COMSAT Laboratories

Volume II

Final Report

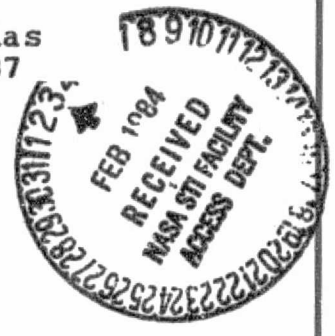

PHASED-ARRAY-FED ANTENNA CONFIGURATION STUDY

Submitted to

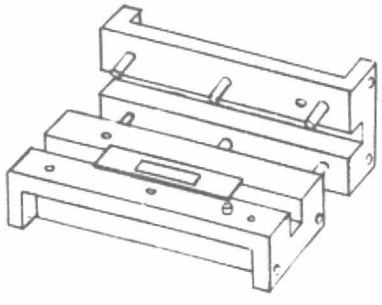

NASA Lewis Research Center
21000 Brookpark Road
Cleveland, Ohio 44135

Under Contract NAS3-23250

October 1983

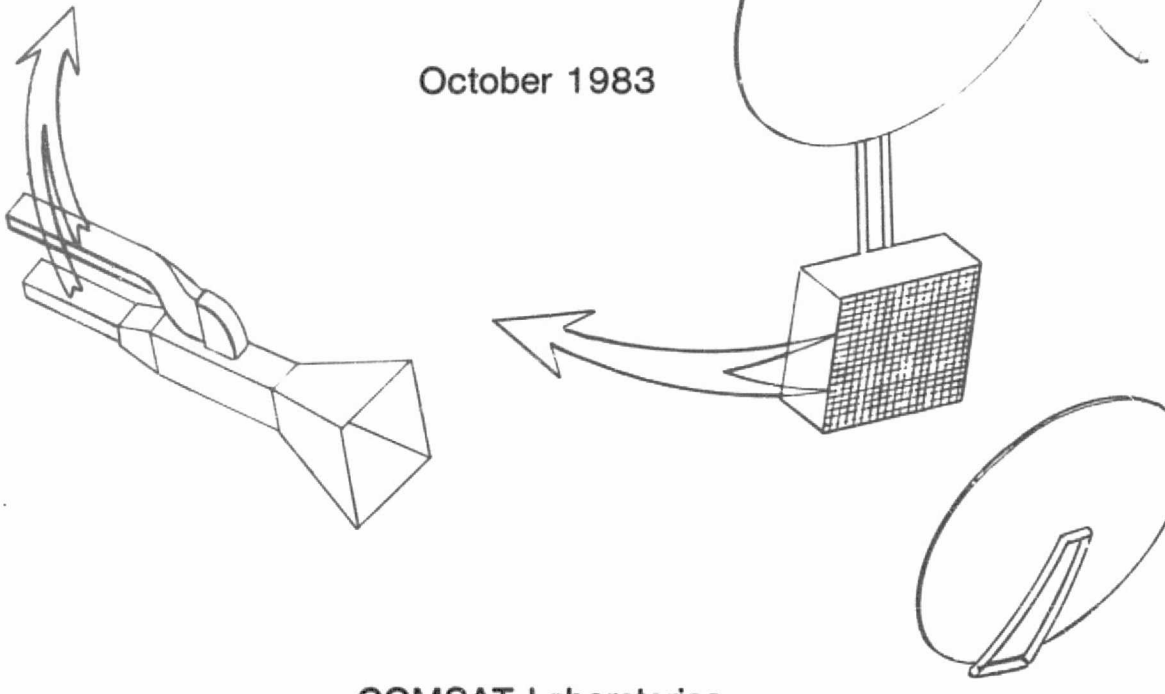

COMSAT Laboratories
Clarksburg, Maryland 20871

1. Report No.	2. Government Accession No.	3. Recipient's Catalog No.
CR168232		

4. Title and Subtitle	5. Report Date
Phased-Array-Fed Antenna Configuration Study Volume II - Final Report	October 1983 6. Performing Organization Code

7. Author(s)	8. Performing Organization Report No.
R. M. Sorbello, A. I. Zaghloul, B. S. Lee, S. Siddiqi, B. D. Geller	10. Work Unit No.

9. Performing Organization Name and Address	11. Contract or Grant No.
Communications Satellite Corporation COMSAT Laboratories Clarksburg, Maryland	NAS3-23250

12. Sponsoring Agency Name and Address	13. Type of Report and Period Covered
National Aeronautics & Space Administration Washington, DC 20546	Contract Report 14. Sponsoring Agency Code

15. Supplementary Notes
NASA Lewis Research Center
Technical Manager, Jerry Smetana, M. S. 54-5
Space Communications Division
Cleveland, OH 44135

16. Abstract

Increased capacity in future satellite systems can be achieved through antenna systems which provide multiplicity of frequency reuses at K_a band. This study addresses a number of antenna configurations which can provide multiple fixed spot beams and multiple independent spot scanning beams at 20 GHz. Each design incorporates a phased array with distributed MMIC amplifiers and phaseshifters feeding a two-reflector optical system. The tradeoffs required for the design of these systems and the corresponding performances are presented. Five final designs are studied in detail. In so doing, a new type of MMIC/waveguide transition is described, and measured results of a breadboard model are presented. Other hardware components developed in conjunction with this study are described. This includes a square orthomode transducer (OMT), a subarray fed with a beamforming network to measure scanning performance, and another subarray used to study mutual coupling considerations. Discussions of the advantages and disadvantages of the final design are included.

17. Key Words (Suggested by Author(s))	18. Distribution Statement
Antenna, Satellite Communications-Dual Reflector, Array Feed, MMIC Active Array	Unclassified - Unlimited

19. Security Classif. (of this report)	20. Security Classif. (of this page)	21. No. of Pages	22. Price*
Unclassified	Unclassified	486	

* For sale by the National Technical Information Service, Springfield, Virginia 22161

PHASED-ARRAY-FED ANTENNA CONFIGURATION STUDY

VOLUME II
FINAL REPORT

by

R. M. Sorbello
A. I. Zaghloul
B. S. Lee
S. Siddiqi
B. D. Geller

Submitted to

NASA Lewis Research Center
21000 Brookpark Road
Cleveland, Ohio 44135

Under Contract NAS3-23250

October 1983

COMSAT Laboratories
Clarksburg, Maryland 20871

ACKNOWLEDGMENTS

The authors wish to express their sincere appreciation to D. F. DiFonzo for his guidance and involvement in the many technical discussions during this study. Thanks are also due to W. Getsinger for his analysis of finline structures, C. Rappaport for his study of the quadrufocal lens, and J. Reisenweber, Jr., for his design of the thermal control system. The efforts of the COMSAT Laboratories' Model Shop, MIC Fabrication Group, and the Technical Publications staff are greatly appreciated.

Finally, the authors would like to acknowledge the efforts of J. Smetana of NASA - Lewis Research Center, with whom they had many helpful discussions throughout the program.

Table of Contents

Table of Contents (Cont'd)

Table of Contents (Cont'd)

List of Illustrations

List of Illustrations (Cont'd)

List of Illustrations (Cont'd)

List of Illustrations (Cont'd)

List of Illustrations (Cont'd)

List of Illustrations (Cont'd)

List of Illustrations (Cont'd)

List of Illustrations (Cont'd)

List of Illustrations (Cont'd)

List of Illustrations (Cont'd)

List of Illustrations (Cont'd)

List of Illustrations (Cont'd)

List of Illustrations (Cont'd)

List of Illustrations (Cont'd)

List of Illustrations (Cont'd)

List of Illustrations (Cont'd)

List of Illustrations (Cont'd)

List of Illustrations (Cont'd)

List of Illustrations (Cont'd)

List of Illustrations (Cont'd)

List of Illustrations (Cont'd)

List of Illustrations (Cont'd)

List of Illustrations (Cont'd)

List of Illustrations (Cont'd)

List of Tables

List of Tables (Cont'd)

1. SUMMARY

This report presents a comprehensive study on scanning and multibeam antenna systems that operate at 20 GHz and utilize monolithic microwave integrated circuit (MMIC) modules to provide both RF power and dynamic phase control. The feasibility of a number of array-fed dual-reflector systems which are capable of achieving six simultaneous independent scanning beams or 18 fixed spot beams is assessed. Some configurations utilize a true phased array to illuminate a pair of confocal parabolic reflectors, while other designs have an array in the focal region of a Cassegrain optical system.

Section 3 postulates a number of scanning beam and multibeam antenna configurations based on the e.i.r.p. and coverage requirements given in the Statement of Work (SOW) and the capabilities of the MMIC modules. An extensive parametric study was performed for each configuration to determine the feasibility of the proposed designs. An important parameter that was determined for each configuration was the DC-to-RF efficiency. Systems which proved to be efficient or competitive with conventional focal-region-fed systems were selected as likely candidates for further investigation. As a result of the parametric study, four configurations (two multiple scanning spot beam and two multiple fixed spot beam) were selected for in-depth analysis. A phased array feeding a pair of confocal parabolas was selected for both a multiple scanning spot beam and multiple fixed spot beam configuration. A focal-region-fed Cassegrain system was selected as the second multiple fixed spot beam system, and a lens-fed confocal parabola was the other multiple scanning spot beam selection.

Section 4 analyzes each of the four selected designs to determine its ultimate performance. In each instance, a specific reflector geometry, feed element, and array or lens design were

developed. Secondary radiation patterns were computed to determine if the required e.i.r.p. levels, sidelobe isolation, and cross isolation could be achieved. These computations verified that both the multiple scanning spot beam and multiple fixed spot beam designs can potentially achieve all the requirements of the SOW. The configurations discussed in this study were limited to a maximum reflector main aperture size of 2.74 m (9 ft). This restricted the system resolution, resulting in interbeam isolations slightly lower than required. By using a larger main aperture size of 3.5 m (11.7 ft), all the SOW requirements can be achieved with the designs discussed in this report.

Section 5 addresses designs for the specific components which comprise the beam-forming networks (BFNs) and the feed array. In addition to "paper" designs, COMSAT also breadboarded and tested each of the key elements in the lens and phased array design. Of note was the development of a waveguide-to-MMIC-to-waveguide transition. This transition is essential for transforming energy in the MMIC to either waveguide or to a radiating horn element. An analysis of the finline structure used in the transition design is also included. Lastly, a linear phased array was built and tested to evaluate mutual coupling effects, grating lobe phenomena, and scan loss performance. The measurements made were in good agreement with calculated predictions.

As a result of this study, COMSAT has demonstrated through both analysis and measured performance the feasibility of the configurations studied. Given the MMIC performances stated in the SOW, phased-array-fed and focal-region-fed dual reflector systems that utilize MMIC modules can be implemented at 20 GHz.

2. INTRODUCTION

To accommodate the continued rapid growth of communications traffic (voice, data, and video), satellites are being required to provide increased capacity. One way of achieving this is to operate at higher frequencies, such as 20 GHz, where large bandwidths of 2.5 GHz provide five times the capacity available at C-band and K_u-band.

Even greater potential for increased capacity is obtainable through advances in frequency reuse antenna technology. Antennas that can provide multiple fixed or scanning beams at 20 GHz and have the potential to provide 6- to 18-times frequency reuse have previously been investigated for NASA. New antenna concepts that can provide a similar number of frequency reuses are addressed in this study. Development of these antennas could provide the capacity required for future communications satellite systems.

NASA-sponsored research and development efforts have investigated the technology required for 20-GHz antenna systems to provide a large number of frequency reuses. The proof of concept (POC) antenna systems developed by FACC [2-1] and TRW [2-2] have examined dual-reflector antenna systems that can provide multiple scanning or multiple fixed spot beams. Both POC antennas are focal-region-fed designs, in which far-field beams are generated by clusters of feeds that comprise part of the total feed array. Scanning in these systems is accomplished by movement of the amplitude distribution in the focal region. The radiated power for each beam is generated by a single traveling wave tube (TWT), which is sized to compensate for any output loss caused by multiplexers and BFNs.

With the advent of MMIC amplifiers and phase shifters, new satellite architectures which incorporate both antenna and transponder technologies are possible. The purpose of this study was to investigate such architectures by considering antenna systems that use distributed amplification and phase control. These antennas were also required to provide a number of scanning and fixed beams, similar to the FACC and TRW POC antenna systems. The major difference in this study is the emphasis on using a true phased array to feed a dual-reflector system.

In this concept, all elements in the array (not just a cluster) are used to generate the far-field beams. Scanning is accomplished by varying the phase taper across the whole array and not by movement of the amplitude distribution in the focal region.

The miniaturization of amplifiers and phase shifters allows these devices to be placed directly behind each radiating element, thus minimizing output loss and offering potential weight and volume savings over the more conventional approaches investigated by FACC and TRW.

This marriage of antenna and transponder technology enables a true systems approach to be employed in the design of these antennas. The antenna concepts addressed in this study have the potential to provide more rapid scanning and a higher e.i.r.p. level than that achievable with the POC concepts of FACC and TRW. With future developments and improvements in MMIC devices, phased-array-fed antenna systems will be a reality at 20 GHz and will be a key contributor to increased satellite capacity.

3. SYSTEM CONFIGURATION STUDY

3.1 SCANNING AND FIXED SPOT BEAM COVERAGE REQUIREMENTS

The coverage requirements for multiple scanning spot beam and multiple fixed spot beam operations dictate the performance prerequisites of the associated antenna systems. The angular field of view (FOV) for the coverage area determines the maximum scan requirements of the antenna system, while the spacing between frequency reuse beams is the driver for the required antenna aperture size.

Figure 3-1 shows computer-generated maps of the contiguous United States (CONUS) in angular coordinates, as seen from geosynchronous altitude at the west longitudes of 90°, 100°, and 105°. The "+" symbols indicate the location of the cities for fixed spot beam coverage as listed in Table 2-2 of Exhibit A of the SOW. Figure 3-2 gives an equivalent antenna coverage for all longitudes, obtained by overlaying individual maps and applying satellite pitch bias of up to $\pm 0.6°$ to minimize the apparent spread of the earth locations across the longitude range. The composite map is representative, but is not necessarily optimized for any single location, although it reflects the SOW's preferred order of the spot beam cities. The FOV for CONUS for this longitude range is $\pm 3.5°$ in azimuth and $\pm 1.5°$ in elevation, and the apparent angular extent of the earth locations varies from small values (e.g., $<0.15°$ for New York and Washington, D.C.) to slightly greater than 0.3° (e.g., Dallas and Houston).

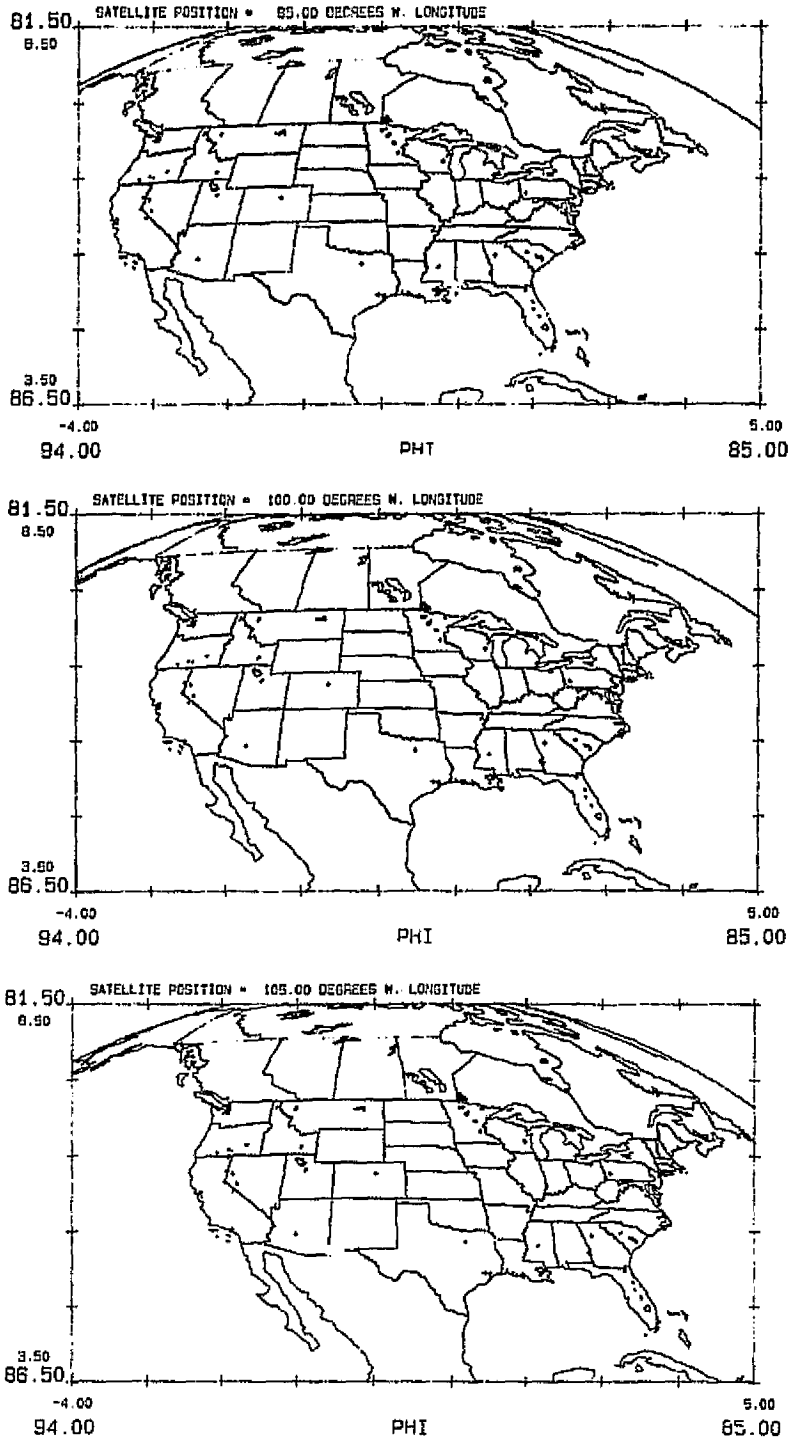

Figure 3-1. CONUS Angular Coordinates as Seen From Geosynchronous Altitude

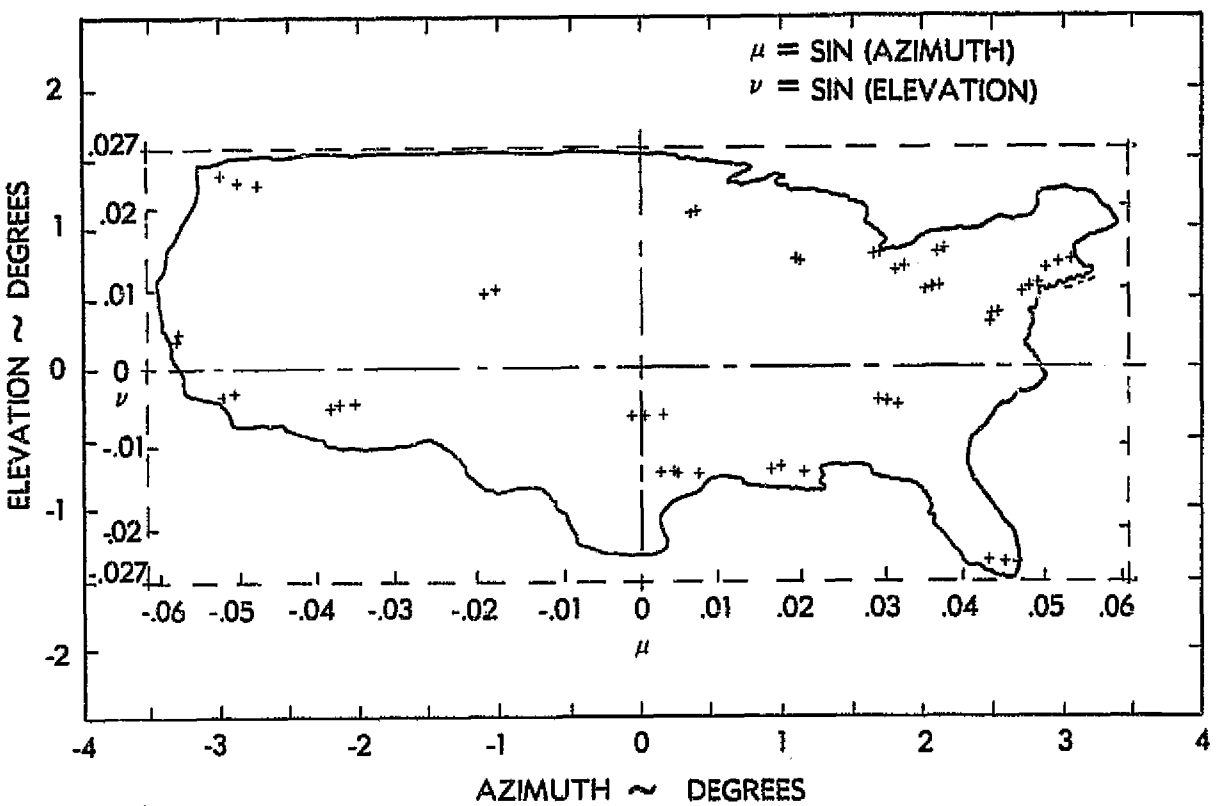

Figure 3-2. Composite Coverage Map of CONUS

Figure 3-3 depicts the selected coverage concepts for the scanning beam and fixed beam systems. In Figure 3-3a, CONUS is divided into six vertical sectors corresponding to the six independent scanning beams required for six-fold frequency use. Each adjacent sector is orthogonally polarized to ensure isolation between co-polarized beams. The 304 beam locations shown in this figure represent the coverage from a scanning beam antenna with a 3.8 m (12.5-ft) aperture which generates a 0.3° beam. For the 2.7 m (9-ft) aperture considered in Subsection 4.2, fewer beams (≅200) will be required over the coverage area, but the segmenting of the coverage is the same as in Figure 3-3.

The 3° x 7° FOV has been used throughout this study to determine the scan performance of the representative antenna designs. For body-stabilized spacecraft, reflectors are positioned on the east and west sides of the bus. This means that east/west scanning in the coverage region will require scanning in the elevation plane of the reflector system of $\pm 3.5°$. Since, in an offset reflector system, elevation plane scanning degrades more severely than azimuth plane scanning, a system with a larger effective focal length would be required for a body-stabilized spacecraft than for spin-stabilized designs which require only $\pm 1.5°$ in elevation scanning. All the configurations chosen are based on the body-stabilized satellite and are designed to produce minimum elevation scan loss.

Figure 3-3b depicts the coverage configuration for the 18-city fixed beam case. Each beam must be isolated from the others, either spatially through sidelobe cancellation or by polarization. Since the interzone spacing between two spatially isolated beams is related to the resolution of the reflector system [3-1],[3-2], the smallest angular spacing required will determine the reflector's main aperture size. This relationship can be expressed as

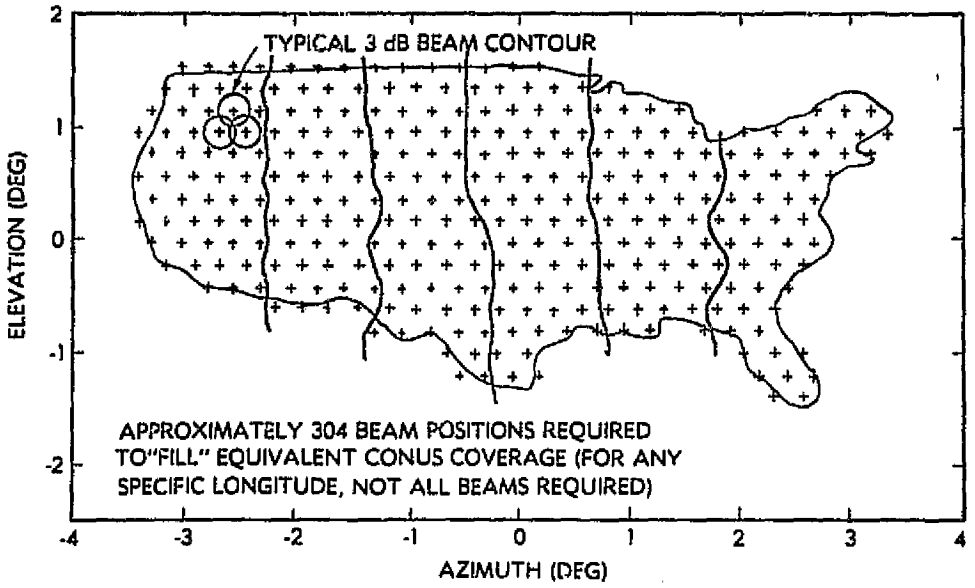

(a) Scanning Beam Coverage Concept

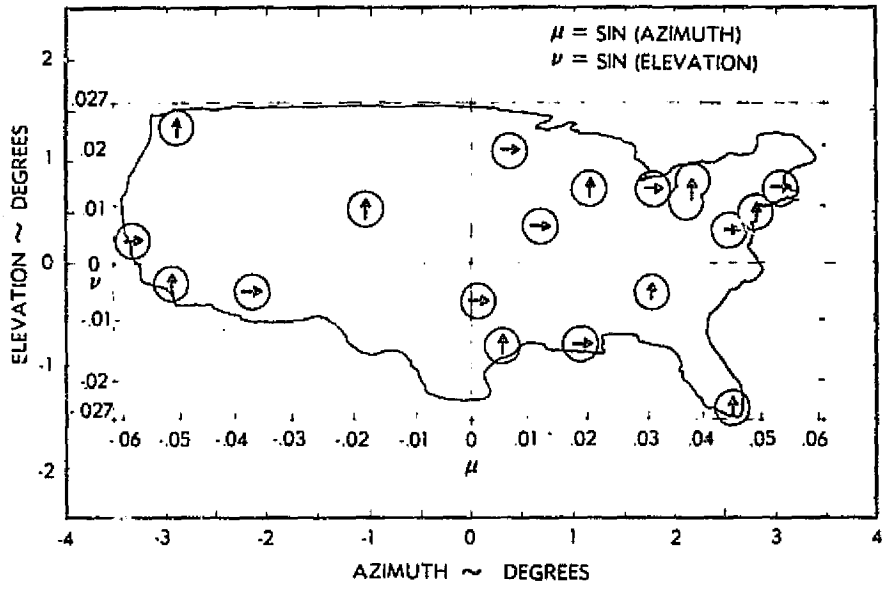

(b) 18-City Fixed Beam Coverage Concept

Figure 3-3. Multiple Scanning and Multiple Fixed Beam Coverages

$$\sigma = \frac{100\lambda}{D} \qquad (3\text{-}1)$$

where σ is the interzone angular spacing in degrees, and D is the required reflector diameter [3-1]. This expression has been derived empirically for a 27-dB interzone isolation and verified on various INTELSAT programs. The Boston-to-Washington spacing is the closest and will be the driver for the main reflector size. At 105°W longitude this spacing minimizes to 0.42°, which implies from the above expression that a reflector size of 3.58 m (11.75 ft) will be needed. For the configurations studied in this report, NASA requested that a main reflector diameter of D = 2.74 m (9 ft) be assumed, because the 2.74-m reflector was available to NASA from a previous contract. This means that a minimum interzone spacing of 0.58° would be necessary to achieve sufficient interzone isolation with this optical system. Subsection 4.6 will elaborate on the coverages achievable with the 2.74-m reflector system and will discuss a design capable of obtaining 30-dB isolation between Boston and Washington.

3.2 PHASED-ARRAY VS FOCAL-REGION-FED SYSTEMS

With the availability of MMIC modules, new satellite system architectures based on an array-fed reflector system with distributed RF power can be attractive alternatives to the conventional focal-region-fed antenna systems, which are employed on most existing satellites. Figure 3-4 depicts two dual-reflector systems, each capable of forming both fixed and scanning beams, but based on different principles.

The phased array system utilizes all the elements in the array to form an incident wave on the subreflector surface.

(a) Phased-Array-Fed System

(b) Focal-Region-Fed System

Figure 3-4. Phased-Array-Fed and Focal-Region-Fed Dual-Reflector Systems

The subreflector exists in the near field of the array, and the optics are designed to transform the approximate plane wave of the array into a magnified version. This is accomplished by using a pair of confocal parabolas, as shown in Figure 3-4 and further discussed in Subsection 4.2. A scanned beam is formed by adjusting the phase shifter setting on each element to vary the phase taper of the incident plane wave. Large e.i.r.p.'s can be achieved with this system via distributed amplifiers. For an amplifier with fixed output, achievable RF powers can be obtained by increasing the number of elements in the array. Since the amplifiers are located close to the radiating elements, complex and lossy feed networks can be used for the array without severely impacting the overall efficiency of the system.

The focal-region-fed system typically employs an optical system that transforms a spherical wave generated by the feed array into a plane wave in the far field. Scanning beams or multibeams are formed by using different portions of the feed cluster in the focal region. Movement of the beams in the far field is accomplished by displacement of the amplitude distribution among a cluster of feed elements. Since only a relatively small number of elements (1, 7, or 19) are used to form each beam, large amounts of RF power cannot be achieved by distributed amplification. Typically, a high-powered TWT is placed before the BFN. Since the BFN can be quite complex (depending on the coverage requirement), the TWT must be of appropriate power to account for the BFN losses and any additional loss (from multiplexers, circulators, switches, etc.) between the output of the tube and the BFN.

With the advent of monolithic amplifier and phase shifter modules, it must be determined under what conditions phased-array-fed systems with distributed amplification are competitive with the conventional focal-region-fed designs. One

parameter that can be used for this comparison is the total DC-to-RF efficiency of each approach. Since the required DC power is an important satellite design parameter, any system that minimizes the total DC power required is extremely attractive. Such a design will minimize the total solar panel area required, which is directly translated into mass savings on the satellite.

To determine the viability of the phased array approach with distributed amplifiers vs the conventional TWT configuration, a system comparison was performed based on the parameter of DC-to-RF efficiency. This comparison was made for the scanning beam case; however, any results obtained are directly applicable to multiple beam configurations.

Table 3-1 summarizes the antenna system requirements for the scanning beam design. The FOV is dictated by the required orbital locations, as described in Subsection 3.1. For the desired range of antenna diameters (2.74-4.27 m or 9-14 ft), achievable edge of coverage (EOC) gains of 50-54 dBi are possible. These are based on an antenna efficiency of 60 percent, which is typical for multibeam applications, and an EOC scan loss of 2.5 dB. This scan loss number will be justified in Subsection 3.5. Depending on the main reflector diameter, between 180 and 450 beam locations will be needed over the coverage area. At any instant, only six beams will exist. For comparison, a baseline 3.81-m (12.5-ft) reflector capable of achieving 53-dBi EOC gain was chosen.

Table 3-2 summarizes the system power requirements for the baseline design (chosen for comparison only). In the scanning beam configurations, the required e.i.r.p. is in the 67-75 dBW range. This necessitates between 25 and 158 W of RF power for each beam, with a total requirement for the six beams of 150-950 W.

Table 3-1. Antenna System Requirements

Parameter	Requirement	Baseline
Field of View	±3.5° E-W, ±1.5° N-S	Same
Main Aperture	2.743-4.267 m	3.81 m
Frequency Range	17.7-20.2 GHz	Same
Bandwidth	500 MHz	Same
Component Bandwidth (3 dB)	0.4°-0.25°	0.27°
Total No. of Beams (6 at any one time)	180-450	304
On-Axis Peak Gain (N = 0.6)	52.5-56.5 dBi	55.5 dBi
Minimum Gain FOV (2.5-dB scan loss)	50-54 dBi	53 dBi

Table 3-2. System Power Considerations

Parameter	Requirement
Antenna Gain (Worst Case)	53 dBi (baseline)
e.i.r.p.	67-75 dBW
Radiated Power/Beam	25-158 W/beam
Total Radiated Power	150-950 W

Given the system antenna and power requirements, Figures 3-5 and 3-6 compare the focal-region-fed vs phased-array-fed approaches. In the conventional approach, a TWT with 35-percent efficiency is assumed. It is also assumed that the total output loss from the TWT to the radiating elements is 4 dB. This number is chosen based on a 3-dB predicted loss for the BFN and a 1-dB

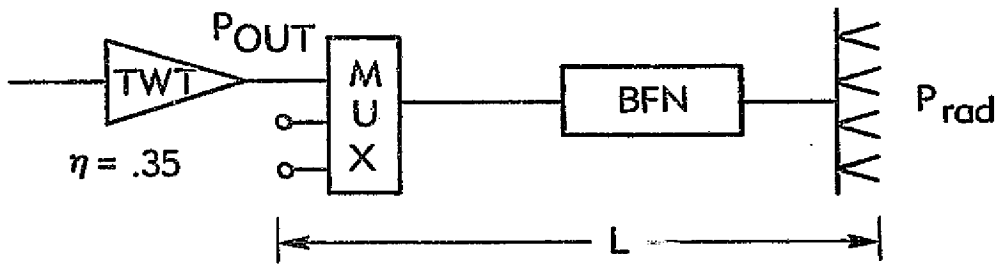

e.i.r.p. (dBW)	Gain (dBi)	P_{rad}/Beam (W)	L* (dB)	η	P_{out}/Beam (W)	P_{DC}/Beam (W)	Total Efficiency (%)
67	53	25	4	0.35	63	180	13.9
71	53	80	4	0.35	200	570	13.9
75	53	158	4	0.35	400	1,140	13.9

*L Includes all output network, BFN, and antenna losses.
Total percent efficiency depends on η and L.

Figure 3-5. Efficiency of Conventional (Focal-Region-Fed) Approach

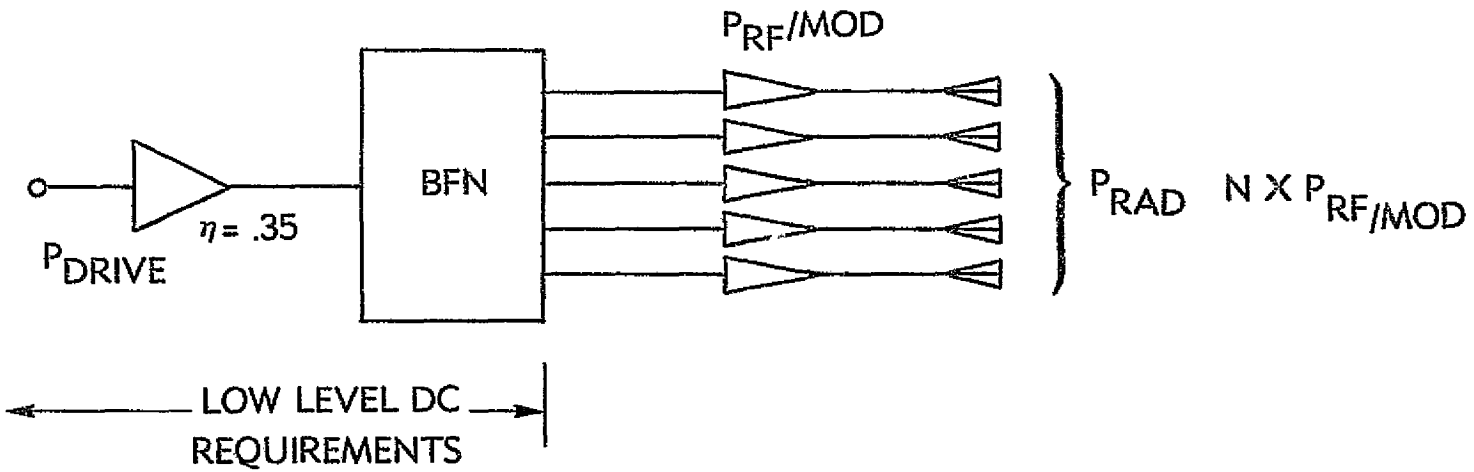

e.i.r.p. (dBW)	Gain (dBi)	P_{rad}/Beam (W)	P_{RF}/MOD (W)	Modulation Efficiency (%)	No. of Elements*	P_{DC}/MOD (W)	P_{DC}/Beam** (W)	Total Efficiency (%)
67	53	25	0.5	15	52	3.3	172	14.2
71	53	63	0.5	15	132	3.3	439	14.2
75	53	158	0.5	15	330	3.3	1,100	14.2

* Assumes 0.2-dB MMIC transition loss.
**Includes RF drive to BFN (driver efficiency ±35 percent).

Figure 3-6. Efficiency of Distributed Amplifier (Phased-Array-Fed) Approach

output multiplexer loss. The BFN loss is based on values predicted by FACC and TRW for the 20/30 GHz POC antenna. Both loss estimates are considered to be conservative, and, depending on the complexity of the system and the number of beams required, total output losses in excess of 4 dB are highly probable. Based on these assumptions, the RF and DC power required per beam ranges between 63-400 W and 180-1,140 W, respectively, for e.i.r.p.'s of 67-75 dBW. The resulting RF-to-DC efficiency for all e.i.r.p. levels is 13.9 percent. As a result of this exercise, it was readily apparent that RF-to-DC efficiency is determined totally by the tube efficiency and the total output loss, L.

Figure 3-6 illustrates a distributed amplifier approach in which similar e.i.r.p. levels and antenna gains are desired. This configuration assumes the existence of a 0.5-W MMIC amplifier module at 15-percent efficiency. Since the amplifiers are placed directly in front of the radiating elements, minimal dissipation of RF power is incurred. For this comparison, a 0.2-dB insertion loss attributable to the MMIC transition is assumed at the output of each amplifier. It is also assumed that the BFN is fabricated in low-loss waveguide. The expected losses for the BFN range from 1.0 to 3.0 dB, based on the required number of elements for the 67- to 75-dBW cases. The bottom line in Figure 3-6 is the percent of DC-to-RF efficiency, which is approximately 14.2 percent for the three cases studied. This reduction in efficiency from the maximum of 15 percent is attributable to the transition loss and the driver tube. The TWT linear drive power required for each case is approximately 1, 2, and 4 W, respectively; well within the range presently achievable.

Construction of the BFN is an important consideration in determining the viability of the design. A BFN fabricated in stripline was initially investigated because its light weight and minimal volumetric requirements appeared attractive. The obvious

disadvantage of stripline is its higher loss. If the BFN is constructed entirely of stripline with a 10-dB insertion loss, the required TWT driver power would be 35 W for the 75 dBW case, and the total efficiency would decline to approximately 12 percent. Since this would be wasteful of power and would require a 20-GHz TWT power level which exceeds the present state of the art, a stripline BFN is not recommended.

Figures 3-5 and 3-6 show that phased array systems with distributed amplifiers can be competitive with conventional approaches when total DC-to-RF efficiencies are compared. When combined output losses in the conventional systems exceed 4 dB, the total efficiency can be competitive with a distributed amplifier system with 15-percent efficient amplifiers. As amplifier efficiencies improve, the tradeoff will be even more favorable to the phased-array-fed systems.

3.3 IMPACT OF SPECIFIED MMIC MODULES ON ANTENNA DESIGNS

3.3.1 AMPLIFIER MODULE LIMITATIONS

Table 3-3 lists the relevant characteristics of the MMIC modules initially assumed for the antenna configuration studies. These characteristics have an important impact on the design and performance of each of the configurations studied. In addition to the two modules specified in the table, the existence of a third module, a variable gain/variable phase transmit module consisting of a 5-bit phase shifter and a variable 0.5-W amplifier, was assumed at NASA's request.

Table 3-3. Characteristics of the Phase Control and Variable Power Amplifier Modules

Characteristic	Variable Phase Control Module	Variable Power Amplifier Module
Frequency (GHz)	17.7 to 20.2	17.7 to 20.2
Impedance	50Ω (nominal)	50Ω (nominal)
VSWR	Less than 1.3:1	Less than 1.3:1
RF Output Power	200 mW	500 mW 125 mW 50 mW 12.5 mW 0 mW
Gain	16 dB	20 dB (at full power)
Gain Variation	1.0 dB (2.5-GHz band) 0.4 dB (any 500-MHz BW)	1.0 dB (2.5-GHz band) 0.4 dB (any 500-MHz BW)
Power-Added Efficiency	15 percent	15 percent 12 percent 9 percent 6 percent * percent
Phase Shifter	Time-delay type	
Control	5 bit	
Lowest Bit	11.25°	
Tolerance	±3°	
Response Time	10 ns	10 ns

*Maximum dissipation = 50 mW.

One initial consideration was to identify the appropriate location of the amplifier/phase shift module for a viable scanning beam configuration. Figure 3-7 shows two possible amplifier locations. To provide six independent scanning beams, it will be necessary to associate a 6-way power combiner with each element, as shown. This implies that all scanning beams would be co-polarized. A more likely arrangement would only have 3-way combiners at each orthogonally polarized port of the dual-polarized feed elements. Subsection 3.4 will discuss this arrangement in greater detail for specific configurations.

Each of the six power combiner ports connects with a BFN which contains the basic N-way power division to distribute

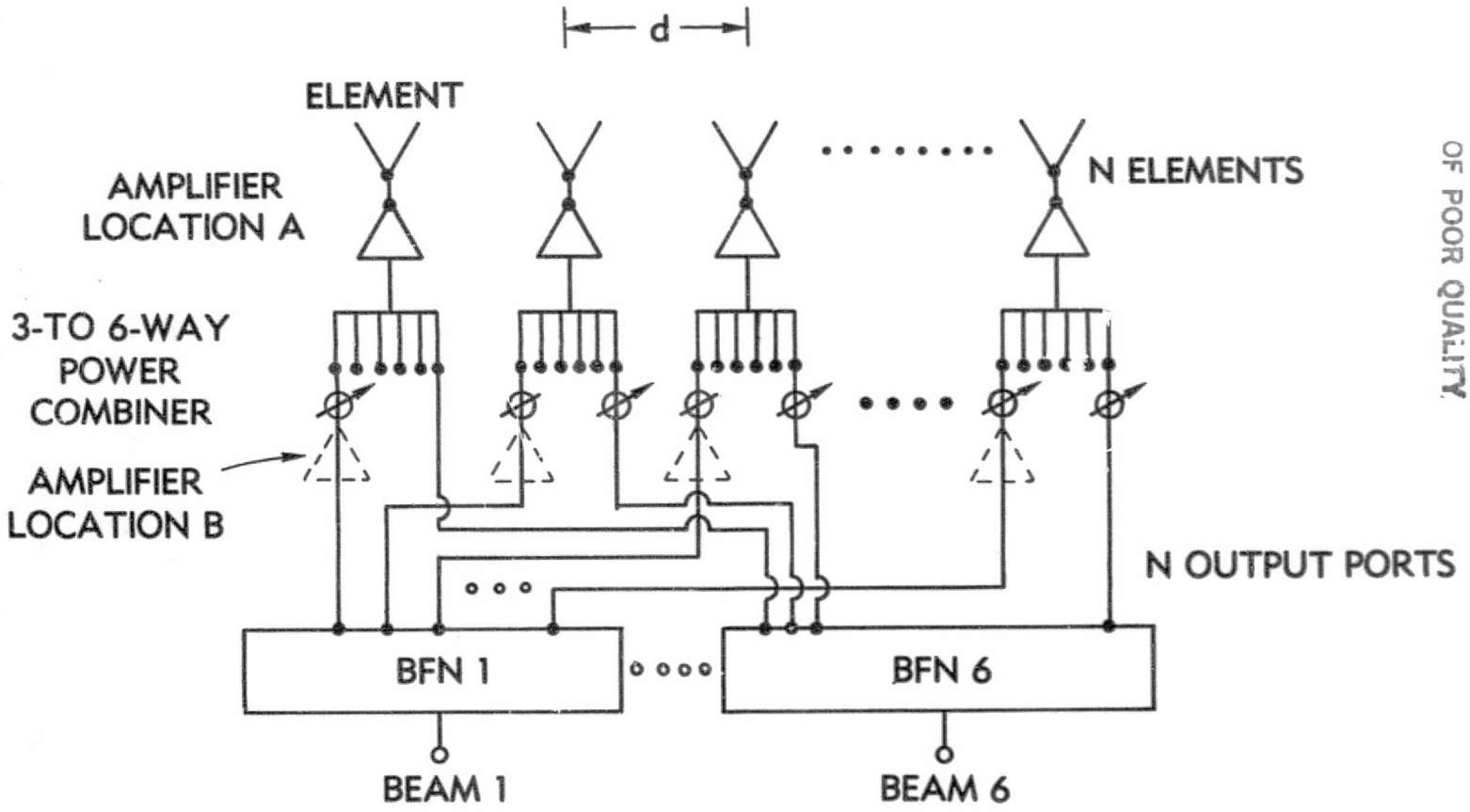

Figure 3-7. Possible Amplifier Locations in a Phased Array BFN

the signal to all elements. For amplifier location A, the active module must provide an average total power, P_o, with each of the six carriers (0.2 W/carrier) coexisting in the amplifier. Since this module is operating as a multicarrier, it must provide linear amplification with an acceptable ratio of carrier-to-intermodulation product power, C/Im.

For amplifier location B, the input to each amplifier is a single 500-MHz signal. If this is a single carrier, the amplifier can operate closer to saturation. However, if these are multiple FDM/TDMA carriers, similar backoff restrictions apply. Because these amplifier outputs must be combined via a 6-way power combiner, five-sixths of the output power will be dissipated in the isolation resistors that must form a part of the combiner design. Therefore, each module must initially produce 1.2 W just to deliver 0.2 W to the radiators. For a system in which cross-polarized beams are used, two-thirds of the output power will be dissipated in a 3-way combiner, which will require each module to produce 0.6 W to deliver 0.2 W.

One of the configurations investigated (discussed in detail in Subsection 3.4) relied on using only the variable phase control module specified in Table 3-3. However, use of this module in a configuration such as that shown in Figure 3-7 presents a dilemma. Since the amplifier and phase shifter sections are an integrated unit, it must be decided which location, A or B, is most appropriate. From a power efficiency viewpoint, the previous discussion has shown that location A is more appropriate. On the other hand, to provide independent scanning control for each beam, the phase shifter must be placed at location B. It was decided early in this study, with NASA's concurrence, that this particular module was not optimum and that, for practical reasons, the phase shift operation and the amplifier should be separated. Further discussions of the configuration studies will assume that the amplifier and phase shifter are separate units,

with the phase shifter having 3 dB of loss and the amplifier having 19 dB of gain to yield 16 dB of module gain overall.

As shown in Subsection 3.2, the performance of the amplifier in terms of efficiency vs output power is the dominant factor in determining the suitability of the active phased array concept. Figure 3-8 shows typical input-output characteristics of a solid-state RF amplifier. An example of the current state of the art for GaAs FET power amplifiers is a 4-GHz, 6.0-W unit that was developed by RCA for INTELSAT and was monitored by COMSAT. The figure depicts the output power and noise-power ratio (NPR), as measured by COMSAT Laboratories. The NPR is representative of the C/Im that would be produced for a large ($\rightarrow\infty$) number of carriers. It is only slightly pessimistic when compared to operation with a large but finite number of carriers. For this amplifier at the 1-dB compression point, the NPR (C/Im) is between 15 and 20 dB, which is in line with the linearity specified for the variable phase shifter (VPS) module and the variable power amplifier (VPA) module.

Also, for this amplifier, the 1-dB compression point represents an input backoff from saturation of 8 dB and a corresponding output backoff of 3.5 dB. This characteristic may be assumed to be typical of FET amplifiers. During this study, it has been assumed that an FDM/TDMA system is being implemented. Based on this assumption, amplifiers placed at either location (A or B) have multicarrier operation and must be operated in the linear region with a maximum of 15-percent efficiency. If, however, a TDMA system consisting of a single broadband 500-MHz carrier were considered, each amplifier at location B could operate at or beyond saturation, resulting in efficiencies approaching 30 percent and an output power level for each module of 0.45 W and 1.12 W for the 0.2-W VPS and 0.5 VPA modules, respectively. As discussed in Subsection 3.2, these levels of efficiency and

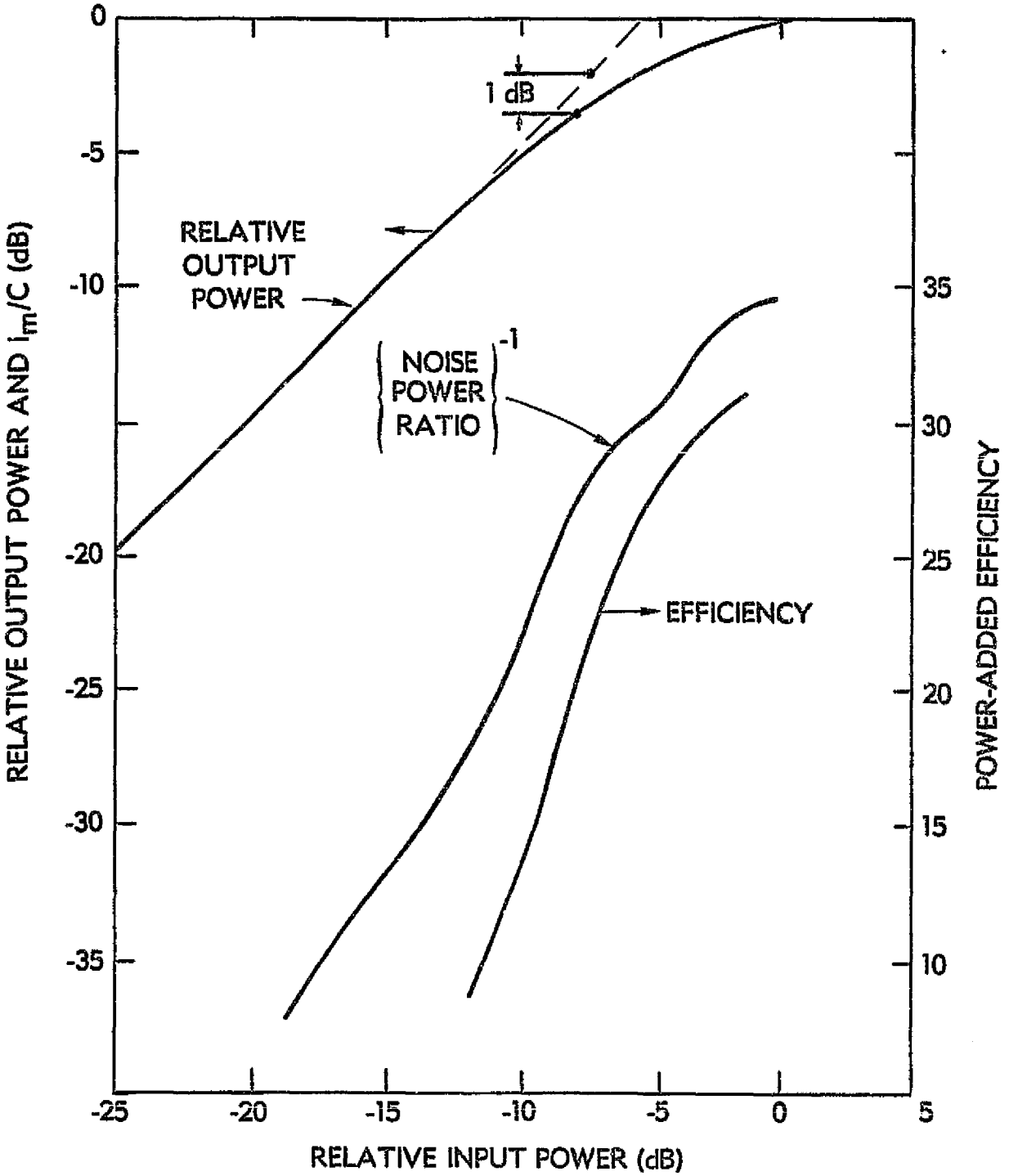

Figure 3-8. FET Output vs Input Response

output powers could have a profound impact on the viability of the distributed amplifier approach. The availability of higher power modules would also result in a decrease in the number of elements required in the array for a specified e.i.r.p. level.

The advantages afforded by this scheme require that the amplifier be placed at location B. For multiple scanning beams, the presence of lossy combiners outweighs the benefits derived from operating the amplifiers at saturation. However, it appears that a two-scanning-beam case with orthogonal polarization could be employed, since the signals are combined via an orthomode transducer (OMT) which results in no combiner loss. A slight benefit in overall performance is even achievable with a four-beam configuration, in which 3 dB of each co-polarized signal are dissipated in the combiners (note that the output backoff was 3.5 dB). This may lead to additional problems associated with heat dissipation which must be traded off against improved performance. For six scanning beams, location A is clearly a more appropriate location for either system approach.

3.3.2 PHASE SHIFTER MODULE LIMITATIONS

The previous subsections have addressed the limitations imposed on the array design by the amplifier modules. Additionally, it can be shown that the discrete 5-bit phase shifting module will impose a limitation on the element size used in the phased array. Two conditions limit element spacing, d, in the phased array: the available phase increment, since it is associated with scanning step requirements; and the grating lobe appearance in the scanning range. The parameters are defined as follows:

f_1, f_2 = lowest and highest frequency of operation

$\theta_3 = \theta_{BW}$ = 3-dB beamwidth in the main reflector far field

M = magnification factor (confocal paraboloid optics)

K = overlapping ratio of the 3-dB beam contours

$\Delta\theta$ = scanning step in the array far field

ϕ_{inc} = smallest available phase increment, including phase shifter errors

θ_s = scanning range in the main reflector far field

The scanning step, $\Delta\theta$, is given as $\Delta\theta = KM\theta_3$; K, defined in Figure 3-9, depends on the array lattice. For a rectangular lattice, K must be less than or equal to 0.707 to ensure that all points lie within the required 3-dB circle. For a triangular lattice, K can have values up to 0.866. As the frequency increases, θ_3 becomes smaller and 3-dB beams overlap less, creating holes between beams where the gain is reduced more than 3 dB from the peak. Therefore, the design must be carried out at the highest frequency in the band. The scanning step must be greater than or equal to the corresponding step achievable through the minimum phase increment. This leads, as shown in Figure 3-10, to $(2\pi d/\lambda) \sin \Delta\theta > \phi_{inc}$, thereby setting a lower limit for the element spacing, d. This expression is valid for small angles of scan from broadside. For the arrays studied in subsequent sections, the maximum scan angle required is ≅12.5°, for which this expression can be shown to be valid. This results in

$$\frac{d}{\lambda} \geq \frac{\phi_{inc}}{2\pi \sin KM\theta_3} \qquad (3\text{-}2)$$

The upper limit of the element spacing is set by the grating lobe criterion. Figure 3-11 shows the grating lobe lattice for rectangular and triangular arrangements. The condition

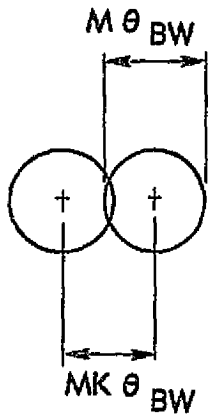

(a) DEFINITION OF OVERLAPPING RATIO K

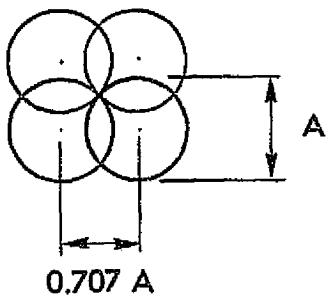

(b) RECTANGULAR LATTICE K = 0.707

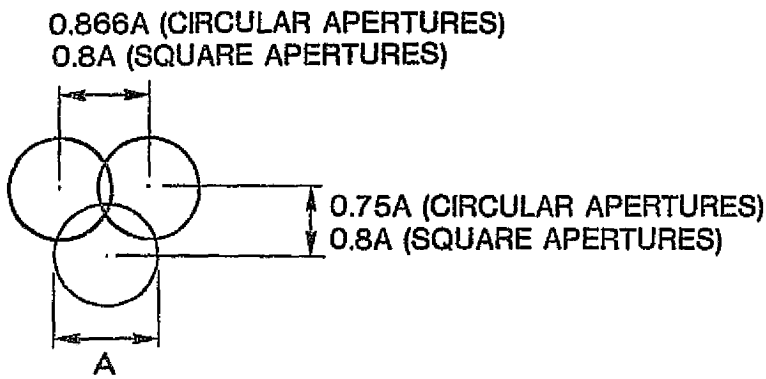

(c) TRIANGULAR LATTICE K=0.75 to 0.866

Figure 3-9. Array Lattice Configurations

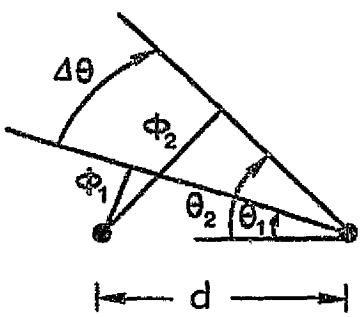

$$\Phi = \frac{2\pi d}{\lambda} \sin(\theta_1)$$

PHASE INCREMENT $\Delta\Phi = \Phi_2 - \Phi_1$

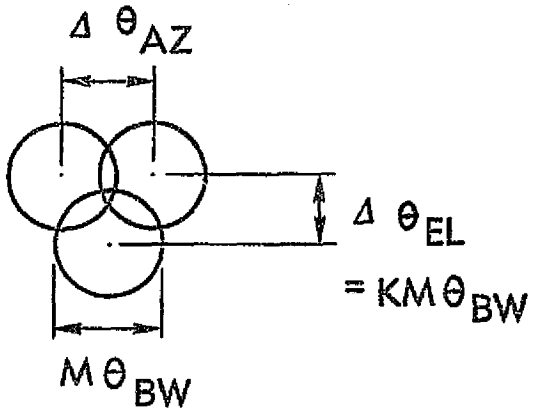

Figure 3-10. Lower Bound on Element Spacing

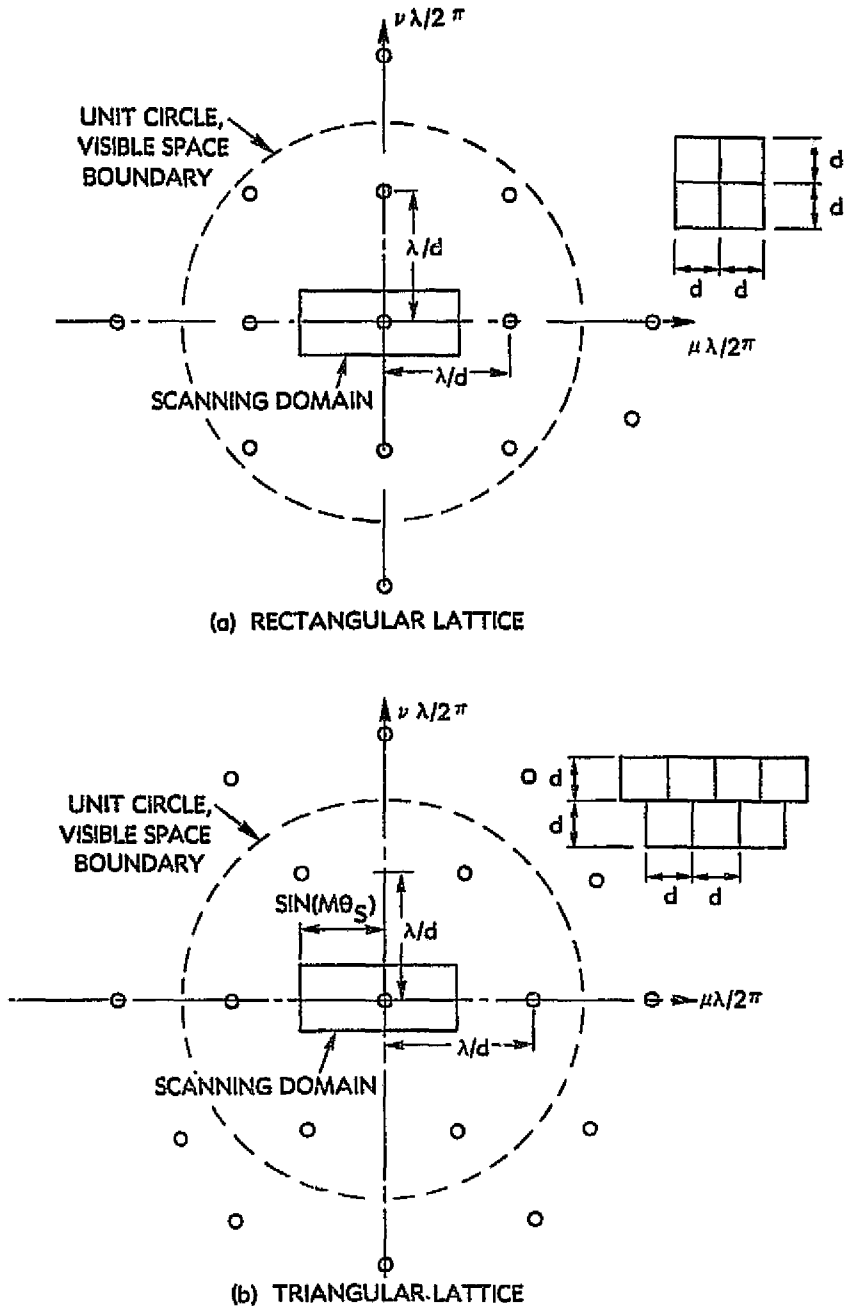

Figure 3-11. Grating Lobe Diagrams for Rectangular and Triangular Lattices

for having the scanning domain free of grating lobes as the main beam scans the CONUS coverage region is $2 \sin (M\theta_s) \leq \lambda/d$, which leads to

$$\frac{d}{\lambda} \leq \frac{1}{2 \sin (M\theta_s)} \tag{3-3}$$

Equations (3-2) and (3-3) give upper and lower bounds on the element spacing, d, as

$$\frac{\phi_{inc}}{2\pi \sin (KM\theta_3)} \leq \frac{d}{\lambda} \leq \frac{1}{2 \sin (M\theta_s)} \tag{3-4}$$

For narrow beams and small scanning angles, the condition for array realizability can be written as

$$\phi_{inc} \leq \frac{180 \sin (K\theta_3)}{\theta_s} \cong \frac{180 \sin (K\theta_3)}{\sin \theta_s} \tag{3-5}$$

Since $K\theta_3$ denotes the scanning step, and $2\theta_s$ is the total scanning range, equation (3-5) leads to the conclusion that, for a realizable system, $\phi_{inc} \leq$ 360/(number of scanning steps in the scanning range).

For the phase shifter module under development by NASA, the smallest phase shift is specified to be 11.25°. Figure 3-12 is a graphical representation of equation (3-4). Parts a and b of the figure are based on an 11.25° increment, a triangular lattice arrangement as shown, and assumed 3-dB beamwidths, θ_3, of 0.3° and 0.4°, respectively. The configurations that have been studied, as addressed in Subsection 4.3, correspond to the $\theta_3 = 0.4°$ case. Figure 3-12 demonstrates the narrow bound imposed on the element size and spacing as a function of the optics magnification. For all the designs subsequently discussed in this report, element sizes within the constraints of equation (3-4) have been used.

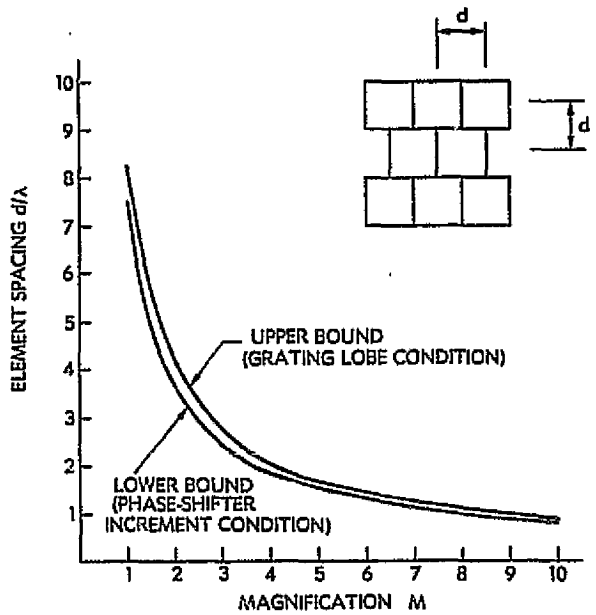

(a) For 0.3° Beamwidth and 5-bit Phase Shifter

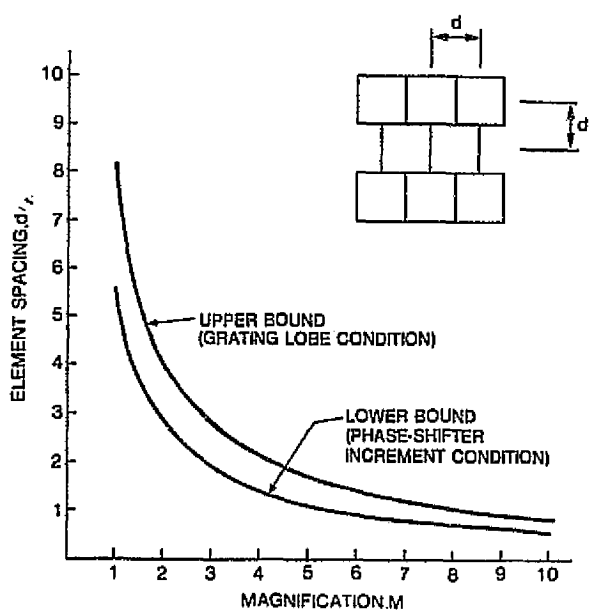

(b) For 0.4° Beamwidth and 5-bit Phase Shifter

Figure 3-12. Upper and Lower Bound on Element Spacing

3.4 INITIAL CONFIGURATIONS STUDIED

Initially, twelve configurations that utilize the monolithic modules described previously were studied to determine the viability of both multiple scanning beam and multiple fixed beam designs. Figure 3-13 depicts seven of the configurations investigated, including four scanning beam designs, two multibeam designs, and a lens configuration. The lens configuration is distinct from the other sets of configurations, since it can accommodate either a scanning beam or fixed multibeam design.

Table 3-4 summarizes the specific electrical requirements for both the scanning beam and fixed beam configurations. The minimum gain required in the SOW is 53 dBi. When the beam is scanned, a loss in gain occurs which must be included in determining the minimum gain. If a reasonable scan loss of 2.5 dB is assumed, then the required non-scan gain would be 55.5 dBi. To achieve this gain, the size of the main reflector is given by

$$D = \frac{\lambda}{\pi}\sqrt{\frac{G}{\eta}} = 4.08 \text{ m } (13.4 \text{ ft}) \qquad (3\text{-}6)$$

Efficiency $\eta = 0.6$ has been assumed. The required power/beam to achieve the maximum e.i.r.p. is 75 - 53.0 = 22.0 dBW = 158.5 W. For the minimum e.i.r.p., the required power/beam is 14 dBW or 25.1 W. For the multiple fixed beam case, RF power ranging from 0.794 to 7.94 W per spot beam is required. The subsequent initial configuration studies are based on these gain and power numbers. The specific designs described in Sections 4 and 5 are based on the gain and e.i.r.p. achievable from a 2.75-m main reflector.

The following list describes the module required for each of the configurations studied. For the multibeam case it was desired that the variability of the phase shifters and amplifiers be used to correct beam pointing.

a. Scanning Beam Configurations

(1) 6 simultaneous scanning beams using the VPS module and consisting of a constant gain amplifier and a 5-bit phase shifter
(2) 6 simultaneous scanning beams using the VPA module and consisting of a variable gain amplifier
(3) 6 simultaneous scanning beams using either a combination of the VPA and VPS modules or a variable gain/variable phase module

b. Fixed Beam Configurations

(1) 10 to 18 fixed beams using the VPS monolithic module with a constant gain amplifier and 5-bit phase shifter
(2) 10 to 18 fixed beams using the VPA monolithic module and consisting of a 5-state variable gain amplifier

c. Additional Configurations

(1) A space-fed lens utilizing the VPS or VPA monolithic modules and capable of forming 6 simultaneous scanning beams or 10 to 18 fixed beams
(2) A directly radiating phased array utilizing the VPS or VPA monolithic modules capable of 6 simultaneous scanning beams or 10 to 18 fixed beams.

MULTIPLE SCANNING BEAM CONFIGURATIONS

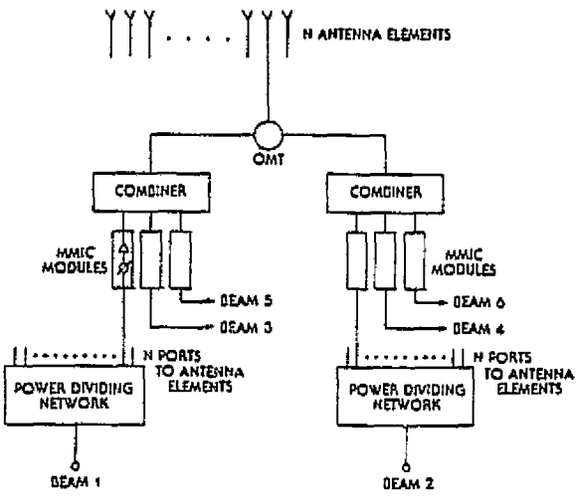

CONFIGURATION A1

-SIX SCANNING BEAMS
-67-75 dBW/BEAM (E.I.R.P.)
-CONSTANT GAIN (.2W MAX OUTPUT) AND 5-BIT VARIABLE PHASE-SHIFTER MMIC

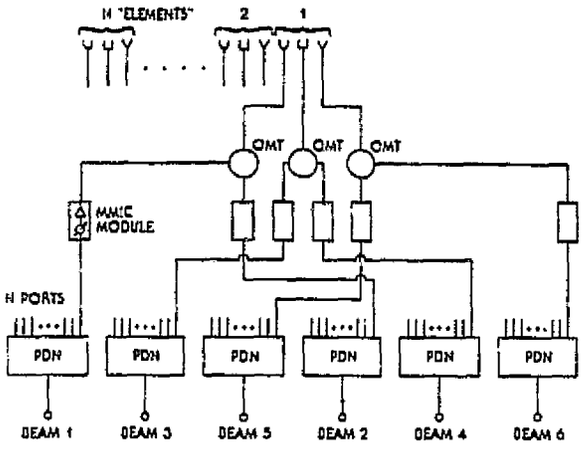

CONFIGURATION A2

-SIX SCANNING BEAMS
-67-75 dBW/BEAM (E.I.R.P.)
-CONSTANT GAIN (.2W MAX OUTPUT) AND 5-BIT PHASE-SHIFTER MMIC

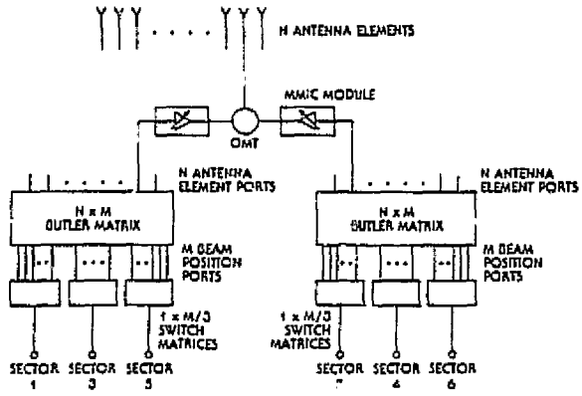

CONFIGURATION B1

-SIX SCANNING BEAMS
-67-75 dBW/BEAM (E.I.R.P.)
-VARIABLE GAIN (3 LEVELS) AMPLIFIER MMIC (.5 W MAX OUTPUT)
-M BEAM POSITIONS ASSUMED (TO COVER CONUS)

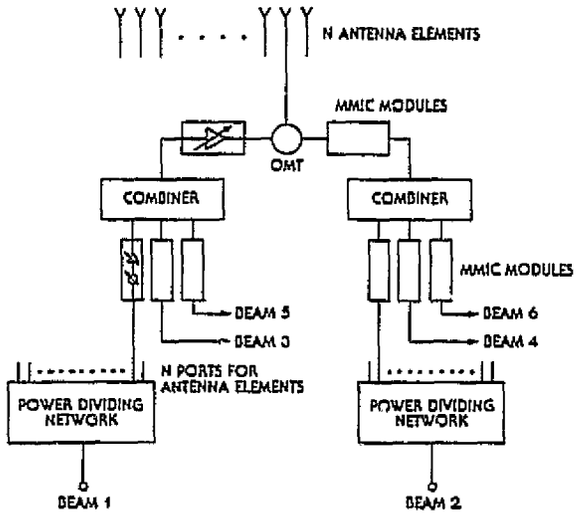

CONFIGURATION C

-SIX SCANNING BEAMS
-67-75 dBW/BEAM (E.I.R.P.)
-VARIABLE GAIN/VARIABLE PHASE MMIC (.5 W MAX OUTPUT. 5 LEVELS/5 BIT) AND VARIABLE GAIN MMIC (.5 W MAX OUTPUT. 5 LEVELS)

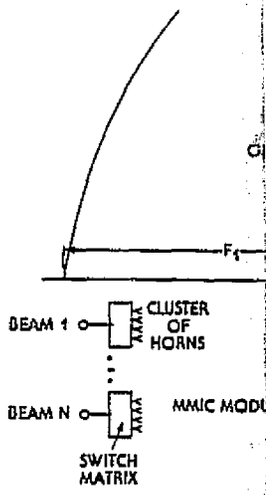

FOLDOUT FRAME

ORIGINAL PAGE IS
OF POOR QUALITY

MULTIPLE FIXED BEAM CONFIGURATIONS

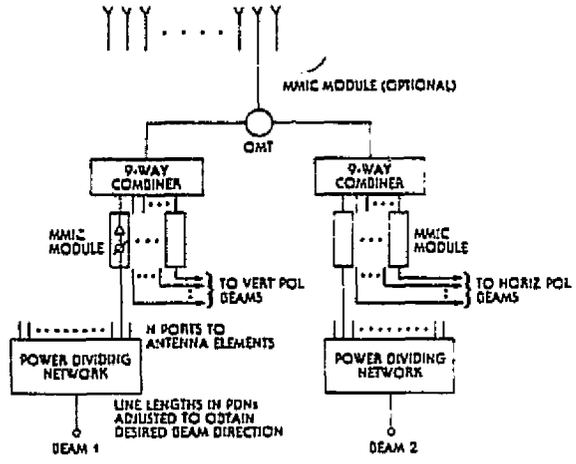

CONFIGURATION D1

- MULTIPLE BEAMS (18)
- 52-62 dBW/BEAM (E.I.R.P.)
- CONSTANT GAIN (.2 % MAX OUTPUT) AND 3-BIT PHASE-SHIFTER (FOR TRIMMING) MMIC

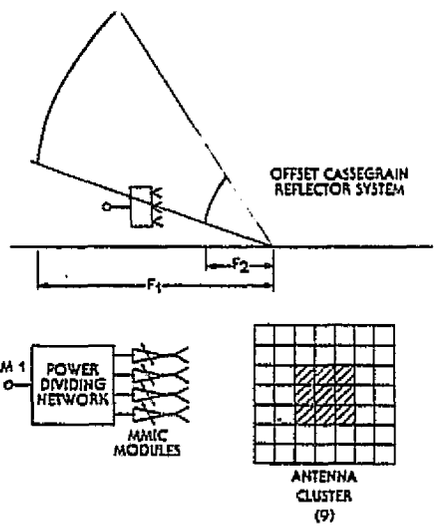

CONFIGURATION E

- MULTIPLE BEAMS (18)
- 52-62 dBW/BEAM (E.I.R.P.)
- VARIABLE GAIN (.5 W MAX OUTPUT, 5 LEVELS) MMIC
- ONE FEED CLUSTER FOR EACH BEAM

LENS CONFIGURATION

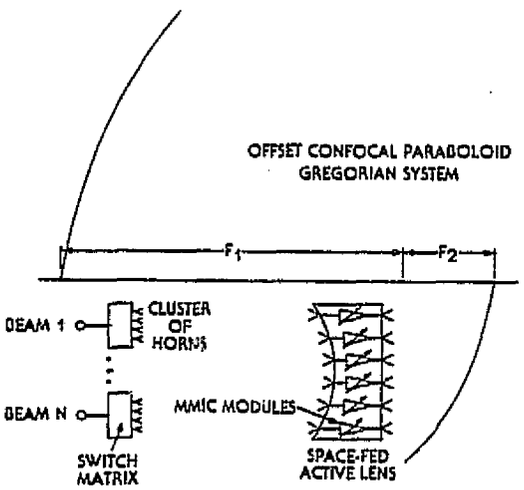

CONFIGURATION F

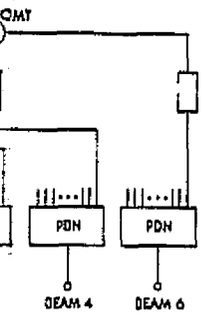

BIT PHASE-SHIFTER MMIC

ENNA ELEMENTS

MODULES

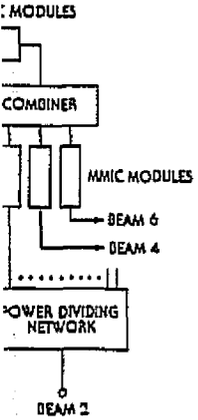

X OUTPUT, 5 LEVELS/5 BIT) LEVELS)

Figure 3-13. Antenna Configurations

2 FOLDOUT FRAME

Table 3-4. Objective Requirements for Multiple Fixed and Multiple Scanning Spot Beam Antennas

Parameter	Beam Configuration	
	Fixed Spot Beam	Scanning Spot Beam
Antenna Size	Shuttle Compatible	Shuttle Compatible
Operation Frequency Range (GHz)		
Down-link	17.7-20.2	17.7-20.2
Up-link	27.5-30.0	27.5-30.0
Number of Beams Operational	10-18	6 Trans
Minimum Gain (dB)		
20 GHz	53	53
30 GHz	56	56
Bandwidth (MHz)		
20 GHz	500	500
30 GHz	500	500
Polarization	Linear	Linear
C/I Performance (DB)*	30	30
Pointing Accuracy (deg)		
E and H Plane	0.02	0.02
Polarization	0.4**	0.4**
Power/Beam (e.i.r.p.) (dBW)	52-62	67-75

*Carrier to interference ratio for each beam relative to all other beams.

**Degrees rotation from reference (i.e., true satellite vertical or horizontal).

3.4.1 MULTIPLE SCANNING BEAM CONFIGURATIONS

3.4.1.1 Configuration A

Configuration A requires six independent scanning beams, each delivering RF power in the range of 25-158 W. MMIC modules capable of providing 0.2 W of power (constant gain) and a 5-bit phase shifter are assumed. These initial studies assumed that the phase shifter and amplifiers were an integral unit (as discussed in Subsection 3.3.1; separate amplifier and phase shift functions are the preferred approach). Three variations of this configuration have been addressed and are compared in Table 3-5 on the basis of the BFN aspects of the system. In this comparison, it is understood that the optics are a confocal paraboloid (Gregorian configuration) with specified magnification, M, and a main reflector aperture sufficient to provide a minimum of 53 dBi of gain over the FOV. The optics will be discussed in detail in Subsection 4.2.1.

3.4.1.1.1 Configuration A1: Full Array With Combiners

Figure 3-14 depicts the candidate feed network proposed for Configuration A1. Six individual power dividing networks (PDNs) are needed for the six scanning beams. Amplitude tapers, which are required to maintain sufficient isolation between sectors, may be generated for each scanning beam by designing the power dividing trees with unequal power dividing elements. There are actually two sets of three PDNs, one set corresponding to the vertically polarized beams and the other to the horizontally polarized beams. Each set of three divider networks is combined to form a set of vertically and horizontally polarized signals at each radiating element.

Table 3-5. Comparison of Configurations A1, A2, and A3

Characteristic	A1 Combining		A2 Interleaving		A3 Side-by-Side	
	Maximum e.i.r.p.	Minimum e.i.r.p.	Maximum e.i.r.p.	Minimum e.i.r.p.	Maximum e.i.r.p.	Minimum e.i.r.p.
Number of Elements	4,000	625	12,000	1,875	12,000	1,875
Size of Elements (M = 3)	1.1λ	2.85λ	0.64λ	1.65λ	0.64λ	1.65λ
Spacing	1.1λ	2.85λ	1.9λ	4.9λ	0.64λ	1.65λ
Number of OMTs	4,000	625	12,000	1,875	12,000	1,875
Number of MMIC Modules	24,000	3,750	24,000	3,750	24,000	3,750
Combiners	8,000	1,250	None	None	None	None
Size of PDN	1 x 4,000	1 x 625	1 x 4,000	1 x 625	1 x 4,000	1 x 625
Heat Wasted in Resistors of Combiners (W)	3,200	500	None	None	None	None

Table 3-5. Comparison of Configurations A1, A2, and A3 (Cont'd)

Characteristic	A1 Combining		A2 Interleaving		A3 Side-by-Side	
	Maximum e.i.r.p.	Minimum e.i.r.p.	Maximum e.i.r.p.	Minimum e.i.r.p.	Maximum e.i.r.p.	Minimum e.i.r.p.
Total Power Generated (W)	4,800	750	4,800	750	4,800	750
Total Power Radiated (W)	1,600	250	4,800	750	4,800	750
Antenna Gain (dBi)	53	53	48	48	48	48
e.i.r.p./Beam (dBW)	77	69	77	69	77	69
Scan Step (K)	2.31	0.866	1.34	0.52	3.86	1.54
Complexity of BFN	Simple	Simple	Complex	Complex	Simple	Simple
Grating Lobes in FOV	No	Yes	No	Yes	No	No

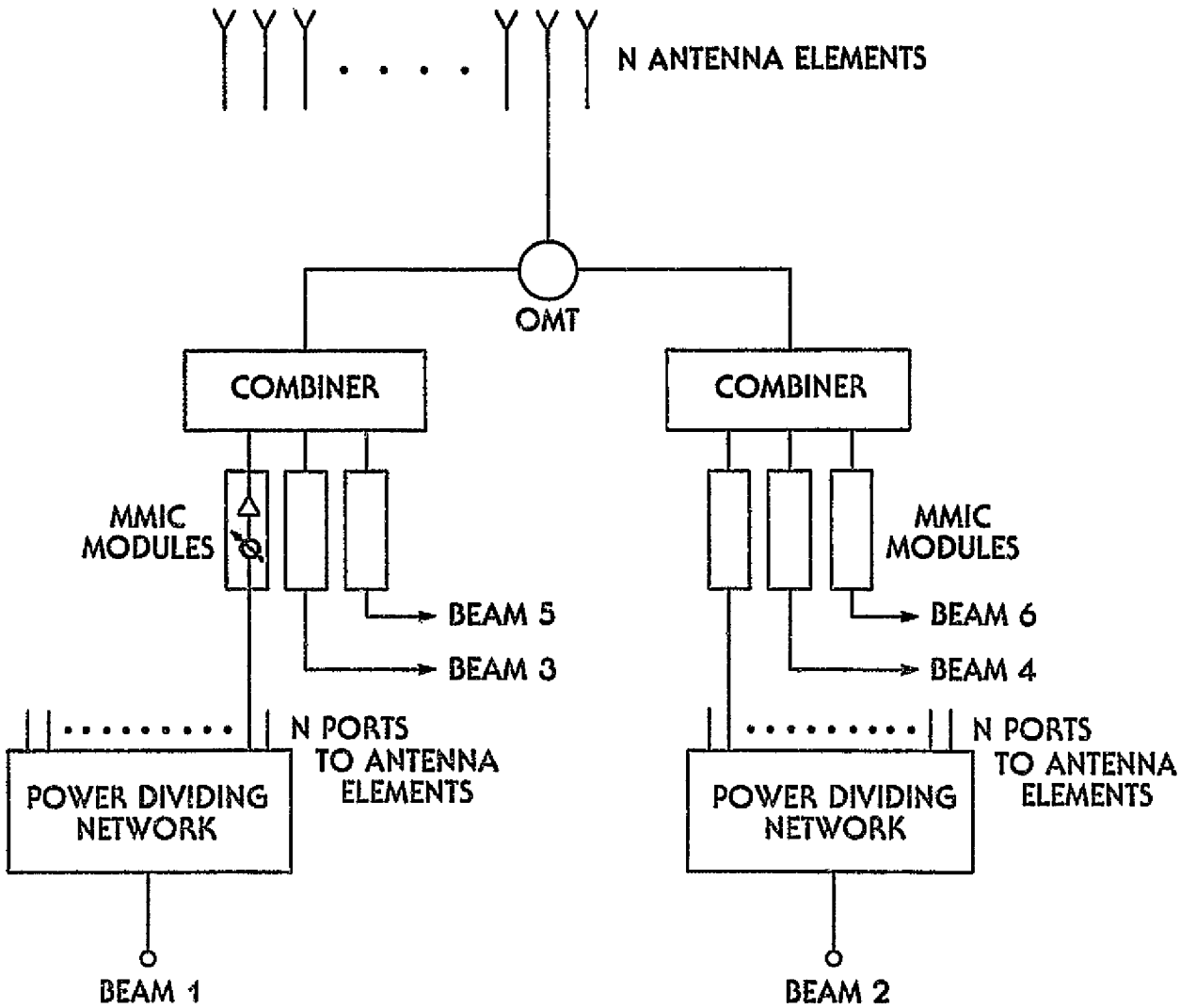

CONFIGURATION A1

- SIX SCANNING BEAMS
- 67-75 dBW/BEAM (E.I.R.P.)
- CONSTANT GAIN (0.2W MAX OUTPUT) AND 5-BIT VARIABLE PHASE-SHIFTER MMIC

Figure 3-14. Configuration A1: Full Array With Combiners

Figure 3-14 also illustrates the interconnection of a single output port of the six PDNs to a single radiating element. The circuitry associated with all other sets of output ports and the associated feed element are identical. A combined monolithic amplifier/phase shifter will be placed at each output port of all six divider networks. By adjusting the phase shifter to the appropriate differential phase settings, a beam may be scanned to its desired location. The three phase shifter/amplifier outputs from sectors 1, 3, and 5 are combined and fed to one port of the OMT located directly behind the radiating element. Similarly, the orthogonal port will contain the three signals combined from the corresponding output ports of sectors 2, 4, and 6.

Since the three sets of signals entering the combiner are necessarily incoherent, approximately 5 dB will be dissipated in the isolation resistors. This represents an extremely inefficient and wasteful approach. One way to overcome this problem is to have separate amplifier and phase shifter modules. The phase shifter precedes the combiners, and amplification occurs after the signals have been combined. This configuration will be discussed further in Section 4.

3.4.1.1.2 Configuration A2: Interleaved Array

In this configuration, the elements are interleaved as shown in Figure 3-15. This avoids the use of a lossy combiner, but makes it necessary to reduce the size of the elements to one-third of their original size. The spacing between elements of the array for one beam is the same as in Configuration A1, which keeps the array factor essentially the same. However, the element factor changes, making the beamwidth broader and the gain smaller.

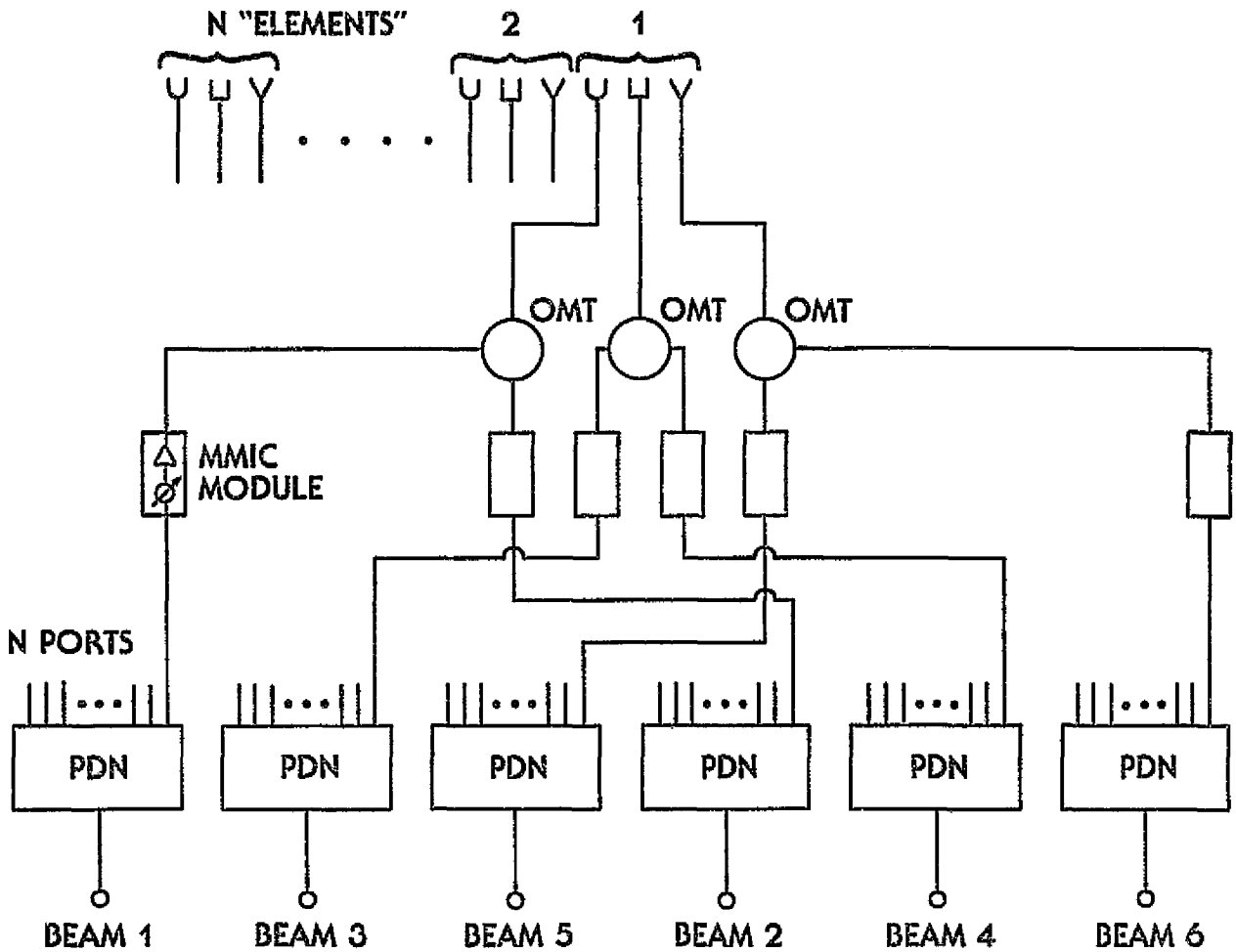

CONFIGURATION A2

-SIX SCANNING BEAMS
-67-75 dBW/BEAM (E.I.R.P.)
-CONSTANT GAIN (.2W MAX OUTPUT) AND 5-BIT PHASE-SHIFTER MMIC

Figure 3-15. Configuration A2: Interleaved Array

The increase in beamwidth introduces larger mutual coupling effects and a reduction in gain which directly impacts the power per beam required to achieve the e.i.r.p. This reduction in gain will be approximately 4.77 dBi (the same as the combining loss); hence, the radiated power should increase by this amount to attain the desired e.i.r.p. Thus, the number of elements needed remains the same. The only difference is that each element now occupies one-ninth of the original area, making it possible to fit three elements of each of the three phased arrays in the area of the original full-sized element. Although this configuration achieves the primary objectives, a major problem is the complexity of the BFN resulting from the interleaved elements. Another point of concern is that little is known about the interaction between the phased arrays. Nevertheless, the interleaving configuration was further investigated to determine what advantages, if any, might be derived from a design which would eliminate the need for combiners.

With a square waveguide aperture as the radiating element in the array, the interleaving of N phased arrays requires one of the two arrangements shown in Figure 3-16 for odd and even N, respectively. Figure 3-16a shows a 3-array interleaving arrangement. For a particular array, the periodic structure has the general appearance shown in Figure 3-17.

Two aspects of array interleaving were studied. The first is the limitations placed on element size, and consequently on element spacing, d. The second is the advantages, if any, in achieving higher e.i.r.p. or higher efficiency than the contiguous arrangement of the same number of arrays.

The element size has an upper bound dictated by the existence of grating lobes in the coverage area, and a lower bound determined by the allowable phase shifter increment and the required scanning step. The grating lobe lattice for the array

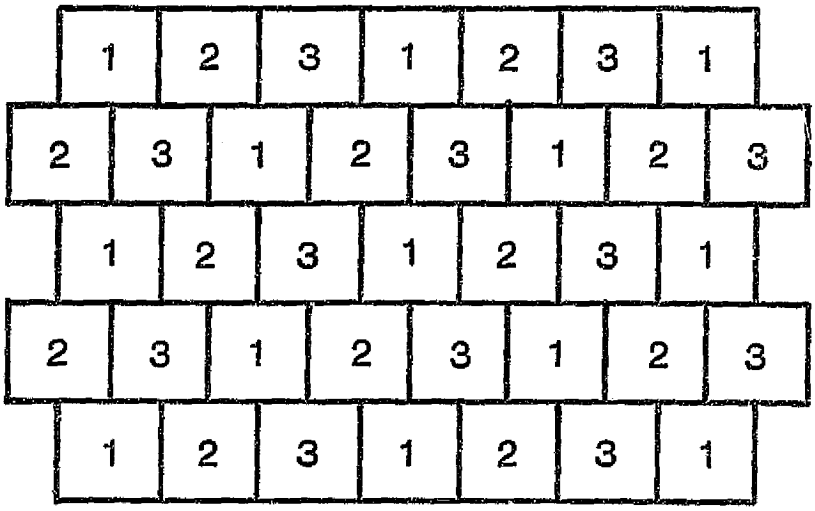

(a) 3-Array Interleaving

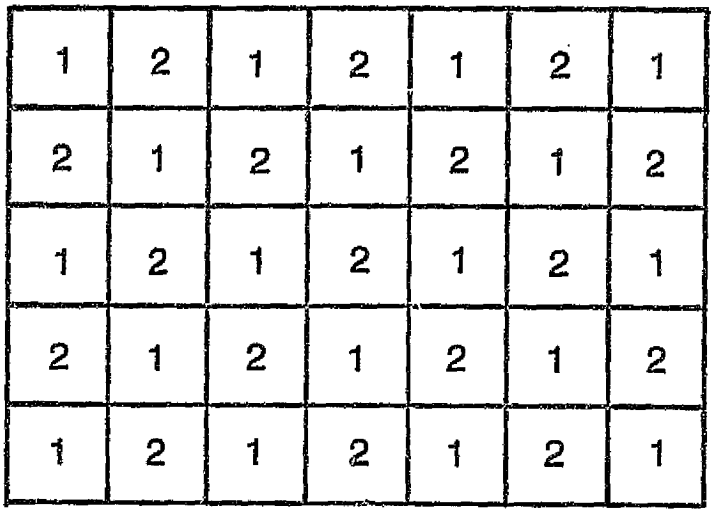

(b) 2-Array Interleaving

Figure 3-16. Array Lattices for 3-Way and 2-Way Interleaving

is shown in Figure 3-18. The coverage area is defined as $\pm\theta_1$ in the angular direction corresponding to the array's x direction, and $\pm\theta_2$ in the angular direction corresponding to the array's y direction. The orientation of the array can be adjusted to make a maximum use of the grating-lobe-free area.

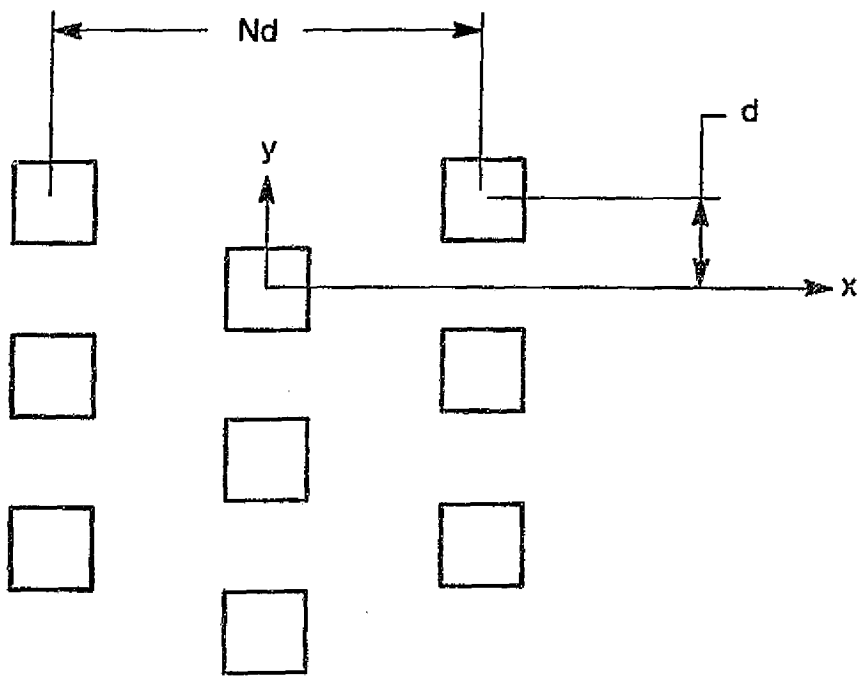

Figure 3-17. Periodic Structure of an Array in N-Array Interleaving Configuration

Generally, it is desired to have no grating lobe in the coverage area as the main beam is scanned from broadside to the edge of coverage. This imposes an upper limit on the element size. This upper limit, normalized to free space wavelength, is given by

$$\frac{d}{\lambda} \leq \frac{1}{2N \sin \theta_1} \tag{3-7a}$$

or

$$\left\{ \begin{array}{c} \frac{d}{\lambda} \leq \frac{1}{N \sin \theta_1} \\ \text{and} \\ \frac{d}{\lambda} \leq \frac{1}{4 \sin \theta_2} \end{array} \right\} \tag{3-7b}$$

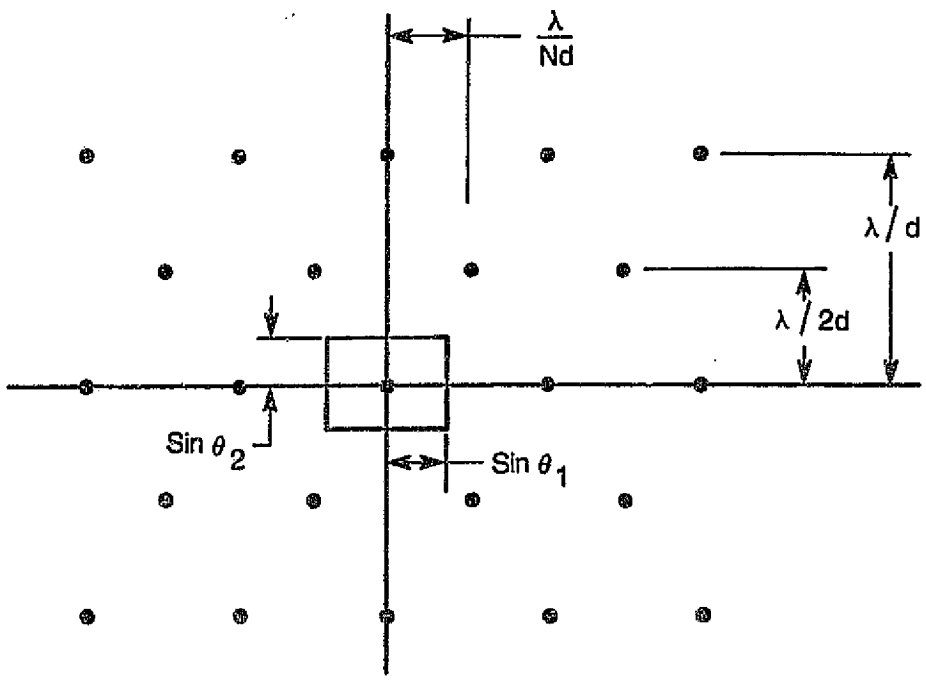

Figure 3-18. Grating-Lobe Lattice for the Periodic Structure of Figure 3-17

For the dual-reflector system, θ_1 and θ_2 will be the magnification factor, M, times the scanning values in the far-field region.

The required scanning step of the array can be expressed in terms of the far-field beamwidth and the interleaving order, N. Figure 3-19 shows the situation in which any point in the scanning range is to be within A degrees from the beam peaks. The scanning step in the y direction between adjacent rows is B, and in the x direction between elements in the same row is NB. From this figure, the relationship between A and B is

$$B = \frac{4N}{N^2 + 4} A \qquad (3\text{-}8)$$

For no interleaving (N = 1 or a triangular array of square horns) B = 0.8A. For N = 2, the obvious relationship is B = A.

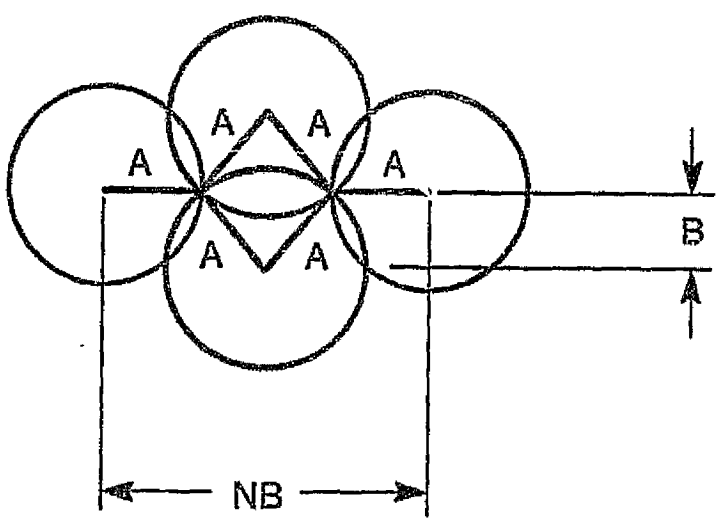

Figure 3-19. Scanning Step Limitation for the Periodic Structure of Figure 3-17

To achieve the scanning step B by using phase shifters of increment $\Delta\phi$, the element size, d, must be above a certain level. For small values of θ_1 and θ_2, the lower bound on d is

$$\frac{d}{\lambda} \geq \frac{\Delta\phi}{2\pi B} \tag{3-9}$$

Equations (3-7) to (3-9) give upper and lower bounds on d/λ for certain levels of interleaving. Inversely, they also give the highest level of interleaving allowable to achieve a feasible system. Figure 3-20 shows the upper and lower limits of d/λ vs the interleaving level for different values of magnification factor, M, and a phase shifter increment of 11.250° (5-bit phase shifter).

For the dual-polarization system, N-level interleaving produces 2N separate scanned beams. This allows the first beam to have opposite polarization with respect to the 2Nth beam. If the grating lobes of the first beam are allowed to appear in the scanning range of the 2Nth beam (thus depending on isolation via polarization) more arrays can be interleaved with feasible values for element size bounds. Figure 3-21 shows the upper and lower limits of d/λ under this condition with 5-bit phase shifters. A comparison of Figures 3-20 and 3-21 reveals that the permissible interleaving level increases from N = 2 to N = 3 if grating lobes are allowed to appear at the edge sector of the scanning range.

To compare the option of array interleaving with the other two options that employ combiners and contiguous arrays, it must be assumed that the three options use the same total aperture area. For a specific value of M and a main reflector diameter of D, the array aperture area is approximately $\pi D^2/4M^2$.

If the aperture is shared between N arrays, the available aperture per array will be $\pi D^2/4M^2N$. For N = 3, this means a loss of 4.77 dB in the available gain due to aperture sharing

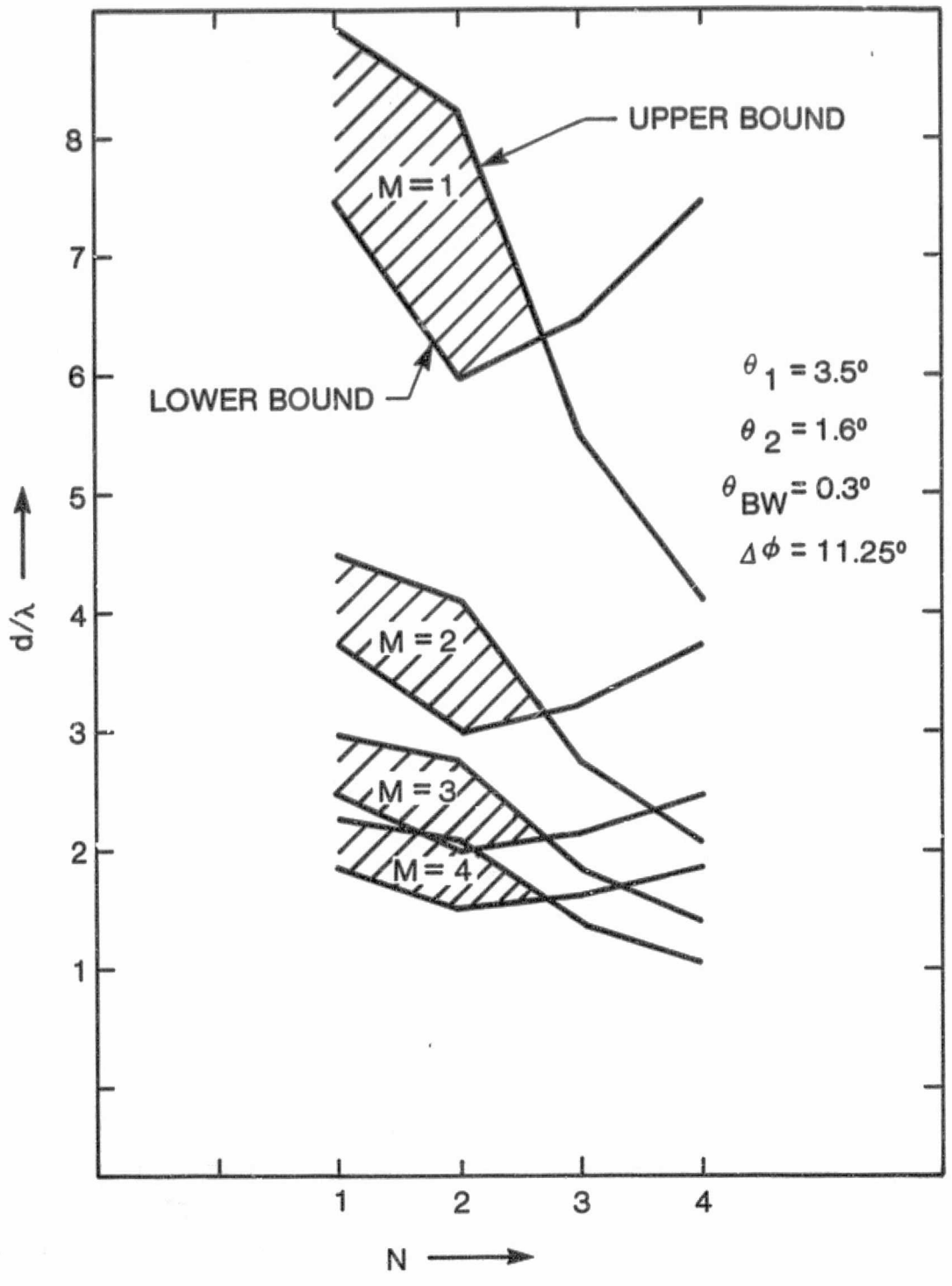

Figure 3-20. Upper and Lower Bounds on d/λ for No-Grating-Lobe Scanning

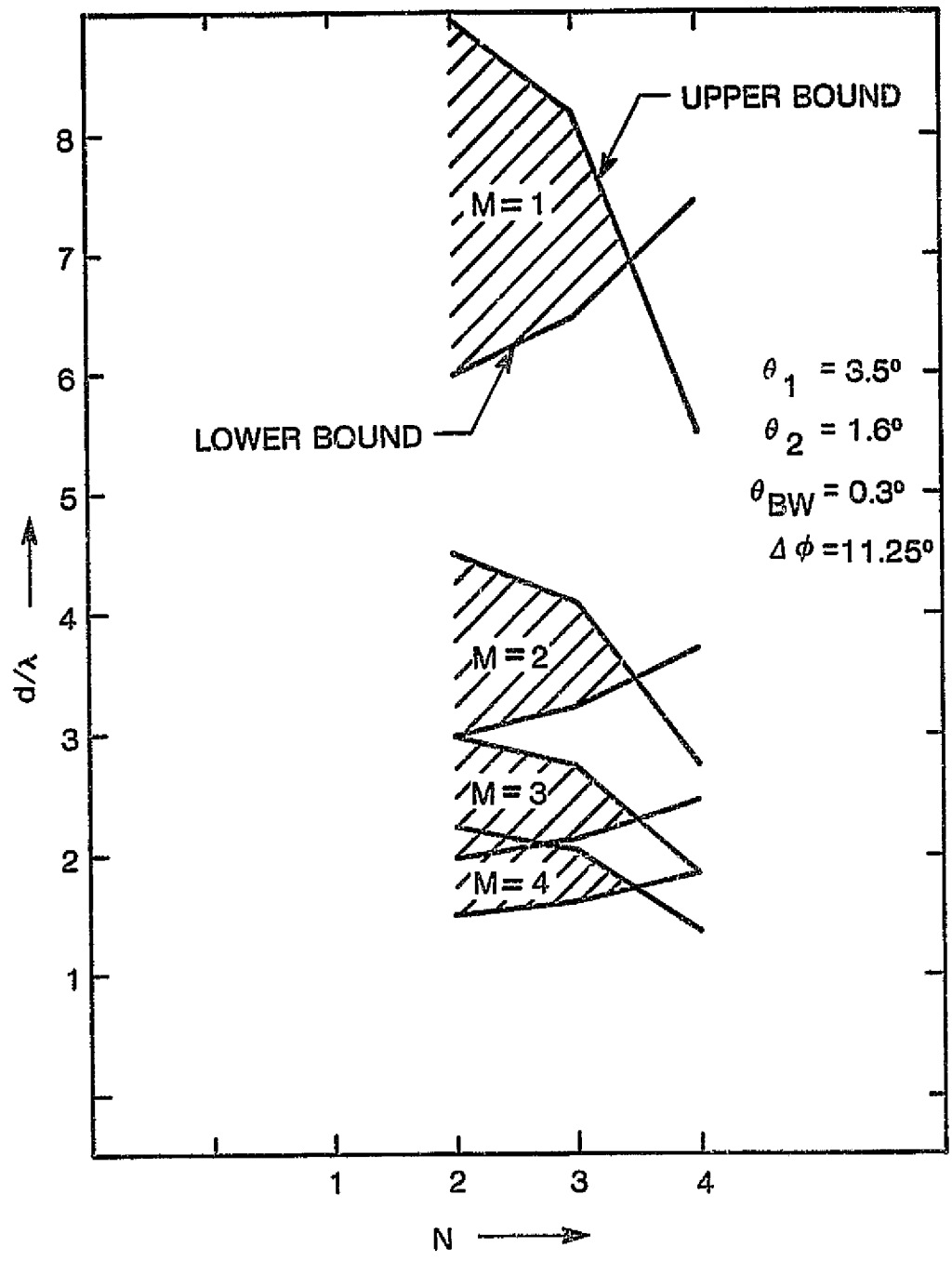

Figure 3-21. Upper and Lower Bounds on d/λ for Scanning With Grating Lobe Allowed at Last Sector

alone. To achieve the same e.i.r.p., the loss in gain must be compensated for by stacking the same number of elements in the new aperture area per array, or in 1/Nth the total aperture area. This is possible if the interleaved arrays use elements 1/Nth the size of the corresponding complete array elements. However, Figures 3-20 and 3-21 show that the allowable element size of interleaved arrays does not decrease as fast as 1/N. In some cases, the element size for M = 3 must be about 2.5λ for N = 1, 2, and 3. This means that the gain loss attributable to aperture sharing cannot be compensated for by increasing the number of elements; thus, the obtainable e.i.r.p. is reduced.

An example is the case in which the desired e.i.r.p. is 70 dBW. For a 13-ft aperture with efficiency $\eta = 0.6$, the available gain is approximately 53 dB. If the aperture is shared by three arrays, the available gain per array becomes 48.23 dB. For the complete aperture array, this results in radiated power per beam of 50.1 W. Assuming M = 3 and f = 20 GHz, the total aperture can accommodate 974 elements of dimensions 2.5λ x 2.5λ. From Subsection 2.1, the element dimension falls within the allowable limits. Thus, the power contribution per horn, assuming lossless horns, is 0.05 W. This is less than 0.067 W that can be achieved by using the available modules in combiner Configuration A1. If the aperture is shared by three arrays, interleaving or contiguous, the element size will have to be about 2.5λ, and the number of elements per array will drop to 325. Assuming lossless systems and 0.2 W per horn, as dictated by the modules, the radiated power/beam will be 65 W. Since the available gain is only 48.23 dB, this will produce an e.i.r.p. of 66.36 dBW. If the same margin for losses is assumed (0.05/0.067), the radiated power/beam will drop to 48.5 W, reducing the e.i.r.p. to 65.09 dBW.

Although the 70 dBW of e.i.r.p. cannot be achieved by interleaving three phased arrays with the same total aperture, interleaving offers a definite advantage in terms of overall efficiency. Assuming 15 percent efficiency for the MMIC modules, the overall efficiency of interleaved arrays can be as high as 13.5 percent, compared with 4.5 percent for the combiner configuration.

A third option in this configuration is to divide the array aperture into three contiguous arrays. This will place the same limitations on the e.i.r.p. as the interleaving option and will deliver the same high overall efficiency. It may, however, result in more scan losses for the edge arrays. These losses can be compensated for by arranging the contiguous arrays on a non-planar surface. The simplicity of the contiguous arrays is an apparent advantage over the complexity of the BFN associated with the interleaved arrays.

Because of the low achievable e.i.r.p. and the complexity of the network for interleaved phased arrays, this option is considered to be inferior to the other scanning array options.

3.4.1.1.3 Configuration A3: Individual Side-by-Side Arrays

A third option investigated employs three individual arrays placed side by side, as shown in Figure 3-22. This approach avoids the unconventional periodicity of the interleaving approach and also eliminates the lossy combiners. In this arrangement, the maximum obtainable e.i.r.p./beam is lower than 75 dBW (the same as that in the previous case (combiner)). The total aperture is shared by the three arrays, and each element radiates 0.2 W, which is sufficient to yield the required minimum e.i.r.p.

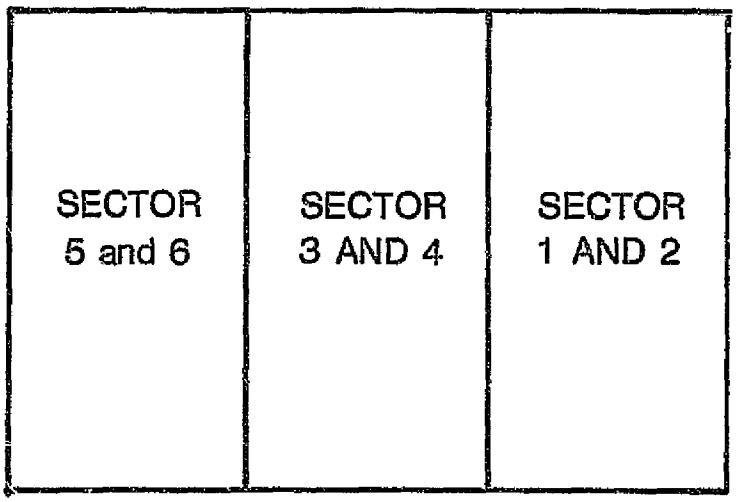

Figure 3-22. Configuration A3: Individual Side-by-Side Arrays

The use of a reduced-size array will also impact the resolution of the antenna system, as well as the degradation in gain. The 3-dB beamwidth will be three times larger than for configurations A1 and A2. This will impact the co-pol isolation between nonadjacent sectors and limit the number of co-polarized scanning beams that can be used. Clearly, the six-beam concept with the coverage shown in Figure 3-3a will be unachievable.

Table 3-5 presents a comparison of the three variations. Both extremes in e.i.r.p. (67-75 dBW) are considered. To determine the number of elements required, losses were assumed from the output of the amplifier module.

3.4.1.2 Configuration B

In this configuration, a variable power module (up to 0.5 W) is utilized to generate six scanning beams with 67- to 75-dBW e.i.r.p. Since phase shifting capability is not available, there are several ways of achieving the scan requirement. One is the Butler matrix approach, with as many beam positions as required to cover the CONUS, and the use of a switch matrix to switch beams to meet the scan requirement. This method uses the variability of the MMIC amplifier module only to introduce a taper in the radiating aperture. The second method, which utilizes MMIC module variability to achieve scanning, is a focal region-fed Cassegrain system. These two approaches are compared in the subsections that follow. A third configuration, the space-fed lens, which is capable of meeting the performance requirements, will be discussed in Subsection 3.4.3.

3.4.1.2.1 Configuration B1: Butler Matrix

In this configuration, shown in Figure 3-23, the MMIC modules are capable of producing up to 0.5 W of power. The number of elements needed to produce maximum e.i.r.p. is given by

$$N = \frac{158}{0.5} = 316\{x\ 3\ \text{(each amplifier shared by three beams)} = 948\} \quad (3\text{-}10)$$

To allow for illumination taper, a more realistic number will be N = 1,600. A lossless Butler matrix produces orthogonal beams with beam crossover levels of -3.92 dB, which is lower than the desired -3 dB. With this crossover level, approximately 250 beam positions are required to cover CONUS. Hence, two Butler matrices, each with 125 input ports and 1,600 output ports, form the basic BFN shown in Figure 3-23. A switch matrix (1 x 42) is used for each of the six regions to accomplish the desired scanning. Higher crossover levels can be achieved if adjacent beams are combined and some energy is lost in the network. This is a fundamental limitation of a Butler matrix. Lossless networks often possess one or more pattern characteristics that can be enhanced when the capabilities of a lossy network are properly traded off. The maximization of available antenna gain at the beam crossover points, for example, is one possible advantage of employing a lossy network instead of a lossless design. Control of near-in sidelobe levels is another.

This configuration has the usual problems associated with phased arrays, namely grating lobes and blind spots. The upper limit of element spacing, as in Configuration A, is not present, and consequently the elements can be made smaller. In terms of the complexity of the BFN, the Butler matrix conforms readily to microstrip medium since its major components are hybrids

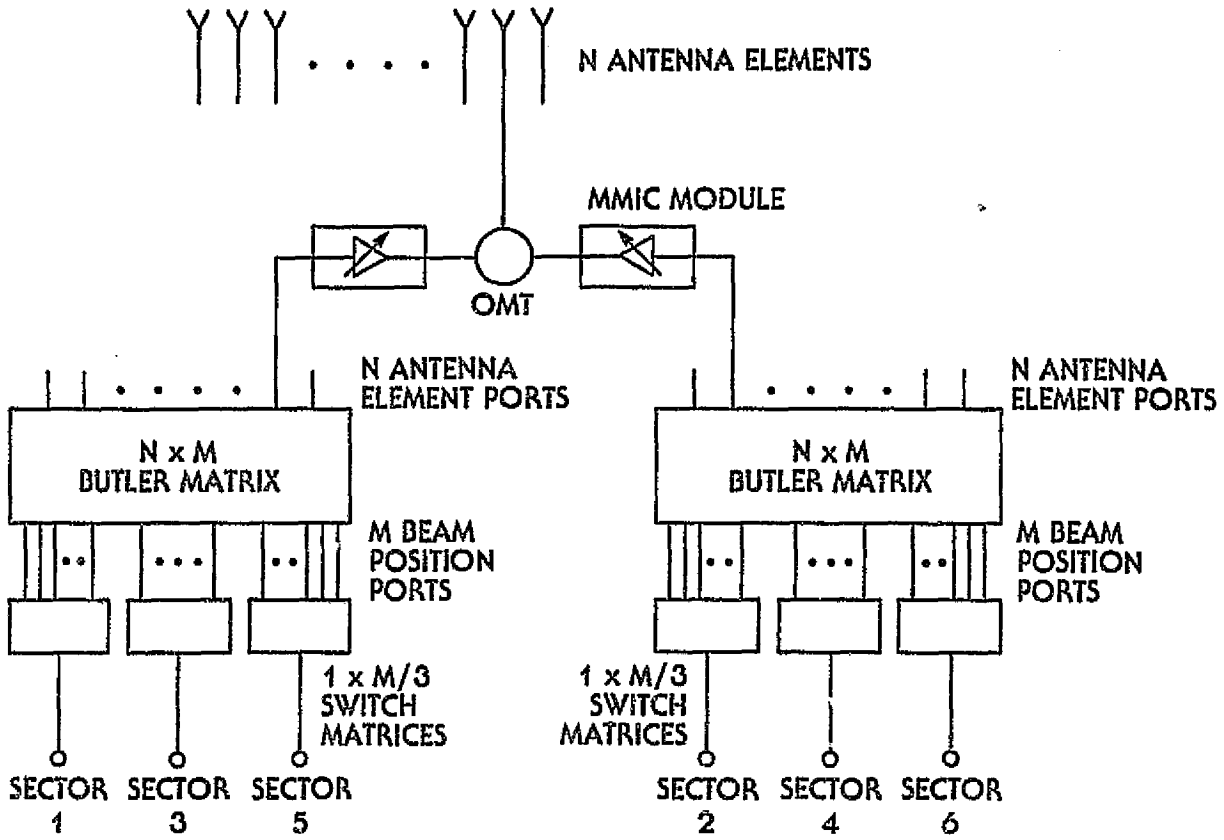

CONFIGURATION B1

-SIX SCANNING BEAMS
-67-75 dBW/BEAM (E.I.R.P.)
-VARIABLE GAIN (5 LEVELS) AMPLIFIER MMIC (.5 W MAX OUTPUT)
-M BEAM POSITIONS ASSUMED (TO COVER CONUS)

Figure 3-23. Configuration B1: Butler Matrix

and line lengths. In this format, the matrix is lossy, and although the amplifiers follow the BFN, the size of the driver tube will be determined by the BFN loss. The MMIC modules can be integrated directly on the same substrate as the Butler matrix, and the conventional switch matrix poses no problems. In terms of the number of components, a 1,600 x 125 Butler matrix requires tens of thousands of hybrids. In addition to the large number of hybrid junctions, 1,600 antenna elements, six 1 x 42 switch matrices, 1,600 OMTs, and 3,200 MMIC modules are needed.

An array of 40 x 40 elements can be formed with element spacings such that the scan step parameter K is more than the required 0.866 to 0.75. This results in crossover levels greater than -3 dB. To obtain K = 0.866 to 0.75 corresponding to -3-dB crossover levels, the Butler matrix becomes lossy.

3.4.1.2.2 Configuration B2: Feed Cluster

This configuration (Figure 3-24), uses a feed cluster to feed a Cassegrain system. A section of the feed cluster forms a beam for one sector of CONUS.

To achieve the maximum e.i.r.p., a minimum of 316 elements, each radiating 0.5 W, is needed. A cluster of 19 elements with a tapered amplitude distribution, and 0.5-W amplifiers on each is capable of producing about 1 W of radiated power if low sidelobes are to be achieved. The cluster can be made larger by adding more elements; however, the number of elements required for 158 W of radiated power will be impractical. The amount of feed sharing required will also be prohibitive. At the lower end (67 dBW) of the e.i.r.p. requirements, 25 W of power is to be radiated by the cluster. Even this will require a large cluster making the antenna system untrackable. Smaller antenna elements can be used but at

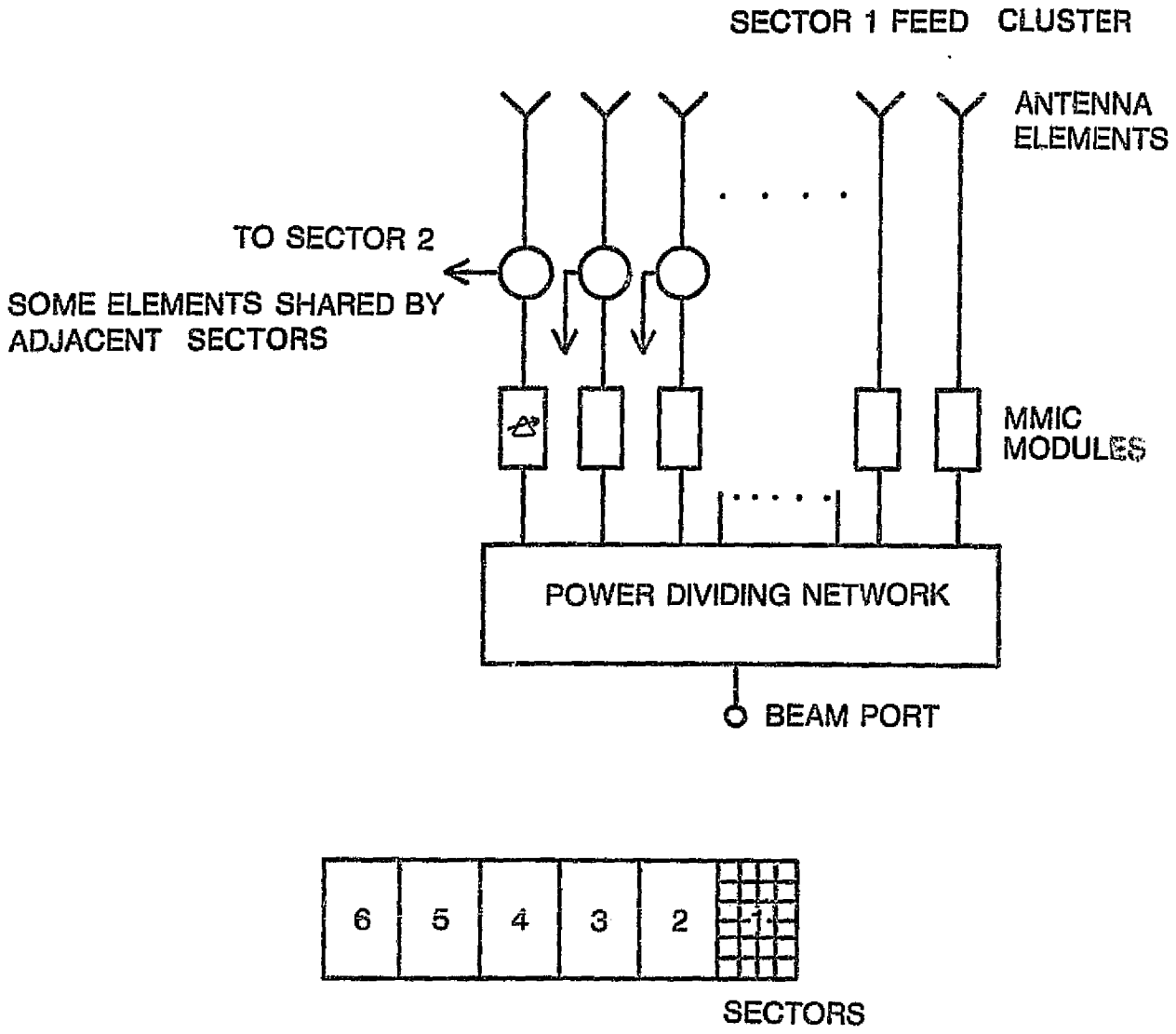

Figure 3-24. Configuration B2: Feed Cluster

the expense of mutual coupling problems without a substantial gain in size of the feed cluster and the antenna system.

Based on the above arguments, it can be concluded that the e.i.r.p. requirement cannot be met with this configuration. It is possible to achieve e.i.r.p. levels that are 10 dB lower than the minimum specification and are of a reasonable size for the feed clusters.

3.4.1.3 Configuration C: Full Array With 3-Way Combiner

This configuration can employ any combination of a VPA module, a VPS module, and a variable power/variable phase (VPA/VPS) module. This design is basically the same as Configuration A except for the use of different MMIC modules. Figure 3-25 shows the combiner technique. A VPA/VPS module is used before the combiner, and a VPA module after the combiner. In this configuration, the VPA/VPS module could be used for two purposes: first, to introduce the correct phase for scanning; and, second, to use the variable power capability to provide just enough power for driving the VPA module without causing excessive power dissipation in the resistor terminations of the combiner. Presumably, the drive level could be set by having the VPA/VPS module on a low gain state. The VPA module is capable of providing 0.5 W at 20-dB gain. With a combining loss of about 4.77 dB, the maximum allowable output power level of the VPA/VPS modules is -23 dBW (5 mW). Therefore, the maximum power dissipated in the combiner would be 10 mW, which is very reasonable.

The number of elements needed to achieve the maximum radiated power/beam of 158 W would be 1,600, the same as in the Butler matrix, Configuration B1. The element size would be divided by the spacing, which is limited by the grating lobes and

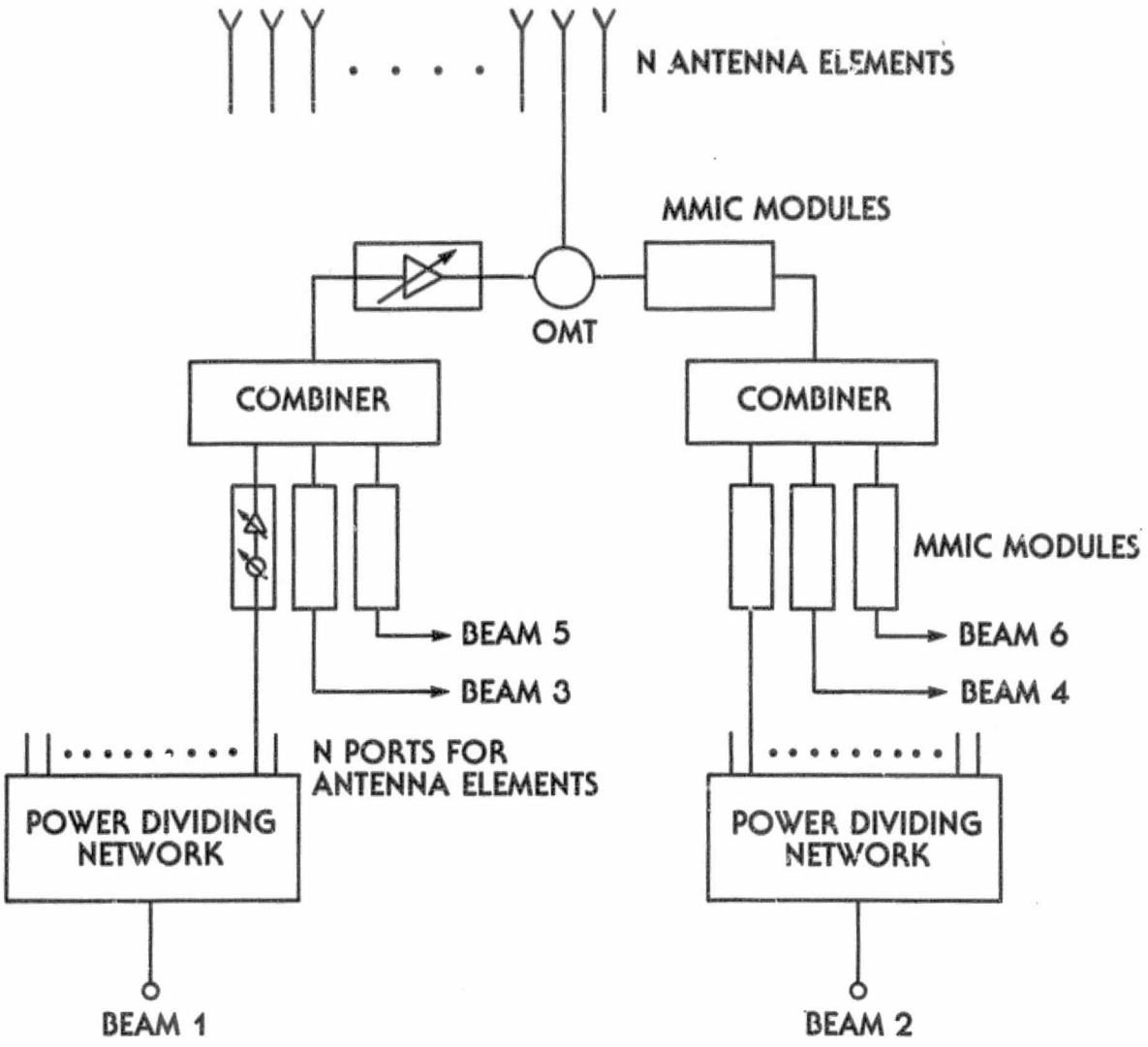

CONFIGURATION C

- SIX SCANNING BEAMS
- 67-75 dBW/BEAM (E.I.R.P.)
- VARIABLE GAIN/VARIABLE PHASE MMIC (.5 W MAX OUTPUT, 5 LEVELS/5 BIT) AND VARIABLE GAIN MMIC (.5 W MAX OUTPUT, 5 LEVELS)

Figure 3-25. Configuration C: Full Array With 3-Way Combiners

beam spacing requirements. The same spacing as in Configuration A1 can be used.

Other features of this BFN configuration are similar to Configuration A1, namely, the power dividing circuits (1 x 1,600) and the OMTs. This configuration seems inherently adaptable to MIC integration techniques, since the power levels up to the input of the VPA module are low. The PDN, the VPA/VPS modules, and the combiners can be integrated into one package.

In terms of the number of components, 1,600 antenna elements, 1,600 OMTs, 3,200 VPA MMIC modules, 3,200 combiners, 9,600 VPA/VPS MMIC modules, and six 1 x 1,600 PDNs are needed to achieve the maximum e.i.r.p.

The other possible configuration is the interleaving method used in Configuration A2. Since the problem of heat dissipation in the combiner, present in Configuration A1, does not exist here, Configuration C is a good candidate for parametric study. Otherwise, if the interleaving method is chosen, the study will be a repetition of Configuration A2 with different values.

3.4.2 MULTIPLE FIXED BEAM CONFIGURATIONS

Table 3-4 presented the system requirements for the multiple fixed beam configurations. The configurations specified in Subsection 3.4, and several variations on each, are discussed in the subsections that follow. For the 4-m reflector assumed in this discussion, each beam requires between 0.8 and 8 W to achieve the range of e.i.r.p.'s specified in Table 3-4.

3.4.2.1 Configuration D

This configuration uses 10 to 18 beams, each with a maximum of 8 W of radiation power. Also addressed is a capability for trimming each beam position independently. Since the MMIC used has a constant power amplifier and a variable phase shifter, the initial beam directions and the trim capability can be achieved by using a phased-array-type radiating system feeding a pair of confocal parabolas.

As in Configuration A, three configurations are possible: a 9-way combiner, interleaving of nine elements, and a side-by-side phased array. Obviously, the 9-element interleaving configuration will be quite complex. In the 9-way combiner configuration, power dissipation poses a problem, since up to 1.6 W of power could be dissipated in the isolation resistors. Table 3-6 presents a comparison between the combiner and a side-by-side phased array. The following subsections summarize a comparison of the three configurations.

3.4.2.1.1 Configuration D1: Full Array With 9-Way Combiners

This configuration (Figure 3-26) is similar to Configuration A1. To achieve the maximum desired e.i.r.p., about 600 elements are needed to allow for amplitude taper. The minimum element spacing required in Configuration A is not a restriction in this case, since the beam is not dynamically scanned. The only requirement is use of the maximum spacing necessary to avoid grating lobes in the FOV. The major concern is heat dissipation.

The PDN for each beam could be constructed of reduced height waveguide, stripline, or MIC. An MMIC module is connected at each output of the PDN. The beams in the desired direction

Table 3-6. Comparison of Combining Technique and Side-by-Side Array

Characteristic	Combining		Side-by-Side	
	Maximum e.i.r.p.	Minimum e.i.r.p.	Maximum e.i.r.p.	Minimum e.i.r.p.
Number of Elements	576	58	5,184	519
Size of Elements, M = 3	3λ	9λ	1λ	3λ
Spacing	3λ	9λ	1λ	3λ
Number of OMTs	576	58	5,184	519
Number of MMIC Modules	10,368	1,036	10,368	1,036
Combiners	1,152	116	None	None
Size of PDN	1 x 576	1 x 58	1 x 576	1 x 58
Heat Dissipation (MMIC not considered) in Resistors (W)	1,843	184	None	None
Power Usage	2,073	207	2,073	207
Power Radiated	230	23	2,073	207
Complexity of BFN	Simple	Simple	Simple	Simple
Grating Lobe in FOV	Yes	Yes	No	Yes

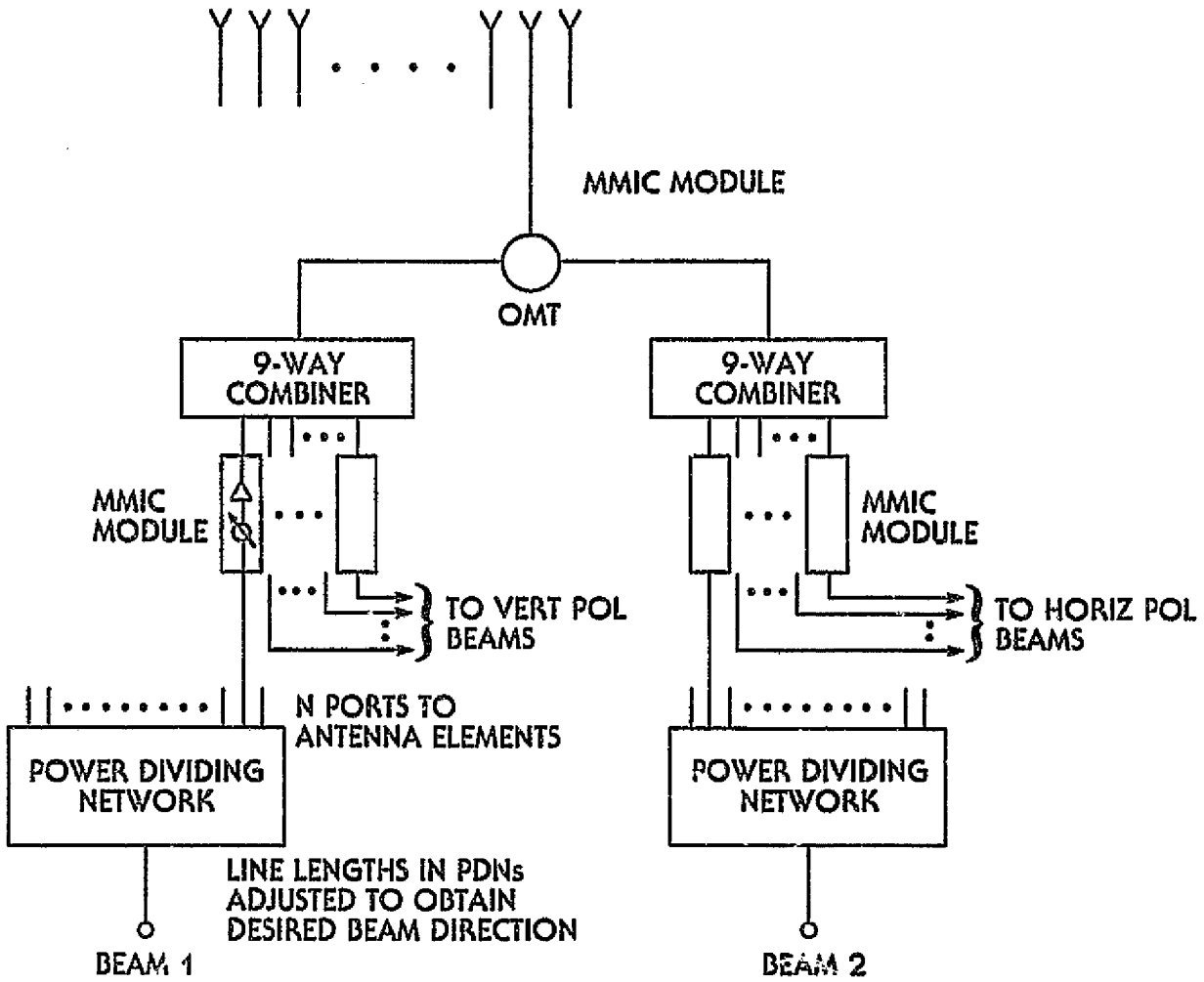

CONFIGURATION D1

-MULTIPLE BEAMS (18)
-52-62 dBW/BEAM (E.I.R.P.)
-CONSTANT GAIN (.2 W MAX OUTPUT) AND 3-BIT PHASE-SHIFTER (FOR TRIMMING) MMIC

Figure 3-26. Configuration D1: Full Array With 9-Way Combiners

are produced by providing the proper phase distribution through the variable phase shifter of the module or by fixed line lengths. Each beam can be trimmed independently through these VPS modules.

3.4.2.1.2 Configuration D2: Interleaved Arrays

The major problem posed by this configuration is the complexity of the interconnections between the antenna elements and MMIC modules, as encountered in Configuration A2. A 24 x 24 element array is needed for each of the nine orthogonally polarized beam pairs. The interleaving of the elements of nine arrays imposes limitations on the size of the element. To avoid grating lobes in the FOV, the spacing between adjacent elements becomes less than one-half wavelength, which is not feasible.

3.4.2.1.3 Configuration D3: Individual Side-by-Side Arrays

Another possibility is to have the nine 24 x 24 element (1λ) phased arrays arranged as shown in Figure 3-27. This configuration removes the complexity of the interleaved-elements arrangement, and provides the capability of individual beam-position trimming.

To obtain the 53-dBi gain from the antenna configuration, the complete radiating aperture must be used. Assuming an equivalent element of size 3λ, about 72 elements can be arranged on one side of a square. Configuration D3 has nine arrays of equal dimensions, which means that each array can have 576 elements of approximately 1λ in size arranged in a 24 x 24 element square. In this case, each element is capable of radiating 0.2 W for each beam, as opposed to 0.022 W in the combiner case, thus providing

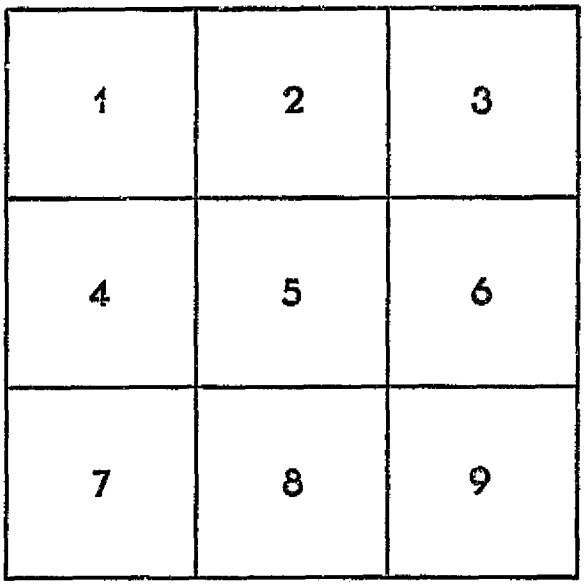

CONFIGURATION D3

- MULTIPLE BEAMS (18)
- 52-62 dBW/BEAM (E.I.R.P.)
- CONSTANT GAIN (.2 W MAX OUTPUT) AND 3-BIT PHASE-SHIFTER (FOR TRIMMING) MMIC

Figure 3-27. Configuration D3: Individual Side-by-Side Arrays

C-2

115 W. With the additional elements, a reasonable amplitude taper can be achieved through a proper selection of power division ratios in the PDN.

The major problem in this configuration is that, through the use of a smaller array, both the gain and the resolution (beamwidth) of the far-field beams are degraded. The increased power can overcome the gain reduction; however, the decrease in resolution will limit the number of beams achievable. Therefore, this is not a recommended configuration.

3.4.2.2 Configuration E: Feed Cluster

Multiple fixed beams (10 to 18) will be generated in specified directions by using 0.5-W VPA modules. An e.i.r.p. of 52-62 dBW per beam and a capability to trim the beam positions individually is required.

Since no phase shifting capability is available, the beams can be generated through a cluster of horns feeding a Cassegrain system, as shown in Figure 3-28. The trimming is achieved by varying the amplitude coefficients of the antenna elements, since the output power of the MMIC modules feeding the antenna elements is controllable.

Approximately 16 uniformly illuminated elements are needed to achieve the desired e.i.r.p. To provide for an amplitude taper and beam position trimming, additional elements will be needed around the periphery. Because feed region space is limited in a Cassegrain system, a smaller cluster such as the square cluster is preferable. Each cluster can produce two orthogonally polarized beams by using an OMT. In view of the trunking locations on CONUS, it is possible to have such feed clusters, each producing two orthogonally polarized beams used for adjacent

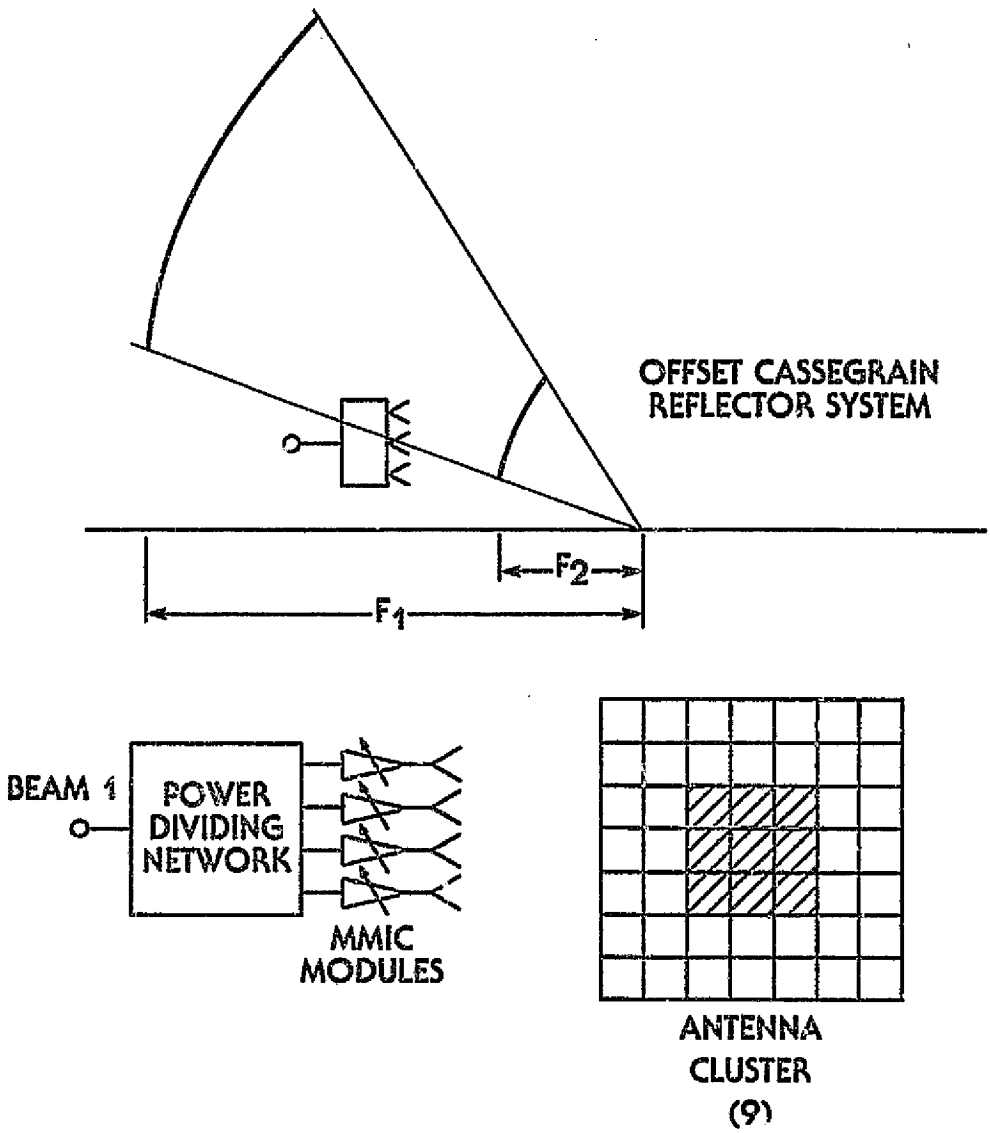

CONFIGURATION E

- MULTIPLE BEAMS (18)
- 52-62 dBW/BEAM (E.I.R.P.)
- VARIABLE GAIN (.5 W MAX OUTPUT, 5 LEVELS) MMIC
- ONE FEED CLUSTER FOR EACH BEAM

Figure 3-28. Configuration E: Feed Cluster

trunking locations, thereby providing isolation through polarization.

In terms of the number of components, 576 antenna elements, 576 OMTs, 576 MMIC modules, and nine PDNs (1 x 64) are needed.

To achieve sufficient beam isolation, a tapered amplitude distribution will be required for each component beam. This will require large feed arrays to be used and will result in a complex BFN which may involve co-polarized feed sharing.

3.4.3 CONFIGURATION F: SPACE-FED PHASED ARRAY--LENS

Both multiple scanning spot beam and multiple fixed spot beam systems can be designed when the phased array is space-fed by using a lens configuration, as shown in Figure 3-29. The beam direction is controlled by a switch in the feed array. The VPA modules are inserted in the lens between the input and output arrays, and the amplifier levels are set to produce the required taper. The levels can be set appropriately for the scanning beam case to maximize the beam isolations.

3.4.4 CONFIGURATION C DIRECT RADIATING PHASED ARRAY

A direct radiating phased array can be used for both the scanning beam and fixed beam cases. The phased array design and its network are similar to Configurations A, C, and D. However, the size of the elements and the array will be multiplied by the magnification factor, which will result in a heavy design that may require a complex deployment mechanism.

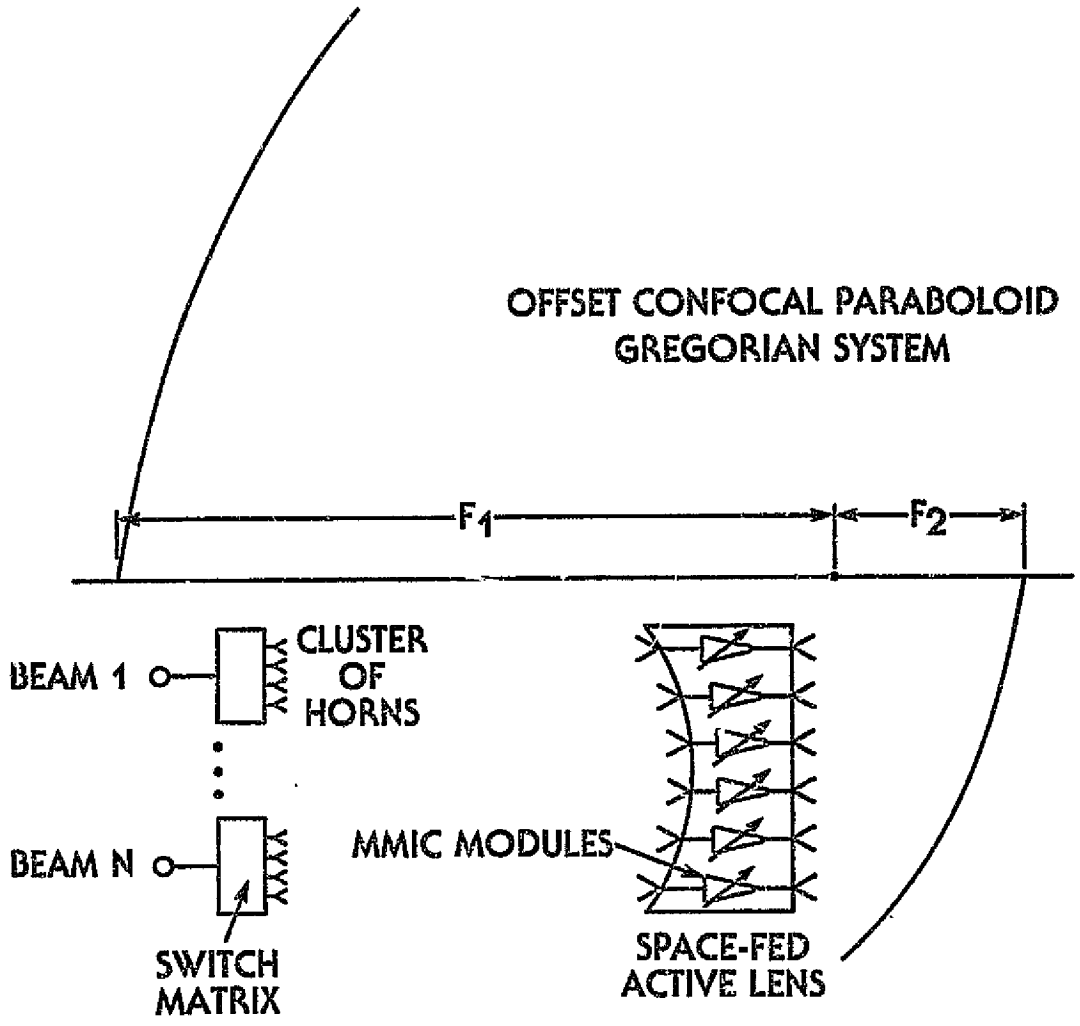

Figure 3-29. Configuration F: Lens

3.5 PARAMETRIC STUDIES

An extensive parametric study was performed in the areas of BFNs, arrays, and reflector optics. Based on the results obtained, it was determined which configurations offer the best potential for future satellite application.

The total power efficiency determined for each configuration represents the single most important parameter in determining system feasibility. Most configurations were investigated from the viewpoint of the e.i.r.p. level specified in the SOW. This requirement, coupled with the desire for six scanning beams, made Configuration A initially noncompetitive with conventional transponder approaches that used TWTs. This was because all amplification was before the combiners at the input of each feed element. In Configuration C, the variable amplifiers preceding the combiner can be driven at a lower power level, with power amplification achieved principally after the combiners. This configuration results in a total power efficiency which is competitive with the TWT approach.

Configuration B results in a complicated combination of optics and feed networks, whether the Butler matrix or lens approach is used. The Butler matrix BFN is extremely difficult to realize, while the lens replaces the Butler BFN with free space. Hence, the lens-fed reflector system was considered as the preferred choice for further study.

In the fixed beam configurations, a true phased array approach is not feasible given the modules, the e.i.r.p., and the initial beam trimming requirements. Configuration D resulted in an inefficient system and was not seriously considered for further study. Several options for Configuration E were studied. In the focal region approach, the required e.i.r.p. is not currently achievable; however, the lens-fed reflector system appears to be

able to meet the e.i.r.p., although beam trimming may not be feasible. A second possibility is an array-fed optical system, but here also beam trimming is impractical. Either or both of these configurations would be a preferred approach.

3.5.1 CONFIGURATION PARAMETRIC STUDIES

A detailed parametric study was undertaken on each of the final BFN configurations and their variations. The output of this undertaking is a set of curves relating relevant parameters for each configuration. Typically, a set contains the following parametric curves:

a. e.i.r.p. vs gain with radiated power as a parameter,
b. radiated power vs number of elements with MMIC module output power as a parameter, and
c. prime power vs radiated power with MMIC module efficiency as a parameter.

In all curves, the values of all power-related parameters (prime power, e.i.r.p., etc.) are per-beam values; consequently, they must be multiplied by the number of beams to achieve the total required power.

In the course of designing a specific configuration, stepping through the set of parametric curves produces a set of design values. In this parametric study, the details of the design are not considered. What is considered is an overall loss occurring in combiners, waveguide runs, and OMTs in each configuration.

The feasibility of the configurations under analysis will indicate which four configurations should be considered for

a more complete parametric study leading to a specific detailed design. The following subsections discuss the parametric curves for the various configurations.

3.5.1.1 Scanning Beam BFNs

The achievable antenna gain from a main reflector of given size is obtained from the optics parametric curves. For example, a 3.96-m (13-ft) diameter parabolic reflector with 60-percent illumination efficiency may yield a gain of 53 dBi. Assuming an e.i.r.p. of 70 dBW/beam as desirable, 50.1 W/beam of power is radiated, as shown in Figure 3-30. The number of antenna elements needed to radiate 50.1 W/beam can be found from the radiated power vs number of elements parametric curves in Figures 3-31 and 3-32. This number is configuration-dependent. Specifically, for Configuration A1 this number is 825, in Configuration A2 it is 2,475, and in Configurations B1 and C it is 325.

Once this number is determined for a given configuration, the total prime power needed to radiate 300.6 W (50.1 W/beam) is determined from the prime power vs radiated power curves given in Figures 3-33 to 3-35. These parametric curves are also configuration-dependent. Specifically, for Configurations A1 and A2, 6,600 W of prime power is necessary, in Configuration B1 this number is 2,250 W, and in Configuration C it is 2,330 W. It is now possible to calculate the overall efficiency of a configuration. In case of Configuration A1, this efficiency is a low 4.5 percent, in Configurations A2 and B1 it is 13.5 percent, and in Configuration C it reduces slightly to 13 percent. Once power considerations are completed, array considerations such as element spacing and size grating lobes can be undertaken.

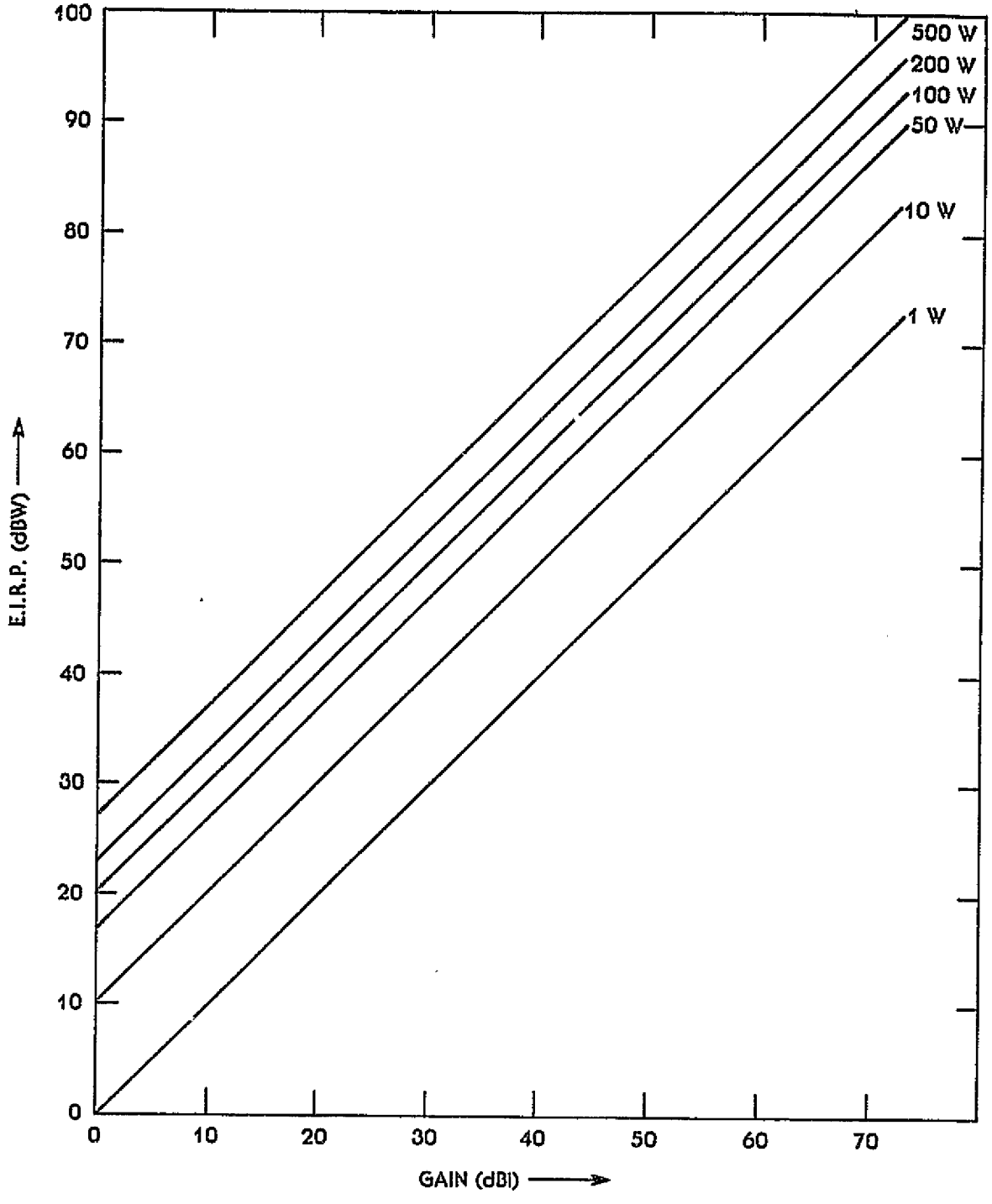

Figure 3-30. e.i.r.p. vs Gain With Radiated Power as Parameter

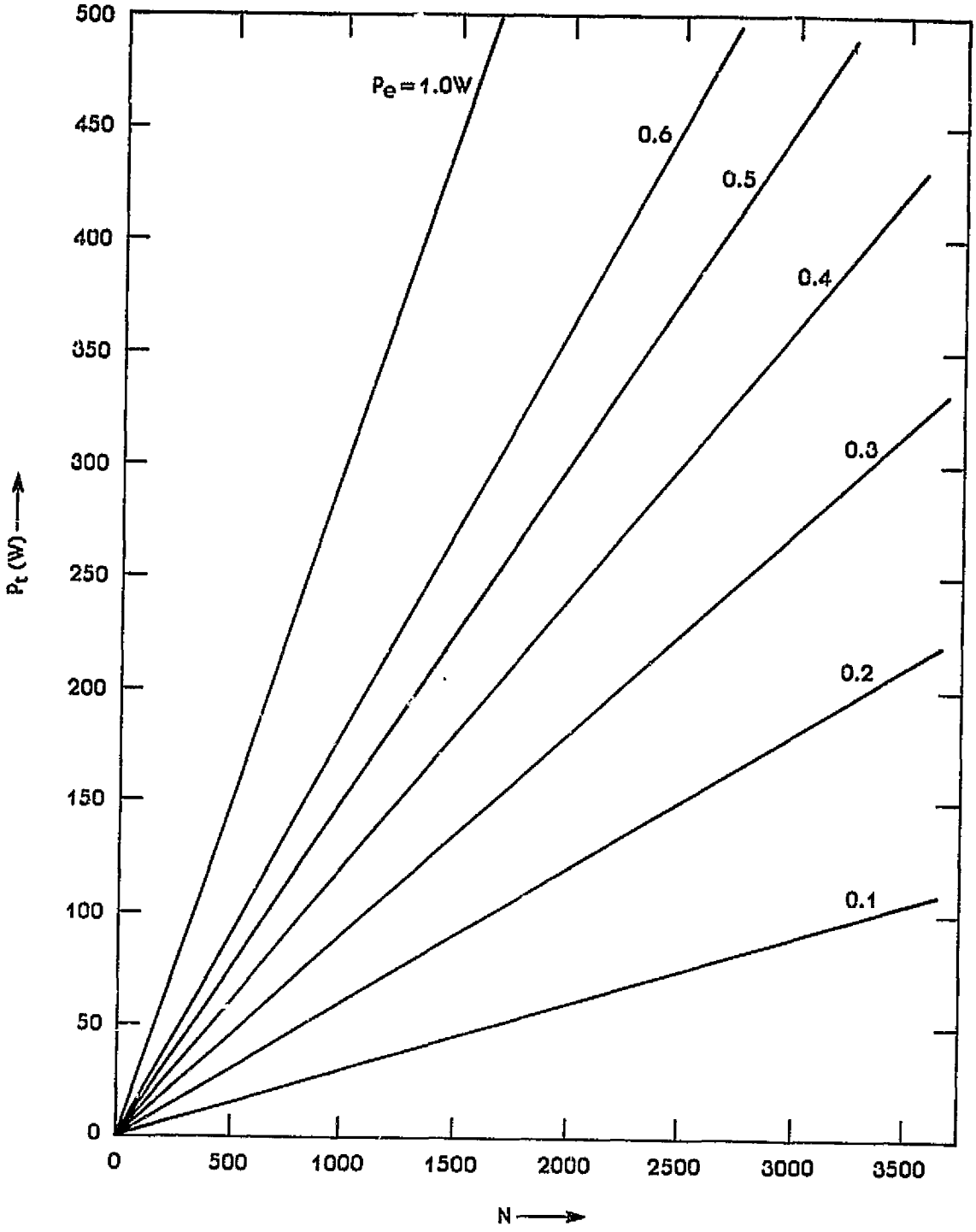

Figure 3-31. Radiated Power vs Number of Antenna Elements With Maximum MMIC Power as Parameter for Configurations A1, B1, and C

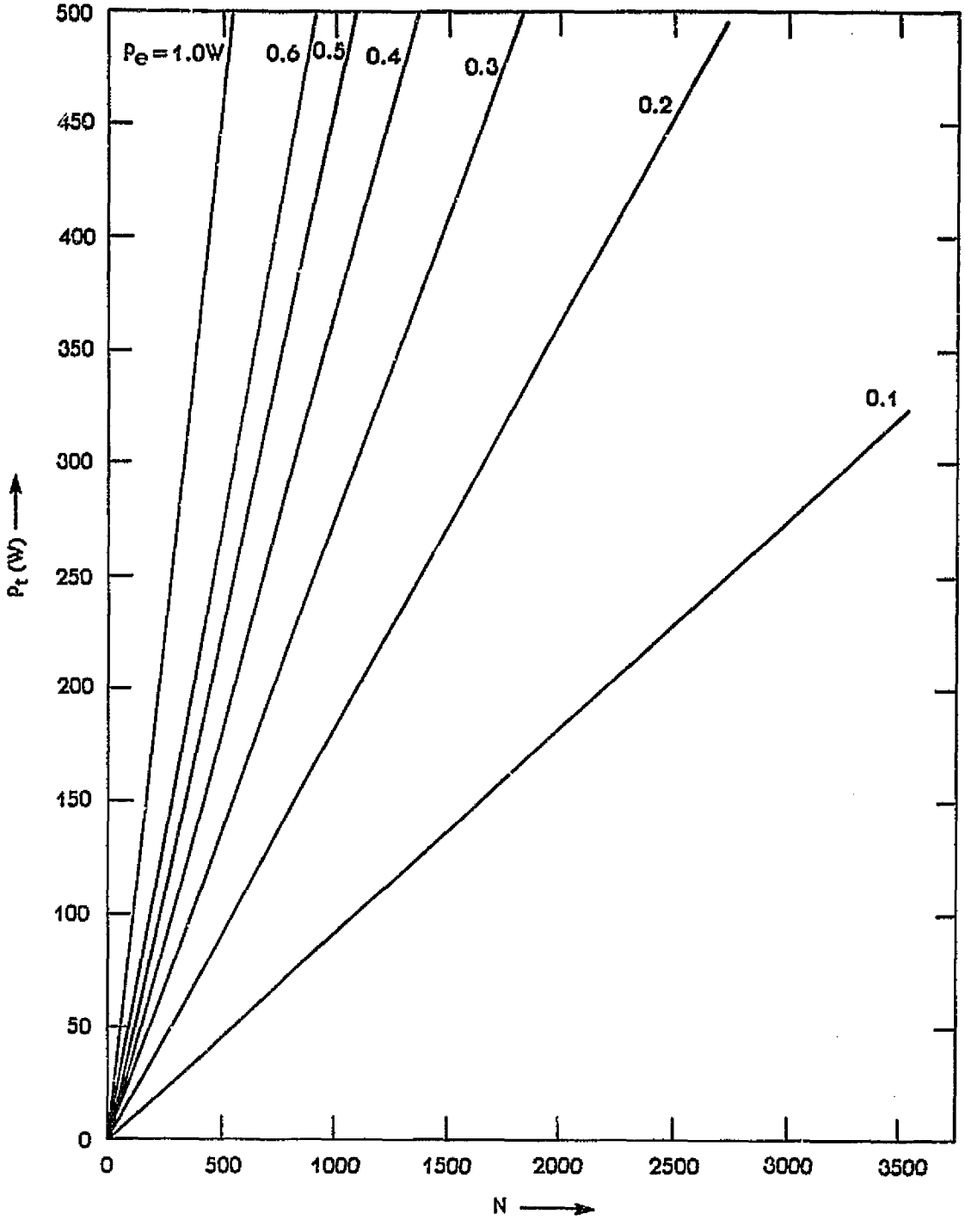

Figure 3-32. Radiated Power vs Number of Antenna Elements With Maximum MMIC Output Power as Parameter for Configuration A2

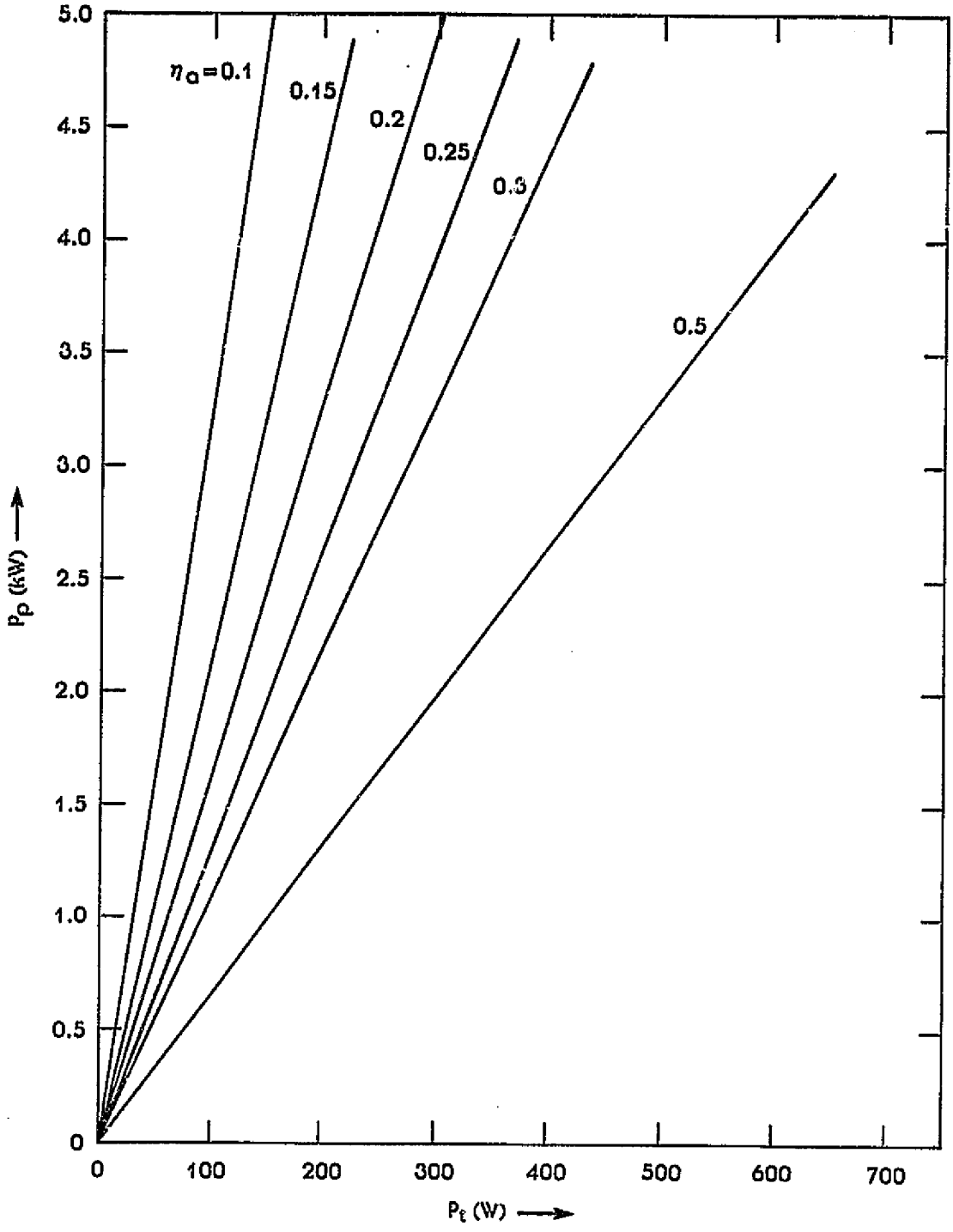

Figure 3-33. Prime Power vs Radiated Power With MMIC Efficiency as Parameter for Configuration A1

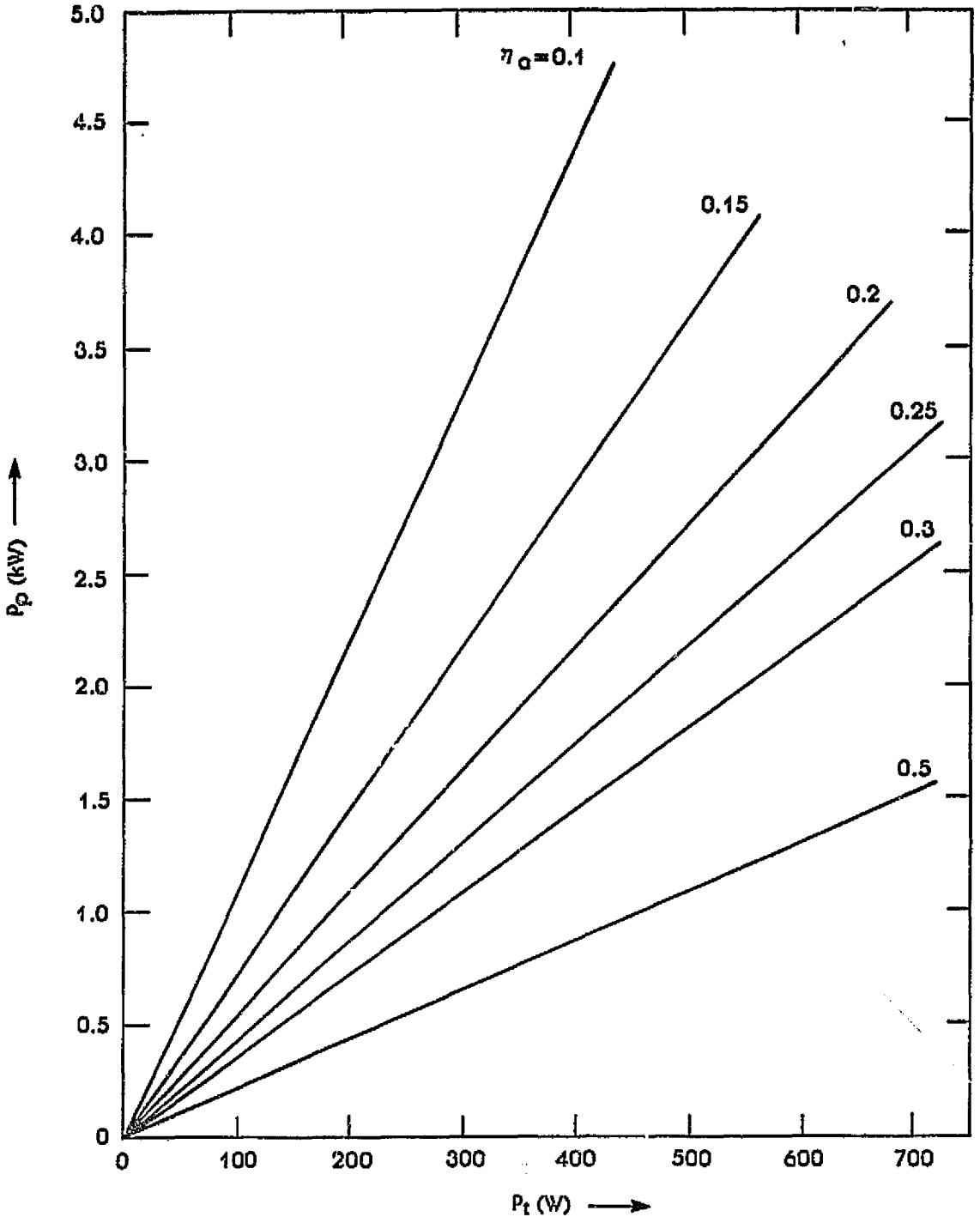

Figure 3-34. Prime Power vs Radiated Power With MMIC Efficiency as Parameter for Configurations A2 and B1

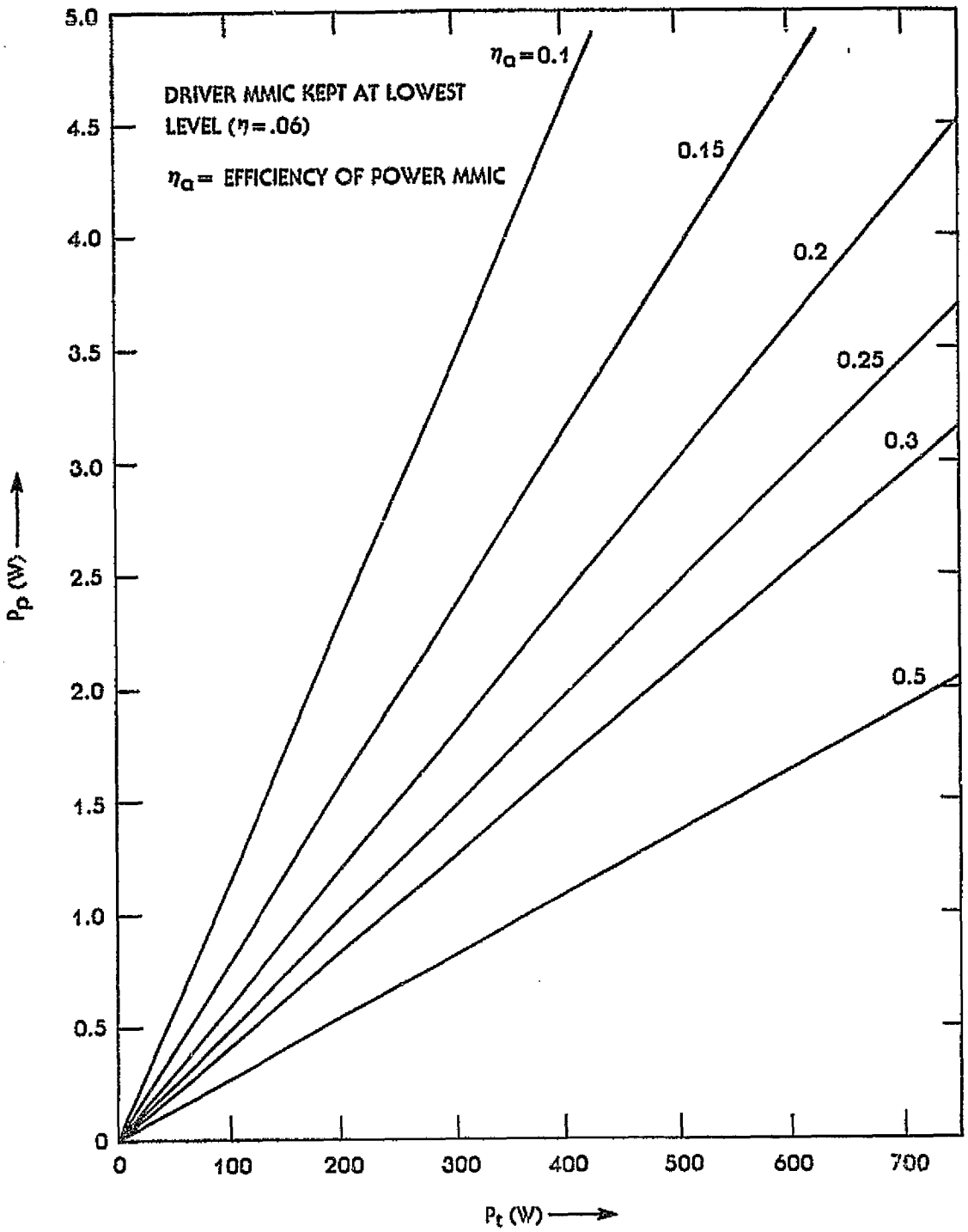

Figure 3-35. Prime Power vs Radiated Power With MMIC Efficiency as Parameter for Configuration C

In scanning beam Configuration B2, which is a single horn/beam-fed Cassegrain system, the desired e.i.r.p. is not achievable. Use of a larger cluster of seven horns per beam will only yield an additional 2.2-dB e.i.r.p./beam, since the outer ring of the cluster will be radiating less than the maximum output power of the MMIC module when a taper is introduced to achieve a low sidelobe level. Hence, a small gain in e.i.r.p. is achieved at the expense of a large increase in the number of elements. To cover the CONUS with a 0.3° beam maintaining a -3-dB overlap, an excessively large number of antenna elements is needed, yet the required e.i.r.p. may not be achieved.

The lens configuration F (Figure 3-29) was subsequently considered as an alternative to the Butler matrix feed, since space can be used to replace the complex BFN and reduce the network loss. An additional complication is that the number of antenna elements required for the lens is almost twice that needed in the Butler matrix configuration. The losses occurring in this configuration consist of waveguide and transition losses, which should be small assuming the periodic lens surface can be matched for all incident angles. Consequently, the overall efficiency of this configuration is better than that of the Butler configuration. The relevant parametric study curves for Configuration F are shown in Figures 3-36 and 3-37.

The directly radiating phased array, Configuration G, is essentially an enlarged version of the smaller phased array used as a feed for the near-field Gregorian system in other configurations. However, there are some basic differences. The total achievable efficiency of a directly radiating phased array can be made higher than that of a phased-array-fed Gregorian system where a maximum of 50 to 60 percent is possible. This is because, in practice, the directly radiating phased array will operate at efficiencies between 70 and 80 percent for sidelobe

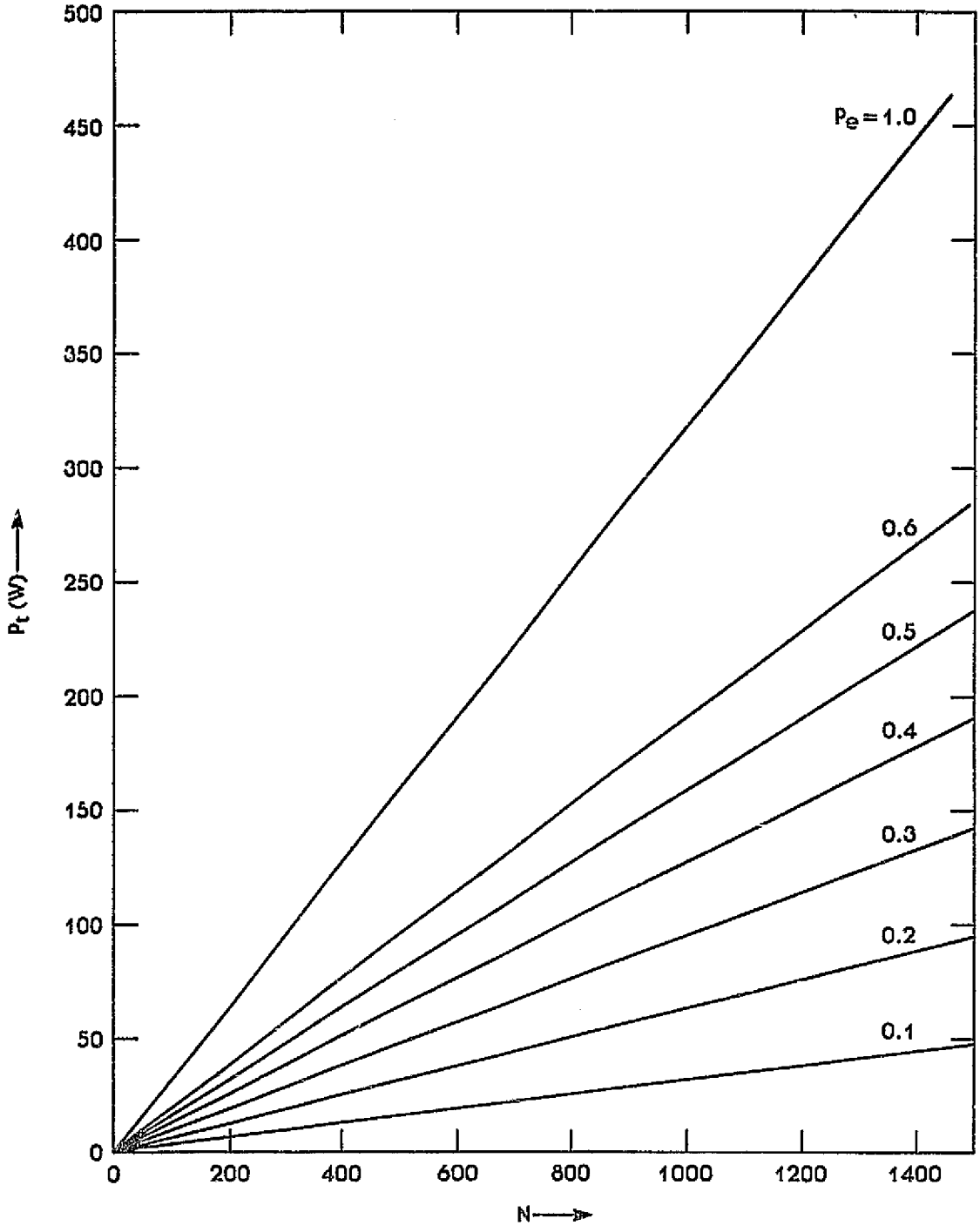

Figure 3-36. Power Radiated vs Number of Antenna Elements With Maximum MMIC Output Power as Parameter for Configuration F

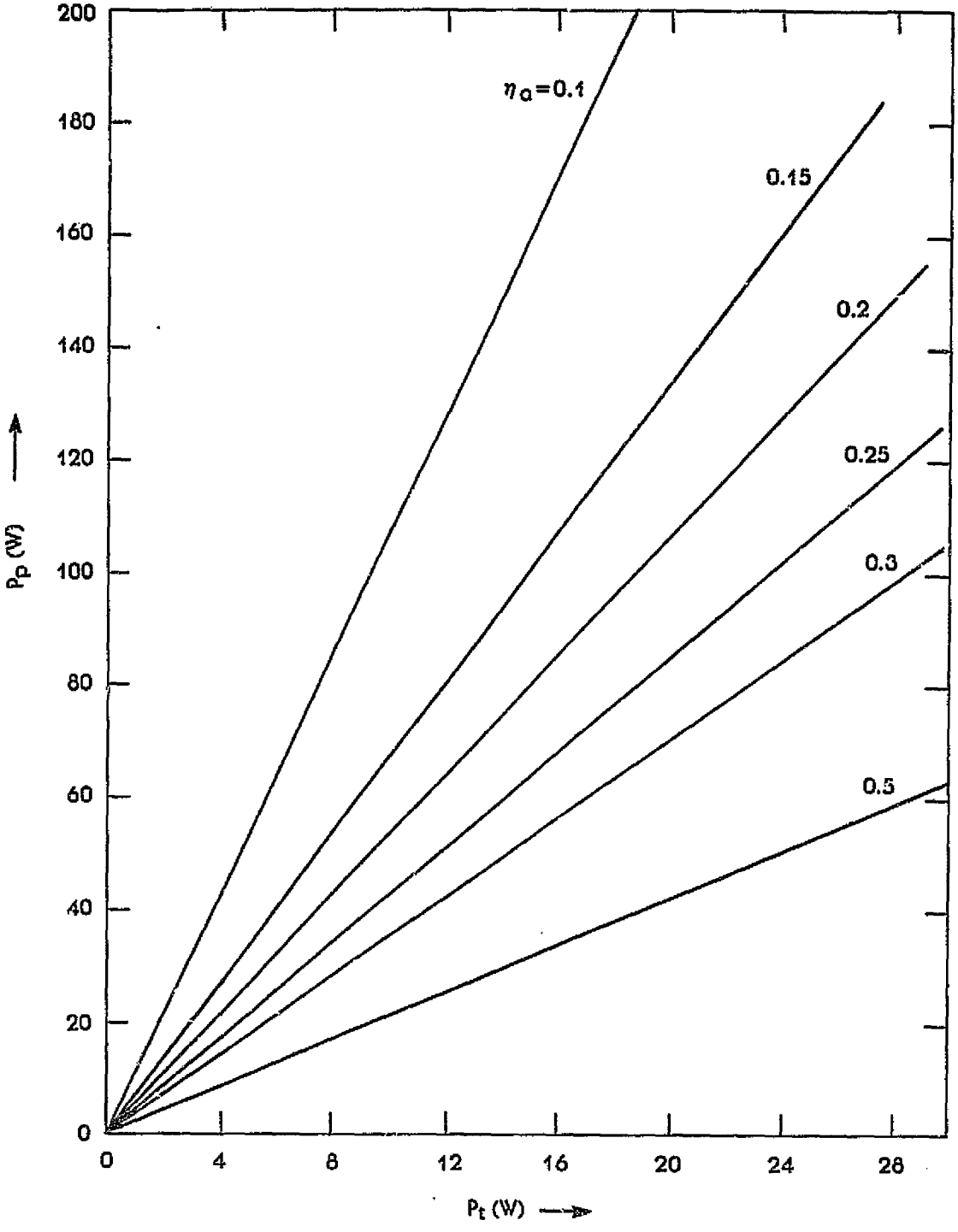

Figure 3-37. Prime Power vs Radiated Power With MMIC Efficiency as Parameter for Configuration F

control, but without the spillover losses associated with optical systems. Consequently, a directly radiating phased array of a size comparable to the main reflector of the Gregorian system will have a potential of up to 1 dB more gain. This means a reduction in the radiated power for the same e.i.r.p. Specifically, for the case under consideration, about 40 W/beam is required to achieve an e.i.r.p. of 70 dBW/beam. The number of antenna elements needed will also be less, but they will be larger. About 260 elements will be required if a directly radiating phased array is implemented in Configuration C. In turn, the prime power requirements are lowered to 1,850 W, while the overall efficiency remains about the same.

3.5.1.2 Fixed Beam BFNs

The starting point for this parametric study is the same as in the scanning beam case, that is, the achievable gain for a main reflector of given size. For uniformity throughout the discussion, the same value (53 dBi) will be used. This leads to the amount of radiated power, which is 2.5 W/beam for an e.i.r.p. of 57 dBW.

For Configuration D1, which uses a 9-way combiner, 125 antenna elements, arranged in a phased array configuration, are needed to radiate 2.5 W/beam in the 18-beam case. The prime power needed is 3,000 W, which makes this configuration highly inefficient (1.5 percent). Figures 3-38 and 3-39 depict the relevant parametric curves. The other possible approach is to use 7-horn clusters for each of the beams in a Cassegrain system. For this case, it is not possible to achieve the desired e.i.r.p. or to trim the beam pointing direction.

In Configuration E, a 9-horn cluster is used for each of 18 beams, also in a Cassegrain system. The desired e.i.r.p.

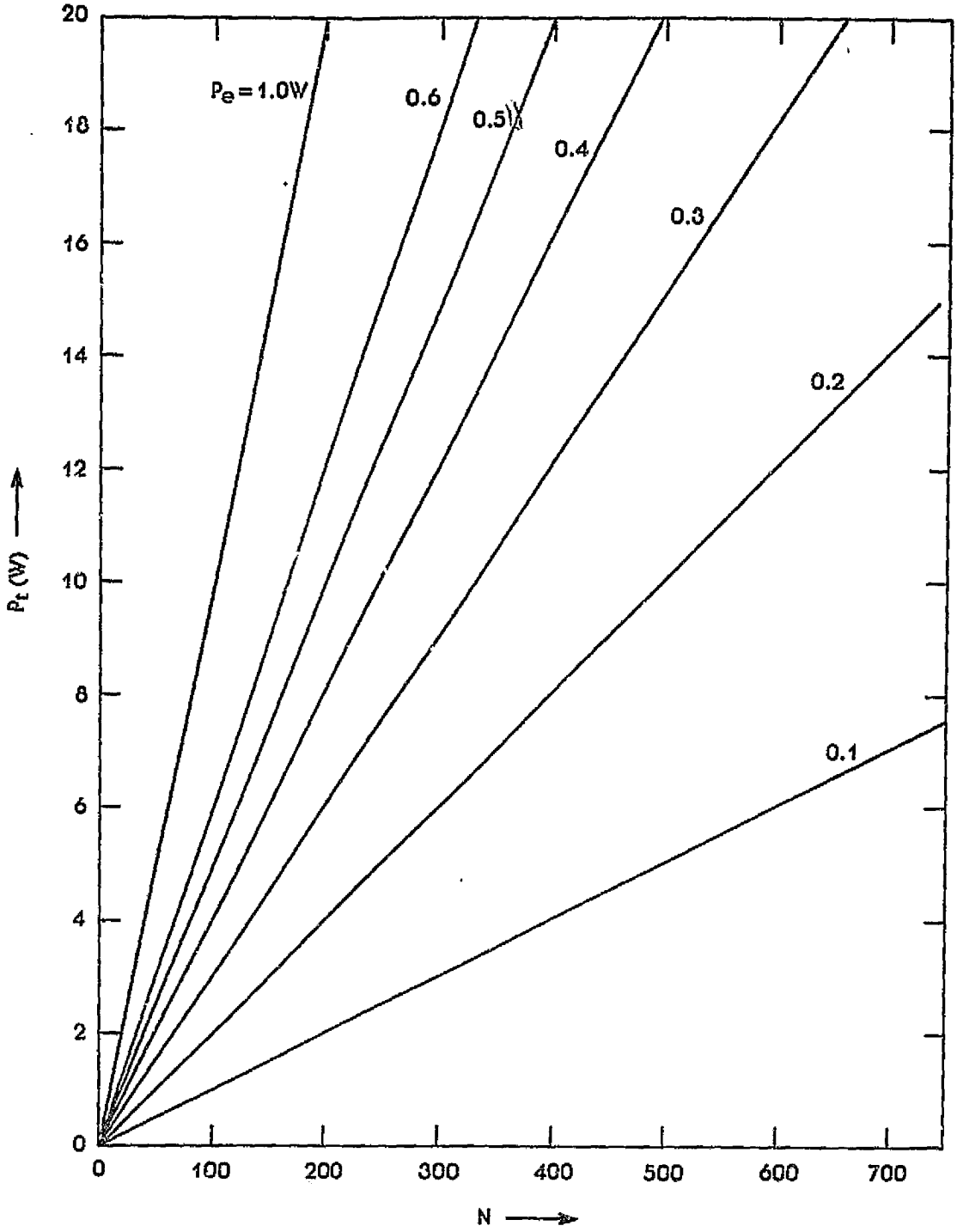

Figure 3-38. Radiated Power vs Number of Antenna Elements With Maximum MMIC Output Power as Parameter for Configuration D1

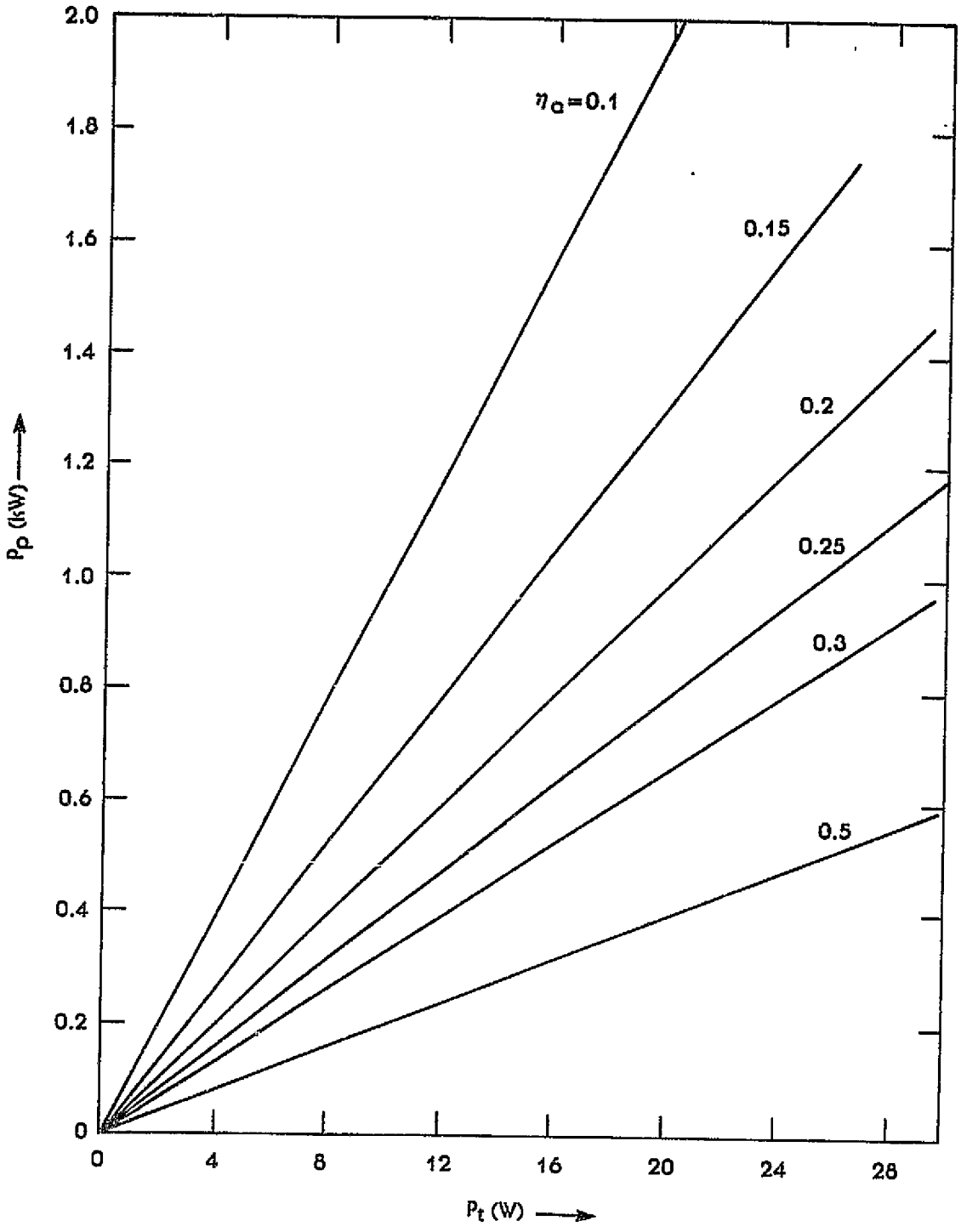

Figure 3-39. Prime Power vs Radiated Power With MMIC Efficiency as Parameter for Configuration D1

of 57 dBW is not achievable; however, it is possible to trim beam pointing direction, since additional antenna elements can be added to surround the 9-horn cluster.

Another possible fixed beam configuration uses the lens and 18 feed elements or clusters to create the 18 beams. This configuration appears to offer some promising features for both the fixed beam and possibly the scanning beam options.

3.5.1.3 Conclusions of Configuration Parametric Studies

All the relevant characteristics for each of the configurations and their variations for a specific e.i.r.p. requirement (70 dBW) and a given main reflector size (4.0 m) are listed in Table 3-7. Based on these numbers in the context of tradeoffs, it is easy to pinpoint the more energy-efficient configurations. It appears that for the scanning beam case, Configuration C the lens, and the directly radiating phased array would be potential candidates for further investigation. The lens and Configuration E represent potential candidates for the multiple fixed beam case.

3.5.2 PHASED ARRAY PARAMETRIC STUDIES

Parametric studies were also performed on the different aspects of the phased array. The upper and lower limits on the element spacing, and consequently the element size, were plotted for various magnification factors, M, and crossover levels. The limiting factors are the existence of grating lobes in the coverage region and the phase-shifter increment of the MMIC device. Studies were made of circular and square horn elements arranged in rectangular and triangular lattices. Also, the number of

Table 3-7. Comparison of the 10 Configurations

Characteristic	Multiple Scanning Beams							Multiple Fixed Beams		
	A1 Combiner	A2 Interleave	B1 Butler Matrix	B2 1-Horn Feed	C Combiner	F Lens	G[a] Phased Array	D1 Combiner	D2 7-Horn Cluster	E 9-Horn Cluster
Desired e.i.r.p. (dBW)	70	70	70	Not possible[b] 50 achievable	70	70	70	57	Not possible[b] 48.2 achievable	Not possible[b] 52.4 achievable
Available Gain (dB) (13 ft. Dia., η = 0.6)	53	48.23	53	53	53	53	>53	53	53	53
Radiated Power per beam (W)	50.1	150.3	50.1	0.5	50.1	50.1	<50.1	2.51	0.34	0.87
Optics	Gregorian	Gregorian	Gregorian	Cassegrain	Gregorian	Gregorian	NA	Grogorian	Cassegrain	Cassegrain
No. of Antenna Elements	825	2475	325	400 (for 400 beam positions)	325	630	<325	125	126	288
Equivalent[c] Element Spacing (Triangular)(λ)	7.5 in both planes	13 in one plane, 8.6 in the other	12 in both planes	1	12 in both planes	12.6 in both planes	>12 in both planes	19 in both planes	1	1
Equivalent[d] Element Size, d(λ)	7.5	4.3	12	1	12	12.6	>12	19	1	1
Beamwidth (deg)	0.3°, pencil	>0.3°, not pencil	0.3°, pencil	0.3°, pencil	0.3°, pencil	0.3°, pencil	0.3°, pencil	0.3°, pencil	0.3°, pencil	0.3°, pencil
Element Periodicity	Triangular d/2 offset	Triangular 3d/2 offset	Triangular d/2 offset	NA	Triangular d/2 offset	Triangular d/2 offset	Triangular d/2 offset	Triangular d/2 offset	NA	NA
Grating Lobes in FOV	No	Yes, not avoidable	Yes[e], but avoidable	NA	Yes[e], but avoidable	Yes[e], but avoidable	Yes[e], but avoidable	Yes[e], but avoidable	NA	NA
Mutual Coupling (adjacent element) (dB)	-18	-15	-20	NA	-20	-21	-20	-16	NA	NA
Maximum Output Power per MMIC (W)	0.2	0.2	0.5	0.5	0.5	0.5	0.5	0.2	0.2	0.5
MMIC Efficiency	0.15	0.15	0.15	0.15	0.15	0.15	0.15	0.15	0.15	0.15
Total Prime Power (W)	6,600	6,600	2,250	40	2,330	2,100	<2,330	3,000	175	6,460

Table 3-7. Comparison of the 10 Configurations (Cont'd)

Characteristic	Multiple Scanning Beams							Multiple Fixed Beams		
	A1 Combiner	A2 Interleave	B1 Butler Matrix	B2 1-Horn Feed	C Combiner	F Lens	G[a] Phased Array	D1 Combiner	D2 7-Horn Cluster	E 9-Horn Cluster
Heat Dissipation (W)										
MMIC	5,610	5,610	1,841.7	37	1,993.4	1,785	<1,993.4	2,550	162	6,424
Combiner	660	--	--	--	6.5	--	<6.5	400	--	--
OMT and Waveguide	29.4	88.2	107.7	--	29.5	14.4	<29.5	4.4	7	20
No. of MMICs	4,950	4,950	650	400	2,600	630		2,250	126	288
No. of Combiners	1,650	NA	NA	NA	650	NA	NA	250	NA	NA
No. of OMTs	825	2,475	325	NA	325	NA		125	NA	NA
PDN Size (Loss) (0.7 dB/Level)	1 x 825 (7 dB)	1 x 825 (7 dB)	1 x 325 (6 dB)	NA	1 x 325 (6 dB)	Switch matrix 1 x No. of beam positions	Smaller than 1 x 325	1 x 125 (5 dB)	1 x 7	1.9
No. of PDNs	6	6	2	NA	6	1	6	18	1	1
Complexity of Network	Simple	Very Complex	Involved	Simple	Simple	Simple	Simple	Simple	Simple	Simple
Overall Efficiency (%)	4.5	13.5	13.5	~15	13	14.3	≥13.5	1.5	3.0	0.2[f]

[a]The values for various parameters are listed as ≥ or ≤ because the aperture efficiency obtained from a directly radiating phased array can be up to 100 percent. Consequently, the gain is higher and radiated power is less (see text).
[b]It is not possible to achieve the required e.i.r.p. without making the number of antenna elements unmanageably large and the system inefficient. The e.i.r.p.s listed are those achievable by normal feed clusters.
[c]Equivalent element spacing is the spacing in the main aperture (reflector) for Gregorian systems. The actual spacing is 1/M times this, where M is the magnification. For Cassegrainian systems, the actual spacing is given.
[d]Equivalent element size is the size in the main aperture for Gregorian systems. The actual size is 1/M times this. For Cassegrainian systems, the actual size is given.
[e]The grating lobes exist in FOV with this spacing, but can be avoided by reducing the spacing between elements. This requires that the number of antenna elements be increased to use the total available aperture. These additional surrounding elements can be excited with lower power levels, thereby having an amplitude taper on the aperture. This will increase the prime power requirements, but only nominally.
[f]The efficiency is low because additional antenna elements are needed to surround the cluster so that the beam pointing direction can be adjusted. The amplifiers feeding these additional elements must be kept on at all times. These dissipate 50 mW at the lowest 'on' level. If beam pointing direction requirements are not necessary, then these additional elements are not needed. This increases the efficiency to 11.3 percent and reduces prime power requirements to 140 W.

scanning steps, or component beams, in the coverage region for the two lattices was determined for different crossover levels. The beamwidth for different beam levels was plotted versus the main reflector diameter for different aperture distributions.

3.5.2.1 Upper Bounds on Element Spacings

The upper limit on the element spacing in the array is determined by the existence of grating lobes in the coverage region for all scanning positions. The relationship between the maximum, d/λ, and the scanning range, $\pm\theta_s$, is

$$d/\lambda \leq \frac{1}{2 \sin (M\theta_s)} \qquad (3\text{-}11)$$

For the CONUS coverage region, $\theta_s = 3.5°$ in azimuth and $\theta_s = 1.6°$ in elevation. Figure 3-40 shows the maximum element spacing in both azimuth and elevation for different magnification factors, M.

3.5.2.2 Lower Bounds on Element Spacings

The lower bound on the element spacing in the array depends on the far-field beamwidth and the phase shifter increment. It also depends on the array lattice shape and, for a triangular lattice, on the array element shape.

To cover the whole region with beams of a certain level below the peak, the individual beams must have an overlapping ratio, K, which depends on the array configuration and element type. For the same phase-shifter increment, the smaller the overlapping ratio, the larger the element spacing must be. For a rectangular lattice, K takes the value of 0.707 for any element shape, as follows:

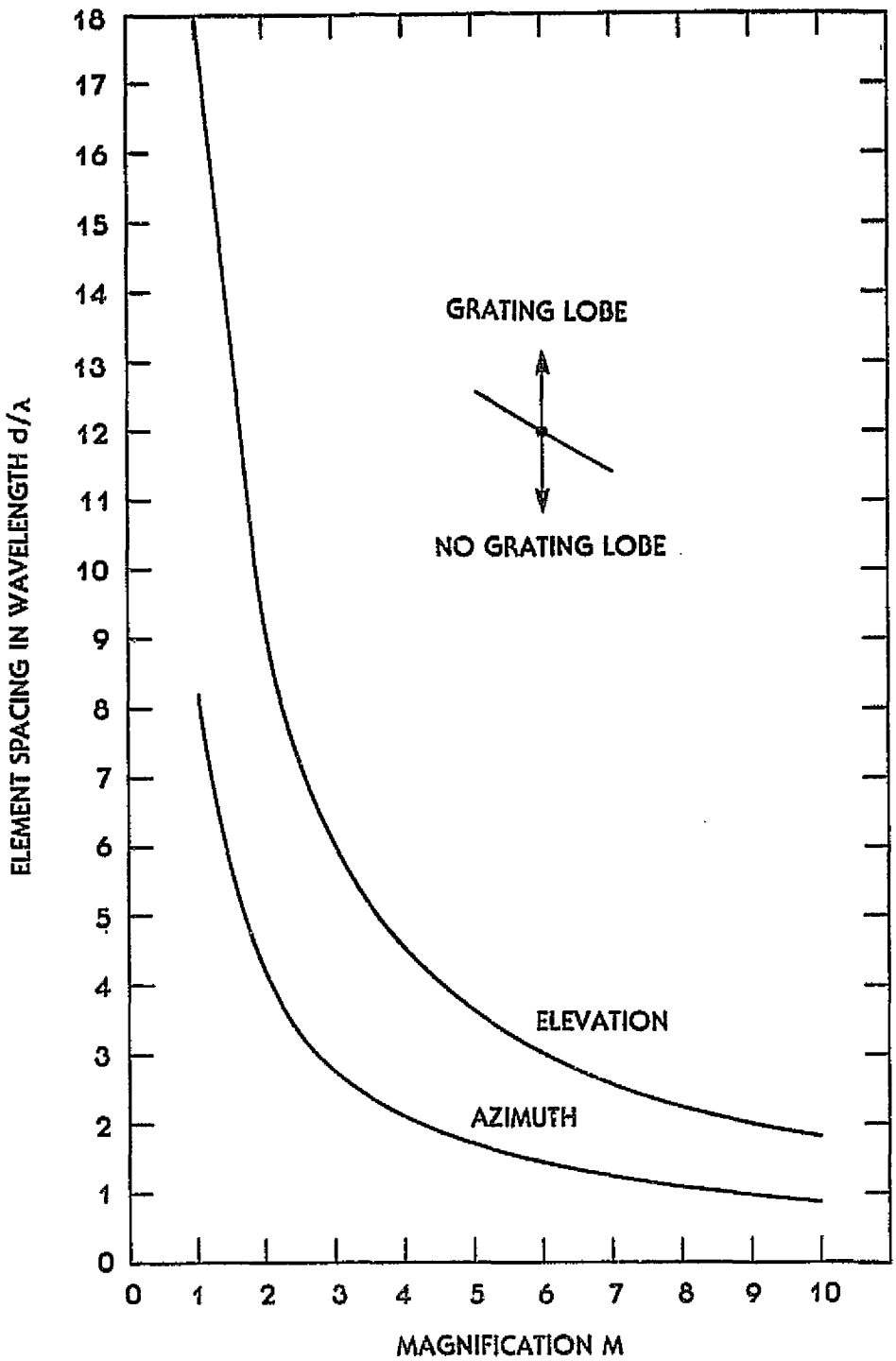

Figure 3-40. Element Spacing vs Magnification for Grating Lobe Criteria Within FOV

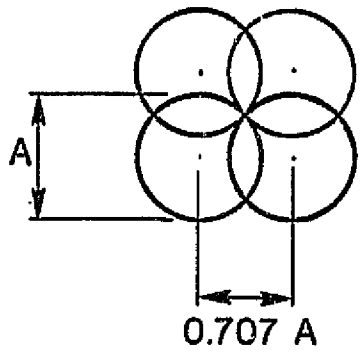

Figure 3-41 plots the minimum element spacing for various phase shifter increments to achieve a K = 0.707.

For a triangular lattice with circular horns, the overlapping ratio differs in azimuth and elevation, as follows:

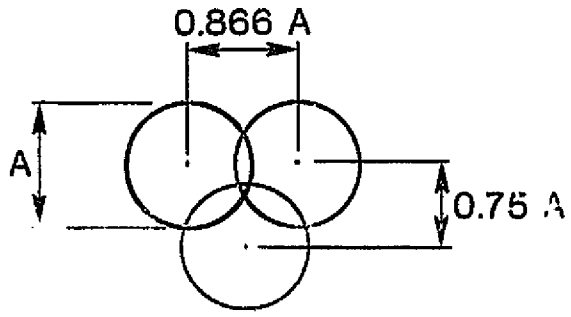

This gives freedom in orienting the array such that the dimension with a larger overlapping ratio is in the direction with wider scanning. Figure 3-42 plots the minimum element spacing for various phase shift bits based on K = 0.75. Figure 3-43 is a plot for a triangular lattice of circular horns in the overlapping direction of K = 0.866.

The triangular lattice with square horns produces the same overlapping ratio (K = 0.8) in both azimuth and elevation, as follows:

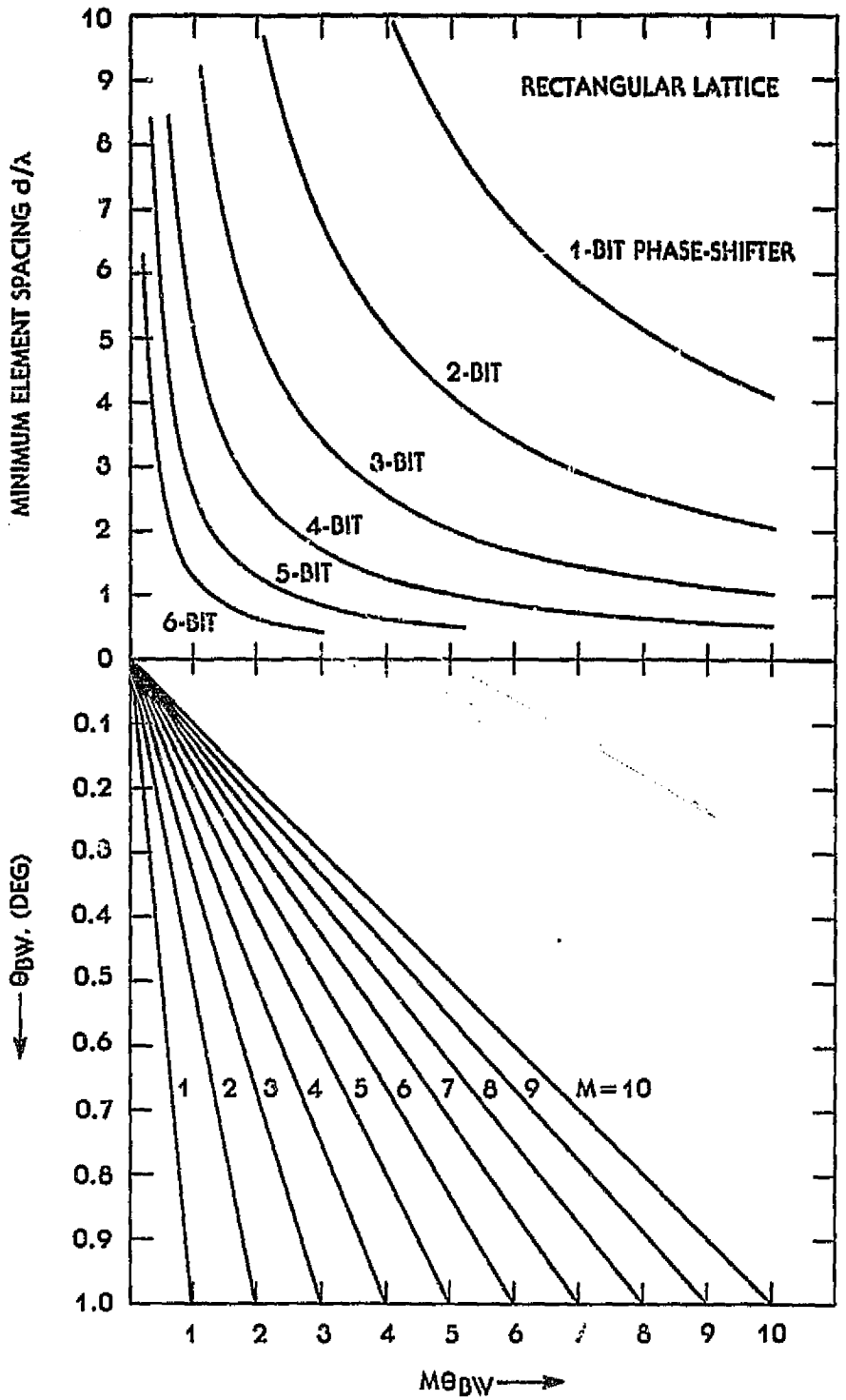

Figure 3-41. Minimum Element Spacing vs Beamwidth With Phase-Shifter Bits as Parameter-- Rectangular Lattice

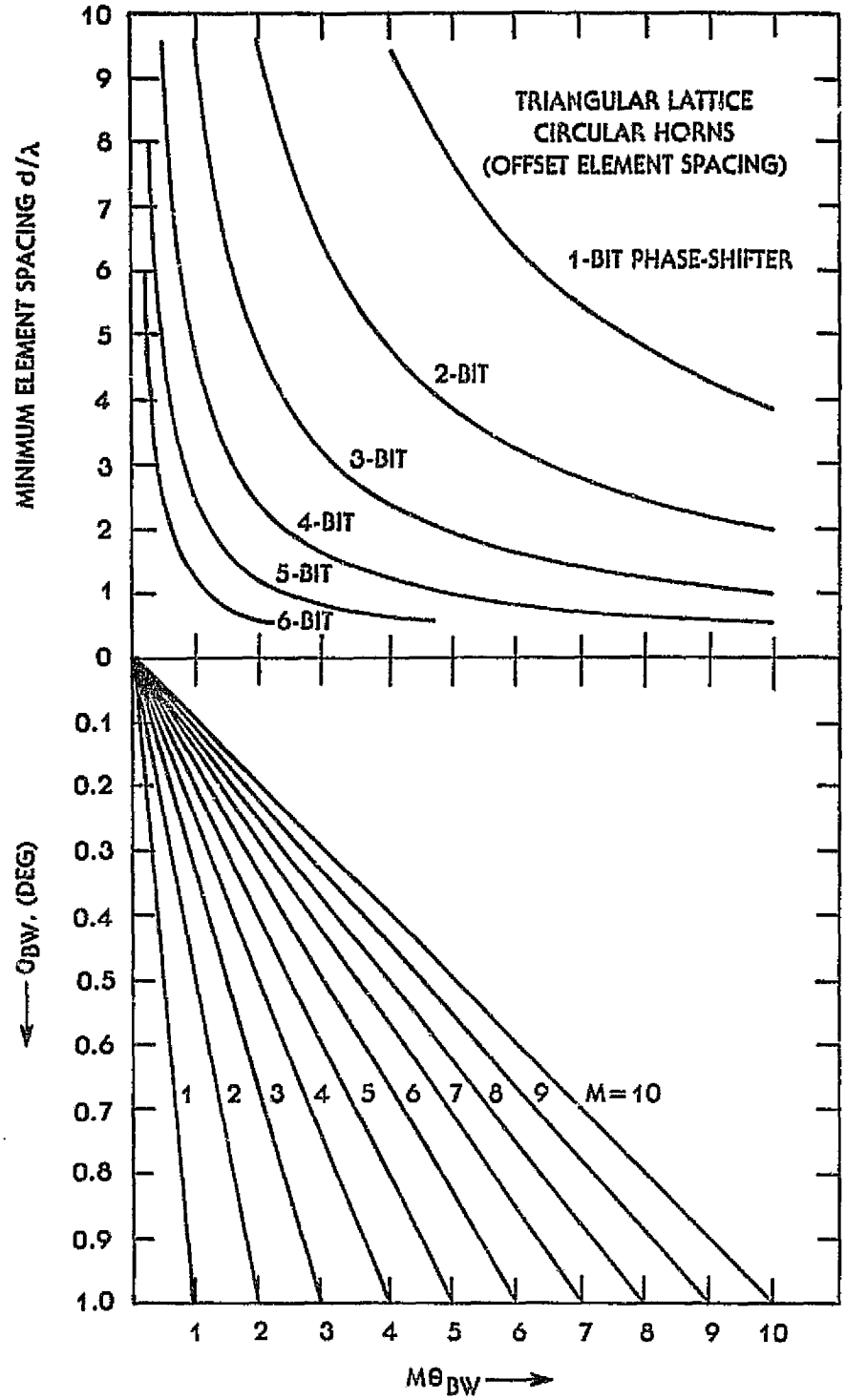

Figure 3-42. Minimum Offset Element Spacing vs Beamwidth With Phase-Shifter Bits as Parameter--Triangular Lattice of Circular Apertures

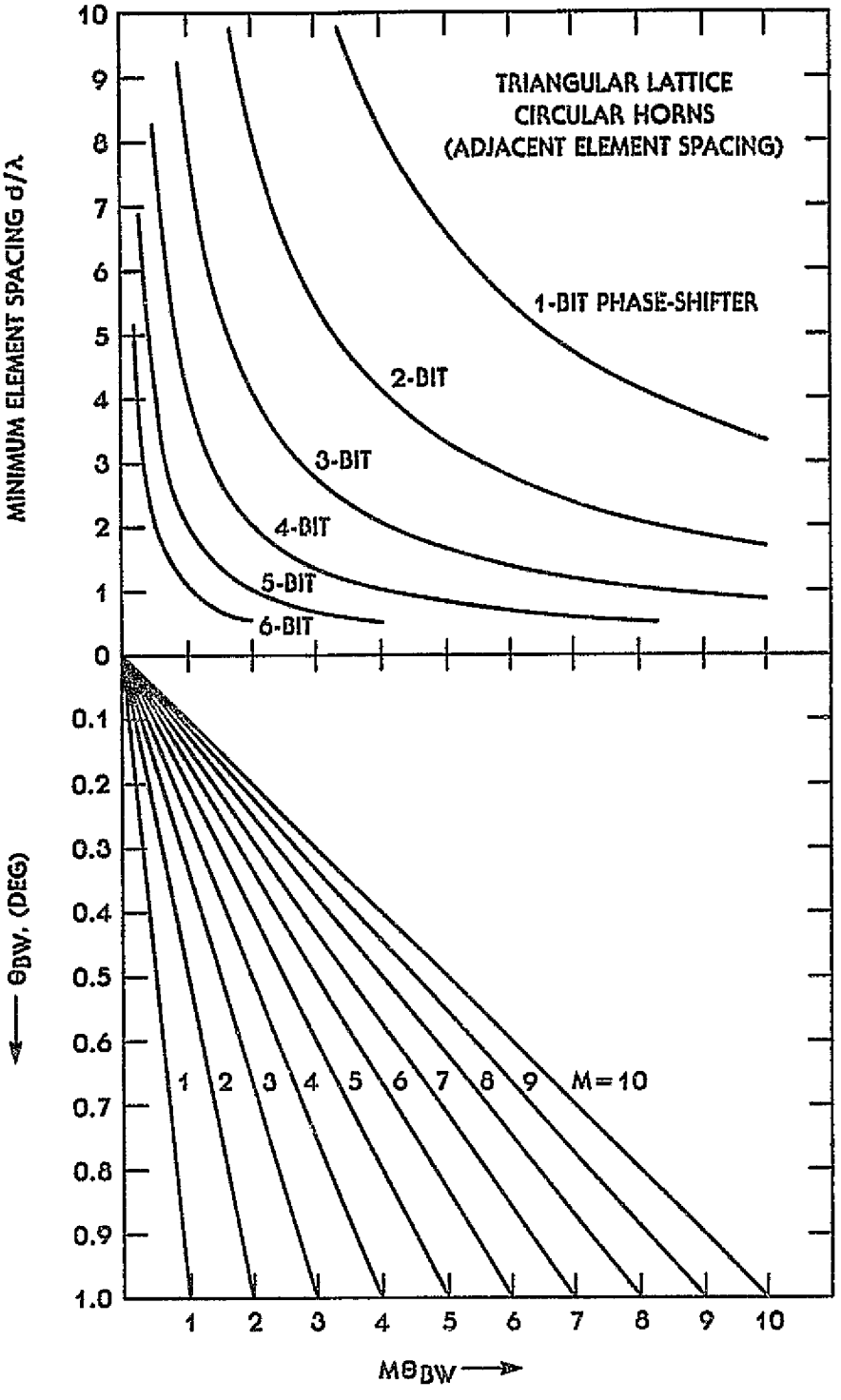

Figure 3-43. Minimum Adjacent Element Spacing vs Beamwidth With Phase-Shifter Bits as Parameter--Triangular Lattice of Circular Apertures

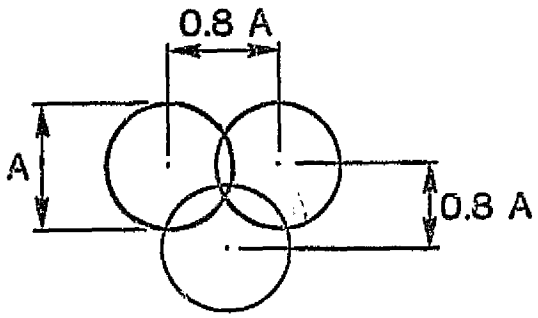

This results in an overall smaller element spacing than the rectangular lattice and more uniform scanning steps than the triangular lattice with circular horns. The minimum element spacing for a triangular lattice of square horns is presented in Figure 3-44.

For the CONUS coverage region, the number of component beams, or scanning steps, depends on the array lattice for a specific beamwidth. The triangular lattice offers a smaller number of scanning steps, as depicted in Figure 3-45.

The beamwidth in the far field is a function of the reflector diameter and the edge taper. The direct relationship between the beamwidth, for a specific beam level and the reflector diameter, D, is determined through the ratio D/λ. This, in turn, is a function of the frequency. The 10-dB edge taper represents a typical value for obtaining efficient illumination of the reflector. Based on this edge taper, Figure 3-46 plots the various beamwidth sizes as a function of D/λ.

A 0-dB edge taper indicates uniform illumination of the reflector. This represents a lower limit on the beamwidth that can be produced by using a specific aperture diameter. Figure 3-47 plots the minimum beamwidths achievable as a function of D/λ.

Figures 3-46 and 3-47 can be used to determine the range of total beam positions for a specific D/λ in the main aperture.

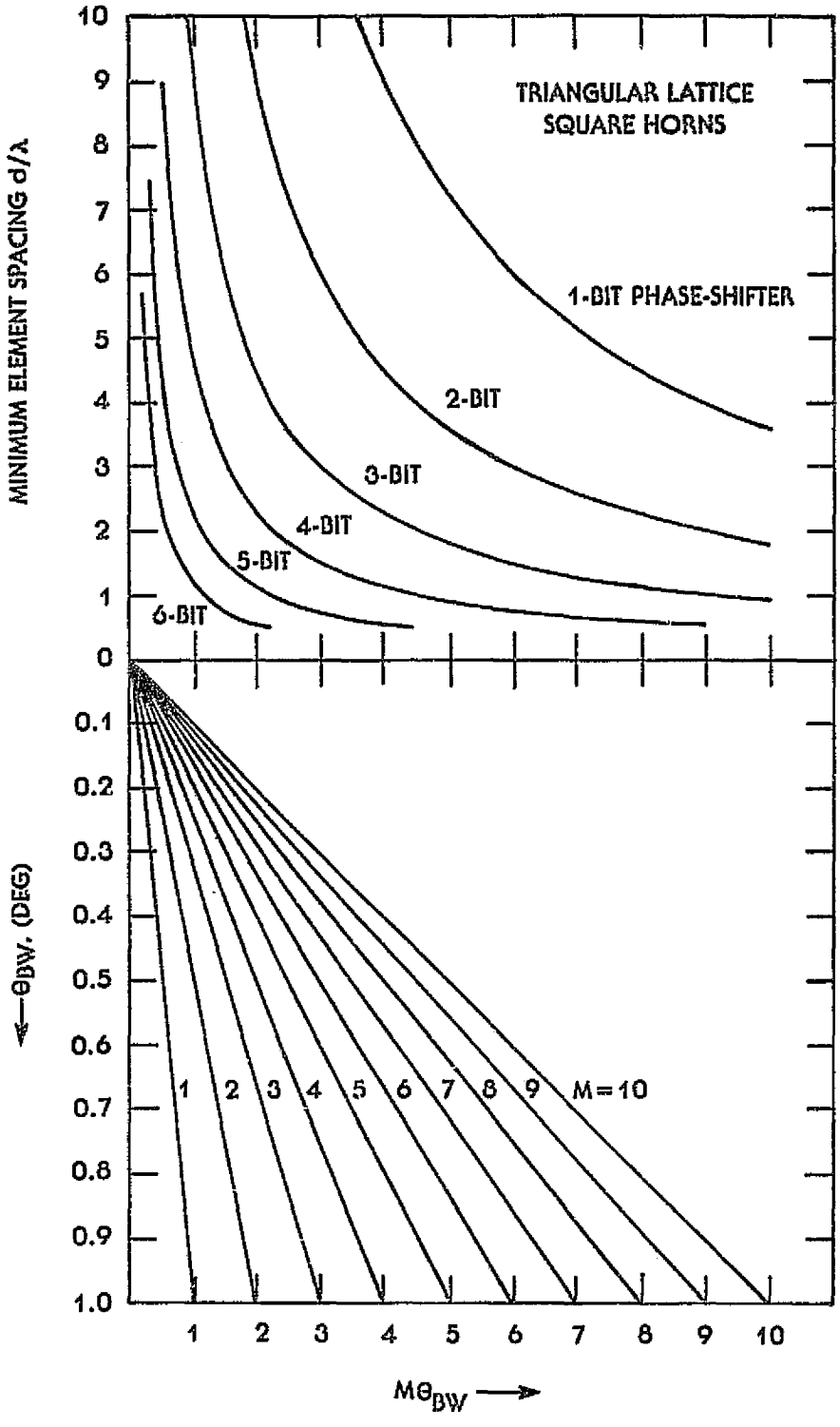

Figure 3-44. Minimum Element Spacing vs Beamwidth With Phase-Shifter Bits as Parameter--Triangular Lattice of Square Apertures

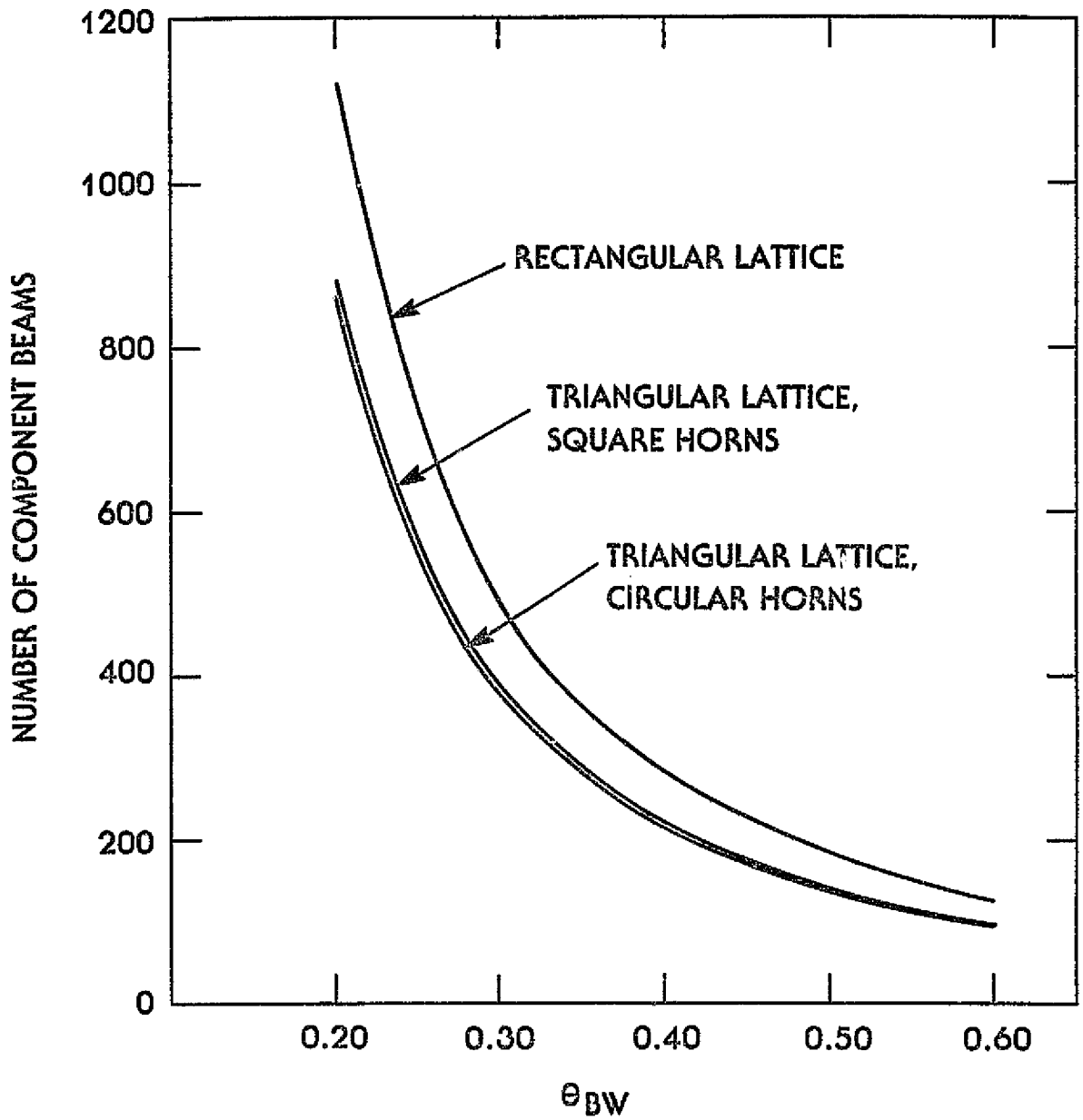

Figure 3-45. Number of Component Beams for CONUS Coverage vs Beamwidth for Different Lattices

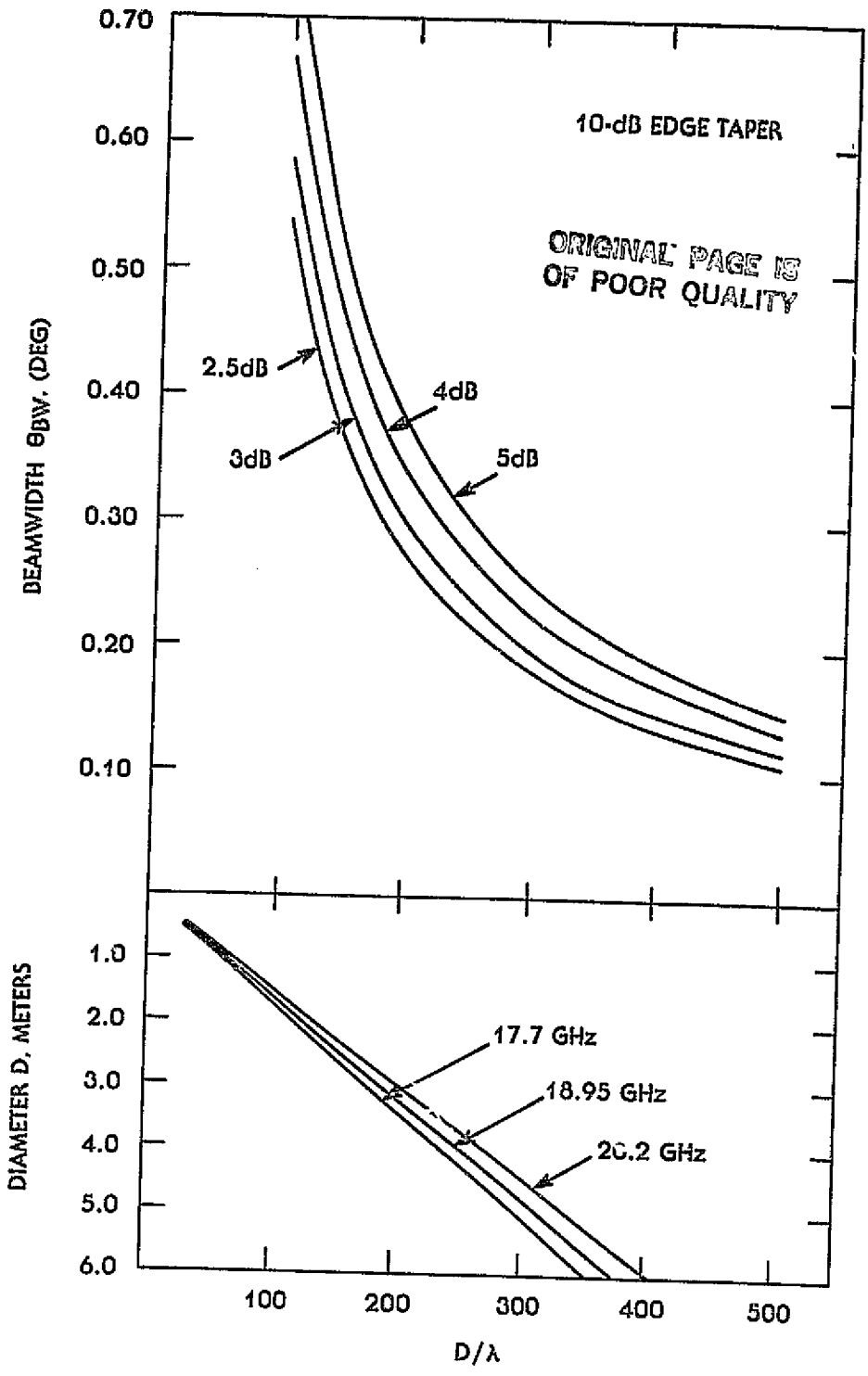

Figure 3-46. Beamwidth vs Main Reflector Diameter With Beam Level as Parameter-- 10-dB Edge Taper

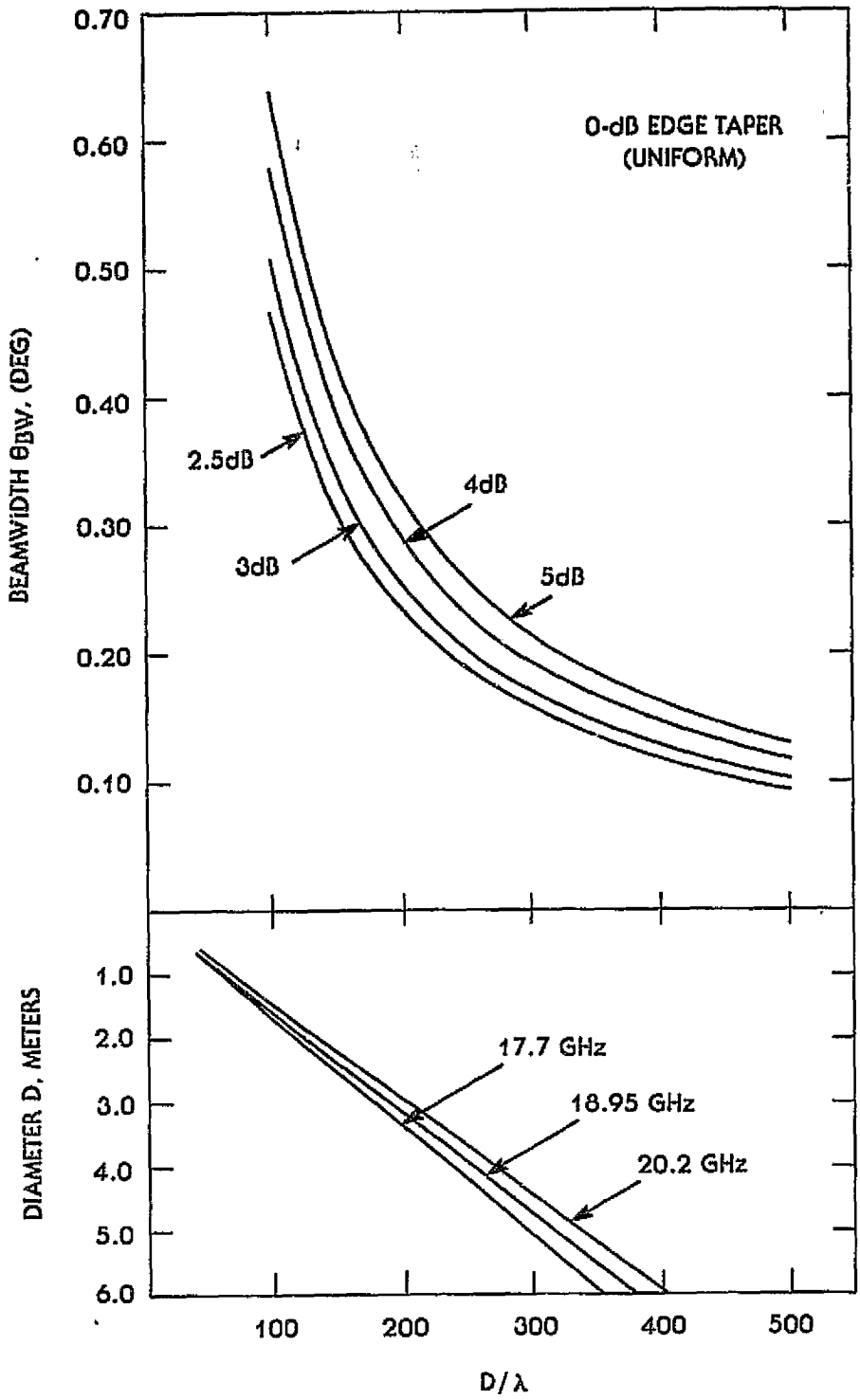

Figure 3-47. Beamwidth vs Main Reflector Diameter With Beam Level as Parameter-- 0-dB Edge Taper

3.5.3 REFLECTOR OPTICS PARAMETRIC STUDIES

3.5.3.1 Confocal Reflectors

To investigate the effect of F/D_p of the main reflector on the performance of the confocal system, two F/D_p values (0.3 and 0.5) are chosen. The size of the main reflector aperture is fixed at D = 271.3 cm (106.8 in.). The focal lengths are 242.6 cm (95.526 in.) and 404.4 cm (159.2 in.), respectively, for these two cases. Since the feed array may consist of thousands of elements, it is not practical to model this array precisely on the computer because of the large amount of CPU time required. In this study, the phased array is modeled by a point source at infinity which has a restricted angular range corresponding to the phased array scan range.

The maximum far-field scan angles are set at $\pm 4°$. Thus, the maximum scan angles for the array are $\pm 4°$ times the magnification factor, M. Subreflector size is determined by the maximum array scan angle, the main reflector size, the magnification factor, and the array position chosen at the conjugate point of the main reflector center.

For each magnification value ranging from 2 to 5, nine beams were generated with scan angles from -4° to 4° in the azimuth, elevation, and diagonal plane, respectively. From this pattern data, curves relating scan loss and sidelobe levels vs scan angles are obtained and given in Figures 3-48 and 3-49. Other parameters, such as array position and offset angles of the reflector, have been investigated and are discussed in greater detail in Section 4. The figures verify that, in this optical configuration, scan losses increase with increased megnification, M, and reduced F/D_p ratios.

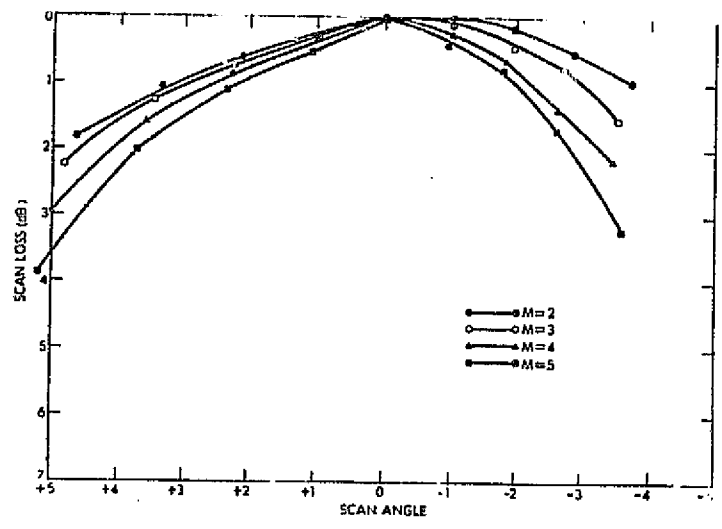

a. $F/D_p = 0.3$

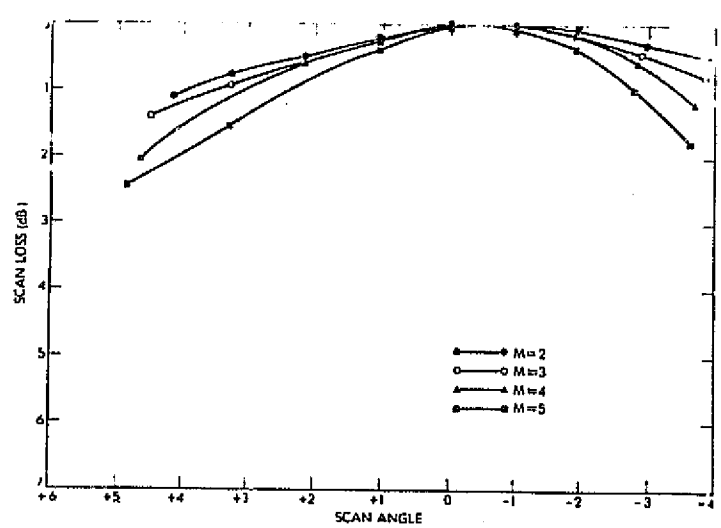

b. $F/D_p = 0.5$

Figure 3-48. Scan Loss vs Scan Angle for Confocal Systems

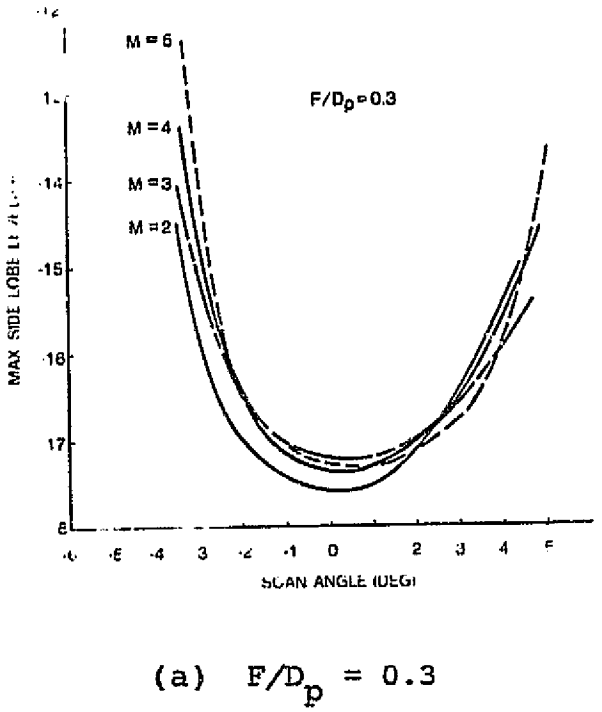

(a) $F/D_p = 0.3$

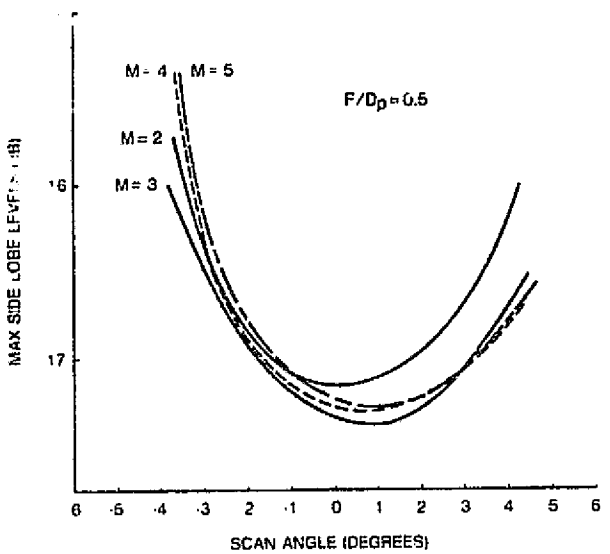

(b) $F/D_p = 0.5$

Figure 3-49. Sidelobe Level vs Scan Angle for Confocal Systems

3.5.3.2 Cassegrain Systems

The main reflector used in this study has a circular aperture size of 271.3 cm (106.8 in.) and an offset height of 142.5 cm (56.12 in.). The focal length for this reflector is 335.3 cm (132 in.). The tradeoff study concentrates on the subreflector and feed parameters. The subreflector parameters include the subreflector size, D, and the focal length. The ratio of the main reflector focal length, F_1, to the subreflector focal length, F_2, is the magnification factor, M. The five subreflector geometries considered in the parametric study are listed in Table 3-8. The magnification factor ranges from 1.5 to 3, and the subreflector sizes are determined for a maximum scan of $\pm 3.5°$. The feeds of these systems are located at the optimum feed locus developed by Krichevsky at COMSAT Laboratories [3-3].

Figure 3-50 shows the scan curves for these five systems. It can be seen that the system with a small magnification has less scan loss. Also, as shown in Figure 3-51, the peak gain from a small-M system is higher. However, the horn spacing between two adjacent beams with fixed crossover level is smaller for a small magnification system. The tradeoff study also includes the blockage caused by the subreflector. As listed in Table 3-8, the subreflector is smaller for larger M. In fact, the clearance angle of the system for M = 1.8 is 3.49°, which is the marginal angle for the CONUS coverage. Parametric tradeoff data for the horn design will be detailed in Section 4.

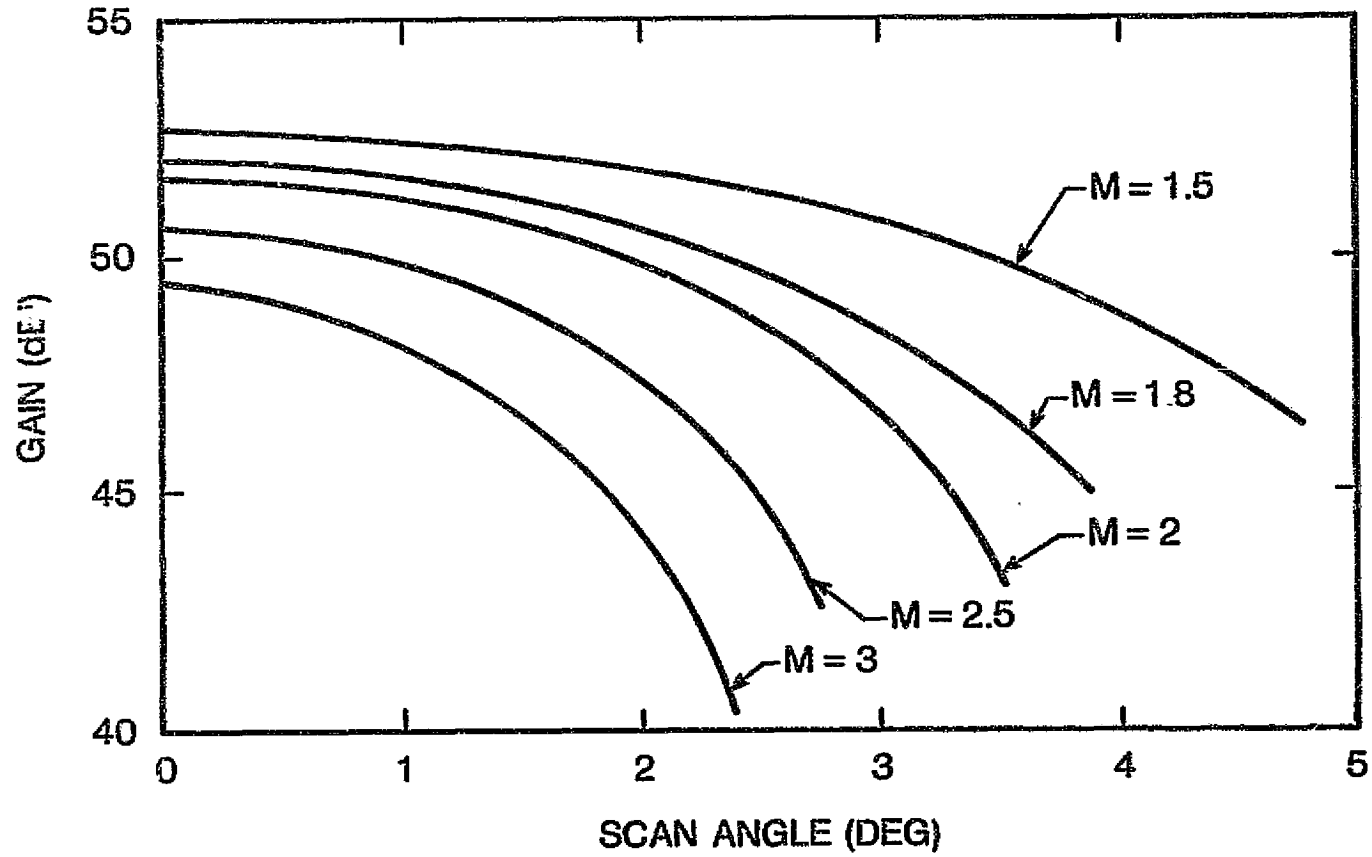

Figure 3-50. Scan Curves of Cassegrain Antenna Systems

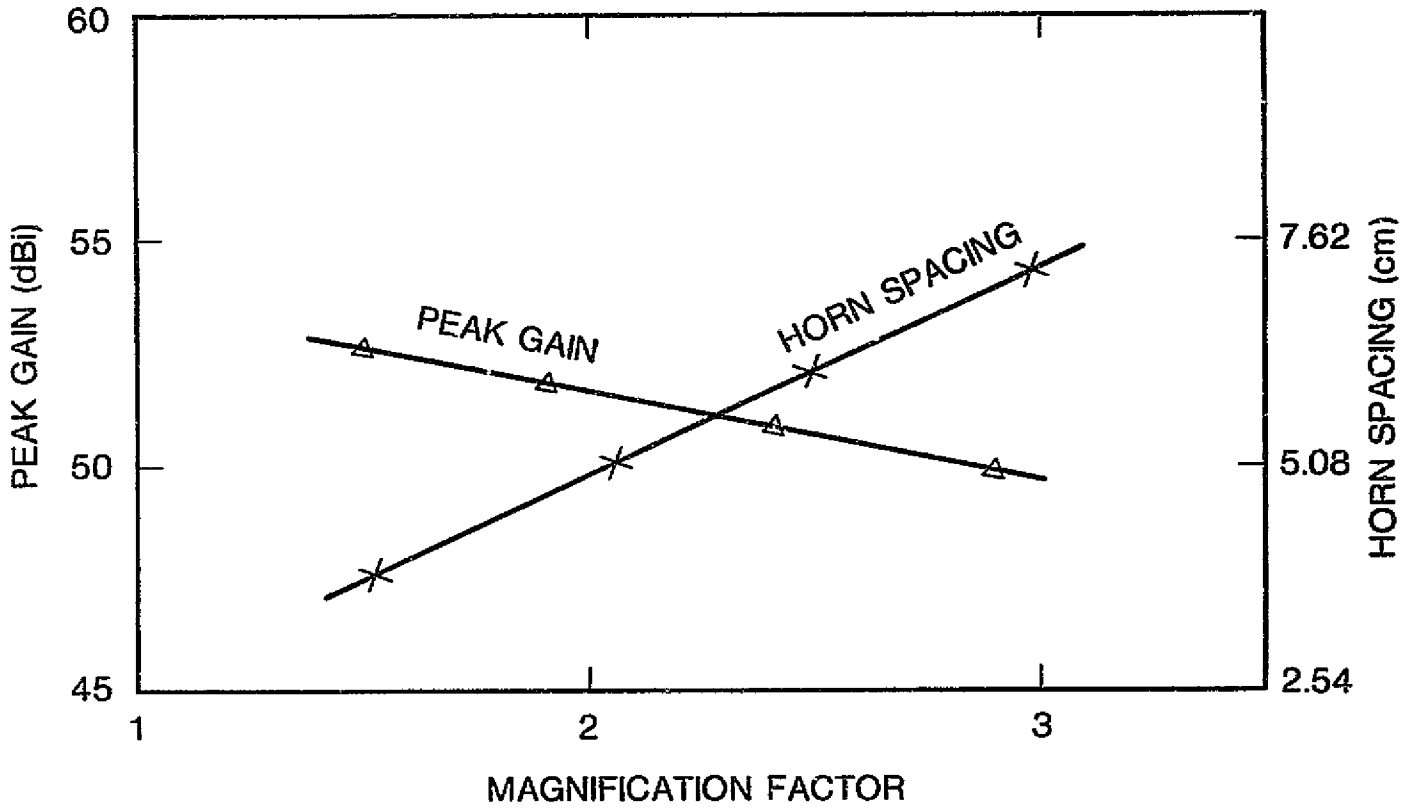

Figure 3-51. Peak Gain and Horn Spacing vs Magnification Factor

Table 3-8. Comparison of Cassegrain Systems

M (cm)	F_1 (cm)	F_2 (cm)	D_1 (cm)
1.5	106.7	71.1	136.1
1.8	114.3	63.5	120.7
2	118.4	59.2	113.5
2.5	127.0	50.8	100.6
3	133.4	44.5	91.9

3.6 RECOMMENDED DESIGNS

The preceding discussions have addressed a number of configurations and some of the important parameters that are required to assess the feasibility of each multiple scanning beam and multiple fixed beam design. Based on these data, COMSAT selected two fixed beam and two scanning beam configurations for the in-depth analysis reported in Section 4.

As discussed, the integration of the phase shifter and amplifier into the VPS module leads to a dilemma in certain configurations. For the design presented in Section 4, COMSAT and NASA agreed that improved performance could be achieved in many of the configurations if the phase shifter and amplifier sections were split. Thus, inefficient designs such as Configurations A1 and D1 could become competitive with the more efficient configurations.

For separate 5-bit phase shifter module and a 0.2-W amplifier module, four configurations were recommended by COMSAT and approved by NASA for further study.

The multiple scanning beam designs chosen were as follows:

a. Configuration C (Figure 3-25), with the provision that the variable gain 0.2-W amplifier preceding the combiner be removed. This configuration employs a 0.5-W variable-gain amplifier and a 5-bit phase shifter.

b. Configuration F, the Lens (Figure 3-29), which uses only a 0.5-W variable-gain amplifier. This design can also be used for multiple fixed beams by removing the dynamic switch matrix and using a fixed number of horns or clusters of horns.

The following multiple fixed beam designs were selected:

a. Configuration D1 (Figure 3-26), with the provision that the amplifier be placed after the 9-way combiner. The configuration then uses a 0.2-W fixed gain amplifier and a 5-bit phase shifter.

b. Configuration E (Figure 3-28), which uses only the 0.5-W variable gain amplifier. This is the only configuration that employs a focal-region-fed optical system.

4. REFINED SYSTEM DESIGN

4.1 INTRODUCTION

Task III of this project dealt with refining the designs of the configurations selected for the scanning beam and multiple fixed-beam systems. As a result of the parametric studies, two designs offered definite advantages for the multiple scanning-beam system: Configuration C, a phased-array-fed confocal paraboloid system; and Configuration F, a lens-fed confocal paraboloid system. For the multiple fixed-beam option, three designs were selected for detailed study: Configuration D1, a a phased-array-fed confocal paraboloid system; Configuration E, a focal-region-fed Cassegrain system; and Configuration F, a lens-fed confocal paraboloid system.

This section presents a detailed analysis of each of these configurations. The optical properties of the confocal paraboloid and the Cassegrain system are studied, and the parameters involved in the element design and array design of the phased array are discussed. To select an optimum scanning performance, two lens designs are considered, bifocal and quadrufocal. To obtain the far-field patterns of the different phased-array designs, the near-field performance of the array must be evaluated. An efficient method of calculating the near field of the array at the subreflector and transferring the results of that calculation into the far field of the confocal paraboloid system is also presented. The far-field patterns of all selected configurations are calculated and assessed.

4.2 FINAL DESIGN CONSIDERATIONS

Two reflector systems are proposed that will generate scanning spot beams and fixed spot beams. An offset near-field Gregorian reflector system with a phased array or lens feed is designed for beam scanning, and an offset Cassegrain system is used to form spot beams for the 18 cities. The design procedures for these two systems will be discussed in detail in the subsections that follow. Numerical data resulting from computer modeling of the antennas are presented to demonstrate that the antennas are capable of meeting the requirements in the critical coverage areas, thus validating the design concepts for the reflector system.

4.2.1 NEAR-FIELD GREGORIAN SYSTEM

For a scanning-beam TDMA satellite application, phased arrays seem attractive because they can provide high gain and narrow spot beams that rapidly scan the coverage area. However, to generate such beams, a phased array with a large radiating aperture must be used. The implications of weight, loss, feed network complexity, and packaging could make a large, passive, directly radiating phased array impractical. An alternative approach to achieve the performance of a large-aperture array is to use two confocal paraboloidal reflectors fed by a phased array [4-1] or a space-fed array (lens). The reflector design will be presented in this subsection, and the phased array and lens designs will be discussed in Subsections 4.3 and 4.4.

4.2.1.1 Reflector Configuration

In a confocal reflector system, a small parabolic subreflector is illuminated by the near field of the phased array or lens, and a large parabolic surface is used as the main reflector. To avoid subreflector blockage, an offset geometry is usually employed. If the array is located so that its center and the center of the main reflector are conjugate points of the optical system, a magnified image of the array is formed on the aperture of the large reflector. The conjugate points in an optical system are defined so that rays originating from one point are transformed by the optical system into rays that pass through another point [4-2].

Since this system is fed by a plane wave source and the subreflector is placed in the near field of the array, it is referred to as the near-field Gregorian system (Figure 4-1). Another type of confocal reflector system is the near-field Cassegrain system shown in Figure 4-2. The advantage of using the Gregorian configuration for the confocal paraboloid arrangement is that the feed array does not block the ray path between the two reflectors, and both reflectors have smaller offset. The disadvantage of this configuration is that it occupies more space, since the spacing between the two reflectors is proportional to $F_1 + F_2$. Conversely, a Cassegrain arrangement provides a larger F/D ratio for the same magnification factor under the same volume constraint. This results in less phase aberrations and thus better sidelobe, cross-polarization, and scan performance for limited angular scan. However, the offset version of this antenna has a severe blockage problem caused by the feed array. Therefore, the Gregorian configuration was chosen for the confocal reflector system design.

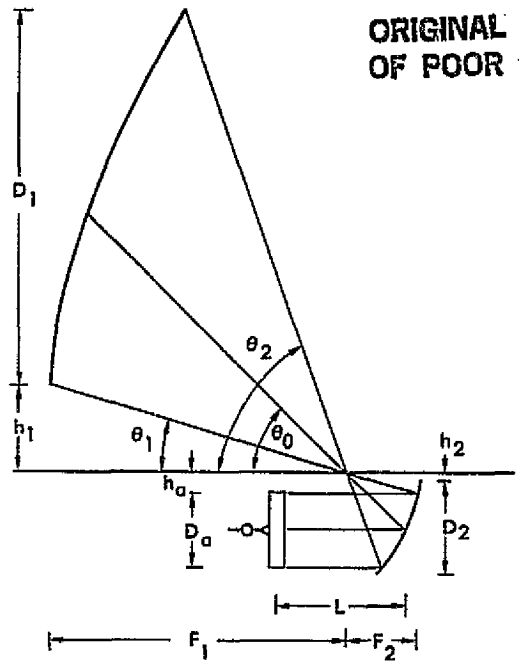

Figure 4-1. Offset Near-Field Gregorian Reflector System

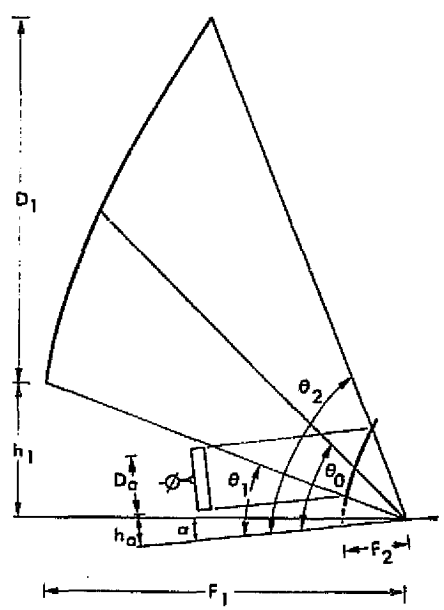

Figure 4-2. Offset Near-Field Cassegrain Reflector System

4.2.1.2 Optical Parameters

The main optical parameters in the design of confocal reflector systems are magnification factor, F/D_p ratio, array location, and offset height, as follows:

a. Magnification Factor. Since the confocal parabolas magnify the field image of a phased array, for a specified main reflector the array aperture is inversely proportional to the magnification factor, M, which is defined by

$$M = \frac{D_1}{D_a} = \frac{F_1}{F_2} \qquad (4\text{-}1)$$

It may be advantageous to use a large M so that a small array feed can be used; however, the scan range is inversely proportional to the magnification [4-1]. That is, the larger the magnification, the wider the array scans will be, and consequently, the larger the aberrations and scan loss will be. On the other hand, a magnification that is too small does not exploit the advantage of magnifying the phased array. Thus, the magnification to be considered in this study is limited to the range from 2 to 5. Since the main reflector size is fixed, variation in magnification implies a change of the subreflector size and its focal length. Table 4-1 lists the subreflector parameters as a function of the magnification for a specified main reflector geometry with diameter D_1 = 271.3 cm, F_1 = 323.5 cm, and offset height h_1 = 133.1 cm. Parameters D_1, F_1, h_1, D_2, F_2, and L are defined in Figure 4-1. The main reflector diameter, D_1, was chosen based on the availability to NASA of a reflector with this dimension.

A set of scan curves generated for this antenna geometry is shown in Figure 3-48. The scan range is limited to approximately $\pm 4°$, since the field of view of the CONUS coverage as seen from the geosynchronized orbit is 7°. These scan curves

Table 4-1. Subreflector Parameter Dimensions

Magnification m	D_2 (cm)	F_2 (cm)
2	207.3	121.3
3	156.5	80.9
4	132.6	60.7
5	118.4	48.5

show that scan loss increases as the magnification factor increases for a fixed scan angle. Sidelobe performance also varies as M changes. Figure 3-49 shows the first sidelobe level vs scan angle for various M values. To illustrate the sidelobe structure of the scanned beams as a function of M, Figure 4-3 shows the elevation cut patterns of M = 2 and M = 5. The contour patterns (-3, -5, and -7 dB) are shown in Figure 4-4 to demonstrate the scan degradation in both gain and beam shape. It is obvious from these figures that scan performance deteriorates more for systems with large M at extreme scan angles. On the other hand, although significantly less beam degradation can be achieved by using a small M system, the subreflector is usually impractically large, as seen in Table 4-1. Therefore, a magnification factor between 3 and 4 is recommended. The magnification for the final design is 3.6, which is obtained by satisfying the requirement imposed by the phased array design described in Subsection 4.4.

b. F/D_p Ratio. In a paraboloidal reflector system, the degradation of a scanned beam corresponding to an offset feed is proportional to the phase aberration that results from feed displacement or feed array scanning. One way to reduce the phase error is to choose a reflector with a large ratio of focal length, f, to parent paraboloid diameter, D_p. The effect of F/D_p can be

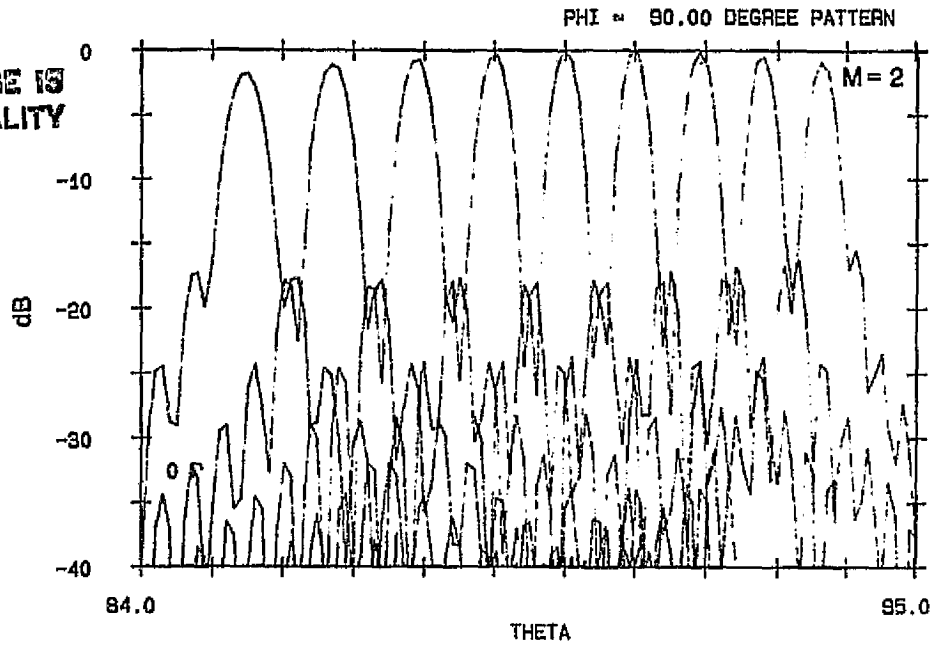

(a) M = 2

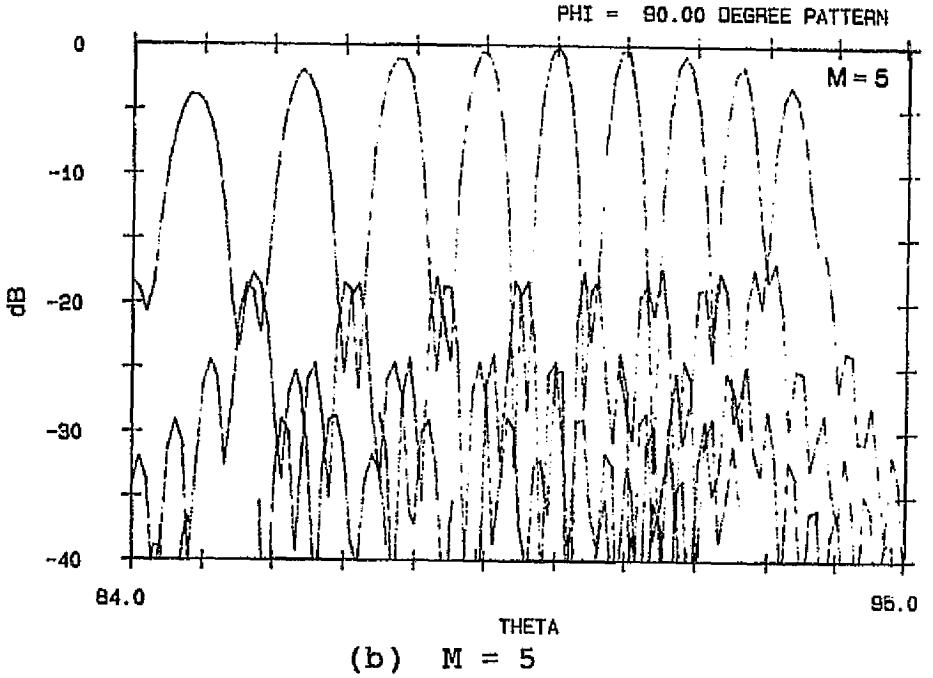

(b) M = 5

Figure 4-3. Elevation Scan Plane Pattern of a Confocal Paraboloidal System

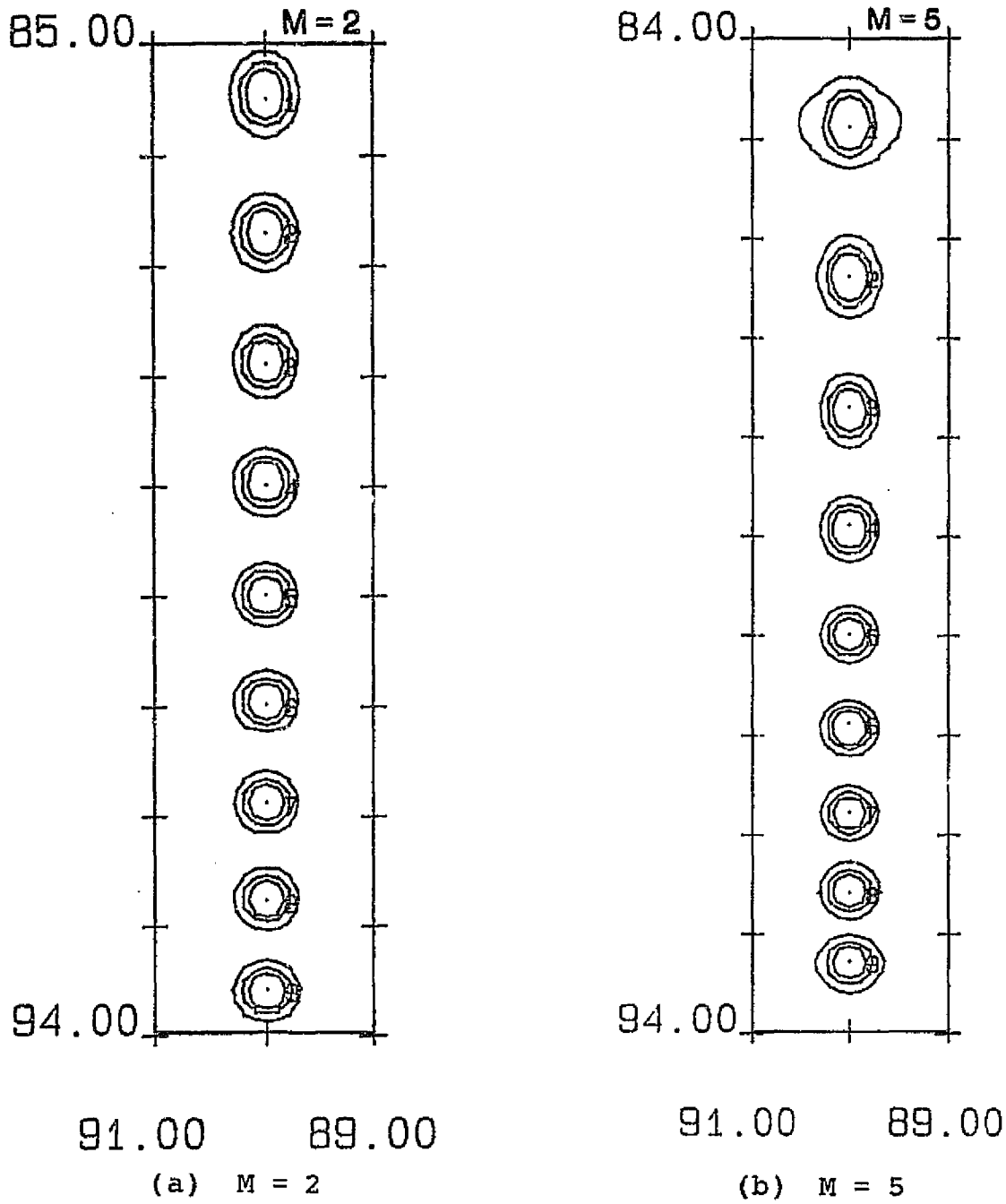

(a) M = 2 (b) M = 5

Figure 4-4. Contour Pattern of a Confocal Paraboloidal System

readily seen from Figure 3-48a and 3-48b. The scan loss for $F/D_p = 0.5$ is always better than that for $F/D_p = 0.3$ for a fixed M value. Unlike the single parabolic reflector system, in which the feed size must be increased to maintain the same tapered illumination on the reflector when a larger F/D_p is used, the feed aperture size in a confocal reflector system is not affected because the phased array feed illuminates the subreflector with plane waves.

The disadvantage of using a large F/D_p is that a larger subreflector is required to maintain the same amount of spillover. For small scanning, the scan angle of the far field, θ, is related to that of the feed array, θ_a, by [4-1]

$$\theta = \theta_a/M \qquad (4\text{-}2)$$

For larger scanning, the relationship is not linear, as demonstrated in Figure 4-5. The deviation depends on M and F/D_p, as well as θ. In practice, equation (4-2) is useful in determining the approximate array scan angle that corresponds to the far-field scan angle. The subreflector size is then limited by the two extreme scan rays on each size of the array.

Another disadvantage of using a large F/D_p is that the spacing between the two reflectors becomes larger, which may cause package problems. The spacings, approximated by $F_1 + F_2$ for various F/D_p and M, are plotted in Figure 4-6. The figure clearly shows that, with $F/D_p = 0.3$, the system has the most compact dimensions; whereas, with $F/D_p = 0.5$, the system occupies the largest volume with the largest subreflector. However, the scan curves in Figure 3-50 show that scan loss is most severe for $F/D_p = 0.3$ and moderate for $F/D_p = 0.5$. Therefore, the tradeoff is between packaging and scan performance. A compromised F/D_p ratio of 0.4 was thus chosen for the final design.

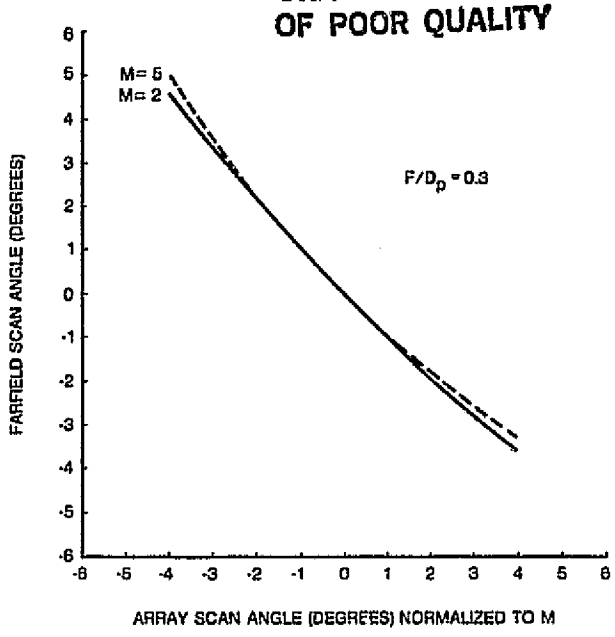

(a) $F/D_p = 0.3$

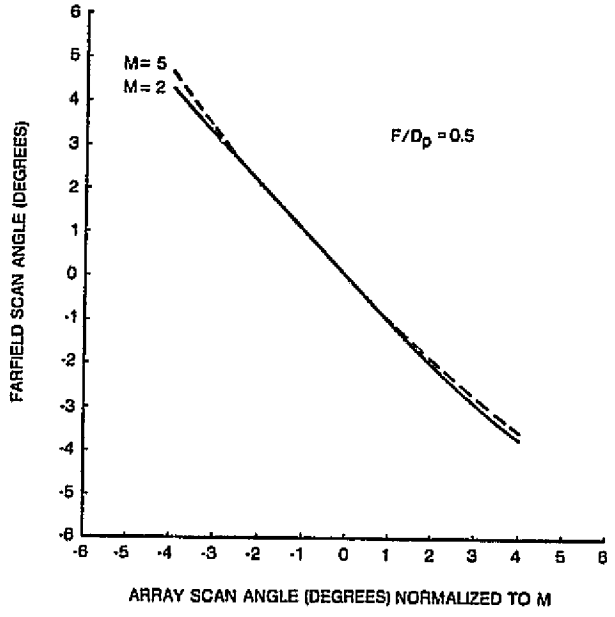

(b) $F/D_p = 0.5$

Figure 4-5. Beam Deviation for Confocal Reflector

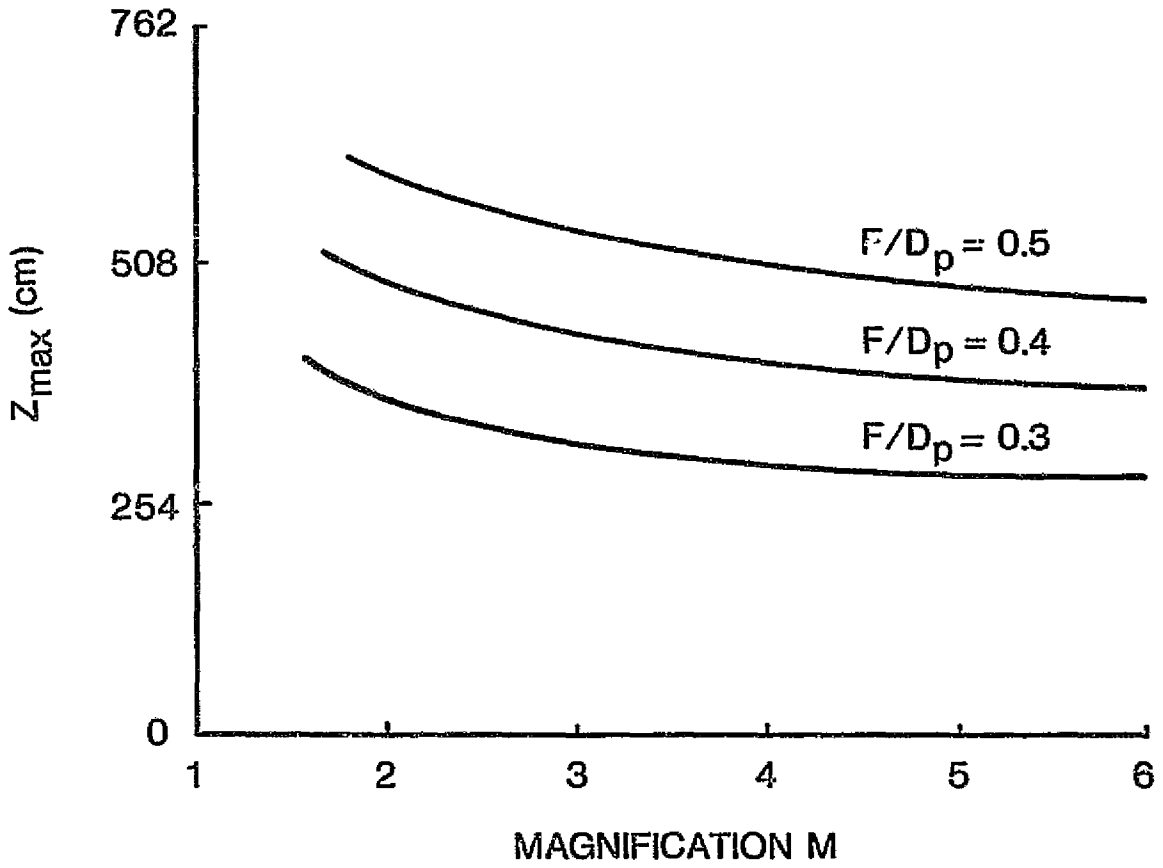

Figure 4-6. Maximum Distance Between Reflectors vs Magnification Factor

c. Array Location. To reduce spillover, the array should be placed close to the subreflector without blocking the ray paths between the two reflectors. The optimum region for array placement can be found by using the conjugate element concept [4-2] based on geometrical optics. To achieve maximum efficiency of illumination, the center of the main reflector and the center of the array must be conjugate points. The distance between the center of the array and the center of the subreflector is given by

$$L = R_s \frac{M + 1}{M} \qquad (4\text{-}3)$$

where R_s is the radial distance from the focal point to the center of the subreflector [4-2]. Since the derivation of equation (4-3) assumes a small incident angle, the array location may not be optimized for moderate or large scanning. However, it still provides a good estimate of where the array should be located, although an adjustment may be needed to determine the final feed position.

To investigate the validity of this approach, a confocal reflector system with $F/D_p = 0.5$ and $M = 3$ is chosen, and scan curves are generated for various array positions, as shown in Figure 4-7. The optimum array position, Z_a, measured from the focal plane is 79.7 cm. The gain curves vary only slightly from $Z_a = 63.5$ cm to 88.9 cm, but degrade severely for $Z_a = 101.6$ cm. Thus, the region adjacent to the conjugate point of the confocal system is the preferred array position, which optimizes both the boresight gain and scan loss. Consequently, the array in the final design will be placed in front of the subreflector at a distance determined by equation (4-3).

d. Offset Height. In an offset parabolic reflector system, the level of the cross-pol component introduced by the asymmetry of the reflector surface is proportional to the amount of

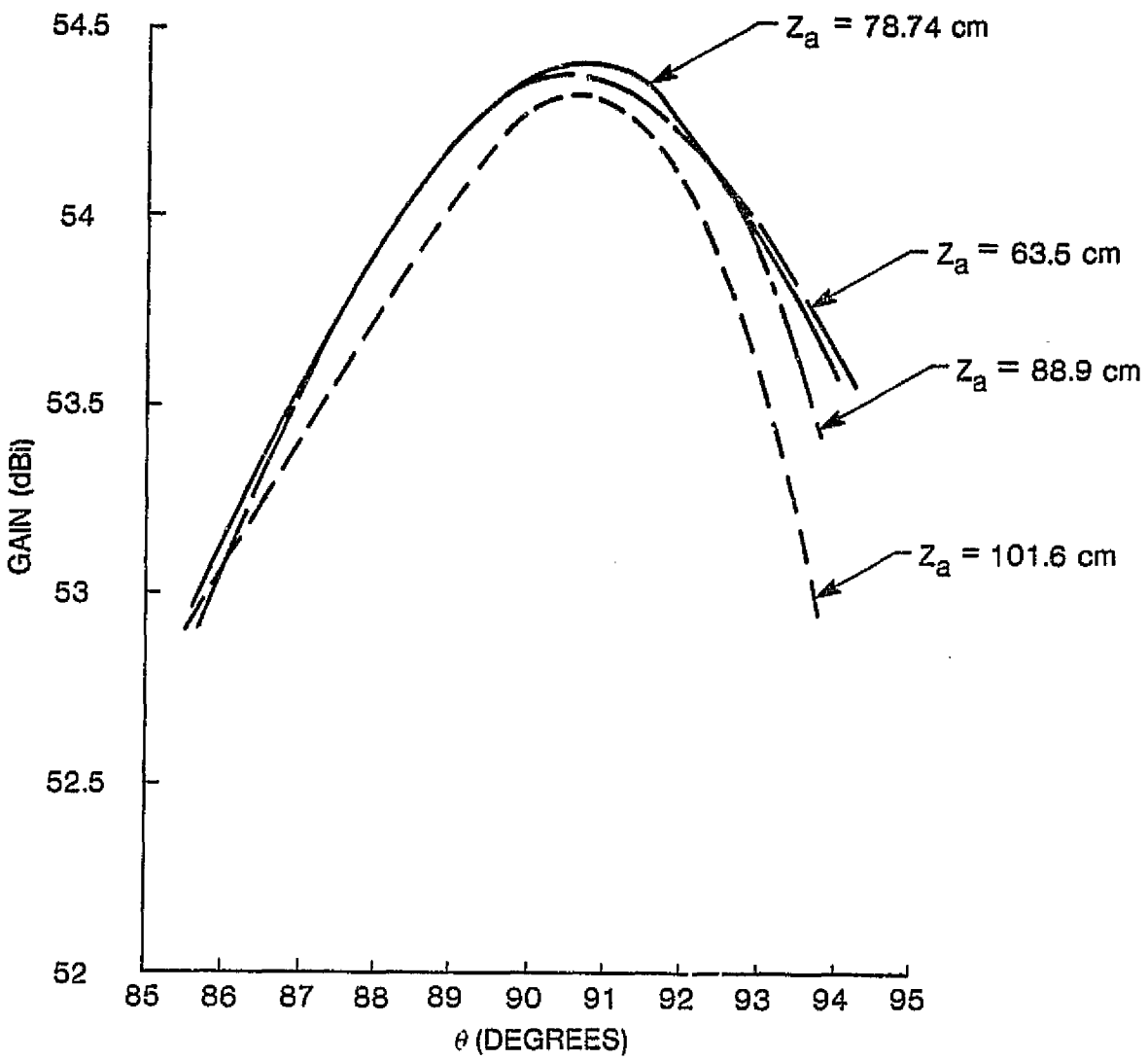

Figure 4-7. Scan Curves for Various Array Positions

offset. Therefore, it is advantageous to use a small offset and to ensure that no blockage is created by the feed array or subreflector. To avoid subreflector blockage, the clearance angle between the main reflector and subreflector must be larger than the maximum scan angle, in this case about 4°. The clearance angle is determined by both the offset height and the size of the subreflector. Subreflector size, in turn, is determined by the magnification, F/D_p, maximum scan angle, and array position. The tradeoff process is complicated because it involves many parameters. A trial and error approach is used to determine the offset height, with a final check made to ensure that the feed array does not block the ray paths. If blockage occurs, the array must be relocated within the optimum region, as discussed in item c of this subsection. If blockage remains, the offset height must be increased. For the final design, the offset height chosen is 133.1 cm.

4.2.1.3 Summary of the Near-Field Gregorian System Design

The final design of the confocal system is derived from the analyses described in Subsection 4.2.1.2. The parameters that define the antenna geometry (see Figure 4-1) are listed in Table 4-2. The numerical results of this antenna design are presented in Subsection 4.6.

Table 4-2. Antenna Parameters for Final Design of the Near-Field Gregorian System

Parameter	Dimension	Parameter	Dimension
D_1	271.3 cm	D_a	76.0 cm
F_1	323.5 cm	h_a	36.7 cm
h_1	133.1 cm	L_a	134.6 cm
D_2	134.6 cm	θ_{oo}	45.11°
F_2	91.1 cm	θ_1	23.25°
h_2	7.4 cm	θ_2	64°
		M	3.6

4.2.2 CONVENTIONAL CASSEGRAIN REFLECTOR SYSTEM

An offset Cassegrain configuration was chosen for the multiple fixed-beam application, since the optics and the feed array design in a focal region feed system for generating fixed spot beams are simple and straightforward. The following subsections describe the design criteria and procedures for deriving the antenna parameters of the reflectors and the horn array.

4.2.2.1 Reflector Configuration

Figure 4-8 shows the geometry of the conventional Cassegrain antenna configuration. The main reflector is a parabola with a circular projected aperture of 271.3 cm, a focal length of 335.28 cm, and an offset height of 142.5 cm. Selection of this reflector is based on NASA's recommendation to investigate the performance of a reflector with the parameters specified above in terms of gain and isolation between adjacent beams. For a reflector of this size, the beamwidth is approximately 0.4° at the downlink frequency of 17.7-20.2 GHz.

The subreflector is a section of a hyperboloid with a circular, projected aperture of 116.8 cm. The focal lengths of the subreflector, 114.3 cm and 63.5 cm, result in a magnification factor of 1.8. The offset height is 67.3 cm and the clearance angle is 3.49°. The offset height and the diameter of the subreflector were chosen to minimize spillover for the maximum scan angle while maintaining a blockage-free configuration. The subreflector parameters chosen were based on a tradeoff study of the magnification factor and the focal lengths of the hyperboloid vs antenna gain. This study was performed under the constraint that a blockage-free condition must be maintained.

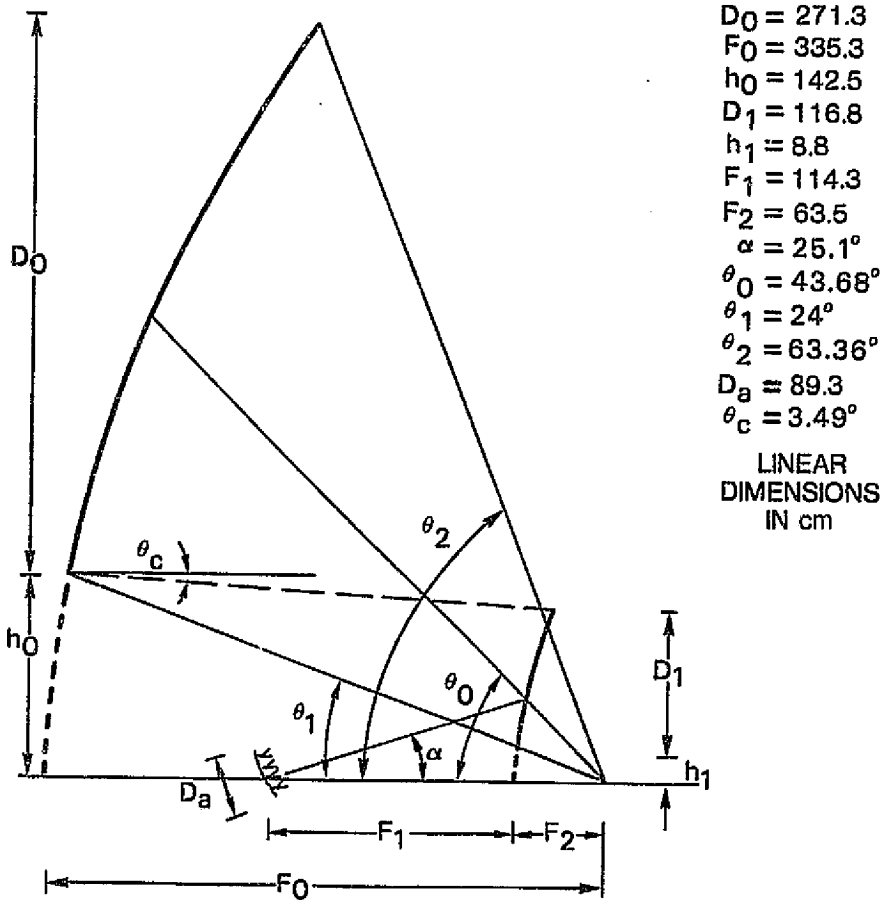

$D_0 = 271.3$
$F_0 = 335.3$
$h_0 = 142.5$
$D_1 = 116.8$
$h_1 = 8.8$
$F_1 = 114.3$
$F_2 = 63.5$
$\alpha = 25.1°$
$\theta_0 = 43.68°$
$\theta_1 = 24°$
$\theta_2 = 63.36°$
$D_a = 89.3$
$\theta_c = 3.49°$

LINEAR DIMENSIONS IN cm

Figure 4-8. Antenna Configuration of the Cassegrain Dual-Reflector System

For a hyperbolic subreflector, the magnification (defined as the ratio of the longer focal length to the shorter one) is proportional to the curvature of the surface. Larger surface curvature implies that the energy reflected from the surface would be more spread out. This greater spread increases the main reflector spillover, especially for large scanning. Therefore, to reduce scan loss, a small-to-moderate magnification is recommended. Conversely, a small magnification system requires a relatively large subreflector, which would cause blockage problems. By placing the focal points closer to the subreflector (that is, by decreasing F_1), subreflector size can be reduced while maintenaining a fixed magnification. Table 3-8 summarizes the geometries of the Cassegrain systems with various magnification factors. All the systems have the same main reflector, with a projected aperture of 271.3 cm, a focal length of 335.28 cm, and an offset height of 142.5 cm. This table shows that the system with the smallest magnification (M = 1.5) has the largest subreflector. On the other hand, the system with the smallest M also has the highest gain at boresight, as indicated in Figure 3-50.

For a small-M system, the spacing between any two horn elements is also reduced (i.e., the size of the horn element is small), resulting in more spillover and less gain. In general, for the same F_1, the spacing between two feed elements corresponding to two scanning directions is proportional to the magnification. Figure 3-51 shows the horn spacing that creates two adjacent beams whose centers are 0.4° apart for the Cassegrain systems investigated. The system with M = 1.5 has the smallest horn space. When cluster feeds are designed for the Boston, New York, and Washington, D.C., areas, the horn sizes of the cluster elements may be impractically small; that is, the system with small M may not meet the isolation requirement. Horn size and cluster design will be discussed in Subsection 4.2.2.2.

The tradeoff between the different subreflector parameters is complex. To establish the final design configuration, a relatively small magnification is chosen that offers the highest gain to meet the isolation requirement while satisfying the blockage-free condition. To demonstrate the performance of the final design system with magnification factors M = 1.8 and F_1 = 113.4 cm (see Figure 4-8), the scan patterns for scan angles ranging from 0° to 4° in the azimuth plane are given in Figures 4-9 and 4-10. The levels presented in Figure 4-10 are -3, -5, -7, and -10 dB. The scan curves for systems with various magnifications are compared in Figure 3-50.

4.2.2.2 Feed Array Configuration

In a reflector antenna system, the performance in gain and beamwidth is normally governed by reflector size. However, feed design is essential for sidelobe control and beam shaping to achieve optimal coverage and beam isolation. For fixed spot beam application, the Boston/New York/Washington region has the most stringent isolation requirements because separation between two cities sharing the same polarization is small. For good isolation between any two copolarized beams, cluster feed, not single element feed, is used to generate each spot beam. Cluster feeds allow adjustment of the power distribution on the component beams and thus control of the sidelobe levels and an increase in isolation. Furthermore, because these three cities are so close together, horn sharing between elements in different clusters must be used to maximize the feed cluster aperture.

The first feed design considered in this study was a seven-horn cluster with horn elements arranged in a triangular lattice. (All the horns are circular, with 1.78-cm diameters.) Two horns are shared between two adjacent clusters, as shown in

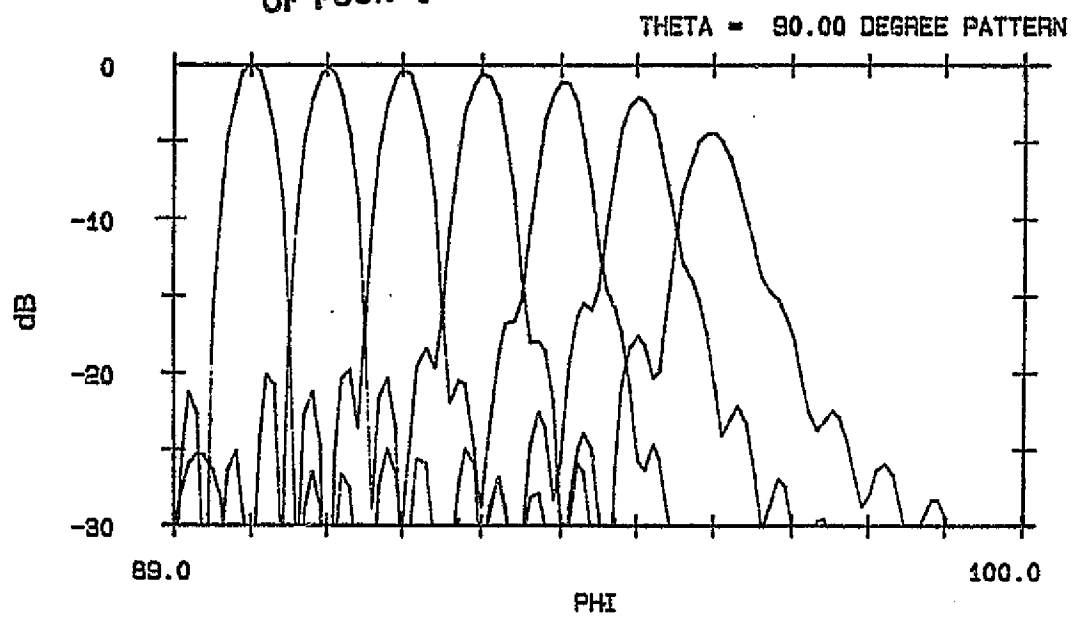

Figure 4-9. Elevation Scan Patterns of the Final Antenna Design

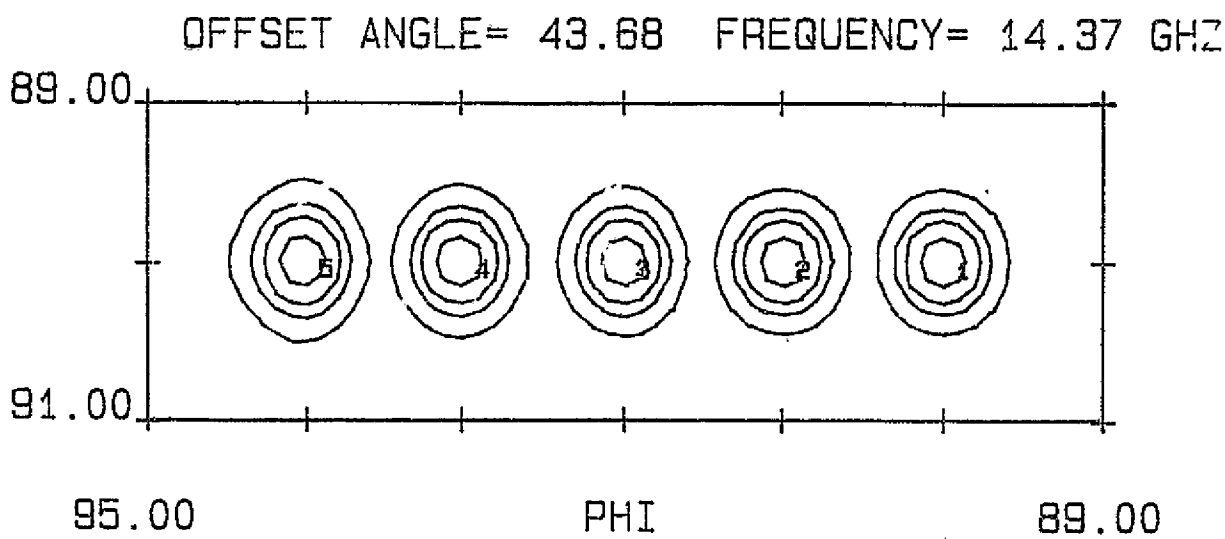

Figure 4-10. Contour Patterns of the Final Antenna Design

Figure 4-11. One advantage of using circular horns is that they can be fed in any convenient polarization, regardless of the feed array orientation (defined by the line connecting the collinear cluster centers). The spot beams generated by these clusters have acceptable peak gain levels of about 50 dBi; however, for some beams, the beam isolation performance is poor. For example, the isolation of Boston from the Washington, D.C., beam is 27 dB, but that of Washington, D.C., from the Boston beam is only 20 dB. To improve beam isolation, another ring of horn elements is required, providing more control over the energy distribution on the clusters and eventua ly on the sidelobe levels. This approach has not been adopted because the horn sizes would be impractically small.

An alternative is to form clusters with rectangular horns. In general, a higher peak gain can be achieved in a reflector system fed by a square horn than in a reflector system fed by a circular horn of the same dimension. Figure 4-12 shows the gain curves vs horn size for the Cassegrain system described above, fed by a square horn and a circular horn, respectively. The gain for a square-horn-fed system is approximately 0.5 dB higher than that of a circular-horn-fed system for a wide range of horn sizes. In addition, a square horn cluster allows finer aperture distribution control. Therefore, for linear polarization applications, it is advantageous to use square or rectangular horns, either as individual feed elements or as clusters.

The next design considered uses square horns to form clusters. The horn arrangement is similar to that of the previous design, except that each cluster consists of nine horns and the horn size is specified, as shown in Figure 4-13. In this arrangement, three horns are shared by the two adjacent clusters. The co-pol and cross-pol orientations are now 45° off the vertical

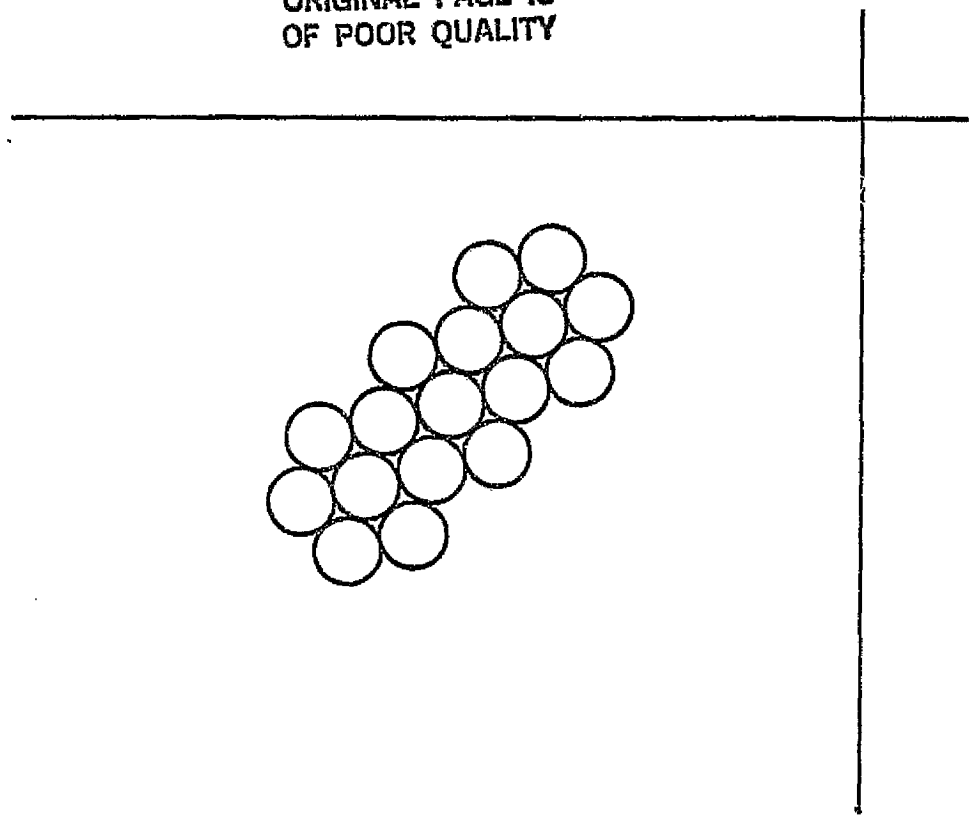

Figure 4-11. Circular Horn Cluster Design

axis, making simulation on the computer somewhat complicated. Although there are more horns in a cluster, the horn aperture size is smaller than that of circular horn described above. The performance of this design offers no significant improvement over that of the previous design.

The final design is a modification of the design shown in Figure 4-13. Each cluster consists of nine horns, each of which is 2.13 cm square, as shown in Figure 4-14. Four horns are shared by two adjacent clusters and one horn is shared by all three clusters. Since the New York beam polarization differs from that of the other two beams, the horn shared by three clusters must transmit one signal with one polarization and two signals

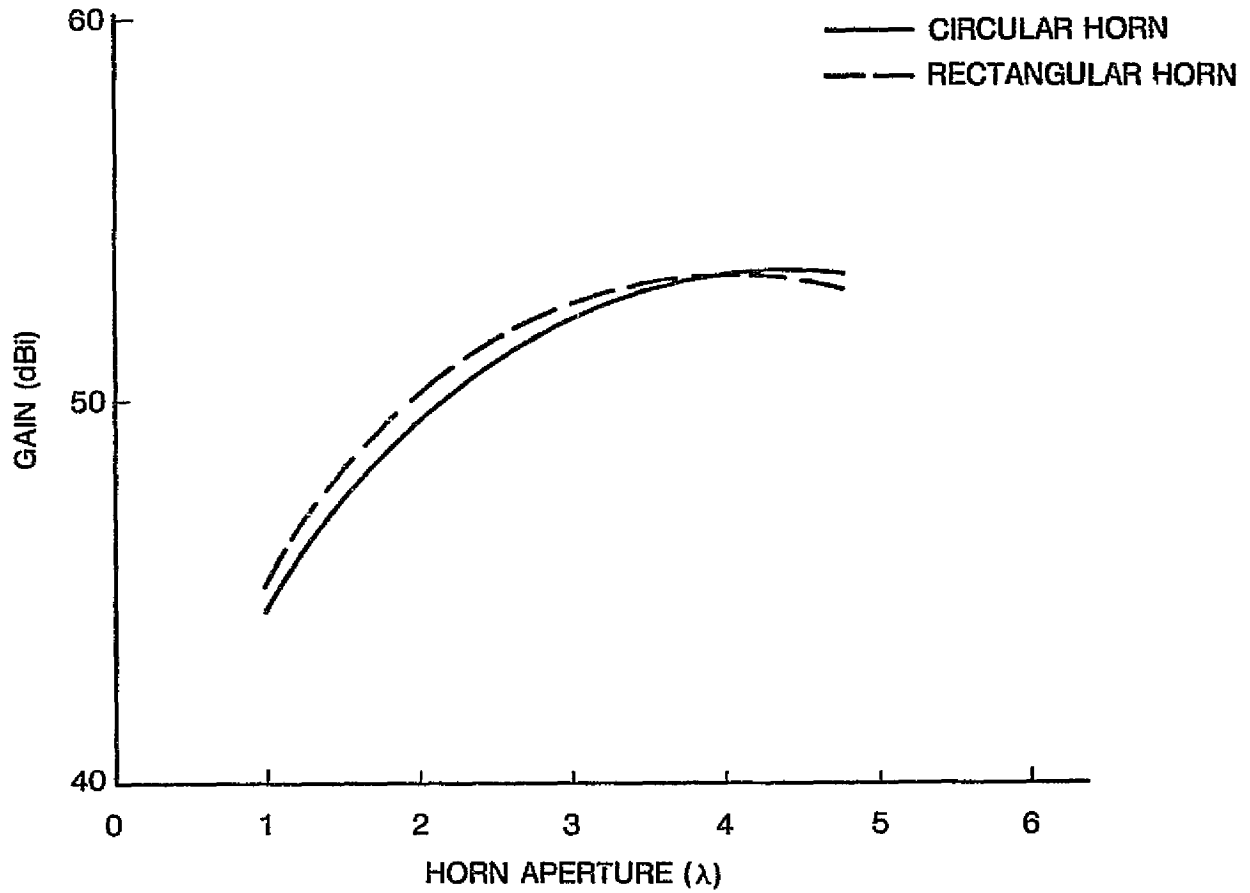

Figure 4-12. Variation of Peak Gain vs Horn Size

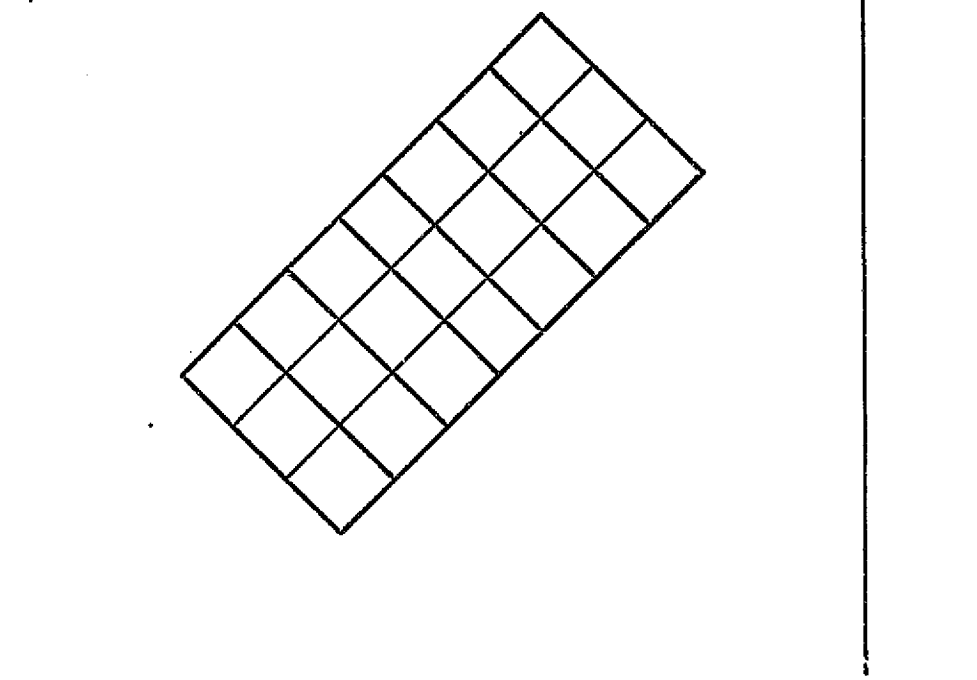

Figure 4-13. Alternative Feed Cluster Design

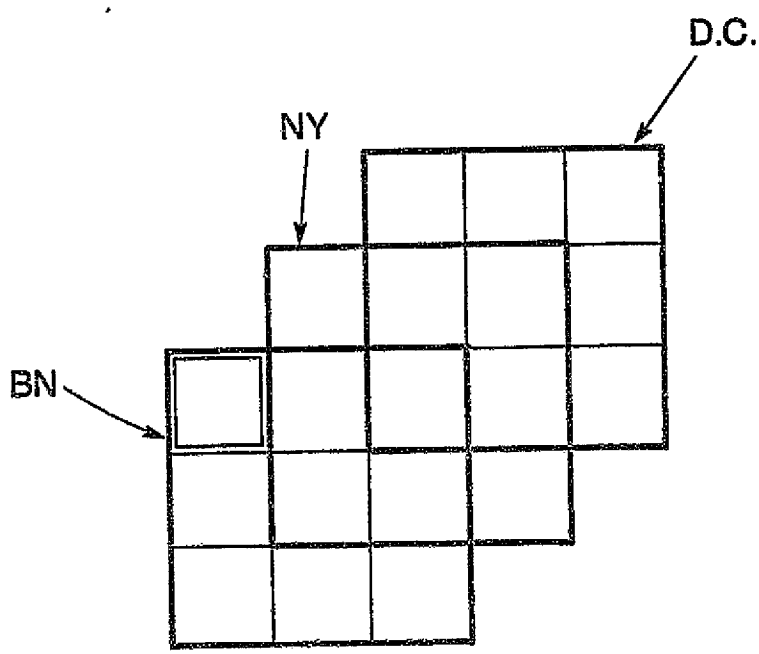

Figure 4-14. Final Design of the Feed Clusters

with the orthogonal polarization. (The circuit design to achieve this operation is described in Subsection 5.6.3.) The horn arrangement shown in Figure 4-14 maximizes the horn aperture size and thus provides good isolation and good gain for a 2.74 m (9-ft) reflector system. Subsection 4.6.2.2 presents calculated beam patterns which demonstrate that the multiple fixed beam antenna system with this feed design either meets or exceeds the isolation specifications.

In addition, feed clusters for Los Angeles, Seattle, and Miami are also generated. These clusters, together with those previously discussed, define the outmost boundary of the feed array as shown in Figure 4-15. Other clusters not shown here can fit within the array area. Some may require horn sharing between adjacent, cross-polarized coverage areas via orthomode transducers (OMTs). Therefore, the feed array of the multiple beam system represents a practical design that provides both good performance and feasibility.

4.3 PHASED ARRAY DESIGN

4.3.1 BASIC PARAMETERS IN PHASED ARRAY DESIGN

The basic parameters in the phased array design are the element type and shape, total array size, number of elements, lattice arrangement, periodic spacing between the elements, and amplitude and phase distributions. Many of these parameters are interlaced to satisfy certain requirements, so that choosing one parameter automatically determines all the rest.

For the present design, a square pyramidal horn is chosen as the array element. This shape satisfies the requirement of

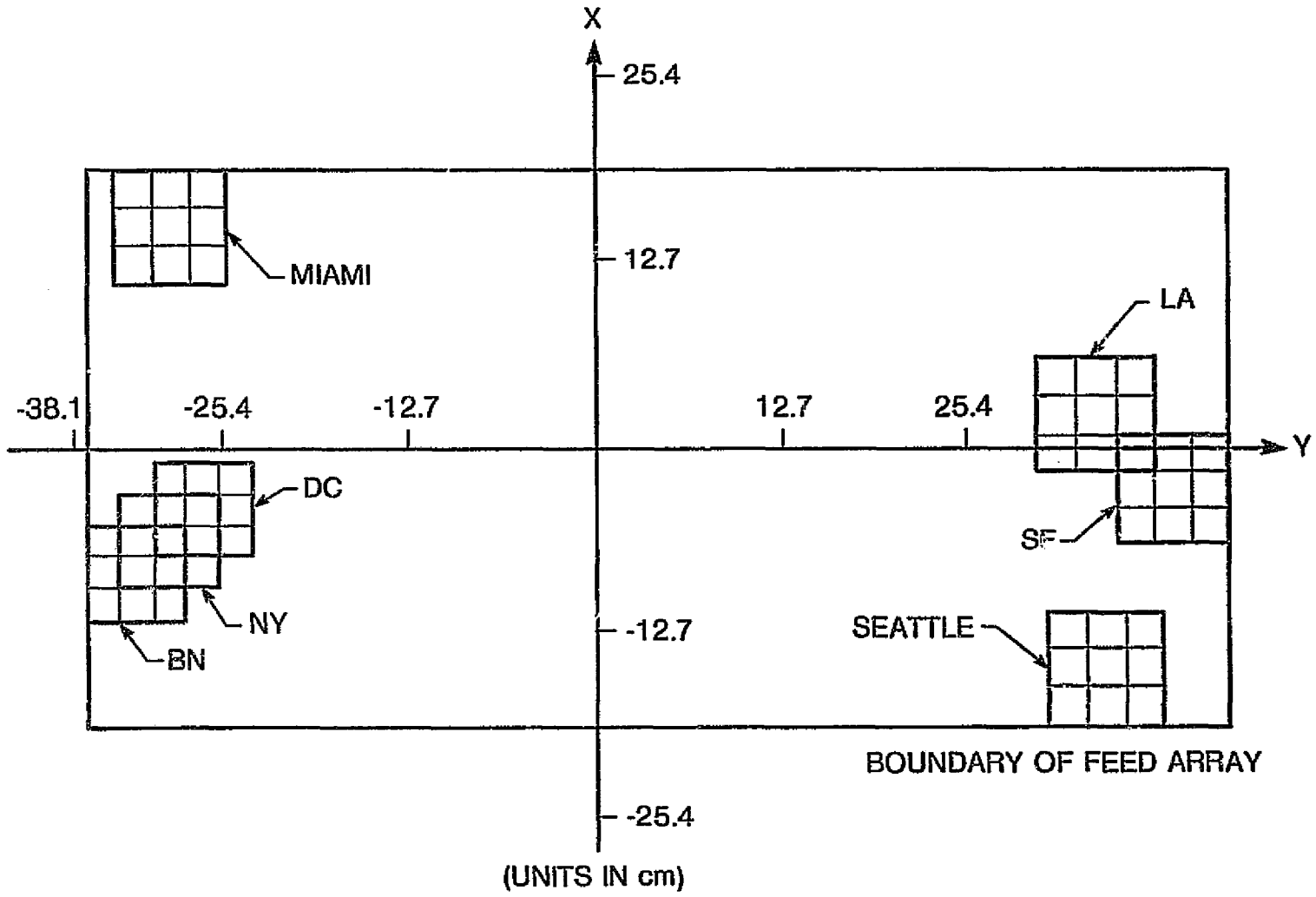

Figure 4-15. Feed Cluster Laycut

dual linear polarization, and the elements can be arranged to make maximum use of the array aperture and achieve the highest gain. The taper angle and length of the horn are chosen to produce a uniform phase front at the horn aperture and to control the modes that could contribute to blind spots in the array pattern.

The total array aperture size is determined from the main reflector size and the magnification factor of the dual-reflector system. The element size and the periodic spacing between the elements are determined from limitations dictated by the grating lobe emergence in the field of view and the phase shifter increment. The total array size and element size directly determine the number of elements in the array, which must also satisfy the power requirements of the array. Limitations on element size is also a function of the lattice arrangement.

High gain can be delivered via the phased array by uniformly illuminating the elements. However, this results in sidelobe levels of about 13 dB below the main beam peak. To satisfy the requirements of high isolation between different scanning beams, amplitude taper is needed. This has the adverse effect of increasing the beamwidth and reducing the average power per element in the array.

4.3.2 SQUARE HORN ELEMENT DESIGN

As pointed out in Section 3, the square aperture dimensions of the horn are limited by the phase shifter increment and the grating lobe locations in the array pattern. By using 5-bit phase shifters with the smallest increment of 11.25° and by assuming a field of view of the CONUS region, Figure 3-12 shows the upper and lower limits on element spacings for different magnification factors, M, when the far-field beamwidth is 0.3° and 0.4°. These

cases occur when the main reflector diameters are 3.658 m and 2.713 m, respectively. The present design uses a main reflector of 2.713 m diameter with a far-field beamwidth of 0.4°.

To avoid excessive scan loss in the dual-reflector system within the CONUS coverage area, the M was chosen to be 3.6. This requires element spacing of between 1.6λ and 2.3λ across the frequency band of 17.7-20.2 GHz. Choosing an element aperture size of 3.166 cm, or 2λ at the band center of 18.95 GHz and assuming a wall thickness of 0.508 mm (0.020 in.) will yield element spacing dimensions within the required range. Table 4-3 shows the element aperture size and element spacing at different frequencies in the band.

Table 4-3. Horn Element Dimensions

Frequency (GHz)	Element Aperture Size (λ)	Element Spacing (λ)
17.70	1.868	1.928
18.95	2.000	2.064
20.20	2.132	2.200

The horn taper is determined by the mode content requirements and allowable phase errors at the horn aperture. The mode content contributes to the existence of blind spots in the array pattern. The most destructive mode is the TM_{12} mode. To eliminate blind spots, the horn taper length must be chosen to effectively short-circuit this mode at the aperture [4-3].

Consider the horn taper shown in Figure 4-16, where A and a are the square aperture and square-feed waveguide dimensions, L is the horn length, and α is the taper angle. The condition for the mode to be short-circuited at the aperture plane is

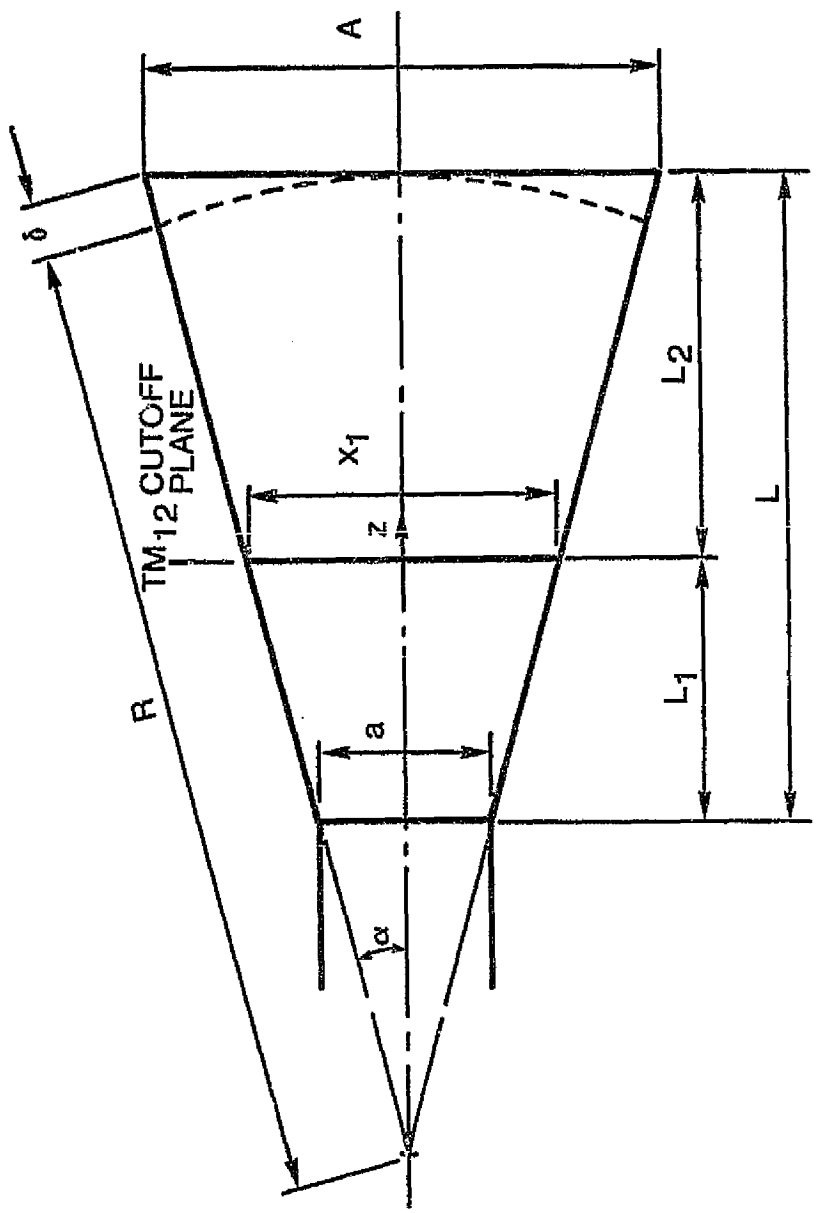

Figure 4-16. Parameters of Horn Design

$$\int_0^{z_{si}} \beta(z)dz = \frac{\pi}{4} + (i - 1)\pi \text{ for TM modes}$$

$$= \frac{3\pi}{4} + (i - 1)\pi \text{ for TE modes} \qquad (4\text{-}4)$$

where z is the distance along the horn axis measured from the cut-off location. The variable z_{si} is the location of the ith shorting plane for that mode, and $\beta(z)$ is the propagation constant determined by the transverse dimensions of the waveguide. For a square pyramidal horn, $\beta(z)$ is given as

$$\beta(z) = \frac{\pi}{x}\sqrt{m^2 + n^2} \text{ for m,n mode}$$

$$= \frac{7.025}{x} \text{ for } TM_{12} \text{ mode} \qquad (4\text{-}5)$$

where x is the cross-sectional dimension at z. Assuming z = 0 or assuming that TM_{12} cutoff cross section occurs at $x = x_1$, $\beta(z)$ can be written as

$$\beta(z) = \frac{7.025}{x_1 + 2z \tan \alpha} \qquad (4\text{-}6)$$

For TM_{12} to be short-circuited at the horn aperture

$$\int_0^{L_2} \frac{7.025}{x_1 + 2z \tan \alpha}\, dz = \frac{\pi}{4} + (i - 1)\pi \qquad (4\text{-}7)$$

which leads to

$$L_2 = \frac{1}{2 \tan \alpha}\left\{e^{[0.2236+(i-1)/1.118]\tan\alpha} - 1\right\} \qquad (4\text{-}8)$$

Using the relation between A, x_1, L_2, and α

$$\frac{A - x_1}{2L_2} = \tan \alpha \qquad (4\text{-}9)$$

and substituting for L_2 from equation (4-8) yields

$$A = x_1 \, e^{[0.2236+(i-1)/1.118]\tan\alpha} \qquad (4\text{-}10)$$

For the TM_{12} mode,

$$x_1 = 1.118\lambda \qquad (4\text{-}11)$$

where λ is the free-space wavelength. This leads to the horn taper angle as a function of the aperture dimension

$$\tan \alpha = \frac{1}{0.2236 + \frac{i - 1}{1.118}} \ln \frac{A}{1.118\lambda} \qquad (4\text{-}12)$$

The total length of the horn, L, is then given by

$$L = \frac{A - a}{2 \tan \alpha} \qquad (4\text{-}13)$$

From equations (4-12) and (4-13), the horn taper and length can be determined for aperture and waveguide dimensions A and α. Another constraint, however, is that the taper must be sufficiently gradual so that the phase difference, δ, between planar and spherical wavefronts at the horn aperture is small compared to wavelength. The phase difference can be shown to be

$$\delta = \frac{A}{2} \frac{1 - \cos \alpha}{\sin \alpha} \qquad (4\text{-}14)$$

The condition for gradual taper is

$$(2\alpha)^2 << \frac{8\lambda}{R} \qquad (4\text{-}15)$$

where R is the radius of a spherical surface at the horn aperture and centered at the pyramidal horn apex.

From Table 4-3, A = 2λ at center frequency (3.166 cm). The waveguide dimension, a, is chosen to be 0.965 cm to control the mode contents in the waveguide for the dual-polarized operation. By using equations (4-12), (4-13), and (4-14), α, L, and δ can be calculated for different values of i. Table 4-4 shows the results for i = 1 through 5.

Table 4-4. Horn Taper, Length, and Phase Front Error

Parameter	i = 1	i = 2	i = 3	i = 4	i = 5
α (deg)	68.97	27.48	16.12	11.31	8.7
L (cm)	0.422	2.113	3.805	5.499	7.188
δ (deg)	247.0	88.0	51.0	35.6	27.4

The value of i = 4 results in δ corresponding to less than 0.1λ. This also satisfies the condition of equation (4-15), where

$$(2\alpha)^2 = 0.039 \text{ rad}^2 \qquad (4\text{-}16)$$

and

$$\frac{8\lambda}{R} = 1.6 \qquad (4\text{-}17)$$

resulting in

$$(2\alpha)^2 << \frac{8\lambda}{R} \qquad (4\text{-}18)$$

The final design values of the horn are listed in Table 4-5.

Table 4-5. Square Horn
Design Parameters

Parameter	Value
Aperture Square Dimension	3.166 cm
Waveguide Square Dimension	0.965 cm
Taper Angle	11.31°
Taper Length	5.499 cm

4.3.3 ARRAY SIZE AND CONFIGURATION

For a magnification factor of 3.6 and a main reflector diameter of 2.74 m (9 ft), the approximate size of the array is 76.1 cm in both dimensions. By using the element size and spacing arrived at in Subsection 4.3.2, the number of elements in the array is determined as 24 x 24 = 576, as shown in Figure 4-17. The total array size is 78.38 x 80.03 cm. The elements are arranged in a triangular lattice with a half-element offset between elements in subsequent rows. The y-axis is parallel to the offset direction of the dual-reflector system, which is in turn parallel to the east-west axis of the spacecraft.

The 576-element array will satisfy the e.i.r.p. requirements with enough margin if the elements are uniformly excited. However, this produces sidelobe levels higher than desired. Restrictions on the sidelobe levels are that the isolation between different scanning beams must be better than 27 dB. This requires that the level of the sidelobe, separated from the main beam by an angle equivalent to one scanning sector, must be less than -27 dB, relative to the main beam. The cross-polarization isolation must also exceed 27 dB.

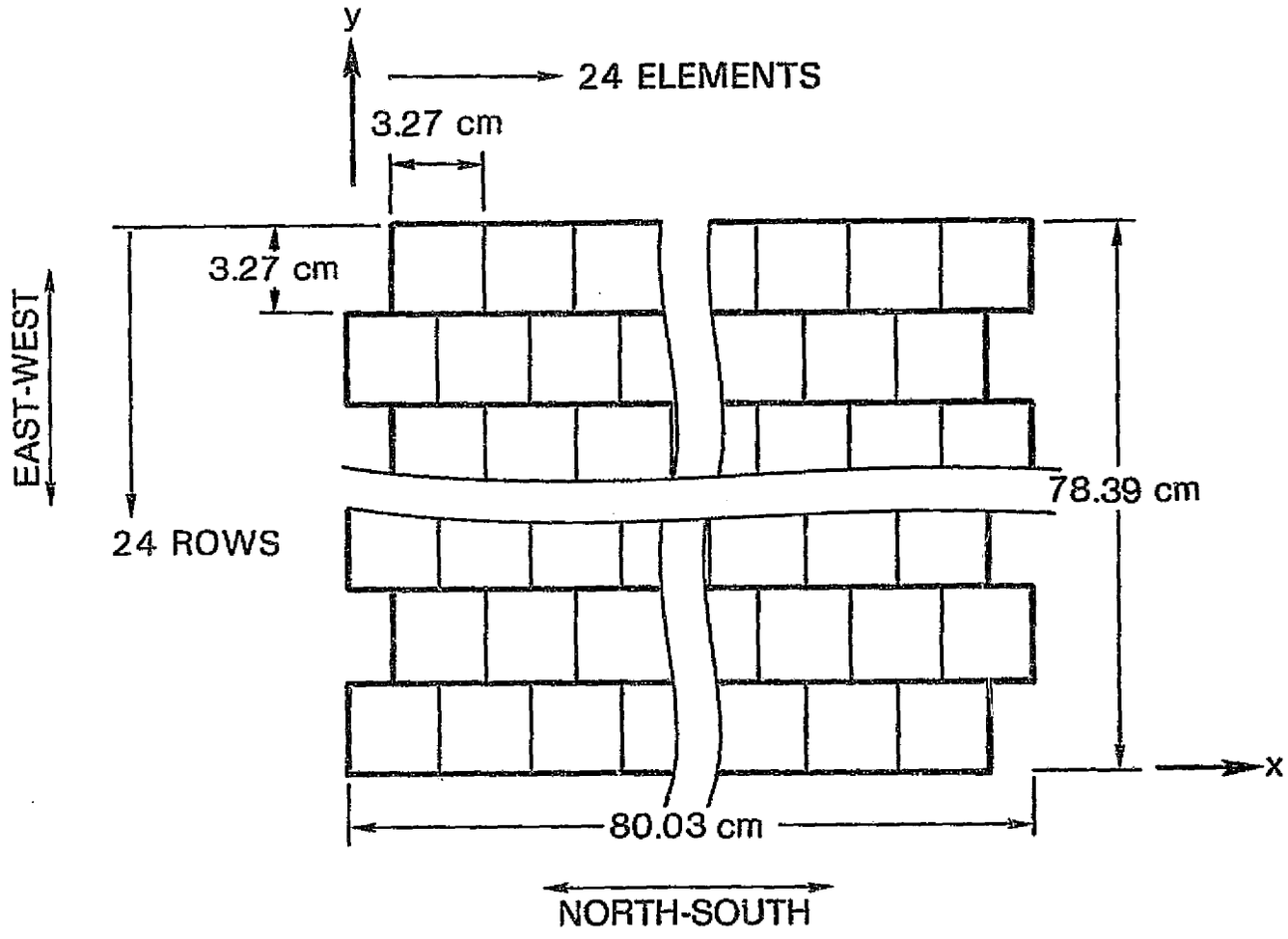

Figure 4-17. 576-Element Phased Array Design

To illustrate that the uniform distribution does not satisfy the isolation requirement, Figure 4-18 shows the radiation pattern of a 24-element linear array with uniform excitation. At 4°, which approximately corresponds to a far-field angle of 1.1° with M = 3.6, the sidelobe level is only 23 dB below the main beam. The cross-polarization level, however, is lower than 50 dB below the co-polarized main beam.

A Taylor distribution was chosen as the means to achieve the required isolation levels. This distribution produces a first sidelobe that is a certain level, R, below the main beam. Successive sidelobes are progressively lower, up to an angle midway between the main beam and the first grating lobe. Because the required low sidelobe is generally not the first one, the distribution can be designed for a higher first sidelobe, resulting in a narrower beam. This level is not achievable by other distributions, such as Tchebyscheff.

The Taylor aperture distribution for the linear array of total size 2a is

$$F(z) = \frac{1}{2a} I_o \left[k_o aC \sqrt{1 - \frac{z}{a}^2} \right], \quad |z| \leq a \qquad (4\text{-}19)$$

where z is the distance from the center of the array, I_o is the modified Bessel function of zero order, k_o is the free-space wave number, and C is a constant determined by the required first sidelobe level. If R is the height of the main beam over the first sidelobe, C is given by:

$$\frac{1}{R} = \frac{4aC}{2\lambda_o \sinh (k_o aC)} \qquad (4\text{-}20)$$

where λ_o is the free-space wavelength.

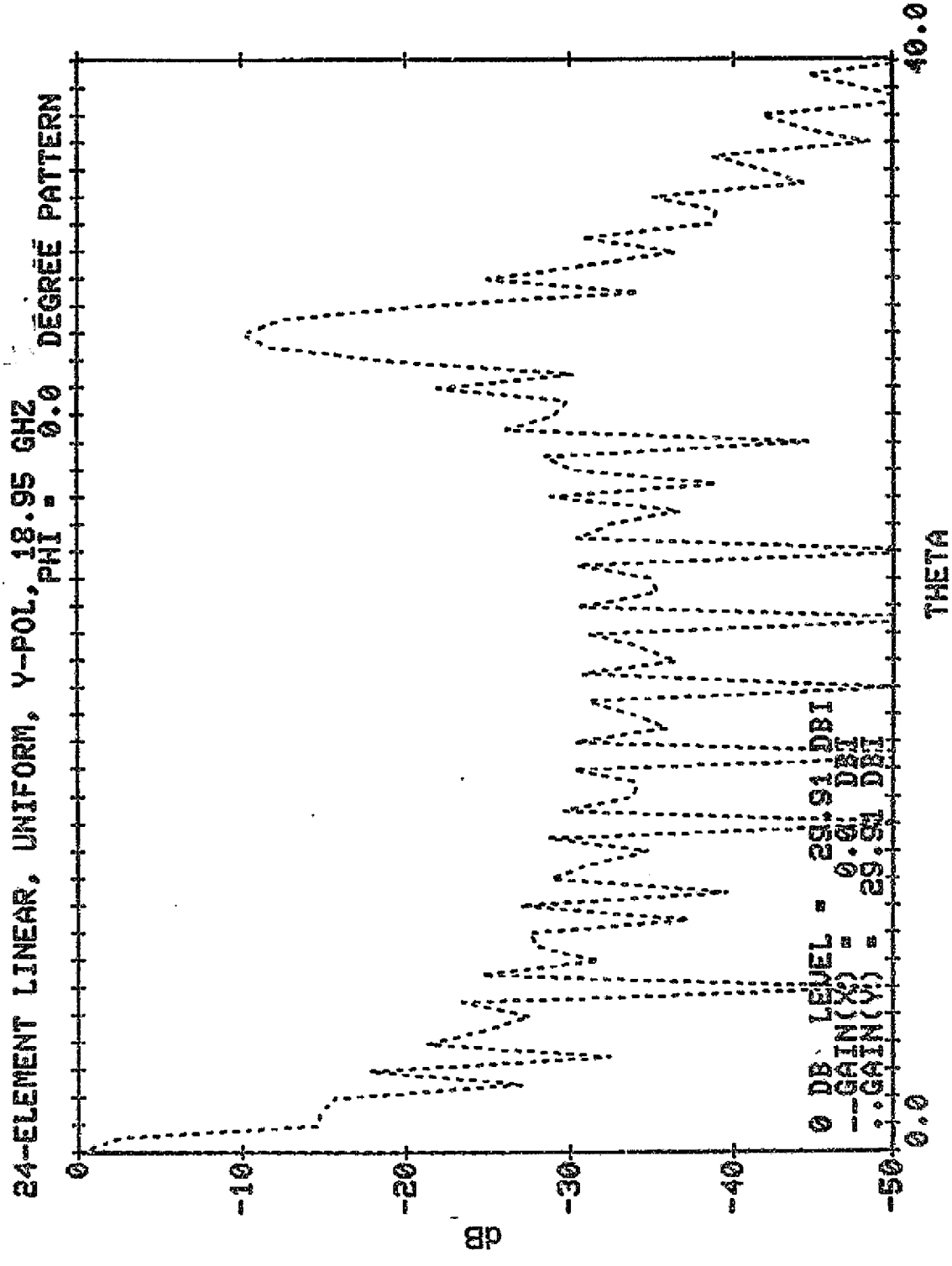

Figure 4-18. Radiation Pattern of 24-Element Linear Array of Uniform Distribution

Figures 4-19 and 4-20 show the radiation pattern of a 24-element array with dimensions that correspond to the present design. The first sidelobe level is -30 dB (relative to the main beam) to allow for implementation margins. Figure 4-19 shows the pattern for broadside radiation. The sidelobe level corresponding to the position of the isolated spots is about -38 dB. As the array scans, the gain degrades according to the element pattern, but the isolation levels remain better than 30 dB. Figure 4-20 shows the scanned beam patterns for different scan angles.

The amplitude coefficients that result in the Taylor patterns seen in Figures 4-19 and 4-20 are given in Table 4-6. This pattern requires a number of amplitude levels that are equivalent to half the number of elements in the array. These levels can be achieved by using a power-dividing network designed to produce the required relative levels. The network outputs are then amplified to attain the e.i.r.p., with amplifiers set at the same bias and gain. This results in low-efficiency operation, since most amplifiers will be operated in a backed-off condition. The dividing network can also be designed to partially achieve the required relative amplitude level and to depend on different prescribed amplifier settings to achieve the final levels, resulting in higher efficiency.

The simplest and most efficient network design can be obtained by using an equal division network and amplifiers set at predefined levels dictated by the 5-step amplifiers available in MMIC form. The five steps are adjusted to power levels of 500, 125, 50, 12.5, and 0 mW, which correspond to relative amplitude levels of 1.0, 0.5, 0.316, 0.158, and 0. This adjustment requires that the coefficients outlined in Table 4-6 be quantized to the five preset levels, resulting in new coefficients which are also given in the Table. The array radiation patterns that use the quantized Taylor distribution are given in Figures 4-21 and 4-22. The sidelobe level at the isolated positions increased to -24 dB relative to the main beam level.

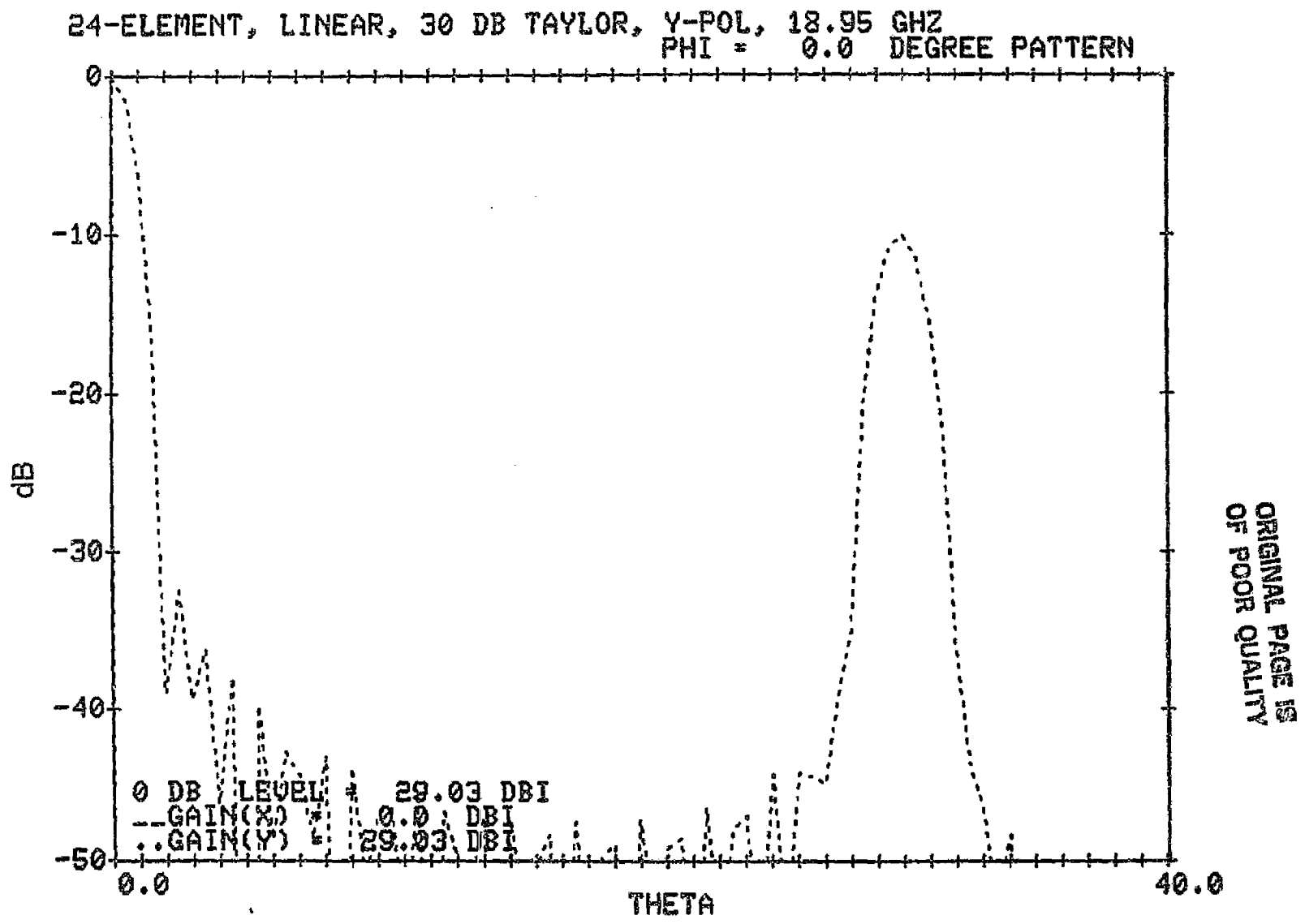

Figure 4-19. Radiation Pattern of 24-Element Linear Array with 30-dB Taylor Distribution

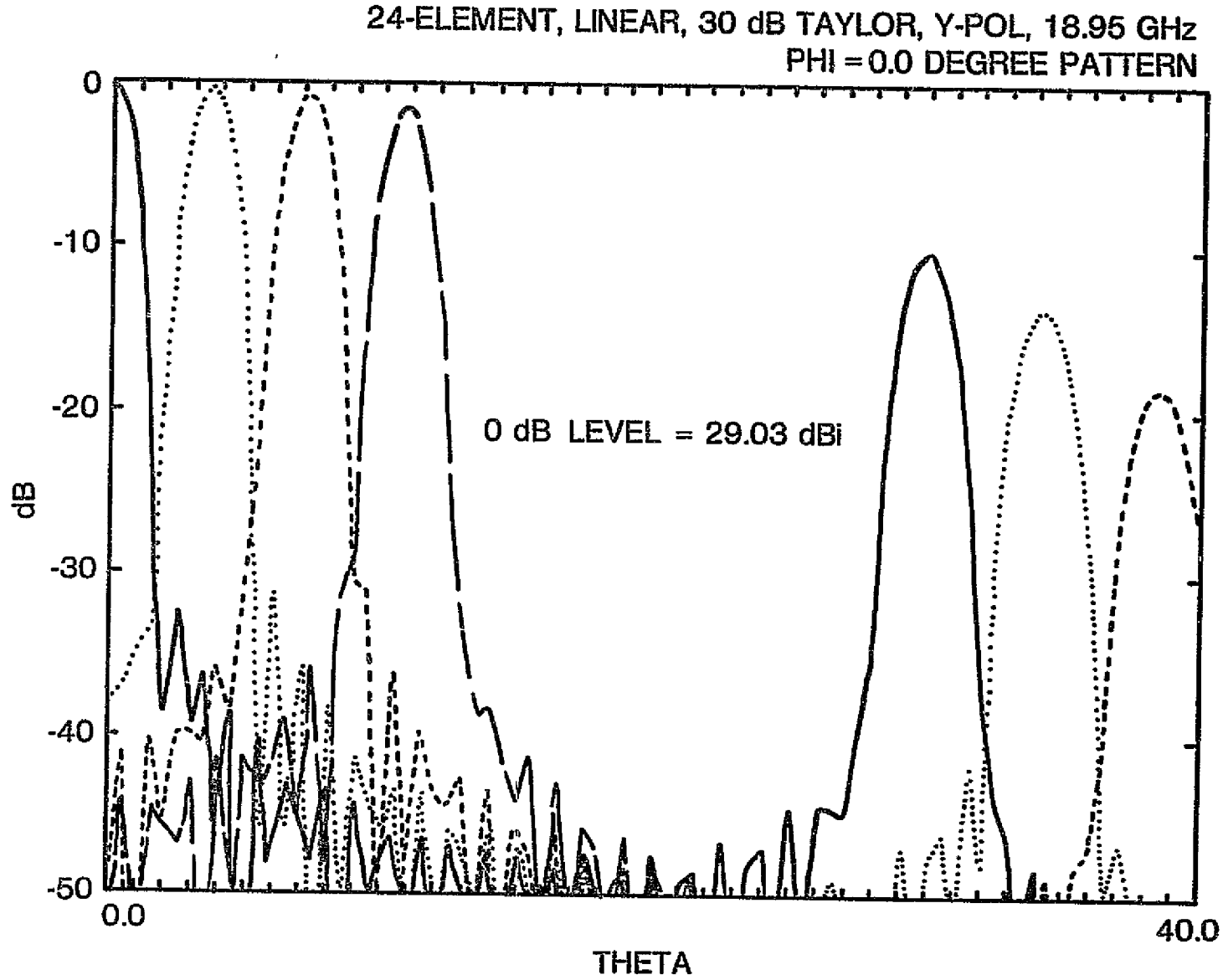

Figure 4-20. Radiation Patterns in Four Scanning Directions of 24-Element Linear Array With 30-dB Taylor Distribution

Table 4-6. Amplitude Coefficients for 24-Element, 30-dB Taylor and Quantized Taylor Distributions

Element Number	Relative Amplitude: 30-dB Taylor	Relative Amplitude: Taylor Quantized to Levels 1, 0.5, 0.316, 0.158, and 0	Relative Amplitude: Taylor Quantized to Levels 1, 0.75, 0.5, 0.25, and 0
1	0.119	0.158	0.0
2	0.193	0.158	0.25
3	0.279	0.316	0.25
4	0.375	0.316	0.25
5	0.478	0.50	0.50
6	0.583	0.50	0.50
7	0.685	0.50	0.75
8	0.780	1.0	0.75
9	0.863	1.0	0.75
10	0.930	1.0	1.0
11	0.976	1.0	1.0
12	1.0	1.0	1.0
13	1.0	1.0	1.0
14	0.976	1.0	1.0
15	0.930	1.0	1.0
16	0.863	1.0	0.75
17	0.780	1.0	0.75
18	0.685	0.50	0.75
19	0.583	0.50	0.50
20	0.478	0.50	0.50
21	0.375	0.316	0.25
22	0.279	0.316	0.25
23	0.193	0.158	0.25
24	0.119	0.158	0.0

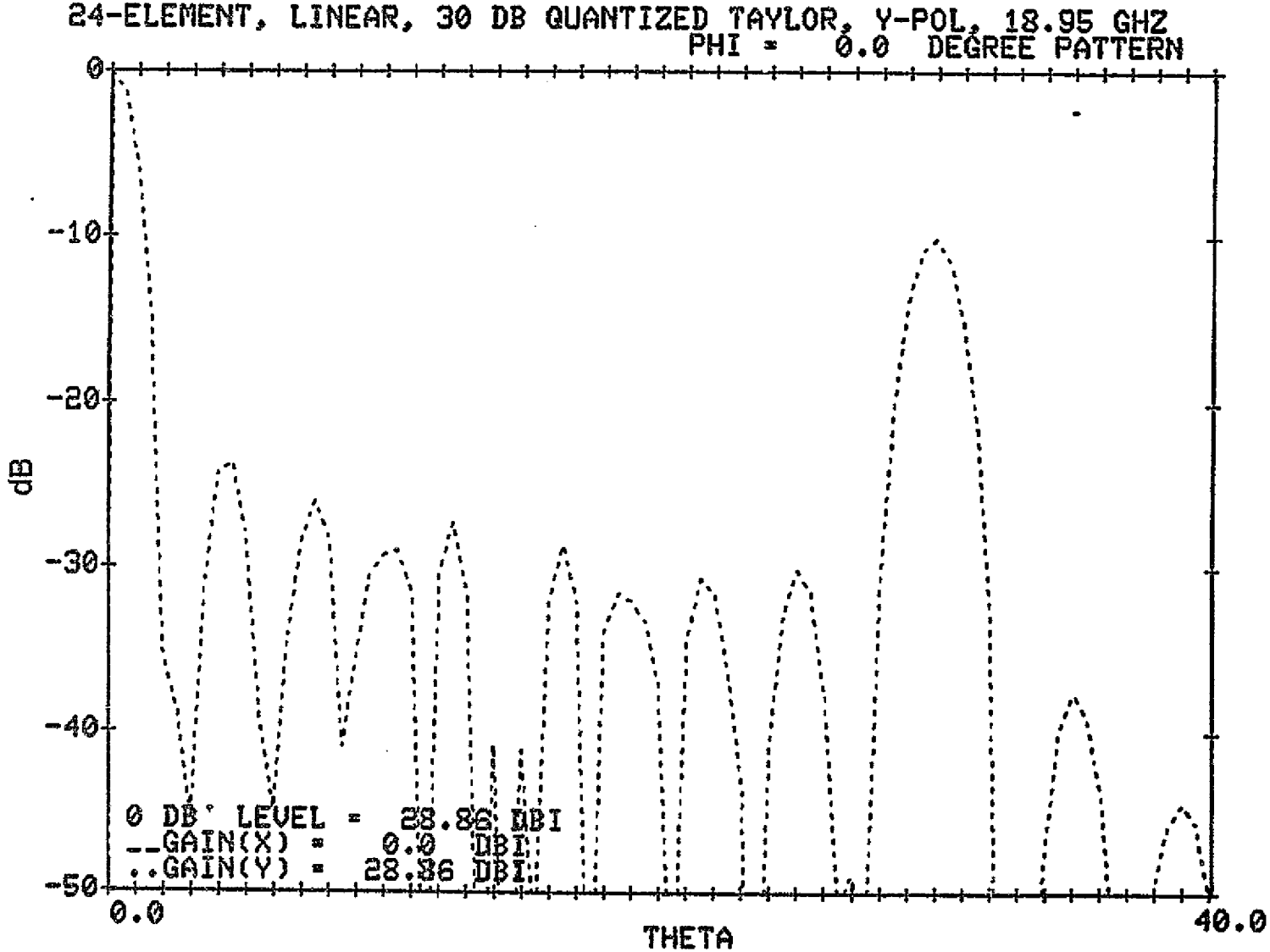

Figure 4-21. Radiation Pattern of 24-Element Linear Array With Quantized 30-dB Taylor Distribution

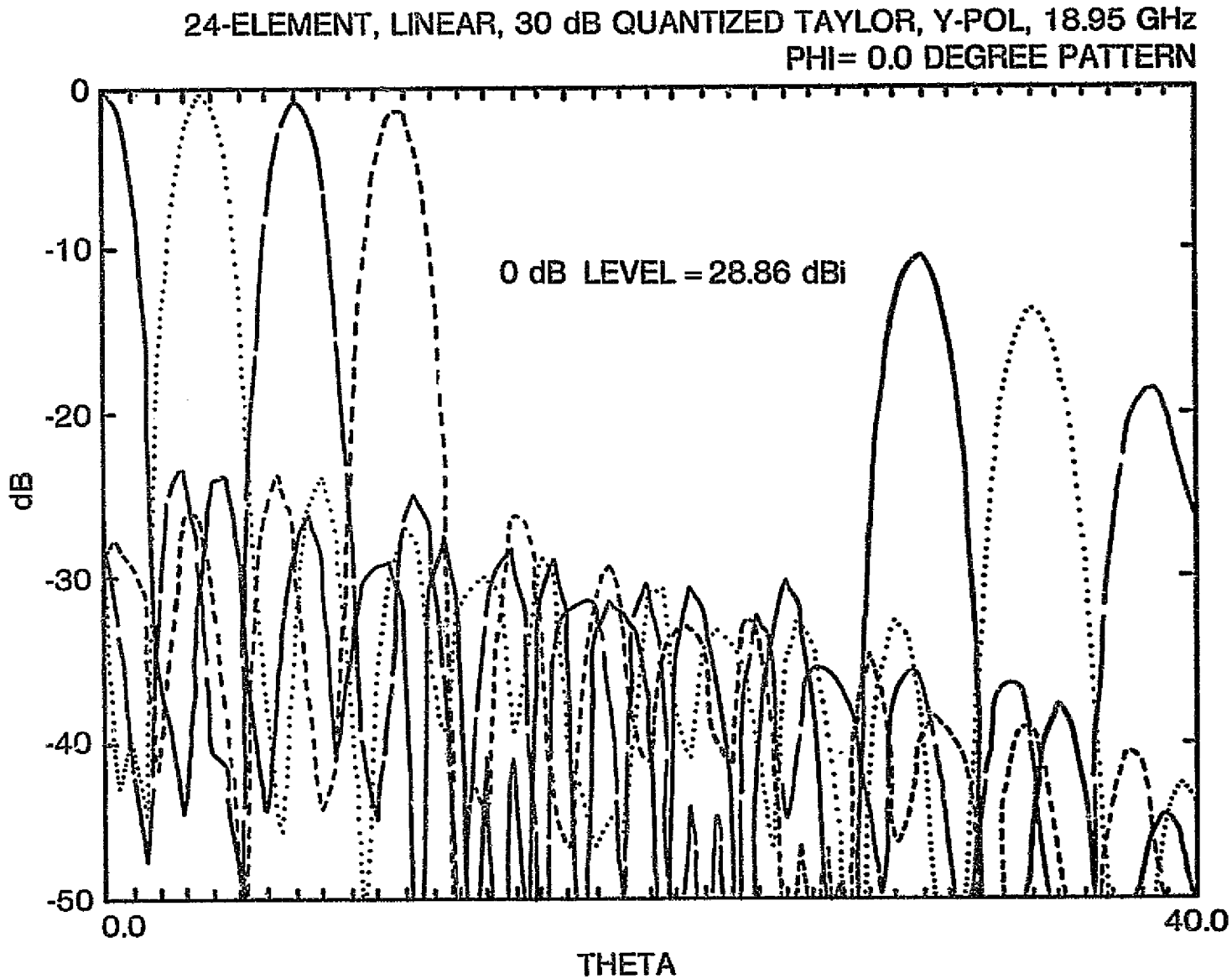

Figure 4-22. Radiation Patterns in Four Scanning Directions of 24-Element Linear Array With Quantized 30-dB Taylor Distribution

The five preset amplifier levels can be optimized to produce a better array pattern. The coefficients in Table 4-6 show that concentrating the four non-zero levels between 1.0 and 0.25 may result in a more gradual quantization between desired levels. For example, if the five levels chosen are 1.0, 0.75, 0.50, 0.25, and 0, the quantized coefficients will be those shown in the last column of the table. The radiation pattern for broadside direction will be those shown in Figure 4-23. The first sidelobe level is now -33 dB below the main beam. The sidelobe level at the isolated positions becomes -27 dB, an improvement over the results shown in Figure 4-21.

Designing the Taylor distribution for a -35-dB sidelobe level and quantizing the resulting amplitudes according to preset levels of 1.0, 0.5, 0.316, 0.158, and 0 produces the amplitudes shown in Table 4-7. The radiation pattern is that shown in Figure 4-24. The sidelobe level in the isolated region increased again to about -24 dB, showing that the proper choice of amplifier setting plays an important role in approaching the Taylor pattern, even if the amplitude distribution is designed with enough sidelobe margin.

The sidelobe and isolation levels are critical mainly for east-west scanning. The north-south sidelobes appear in the same sector as the main beam, simplifying the aperture distribution in the x-direction of the array or in individual rows. A uniform distribution can be used in this direction, which helps to increase the average power per element and thus achieve the required e.i.r.p. levels. The combined x-y aperture distribution of uniform and quantized Taylor distribution of Table 4-6 produces an average power per element of 0.5 of the maximum available power, or 0.25 W per element. Figure 4-25 shows an example of the two-dimensional pattern contours of such a system for broadside radiation.

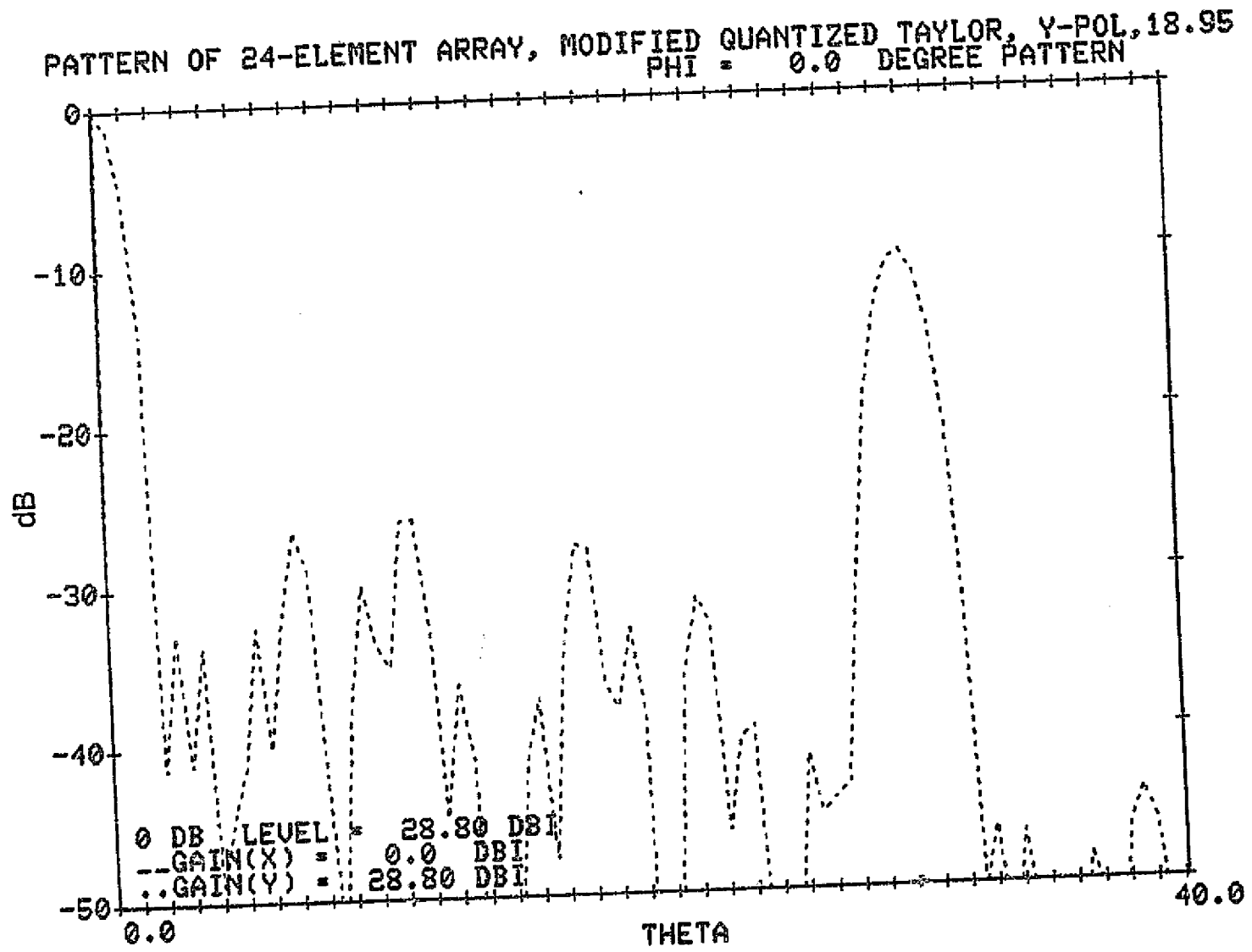

Figure 4-23. Radiation Pattern of 24-Element Linear Array With Modified Quantized 30-dB Taylor Distribution

Table 4-7. Amplitude Coefficients for 24-Element, 35-dB Quantized Taylor Distribution

Element Number	Relative Amplitude Quantized to Levels 1, 0.5, 0.316, 0.158, and 0
1	0.0
2	0.158
3	0.158
4	0.316
5	0.316
6	0.50
7	0.50
8	0.50
9	1.0
10	1.0
11	1.0
12	1.0
13	1.0
14	1.0
15	1.0
16	1.0
17	0.50
18	0.50
19	0.50
20	0.316
21	0.316
22	0.158
23	0.158
24	0.0

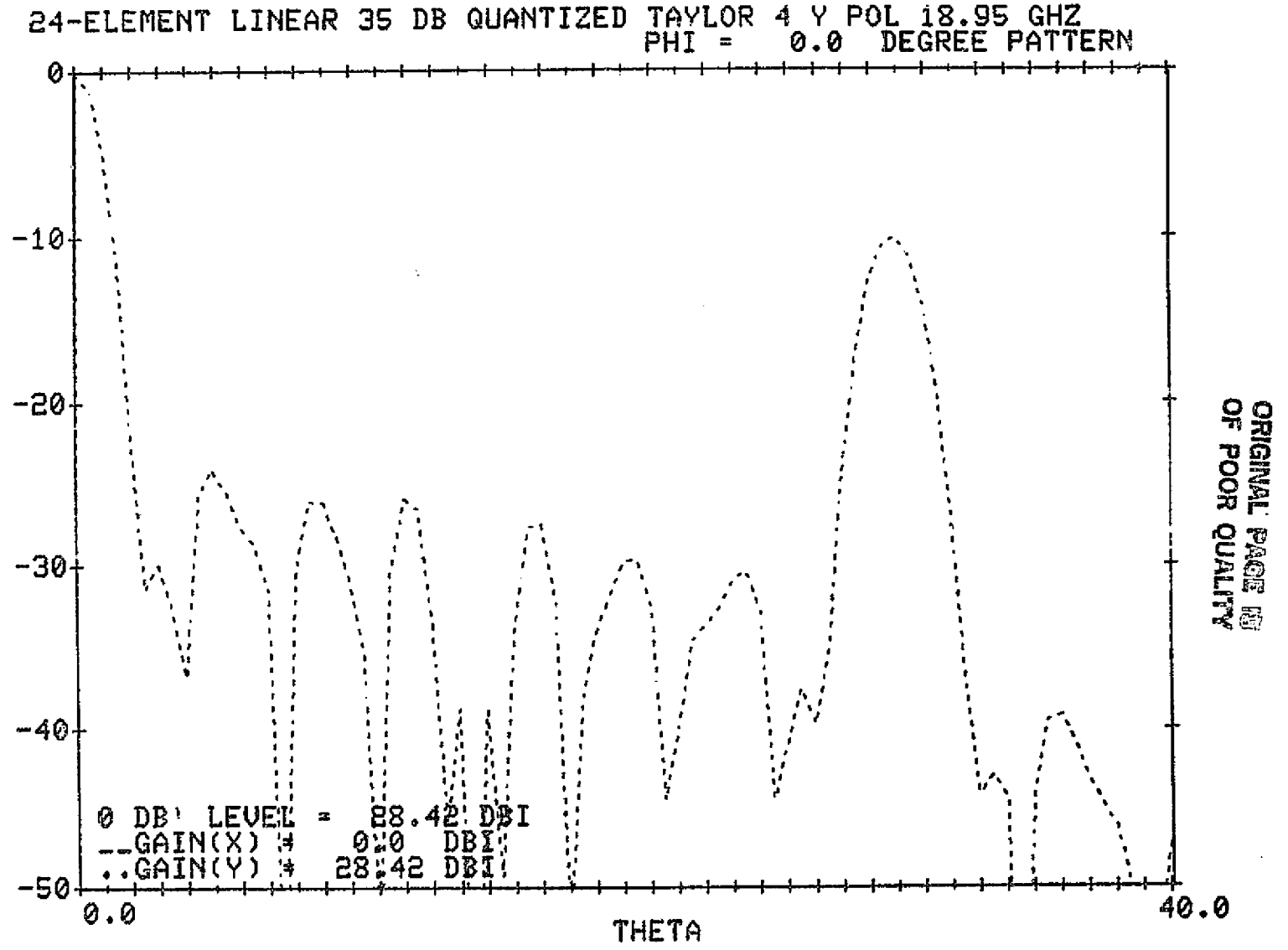

Figure 4-24. Radiation Pattern of 24-Element Linear Array With Quantized 35-dB Taylor Distribution

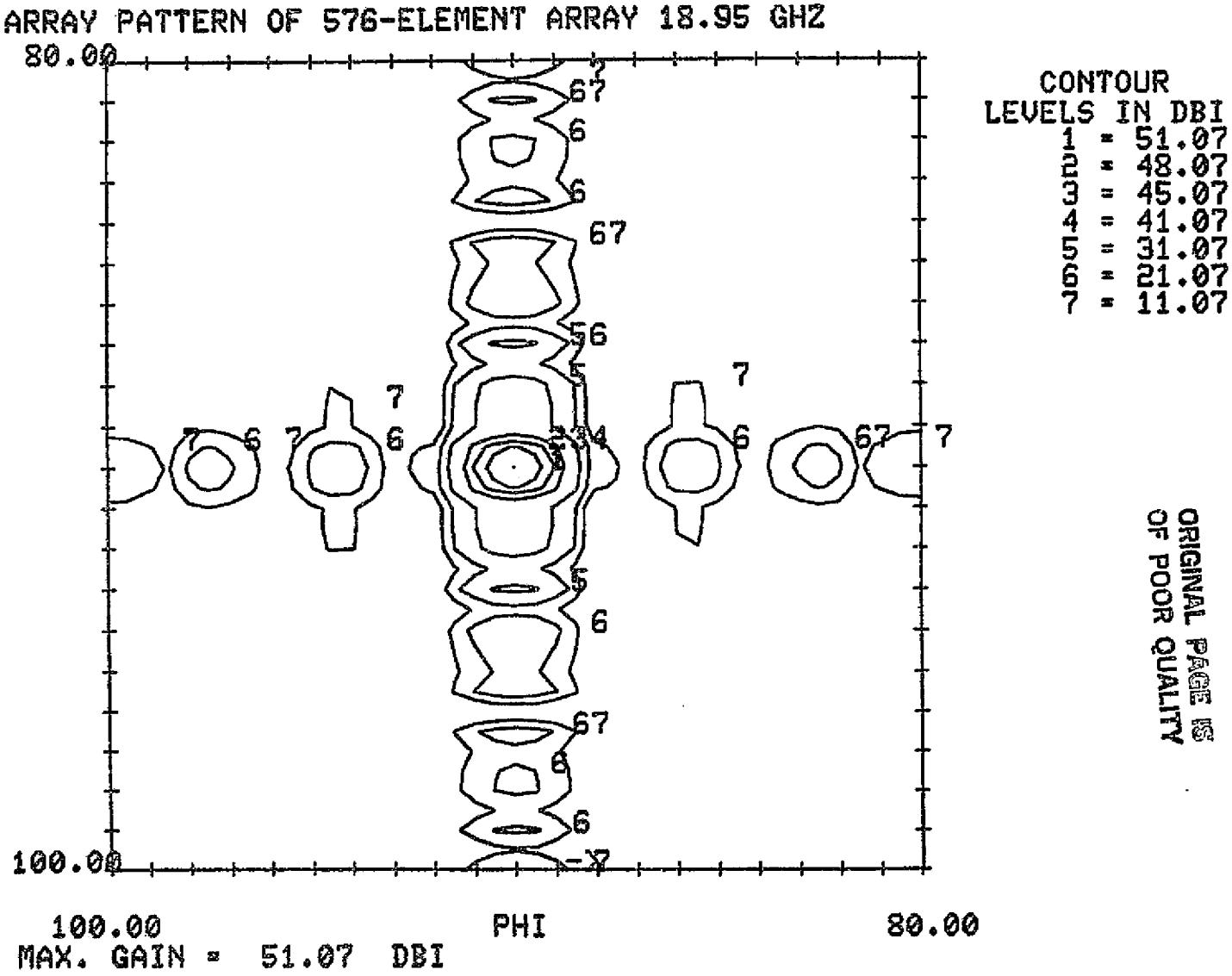

Figure 4-25. Radiation Pattern Contours of the 576-Element Array

4.4 LENS DESIGN

Among the different configurations for microwave lenses, the bootlace or Rotman lens [4-4] offers the simplest and most convenient design for the present application. Three different arrays must be designed for such a lens: a feed array, a lens input array, and a lens output array. The feed array has a number of elements that correspond to the scanning spots in the far field. The number of elements, element size, and array lattice of the output array follow steps similar to those of the phased array discussed in Subsection 4.3. The input array has the same number of elements as the output array, but the element types need not be the same. One major design effort is the determination of the array surface shapes, which depend on the number of focal points in the lens. For this purpose, two lens designs were studied: bifocal and quadrufocal.

A two-dimensional analysis of both designs has been available in the literature for a number of years. Recently, a three-dimensional analysis was introduced [4-5] with results only in two orthogonal planes and with no attempt to improve the lens performance in scan directions other than the perfect focal points. In the present effort, both bifocal and quadrufocal lenses were analyzed in general scan directions. Feed-array element locations were optimized to produce minimum path length error in all directions.

4.4.1 BIFOCAL LENS

The bifocal lens offers a simple design in which the output array lies on a planar surface. The two scan directions corresponding to the perfect focal points are symmetrical about the lens boresight direction. Figure 4-26 shows the geometrical

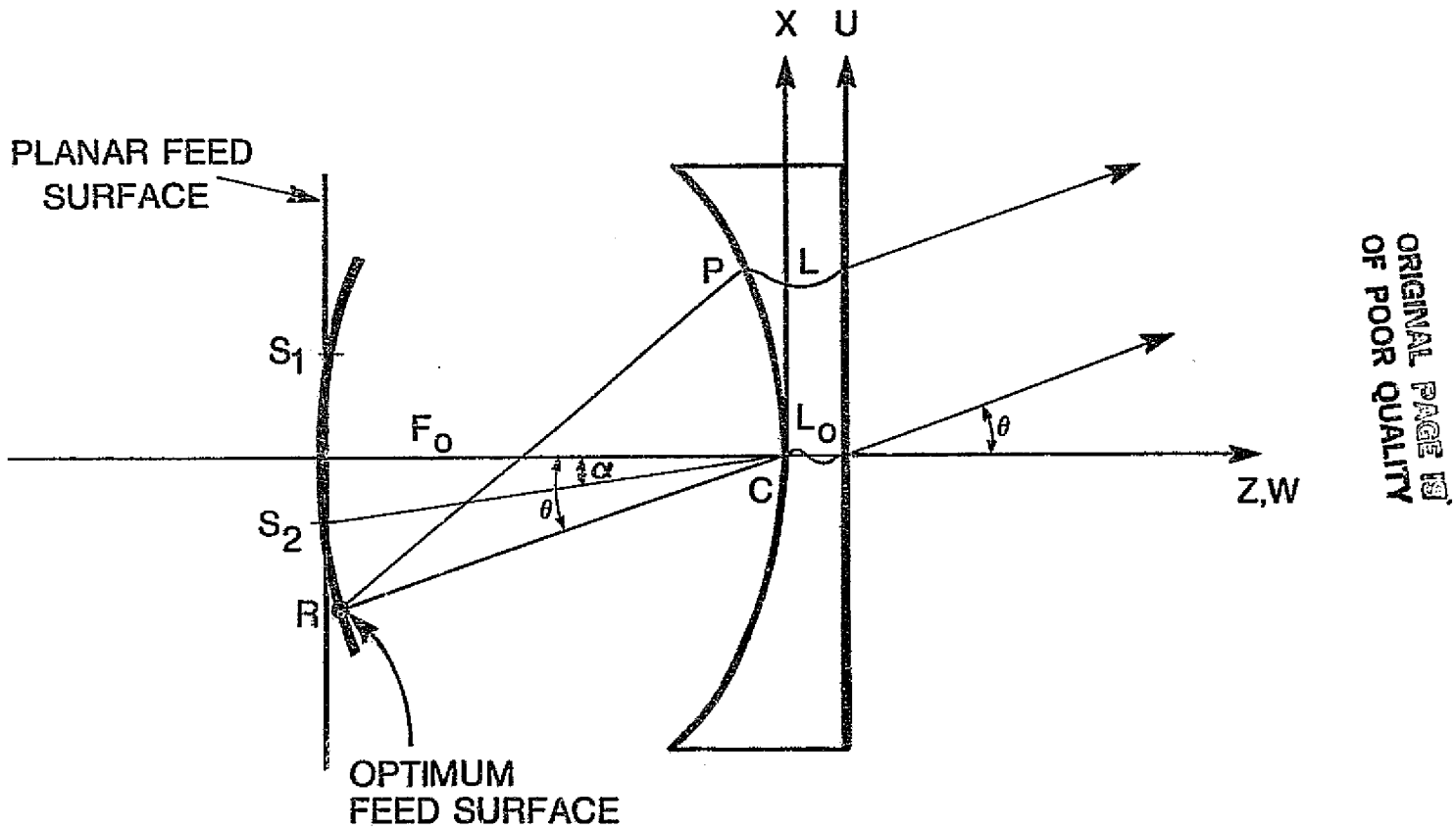

Figure 4-26. Bifocal Lens Geometry

parameters of the lens. The perfect focal points are S_1 and S_2, subtending an angle α with the lens axis Z. The inner surface of the lens is given by

$$X^2 \cos^2 \alpha + Y^2 + (Z + F_o)^2 = F_o^2 \qquad (4\text{-}21)$$

where F_o is the focal length measured along the Z axis from the lens center, C, to the focal line S_1 and S_2. The inner surface is symmetrical about the line S_1S_2. The outer surface is defined by the plane UV in the UVW coordinate system, where Z and W axes are the same. For the bifocal lens, U = X is an added constraint compared to trifocal and quadrufocal lenses. The connecting transmission line lengths between the inner and outer surfaces are equal, that is, $L = L_o$.

For feeds placed at the two focal points, the wavefronts emitting from the secondary array are plane waves in directions $(\pm\alpha, 0)$ in the (θ, ϕ) coordinates. Coordinate θ is measured from the Z (or W) axis, and ϕ is measured in the UV plane from the U axis. For feeds placed at other points on the feed surface, the wavefront will have some phase errors. This analysis revealed that, instead of locating the feeds on a planar surface parallel to the XY-plane, a first-order optimum surface can be produced by moving the feeds parallel to the Z-axis to minimize the maximum path length error.

The path length error for a feed located at point R is

$$\Delta L = L_P - LC \qquad (4\text{-}22)$$

where

$$L_P = \overline{RP} + L - U \sin\theta \cos\phi - V \sin\theta \sin\phi \qquad (4\text{-}23)$$

$$L_C = \overline{RC} + L_o \qquad (4\text{-}24)$$

$$\overline{RP}^2 = (X_P - X_R)^2 + (Y_P - Y_R)^2 + (Z_P - Z_R)^2 \qquad (4\text{-}25)$$

$$\overline{RC}^2 = X_R^2 + Y_R^2 + Z_R^2 \qquad (4\text{-}26)$$

$$X_R = -F_o \tan\theta \cos\phi \qquad (4\text{-}27)$$

$$Y_R = -F_o \tan\theta \sin\phi \qquad (4\text{-}28)$$

$$Z_R = -F_o \qquad (4\text{-}29)$$

$$X_P^2 \cos^2\alpha + Y_P^2 + (Z_P + F_o)^2 = F_o^2 \qquad (4\text{-}30)$$

Equations (4-22) through (4-30) lead to the path length error normalized to focal length F_o as

$$\frac{\Delta L}{F_o} = -u \sin\theta \cos\phi - v \sin\theta \sin\phi - \frac{1}{\cos\theta} + \sqrt{\frac{1}{\cos^2\theta} + u^2 \sin^2\alpha + 2u \tan\theta \cos\phi + 2v \tan\theta \sin\phi} \qquad (4\text{-}31)$$

where

$$u = U/F_o$$

and

$$v = V/F_o \qquad (4\text{-}32)$$

If the feed element position is perturbed in the Z-direction by a normalized amount ζ, equation (4-29) is rewritten as

$$Z_R = -F_o + \zeta F_o \tag{4-33}$$

The normalized path length error at an output array location of (U,V) for feed with incidence direction (θ,ϕ) can be shown to be

$$\Delta L = -u \sin\theta \cos\phi - v \sin\theta \sin\phi - \left[\frac{1}{\cos^2\theta} + \zeta^2 - 2\zeta\right]^{1/2}$$

$$+ \left[\frac{1}{\cos^2\theta} + u^2 \sin^2\alpha + 2u \tan\theta \cos\phi + 2v \tan\theta \sin\phi\right.$$

$$\left. + \zeta^2 - 2\zeta \sqrt{1 - u^2 \cos^2\alpha - v^2}\right]^{1/2} \tag{4-34}$$

When $\theta = \alpha$ and $\phi = 0$, equations (4-31) and (4-34) both give zero path length error at all values of U and V, as expected. The feed location axial parameter, ζ, can be optimized to produce minimum peak error for every scan direction. The peak error is the maximum path length error for all values of U and V in the output array. Consequently, the peak error and the optimum ζ are functions of the shape and size of the outer array aperture.

For an outer array configuration similar to the one used for the phased array in Figure 4-17, and for focal length equal to the largest array dimension (F/D = 1.0), the perfect focus angle, α, is chosen to produce minimum path length error within the scanning range. Figure 4-27 shows the variation of the maximum relative path length error with scan angle for different values of α. The scan angle is limited in the θ direction by 15° and is 0° in the ϕ direction. This shows scanning in the principal plane XZ of the lens.

For the present design, the principal plane is assumed to be the offset plane of the dual-reflector system. This means that the path length error curves of Figure 4-27 are for east-west scanning, which is limited to $\pm 13°$ for a magnification factor of 3.6. To obtain phase front error as uniformly as possible within the scanning range, it is desirable to equalize the path length error at the two edges of the scanning range, 0° and 13°. Figure 4-28 is used to determine α, which satisfies this requirement. The maximum path length error is plotted at $\theta = 0°$ and 13° vs the perfect focus angle, α. This figure shows that $\alpha = 10.5°$ satisfies the requirement of a nearly uniform path length error. Figures 4-27 and 4-28 both use the optimized axial perturbations of the feed elements or the optimum feed surface, as defined earlier.

Once α is determined, the optimum feed surface and the corresponding maximum path length errors can be calculated for all scanning directions. Figures 4-29 and 4-30 show the optimum axial feed locations and the maximum relative path length error in different ϕ planes from 0 to 90°. The equation $\phi = 90°$ corresponds to north-south scanning. In these figures, the output array assumes the same configuration as that of Figure 4-17. The focal length F_o is assumed to be equal to the array side dimension, or in optical terms, $F/D = 1.0$. To compare the optimized results with those obtained when the feed array is located on a planar surface, Figure 4-30 also shows the maximum path length error when $\zeta = 0$. Improvements of up to 30 percent are obtained when the optimum feed surface is used.

This analysis leads directly to an examination of the phases of the different elements in the outer array. The amplitude distribution is set through the amplifiers, which are inserted between the input and output arrays. As in the case of the phased array, the amplitude distribution is set to be uniform in the north-south direction (in the same row of the triangular

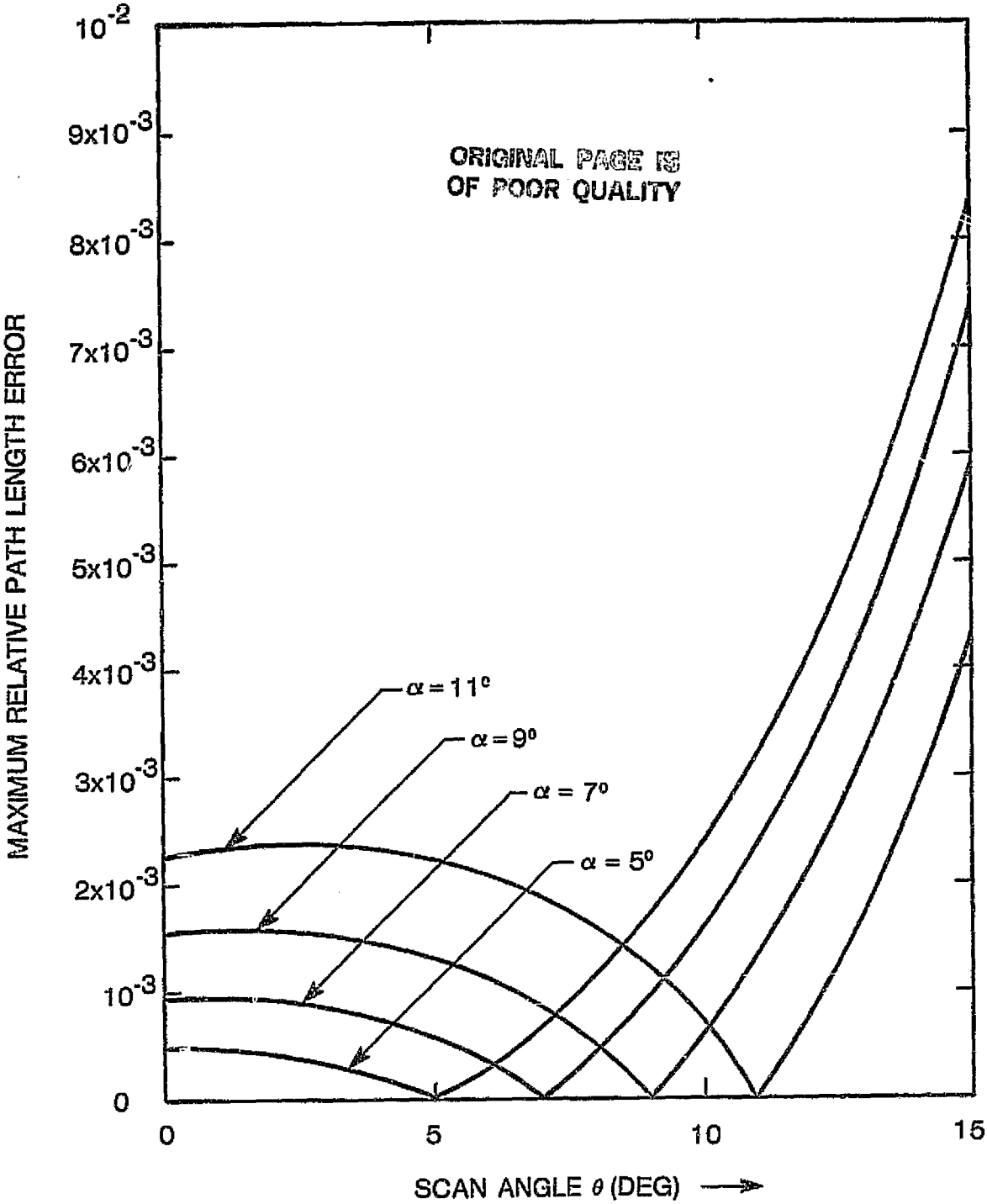

Figure 4-27. Maximum Relative Path Length Error vs Scan Angle for Different Values of α

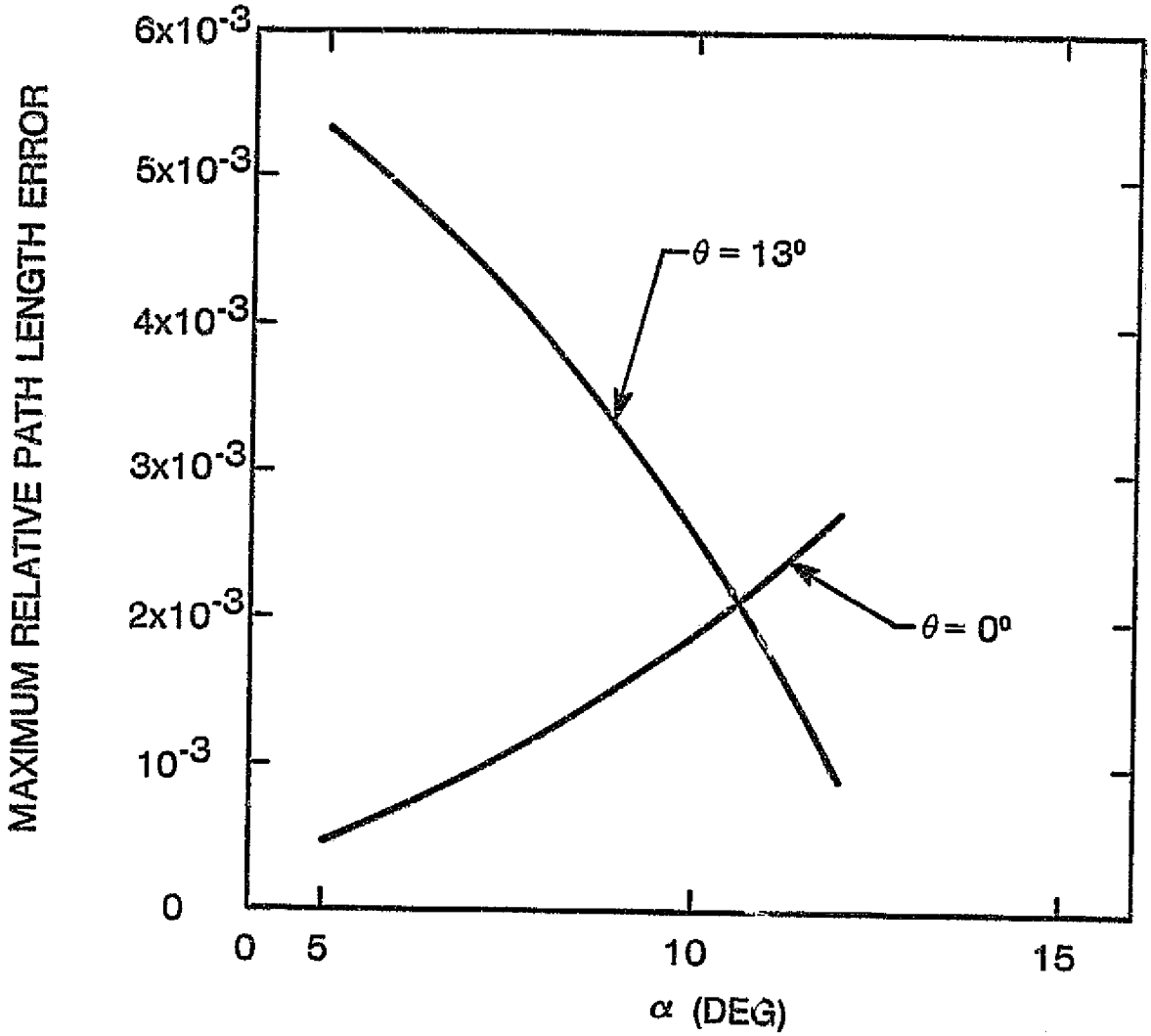

Figure 4-28. Maximum Relative Path Length Error at Broadside and Scan Edge vs Angle α

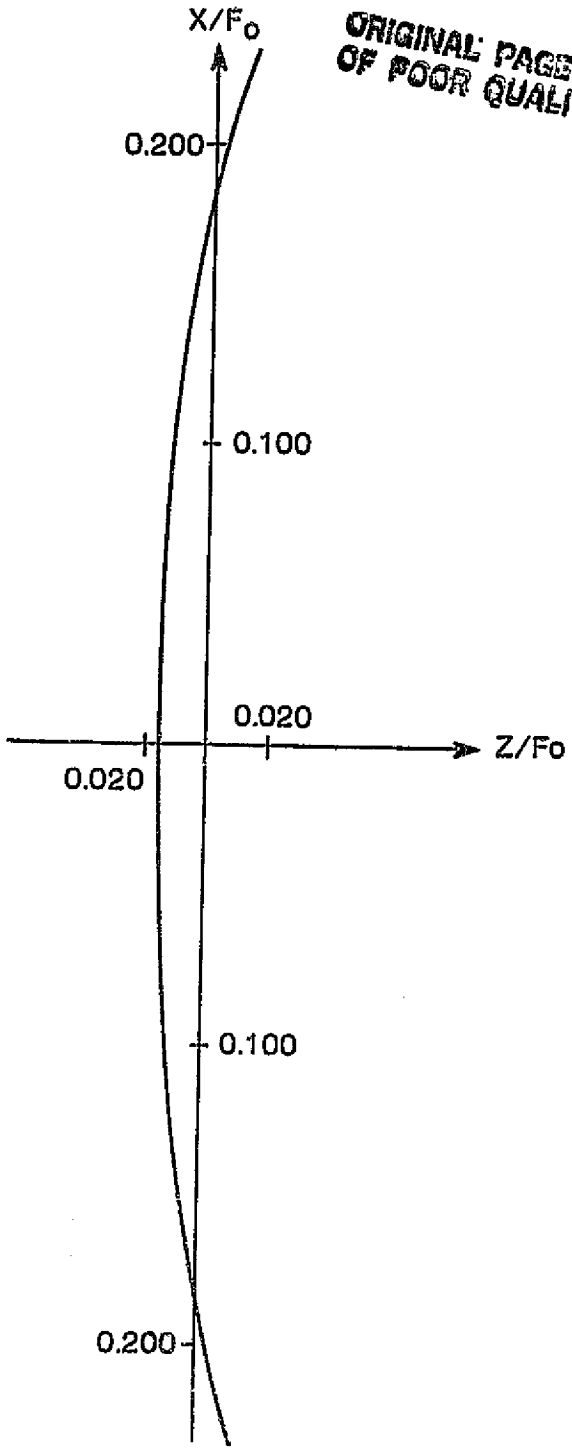

Figure 4-29. Optimum Feed Locus in XZ-Plane

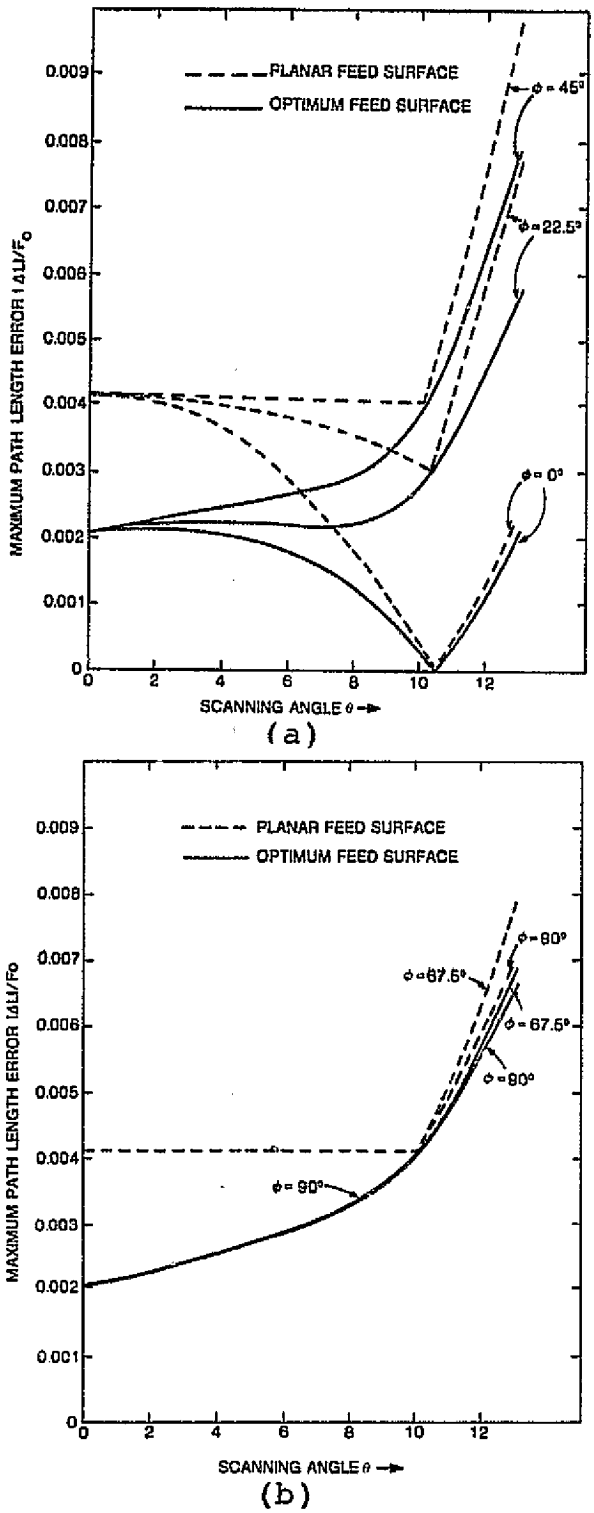

Figure 4-30. Maximum Relative Path Length Error vs Scanning Angle in Different Planes for $\alpha = 10.5°$

C-3

lattice), and quantized Taylor distribution is set in the east-west direction (between the different rows). The quantization levels are set according to allowable levels of the amplifier modules. Examples of east-west pattern cuts with this distribution are shown in Figures 4-31 and 4-32. A comparison of these examples with those portrayed in Figure 4-22 shows the overall effect of the path length errors on scanning in the principal east-west plane.

4.4.2 QUADRUFOCAL LENS

The four adjustable constraints on the bootlace lens, the shapes of the inner and outer surfaces, the electrical length of each transmission line connecting the elements of the two surfaces, and the mapping from an element on the inner surface to one on the outer surface, provide four degrees of freedom. Thus, it is possible to design a lens with four perfect focal points, one for each of four separate output directions. These four points can be spread across the focal region to provide a wide field of view with a minimal amount of aberration.

Rao [4-5] has devised a method of generating three-dimensional bootlace lenses with two, three, and four focal points. Based on equations similar to those of Rotman [4-4], and with a restriction that all of the design foci be collinear, the three-dimensional lens is generated by revolving the derived two-dimensional profile around the focal line. These lenses are not rotationally symmetrical around the Z axis. Having a fourth focal point substantially increases the field of view over the previous trifocal designs; however, the phase errors for beams that fall between the designed scan directions are relatively large.

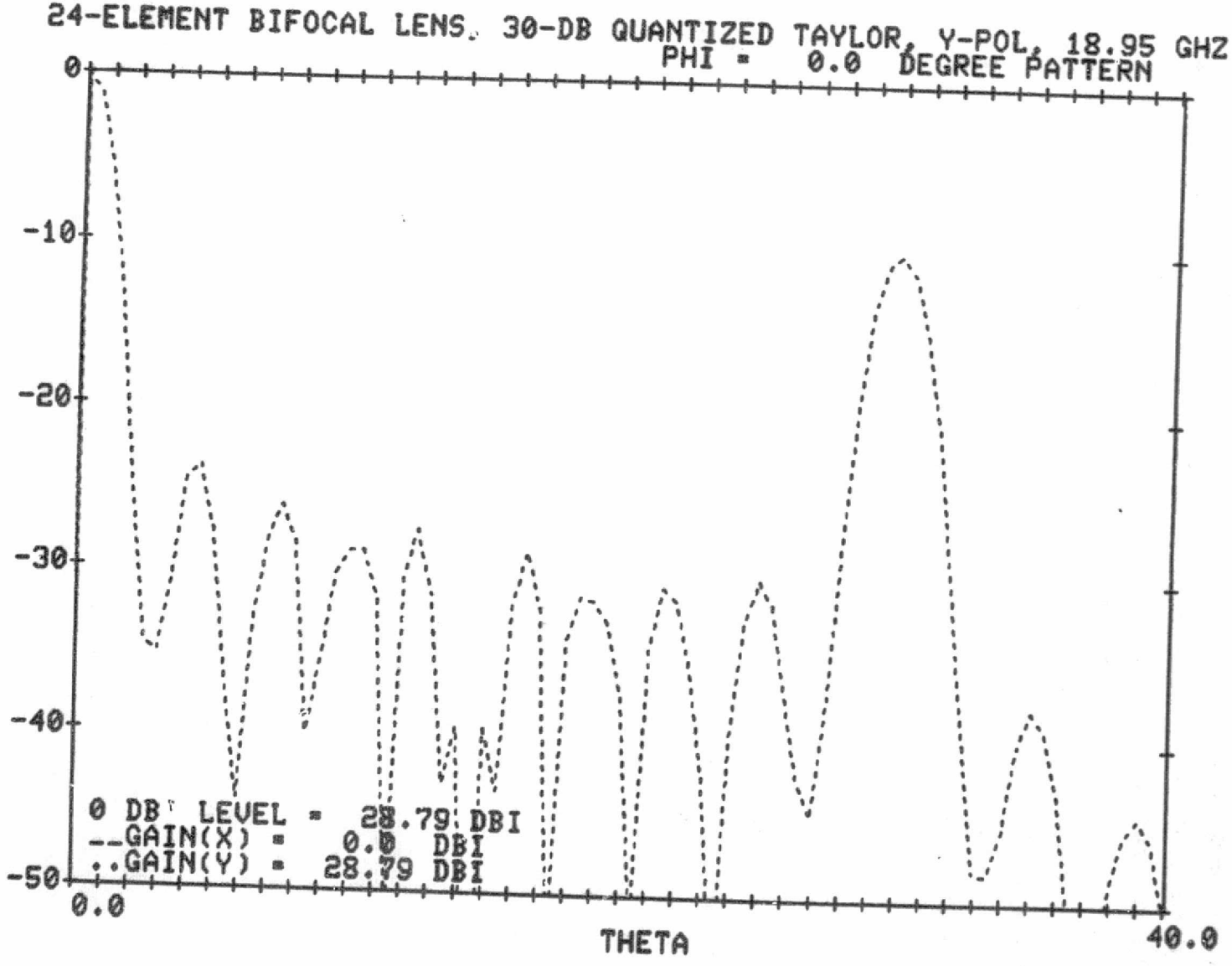

Figure 4-31. Radiation Pattern of 24-Element Linear Bifocal Lens With 30-dB Quantized Taylor Distribution

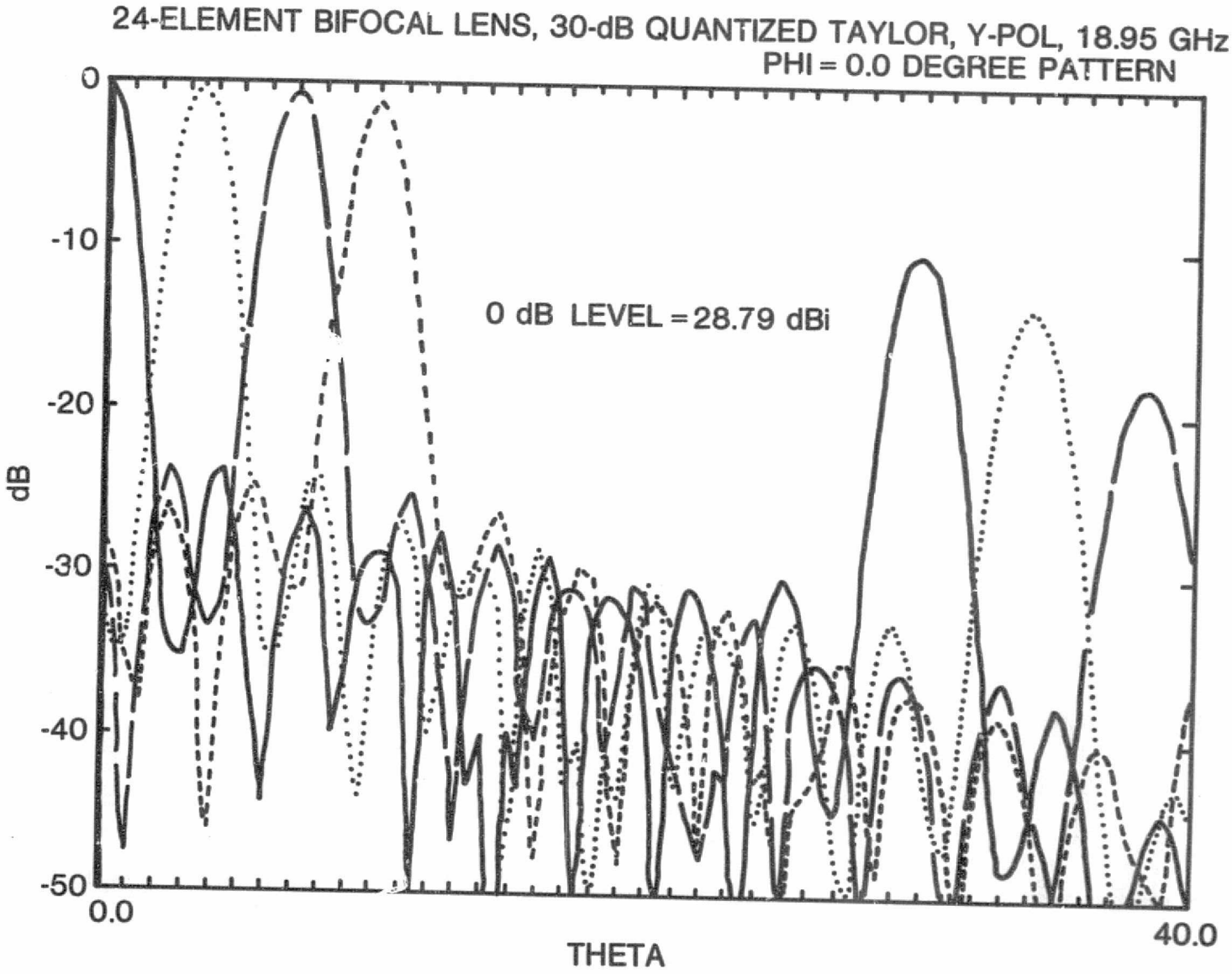

Figure 4-32. Radiation Pattern of 24-Element Linear Bifocal Lens in Four Scanning Directions with 30-dB Quantized Taylor Distribution

The use of a curved focal arc for a three-dimensional quadrufocal bootlace lens makes the design procedure more difficult. However, this new concept may significantly improve scan performance.

Figure 4-33 shows the geometry of the quadrufocal bootlace lens. There are four path length conditions, which are stated as

$$F_i = \sqrt{(Z + F_i \cos\theta_i)^2 + Y^2 + (X - F_i \sin\theta_i)^2} + L + U \sin\theta_i - W \cos\theta_i; \qquad (4\text{-}35)$$

$$i = 1,2 \quad ; \quad \theta_1 = \pm\alpha \quad ; \quad \theta_2 = \pm\beta$$

with $V = Y$.

The following algebra solves the above equations for Y, U, W, and L for variables X and Z and for parameters F_i, θ_i. Subtracting equation (4-35) from the same equation with θ_i replaced by $-\theta_i$ yields

$$0 = \sqrt{F_i^2 + R^2 + 2F_i(Z\cos\theta_i - X\sin\theta_i)} - \sqrt{F_i^2 + R^2 + 2F_i(Z\cos\theta_i + X\sin\theta_i)} - 2U\sin\theta_i \qquad (4\text{-}36)$$

where $R^2 = X^2 + Y^2 + Z^2$. Regrouping, squaring equation (4-36), and rearranging produces

$$\frac{F_i X}{U} = U\sin\theta_i + \sqrt{F_i^2 + R^2 + 2F_i(Z\cos\theta_i - X\sin\theta_i)}$$

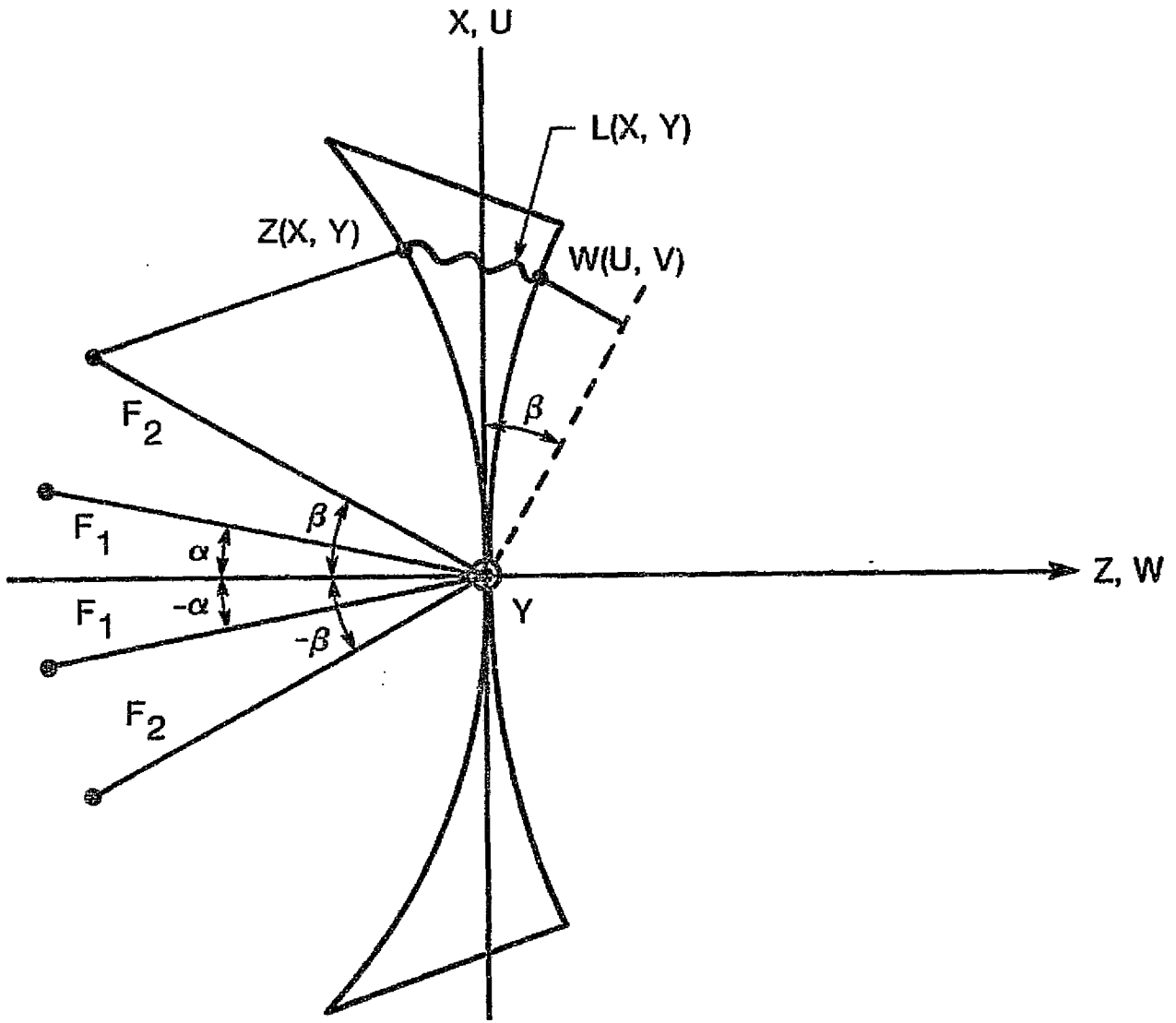

Figure 4-33. Geometry of the Quadrufocal Lens

Regrouping and squaring again gives

$$Y^2 = \left(\frac{F_i X}{U}\right)^2 + U^2 \sin^2 \theta_i - (F_i^2 + X^2 + Z^2 + 2F_i Z \cos \theta_i) \quad (4\text{-}37)$$

Subtracting equation (4-37) with $\theta_i = \alpha$ from equation (4-37) with $\theta_i = \beta$ yields

$$U^4 A + U^2 B + C = 0 \quad (4\text{-}38)$$

where

$$A = \sin^2 \beta - \sin^2 \alpha$$
$$B = 2Z(F_1 \cos \alpha - F_2 \cos \beta) + F_1^2 - F_1^2$$
$$C = (F_2^2 - F_1^2) X^2$$

Thus, U is found in terms of X and Z by applying the quadratic formula. Equation (4-37) gives Y as a function of X, Z, and U.

By using equation (4-38), equation (4-37) can be manipulated to specify Y as a function of only U and Z. Equation (4-38) is rewritten as

$$X^2 = \frac{AU^4 + BU^2}{F_1^2 - F_2^2} \quad (4\text{-}39)$$

Now, equation (4-37) is written as

$$Y^2 = U^2 \sin^2 \theta_i - (F_i^2 + Z^2 + 2F_i Z \cos \theta_i) + \frac{AU^4 + BU^2}{F_1^2 - F_2^2} \left(\frac{F_i^2}{U^2} - 1\right) \quad (4\text{-}40)$$

with A and B defined in equation (4-38).

Simplifying equation (4-40) yields

$$Y^2 = U^2 \left(\sin^2 \theta_i + \frac{AF_i^2}{F_1^2 - F_2^2} \right) - \frac{AU^4}{F_1^2 - F_2^2}$$

$$+ F_i^2 \left(-1 + \frac{B}{F_1^2 - F_2^2} \right) - \frac{BU^2}{F_1^2 - F_2^2} - 2F_iZ \cos \theta_i - Z^2 \qquad (4\text{-}41)$$

Letting i = 1 and substituting for A and B yields

$$Y^2 = - \frac{AU^4}{F_1^2 - F_2^2} + U^2 \frac{(F_1^2 \sin^2 \beta - F_2^2 \sin^2 \alpha)}{F_1^2 - F_2^2}$$

$$- U^2 \left[\frac{F_1^2 - F_2^2 + 2Z(F_1 \cos \alpha - F_2 \cos \beta)}{F_1^2 - F_2^2} \right]$$

$$+ F_1^2 \left[\frac{2Z(F_1 \cos \alpha - F_2 \cos \beta)}{F_1^2 - F_2^2} \right] - 2F_1Z \cos \alpha - Z^2 \qquad (4\text{-}42)$$

or

$$Y^2 = - \frac{AU^4}{F_1^2 - F_2^2} + U^2 \frac{F_2^2 \cos^2 \alpha - F_1^2 \cos \beta}{F_1^2 - F_2^2}$$

$$+ Z \left(\frac{2}{F_1^2 - F_2^2} \right) [(F_1F_2)(F_2 \cos \alpha - F_1 \cos \beta)$$

$$+ U^2(F_2 \cos \beta - F_1 \cos \alpha)] - Z^2 \qquad (4\text{-}43)$$

Finally, casting this equation into the canonical equation for a circle results in

$$Y^2 + \left\{ Z - \left(\frac{1}{F_1^2 - F_2^2} \right) [F_1 F_2 (F_2 \cos \alpha - F_1 \cos \beta) + U^2 (F_2 \cos \beta - F_1 \cos \alpha)] \right\}^2$$

$$= -U^4 \left(\frac{1}{F_1^2 - F_2^2} \right)^2 (F_2 \cos \alpha - F_1 \cos \beta)^2$$

$$+ U^2 \left(\frac{1}{F_1^2 - F_2^2} \right)^2 [-(F_1^4 \cos^2 \beta + F_2^4 \cos^2 \alpha)$$

$$+ 2F_1 F_2 (F_1^2 + F_2^2) \cos \alpha \cos \beta - F_1^2 F_2^2 (\cos^2 \alpha + \cos^2 \beta)]$$

$$- \left(\frac{F_1 F_2}{F_1^2 - F_2^2} \right)^2 (F_2 \cos \alpha - F_1 \cos \beta)^2 \qquad (4\text{-}44)$$

or

$$Y^2 + \left\{ Z - \left[Z_0 + \frac{U^2}{F_1^2 - F_2^2} (F_2 \cos \beta - F_1 \cos \alpha) \right] \right\}^2$$

$$= -Z_0^2 \left[\frac{U^4}{F_1^2 F_2^2} - U^2 \frac{(F_1^2 + F_2^2)}{F_1^2 F_2^2} + 1 \right] \qquad (4\text{-}45)$$

where

$$Z_0 = \left(\frac{F_1 F_2}{F_1^2 - F_2^2} \right)^2 (F_2 \cos \alpha - F_1 \cos \beta) \qquad (4\text{-}46)$$

Now W and L must be determined. Let $S_i = F_i - L + W \cos \theta_i$. From the equation

$$(S_i - U \sin \theta_i)^2 = F_i^2 + X^2 + Y^2 + Z^2 + 2F_i (Z \cos \theta_i - X \sin \theta_i) \qquad (4\text{-}47)$$

Subtracting the same equation with θ_i replaced by $-\theta_i$ yields

$$-4S_iU \sin \theta_i = -4F_iX \sin \theta_i \tag{4-48}$$

which leads to

$$X = \frac{S_iU}{F_i} \tag{4-49}$$

and so

$$F_1S_2 = F_2S_1 \tag{4-50}$$

$$-LF_1 + WF_1 \cos \beta = -LF_2 + WF_2 \cos \alpha \tag{4-51}$$

implying that

$$L = \left(\frac{F_1 \cos \beta - F_2 \cos \alpha}{F_1 - F_2} \right) W \tag{4-52}$$

Substituting this result into equation (4-49)

$$X = \left(\frac{F_i - L + W \cos \theta_i}{F_i} \right) U \tag{4-53}$$

and choosing $\theta_i = \alpha$, and $F_i = F_1$ yields

$$X = \left[1 + \frac{W}{F_1} \left(\cos \alpha - \frac{F_1 \cos \beta - F_2 \cos \alpha}{F_1 - F_2} \right) \right] U \tag{4-54}$$

$$W = \left(\frac{X}{U} - 1 \right) \frac{F_1 - F_2}{\cos \alpha - \cos \beta} \tag{4-55}$$

Thus, given Z and U, Y is determined by equation (4-46), X follows from equation (4-39), L from equation (4-52), and W from equation (4-55).

Although the scan angles α and β are known parameters, the focal lengths F_1 and F_2 are unspecified. The proper selection of these lengths is critical to providing a minimum amount of aberration for beams scanned at angles that fall between the designated values α and β.

For simplicity, it is assumed that the four focal points lie on a second-degree curve, either an ellipse or a hyperbola. The polar coordinate representation of an ellipse is

$$r^2 = \frac{a^2 b^2}{a^2 \sin^2 \theta + b^2 \cos^2 \theta} \tag{4-56}$$

In terms of the focal point variables, this becomes

$$F_i^2 = \frac{a^2 b^2}{a^2 \sin^2 \theta_i + b^2 \cos^2 \theta_i} \tag{4-57}$$

Solving for b^2 produces

$$b^2 = \frac{F_i^2 a^2 \sin^2 \theta_i}{a^2 - F_i^2 \cos^2 \theta_i} \tag{4-58}$$

Since this equation holds for both i = 1 and i = 2, it can be seen that

$$\frac{F_1^2 \sin^2 \alpha}{a^2 - F_1^2 \cos^2 \alpha} = \frac{F_2^2 \sin^2 \beta}{a^2 - F_2^2 \cos^2 \beta} \tag{4-59}$$

Solving for a^2 results in

$$a^2 = \frac{F_1^2 F_2^2 (\sin^2 \beta \cos^2 \alpha - \sin^2 \alpha \cos^2 \beta)}{F_2^2 \sin^2 \beta - F_1^2 \sin^2 \alpha} \tag{4-60}$$

Substituting back into equation (4-58) yields the remaining ellipse axis equation

$$b^2 = \frac{F_1^2 F_2^2 (\sin^2 \beta \cos^2 \alpha - \sin^2 \alpha \cos^2 \beta)}{F_1^2 \cos^2 \alpha - F_2^2 \cos^2 \beta} \qquad (4\text{-}61)$$

Thus, given the two focal lengths and angles to the focal points, the focal arc is specified.

At this stage, one additional condition must be specified to fully constrain the lens. A possible choice would be no phase variation along the transverse (Y) axis of the lens for rays from a source on the Z-axis, that is, for the summation of L(),Y) and the distance from (0,0,-a) to the point (0,Y,Z) to be constant. This condition simplifies the design considerably, yielding $F_1 = F_2$ as one solution. As with the Rotman lens, the focal arc is a circle; and referring to equation (4-55), W = 0. Unlike the Rotman lens, however, this configuration has four perfect foci and so has a field of view four-thirds as large, in addition to being three dimensional. The lost degree of freedom, that W is zero, is plausible because with $F_1 = F_2$, there are only three input parameters: α, β, and F_1.

The simplified equations are

$$Z = -U^o \frac{\cos \alpha + \cos \beta}{2F_1} \qquad (4\text{-}62)$$

from equation (4-38), and

$$X = \frac{F_1 - L}{F_1} U \qquad (4\text{-}63)$$

from equation (4-49), which leads to

$$L = F_1 \left(1 - \frac{X}{U}\right) \qquad (4\text{-}64)$$

Also, from equation (4-37), using equation (4-62) to solve for U, and with i = 1, gives

$$Y^2 = -\left[F_1^2 + Z^2 + Z\left(2F_1 \frac{\cos\alpha\cos\beta + 1}{\cos\alpha + \cos\beta}\right) + X^2\left(1 + F_1 \frac{\cos\alpha + \cos\beta}{2Z}\right)\right] \quad (4\text{-}65)$$

In equation (4-64), Y is a well-defined function of X and Z everywhere except at Z = 0. From equation (4-62), U = 0 when Z = 0, and by equation (4-63), X = 0 also. From these equations, it is apparent that

$$\frac{X^2}{Z} = -\frac{2(F_1 - L)^2}{F_1(\cos\alpha + \cos\beta)} \quad (4\text{-}66)$$

Therefore, in the plane X = 0, the inner lens profile is a line Z = 0 and has Y related to L by

$$Y^2 = (F_1 - L)^2 - F_1^2 \quad (4\text{-}67)$$

To find the inner lens profile in the plane Y = 0, approximate $F_1 >> Z$ and use equation (4-65), as

$$0 \cong -F_1^2 - X^2 F_1 \frac{\cos\alpha + \cos\beta}{2Z} \quad (4\text{-}68)$$

which becomes

$$Z \cong -X^2\left(\frac{\cos\alpha + \cos\beta}{2F_1}\right) \quad (4\text{-}69)$$

Thus, the optimum lens has a flat outer surface, W(U,V) = 0, and an inner surface that is approximately parabolic in one plane and constant in the other.

It is clear that the distance from the point on the lens axis (also on the focal circle) $(0,0,-F_1)$ to any point $(0,Y,Z)$, plus $L(0,Y)$, is $\sqrt{Y^2 + F_1^2} + [F_1 - \sqrt{Y^2 + F_1^2}]$, which is just F_1, the required constant. Further, since the focal arc is a circle of radius F_1, this property holds for every point on the circle. Although this does not hold in general for every plane for which X equals a constant, it does imply little additional phase error in the region near the Y axis of the lens.

An analysis was made of a quadrufocal bootlace lens with parameters similar to those of the bifocal lens mentioned above. To minimize the maximum phase error across the output aperture for all scan angles from -13° to +13°, the focal points were chosen with angles α = 5°, β =12°, and length F_0 the same as for the bifocal. Figure 4-34 shows the configuration of the lens and its focal arc, with the perfect focal points indicated. Using the same focal length for each focal point yields a lens design with a planar output surface. Table 4-8 compares the computed values for samples of X and U and gives the effective transmission line lengths, L, in inches (2.54 cm) for each of these values for a lens with focal length F = 76.2 cm. Although the difference between X and U is a crucial degree of freedom in the quadrufocal lens, it is nonetheless small. Also, the values of L are small compared to the focal length.

Figure 4-35 plots the maximum phase error across the square aperture bounded by (F/D = 1) for beams scanned in the scan plane as a function of angle. Since the scan plane is the plane that includes the focal point, Figure 4-36 plots the scan performance in the optimum direction. As expected, there are two nulls in the phase error plot. These represent the two positive, perfectly focused beam directions. The worst error for beams scanned in the scan plane within $\pm$13° for the F/D = 1 case is 0.145°, or 8.5×10^{-6}F. This error is practically insignificant.

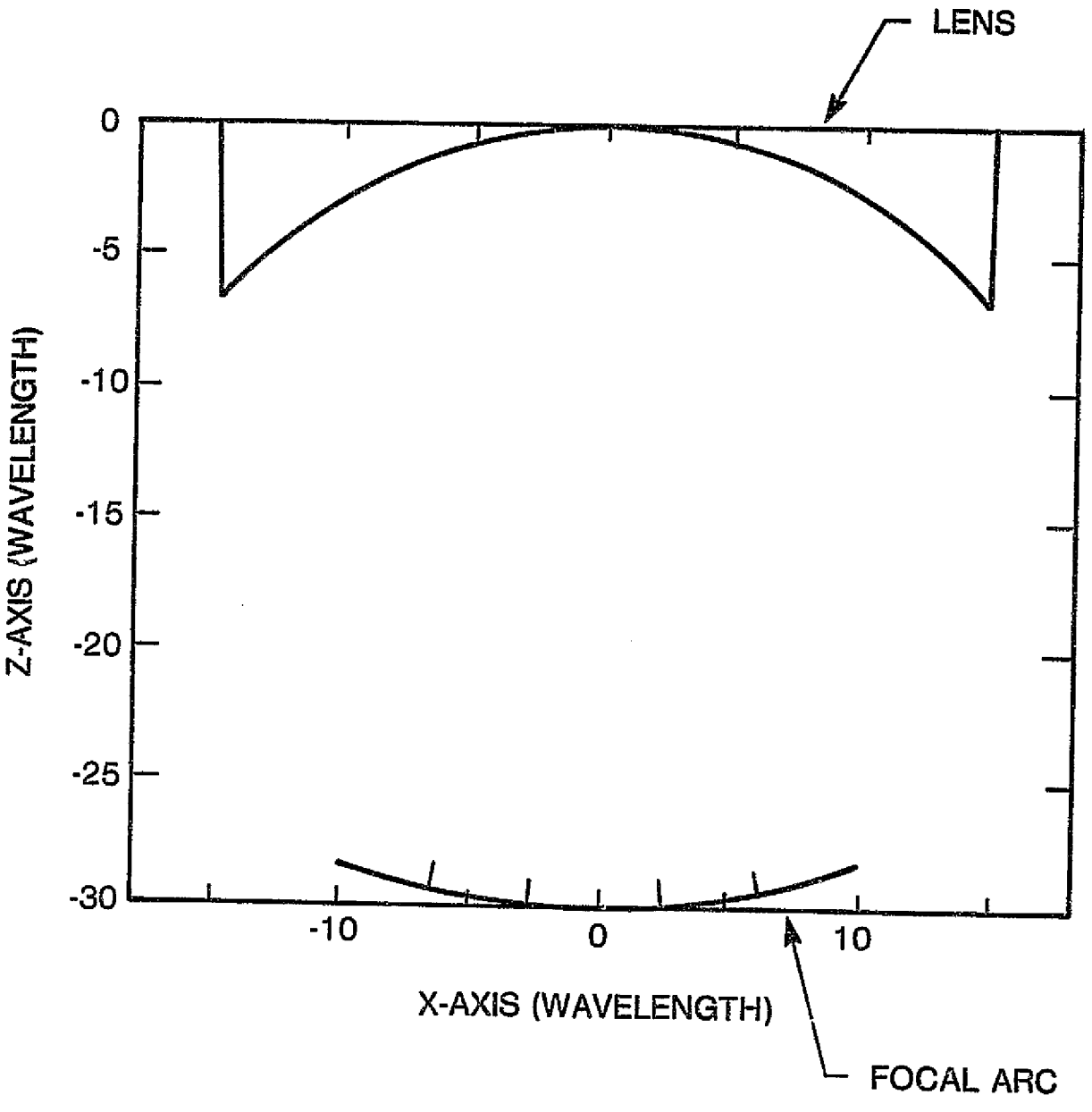

Figure 4-34. Quadrufocal Lens Profile in Y = 0 Plane

Table 4-8. Quadrufocal Lens Design Parameters
(In units of 2.54 cm)

X	Y	Z	U	W	L
0.0	0.0	0.0	0.0	0.0	0.0
2.5104	0.0	-0.2094	2.5192	0.0	0.1035
3.5379	0.0	-0.4188	3.5626	0.0	0.2074
4.3179	0.0	-0.6282	4.3633	0.0	0.3117
4.9682	0.0	-0.8376	5.0383	0.0	0.4163
5.5349	0.0	-1.0471	5.6330	0.0	0.5213
6.0414	0.0	-1.2565	6.1707	0.0	0.6267
6.5019	0.0	-1.4659	6.6651	0.0	0.7324
6.9255	0.0	-1.6753	7.1253	0.0	0.8386
7.3187	0.0	-1.8847	7.5575	0.0	0.9451
7.6861	0.0	-2.0941	7.9663	0.0	1.0520
8.0313	0.0	-2.3035	8.3551	0.0	1.1594
8.3570	0.0	-2.5129	8.7266	0.0	1.2671
8.6654	0.0	-2.7224	9.0830	0.0	1.3752
8.9584	0.0	-2.9318	9.4258	0.0	1.4837
9.2372	0.0	-3.1412	9.7567	0.0	1.5927
9.5033	0.0	-3.3506	10.0767	0.0	1.7021
9.7577	0.0	-3.5600	10.3868	0.0	1.8119
10.0012	0.0	-3.7694	10.6879	0.0	1.9221
10.2346	0.0	-3.9788	10.9808	0.0	2.0328
10.4587	0.0	-4.1882	11.2660	0.0	2.1439
10.6739	0.0	-4.3977	11.5443	0.0	2.2554
10.8809	0.0	-4.6071	11.8159	0.0	2.3674
11.0800	0.0	-4.8165	12.0815	0.0	2.4799
11.2717	0.0	-5.0259	12.3413	0.0	2.5928
11.4564	0.0	-5.2353	12.5958	0.0	2.7062
11.6344	0.0	-5.4447	12.8453	0.0	2.8201
11.8060	0.0	-5.6541	13.0900	0.0	2.9344
11.9715	0.0	-5.8635	13.3302	0.0	3.0493
12.1311	0.0	-6.0729	13.5661	0.0	3.1646

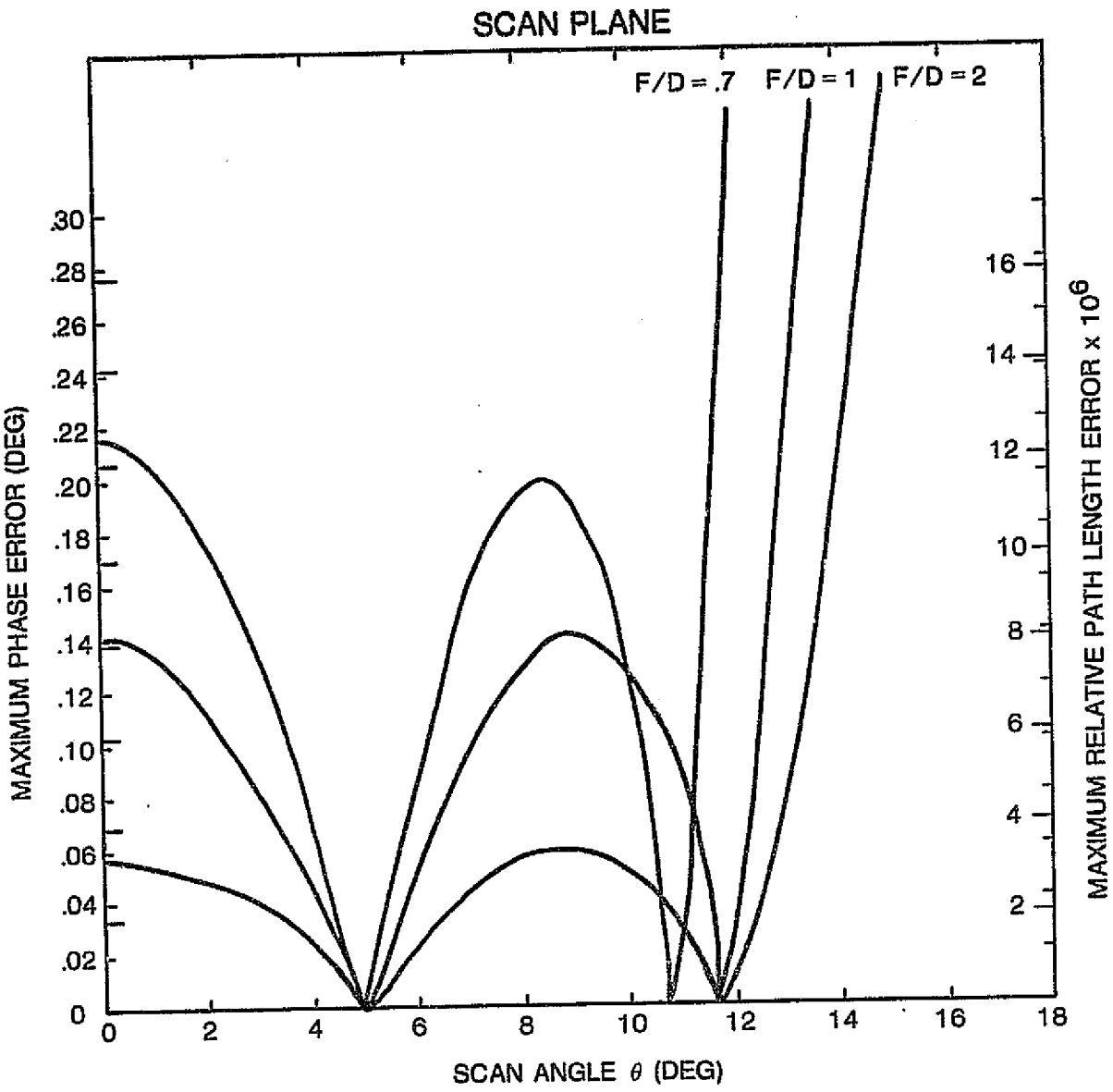

Figure 4-35. Relative Path Length Error and Relative Phase Error vs Scan Angle in Principal Plane for Different Values of F/D

For scanning in a direction perpendicular to the scan plane, the results are not as good. Figure 4-36 shows that errors at 5.5° of scan in the orthogonal plane are about 63°, 3.6×10^{-3}F. Figure 4-37 shows the error at the edge of the scan range (13° x 5.5°) as a function of the U and V dimensions of the aperture.

4.4.3 CONCLUSIONS ON LENS DESIGN

The previous subsections showed that the quadrufocal lens can produce less path length errors in the principal plane of scanning than does the bifocal lens. In the orthogonal and other planes, however, the bifocal lens can produce path length errors of the same order of magnitude. The quadrufocal lens, on the other hand, produces path length errors about 10^3 times those of the principal plane. For two-dimensional scanning, the bifocal lens offers more uniform path length errors across the coverage region, whereas the quadrufocal lens prefers one plane at the expense of the rest of the coverage area. This translates into less phase aberrations and thus less scan loss for the bifocal lens than for the quadrufocal lens. This difference will be demonstrated in the discussion of far-field pattern contours of the dual-reflector system (Subsection 4.6).

The bifocal lens has the added advantage of design simplicity. Its line length between the input (inner) and output (outer) arrays is the same for all elements, whereas the quadrufocal lens requires different line lengths for different elements in the two arrays. For these reasons, the bifocal lens has been chosen as the baseline design for the space-fed phased array.

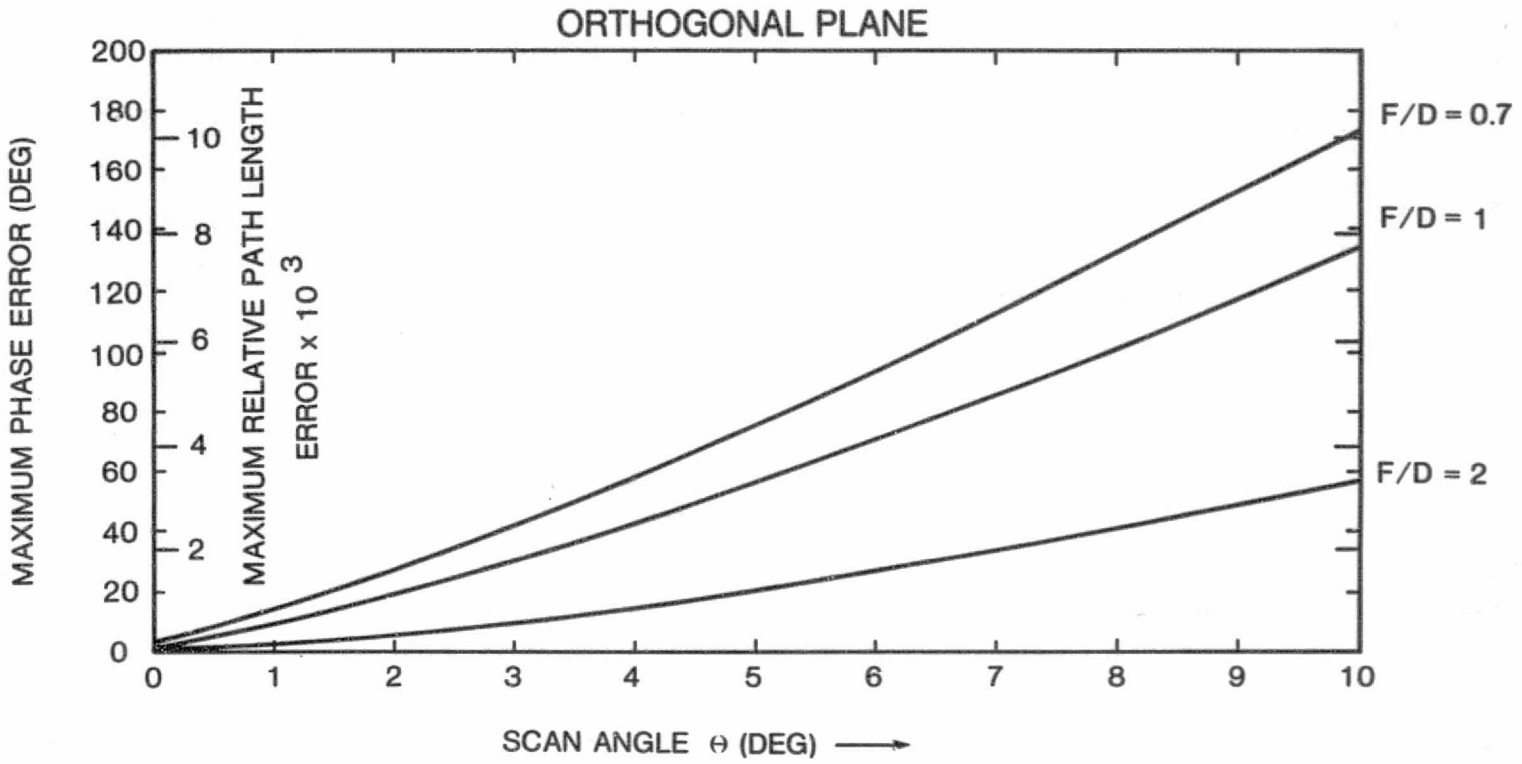

Figure 4-36. Relative Path Length Error and Relative Phase Error vs Scan Angle in Orthogonal Plane for Different Values of F/D

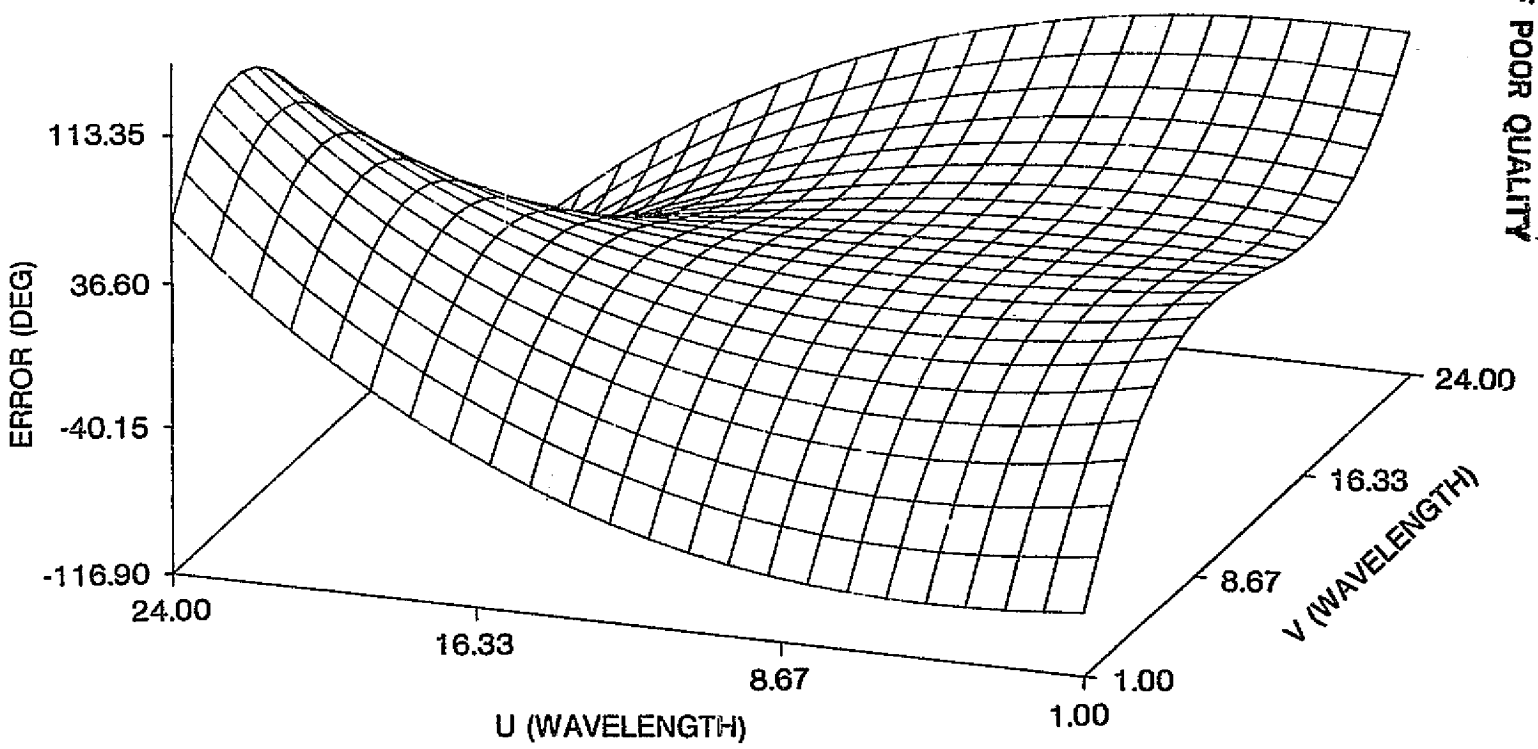

Figure 4-37. Phase Error for Quadrufocal Lens

4.5 ANALYSIS OF PHASED-ARRAY-FED CONFOCAL REFLECTOR SYSTEMS

4.5.1 NEAR-FIELD ANALYSIS OF A PHASED ARRAY

A near-field analysis of an array of open-ended rectangular waveguides was conducted. The results are based on the assumption that, when radiating individually, the observation point falls in the far field for each waveguide, but falls in the near field of the total array. This assumption is valid because the $2D^2/\lambda$ farfield criterion is satisfied for individual waveguides.

Initially, a field distribution in each waveguide aperture is assumed (TE_{10}). The far field resulting from this aperture distribution is calculated at an observation point in front of the array. Expressions for the far field (in closed form) are available in the literature [4-6]. This far-field contribution from each waveguide aperture is calculated, then added vectorially, taking into account respective amplitude and phase weights. No approximation is made in the magnitude or phase of this field. The electric far-field vector resulting from each waveguide aperture generally has a different direction in the array coordinate system because the observation point is in the near field of the complete array. The resulting expression for the system shown in Figure 4-38 takes the form

$$\vec{E}(R,\theta,\phi) = \sum_n \sum_m A_{nm} \; F\left\{\vec{\psi}_{10}(\theta,\phi)\right\} \frac{e^{-j\vec{k}_{nm}\cdot\vec{R}_{nm}}}{|\vec{R}_{nm}|} \qquad (4\text{-}69)$$

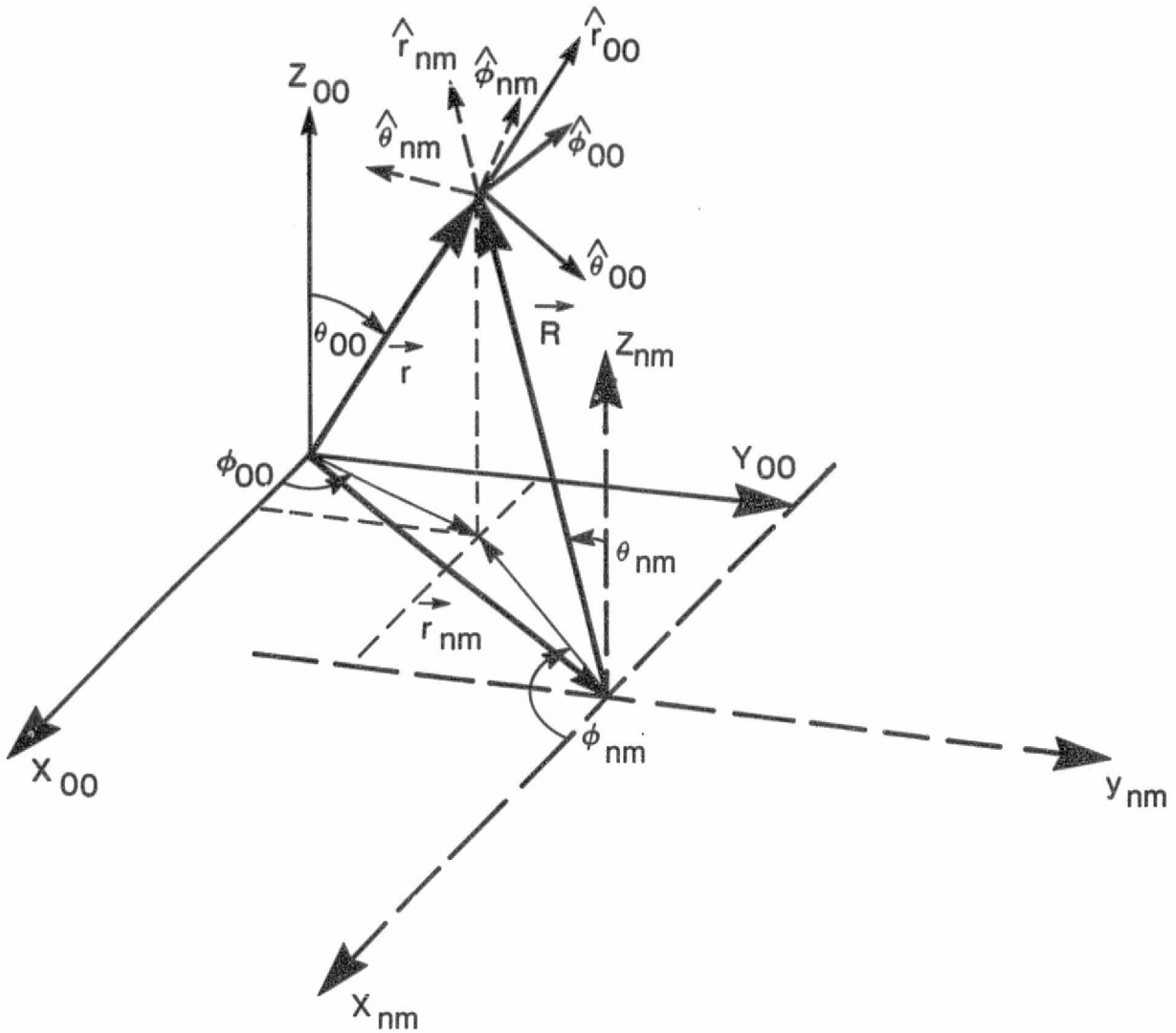

Figure 4-38. Coordinate System Definitions

where

A_{nm} = a complex number with the magnitude and phase of the (n,m)th element

$\vec{\psi}_{10}(\theta_{nm}, \phi_{nm})$ = vector far field of the TE_{10} waveguide mode in the local coordinate system attributable to the (n,m)th element

F = transformation from the local coordinate system [(n,m)th] into the array coordinate system (same as the (0,0) element coordinate system)

$\vec{R}_{nm} = \vec{r} - \vec{r}_{nm}$ is a vector from the (n,m)th element to the observation point $(R_{00}, \theta_{00}, \phi_{00})$

$\vec{r}$ = vector from the origin of the array to the observation point $(R_{00}, \theta_{00}, \phi_{00})$

$\vec{r}_{nm}$ = vector from the array origin to the origin (n,m)th element

$\vec{k}_{nm}$ = wave vector in the local coordinate system for (n,m)th waveguide

This expression is different from the far-field expression of a phased array because it is not separable into an element factor and an array factor. This is caused by the transformation, F, that operates on the element factor. When the exponent is expanded, the phase factor $e^{-jk_{nm}R_{nm}}$ has an additional term, besides the usual k d sin θ type terms. This additional term results because $\vec{r}$ and $\vec{r}_{nm}$ are not in the same direction, as approximated in the far-field case. When the array is scanned by introducing the proper phase taper across the aperture, an error in the scan direction of the near field is observed because of this additional term in the phase factor.

The phase-amplitude function A_{nm} usually takes the form $A_{nm}\, e^{j\Phi_{nm}(x,y)}$. The phase term $\Phi_{nm}(x,y)$ is a function of the

scan angle and the array geometry. The term A_{nm} is a function of the type of amplitude distribution.

The near field of the array generally consists of all three components: E_θ, E_ϕ, and E_r. A computer program has been written to simulate the near field that results from an array of open-ended waveguides arranged in rectangular or triangular grids. The near field can be calculated on any surface (representable by an algebraic expression) placed in front of the array. The calculation can also be performed for any mode propagating in the waveguide. For this particular application, the near field is calculated on the subreflector of a confocal parabolic system.

Consider an array of identical waveguide elements arranged in a triangular grid in the x-y plane of the array coordinate system (x_A, y_A, z_A) located at the center of the array (Figure 4-17). The origin of the array coordinate system is at $(0, h, -\ell)$ in the main coordinate system (reflector system). The parabolic subreflector with a focal length F_2 is located in front of the array, and the parabolic primary reflector with a focal length F_1 is so placed as to form a confocal paraboloidal system, as shown in Figure 4-39.

Assume that the far field of the waveguide element is represented by

$$\vec{e}(r_1\theta_1\phi) = C\vec{\psi}(\theta,\phi)\,\frac{e^{-j\vec{k}\cdot\vec{R}}}{|\vec{R}|}, \quad C = \text{constant} \qquad (4\text{-}70)$$

where $\vec{\psi}(\theta,\phi)$ is the angular dependence, and the second factor is the usual R-dependence in the far field. Assume also that $(F_2 + \ell)$ is much less than $2D_A^2/\lambda$ (where D_A is the maximum dimension of the array) but greater than $2d^2/\lambda$ (where d is the maximum dimension of the waveguide).

Figure 4-39. Coordinate System in Relation to Reflector Configuration

To calculate the field that results from the array at a point (R_A,θ_A,ϕ_A) on the subreflector, the subreflector is first represented in the array coordinate system. The intersection of a cone of rays with the cone's axis along the scan direction, and the subreflector are calculated at $\Delta\theta_A$ increments along each ϕ_A-cut, yielding the respective R_A^is. The field is calculated at these coordinate points $(R_A^i,\theta_A^i,\phi_A^i)$ on the subreflector in the following order.

The points on the subreflector $(R_A^i,\theta_A^i,\phi_A^i)$, which are also the points in the (0,0)th coordinate system, are transformed into the local coordinate system of the (n,m)th waveguide, yielding $(R_{nm}^i,\theta_{nm}^i,\phi_{nm}^i)$. The local far-field components (usually $E_{\theta nm}^i$ and $E_{\phi nm}^i$) are calculated and then transformed to E_{xnm}^i, E_{ynm}^i, and E_{znm}^i components. This procedure is followed for all waveguides in the array. The respective rectangular components of the field that result from each waveguide are added algebraically, since the local coordinate systems are only translated into the (0,0)th system.

The total x-, y-, z-components of the total field at a point, i, on the subreflector are given by

$$\begin{pmatrix} E_x \\ E_y \\ E_z \end{pmatrix}^{(R_A^i,\theta_A^i,\phi_A^i)} = C \sum_n \sum_m A_{nm} \begin{pmatrix} \psi_x \\ \psi_y \\ \psi_z \end{pmatrix}^{(\theta_{nm}^i,\phi_{nm}^i)} \cdot \frac{e^{-j\vec{k}_{nm}\cdot\vec{R}_{nm}^i}}{\vec{R}_{nm}^i} \qquad (4\text{-}71)$$

where $A_{nm} = A_{nm}\, e^{-j(n\delta x+m\delta y)}$, and δ_x and δ_y are the phase increments in x- and y- directions, respectively. The quantities

$$\psi\begin{pmatrix} x \\ y \\ z \end{pmatrix}(\theta^i_{nm},\ \phi^i_{nm})$$

are the x-, y-, z-components of the (nm)th waveguide field at point i on the subreflector. The vector $\vec{k}_{nm}$ is defined in equation (4-69). When expanded, the exponent of the exponential term yields

$$\vec{k}_{nm} = k(\sin\theta_{nm}\cos\phi_{nm}\,\hat{x}_o + \sin\theta_{nm}\,\hat{y}_o + \cos\theta_{nm}\,\hat{z}_o) \qquad (4\text{-}72a)$$

$$\vec{R}^i_{nm} = \vec{R}^i_A - \vec{\rho}_{nm} \quad ; \quad \vec{\rho}_{nm} = (nd_x + ms)\,\hat{x}_o + nd_y\hat{y}_o \qquad (4\text{-}72b)$$

$$\vec{R}^i_A = R^i_{oo}(\sin\theta^i_{oo}\cos\phi^i_{oo}\,X_o + \sin\theta^i_{oo}\,\hat{y}_o + \cos\theta^i_{oo}\,\hat{z}_o) \qquad (4\text{-}72c)$$

$$\vec{k}_{nm}\cdot\vec{R}^i_{nm} = kR^i_{oo}(\sin\theta_{oo}\sin\theta_{nm}\cos(\phi_{nm}-\phi_{oo}) + \cos\theta_{oo}\cos\theta_{nm}) - kR^i_{oo}\{(nd_x + ms)\cos\phi_{nm}\sin\theta_{nm} - md_y\sin\theta_{nm}\sin\phi_{nm}\} \qquad (4\text{-}73)$$

The second term in equation (4-73) is the term usually present in the far-field expression of a phased array. The first term is a phase contribution in the near field that couples the element factor and the array factor. This term goes to zero in the far field, since $\theta_{nm} \to \theta_{oo}$ and $\phi_{nm} \to \phi_{oo}$.

The phase taper across the aperture that scans the array to (θ_o,ϕ_o) is provided by $n\delta_x + m\delta_y$, where

$$\delta_x = kd_x \sin\theta_0 \cos\phi_0$$

$$\delta_y = k \sin\theta_0 \, (d_y \sin\phi_0 + s \cos\phi_0). \qquad (4\text{-}74)$$

The phase error, the first term in equation (4-73), introduces no degradation in the far-field scan position.

To input the field calculated on the subreflector to the General Antenna Program (GAP), a fictitious point source is located along the scan direction, far from the subreflector (Figure 4-39). This location is on a sphere of radius R, whose center is at the origin of the phased array. The feed is defined in such a way that it produces a plane wave field on the subreflector which is the same as that of the array calculated previously. The coordinate system of the feed is defined so that the positive z_f-axis is along the scan direction and the x_f-y_f plane is tangent to the sphere. The subreflector equation is transformed into the (x_f, y_f, z_f) coordinate system. The intersections of a cone of rays ($0 \le \theta_f^i \le \theta_{max}$, $0 \le \phi_f^i \le 360°$) and the parabola are calculated at $\Delta\theta_f$ increments along each ϕ_f-cut, yielding the respective R_f^is. These points $(R_f^i, \theta_f^i, \phi_f^i)$ on the subreflector are transformed into corresponding points in the array coordinate system $(R_A^i, \theta_A^i, \phi_A^i)$. The procedure then followed is identical to that described in the preceding paragraphs. Once the rectangular components of the field in the array coordinate system are calculated at the points $(R_A^i, \theta_A^i, \phi_A^i)$, they are transformed to corresponding rectangular components in the fictitious feed system (x_f, y_f, z_f). The data are then fed to GAP, which traces the fictitious feed through the two reflectors and calculates the far field.

A 12 x 12 array of 2λ square waveguides (TE_{10} mode), arranged in a triangular grid, was simulated in a confocal paraboloid system. The array had Taylor distribution with a 30-dB amplitude taper along the y-axis and a uniform distribution along

the x-axis. The electric field was calculated on the subreflector in a region occupied by the base of a cone defined by the half-cone angle θ_f = 0.2° in the fictitious feed coordinate system located 25,400 cm (R) from the array origin. This was done for four different positions of the array (ℓ = -38.7, 0, 60.27, and 101.6 cm). Figure 4-40a, b, c, and d shows the plots of the electric field on the reflector in one principal plane (x-axis). The fictitious feed angle, θ_f, is plotted along the abscissa. The range over which the array and the subreflector extend is also shown. For the case ℓ = 60.27 cm, which corresponds to the conjugate point of the confocal system, Figure 4-41 shows the plot of the electric field in the other principal plane (y-axis) of the amplitude taper.

4.5.2 COMPUTER MODELING OF A PHASED-ARRAY-FED REFLECTOR SYSTEM

To simulate a phased-array-fed confocal reflector system, the near-field array program is incorporated into GAP. The GAP program can handle multisurface systems of arbitrary geometry with multiple feeds. The radiation field calculation in this program is based on a current integration method. In setting up the surface currents on the main reflector, the program traces all the rays from each horn to the main reflector. With a reasonable number of feed elements, the ray-tracing procedure provides the most efficient approach to computing the surface currents in a multiple reflector system. For a phased array feed consisting of thousands of feed elements, tracing all the rays from all feed elements is time-consuming and impractical. Therefore, an alternative approach was developed to simulate the field of the phased array in the GAP program.

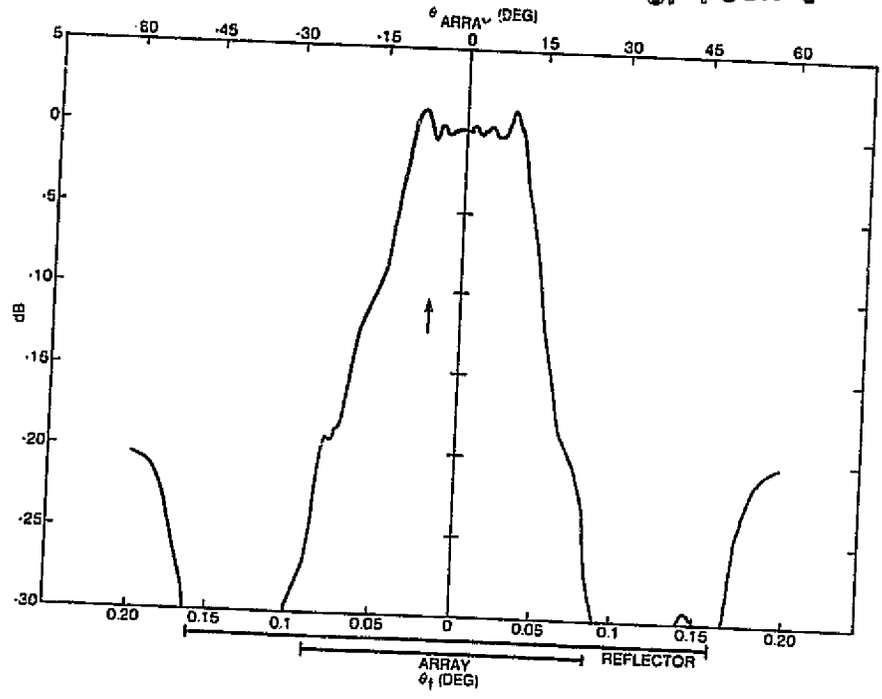

(a) ℓ = -38.7 cm

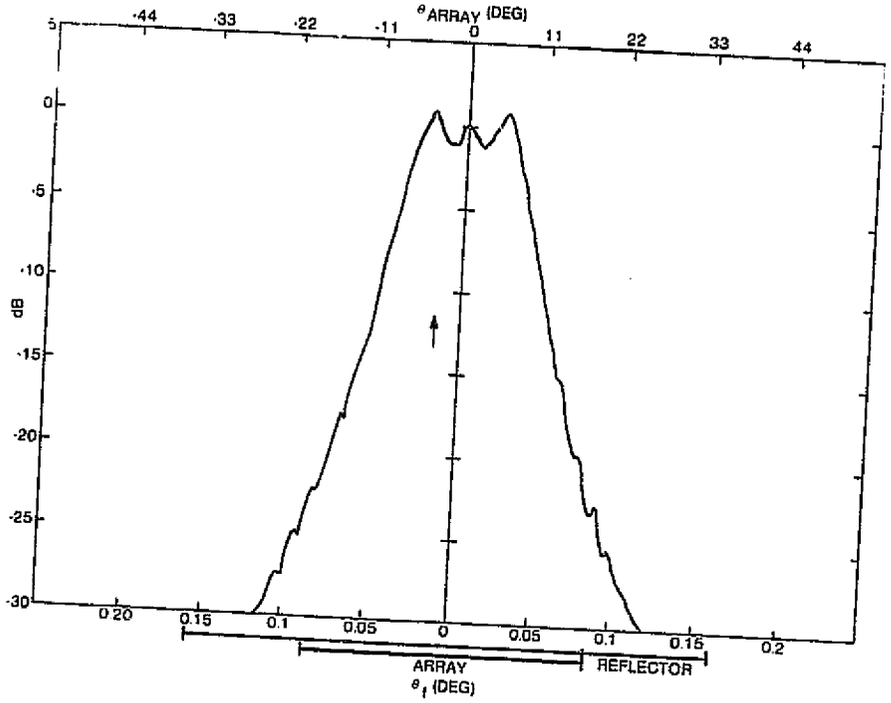

(b) ℓ = 0 cm

Figure 4-40. Electric Field Distribution on the Subreflector in the x-Axis Plane

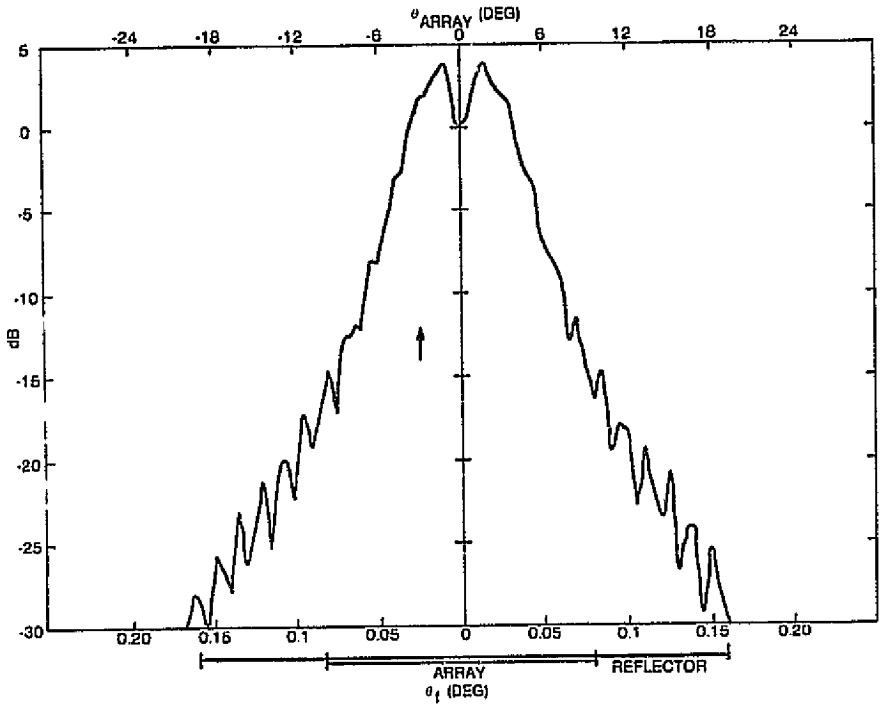

(c) ℓ = 60.27 cm

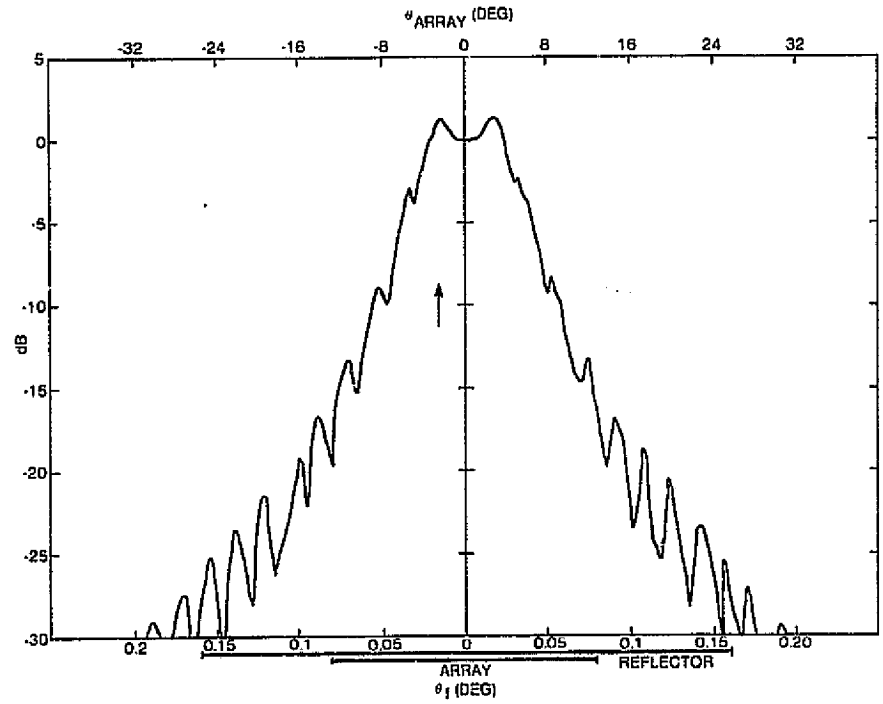

(d) ℓ = 101.6 cm

Figure 4-40. Electric Field Distribution on the Subreflector in the x-Axis Plane (Cont'd)

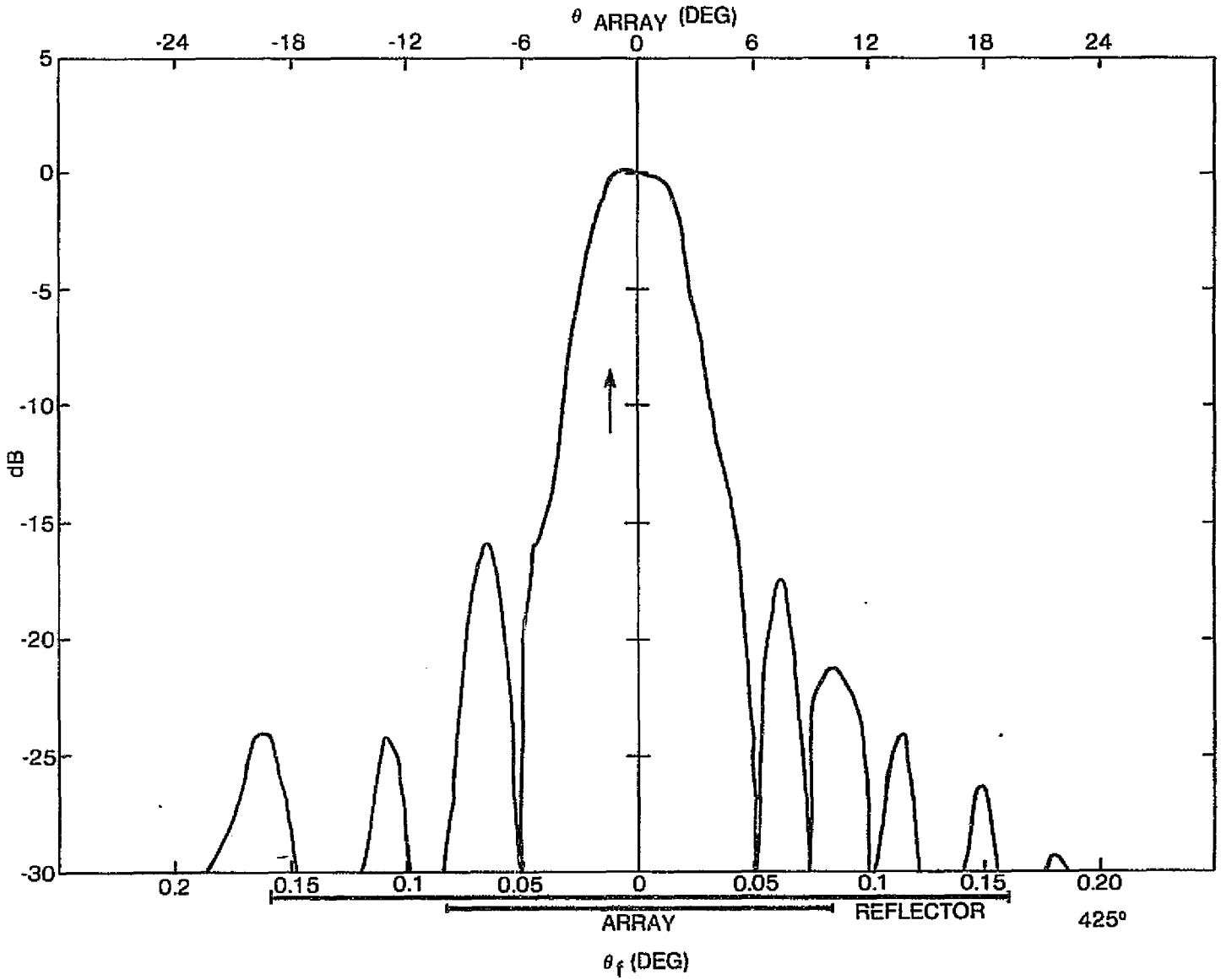

Figure 4-41. Electric Field Distribution on the Subreflector in the y-Axis Plane for ℓ = 60.27 cm

Since the phased array has a plane wave pattern, it seems natural to use a plane wave source to simulate a phased array and avoid extensive computations. However, the ray-tracing scheme used in GAP assumes that all rays originate from a point source, i.e., that all rays from the feed have spherical wavefronts. Therefore, a plane wave source is not available in the current feed library. To model a plane wave source, a feed may be located far from the subreflector so that the amplitude and phase of the incident field are almost uniform in the vicinity of the subreflector. In a phased-array-fed antenna system, the subreflector is in the near-field region of the feed array. The near field of the array is a quasi-plane wave with ripples in both phase and amplitude. Therefore, the phased array in this system cannot be modeled by a true plane wave source. However, if the plane waves are modified by adding the desired amplitude and phase pattern, this modified quasi-plane wave can be used to represent the near field of a phased array.

To simulate the near field of a phased array in a confocal reflector system, a feed routine was established in GAP. This feed routine interpolates the input feed data, which may be obtained by taking the sampled values of a measured pattern or calculated by a separate program. In this application, the feed data are computed by the phased array program described in the Subsection 4.5.1. These feed data are input to the GAP program in each constant ϕ cut. To find the field value in a specified direction (ψ,ϕ), the feed routine first linearly interpolates the field values in ψ in the two planes adjacent to ϕ, then linearly interpolates the field value in ϕ. In Figure 4-42, the feed pattern value $f(\psi)$ at an angle ψ is calculated by

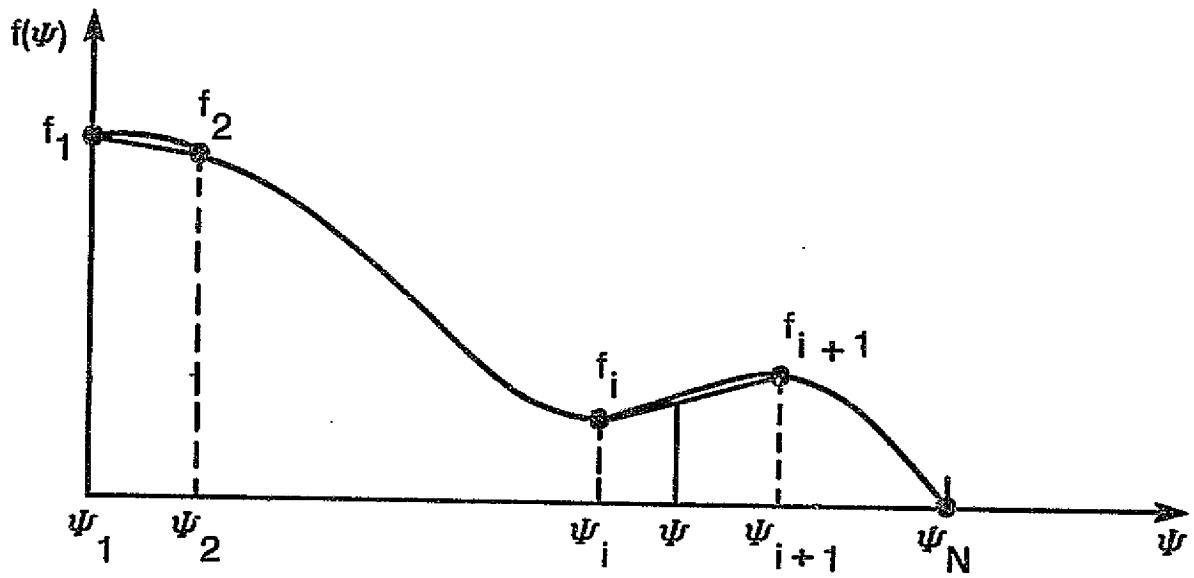

Figure 4-42. Interpolation Scheme for Input Feed Data

$$f(\psi) = f_i \cdot (1 - d_\psi) + f_{i+1} \cdot d_\psi \qquad (4\text{-}75)$$

where

$$d_\psi = \frac{\psi - \psi_i}{\psi_{i+1} - \psi_i} \qquad (4\text{-}76)$$

and f_i's are the input feed pattern data sampled at the ψ_i angles.

For feeds with circular symmetry, the field patterns can be obtained by interpolating between the E- and H-plane patterns, as

$$E_\psi(\psi \cdot \phi) = f_E(\psi)(A_x \cos \phi + A_y \sin \phi) \qquad (4\text{-}77)$$

$$E\phi(\psi \cdot \phi) = -f_H(\psi)(A_x \sin \phi - A_y \cos \phi) \qquad (4\text{-}78)$$

where f_E and f_H represent the E- and H-plane patterns, respectively, and A_x and A_y are the complex coefficients for x and y excitations of the feed.

For feed patterns that do not have the symmetry property in ϕ, multiple-plane pattern cuts are required to represent field variations. This is the case with the near field of the phased array on the subreflector surface. In this case, field values obtained from equation (4-75) on two adjacent ϕ planes are interpolated in x, y, and z components and the resulting field values are given by

$$f(\phi,\psi) = f_j(1 - d_\phi) + f_{j+1} \cdot d_\phi \qquad (4\text{-}79)$$

for all three components, where

$$d_\phi = \frac{\phi - \phi_j}{\phi_{j+1} - \phi_j} \qquad (4\text{-}80)$$

and f_j's are the field values interpolated in the ϕ_j and ϕ_{j+1} planes, as calculated by equation (4-75).

By defining a new feed that reads and interpolates the calculated phased array near-field data on the subreflector, this feed modeling technique provides an accurate estimate, in magnitude and phase, of fields on the subreflector. Locating this feed far from the subreflector also ensures that the incident waves have basically a plane nature, which is essential to a confocal reflector system. Thus, this feed model, which generates a modified plane wave that matches the fields of a phased array on the subreflector, can simulate a phased array feed in a confocal reflector system.

4.6 SECONDARY PATTERN CALCULATIONS

4.6.1 MULTIPLE SCANNING BEAM CALCULATIONS

The final array design of 24 x 24, 2λ waveguide elements uses a 30-dB Taylor distribution in the east-west direction (y-axis) to achieve the required co-pol (sidelobe) isolation between two sections with the same polarization. The array, used as a feed in the confocal paraboloid system with a magnification factor of 3.6, is simulated by using the computer program described. Figure 4-43 shows the performance of the array. The various beams, 2-dB contours calculated at 18.95 GHz, show the scanned positions when the element phase shifts are incremented by 11.25 degrees. The angular dimensions of CONUS, as viewed from the satellite,

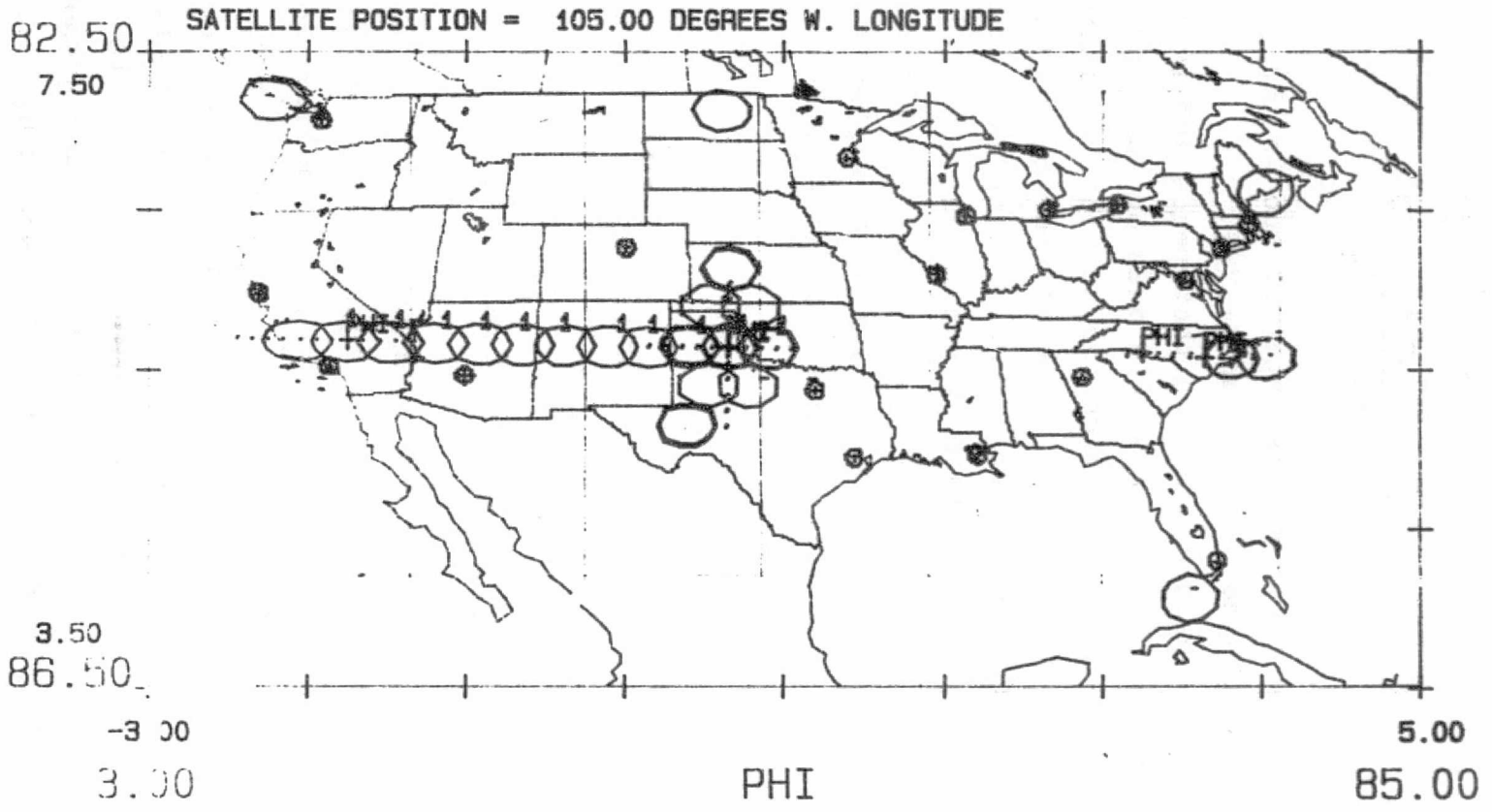

Figure 4-43. 2-dB Contours of Scanned Beams Over CONUS

are 6.6° east-west and 3° north-south. The no-scan position of the array is biased 0.15° to the west to make the scan loss equal at the east and west extremities. This results in a scan extent of 3.15° to the west (scan loss = 1.54 dB) and 3.45° to the east (scan loss = 1.86 dB). Figure 4-43 shows a cluster of beams at the center. The level of contour overlap between the beams is about 2 dB. The figure also shows beams scanned to the northwest, northeast, southeast, and extreme north positions.

4.6.1.1 Configuration C: Phased Array Confocal System

In this configuration, the variable gain amplifiers have five quantized levels (1, 0.5, 0.315, 0.158, and 0), as specified in the amplifier module characteristics. The array performance shown in Figure 4-43 has a 30-dB Taylor distribution at these quantized levels. Sidelobe isolation was studied by scanning the beam to a point at the north edge of Sector I, and the sidelobes falling in Sector III, which has the same polarization, were also observed. Figure 4-44a shows the main beam and the sidelobes. The first sidelobe falling in Sector III is about 23 dB down from the peak (51.92 dBi). The gain of the main beam scanned to where the sidelobe falls in Sector III is 52.7 dBi, which results in co-pol isolation of about 24 dB. This high sidelobe level (24 dB) instead of the designated one (30 dB) can be attributed to the error introduced by quantization. The cross-polarization of this beam is shown in Figure 4-44b. The first contour, which does not fall in Sector II, is 30 dB down from the peak, resulting in cross-pol isolation of at least 30 dB. The cross-pol in this figure and in subsequent configurations is expressed in spacecraft coordinates. Cross-pol isolation expressed in localized coordinates will be much higher.

The choice of quantized levels can help improve the cross-pol isolation. A new set of quantized levels (1, 0.75, 0.5,

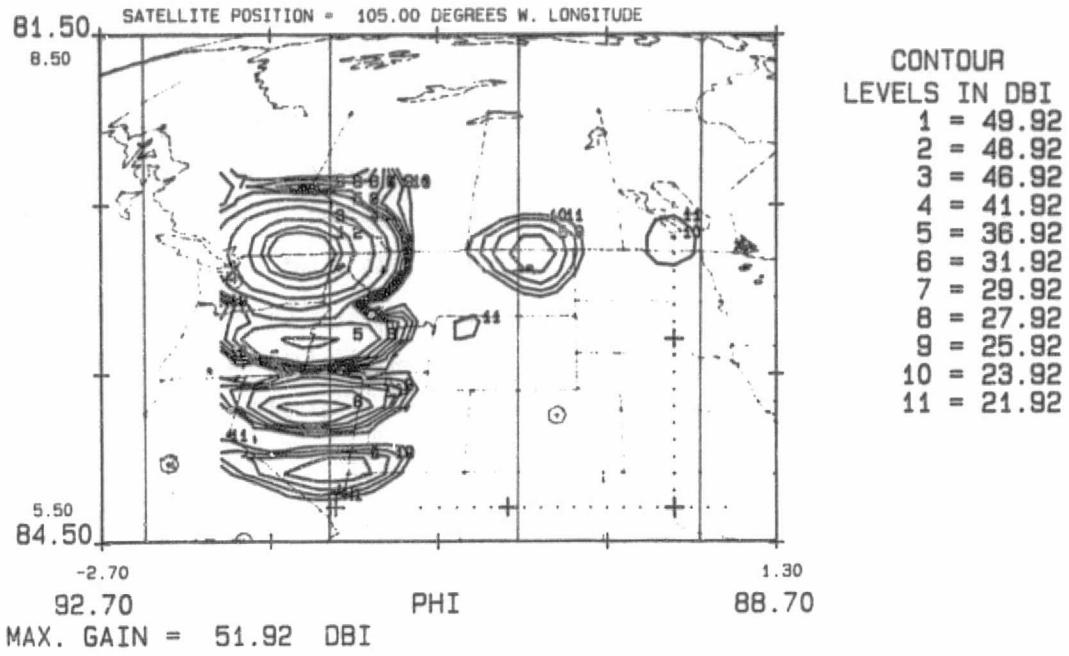

(a) Co-Pol

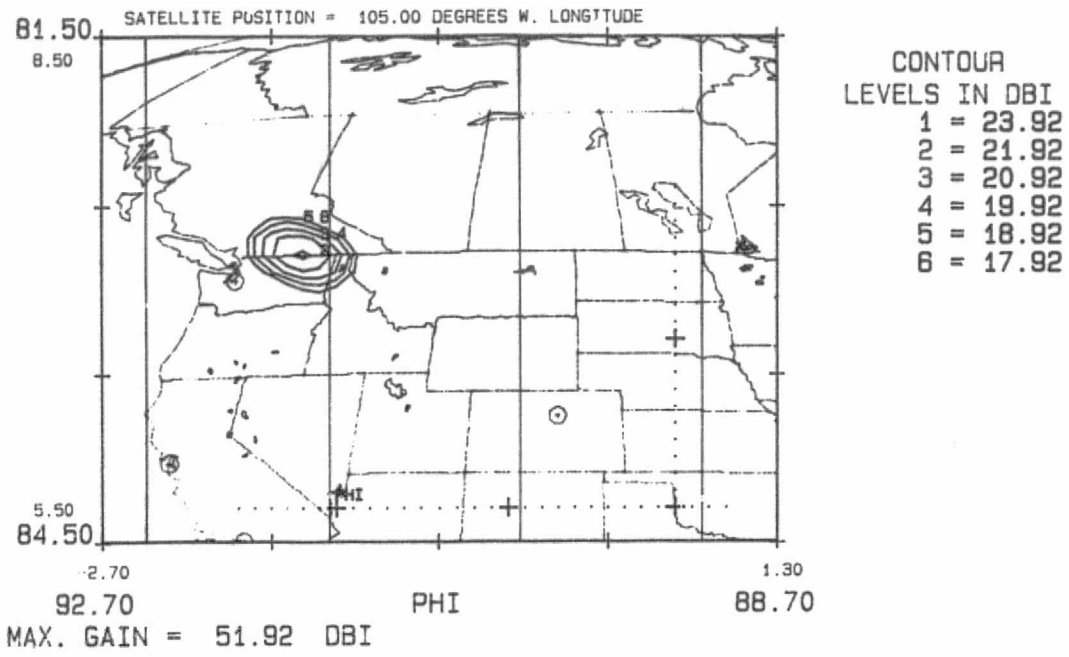

(b) Cross-Pol

Figure 4-44. Isolation for Worst-Case Scanned Position Using Quantized Levels of 1, 0.5, 0.315, 0.158, and 0

0.25, and 0) was selected, based on the far-field array performance outside of the reflector system. Figure 4-45a shows a plot of the same beam with the sidelobe levels. The first sidelobe is 27 dB down from the peak, resulting in co-pol isolation of more than 27 dB. The 30-dB isolation could easily be achieved by using a larger aperture.

If continuous 30-dB Taylor distribution were used, the required 30-dB co-pol isolation could be achieved with enough margin. However, as pointed out in Subsection 4.3.3, this results in a less efficient operation. The contours of a beam at the edge of Sector I are shown in Figure 4-45b, indicating a co-pol isolation level in Section III of better than 33 dB.

4.6.1.2 Configuration F: Lens-Fed Confocal System

The lens designs discussed in Subsection 4.4 were simulated by using the computer program discussed in Subsection 4.5 with the appropriate phase errors derived in Subsection 4.4. Figure 4-46a shows the performance of the bifocal lens. The focal plane of the lens lies in the east-west direction. Unscanned beam gain is 52.90 dBi. Scan loss is 1.14 dB at the extreme west position and 1.7 dB at the extreme east position. At the extreme north position, scan loss is only 0.36 dB.

Figure 4-46b shows the performance of the quadrufocal lens. In this case, the unscanned beam gain is 53.16 dBi, which is higher than that for the bifocal lens. Scan loss is 1.3 dB at the extreme west position and 2.06 dB at the extreme east position. At the extreme north position, scan loss is 0.74 dB. The scan loss performance of the bifocal lens is better, especially in the orthogonal plane, than that of the quadrufocal lens. This inferior scan loss performance by the quadrufocal lens is expected to prevail in all planes, since this lens is heavily biased with four foci in one plane. Analysis of the lens performance for multiple fixed beams is presented in Subsection 4.6.2.3.

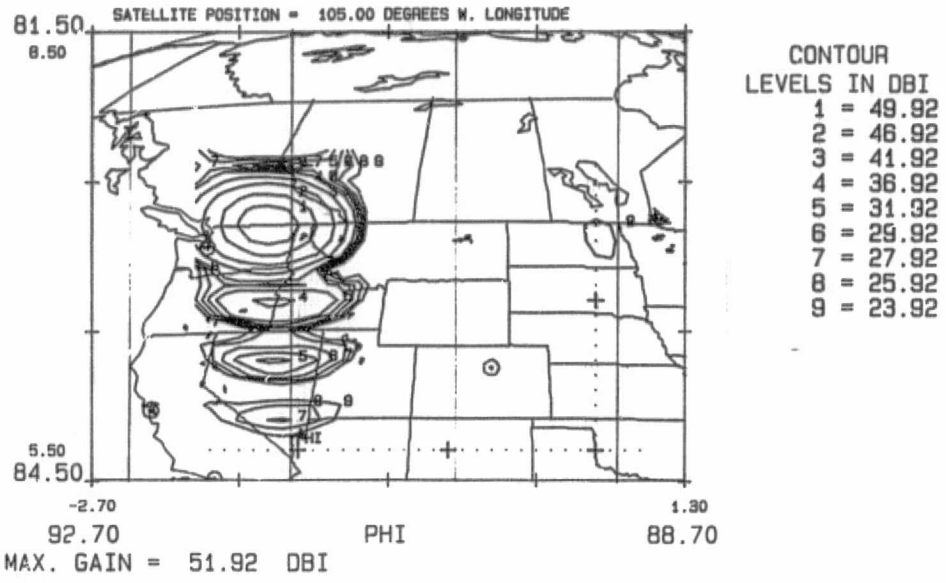

(a) Using Modified Quantized Levels of 1, 0.75, 0.5, 0.25, and 0

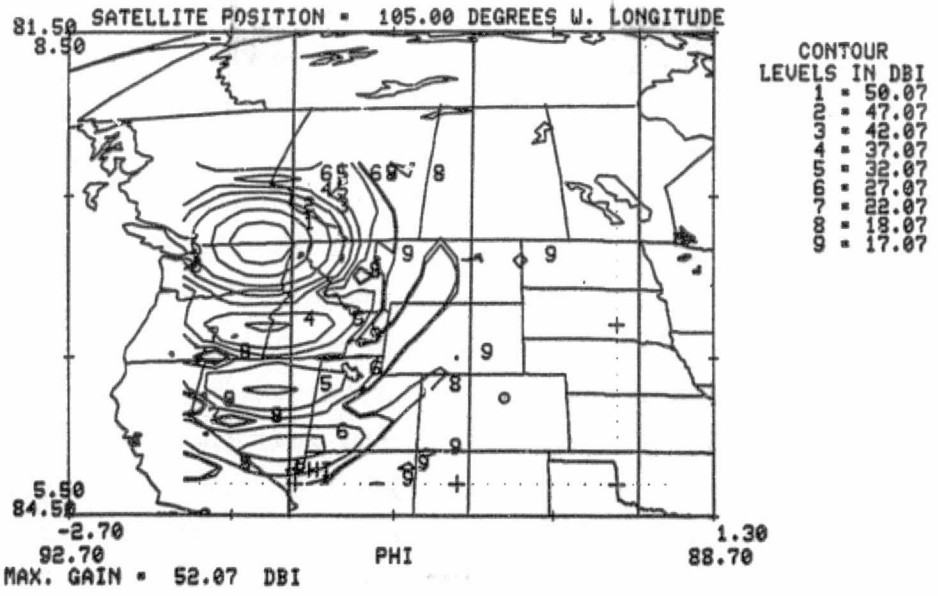

(b) Using Continuous 30-dB Taylor Levels

Figure 4-45. Sidelobe Isolation for Worst-Case Scanned Beam

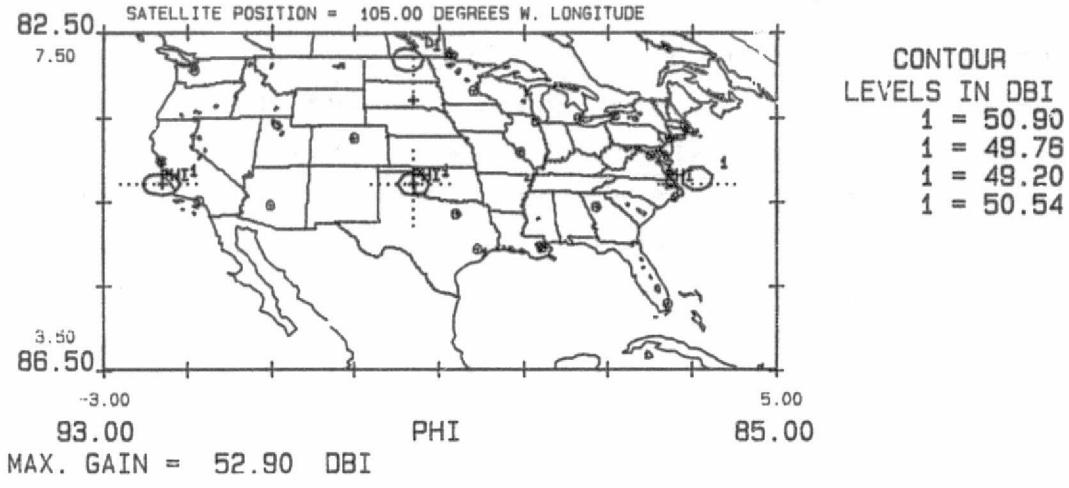

(a) Bifocal

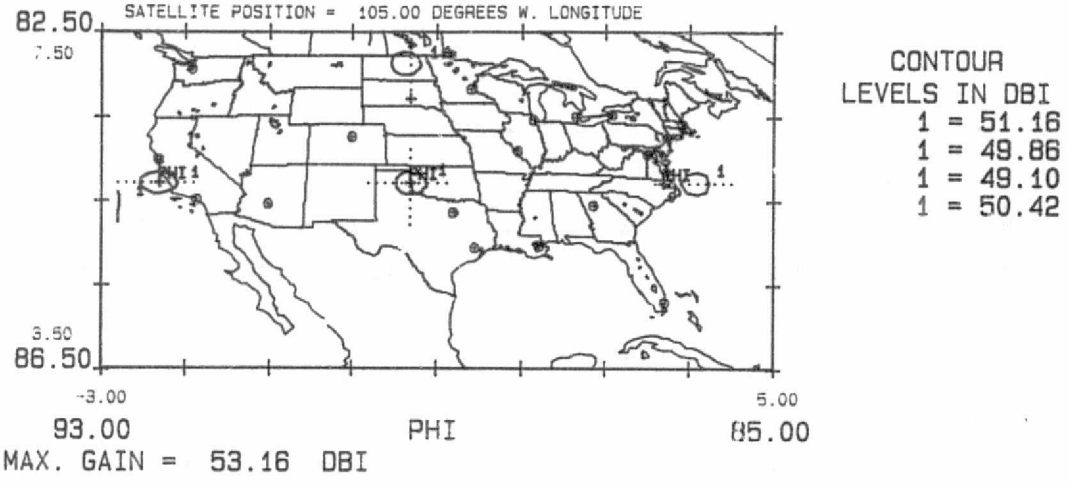

(b) Quadrufocal

Figure 4-46. Lens Scan Performance Over CONUS

4.6.2 MULTIPLE FIXED BEAM CALCULATIONS

This subsection discusses the numerical results of fixed spot beams generated by a phased-array-fed confocal system, a focal-region-fed Cassegrain system, and a lens-fed confocal system. The confocal systems that employ lens or phased array feed demonstrate good performance in both gain and isolation. However, these systems require a complicated beam-forming network (BFN), and, to achieve the required isolation with a 2.74-m reflector, continuous Taylor distribution must be used in the orthogonal planes of the array, resulting in a low-efficiency operation. The Cassegrain system, on the other hand, has reasonable e.i.r.p. and good co-pol and cross-pol beam isolation. From these results, it is concluded that a Cassegrain antenna is an attractive design for generating spot beams.

4.6.2.1 Configuration D1: Phased-Array-Fed Confocal System

The cities that are closest to each other and have the same polarization are Boston and Washington, D.C. The separation between them is the smallest for a satellite position of 105° W. Consequently, studies for the multiple-beam case with this configuration are conducted using this satellite position for both cities. The argument is that if co-pol isolation is met in this case, then it should be easily achievable for all other longitudes. The no-scan position of the array is biased slightly toward the eastern U.S. to optimize the co-pol isolation between Boston and Washington. Figure 4-47a shows the spot beam on Boston. The sidelobe level on Washington is only 19 dB down from the peak of 51.27 dBi. The peak gain of the spot beam on Washington is 52.00 dBi. Hence, the co-pol isolation between Boston and Washington, with the spot beam on Boston, is about 19.8 dBi. Once again, with a larger

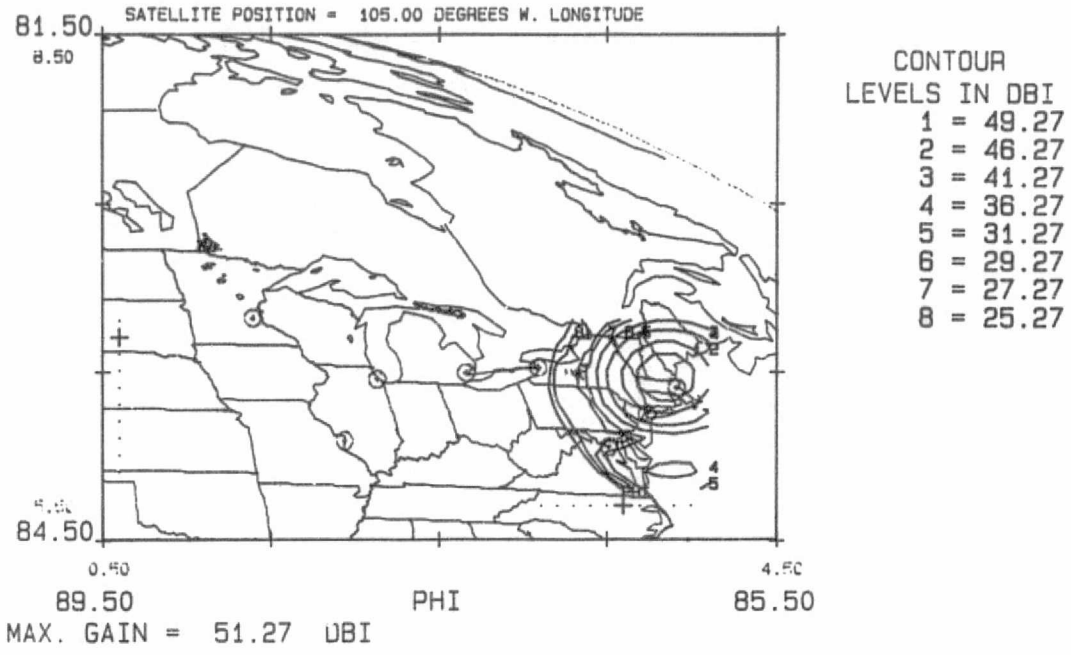

(a) Co-Pol Contours

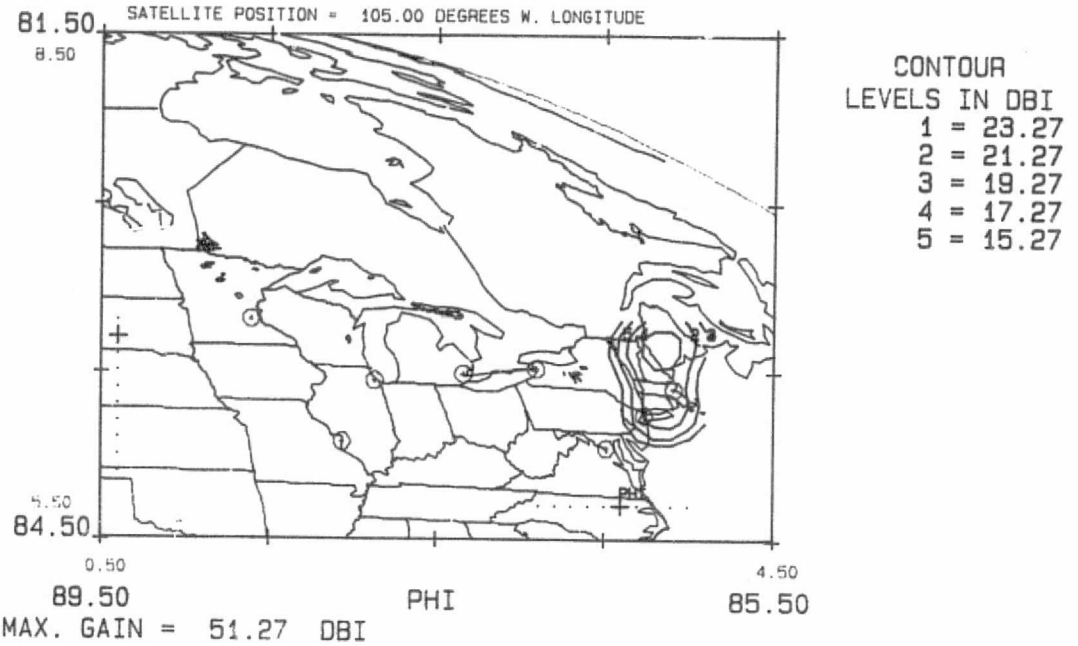

(b) Cross-Pol Contours

Figure 4-47. Fixed Spot Beam Over Boston Using Phased Array Configuration

aperture, the 30-dB isolation should be achievable. Figure 4-47b shows the cross-pol contours of the beam on Boston.

The next closest cities with the same polarization are New York and Buffalo. Figure 4-48a shows the co-pol contours of the spot beam on New York. The sidelobe level on Buffalo is 30 dB down from the peak of 51.75 dBi. The peak gain of the spot beam on Buffalo is 52.2 dBi, making the co-pol isolation between these cities at least 30 dB. Figure 4-48b shows the cross-pol contours of the beam on New York. The cross-pol level at Boston caused by the beam at New York is at least 33 dB down, and the level at Washington is 36 dB down, resulting in similar cross-pol isolation levels. One of the causes of poor co-pol isolation between Boston and Washington is the uniform distribution along the north-south direction and the quantized Taylor distribution along the east-west direction of the array aperture.

As mentioned in the discussion of configuration C in Subsection 4.6.1.1., it is possible to improve the isolation by using continuous 30-dB Taylor distribution along both the east-west and north-south paths. This satisfies e.i.r.p. requirements and results in higher isolation, although at the expense of efficiency and BFN simplicity. An example of such a result is shown in Figure 4-49 for the co- and cross-pol contours of the Boston beam when the array is excited by the 30-dB Taylor distribution in orthogonal planes. The co-pol isolation over Washington increases to about 27 dB measured from the peak at the Washington beam.

4.6.2.2 Configuration E: Focal-Region-Fed Cassegrain System

The Cassegrain system, as described in Subsection 4.2.2, is designed to generate all 18 fixed spot beams for the cities specified by NASA. Of these 18 beams, the Boston, New York City, and Washington, D.C., beams impose the most stringent isolation

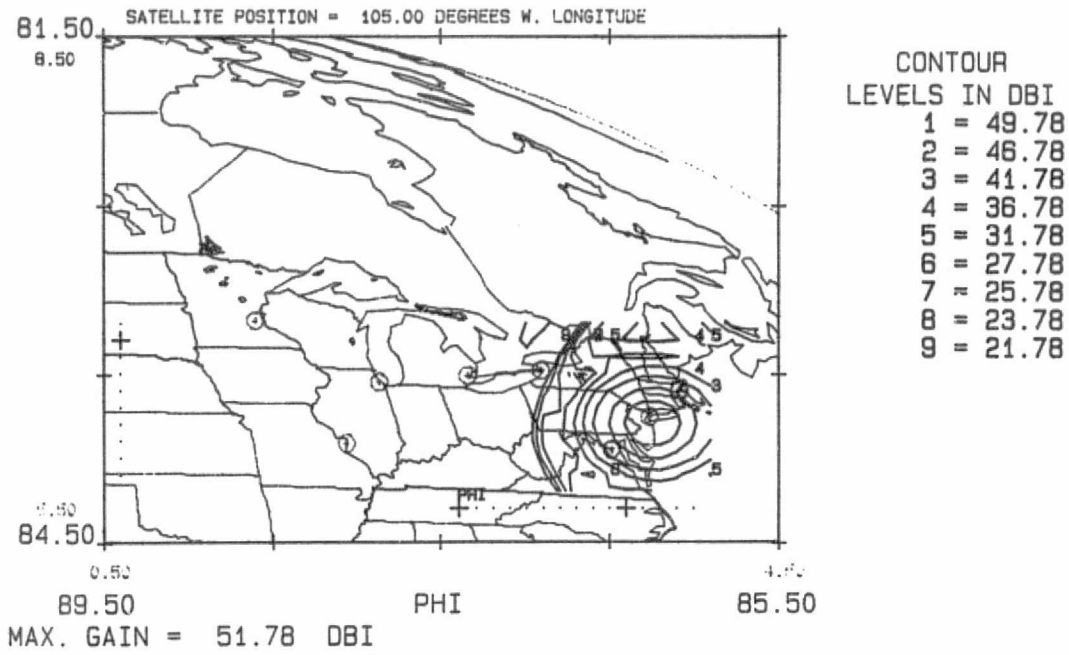

MAX. GAIN = 51.78 DBI

(a) Co-Pol Contours

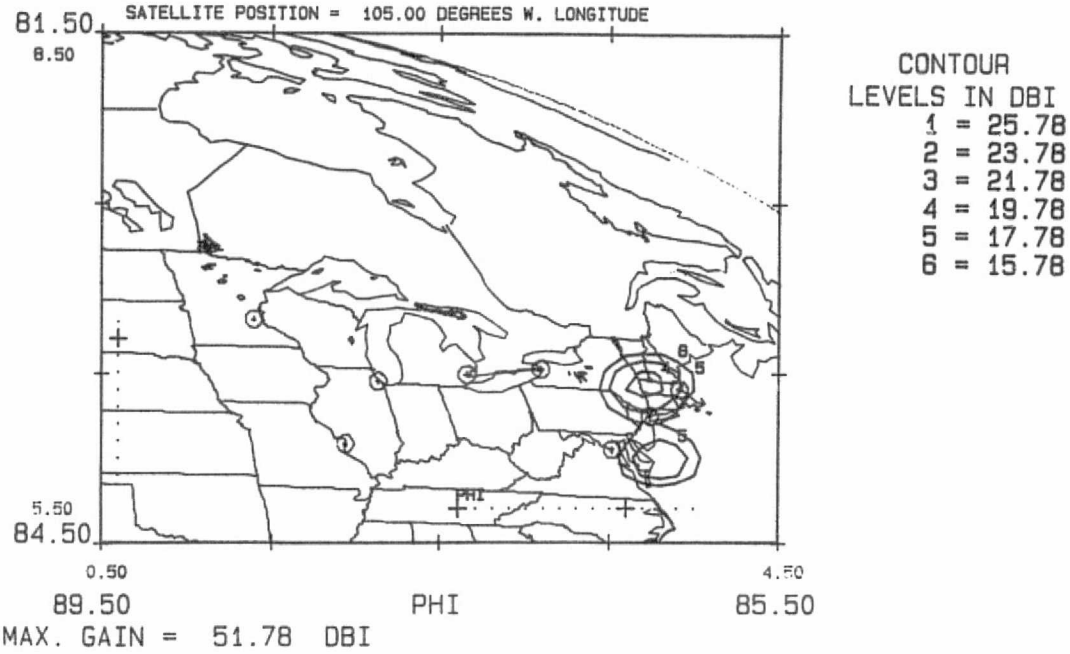

MAX. GAIN = 51.78 DBI

(b) Cross-Pol Contours

Figure 4-48. Fixed Spot Beam Over New York City Using Phased Array Configuration

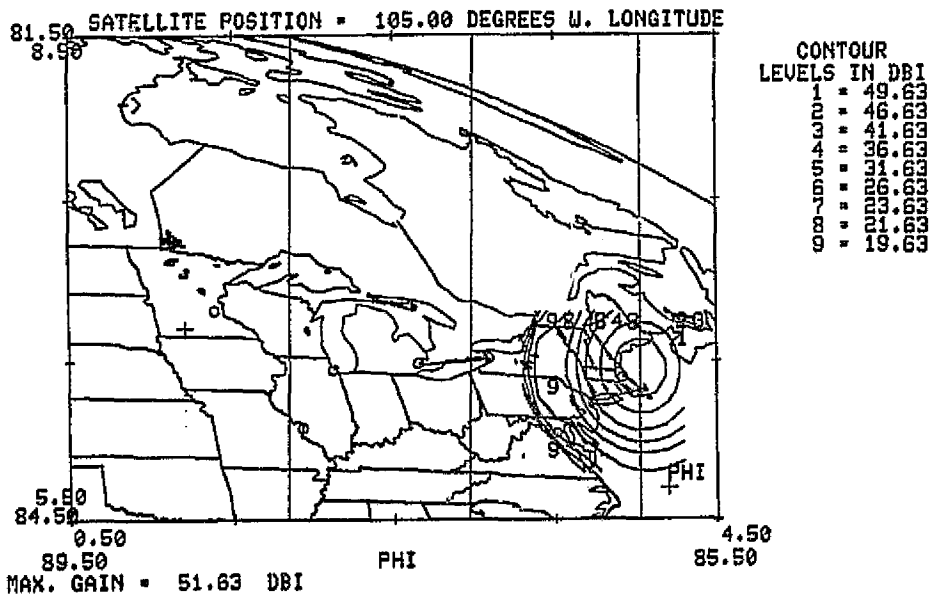

(a) Co-Pol Contours

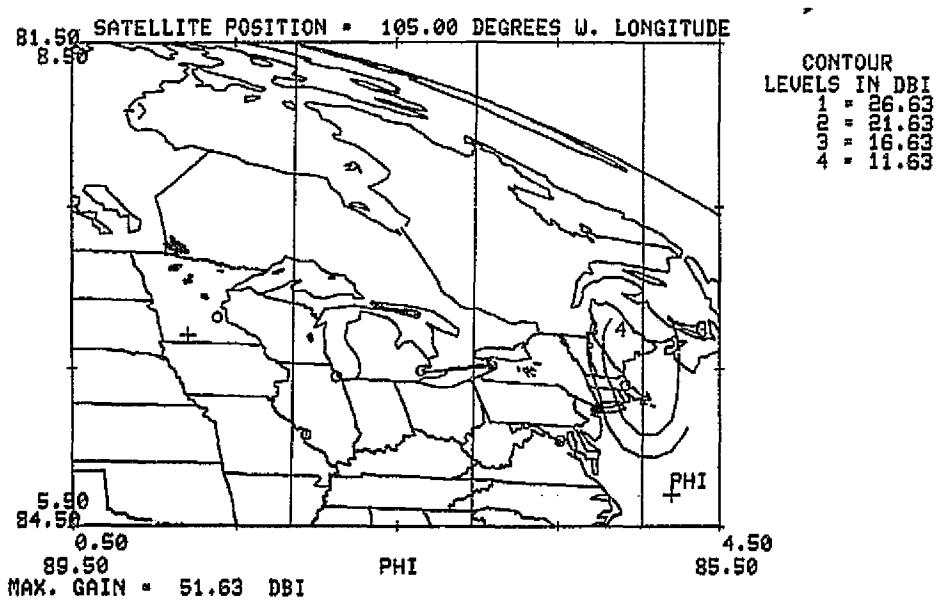

(b) Cross-Pol Contours

Figure 4-49. Fixed Spot Beam Over Boston Using Phased Array Configuration With Continuous Taylor Distribution in Orthogonal Planes

and feed size requirements. Therefore, to demonstrate the validity of this antenna design, the contour patterns of these three cities were calculated and will be presented in this section. For the computation of these scanned beams, the boresight of the antenna was located at Oklahoma, or more precisely, 0.99° east and 5.65° north of the subsatellite point of a satellite at a west longitude of 105°. The satellite longitude of 105° represents the worst-case coverage, since spatial distances between these cities are the smallest of the three longitude angles recommended by NASA. The boresight was chosen to minimize the amount of scanning for these beams, while ensuring that the spot beams on the west coast achieve the same level of isolation. Consequently, in additon to the three most critical beams on the east coast, the San Francisco beams were also calculated and are presented to demonstrate the west coast performance. All patterns were calculated at the mid-band frequency of 18.95 GHz.

Figure 4-50 shows the component beams of the Boston, New York City, and Washington, D.C., coverage. The horn layout and the coordinates of the horn locations are presented in Subsection 4.2.2. The co-pol and cross-pol patterns of these three cities are shown in Figures 4-51 through 4-53. These co-pol contour patterns show that all three beams meet or exceed a 30-dB isolation from the adjacent cities that use the same sense of polarizaton. The cross-pol patterns show that the cross-polarization field introduced by the reflector optics is negligible.

The coefficients used to optimize these beams are quantized based on the gain level specifications of the variable power amplifier module and on the phase-step increment of the variable phase shifter, although the phase shift will be implemented in waveguide, as discussed in Subsection 5.6.3. Table 4-9 lists the coefficients for these three beams; the beam numbers refer to those of Figure 4-50.

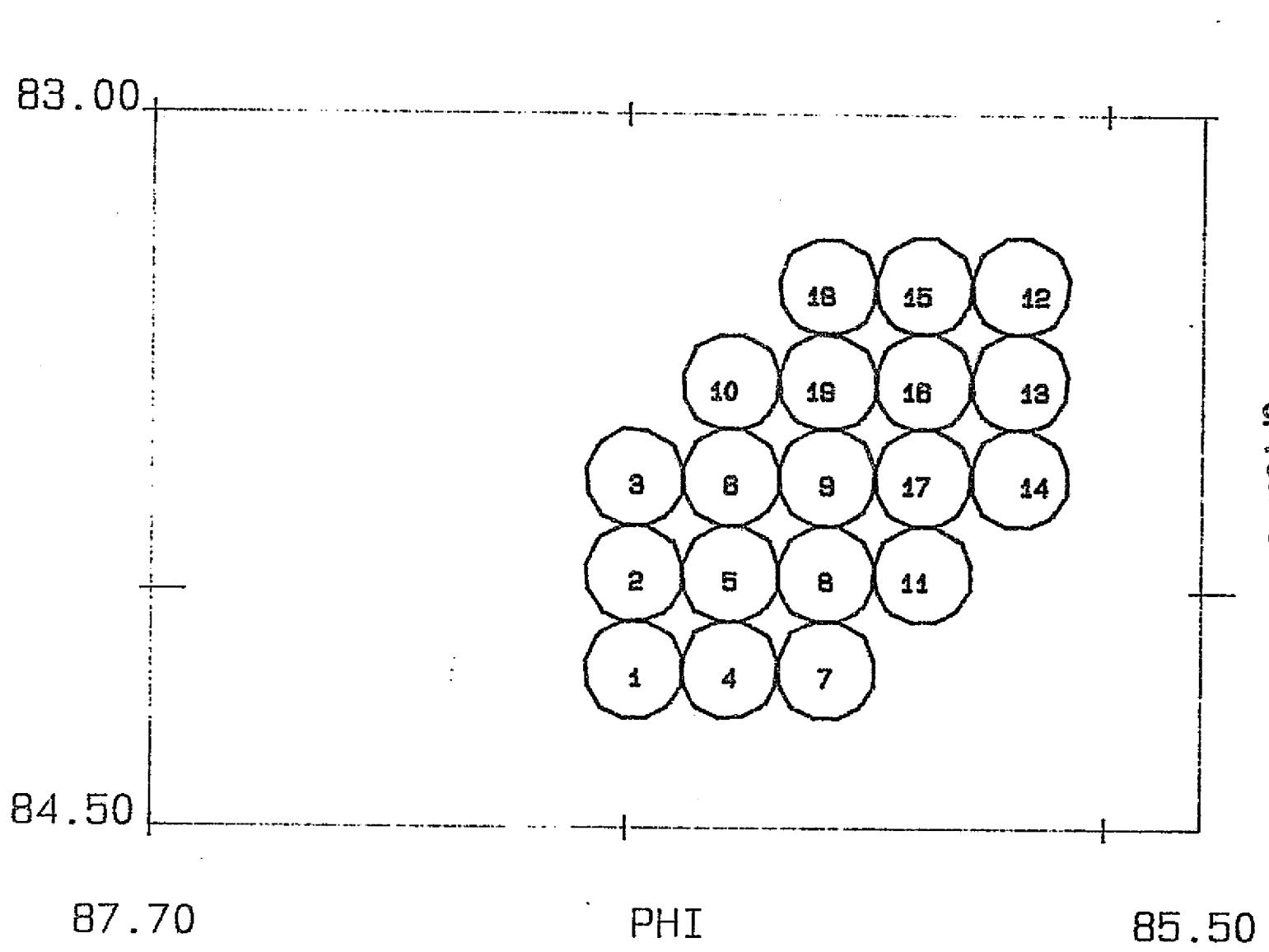

Figure 4-50. Component Beams for Boston, New York, and Washington, D.C. Coverage

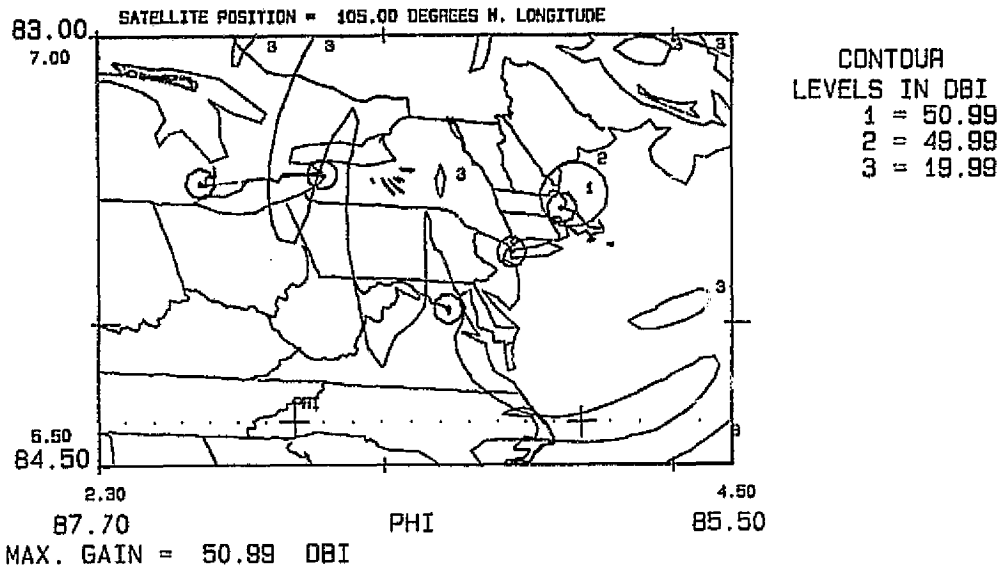

(a) Co-Pol Contours

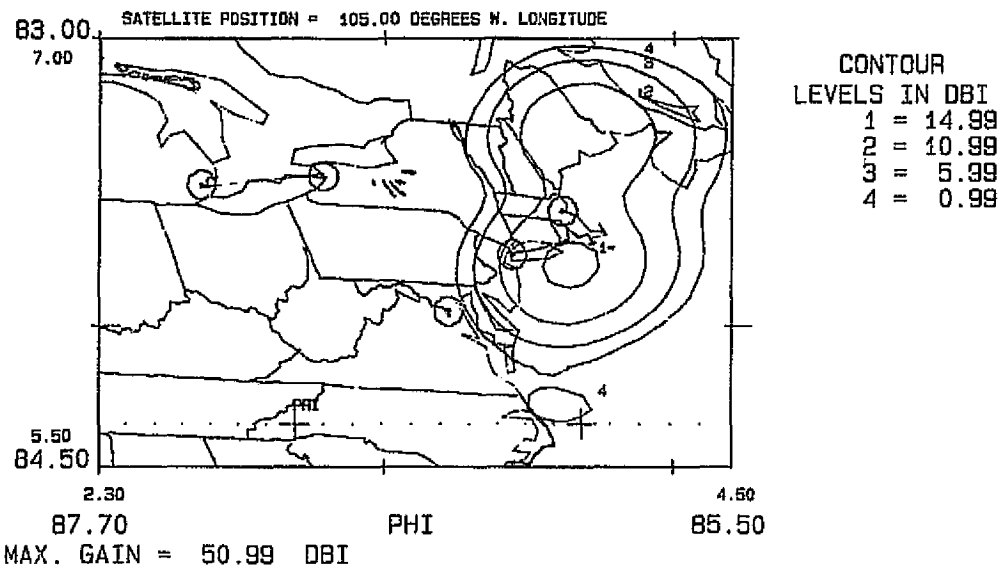

(b) Cross-Pol Contours

Figure 4-51. Fixed Spot Beam Over Boston Using 9-Horn Cluster

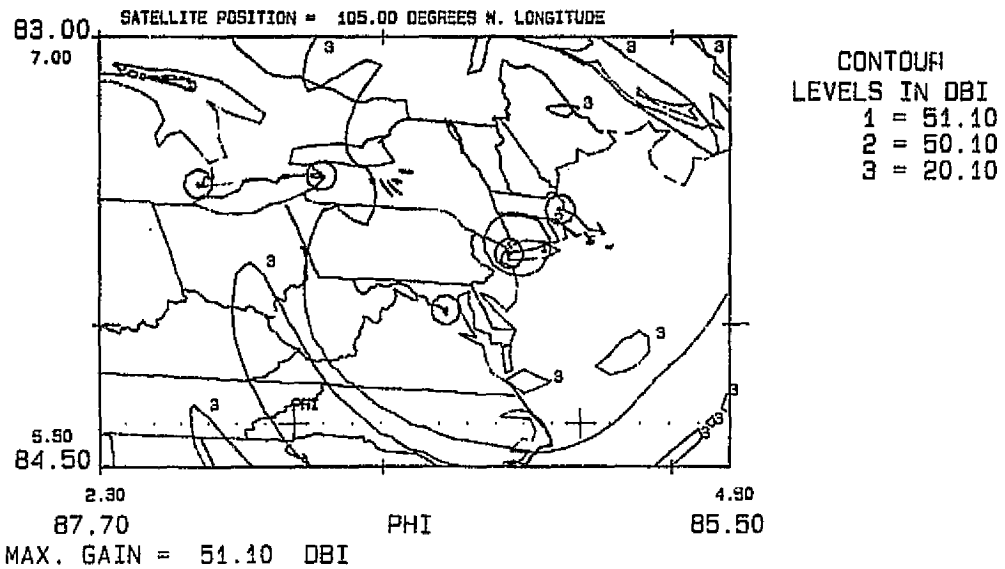

(a) Co-Pol Contours

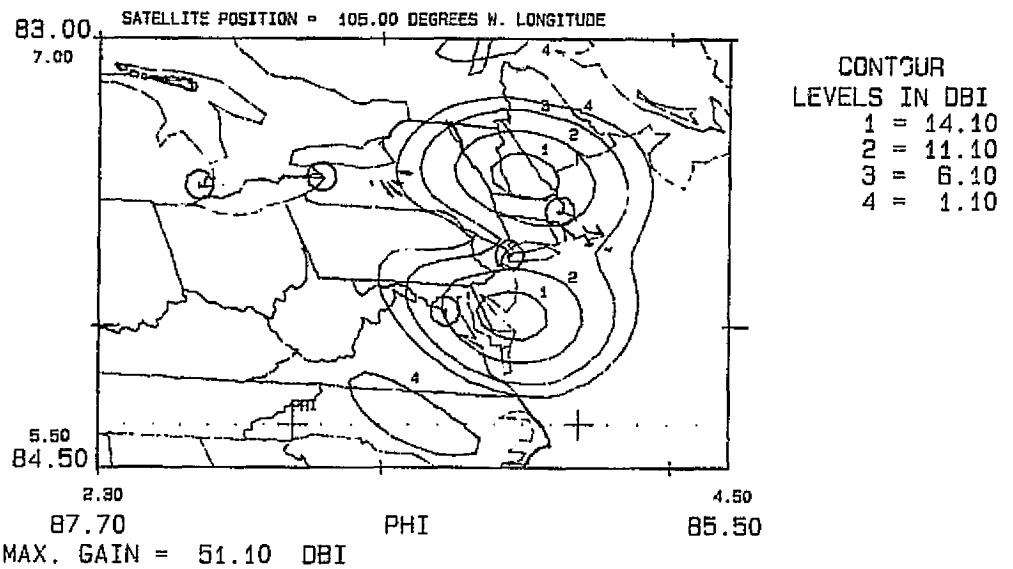

(b) Cross-Pol Contours

Figure 4-52. Fixed Spot Beam Over New York Using 9-Horn Cluster

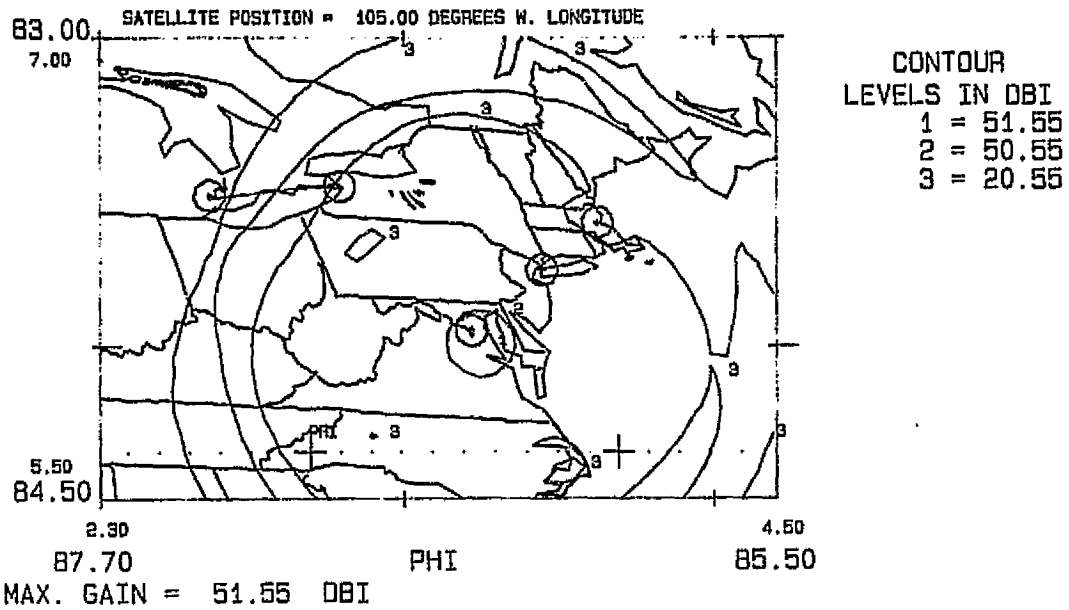

(a) Co-Pol Contours

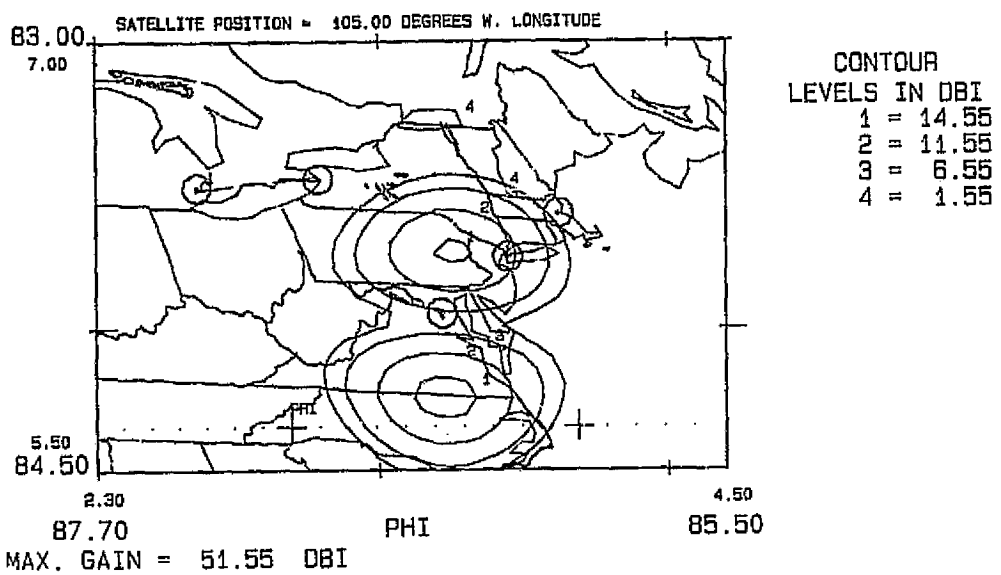

(b) Cross-Pol Contours

Figure 4-53. Fixed Spot Beam Over Washington, D.C., Using 9-Horn Cluster

Table 4-9. Coefficients for Washington, D.C., New York, and Boston Beams

Component Beam No.	Washington, D.C.		New York		Boston	
	Amplitude	Phase	Amplitude	Phase	Amplitude	Phase
1	0	0				
2	0.32	56.25				
3	0.16	33.75				
4	0.5	0				
5	1.0	0	0.32	180		
6	0	0	0.32	67.5		
7	0.32	0				
8	0.32	-56.25	0.32	90		
9	0.32	-45.0	1	0	0.32	-135
10			0.32	22.5		
11			0.32	0		
12					0	0
13					0	0
14					0.16	0
15					0.32	45
16			0.5	-11.25	1	45
17			0.5	-11.25	0.5	11.25
18					0.5	-101.25
19			0.32	22.5	0.32	-78.75

For the San Francisco fixed beam coverage, a 9-horn cluster is used. All feed elements are 2.54-cm (1in.) square horns. The component beams for San Francisco coverage are shown in Figure 4-54, and the composite co-pol and cross-pol contour patterns are shown in Figure 4-55. Again, the 30-dB isolation is readily achieved, and the cross-pol levels are almost 45 dB at the closest city (Los Angeles). The coefficients of the component beams are given in Table 4-10.

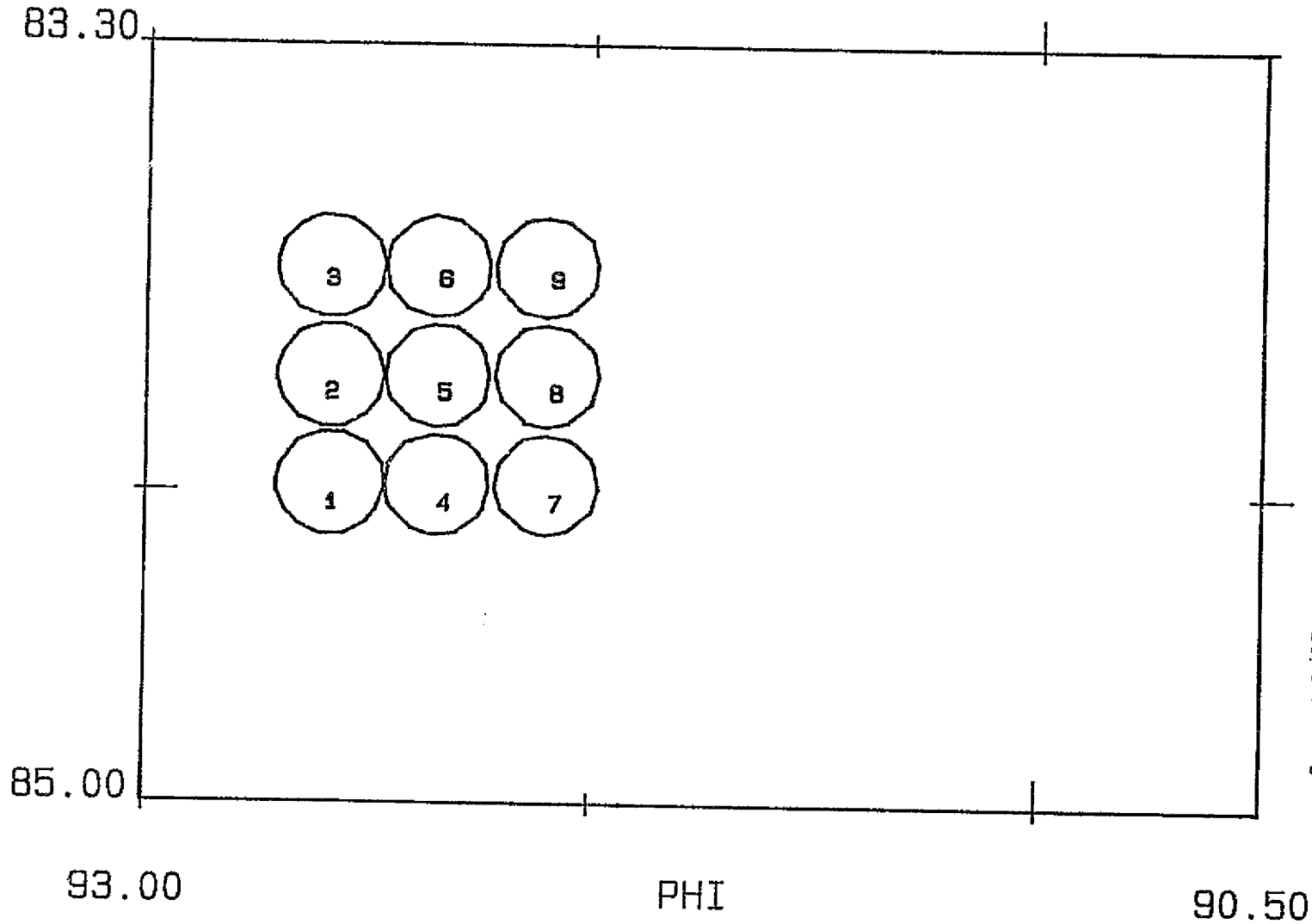

Figure 4-54. Component Beams for San Francisco Coverage

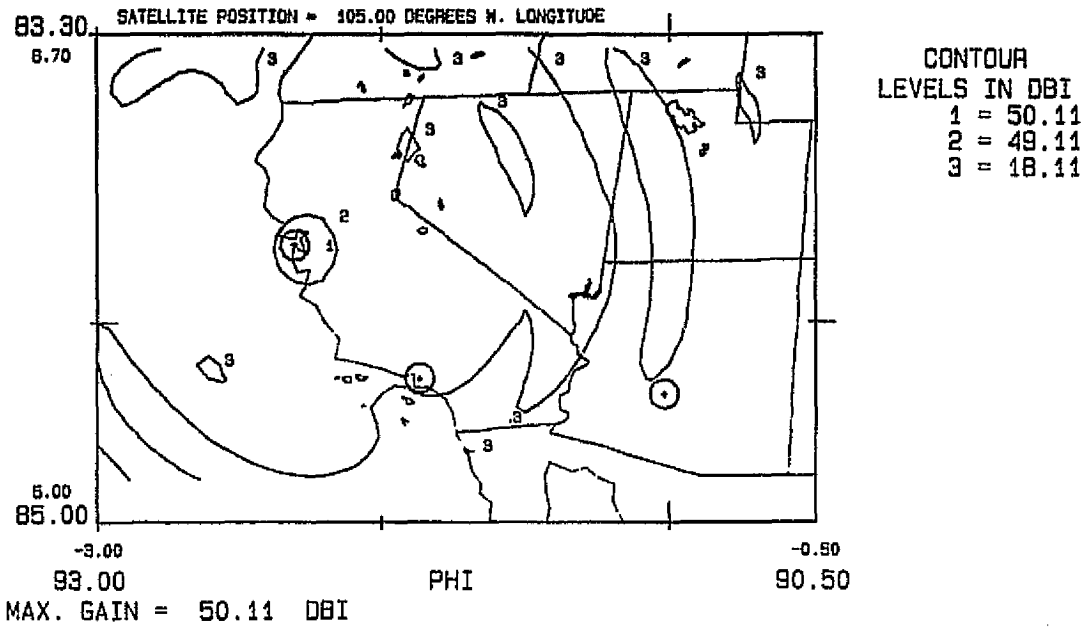

(a) Co-Pol Contours

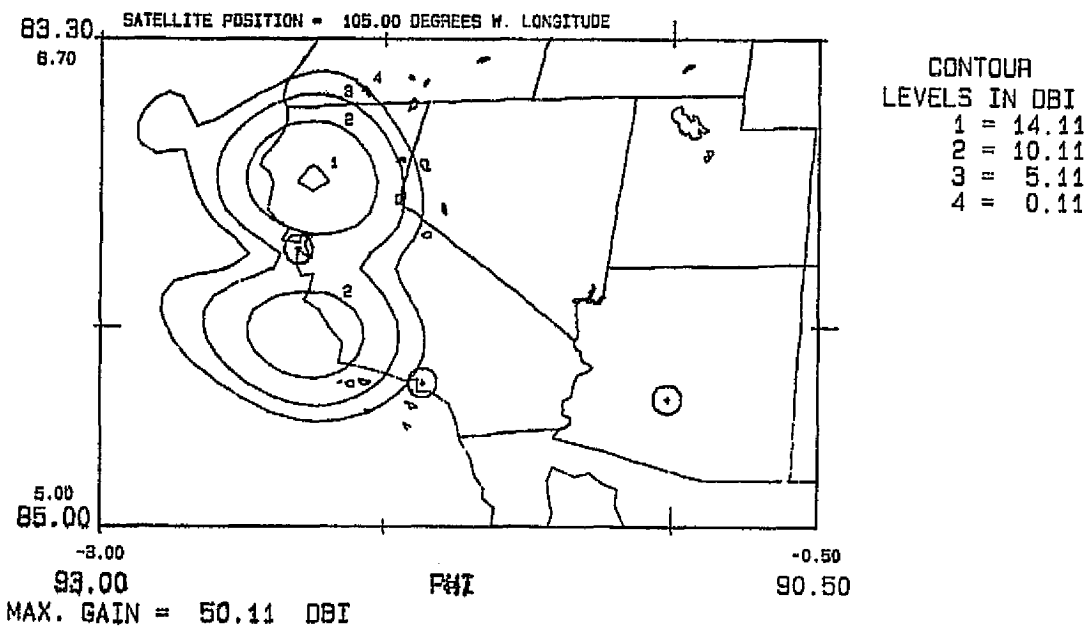

(b) Cross-Pol Contours

Figure 4-55. Fixed Spot Beam Over San Francisco Using 9-Horn Cluster

Table 4-10. Coefficients for San Francisco Fixed Beam Coverage

Component Beam Number	Amplitude	Phase
1	0	0
2	0	0
3	0.16	0
4	0.32	45
5	1	45
6	0.5	11.25
7	0.5	-101.25
8	0.32	-78.75
9	0.32	-135

The e.i.r.p. of any beam coverage is defined by

$$\text{e.i.r.p.} = \text{gain}_{(\text{dBi})} + \text{power}_{(\text{dBW})} - \text{loss}_{(\text{dB})} \qquad (4\text{-}81)$$

where gain is the maximum edge gain of each spot beam, and the total input power is the total power delivered by the variable gain amplifier module. The loss term includes the loss from the VPA module to the radiating element. Table 4-11 summarizes the e.i.r.p., edge gain, highest sidelobe level, and the isolation at the closest city that shares the same polarization. The e.i.r.p. number in the table was evaluated by adding the gain number to the sum of the power at the amplifier stage of all elements for each cluster. A 0.2-dB loss was assumed for the MMIC transition since the maximum output power from a variable-power amplified module is 0.5 W, the total input power available to the clusters ranges from 0.84 W to 1.06 W, which results in almost identical e.i.r.p. and gain numbers for all beams.

Table 4-11. Antenna Performance at Selected Cities

City	e.i.r.p.	Edge Gain	Cross-Pol	Isolation*
Washington, D.C.	50.33	50.6	37	30
New York	50.02	50.2	37	32
Boston	49.91	50.1	36	30
San Francisco	48.96	49.2	44	32

*Sidelobe level at the closest co-pol city.

4.6.2.3 Configuration F: Lens-Fed Confocal System

The performance of the bifocal lens used in the multiple fixed spot beam case is evaluated here for two cities. Figure 4-56a shows, the Boston beam with the same satellite bias (0.7°E, 5.7°N) as in the phased array case. However, the peak of the beam is not exactly on Boston. This inaccuracy is attributed to phase errors introduced by the lens and suggests the need for a finer adjustment of the primary feed horn. Note that, without the lens phase error, the beam will be accurately pointed. Co-pol isolation between Boston and Washington, D.C., is not greater than 20 dB. Figure 4-56b is another example of this configuration, showing the New York beam, with the same satellite bias. In this case also, due to the phase errors, the beam is not in the correct position over New York and will require a finer adjustment of the primary feed horn. Because of the New York beam, co-pol isolation at Buffalo is not better than 27 dB.

As mentioned earlier in the phased array cases, the use of continuous Taylor distributions in orthogonal planes will result in higher isolation numbers and a lower efficiency. It appears that, when using a lens with the multiple fixed-beam, all feed horns that are not in or close to the focal plane will require finer adjustments to achieve proper beam pointing.

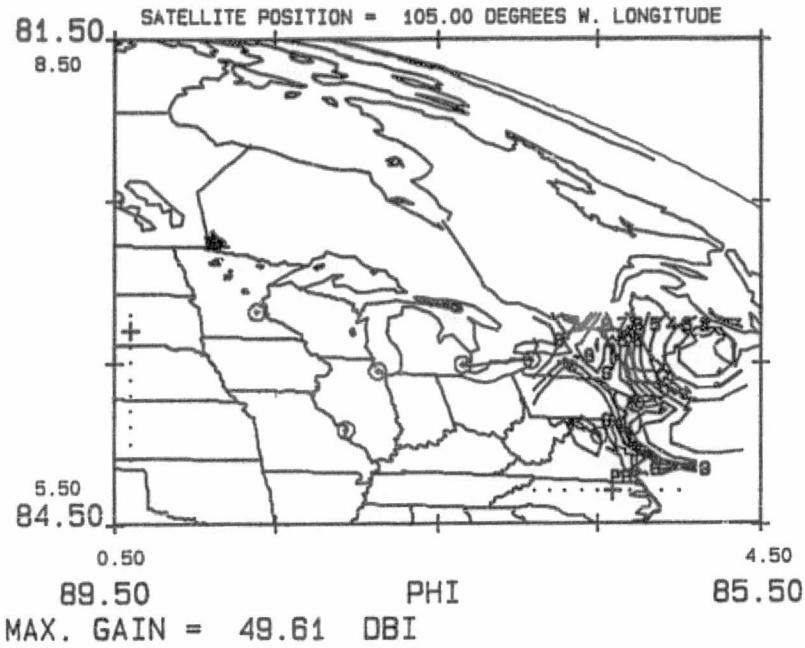

(a) Boston Co-Pol Contours

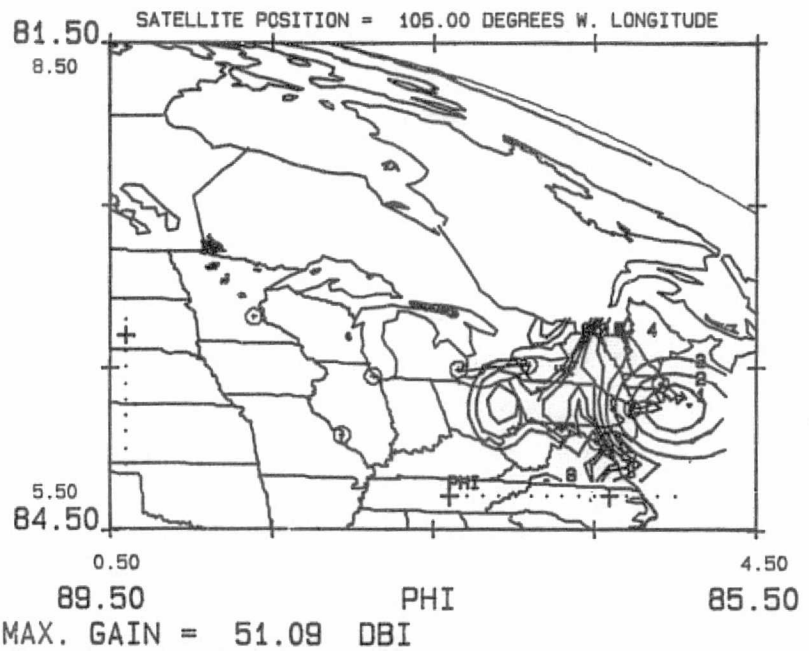

(b) New York Co-Pol Contours

Figure 4-56. Fixed Spot Beam With Bifocal Lens

4.7 INTEGRATED SPACECRAFT ANTENNA CONCEPT

A shuttle-compatible communications spacecraft configuration, shown in Figure 4-57, was developed to illustrate techniques for packaging antenna systems of the type discussed in this section. A large spacecraft is assumed because of the power and thermal requirements of the antenna subsystem. An undefined upper stage is used, with the yaw axis of the spacecraft coincident with the longitudinal axis of the shuttle bay. This launch position permits the entire shuttle bay diameter of 15 ft to be used for the reflector, if required. The spacecraft configuration shown has two distinct antenna subsystems. The DC input power for the scanning beam and fixed beam arrays was estimated to be as high as 7 and 1.5 kW respectively. If the amplifiers are about 15-percent efficient, a total of 7.2 kW will be radiated as waste heat. This radiator (approximately 28 m^2) is identified in Figure 4-57 as having north/south facing surfaces. The actual location of the radiator depends on the spacecraft configuration. It is assumed that a separate spacecraft configuration study will locate the radiator on the basis of the temperatures and heat rejection requirements established in this study.

The large deployable reflectors are stowed one above the other; launch locks carry the loads from the top reflector through the second reflector to the tower. The top reflector requires two hinges to achieve the necessary deployed geometry. The second hinge, however, will aggravate mechanical misalignment and possibly thermal distortion problems. Detailed configuration work with alternate optical arrangements, in addition to those illustrated in the figure, will be necessary to establish the optimum design with respect to RF performance and the mass and volume of the antenna subsystem. The consideration of folded optics recognizes the importance of the shuttle-launch cost incentive to minimize spacecraft length.

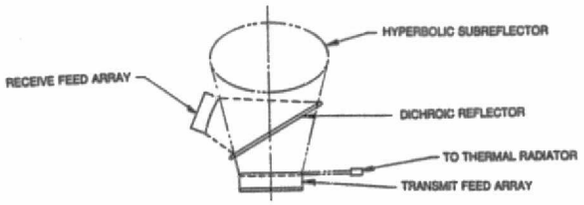

VIEW **B-B**
ROTATED INTO PLANE

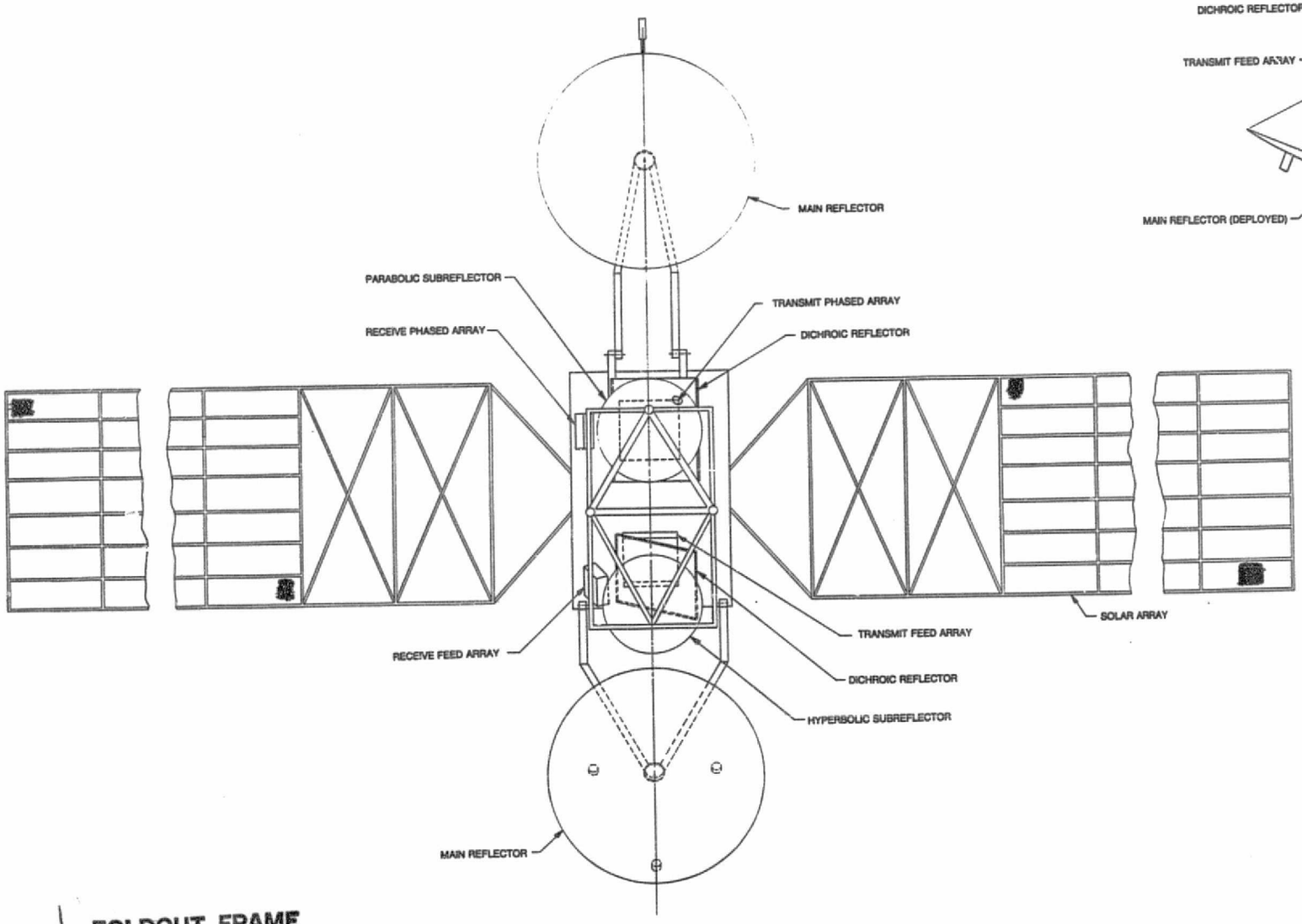

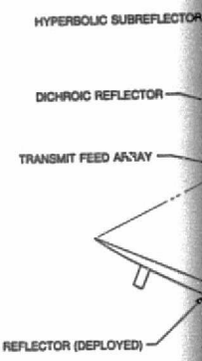

FOLDOUT FRAME

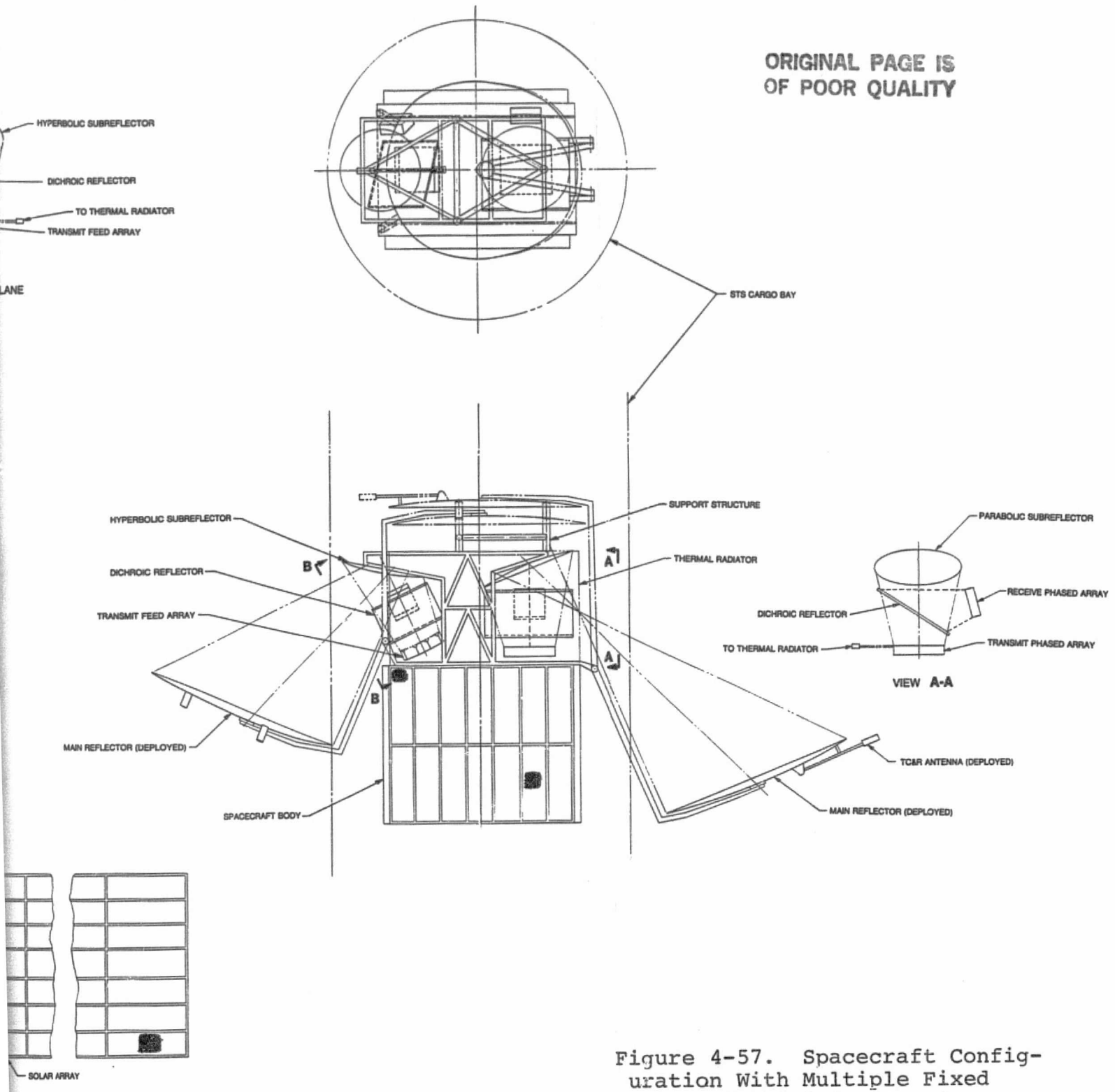

Figure 4-57. Spacecraft Configuration With Multiple Fixed Beam and Multiple Scanning Beam Antennas

2 FOLDOUT FRAME

5. FEED ARRAY DESIGN

5.1 INTRODUCTION

Task IV of this project dealt with the detailed aspects of the feed array design for both multiple scanning beam and multiple fixed beam antennas. Based on the studies performed under Task III and presented in Section 4, a phased-array feed element was fabricated and tested. This element included the radiating square horn, the orthomode transducer, and the MMIC/waveguide transitions. Also a lens element comprising MMIC/waveguide transitions in square waveguides for dual polarization was assembled. The mutual coupling effects in the array were thoroughly assessed, both analytically and through measurements. To study the scanning performance of the phased array, a 34-element subarray was fabricated and tested for different kinds of amplitude tapers. The MMIC was integrated into the feed element by using MMIC/waveguide transitions designed for rectangular and square waveguides. The propagation characteristics in finline structures were analyzed to assist in the design procedure. Also under Task IV, a comprehensive study of the beam-forming network (BFN) for all the final configurations was carried out, and a design for the thermal control system was studied.

5.2 FEED ELEMENT DESIGN

5.2.1 RADIATING ELEMENT

As mentioned in Subsection 4.3, a square horn of aperture dimension 2.0λ at band center was selected as the radiating element for the phased array, for both the scanning array and the multiple beam array. For the multiple beam feed array in the Cassegrain system of Configuration E, the element is also a square horn, but with the smaller aperture dimension of 1.3λ at band center.

For the phased array, the element aperture size, the length, and taper satisfied all the requirements of scanning step criteria, avoiding grating lobe, suppressing the TM_{12} mode at the horn aperture, and reducing aperture phase errors. The square waveguide dimensions at the horn input were chosen to allow for dual linear polarization, as discussed in Subsection 5.2.2.

A horn with the design parameters outlined in Table 4-5 was fabricated and tested and is shown in Figure 5-1. The E- and H-plane radiation patterns of this horn were measured at three frequencies in the 17.7-20.2 GHz band. Figure 5-2 shows the measured patterns.

5.2.2 ORTHOMODE TRANSDUCER

An orthomode transducer (OMT) is used to feed the radiating element with dual polarization. Figure 5-3 is a cross-sectional sketch of the OMT, where the two perpendicularly polarized signals are fed through the shunt and the back (or through) ports. The shunt port carries the horizontal polarization, which

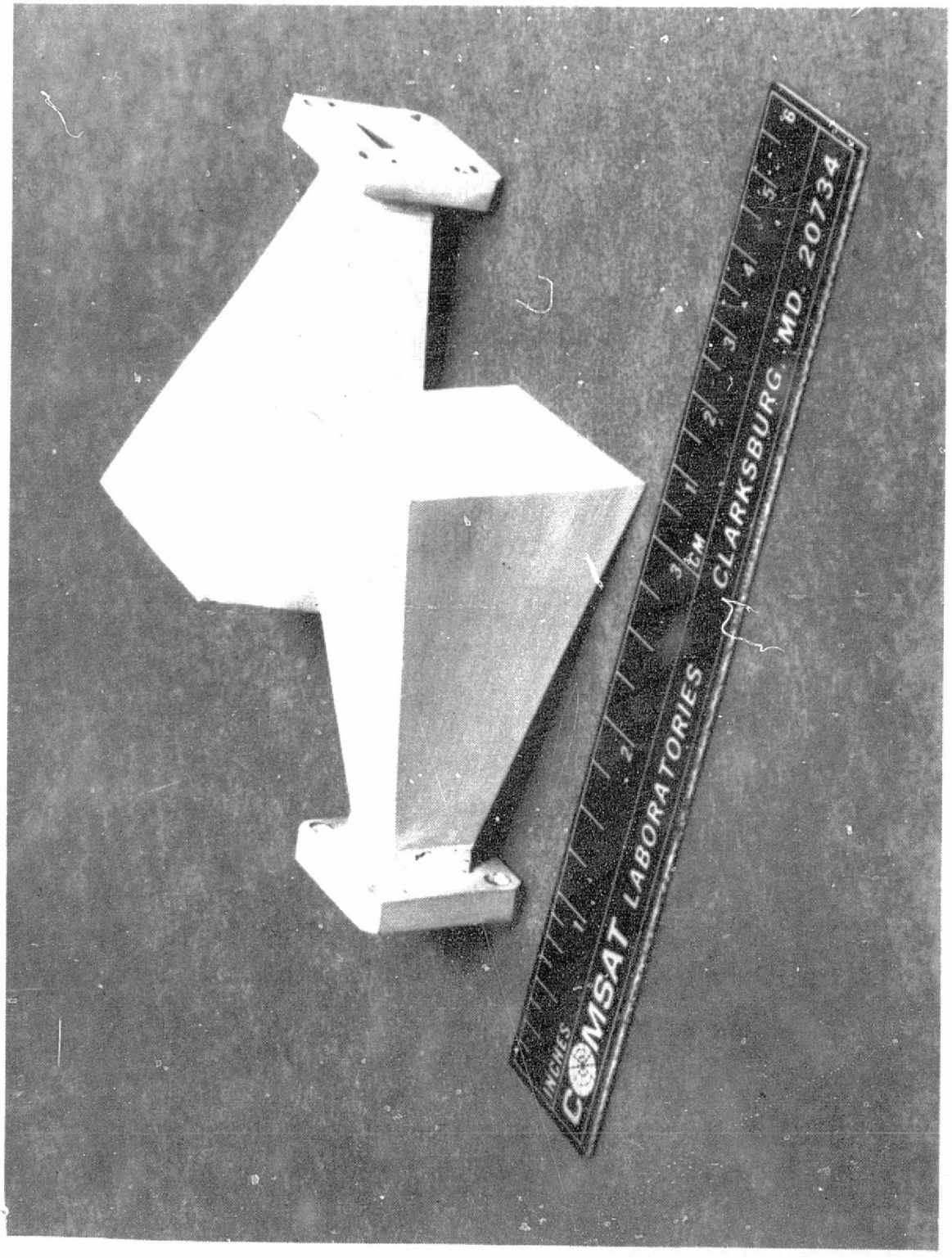

Figure 5-1. Horn Element for Scanning Beam Array

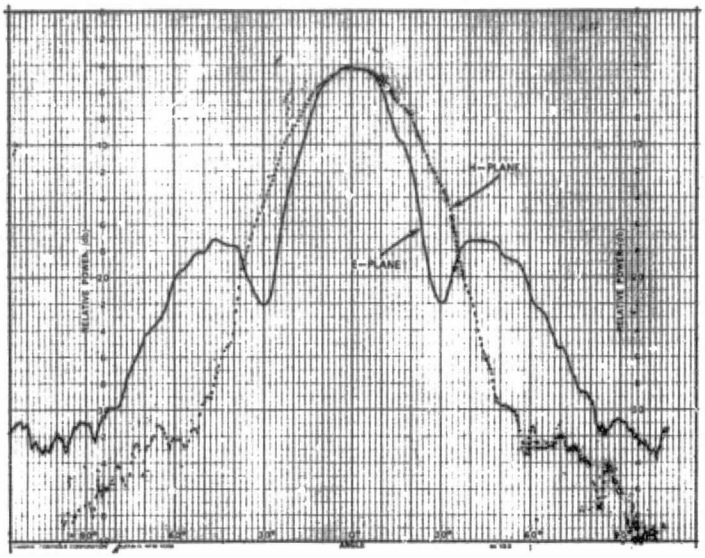

(a) 17.9 GHz

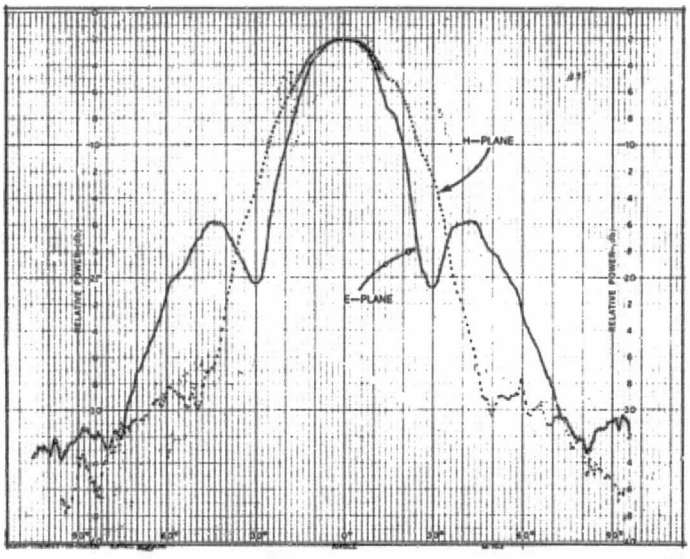

(b) 18.95 GHz

Figure 5-2. E-Plane and H-Plane Radiation Patterns for Square Horn

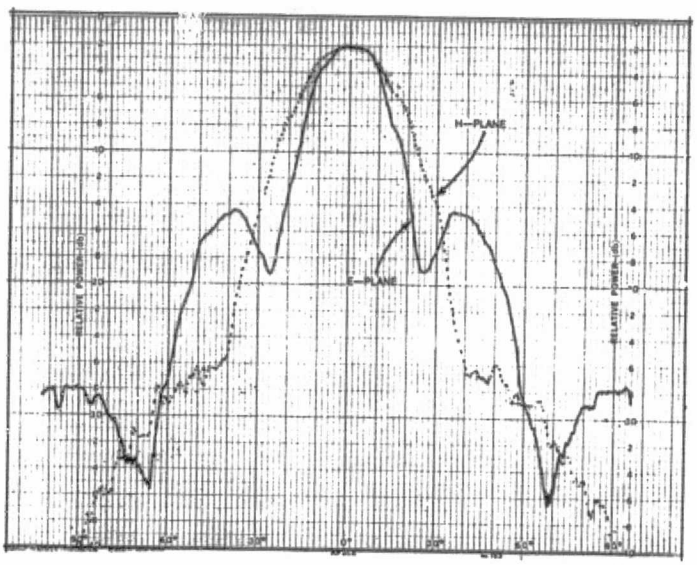

c. 20.2 GHz

Figure 5-2. E-Plane and H-Plane Radiation Patterns for Square Horn (Cont'd)

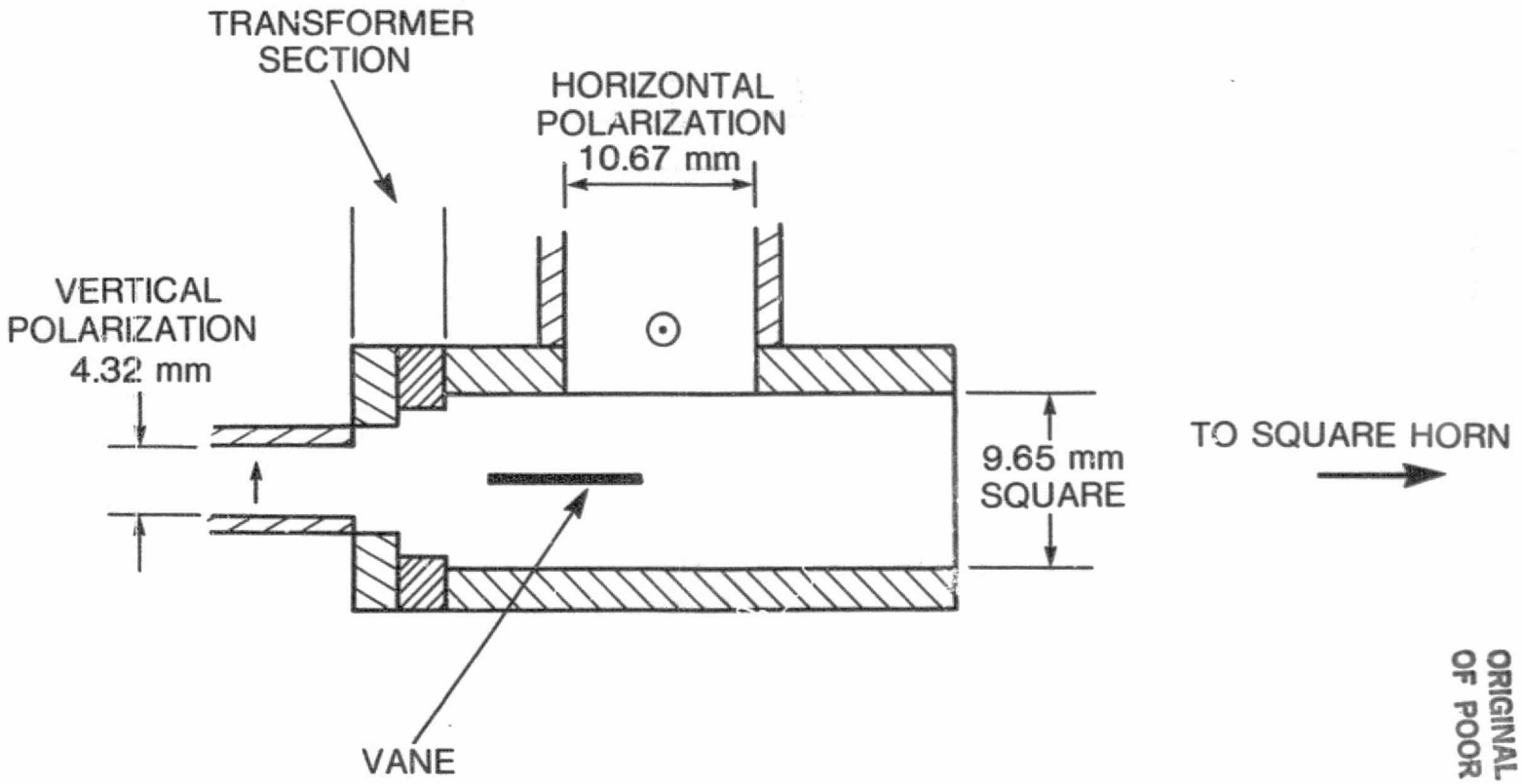

Figure 5-3. Dimensions of OMT Design

is reflected at the horizontal vane and propagates toward the horn. The vertical polarization, fed through the back port, is normal to the vane and propagates directly to the horn. Both input ports have standard WR-42 waveguide cross sections. To match the back port to the square cross section of the OMT, a two-section, quarter-wavelength transformer is used.

The square cross-sectional dimensions of the OMT must be chosen to allow only TE_{10} modes of both polarizations to propagate. Table 5-1 lists the cutoff frequencies for the TE_{10}, TE_{11}, and TE_{20} modes in square waveguides of different dimensions. The 0.965-cm (0.38-in.) square waveguide offers an operating band enclosing the 17.7-20.2 GHz band about its center. This dimension is chosen for the OMT and, consequently, for the radiating horn and other square waveguide sections in the system.

Table 5-1. Cutoff Frequencies for Rectangular Waveguides

Waveguide Size (cm)	Cutoff Frequency (GHz)		
	TE_{10} Mode	TE_{11} Mode	TE_{20} Mode
WR-42 1.067 x 0.432	14.05	37.45	28.10
Square 1.067 x 1.067	14.05	19.87	28.10
Square 1.016 x 1.016	14.75	20.86	29.50
Square 0.965 x 0.965	15.53	21.96	31.06
Square 0.914 x 0.914	16.39	23.18	32.78

A breadboard model of the OMT was fabricated and tested. Figure 5-4 is a photograph of the OMT showing its different sections. The final matching is achieved through two tuning screws at the two inputs. Figures 5-5 through 5-7 show the measured

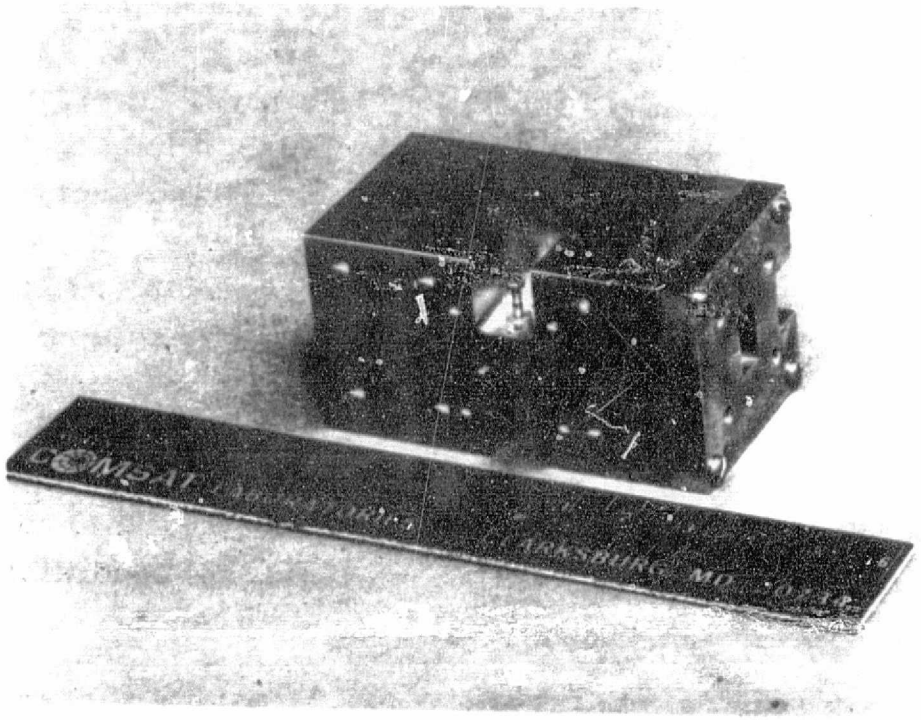

(a) Outside View

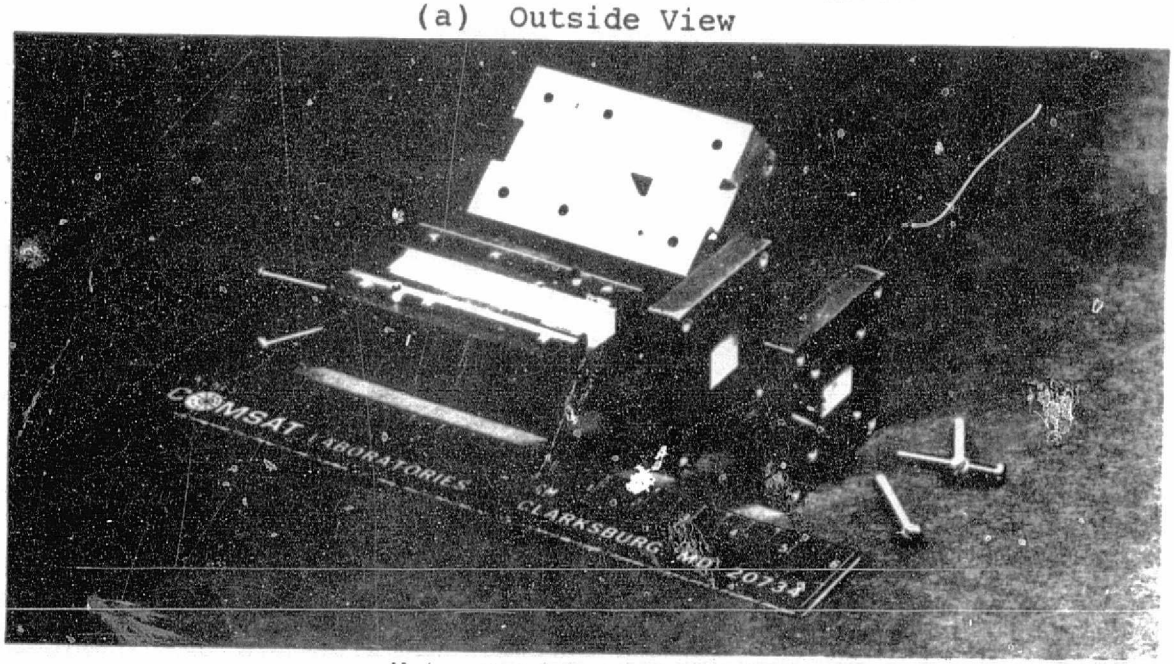

(b) Inside Details

Figure 5-4. 20-GHz Prototype OMT

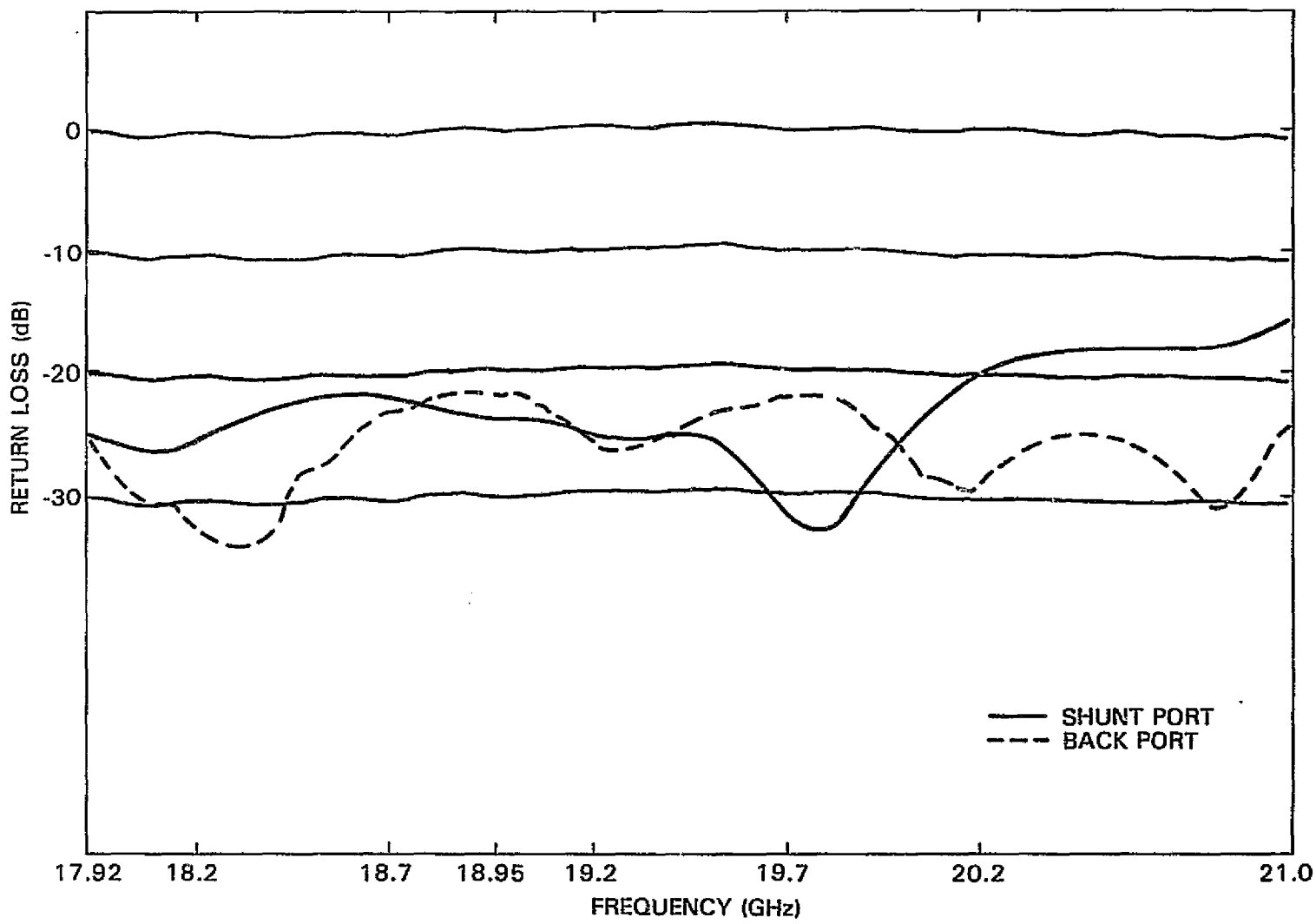

Figure 5-5. Return Loss of OMT

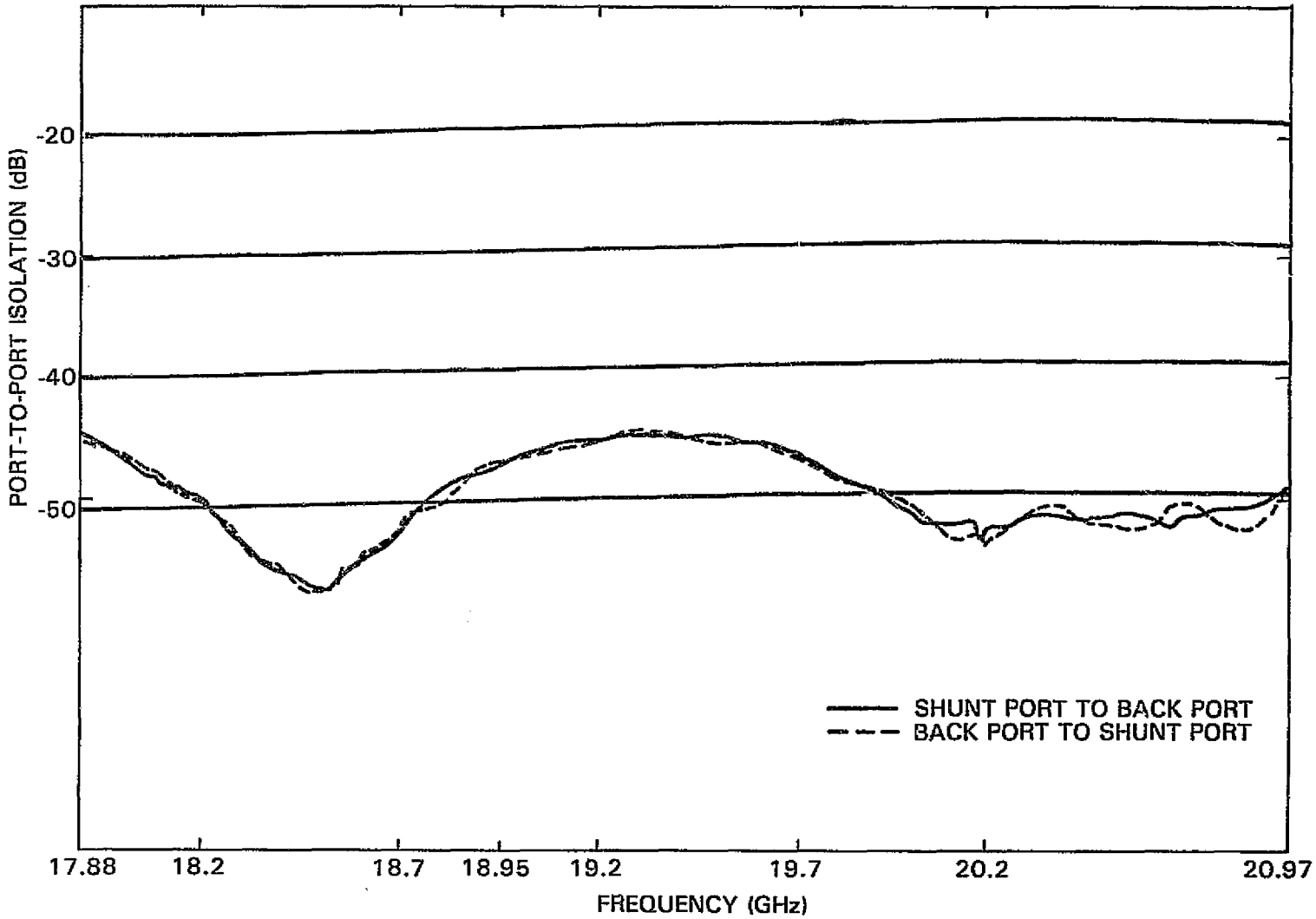

Figure 5-6. Port-to-Port Isolation of OMT

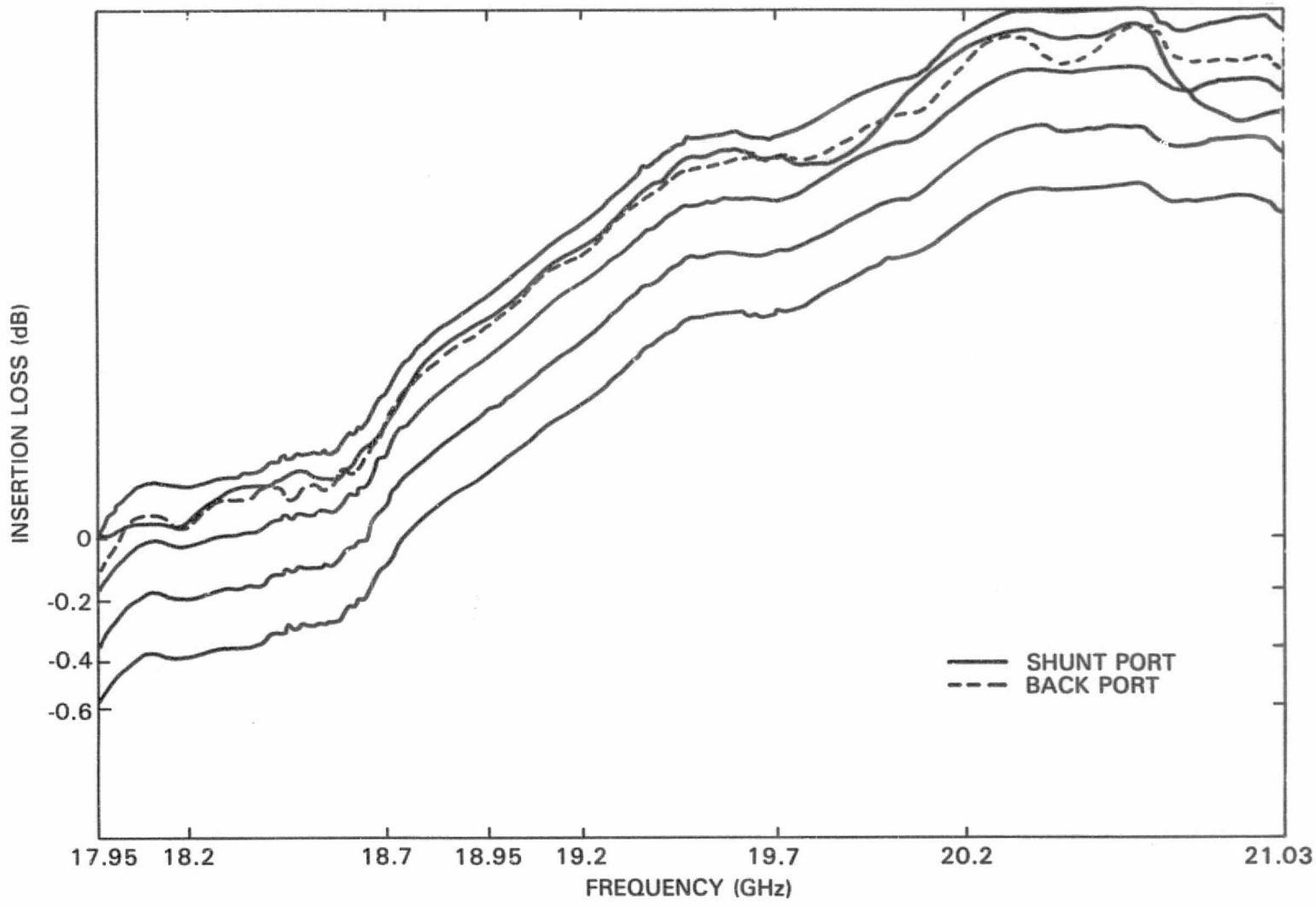

Figure 5-7. Insertion Loss of OMT

performance of the OMT across the operating frequency band. The obtained return loss, shown in Figure 5-5, exceeds 20 dB for frequencies less than the upper band limit of 20.2 GHz. The port-to-port isolation, Figure 5-6, is better than 45 dB across the band. The insertion loss is measured between each input and the WR-42 side of a 9.65-mm-square-to-WR-42 waveguide taper. Figure 5-7 indicates insertion losses of about 0.08 dB.

5.2.3 PHASED ARRAY ELEMENT

The complete phased array element consists of the radiating horn fed by the OMT, which in turn is fed through the two orthogonal ports via waveguide sections containing the MMIC amplifier modules. A detailed discussion of this waveguide/MMIC/waveguide transition section is given in Subsection 5.7. Assembly of the horn, the OMT, and two transitions results in the phased array element shown in Figure 5-8.

The overall performance of this breadboard element was measured. The return losses, port-to-port isolation, and insertion losses are shown in Figures 5-9 through 5-11, respectively. Because of the limitations of the MMIC/waveguide transitions, the bandwidth of the whole phased array element is reduced to about 1 GHz for a return loss better than 15 dB. The port-to-port isolation is higher than 47 dB across the full band. The insertion loss without the radiating horn, however, is about 1.1 dB across a 1-GHz bandwidth. This loss reflects mainly the 50-Ω line loss inside the transition, as pointed out in Subsection 5.7. It should be noted that the bandwidth restrictions of the transition are dictated by the stepped transformer sections in the circuit, which are used to match the 50-Ω MIC line to the waveguide impedance. A continuous taper transformer design may increase the bandwidth to nearly the full 2.5 GHz, as discussed in Subsection 5.7.

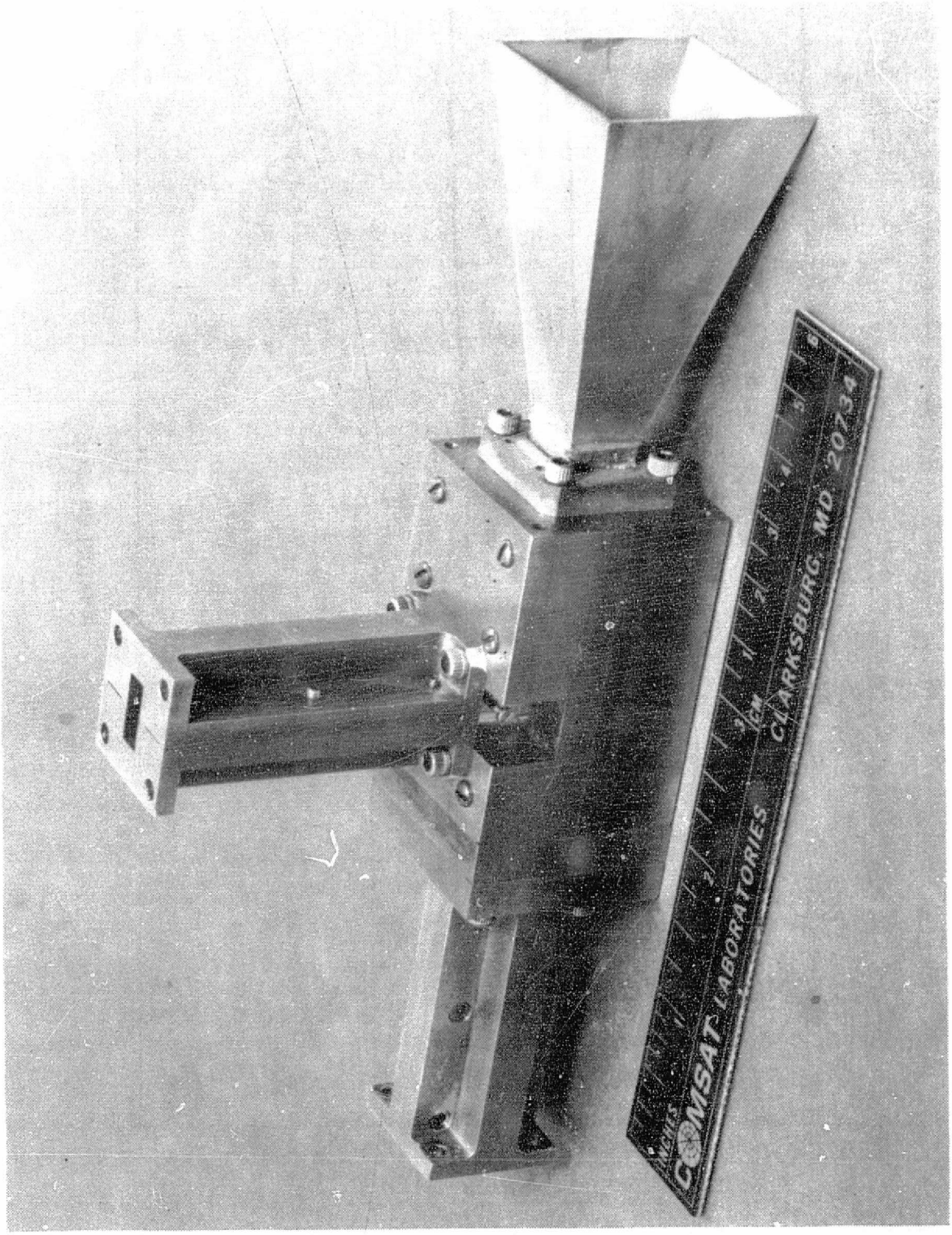

Figure 5-8. Complete Breadboard Model of Array Element

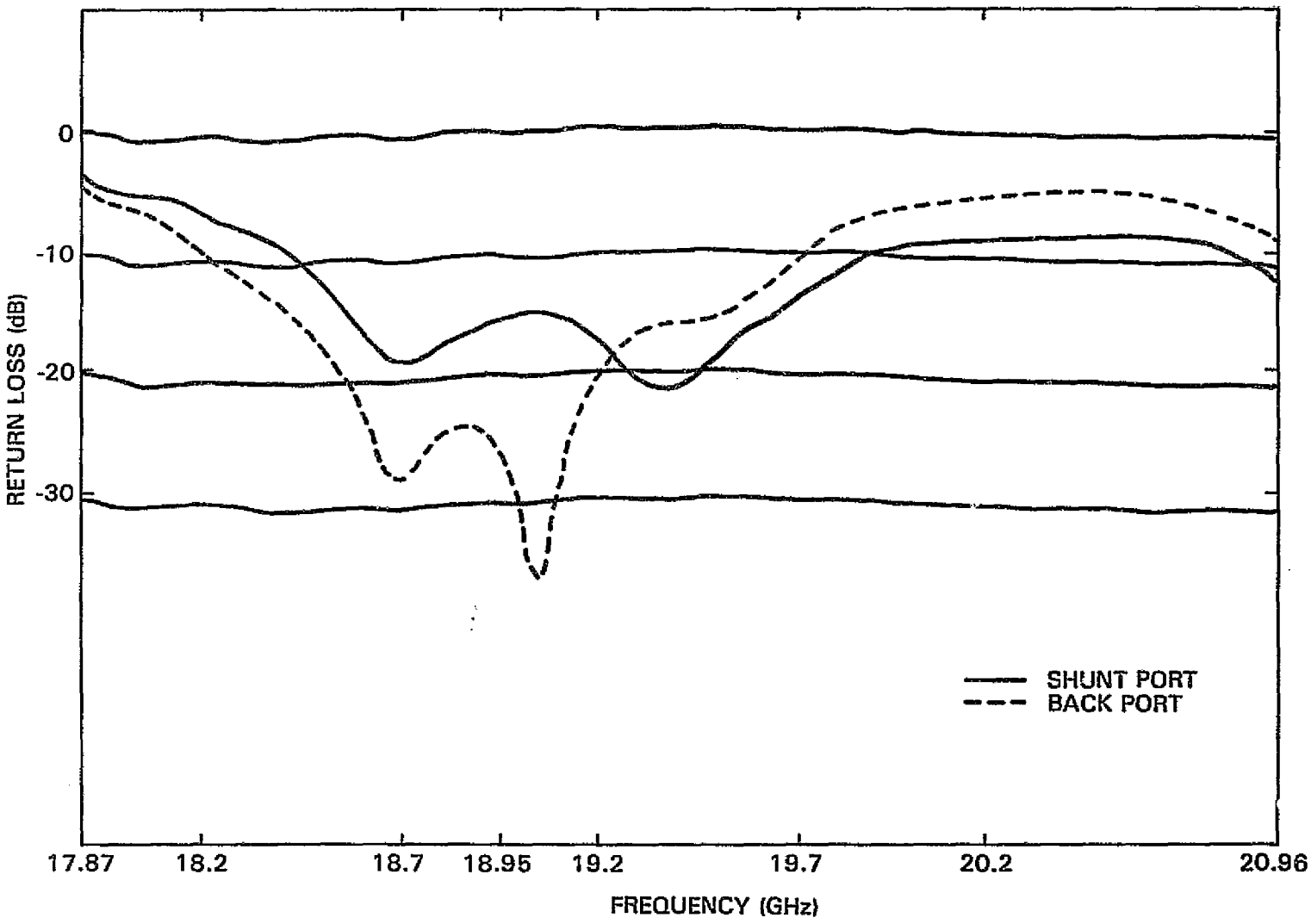

Figure 5-9. Return Loss of Breadboard Array Element

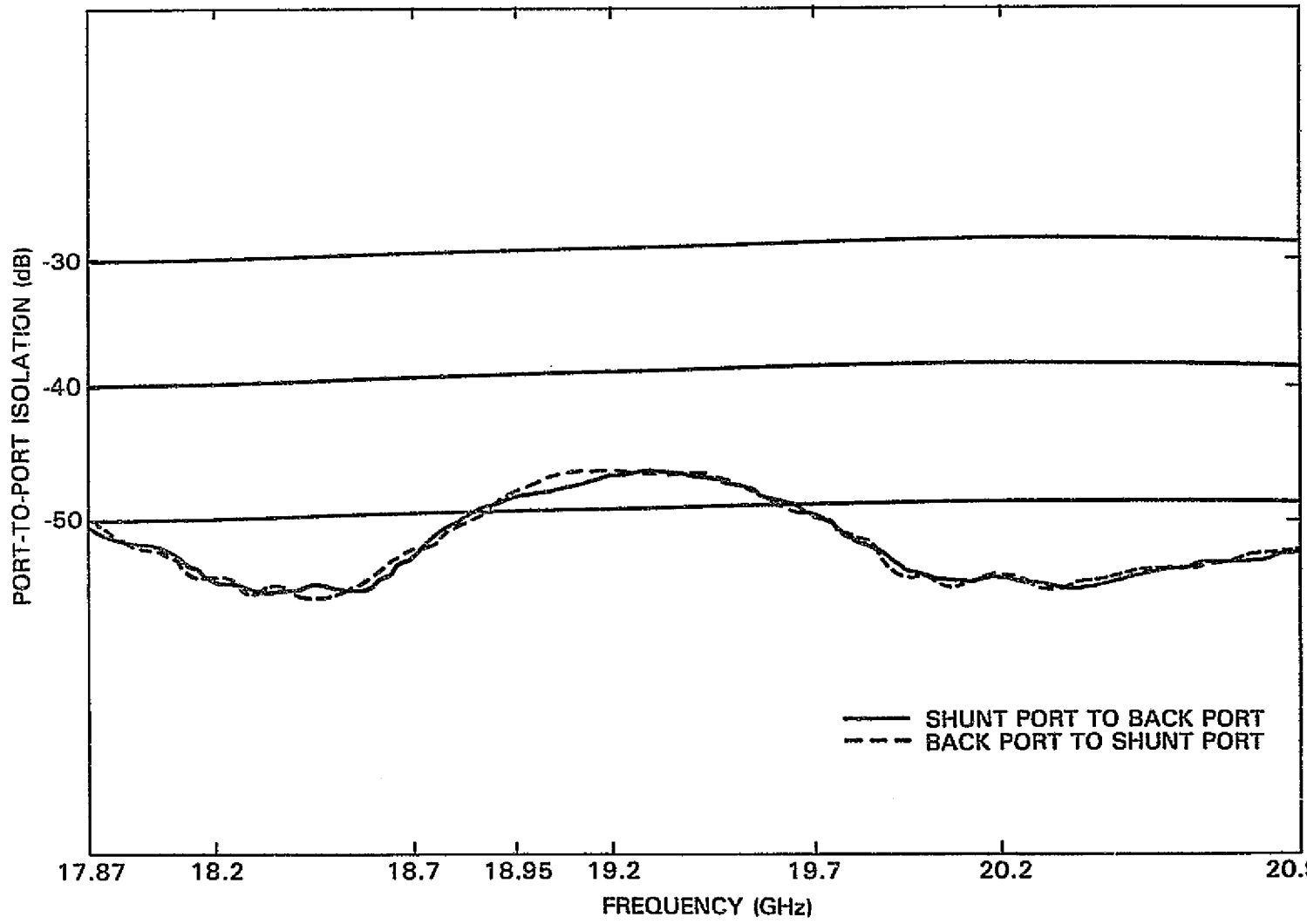

Figure 5-10. Port-to-Port Isolation of Breadboard Array Element

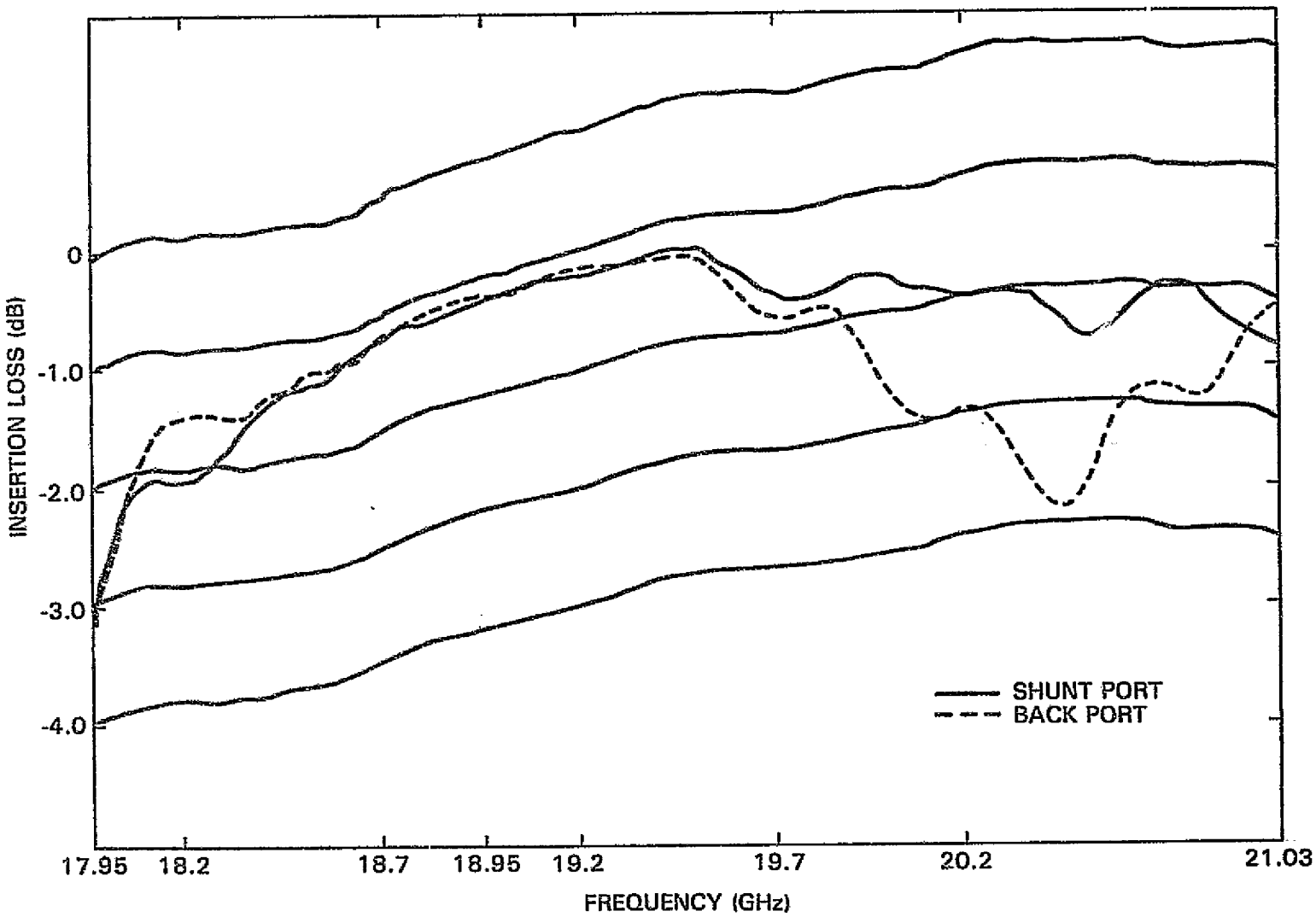

Figure 5-11. Insertion Loss of OMT-MMIC/Waveguide Transition in Breadboard Array Element

5.2.4 LENS ELEMENT

The complete lens element consists of an input radiating horn, two square waveguide sections containing the MMIC amplifier modules, and an output radiating element. The amplifier modules are placed inside the square waveguide/MMIC/waveguide transition sections. The square waveguide has the same dimensions as the horn input and supports both vertical and horizontal polarizations. The MMIC/waveguide transition is designed so that it supports no coupling between the two orthogonal polarizations. A discussion of this transition is given in Subsection 5.7.3. Figure 5-12 shows an assembled breadboard model of the lens element.

To form the inner lens surface, the physical length of the square waveguide section in the lens element will be different for different elements. To make the electrical length between the input and output horns conform to a given design length, an extra line length can be added in the MIC circuit.

5.3 MUTUAL COUPLING EFFECTS

For an array of square horns, the significance of mutual coupling effects depends on the size of the individual horn aperture and the spacing between horns. A computer program has been developed at COMSAT Laboratories to calculate the mutual coupling between rectangular apertures in a plane [5-1]. The program uses the correlation matrix technique to evaluate the scattering and admittance matrices. The results of the computer program have been compared with experimental results in the past and have shown very good agreement.

The horn sizes considered in this study range from 1.3λ for the multiple beam focal-region-fed Cassegrain system to 2λ

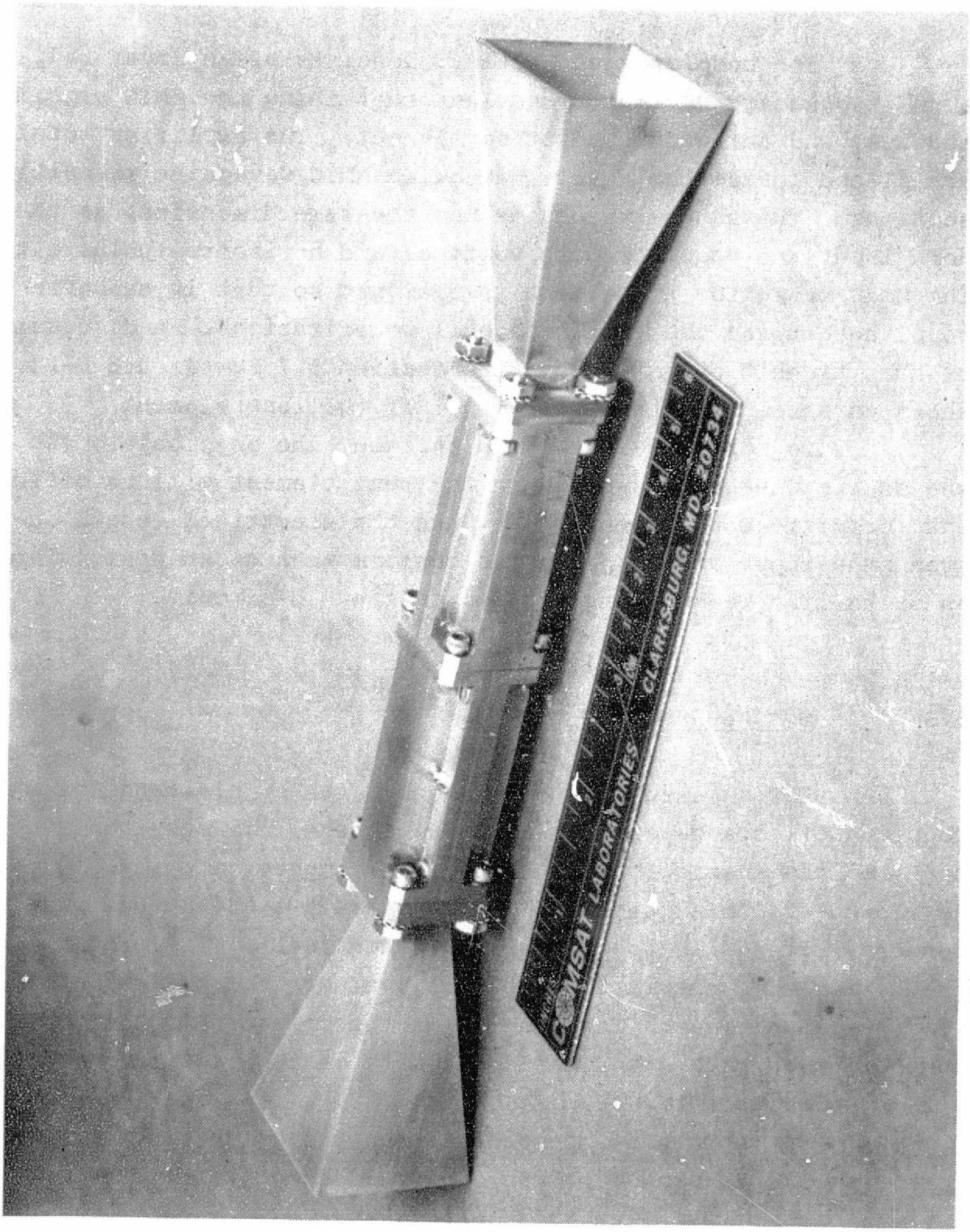

Figure 5-12. Complete Breadboard Model of Lens Element

for the phased array. For the larger elements of 2λ, the mutual coupling is expected to be much less than for the smaller elements. To study the mutual coupling effects, an array of square horns was fabricated. Because of the existence of hardware at the K_u band (11.7-12.2 GHz), the horns were designed for this frequency band. The horn size chosen was about 1.3λ, with element spacing of 1.43λ at the center frequency of 11.95 GHz. This spacing is similar to that of the smaller horns considered for the design under consideration, and this size would demonstrate the worst-case mutual coupling effects.

Figure 5-13 shows the square horn array built to study the coupling effects. The elements of the array are fed with OMTs to excite vertical and horizontal polarizations. The array mounting frame is designed to allow for reconfiguration of the elements in the array into triangular lattices. The arrangement shown in Figure 5-14 is used to calculate and measure the mutual coupling in a 12-element array, and Figure 5-15 shows calculated coupling coefficients between different elements. Figure 5-16 shows measured mutual coupling coefficients across the frequency band between two adjacent horizontally polarized elements and two adjacent vertically polarized elements. The corresponding values calculated using COMSAT's mutual coupling program are shown on the same figure for comparison.

From Figures 5-15 and 5-16, the coupling coefficients between two 1.3λ square apertures spaced 1.4λ apart is less than -28 dB. The coupling is higher between two colinear apertures with horizontal polarization, such as horns 7 and 8. For adjacent vertically polarized horns, the electric fields go to zero at the common edge and the coupling becomes less. Also, for offset vertically polarized horns (such as horns 6 and 10), the electric field distribution in the two apertures is such that strong field in one horn is colinear with almost zero field in the other horn,

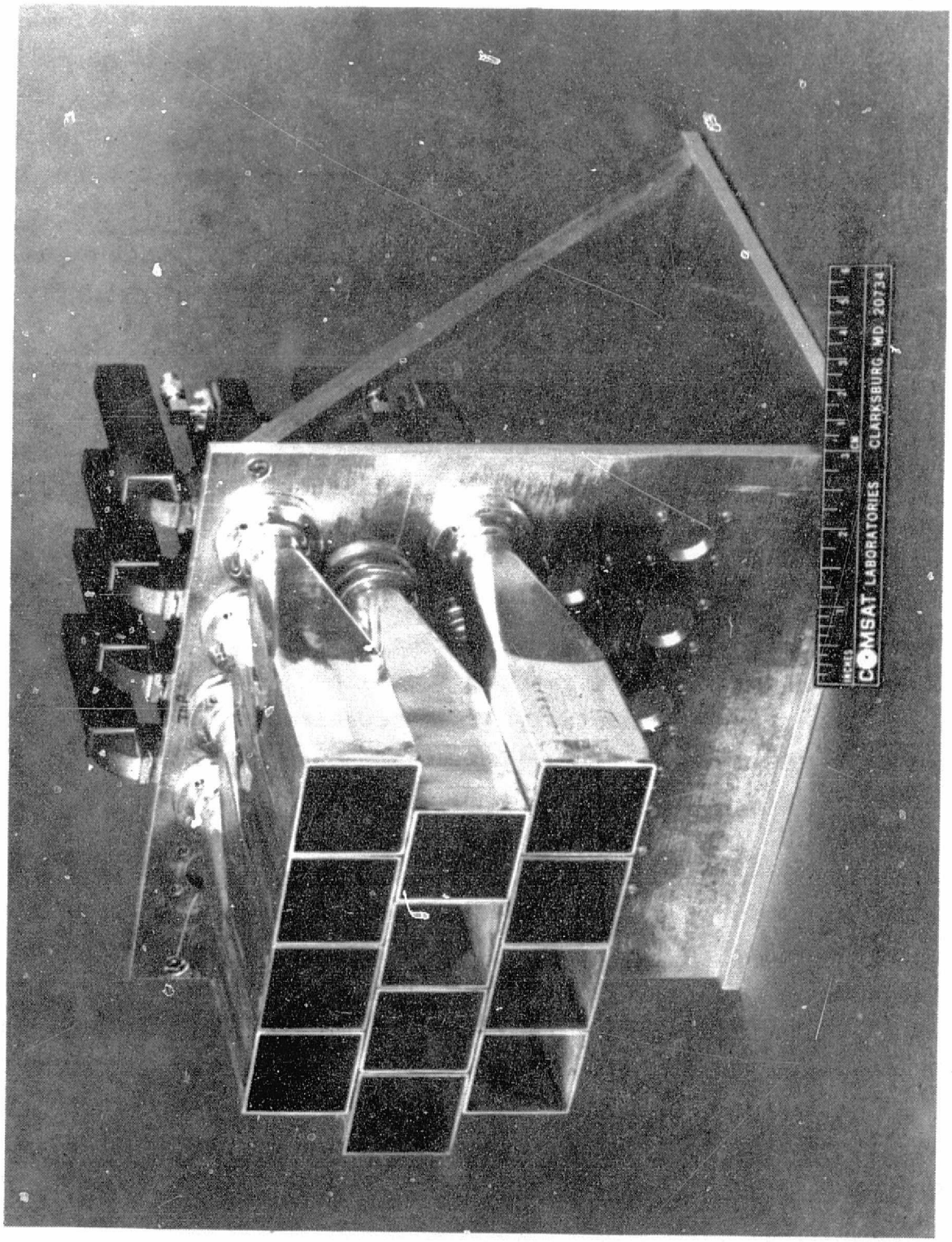

Figure 5-13. 12-Element K_u-Band Dual-Polarized Square Horn Array

thus resulting in weaker coupling. As the frequency increases, the horn sizes increase electrically and the mutual coupling decreases accordingly. This means that, for larger elements of 2λ square apertures, the coupling will be less than the -30 dB observed for the 1.3λ apertures.

To study the effects of mutual couplings on the radiation pattern of the array, a 14-element array was configured as shown in Figure 5-17. The element patterns of the central element, 10, and the edge element, 1, and the isolated pattern of a single horn were measured for both orthogonal polarizations. Figure 5-18 shows the E-plane, H-plane, and 45°-plane patterns for element 10 at 11.7 GHz when this element is excited with vertical polarization through the back port of the OMT. The other elements in the array are terminated with matched terminations. These patterns represent the large array element pattern, or the

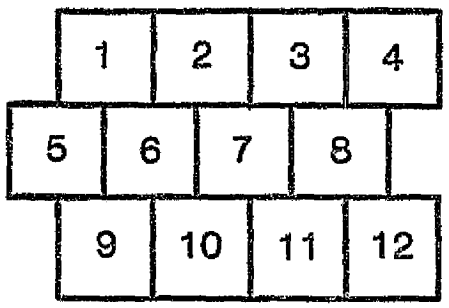

Figure 5-14. 12-Element Array Configuration

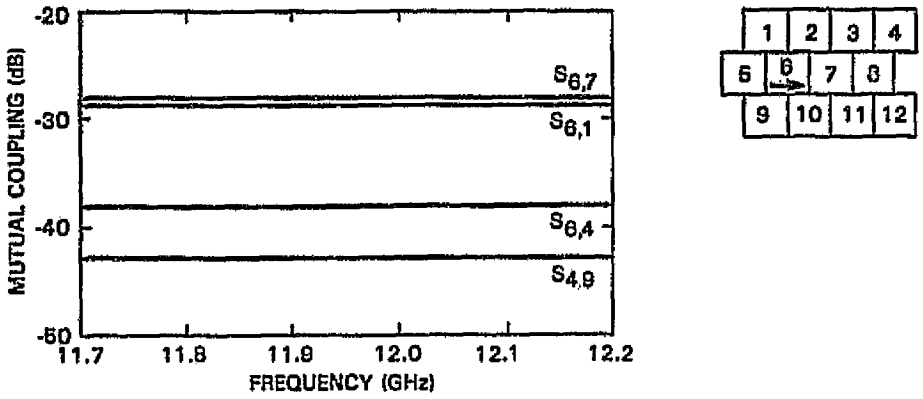

(a) Mutual Coupling Between Horizontally Polarized Elements

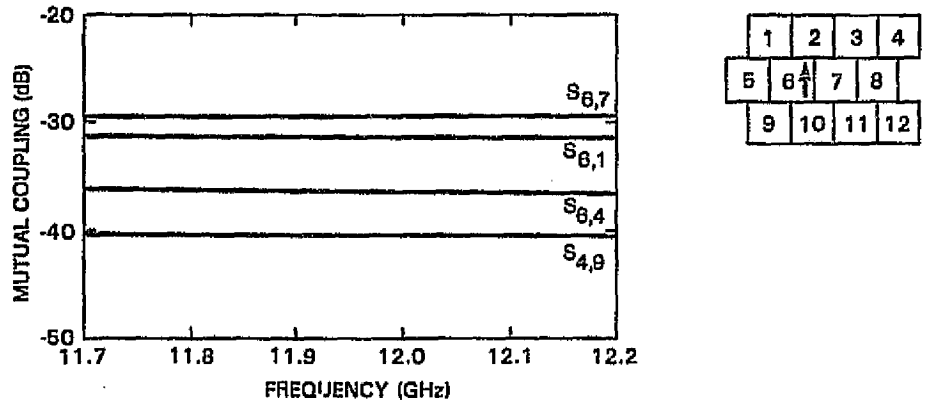

(b) Mutual Coupling Between Vertically Polarized Elements

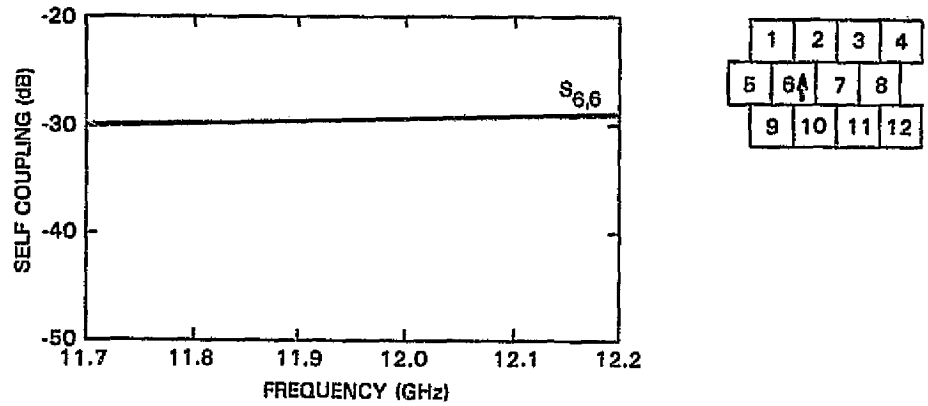

(c) Self Coupling of Vertically Polarized Element

Figure 5-15. Calculated Couplings Between Elements

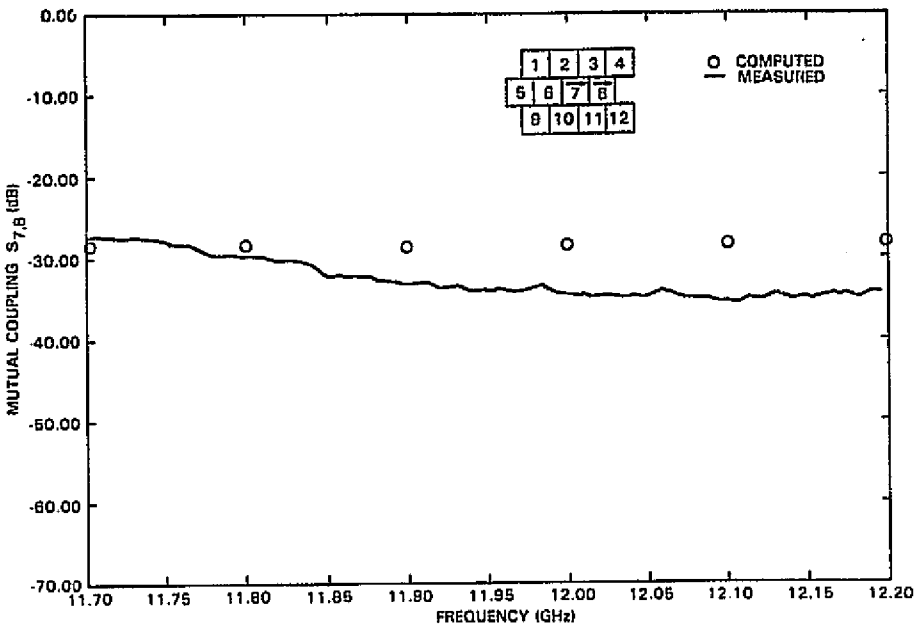

(a) Horizontally Polarized Elements

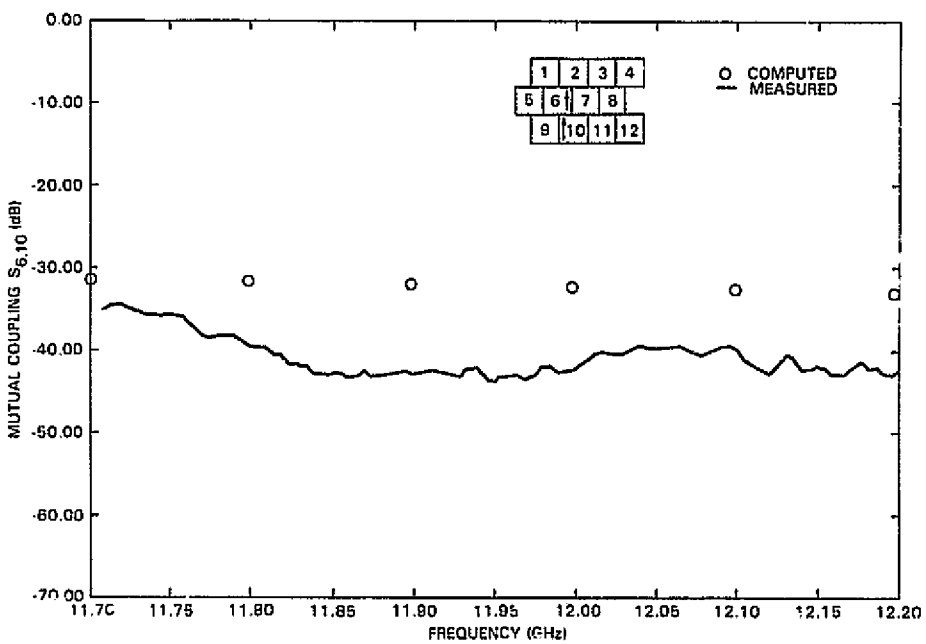

(b) Vertically Polarized Elements

Figure 5-16. Calculated vs Measured Mutual Couplings

scanning pattern of the complete array. Because of the central position of the element being measured, the contributions of the mutual couplings between this element and the other elements in the array add in a symmetric manner, resulting in a symmetric pattern. The cross-polarization patterns are shown in the same figure for the E-plane, H-plane, and 45°-cut plane.

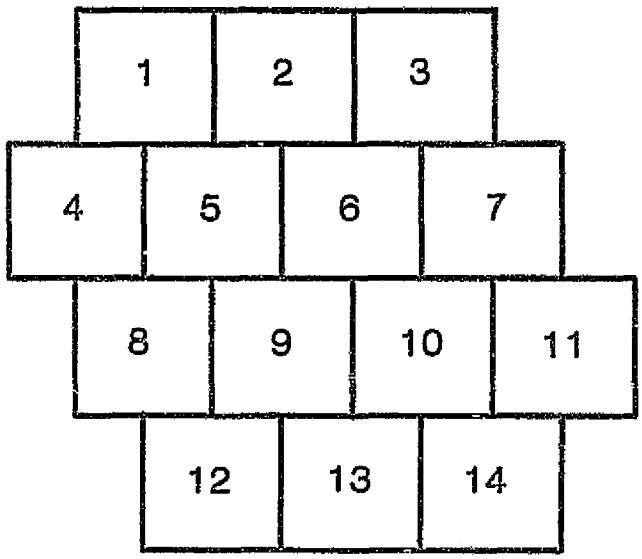

Figure 5-17. 14-Element Array Configuration

For edge element 1, the mutual coupling contributions do not add symmetrically. Figure 5-19 shows the E-plane, H-plane, and 45°-plane patterns for this element at 11.7 GHz when it is excited with vertical polarization. The asymmetry of the pattern is especially apparent in the E-plane pattern. This shows that, although the individual mutual coupling coefficients may be small, their accumulation can have a significant effect on the pattern of the edge elements.

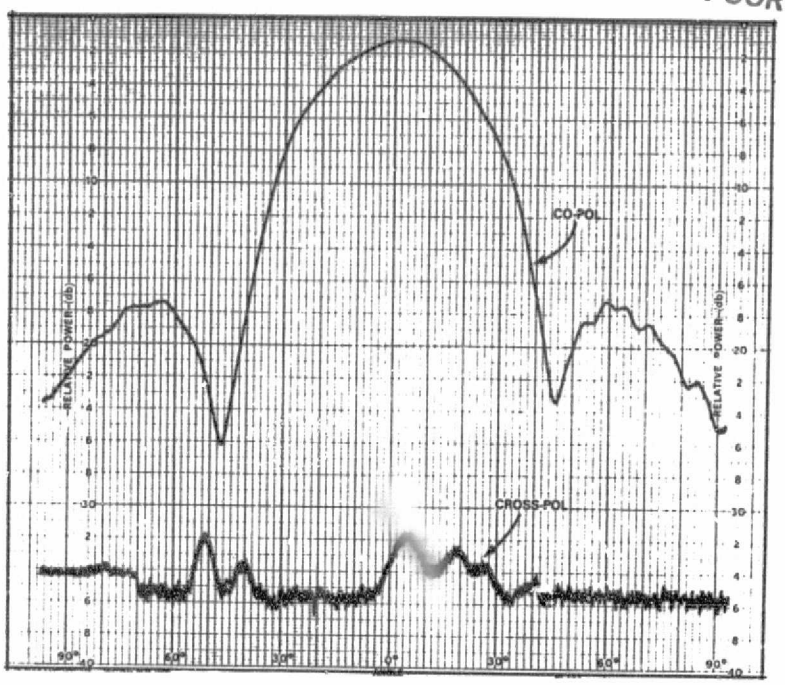

(a) E-Plane

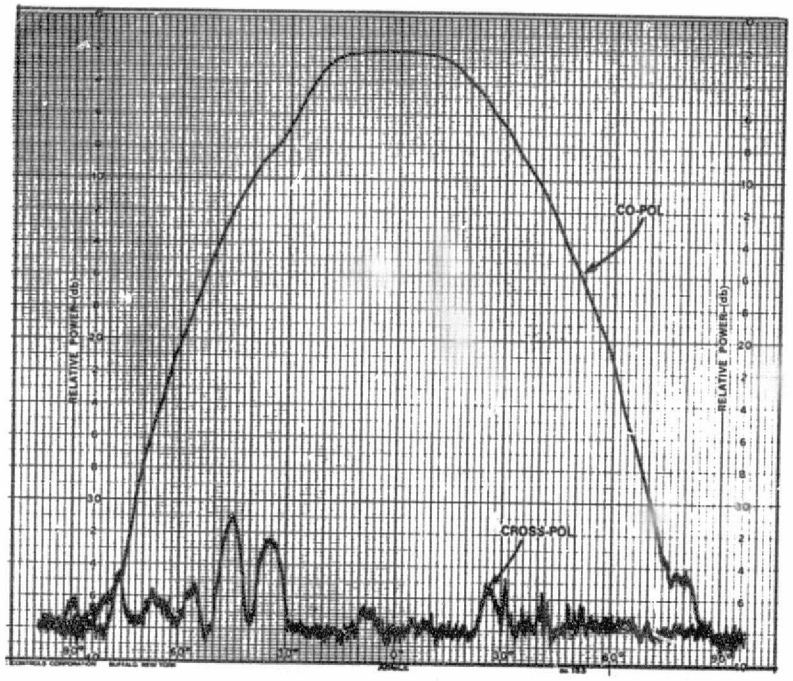

(b) H-Plane

Figure 5-18. Co- and Cross-Pol Radiation Patterns of Vertically Polarized Central Element 10 at 11.7 GHz

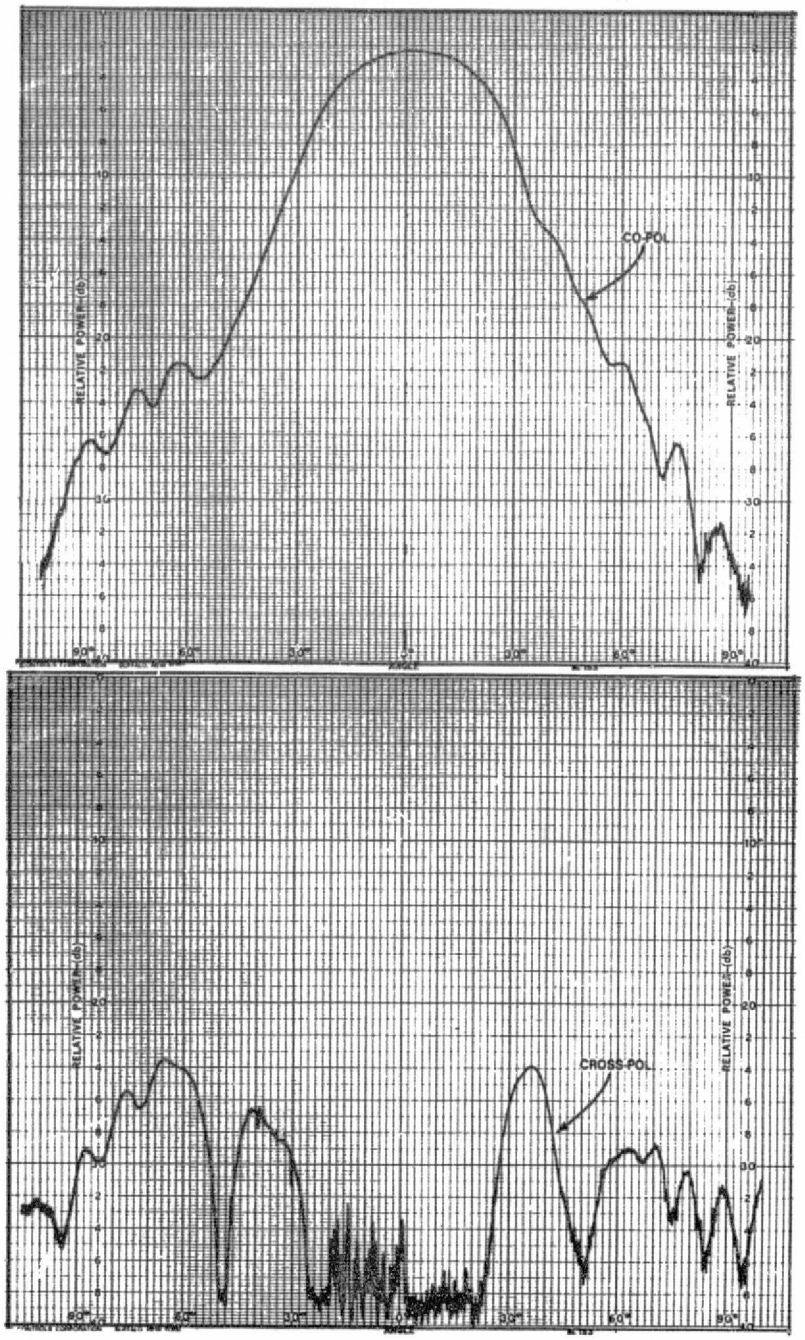

(c) 45° Plane

Figure 5-18. Co- and Cross-Pol Radiation Patterns of Vertically Polarized Central Element 10 at 11.7 GHz (Cont'd)

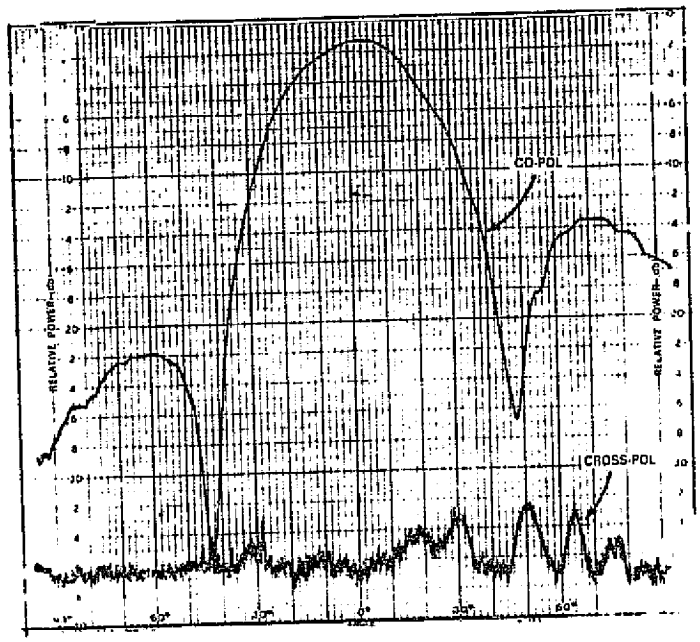

(a) E-Plane

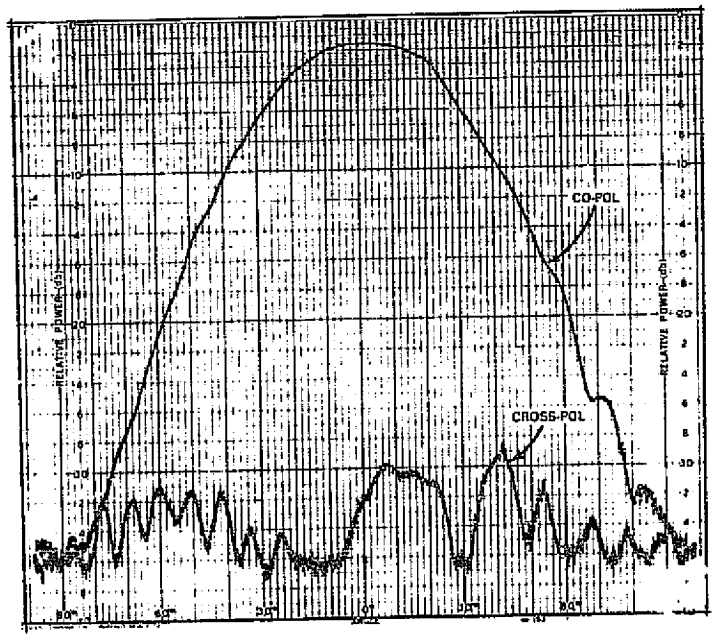

(b) H-Plane

Figure 5-19. Co- and Cross-Pol Radiation Patterns of Vertically Polarized Edge Element 1 at 11.7 GHz

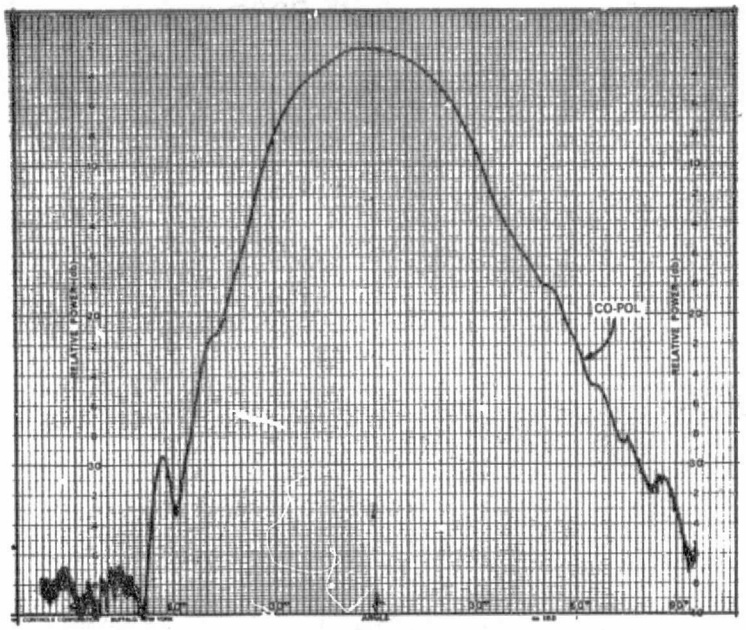

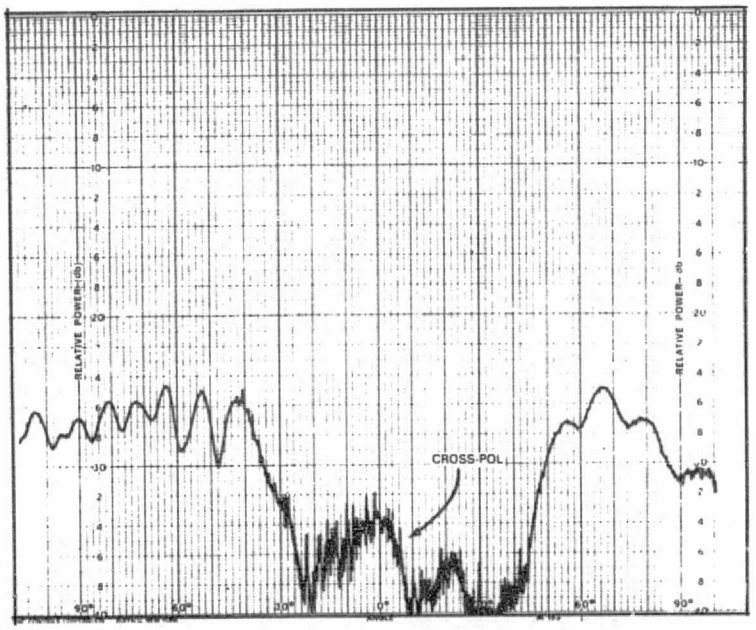

(c) 45° Plane

Figure 5-19. Co- and Cross-Pol Radiation Patterns of Vertically Polarized Edge Element 1 at 11.7 GHz (Cont'd)

To compare the patterns of the array elements with the single horn patterns, Figure 5-20 shows the E-plane, H-plane, and 45°-plane patterns of an isolated horn at 11.7 GHz.

A complete set of pattern measurements was taken at three frequencies in the band, 11.7, 11.95, and 12.2 GHz, for the central element, the edge element, and the isolated single horn. These measurements are included in Appendix A. The measurements show again that, as the frequency increases, the element size and element spacing increase in terms of wavelength, and this leads to reductions in the mutual coupling effects. This is apparent in the patterns of the edge element where the asymmetry becomes less as the frequency increases. As mentioned earlier, the element patterns show, in addition to the mutual coupling effects, the complete array scanning patterns in different planes. This information is considered in Subsection 5.5 in a discussion of the scanning performance of the array.

5.4 COMPLETE ARRAY DESIGN

As discussed in Subsection 4.3, the complete phased array contains 576 elements, arranged in a triangular lattice of 24 rows. The building unit of the array is the feed element discussed in Subsection 5.2, of which a breadboard model is shown in Figure 5-8. However, to accommodate the OMT and transition sections within the overall dimensions of the array aperture, the horizontal polarization must be fed through a 90° H-plane bend. Also, to allow for uniform design of the BFNs of both polarizations and for the widest surface areas available for thermal conduction via heat pipes, a 90° twist is used to bring the horizontal polarization arm of the OMT parallel to the vertical polarization arm. Figure 5-21 is a conceptual drawing of the dual-polarized

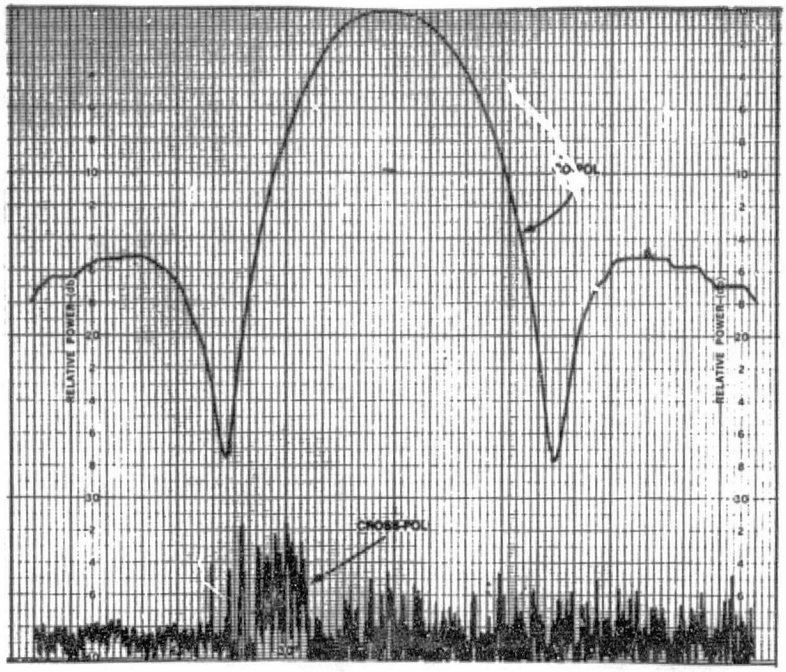

(a) E-Plane

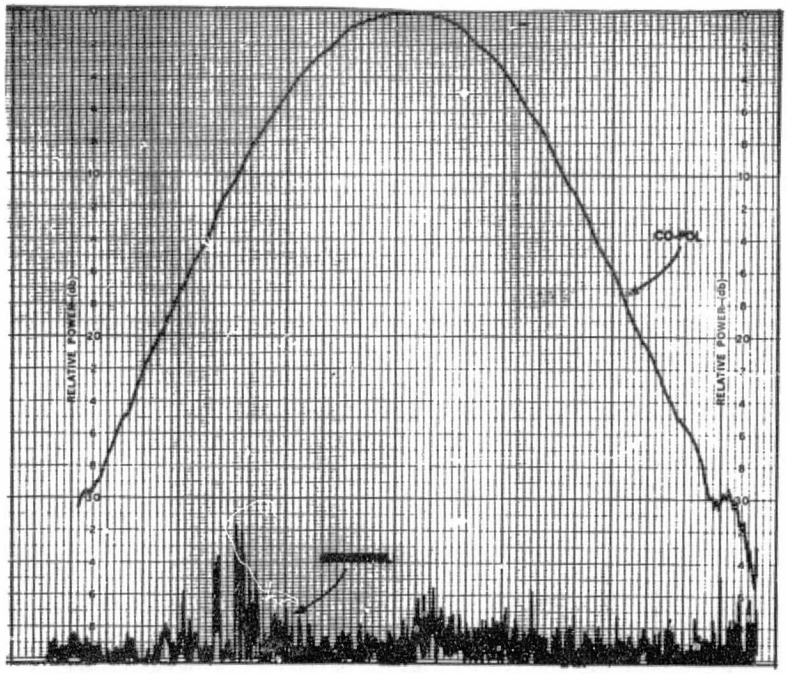

(b) H-Plane

Figure 5-20. Co- and Cross-Pol Radiation Pattern of an Isolated Element at 11.7 GHz

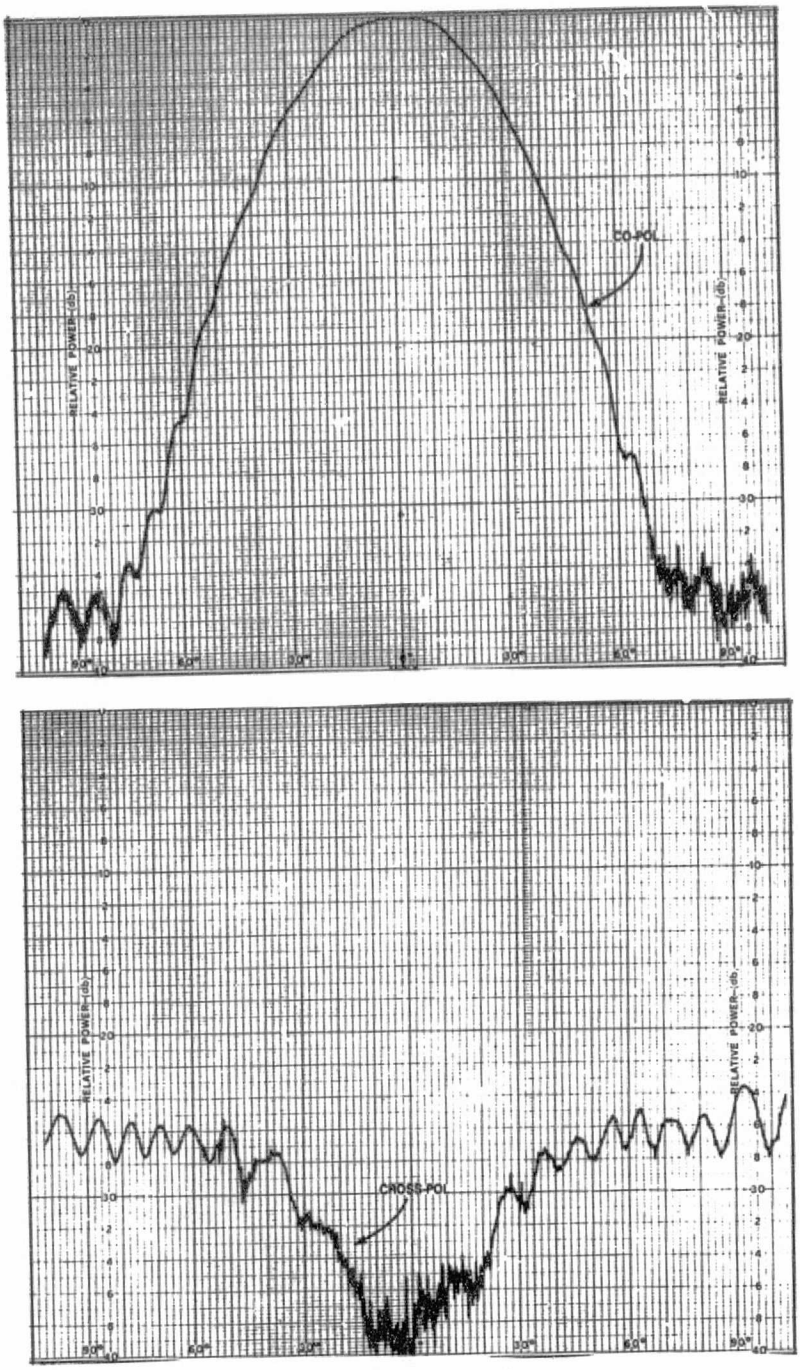

(c) 45° Plane

Figure 5-20. Co- and Cross-Pol Radiation Pattern of an Isolated Element at 11.7 GHz (Cont'd)

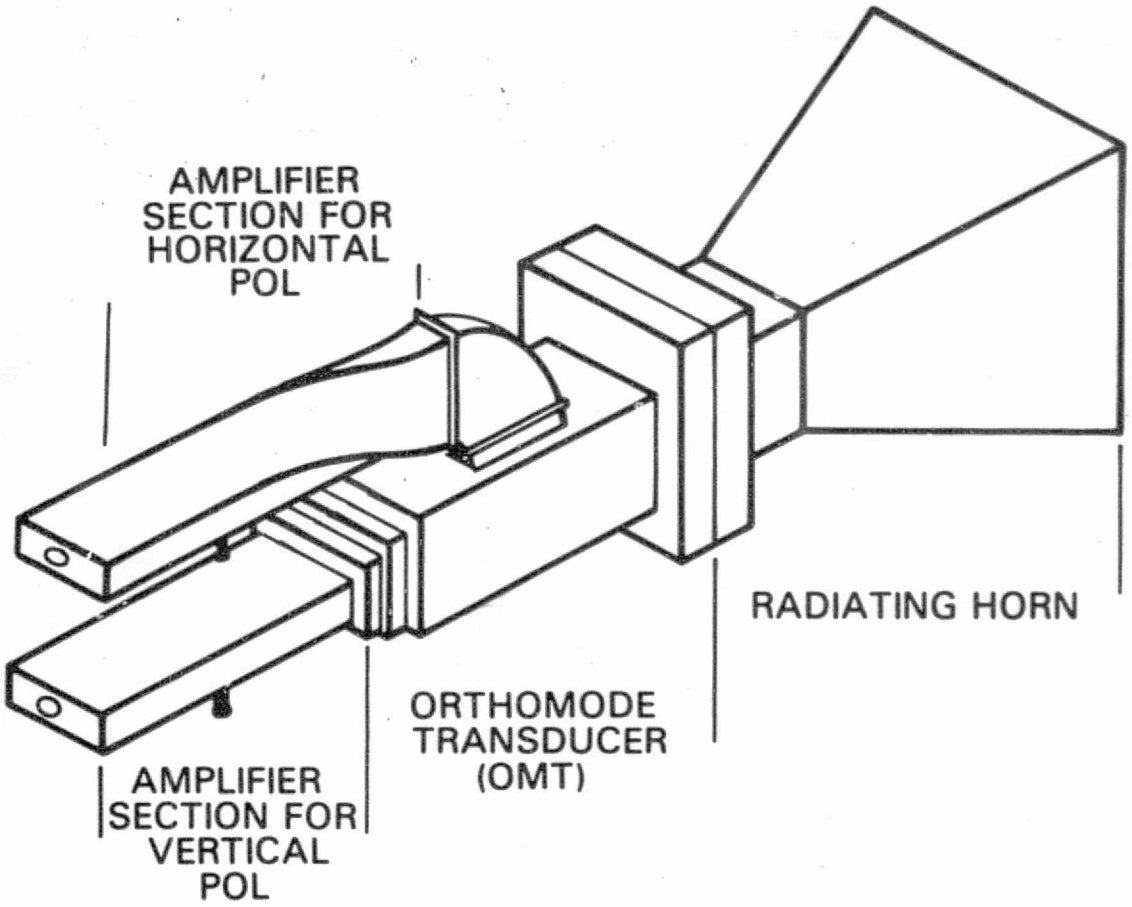

Figure 5-21. Conceptual Drawing of Dual-Polarized Array Element

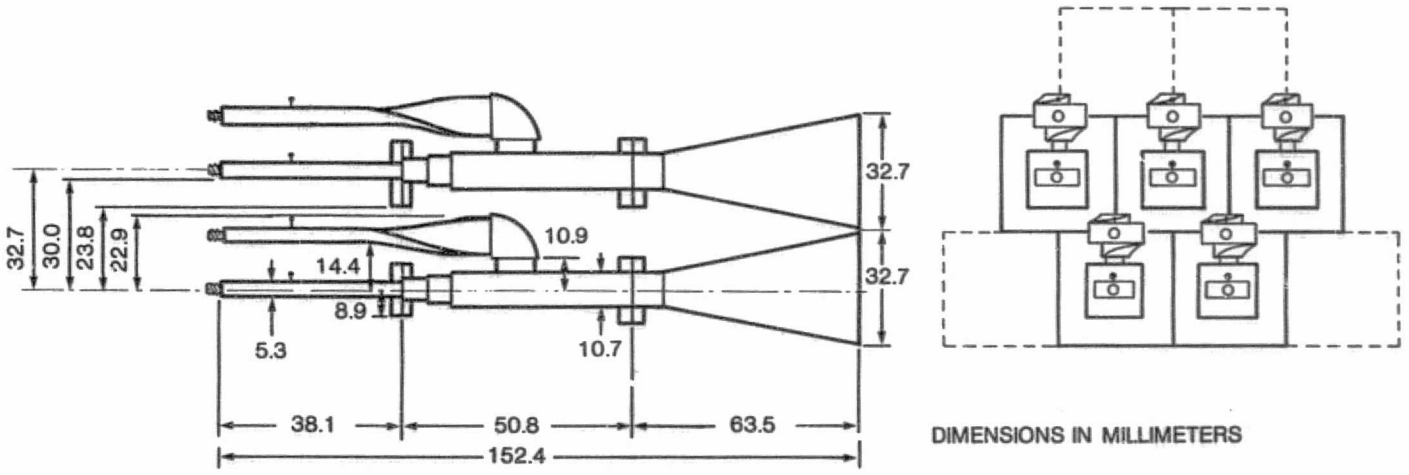

Figure 5-22. Conceptual Drawing With Dimensions of Arrangement of Several Elements in the Array

element, and Figure 5-22 is a detailed drawing showing the arrangement of the dual-polarization inputs of the array. As discussed in Section 3, the spacing between parallel rows should allow for the six BFNs of the six scanning beams. This imposes severe restrictions on the size of the BFN, as will be discussed in Subsection 5.6. The lens array will have the basic element shown in Figure 5-23.

5.5 MEASURED SCANNING PERFORMANCE

To study the scanning performance of the array, a 34-element dual-polarized phased array was fabricated and tested. The array was built for the frequency band of 11.7-12.2 GHz and the elements described in Subsection 5.3 were used. The element size of 1.3λ and spacing of 1.43λ at band center corresponds to the use of a dual-reflector system of magnification factor 5, according to Figure 3-12. The array configuration is shown in Figure 5-24. Eight central colinear elements were fed by using a BFN designed and assembled for this purpose. The eight elements formed a linear array of dual polarization. The 26 other elements were terminated with matched loads, thus providing the environment of a large array. Figure 5-25 shows the array and the BFN, and Figure 5-26 shows the details of the BFN where the eight outputs can be adjusted continually to produce any desired amplitude and phase distribution.

Three different distributions were considered in the measurements: uniform distribution, Taylor distribution, and quantized Taylor distribution. The beam was scanned from 0 to 20°. For the magnification factor of 5, this corresponds to far-field scanning of the dual-reflector system of 4°. To adjust the amplitudes and phases of the BFN, the electric field of the corresponding polarization was probed at the horn aperture by using a similar

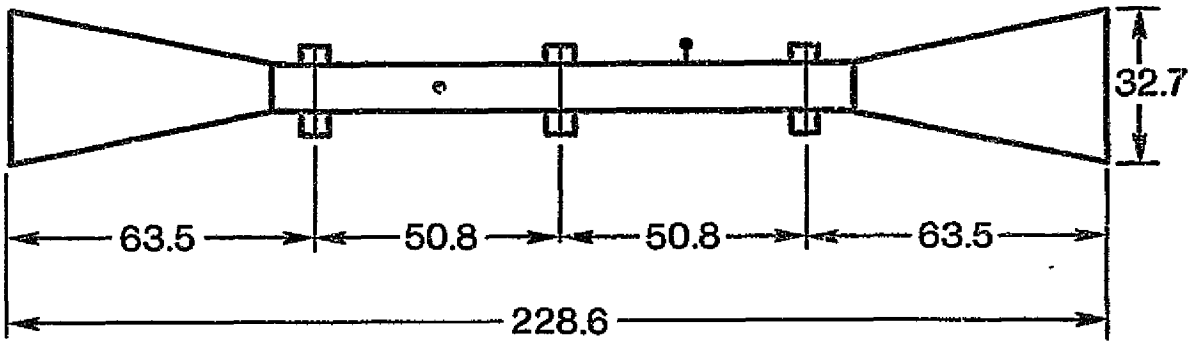

DIMENSIONS IN MILLIMETERS

Figure 5-23. Dimensions of Lens Element

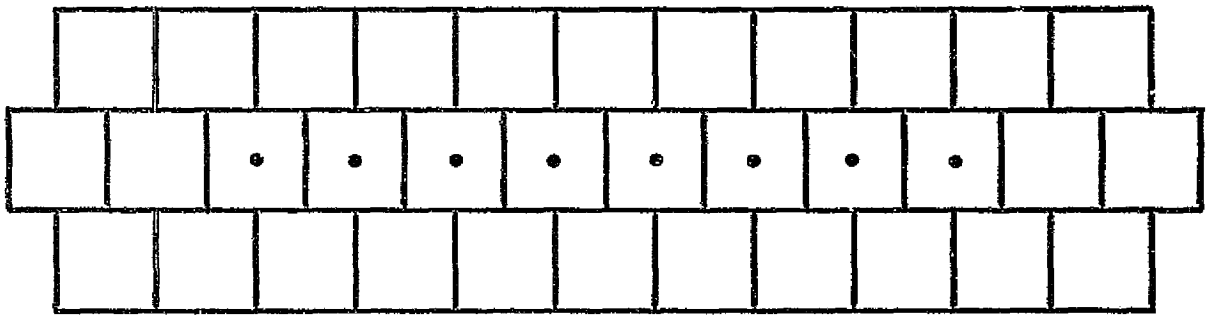

34 - ELEMENT ARRAY OF 1.4λ x 1.4λ

• DENOTES EXCITED ELEMENTS

Figure 5-24. 34-Element Array of 1.4λ x 1.4λ

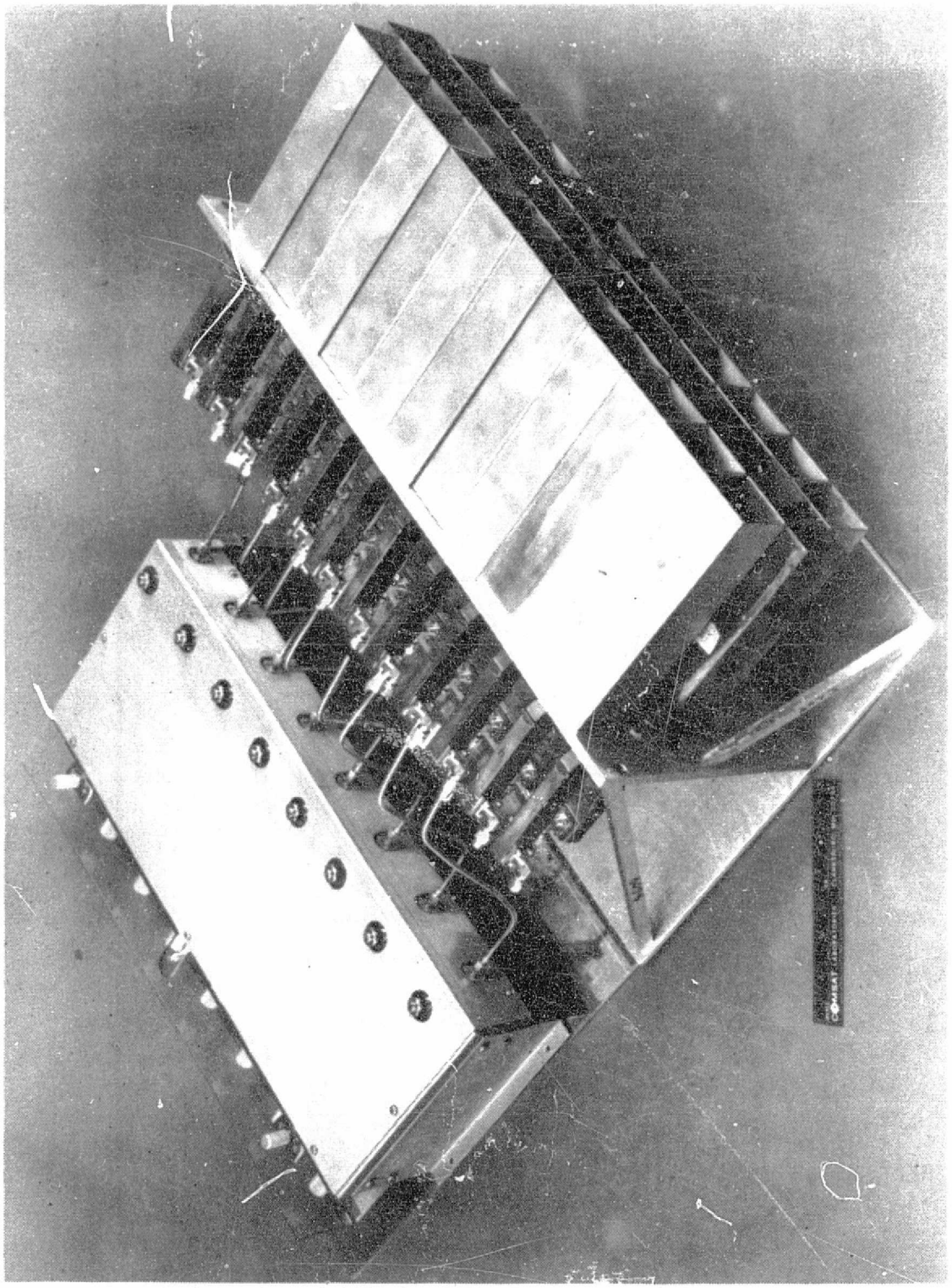

Figure 5-25. 34-Element Array and BFN

C-4

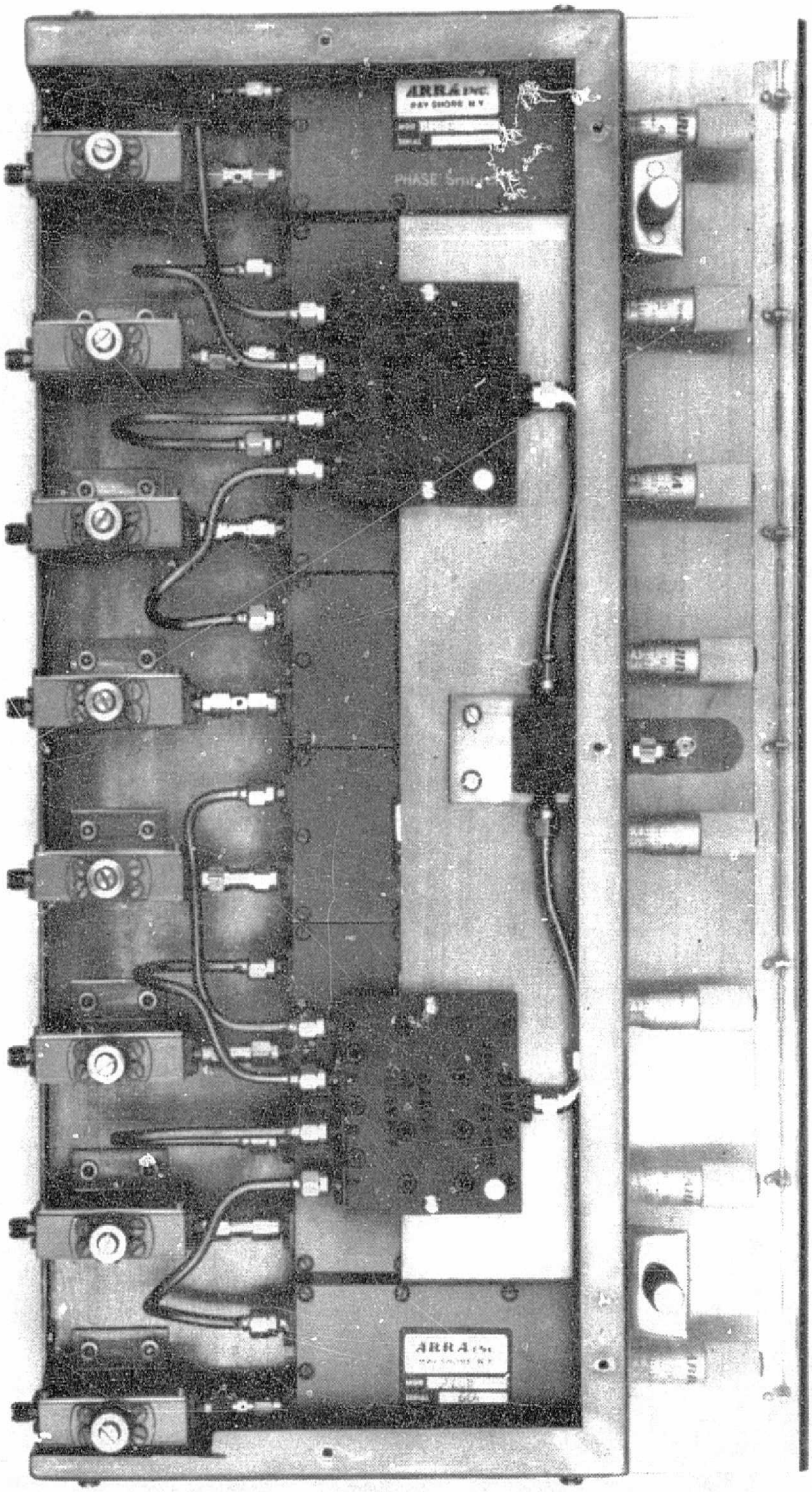

Figure 5-26. Details of the BFN for the 8-Element Array

horn as a probe. This takes into account any differences in phase or amplitude responses of the OMTs or the cables connecting the BFN to the OMT ports. Examples of the amplitude and phase distributions measured at the array aperture are shown in Figures 5-27 through 5-29 for three scanning directions. Uniform amplitude distribution is obtained in the three cases across the frequency band of 11.7-12.2 GHz, with a deviation of $\pm$0.4 dB. The three cases represent equal phases, 90° phase-shift, and 180° phase-shift between adjacent horns. The phase deviations are within $\pm$4°.

For uniform distribution, the array's E-plane pattern was measured when the elements were horizontally polarized, and the H-plane pattern was measured when the elements were vertically polarized. The measurements were repeated at the three frequencies of 11.7, 11.95, and 12.2 GHz. Figure 5-30 shows the E- and H-plane patterns at 11.95 GHz when all elements are in phase. The grating lobes that appear at $\pm$44° are more prominent in the H-plane pattern because of the wider element pattern in that plane. With a magnification factor of 5, this corresponds to far-field grating lobes of $\pm$8.8°, which means that the scanning range free of grating lobes is about $\pm$4.4°. The required CONUS coverage is well within this range.

When the array is fed with uniform distribution and progressive phase, the beam scans as shown in Figures 5-31 and 5-32 for 90° and 180° phase shifts, respectively. These figures show the E- and H-plane patterns at 11.95 GHz. As expected, the main beam scans about 10° for the 90° and about 20° for the 180° phase shifts. The grating lobe level increases as it moves in the same direction as the main beam. For the 180° phase shift, the out-of-phase excitation case occurs, in which the main beam and the grating lobe have the same level and are in equal angular directions about broadside. A complete set of pattern measurements for the

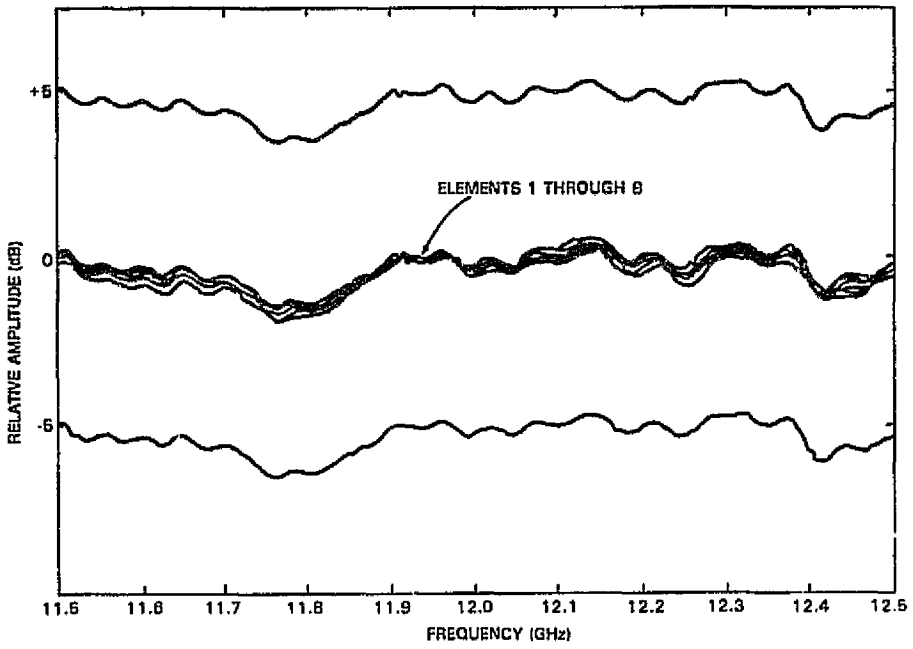

(a) Uniform Amplitudes

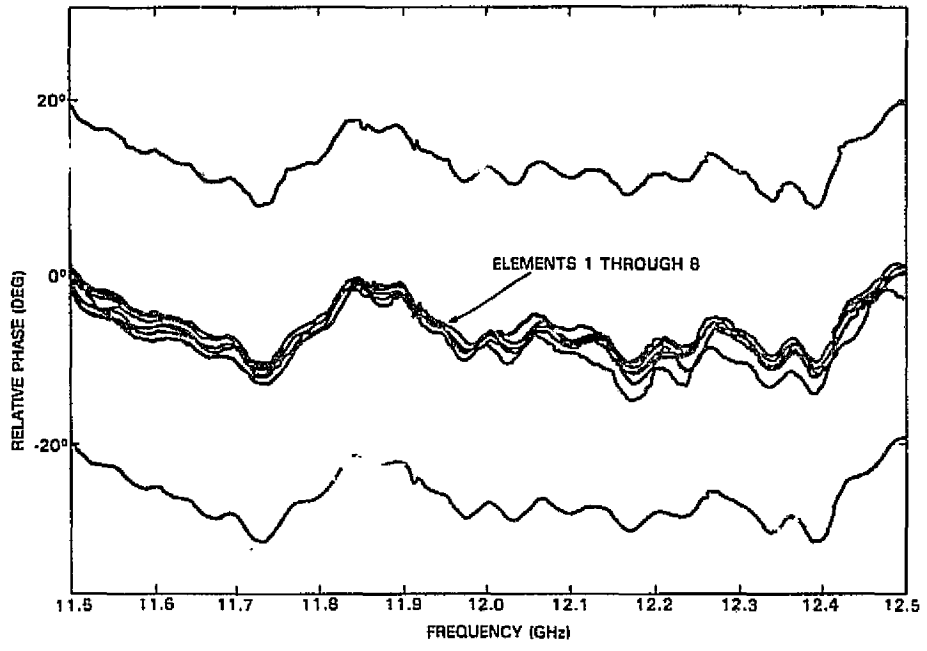

(b) Uniform Phases

Figure 5-27. Probed Coefficients Measured at the Horn Apertures for the Eight Elements: Uniform Amplitudes, Uniform Phases

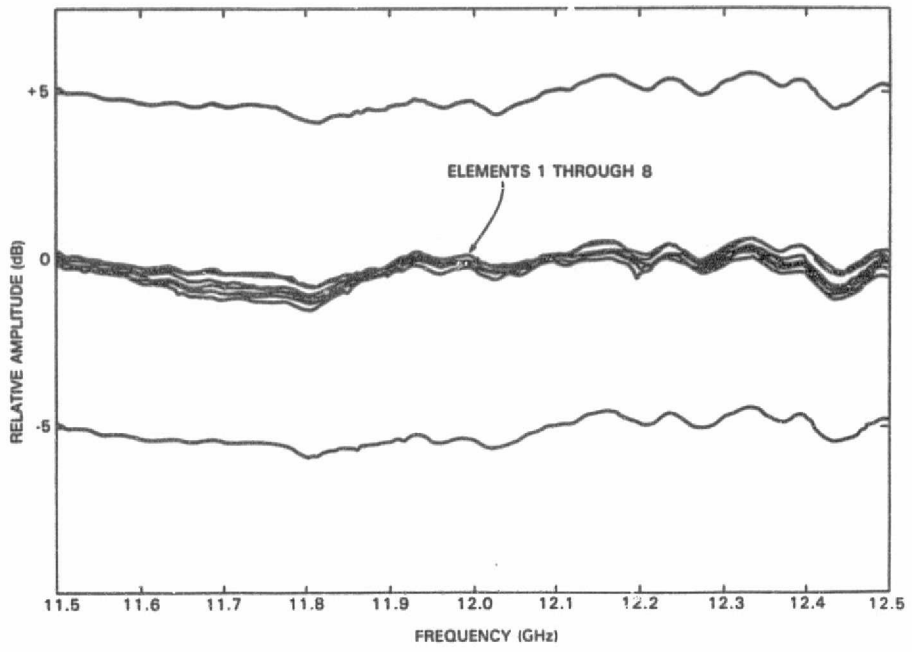

(a) Uniform Amplitudes

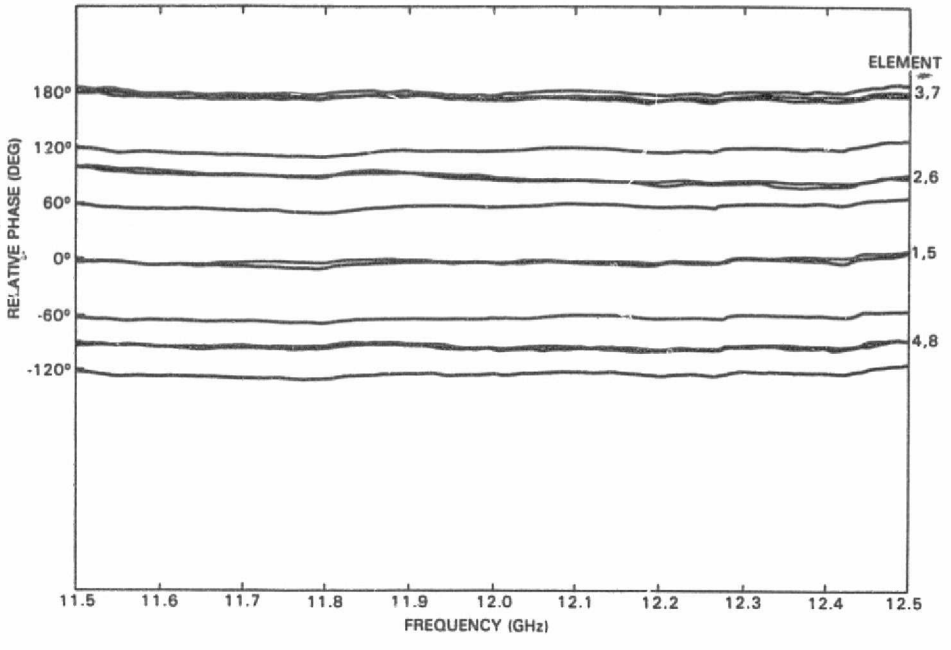

(b) 90° Progressive Phase Differences

Figure 5-28. Probed Coefficients Measured at the Horn Apertures of the Eight Elements: Uniform Amplitude, 90° Progressive Phase Differences

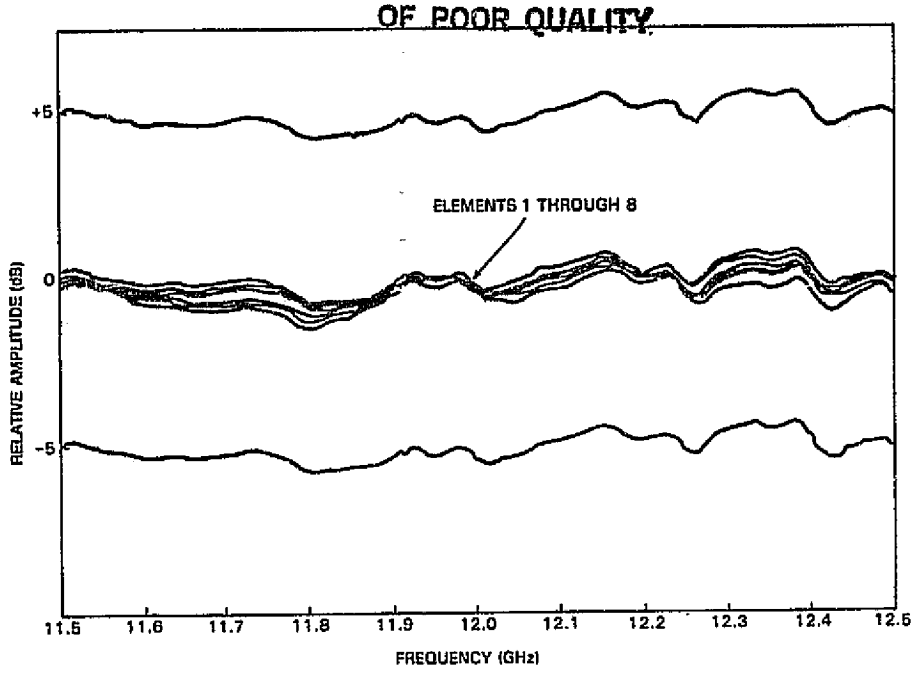

(a) Uniform Amplitudes

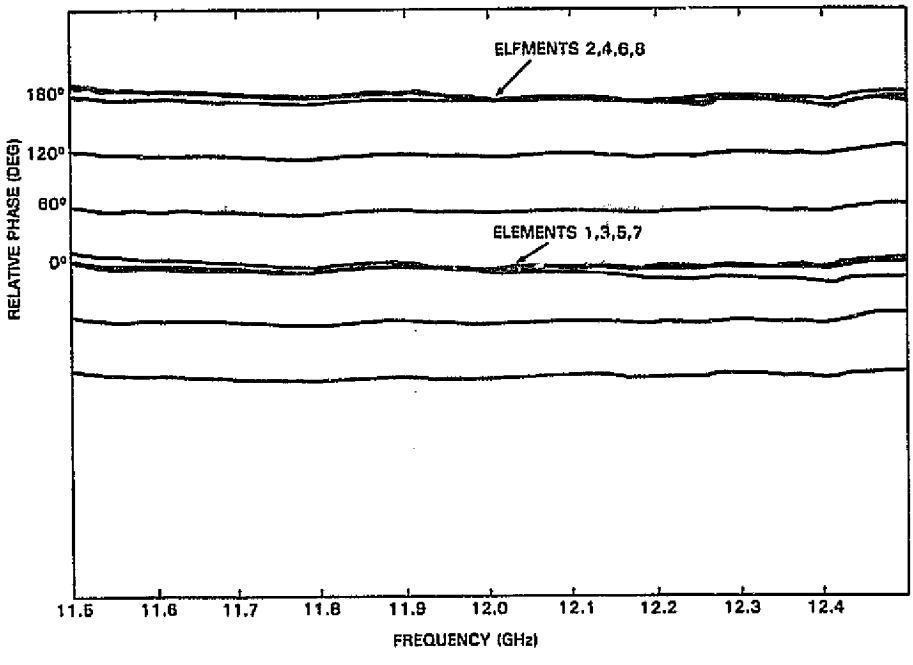

(b) 180° Progressive Phase Differences

Figure 5-29. Probed Coefficients Measured at the Horn Apertures of the Eight Elements: Uniform Amplitudes, 180° Progressive Phase Differences

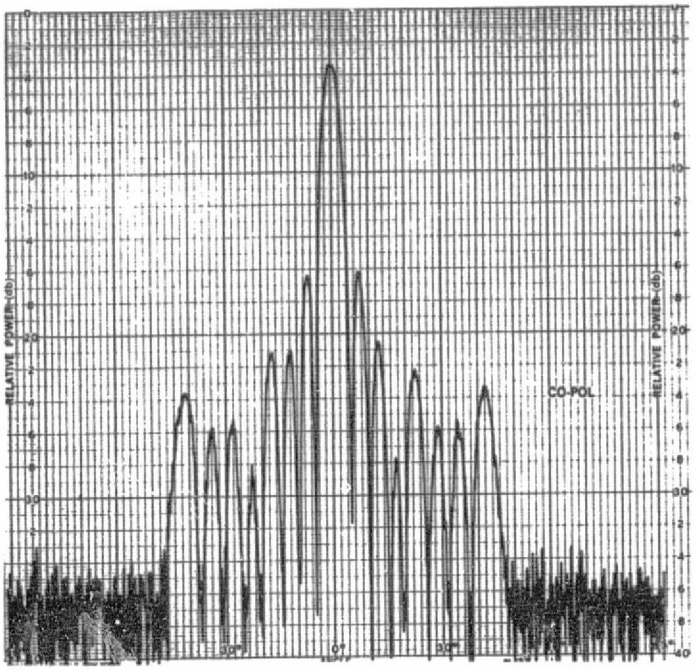

(a) E-Plane of Horizontal Polarization

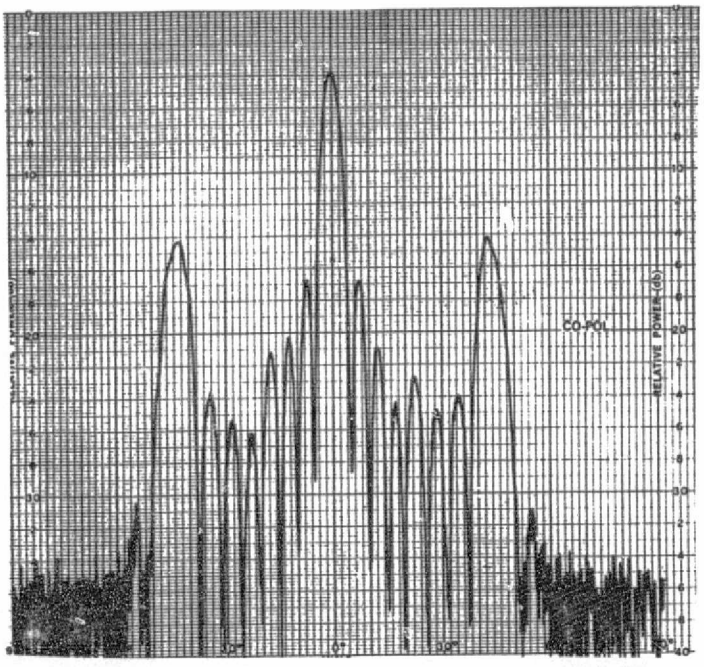

(b) H-Plane of Vertical Polarization

Figure 5-30. Radiation Pattern of 8-Element Array at 11.95 GHz: Uniform Amplitude, Uniform Phase

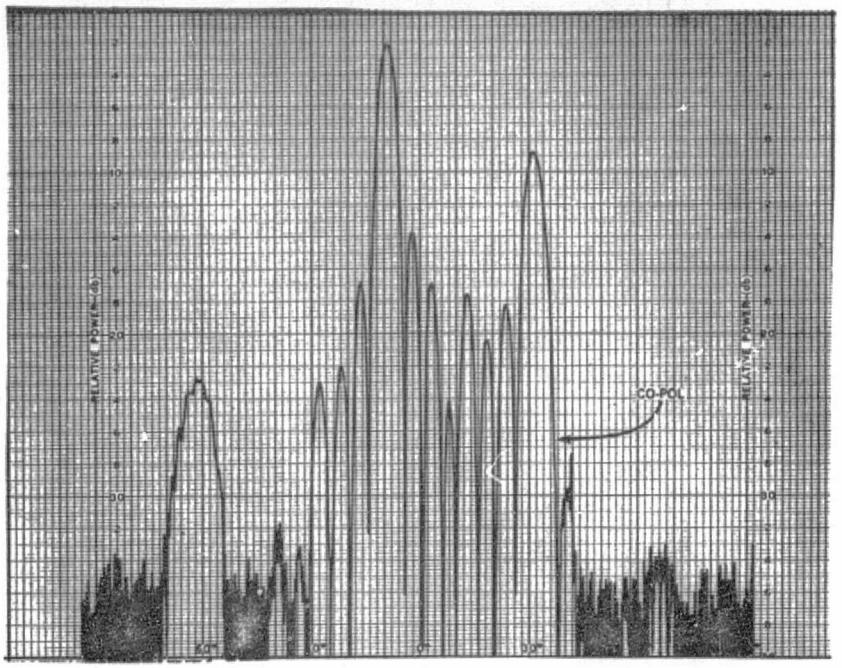

(a) E-Plane of Horizontal Polarization

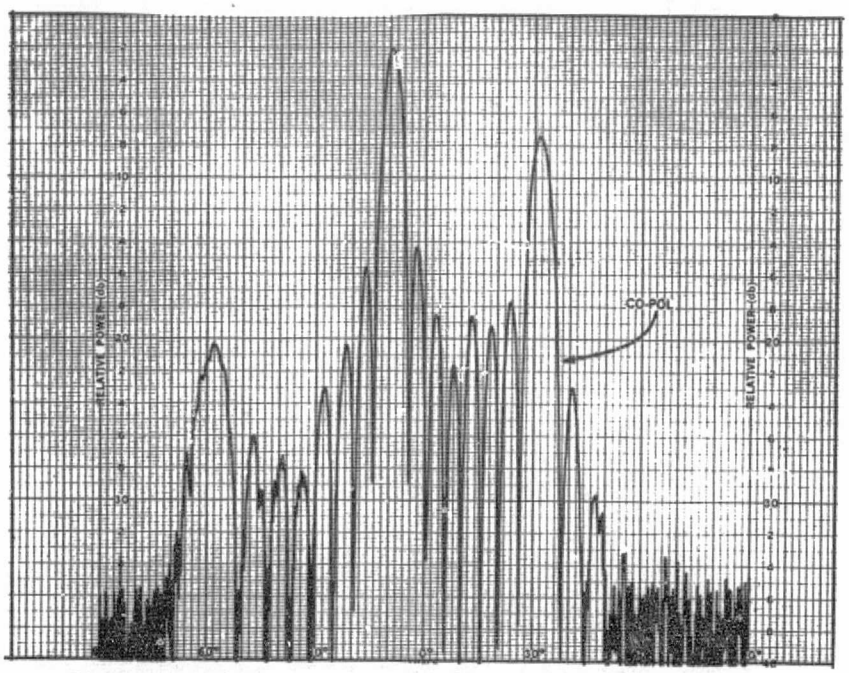

(b) H-Plane of Vertical Polarization

Figure 5-31. Radiation Pattern of 8-Element Array at 11.95 GHz: Uniform Amplitude, 90° Progressive Phase Shift

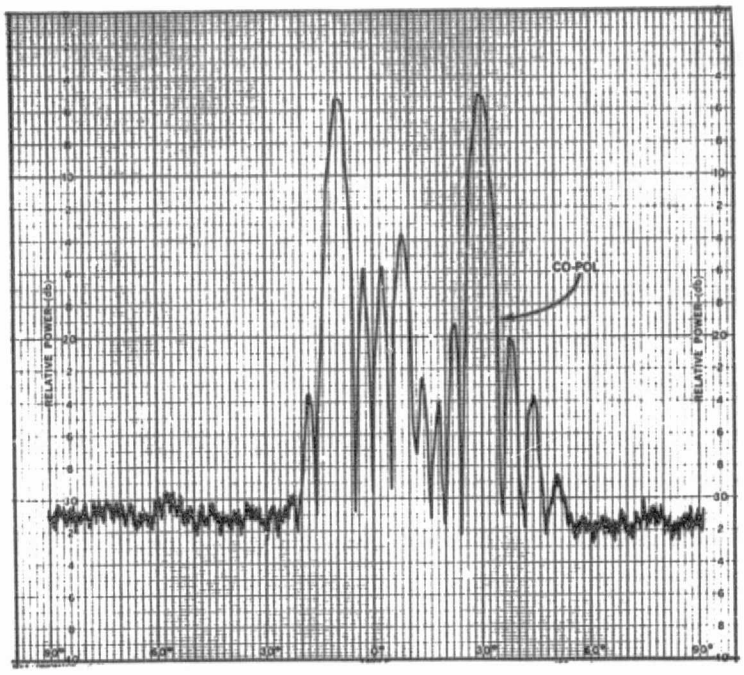

(a) E-Plane of Horizontal Polarization

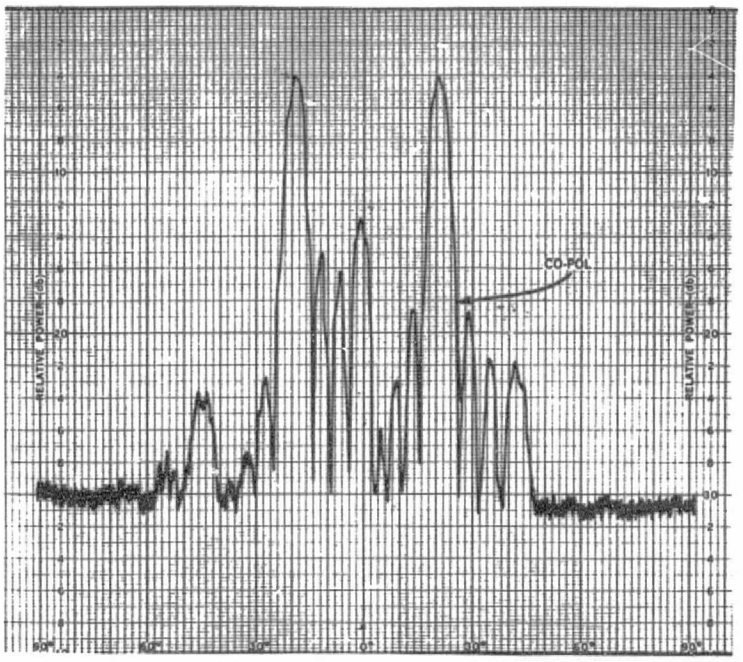

(b) H-Plane of Vertical Polarization

Figure 5-32. Radiation Pattern of 8-Element Array at 11.95 GHz: Uniform Amplitude, 180° Progressive Phase Shift

E- and H-planes at 11.7, 11.95, and 12.2 GHz, with progressive phase shifts of 0, 45°, 90°, 135°, and 180°, are given in Appendix B.

The reduction in gain as the main beam scans, or the array scan loss, was also measured for both horizontal and vertical polarization (E- and H-planes). Figure 5-33 shows the gain variation as the array scans to ±20°. The measured embedded element patterns are given on the same figure to show how the array scanning pattern follows the element pattern, as expected. The H-plane scan has about 2 dB of scan loss at 20°, while the E-plane has as much as 4 dB. Figure 5-34 shows the measured vs calculated scan loss for E- and H-plane scanning at the three frequencies.

The second type of excitation considered for these measurements is the Taylor distribution. Table 5-2 shows the amplitude coefficients of the eight elements to produce a 30-dB Taylor pattern. Examples of the measured patterns are shown in Figure 5-35 for broadside radiation in the E- and H-planes at 11.95 GHz. The sidelobe levels are reduced to about 25 dB below the main beam in the E-plane and about 24 dB in the E-plane. Additional measured results at other frequencies and other scan directions are included in Appendix B. The gain variation with scanning for this kind of amplitude distribution is shown in Figure 5-36 for the E- and H-planes. The scan loss is about the same as in the case of uniform distribution.

The third type of excitation is the Taylor distribution quantized to fit the predetermined levels set by the amplifier modules. Table 5-2 shows the quantized levels corresponding to the original Taylor distribution. Examples of the measured patterns are shown in Figure 5-37. The broadside radiation patterns at 11.95 GHz show sidelobe levels about 20 dB below the main beam peak for both E- and H-planes. The increase in the sidelobe

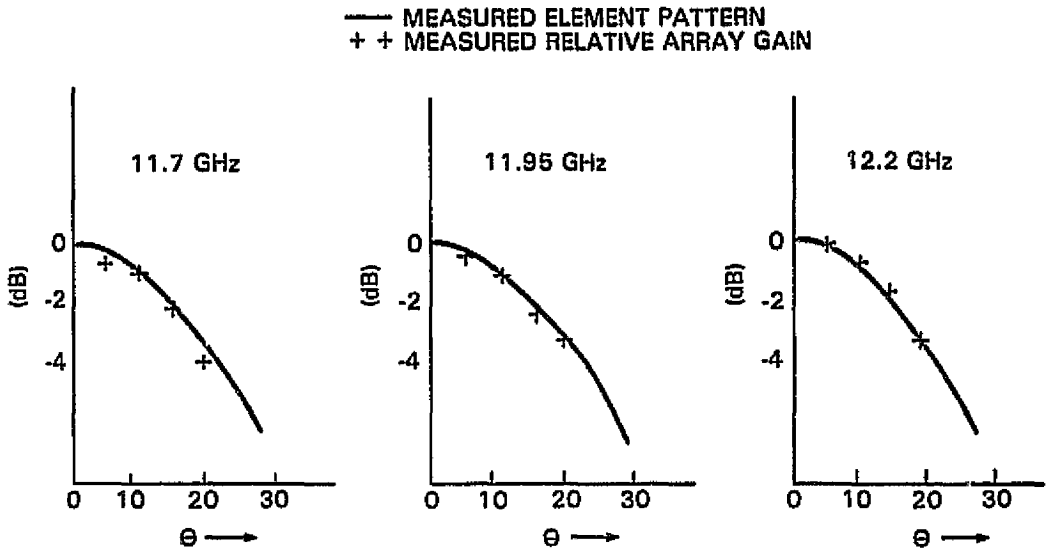

(a) E-Plane of Horizontal Polarization

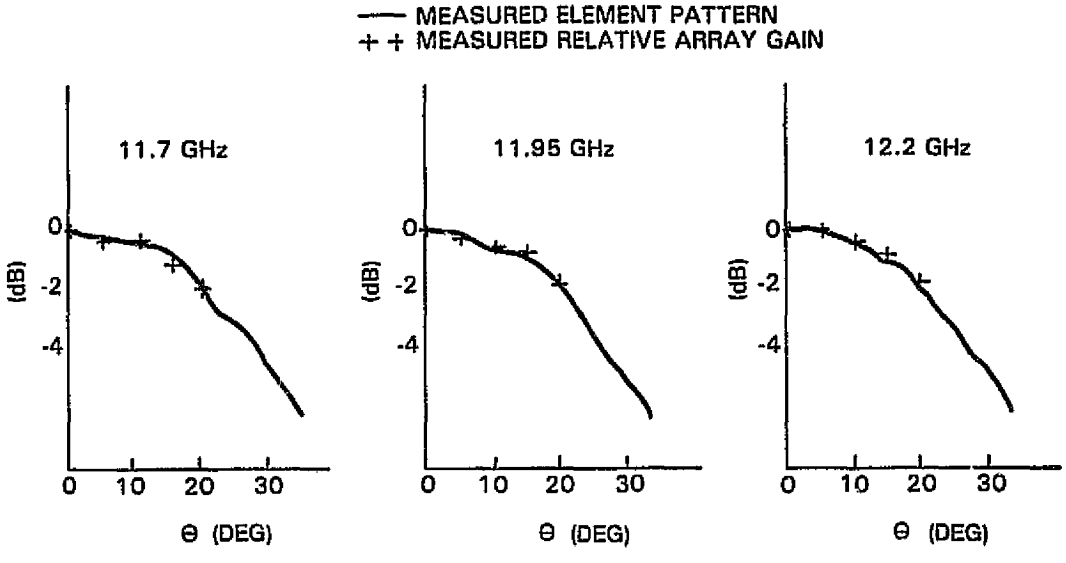

(b) H-Plane of Vertical Polarization

Figure 5-33. Measured Gain Variations vs Scan Angle for 8-Element Array: Uniform Distribution

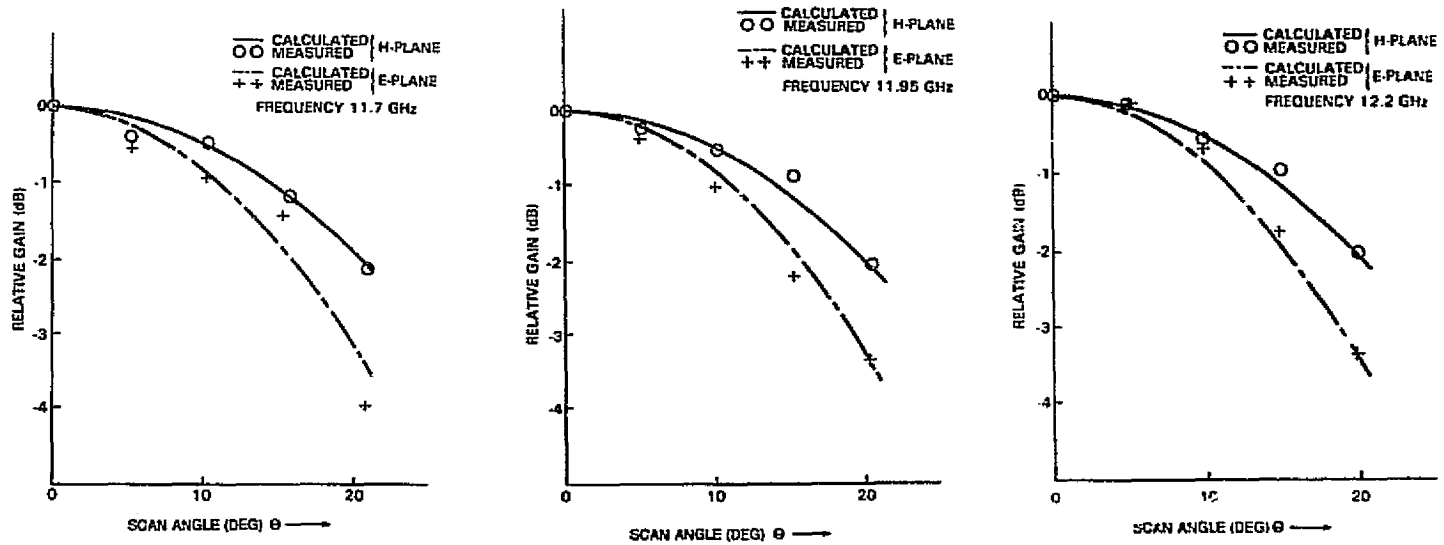

(a) 11.7 GHz (b) 11.95 GHz (c) 12.2 GHz

Figure 5-34. Calculated vs Measured Gain Variations With Scan Angle for 8-Element Array: Uniform Distribution

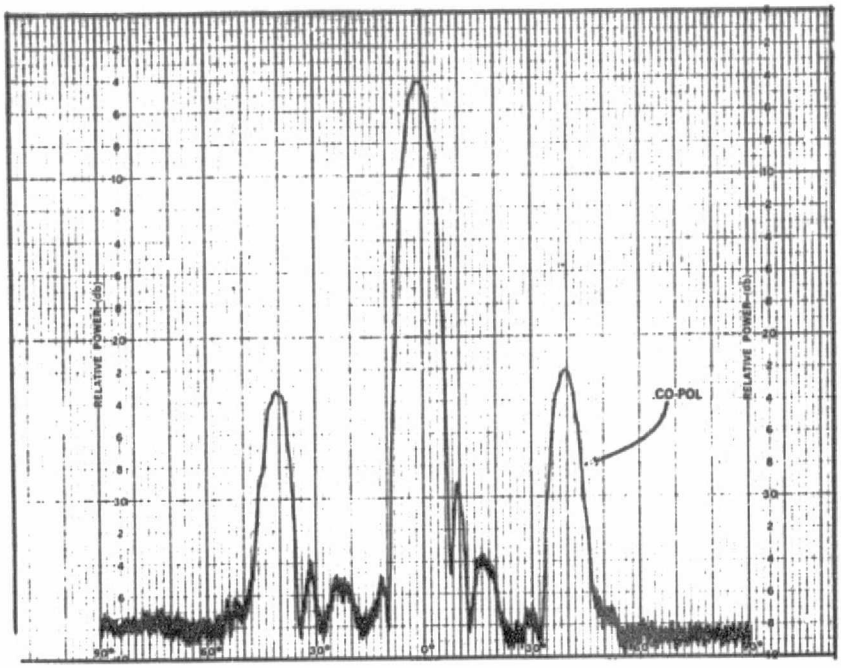

(a) E-Plane of Horizontal Polarizatio:

(b) H-Plane of Vertical Polarization

Figure 5-35. Radiation Pattern of 8-Element Array at 11.95 GHz: 30-dB Taylor Distribution, Uniform Phase

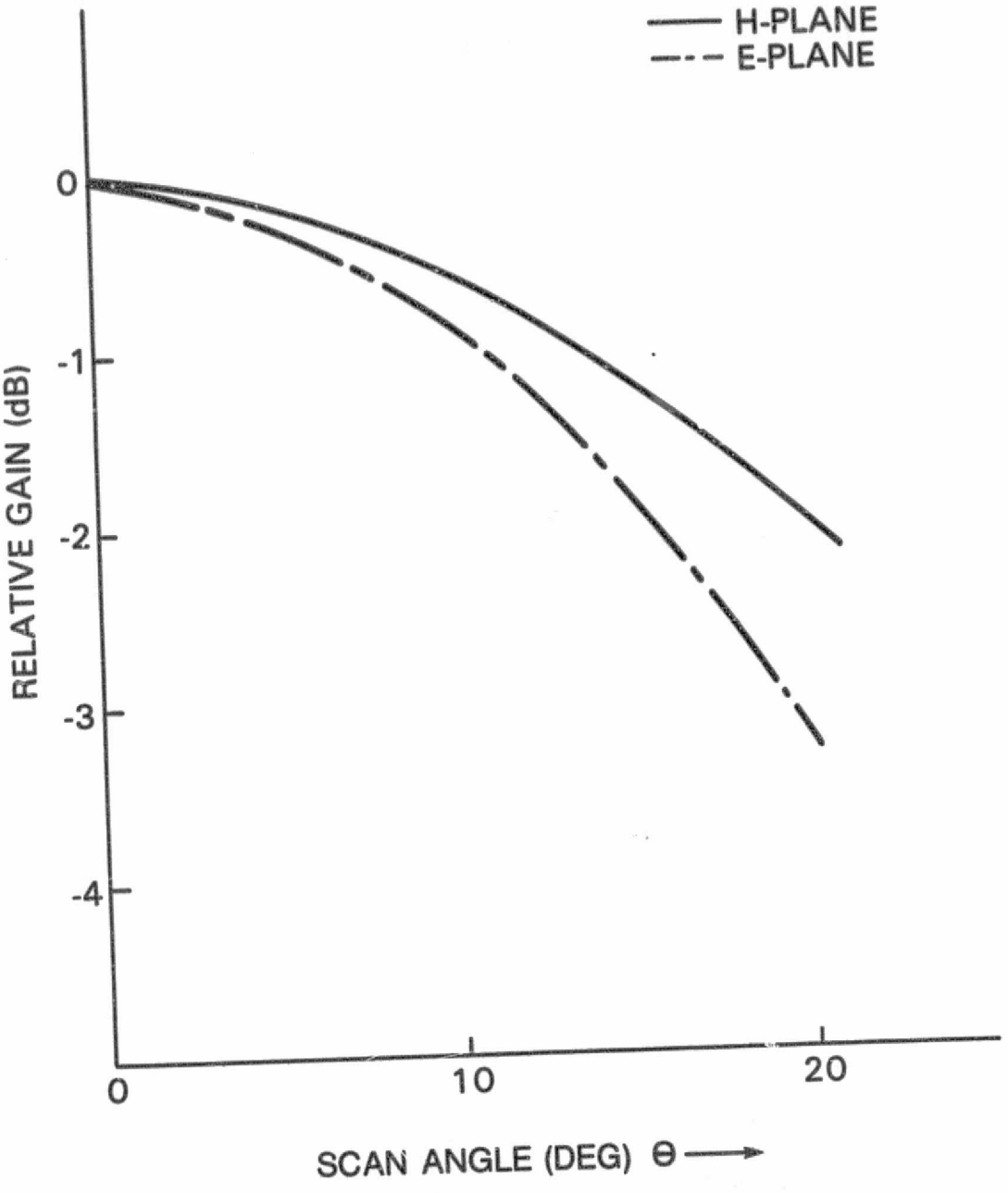

Figure 5-36. Relative Gain Variation With Scan Angle for 8-Element Array at 11.95 GHz: 30-dB Taylor Distribution

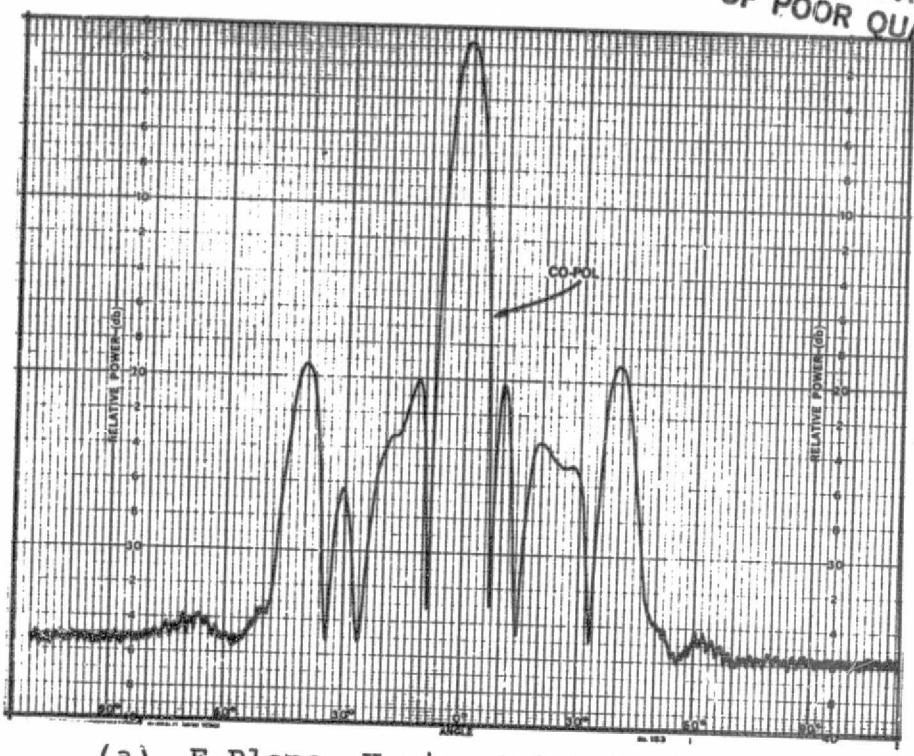

(a) E-Plane, Horizontal Polarization

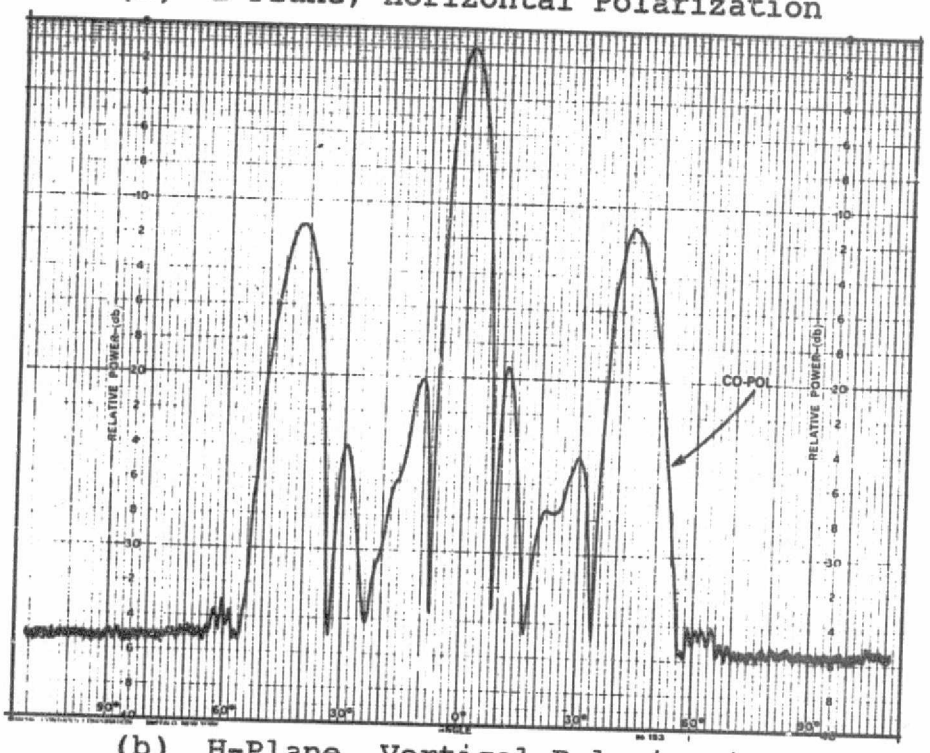

(b) H-Plane, Vertical Polarization

Figure 5-37. Radiation Pattern of 8-Element Array at 11.95 GHz: Quantized 30-dB Taylor Distribution, Uniform Phase

level is expected and is consistent with the discussion presented in Subsection 4.3. Additional measured results at other frequencies and other scan directions are included in Appendix B. Figure 5-38 shows the gain variation with scanning for the quantized Taylor distribution. As for Taylor distribution, the scan loss is about the same as in the uniform distribution case.

Table 5-2. Amplitude Coefficients for 8-Element 30-dB Taylor and Quantized Taylor Distributions

Element Number	Relative Amplitude Level	
	30-dB Taylor	30-dB Quantized Taylor
1	0.197	0.158
2	0.489	0.500
3	0.799	1.000
4	1.000	1.000
5	1.000	1.000
6	0.799	1.000
7	0.489	0.500
8	0.197	0.158

5.6 BEAM-FORMING NETWORK DESIGN

5.6.1 CONFIGURATION C

As shown in Figure 3-25, the BFN comprises a 1-input, 576-output power dividing network (PDN); phase shifters on each of the outputs; 3-way combiners combining corresponding outputs of each of the two sets of three PDNs each; followed by amplifiers before feeding the two ports of the OMTs at each antenna element. Figure 5-39 is a schematic representation of the general configuration of a BFN for one beam. A vertical 1-input, 24-output PDN

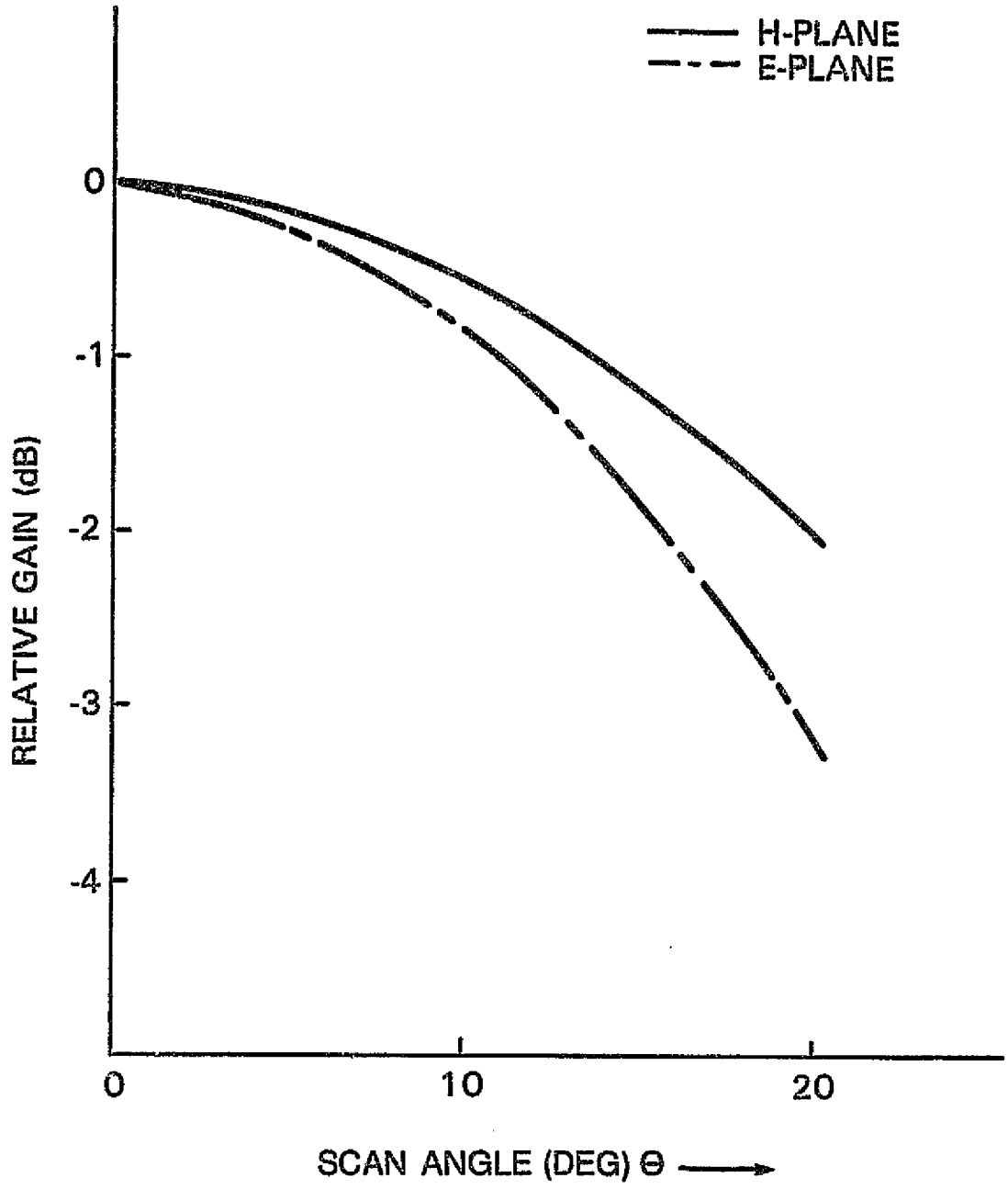

Figure 5-38. Relative Gain Variation With Scan Angle for 8-Element Array at 11.95 GHz: Quantized 30-dB Taylor Distribution

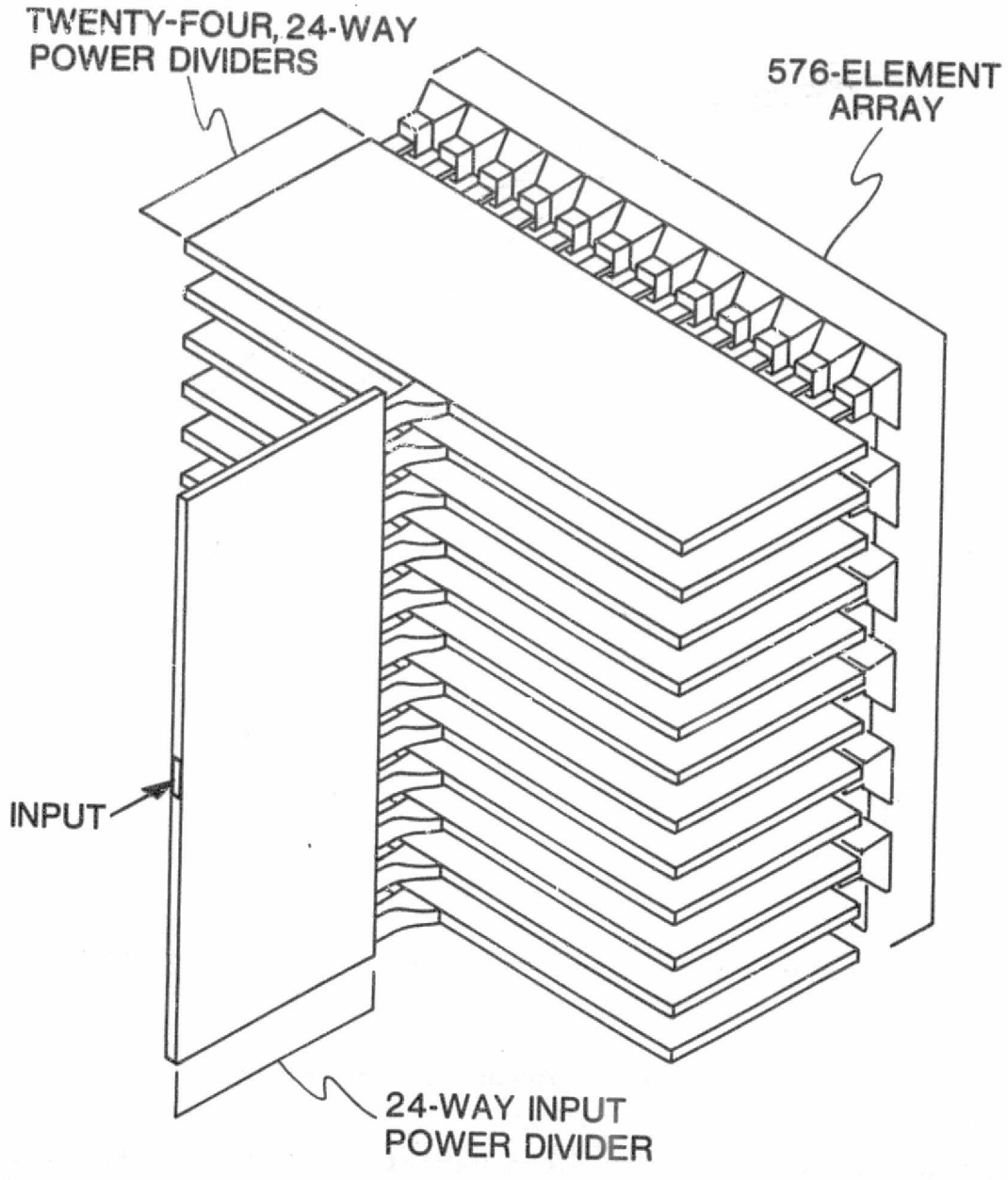

Figure 5-39. Conceptual Drawing of the BFN Design of One Beam in the Multiple Scanning Beam Array

feeds 24 similar 1-input, 24-output PDNs positioned horizontally. The 24-way power divider is schematically shown in Figure 5-40. The output ports of the horizontal PDNs lie just behind the arrayed antenna elements. Since the array has a triangular lattice, alternate horizontal PDNs will have their outputs offset by an appropriate amount.

Figure 5-41 shows how the three networks corresponding to the same polarization are interlaced to form a compact BFN. The other three BFNs are handled in the same fashion. Each of the six vertical networks are offset from the previous one to accommodate feeding the respective horizontal networks. This offset is different from the offset in the outputs of the horizontal PDNs, and is about equal to the PDN thickness. Since the physical size of the array is fixed by design, the height of a PDN layer cannot be excessive because the outputs of the combiners of vertically and horizontally polarized beams, respectively, must be positioned close to the antenna/OMT element they will be feeding.

The PDNs and combiners could be implemented in any one of the many transmission line media. Three types of media offer the most advantages in implementing the PDNs: striplines, microstrip lines, and reduced-height waveguides. The stripline and microstrip PDNs have the advantage of being simple and less costly to fabricate. However, they are lossier and are not amenable to simple tuning once they are built. They satisfy the thickness constraint, but, on the other hand, require input and output connectors which may pose a significant impedance matching problem at this frequency band. Also, to fall within the required thickness, the connectors must be of the snap-on or slide-on type, which may add to the matching problem.

The waveguides are much less lossy than their stripline and microstrip counterparts. Waveguide dividers are wideband, low-loss, and can be tuned through screws in the top or bottom

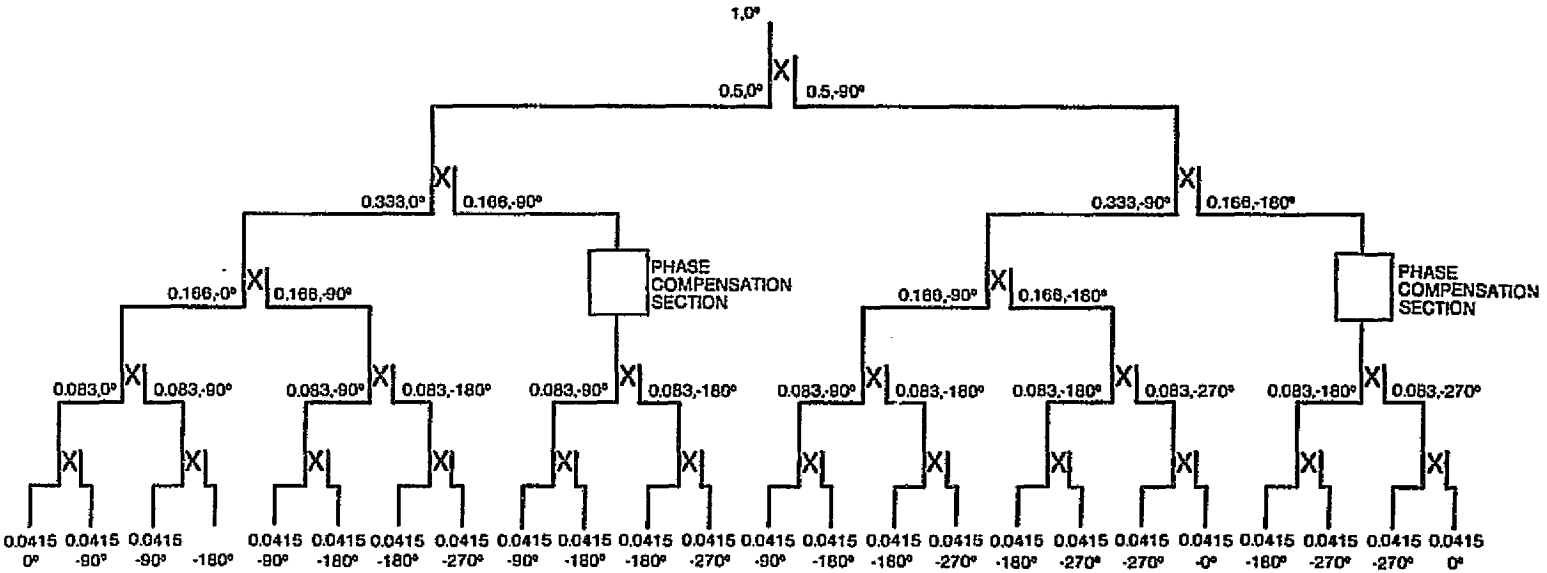

Figure 5-40. Schematic of 24-Way Power Divider

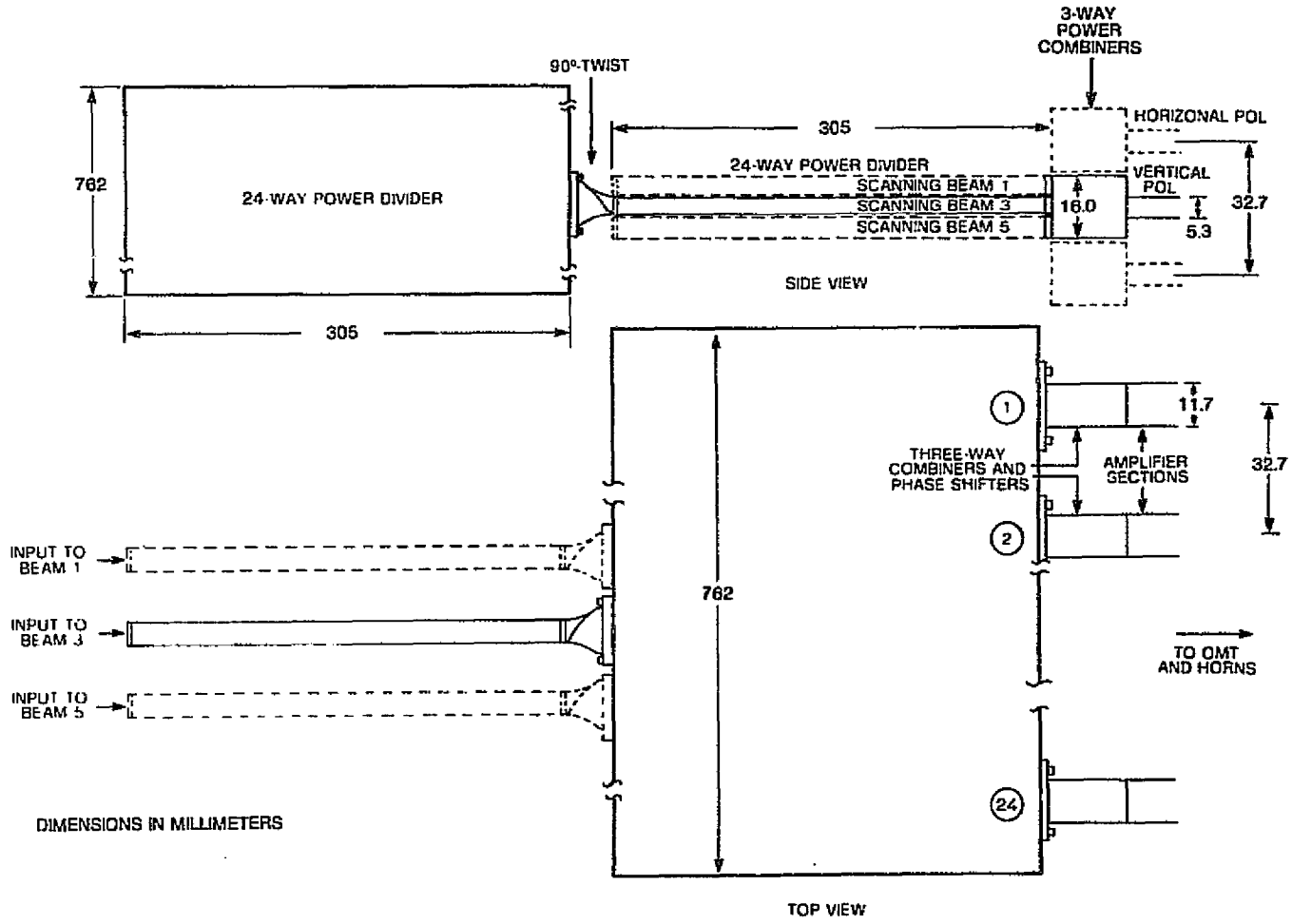

Figure 5-41. Layout Drawing of Scanning Beam BFN Design

plates. Reduction of the waveguide height increases the attenuation, but still offers an attractive alternative to stripline and microstrip line. Table 5-3 gives an estimate of losses in dB/cm and total dissipative losses of the network for waveguide of standard 1.067-cm (0.42-in.) width with different heights, as compared with stripline and microstrip line losses.

Table 5-3. Loss Estimates at 18.95 GHz for Waveguide and Stripline Networks

Transmission Line Type	Attenuation (dB/cm)	Estimated Total Network Dissipative Loss (dB)
Standard WR-42 (1.067 x 0.432 cm)	0.006	0.65
Reduced-Height 0.305 cm (1.067 x 0.305 cm)	0.008	0.88
Reduced-Height 0.254 cm (1.067 x 0.254 cm)	0.009	1.0
Reduced-Height 0.203 cm (1.067 x 0.203 cm)	0.011	1.18
Stripline	0.059	5.7
Microstrip Line	0.098	9.5

Although the realizable e.i.r.p. depends mainly on the output power delivered by the amplifier modules, the BFN dissipative loss and the maximum amplifier gain determine the size of the RF driver feeding the amplifier modules. It is desirable to keep the input power level as low as possible. From Table 5-3, assuming an average input power per element of 2.5 mW (based on 50-percent amplitude taper and 20-dB gain of the 0.5-W modules), the stripline-fed 576-element array will need an RF driver of 5.38 W. A microstrip-line-fed network is even lossier and will

require more than 10 W of RF driver power. A 0.254-cm reduced-height waveguide BFN, however, will require only 1.81 W of RF power.

Considering all the factors, the reduced-height waveguide BFN is the best candidate for this configuration. It can be fabricated with inside dimensions of 1.067 x 0.254 cm, and the H-plane power divider can be channeled in one aluminum block of dimensions 76.2 x 30.5 x 0.508 cm. The waveguide top is provided in the form of a 0.051-cm cover, which is screwed on recessed portions of the waveguide walls to guarantee perfect top-to-sidewall contacts for the waveguides.

Figure 5-42 is a schematic diagram of part of the PDN, which contains a number of 3- and 4.8-dB couplers. The 3-dB coupling is achieved by using sidewall short slot hybrid couplers, which provide an equal power split with 90° phase shift. The 4.8-dB coupler uses sidewall hole coupling to produce a one-third to two-thirds power split. The connections between the horizontal "shelves" and the vertical "shelf," and between the horizontal shelves and the 3-way combiner or the phase shifter circuit, are all made in waveguides. This guarantees repeatable performance with low loss. Because of the size limitations, special ear-type flanges must be used, as shown in Figure 5-43. To use the same design for horizontal and vertical dividers, a 90° twist is connected between the outputs of the vertical dividers and the inputs of the horizontal dividers.

5.6.2 CONFIGURATION D1

The BFN concept for this configuration is similar to that of Configuration C. A 9-way combiner is used instead of a 3-way combiner to combine the outputs of two sets of nine PDNs interlaced in the same fashion. Assuming a 0.508-cm thickness

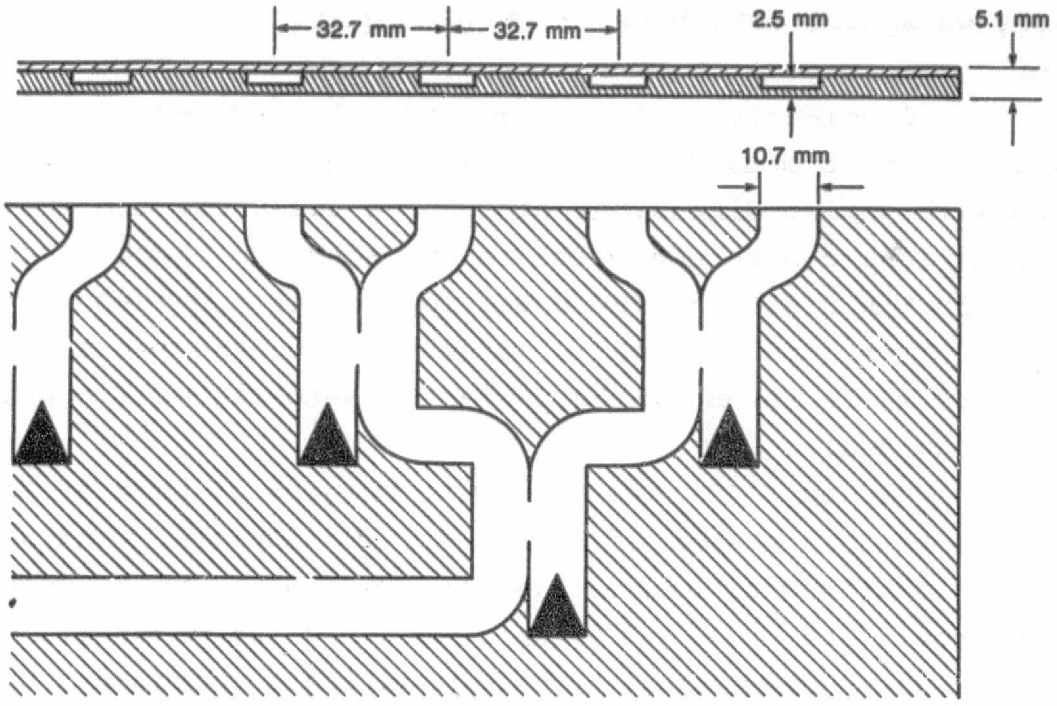

Figure 5-42. Conceptual Drawing of a Portion of the Waveguide Power Dividing Network

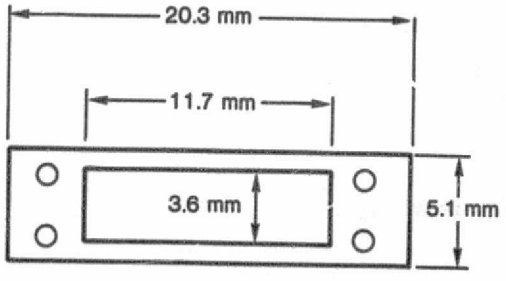

Figure 5-43. Ear-Type Flange

for one PDN, there will be about 9.144 cm between adjacent copolarized outputs (Figure 5-44). Since the spacing between copolarized OMT ports at the antenna element array is only 3.266 cm, the connecting waveguides must be snaked around, as shown. These additional waveguide sections (not present in Configuration C) increase the BFN loss slightly.

The 18 interlaced feed networks form a BFN that is very large, about 76.2 x 213.36 cm. The 213.36-cm dimension can be reduced by employing waveguides of still shorter heights (0.203 cm) so that the PDN is 0.330 cm thick. This reduces the BFN dimensions to 76.2 x 142.24 cm, but may result in additional practical implementation problems.

5.6.3 CONFIGURATION E

In this configuration, a nine-horn cluster for each beam is envisioned. For most cities, these clusters will be independent. However, because of the proximity of New York, Boston, and Washington, D.C., some horns must be shared. Figure 5-45 shows a layout of the BFN for these cities. Horn 9 is shared by all three cities, and hence a combiner is used for Boston and Washington, D.C., before the OMT port. Because of the additional loss in these lines, the next higher state of amplifier outputs will be used.

The PDNs consist of couplers and phase shifters which are made in waveguide. The phase shifter and the amplifier modules can be mounted in waveguide sections, for which transitions were constructed and tested as discussed in Subsection 5.7. A 2-way combiner is needed to combine one output from each of the Washington, D.C., and Boston BFNs. The output ports are arranged so that they mate into the respective antenna elements of the cluster. Outputs of these networks are connected to the respective antenna

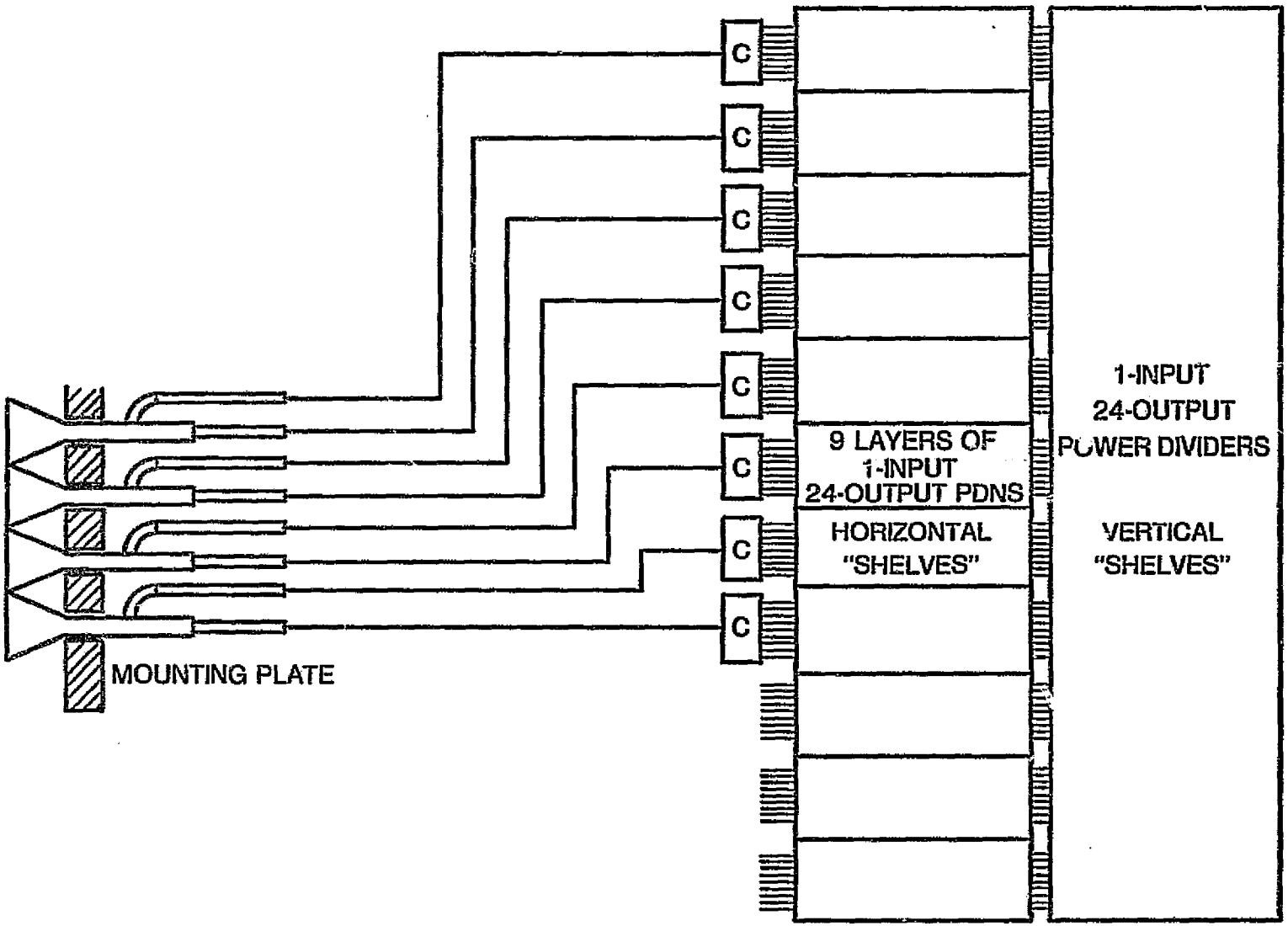

Figure 5-44. BFN Concept for 18 Spot Beam Phased Array Configuration (Configuration D1)

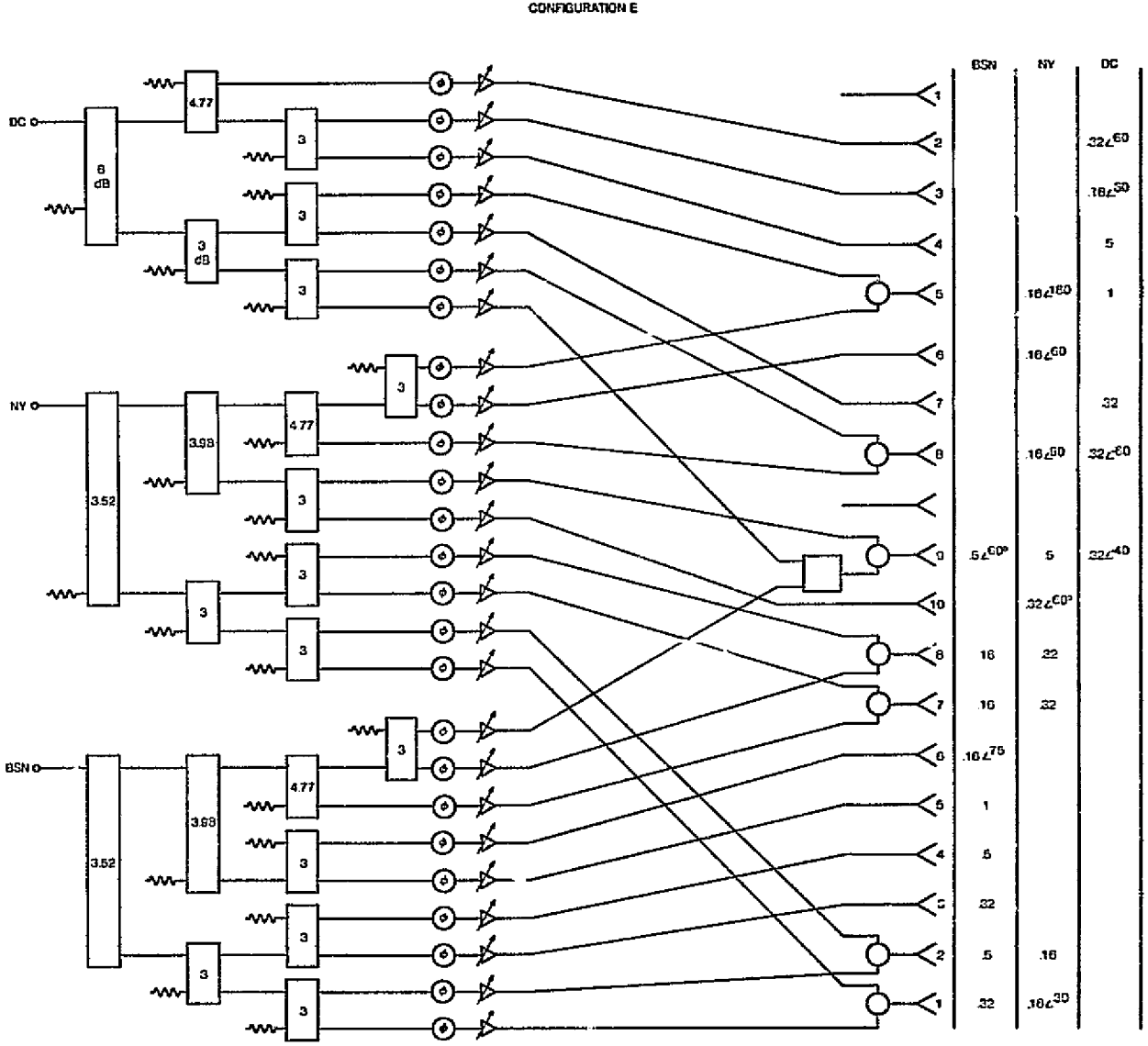

Figure 5-45. BFN for Boston, New York City, and Washington, D.C. Spot Beams (Configuration E)

elements through waveguide sections with the phase shifters and amplifiers. In this case, standard WR-42 waveguides are used, since there is no interlacing.

Based on the attenuation values given in Table 5-3, the total network dissipative loss for each of the three networks will be about 0.25 dB.

Similar BFNs are envisioned for the remaining 15 cities. In all these cases, the BFNs are relatively simple in design. None of the remaining feed arrays require co-polarized feed sharing, and all other feed sharing is performed via an OMT.

5.6.4 IMPLICATIONS FOR 30-GHz BFNs

At the receive frequencies, the BFN passive components for the various configurations will be scaled versions of the 20-GHz components. The combiners will be used as dividers. Use of the waveguide transmission line medium will be made attractive based on loss considerations. In waveguide, all components can be scaled to the appropriate frequency; therefore, no implementation problem is foreseen. On the other hand, the active components such as phase shifters and low-noise amplifiers must be developed in MMIC form at 30 GHz.

5.7 DESIGN AND ANALYSIS OF MMIC-TO-WAVEGUIDE TRANSITION

Two dual-polarization phased array transition configurations were investigated and prototypes were built. One is a single polarization transition, and the other is an orthogonal dual-polarization transition. In both versions, the MMIC circuit is mounted on a dielectric (beryllia) substrate which includes impedance matching and bias circuits. The substrate assembly is

mounted vertically (in the E-plane) in a square or rectangular waveguide section, as shown in Figure 5-46.

For both lens and phased array applications, two transitions are required, one for each polarization. In the phased array configuration, the two transitions are mounted in standard height (rectangular) waveguide housings. Since the OMT will couple only vertically or only horizontally polarized components to each of the two output ports (within the isolation limits of the structure), each of the transitions will be in a single polarization environment. In the lens configuration mode, separation is accomplished through orthogonal mounting of the two transitions in a section of square waveguide, as shown in Figure 5-47. Mode isolation in this case depends on control of the mechanical and physical parameters of the structure.

5.7.1 DESIGN PROCEDURE

For both the square and rectangular transitions, the design began with a calculation of the propagation characteristics and characteristic impendances for the chosen geometries and dielectrics. Although some material is available in the literature on finlines, much of it is restricted to special waveguide geometries or dielectrics (RT-Duroid being the most popular) [5-2], [5-3]. The requirement for nonstandard waveguide goemetries and a previously unanalyzed dielectric, namely 0.635-mm (0.025-in.) beryllia chosen for its high thermal conductivity, made it necessary to calculate the required parameters.

Two approaches were taken for the calculation of the effective dielectric constant. The first was an approximate technique, which also yielded characteristic impedance. At one

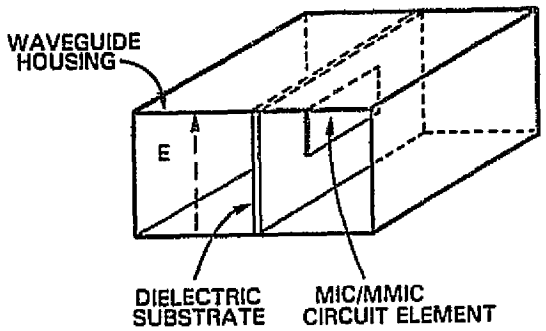

Figure 5-46. Single Polarization MMIC-to-Waveguide Transition Assembly

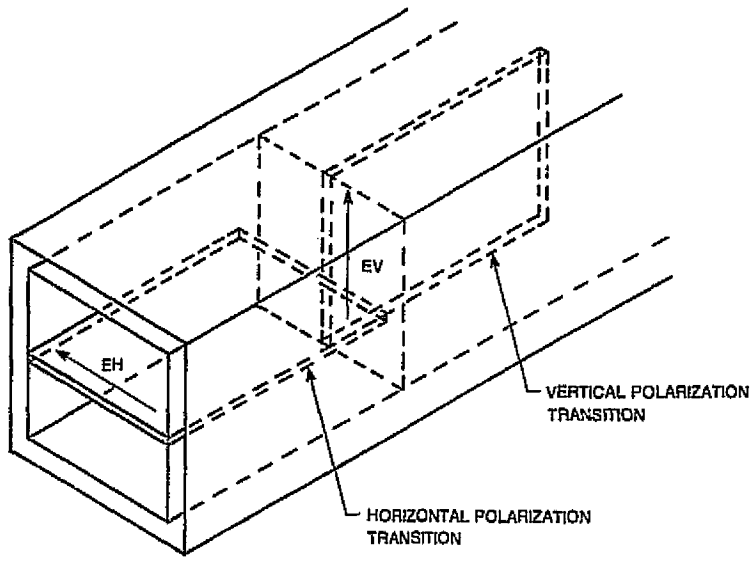

Figure 5-47. Dual-Polarization Transition Assembly

gap extreme, the finline was modeled as a slotline and, at the other extreme, as a slab-loaded waveguide. For the slotline, data are available in either graphical [5-4] or closed form, or in the circuit analysis program Super-Compact. For the slab-loaded guide, an exact solution was found by using the theory developed in Reference 5-5. This process resulted in one set of points for Z_0 and ε_{eff} for narrow gaps, and one solution for Z_0 and ε_{eff} for a full height gap. A curve was fitted to interpolate between the two extremes.

The following subsection discusses the second approach (spectral domain), which yields data for ε_{eff} over the entire range of gaps.

5.7.1.1 Calculation of Propagation Characteristics in Finlines Using Spectral Domain Analysis

This subsection is concerned specifically with the analytical determination and computation of the propagation constant of finline. The analytical approach selected as most suitable for this work is known as spectral domain analysis. The techniques described in this subsection were followed in the development of a computer program named SAIL (Spectral Analysis of Inhomogeneous Lines). At this writing, SAIL gives accurate values of propagation constant for empty rectangular waveguide, dielectric-slab-loaded rectangular waveguide, finline for the entire range of fin widths, and microstrip and suspended-substrate transmission lines. Microstrip was included in SAIL because its analysis requires only a slight rearrangement of finline coding, and extensive and reliable data on microstrip are available in the literature to verify the SAIL computations.

Figure 5-48 represents uniform finline supporting propagation along the z-axis. Because both TE and TM modes are needed to describe the electromagnetic conditions at the air/dielectric interfaces, the solution to the boundary value problem is often referred to as a hybrid-mode solution.

The essence of the spectral domain technique of hybrid-mode analysis is Fourier transformation in space of the assumed tangential field or current distribution along the fin/gap interface. Ideal thin conductors are assumed for the fins.

The first successful use of this technique was Denlinger's [5-6] application to open microstrip. After determining the fields in the Fourier domain, Denlinger reverted to the space domain to set up a pair of coupled integral equations for solution of the propagation constant along the z-axis. Itoh and Mittra [5-7] explained that, by remaining in the Fourier domain, the coupled integral equations were represented by coupled algebraic equations relating imposed currents to resulting fields at the air/dielectric interface. Then, following the moment method [5-8], they formed an inner product of each term of the coupled equations by using the assumed fields or currents as weighting functions (Galerkin's method). This yielded a matrix equation whose determinant was shown to equal zero when the proper value of propagation constant was used. Harrington [5-8] has proved that the moment method has a variational interpretation and thus leads to accurate values of propagation constant for only approximate descriptions of current density or field.

Next, Davies and Mirshekar-Syahkal [5-9] demonstrated that this approach could be applied to structures with a multiplicity of dielectric layers. Finally, Itoh [5-10] proposed a simple coordinate transformation from the imposed z- and x-directions which yielded fields (or currents) that generated

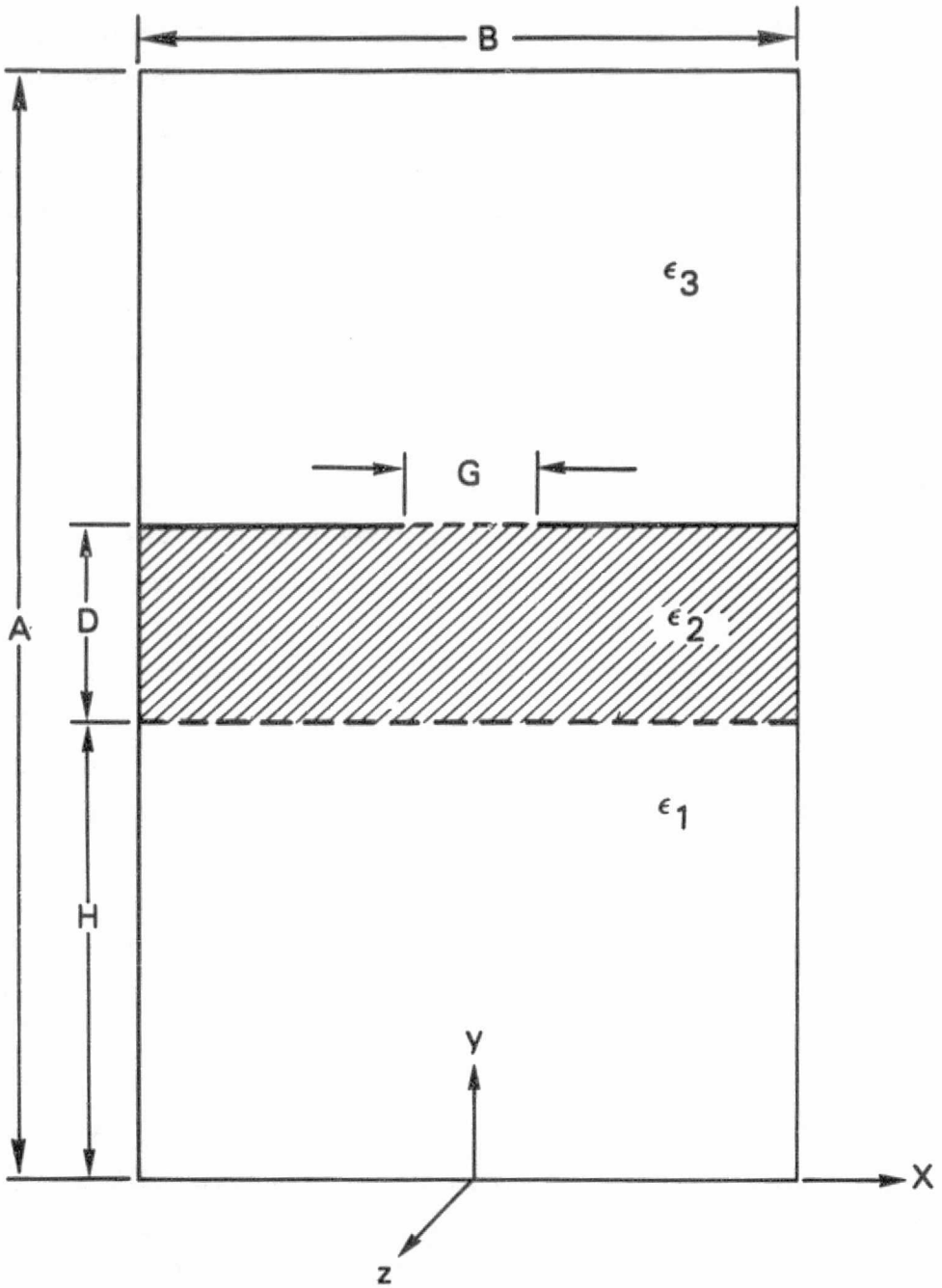

Figure 5-48. Finline Structure Used in Spectral Domain Analysis

only TE-to-y or only TM-to-y solutions for the fields in the structure. He then showed that the variation of these mode fields in y could be determined by straightforward transmission-line analysis. This led to a simpler, more intuitively satisfying way of setting up the final matrix, whose determinant is set to zero by iteratively searching for the correct value of propagation constant. The above concepts were used in the development of SAIL.

For narrow gaps ($G \leq B/2$), the gap field (basis function) in SAIL is assumed to have single x- and z-components. The x-component is taken to be proportional to $1/\sqrt{(G/2)^2 - x^2}$ and the z-component proportional to $\sin(\pi x/G)\sqrt{(G/2)^2 - x^2}$. For wide gaps ($G \geq B/2$), the basis functions are chosen to represent the currents on the fins. (Different approaches are used for narrow and wide gaps because reasonably simple field or current approximations hold best for small conductors or gaps, and because the basis functions chosen must be Fourier transformable with simplicity.) An electric wall is passed between the fins and the origin of the coordinate axes moved along x by B/2. Thus, the problem actually solved is the first higher order mode on microstrip, which is completely equivalent to wide finline. In this case, the transverse current density is proportional to $\cos(\pi x'/2)\sqrt{1 - (x')^2}$ where $x' = (1 - 2x/B)/(1 - G/B)$. The longitudinal current is taken to be proportional to the derivative with respect to x' of the transverse current density, as suggested by Jansen [5-11].

For the empty or dielectric-loaded waveguide (no fins), the field is uniform across B, and only a single (TE-to-y) mode is needed for solution. However, when fins are present, it is necessary to use about 200 terms in the Fourier expansions to accurately accommodate the singularities of the basis functions.

Figure 5-49 illustrates the agreement for the three separate solutions: narrow gap, wide gap, and empty waveguide.

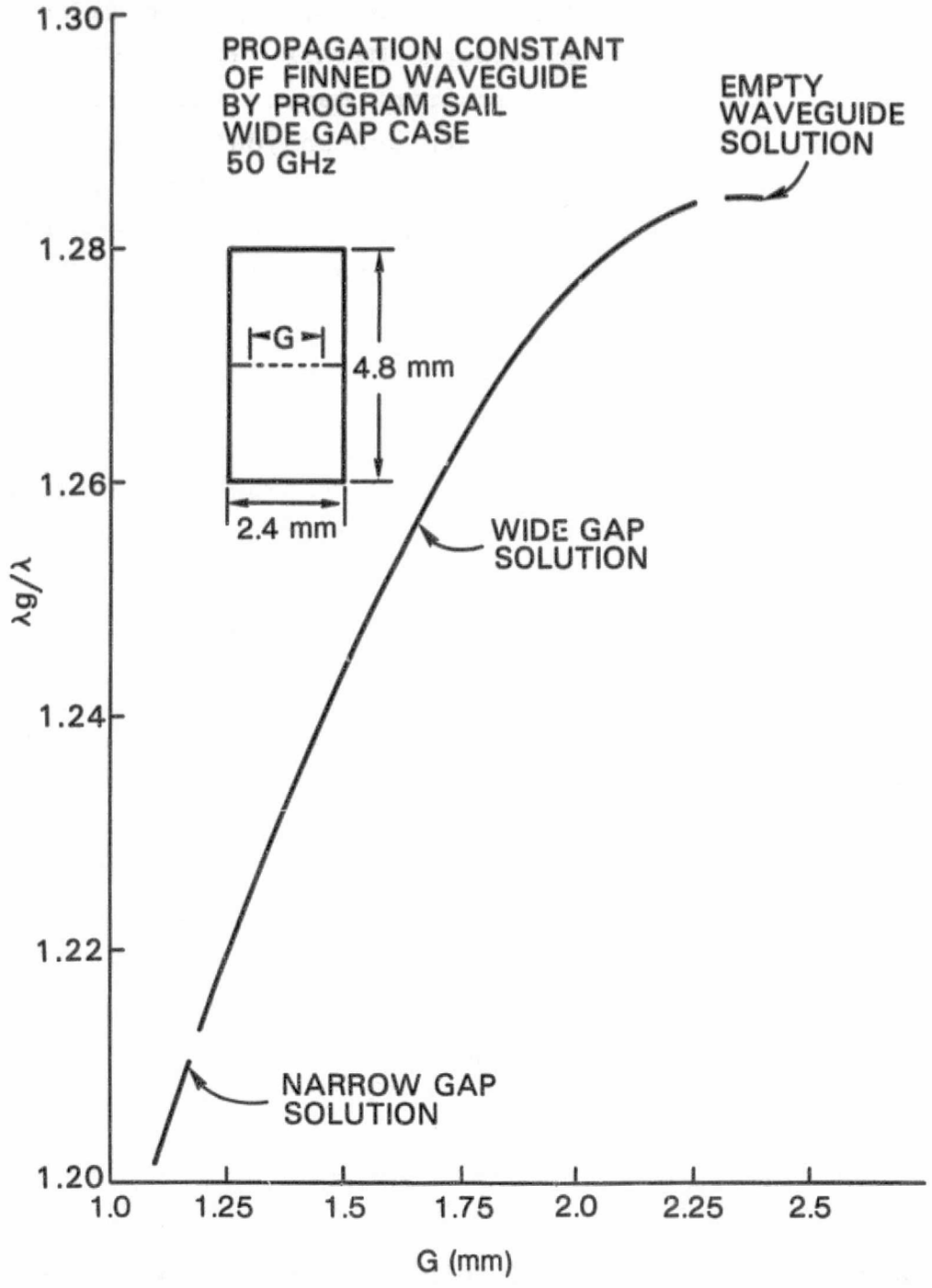

Figure 5-49. Combined Plot of Narrow Gap, Wide Gap, and Empty Waveguide Solution for $\lambda g/\lambda$ vs Gap Width

Computations by SAIL showed no perceptible difference from Bryant and Weiss' [5-12] program MSTRIP (within MSTRIP's range of best accuracy) for microstrip, Davies and Mirshekar-Syahkal's [5-9] finline graph, Knorr and Shayda's [5-13] dielectric-loaded waveguide and finline results (when SAIL used the same simplified basis function used by Shayda), Jansen's [5-14] finline graphs, and Cohn's [5-15] slotline results.

5.7.1.2 Characteristic Impedance

It is well-known that a unique characteristic impedance exists in TEM transmission lines and that it can be calculated from any of the following [5-16]:

$$Z_0 = \frac{V}{I} \; ; \; Z_0 = \frac{2W}{II^*} \; ; \; Z_0 = \frac{VV^*}{2W} \qquad (5\text{-}1)$$

This property is attributable to the uniqueness of the current and voltage at a given point along the line. In waveguides and finlines, however, no such unique definition of current and voltage exists, and the determination of Z_0 must be done carefully and with recognition of the limitations of the concept.

From Reference 5-16, for the case of rectangular waveguide

$$Z_0(V,I) = \frac{\pi b}{2a} \frac{W\mu}{\beta} = \frac{\pi b}{2a} Z_z$$

$$= \frac{\pi b \eta}{2a\sqrt{1 - (f_c^2/f^2)}} \qquad (5\text{-}2)$$

where a and b are the width and height of the waveguide, respectively. Similarly,

$$Z_0(W,I) = \frac{\pi^2 b}{8a} Z_z = \frac{\pi}{4} Z(V,I) \qquad (5\text{-}3)$$

$$Z_0(W,V) = \frac{2b}{a} Z_z = \frac{4}{\pi} Z(V,I) \qquad (5\text{-}4)$$

For a given guide, all three definitions are equally valid (or equally arbitrary), and a single definition should be used consistently.

A problem occurs, however, at the junction between two transmission media. Assuming that a unique impedance match does exist at the junction, a question arises as to what definition should be used if one line is a waveguide (or finline) and the other is, for example, microstrip. A reasonable approach would be to establish whether current or voltage is the more readily calculable at the junction and use that definition [5-18]. For the case of the microstrip/slotline or finline junction, the power-current definition was chosen as the more appropriate. All computations were carried out in power-voltage and subsequently transformed by the constant $(\pi/4)^2$ [equations (5-3) and (5-4)] to power-current. Although this constant was derived for rectangular waveguide, it was assumed that it would be approximately correct for finlines and slotlines. This assumption is supported by Cohn's observation [5-4] that a 50-Ω coax line matches well to a 75-Ω (power-voltage) slotline.

Figure 5-50 presents the transmission properties of finline on 0.635-mm (0.025-in.) beryllia centered in rectangular WR-42 waveguide. The parameters, which are included, are Z_0, λ_g/λ_0, and α.

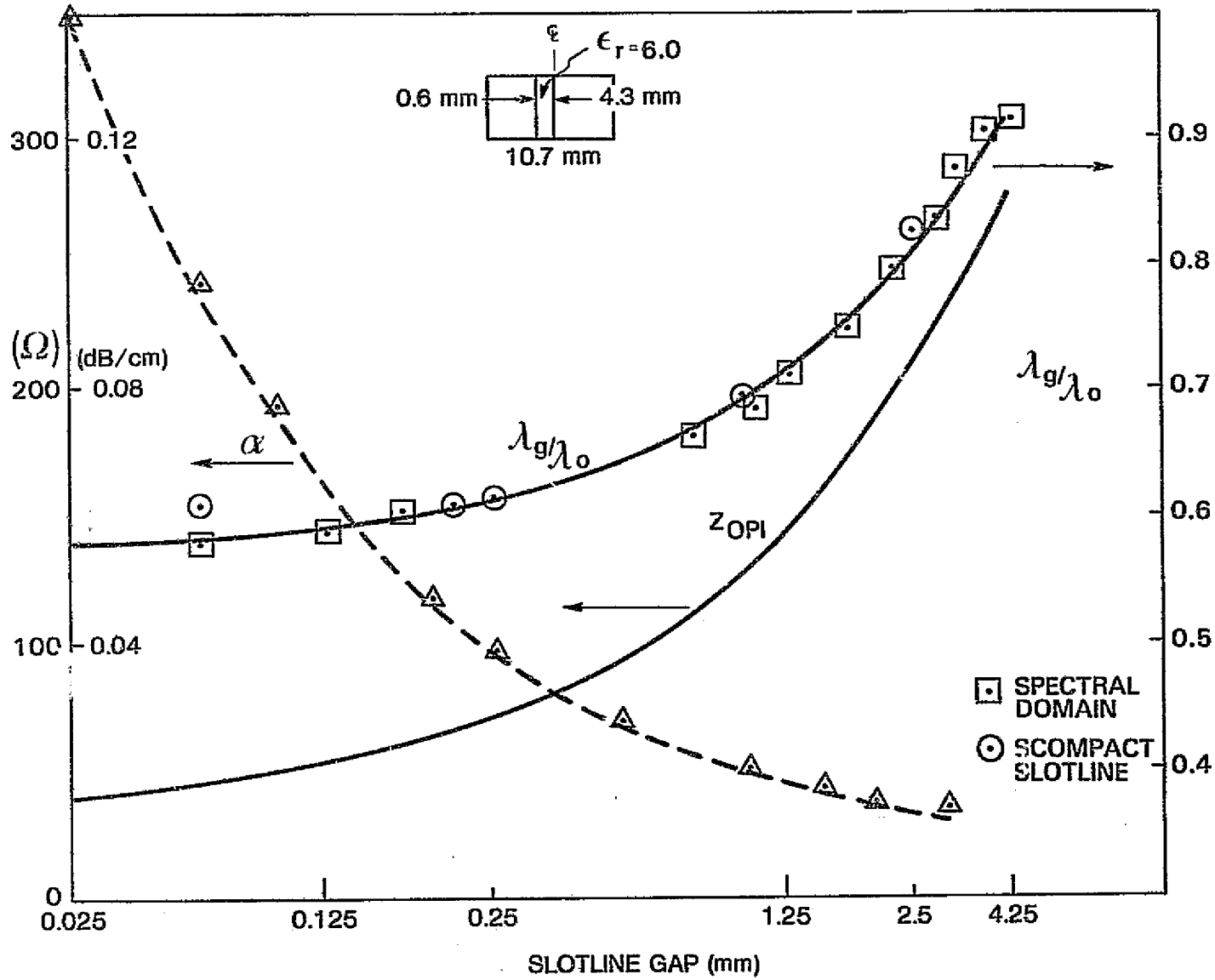

Figure 5-50. Transmission Properties of Finline on 0.635-mm (0.025-in.) Beryllia in WR-42 Waveguide

5.7.2 RECTANGULAR WAVEGUIDE TRANSITION

The rectangular waveguide transition consists of a three-step $\lambda/4$ transformer and a balun which converts the balanced slotline to the unbalanced microstrip. Figure 5-51 illustrates the balun and gives an equivalent circuit. The length, ℓ, is normally $\lambda/4$ at the center frequency, but in this case it is slightly longer to resonate out the bondwire inductance.

The circuit was modeled on Super-Compact by using a TEM approximation to the finlines and slotlines. Therefore, the results should be considered valid only in the vicinity of the center frequency. Figure 5-52 is the Super-Compact circuit file, and Figures 5-53 and 5-54 are the calculated return loss and insertion loss, respectively. The predicted return loss is better than 20 dB around 19 GHz, and the insertion loss is in the vicinity of 0.5 dB. Note that this figure includes the loss of the microstrip line (~0.35 dB) and both input and output transitions.

Figure 5-55 is the measured return loss and insertion loss of the same circuit. The insertion loss is approximately 1 dB over the 18.5-19.5-GHz range. This includes 0.4 dB for the 50-Ω line that simulates the MMIC module, plus the input and output transitions, which are 0.3 dB each. The return loss over this same range is better than 15 dB, and is about 25 dB at 19 GHz.

The isolation between input and output was measured by removing the input and output ribbons. The resulting coupling, -30 dB, is caused primarily by leakage through the waveguide beyond cutoff in the vicinity of the 50-Ω microstrip and is illustrated in Figure 5-56. Figure 5-57 is a photograph of the disassembled rectangular waveguide transition.

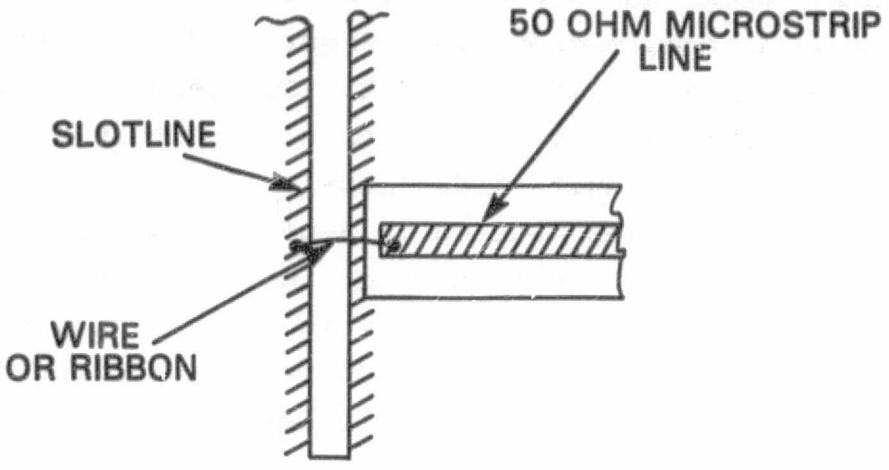

(a) Drawing

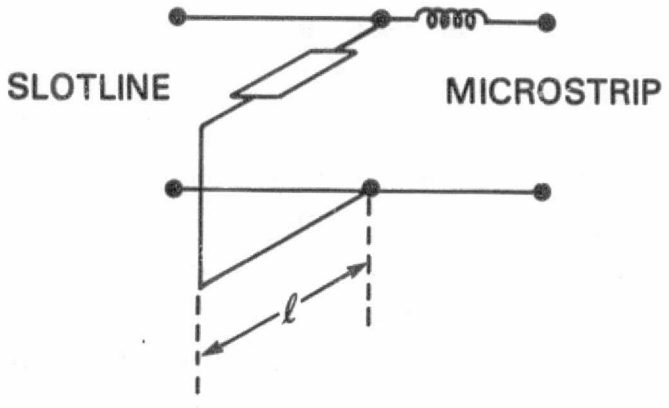

(b) Equivalent Circuit

Figure 5-51. Simple Microstrip/Slotline Balun

```
LAD
TRL 1 2 Z 280 E .1 F 19GHZ A .05
TRL 2 3 Z 149.31 P .112IN K 1.93 A .04/IN
TRL 3 4 Z 74.9 P .096IN K 2.60 A .09/IN
TRL 4 5 Z 62 P .097IN K 2.78 A .12/IN
SST 5 0 Z 62 P .119IN K 2.78 A .12/IN
IND 5 6 L .2NH
TRL 6 7 Z 50 P .236IN K 8.3 A .75/IN
A:2POR 1 7
END
BLK
A 2 3
A 4 3
B:2POR 2 4
END
FREQ
STEP 15GHZ 25GHZ .2GHZ
END
OUT
PRI B S R1 280 R2 280
END
OPT
B F 19.5GHZ 20GHZ
MS11 -40DB LT
END
```

Figure 5-52. Circuit File Used in Analysis of Balun

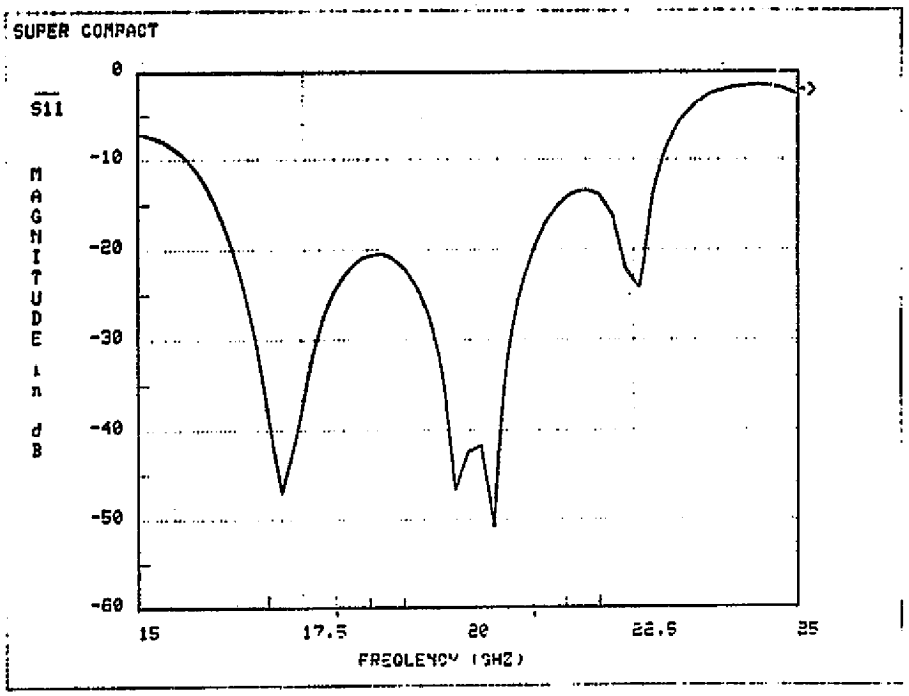

Figure 5-53. Calculated Balun Return Loss

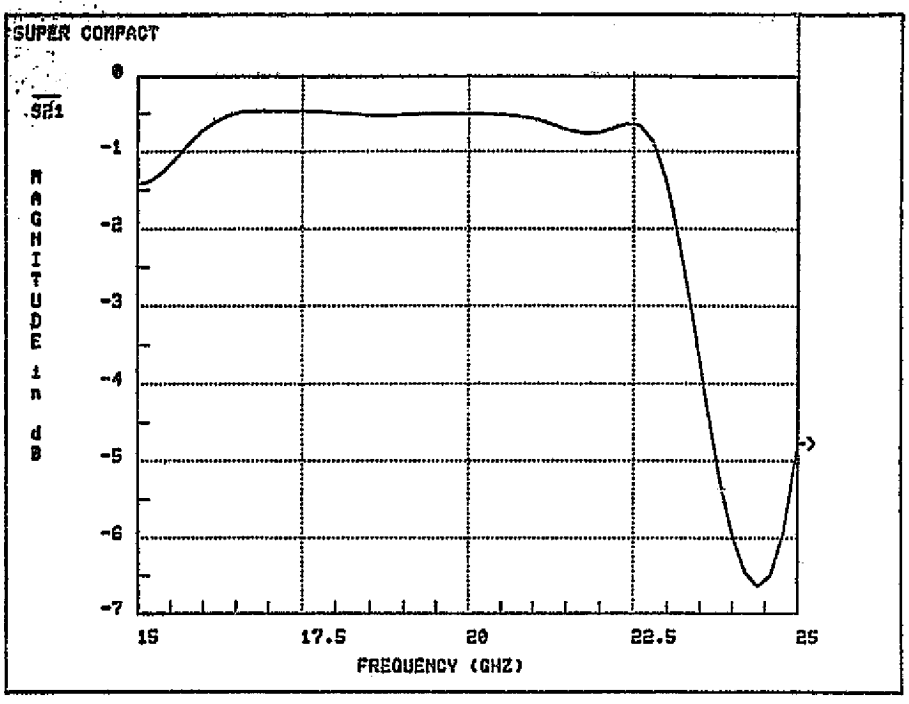

Figure 5-54. Calculated Balun Insertion Loss

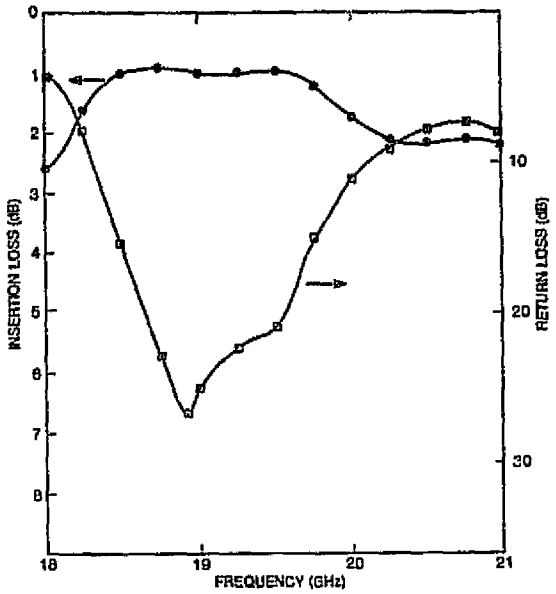

Figure 5-55. Measured Insertion Loss and Return Loss of Rectangular Waveguide Transition

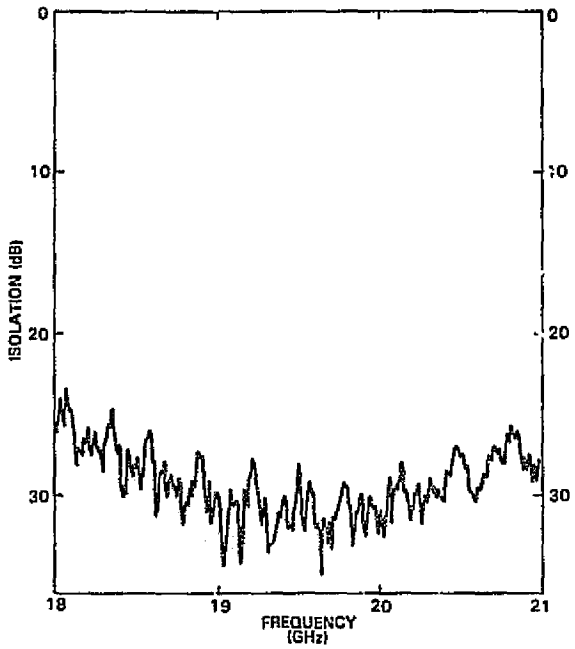

Figure 5-56. Measured Isolation of Rectangular Waveguide Transition

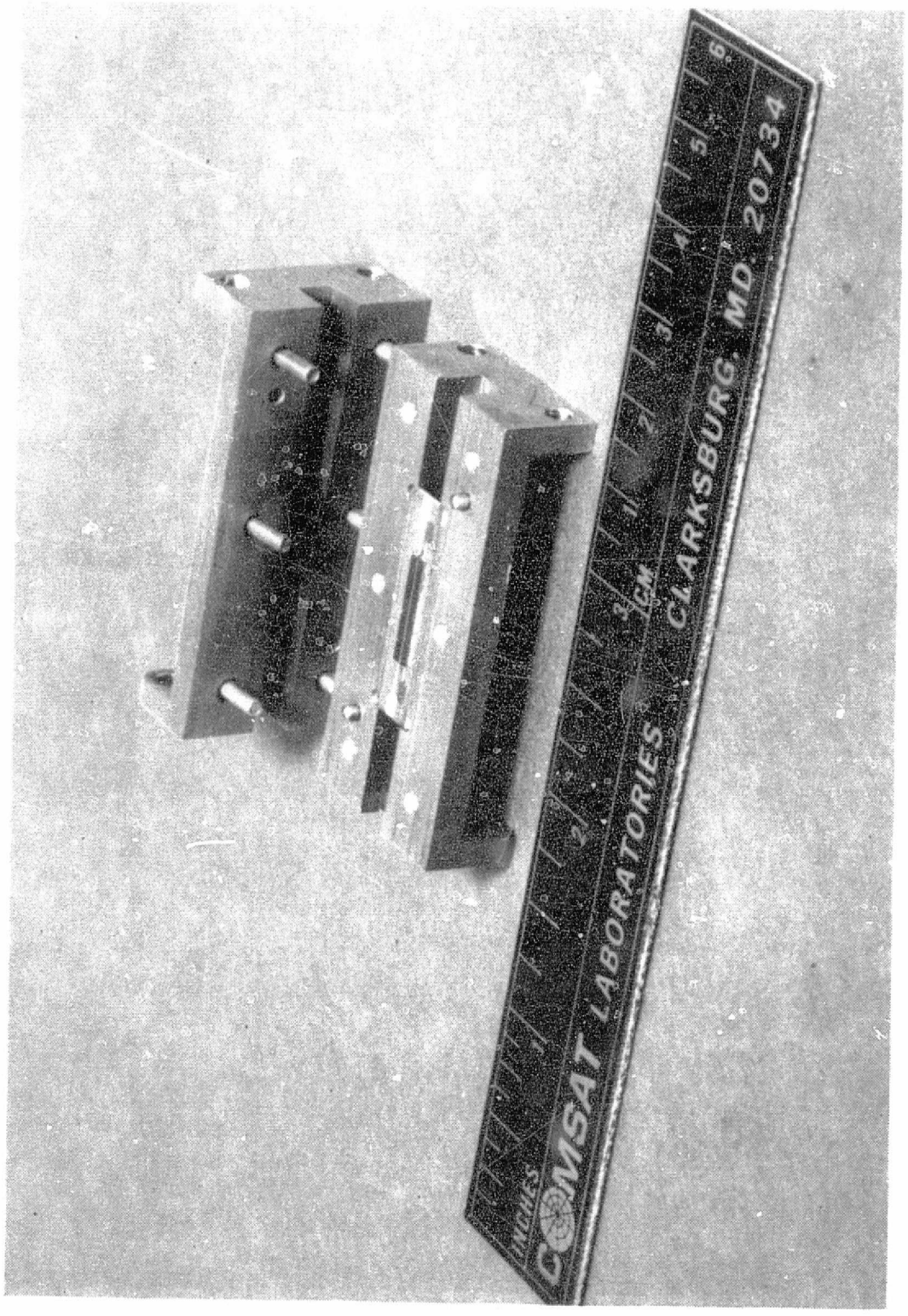

Figure 5-57. Rectangular Waveguide Transition (Disassembled)

5.7.3 SQUARE WAVEGUIDE TRANSITION

The purpose of the square waveguide transition is to allow selective coupling to one polarization while appearing transparent to the other. The dual-polarization lens element includes of two single transitions oriented orthogonally to each other, as illustrated in Figure 5-47. Each substrate contains a printed circuit that allows coupling to either a vertically or horizontally polarized wavefront, but not to both. A single such transition is shown disassembled in Figure 5-58. The beryllia substrate is 25.4 x 12.7 mm (1.0 x 0.5 in.) and is centered in the 9.65-mm (0.38-in.) square waveguide section. A pair of spring-fingered beryllium-copper rails are mounted on the edges of the substrate to make contact between the gold metallization of the substrate and the waveguide walls. The rails fit into a milled-out step and are clamped in place when sandwiched between the top and bottom halves of the housing.

Previous work [5-17],[5-19] using an antipodal (two-sided) finline structure, had the drawbacks of coupling to orthogonal modes and poor access to the ground plane at the MMIC mounting location. The present design allows mounting of the MMIC on the surface of a metallized dielectric substrate, giving good contact to ground, while contact to input and output is made by gold ribbons or wire bonds. The pattern is etched on only one side of the beryllia substrate, the other side is blank. The pattern consists of a waveguide-to-MMIC-to-waveguide transition made up of three sub-circuits, a four-step finline transformer, a slotline-to-microstrip balun, and a vertical septum (on which the MMIC is mounted) that divides the waveguide into two sections of guide below cutoff. Since the circuit is virtually coplanar, it lies on an equipotential surface for a horizontally polarized electric field and appears transparent to that polarization. The parasitic reactances associated with both vertical and horizontal septa have been neglected here.

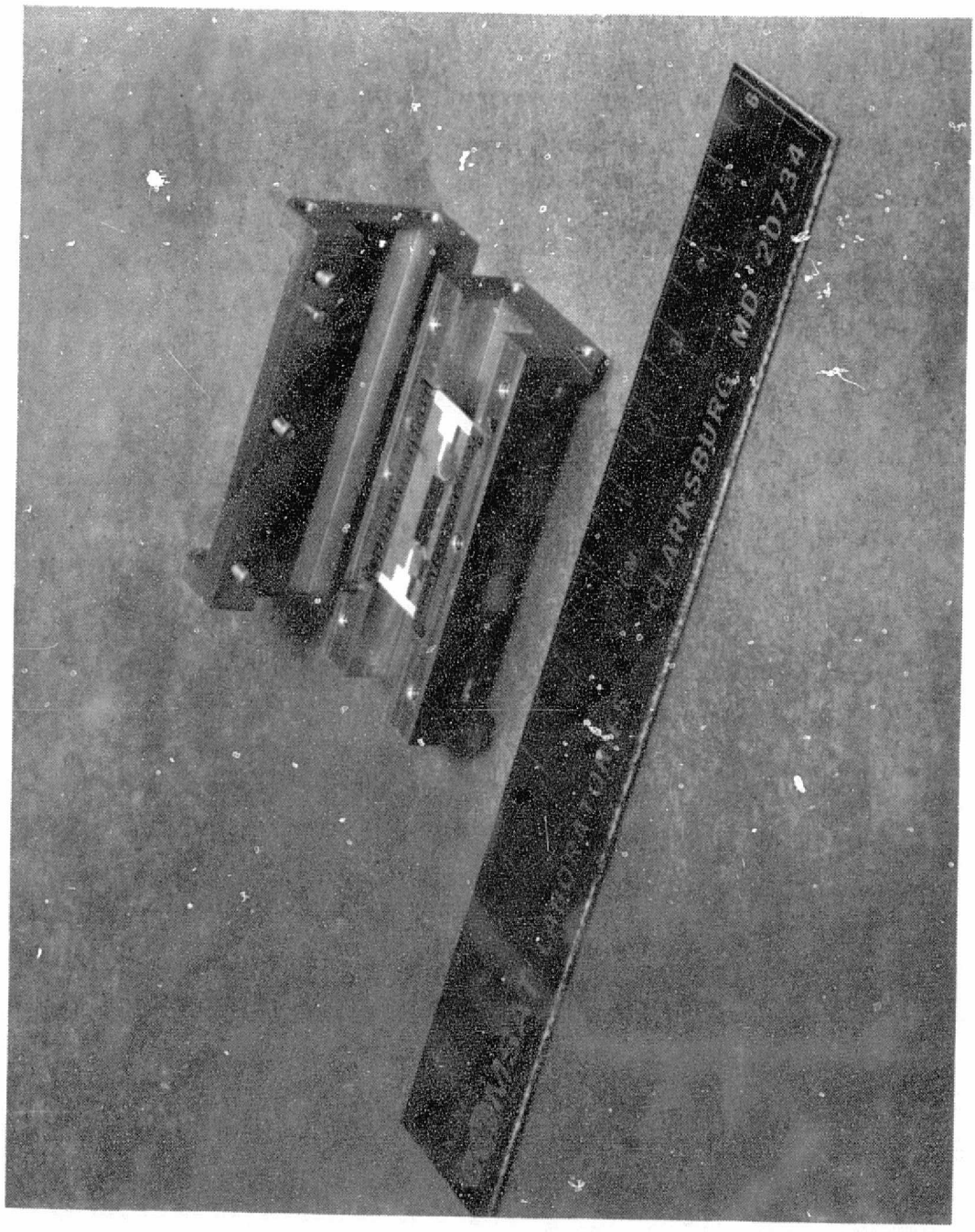

Figure 5-58. Square Waveguide Transition (Disassembled)

Calculation of the thermal resistance of the beryllia substrate indicated a value of 5°C/W. For example, for a 0.25-W amplifier operating with a gain of 4 dB and an efficiency of 20 percent, this would result in a temperature rise of only 3°C.

Two square waveguide cross sections were evaluated. The first was 10.7 mm (0.42 in.) square, and the second was 9.65 mm (0.38 in.) square. The choice of the 10.7-mm (0.42-in.) waveguide was based on the ease of tapering to standard WR-42 waveguide and the reasonably low cutoff frequency, resulting in a moderate characteristic impedance.

The characteristic impedance of rectangular waveguide is given by [5-16]

$$Z_0(V,I) = \frac{\pi b \eta}{2a\sqrt{1 - (f_c/f)^2}} \tag{5-5}$$

For the case of a square waveguide a = b; therefore,

$$Z_0(P,I) = \frac{\pi}{4} Z_0(V,I) = \frac{\pi^2 \eta}{8\sqrt{1 - (f_c/f)^2}} \tag{5-6}$$

$$Z_0(P,I) = \frac{\pi^2 \eta}{8\sqrt{1 - (\lambda_0/2a)^2}} \tag{5-7}$$

Equation (5-7) is plotted at 20 GHz in Figure 5-59. Note that Z_0 increases as a is decreased and asymptotes to 465 Ω for large a. At 10.7 mm, Z_0 is 650 Ω, and at 9.65 mm it is 750 Ω.

Figure 5-60 illustrates the computed propagation characteristics using a 0.635-mm beryllia substrate as a function of the relative gap width.

Accurate design of a multistep finline transformer network depends on an accurate knowledge of propagation characteristics, including effective dielectric constant, characteristic impedance, and losses. Although some data are available in the literature, little is applicable to the materials and geometries chosen here. Therefore, a separate effort was undertaken to write

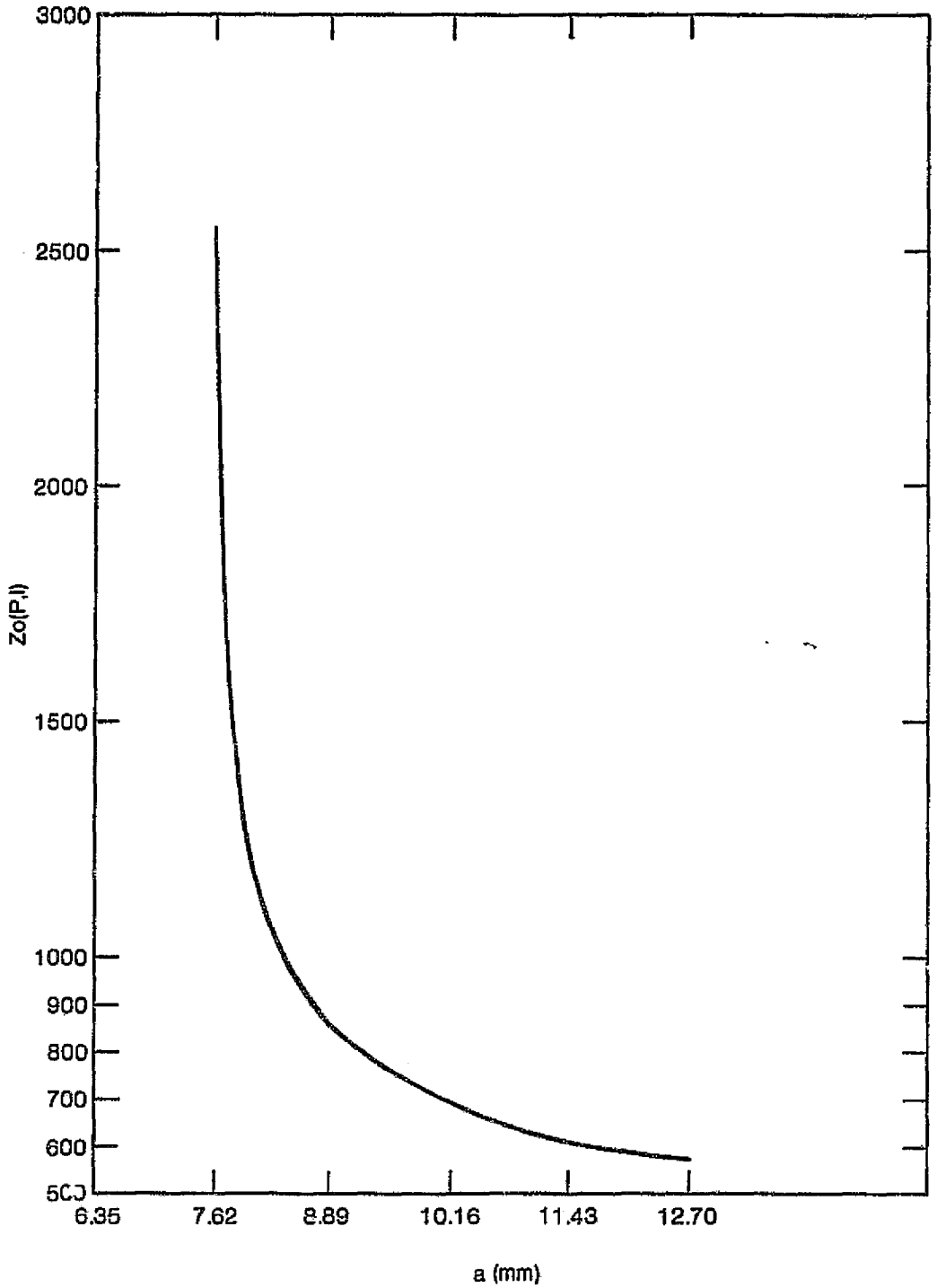

Figure 5-59. Characteristic Impedance (Power/Current) of Square Waveguide at 20 GHz

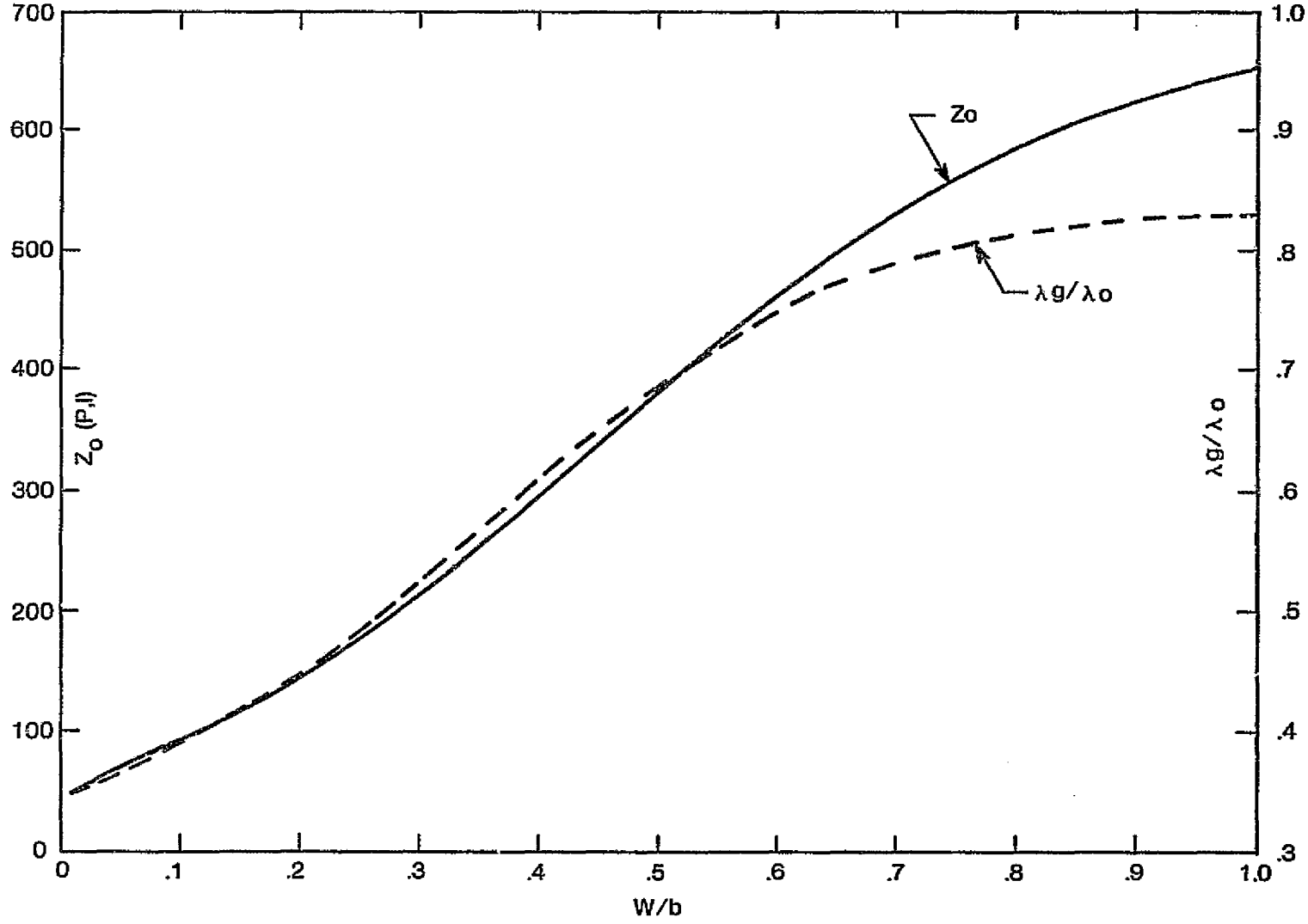

Figure 5-60. Computed Propagation Characteristics of Finline on 0.635-mm (0.025-in.) Beryllia in 10.7-mm (0.42-in.) Square Waveguide

a computer program that could be used to calculate the effective dielectric constant and characteristic impedance of a generalized finline structure. At the beginning of the project, however, this program was not yet available and design data were based on approximation and the interpolation of existing data. Figure 5-61 is a photograph of the original transition, designed for 10.7-mm (0.42-in.) square waveguide and incorporating a coplanar waveguide (CPW) 50-Ω transmission line section between input and output networks. The CPW section was subsequently replaced with an equal length section of 50-Ω microstrip line on 0.3-mm (0.012-in.) GaAs to more accurately simulate the MMIC circuit that would actually be used. The only tuning element on this circuit, and in all of the circuits to be discussed, is the length of the short-circuited slotline stub, which is in parallel with the microstrip input and output. This length is nominally 90 degrees at the center frequency, but is extended to about 115 degrees to tune out the bondwire or ribbon inductance.

Figure 5-62 is a plot of insertion loss and return loss for this structure. The total insertion loss, which includes the loss of the microstrip section, is about 1.0 dB over a 1-GHz bandwidth centered at 19.0 GHz. The loss of each of the two transitions is about 0.3 dB. The return loss is better than 14 dB over this range. However, the predicted insertion loss for each individual transition is about 0.15 dB, and return loss is better than 20 dB over a 25-percent bandwidth. The poor quantitative correlation with experimental data is believed to result from the following problem areas:

a. finline transformer discontinuity effects,
b. poorly defined characteristic impedance,
c. dispersion effects, and
d. surface roughness of the beryllia substrates.

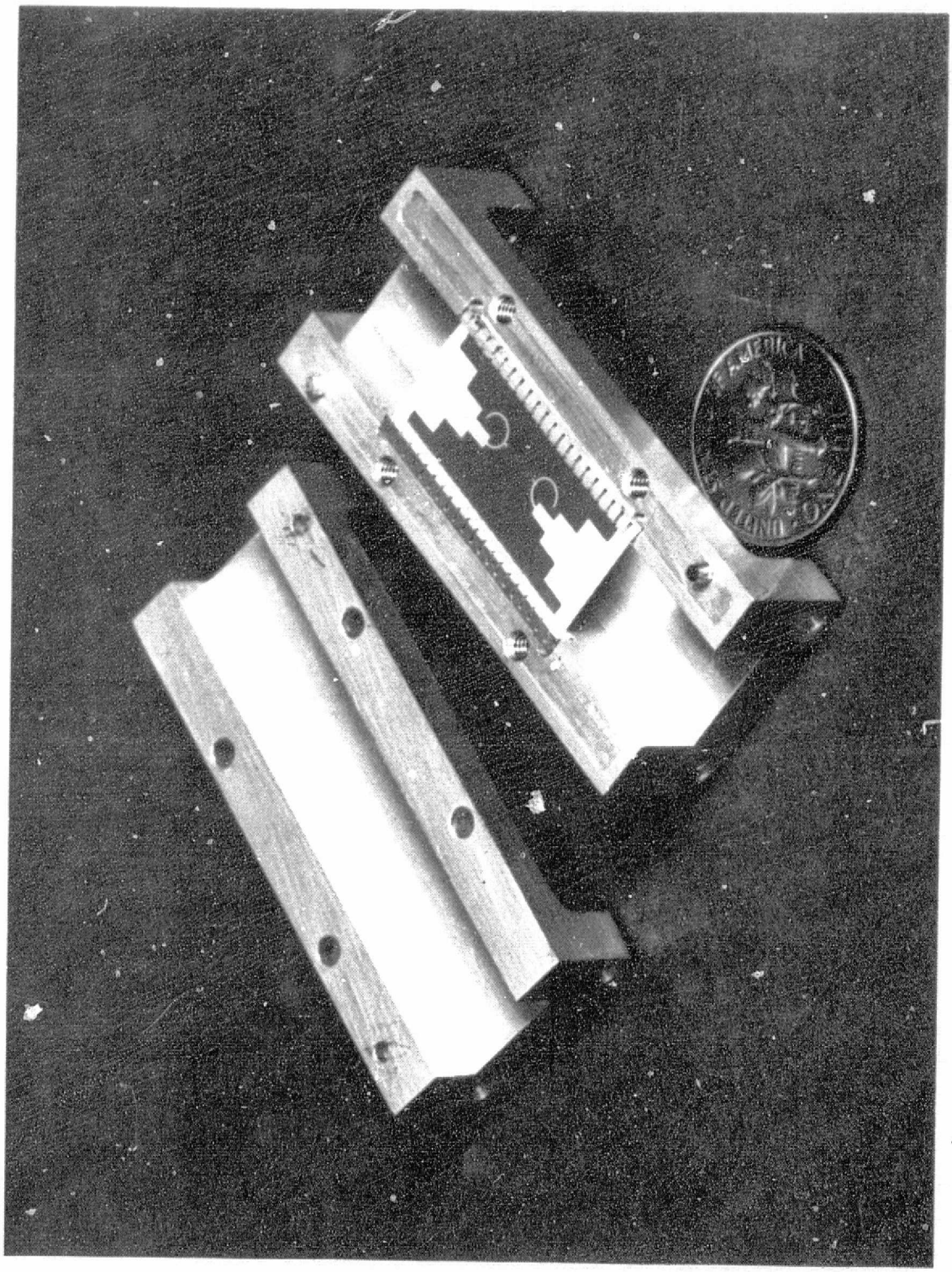

Figure 5-61. Original 10.7-mm (0.42-in.) Square Waveguide Transition

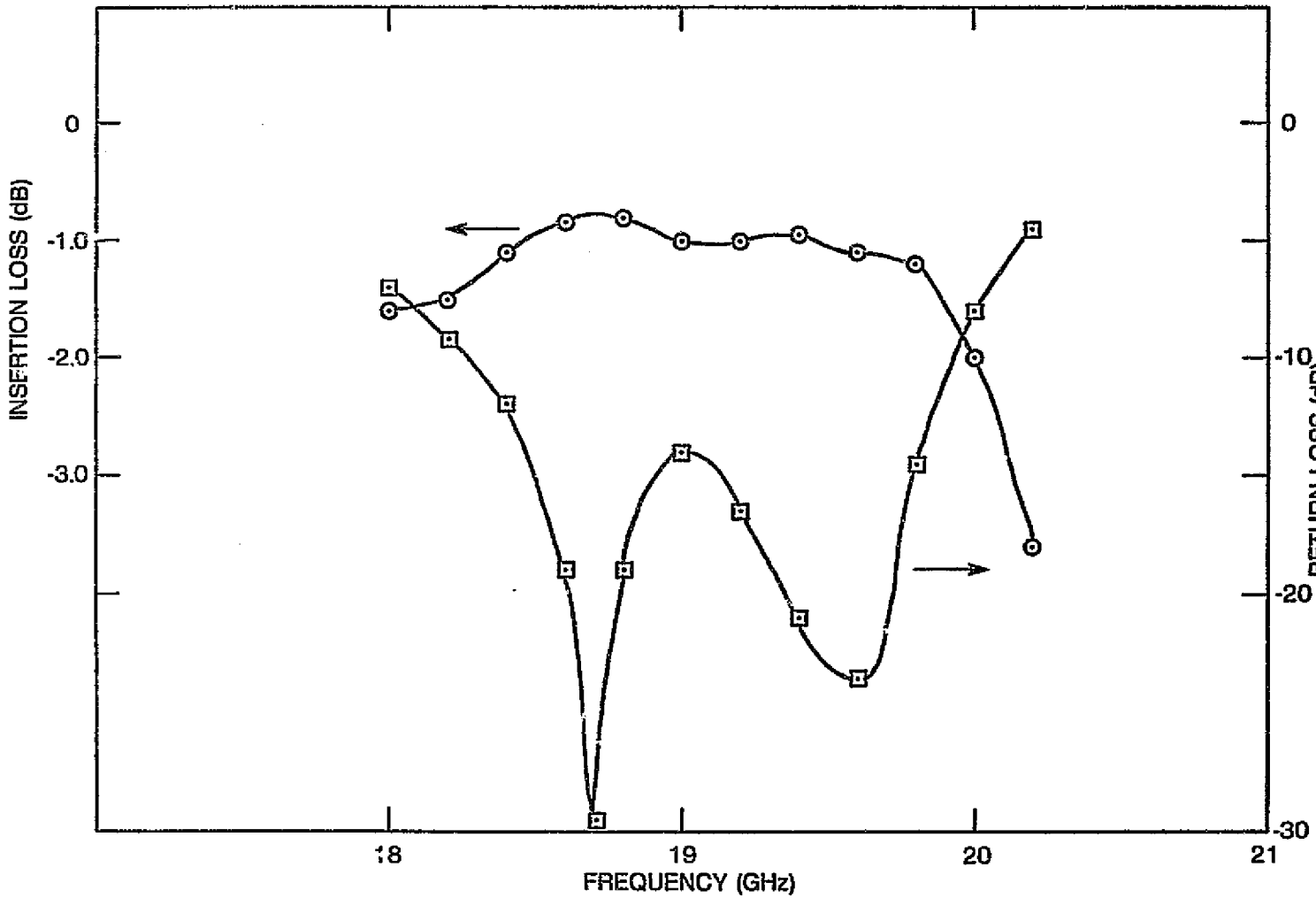

Figure 5-62. Insertion Loss and Return Loss of Original Square Waveguide Transition (includes 0.4 dB for microstrip section)

Figure 5-63 is a plot of the vertical-to-horizontal mode conversion for this transition. Over the operating band, the vertical-to-horizontal ratio is about 30 dB; however, outside this range, and especially at the high-frequency end, several high Q passbands appear. These may be attributed to the presence of high-order modes that are excited by asymmetries in the structure.

By using improved finline data for both characteristic impedance and effective dielectric constant, a new four-step transition was designed for the 10.7-mm (0.42-in.) housing, and a new design was begun for a transition in 9.65-mm (0.38-in.) square waveguide. The latter design was based on the hypothesis that vertical-to-horizontal ratio could be improved by raising the cutoff frequencies of the higher order modes mentioned above.

Figure 5-64 is a drawing of the revised 10.7-mm (0.42-in.) transition. Table 5-4 gives the pertinent dimensions and electrical parameters (the section numbers are defined later in Figure 5-67), and Figure 5-65 is a plot of the measured insertion loss and return loss for this structure. The total insertion loss is about 0.6 dB, which is close to the predicted value, and the return loss is better than 15 dB over the 18.2-19.6-GHz frequency range. Vertical-to-horizontal mode conversion is plotted in Figure 5-66 and is poorer than in the original design, probably because of mechanical imperfections and uncontrolled field fringing.

Table 5-4. Characteristics of 10.7-mm (0.42-in.) Transition

Section	Z_0(P,I) (Ω)	W (mm)	ℓ (mm)
1	472	6.60	2.84
2	248	3.73	2.13
3	130	1.93	1.63
4	69	0.48	1.35

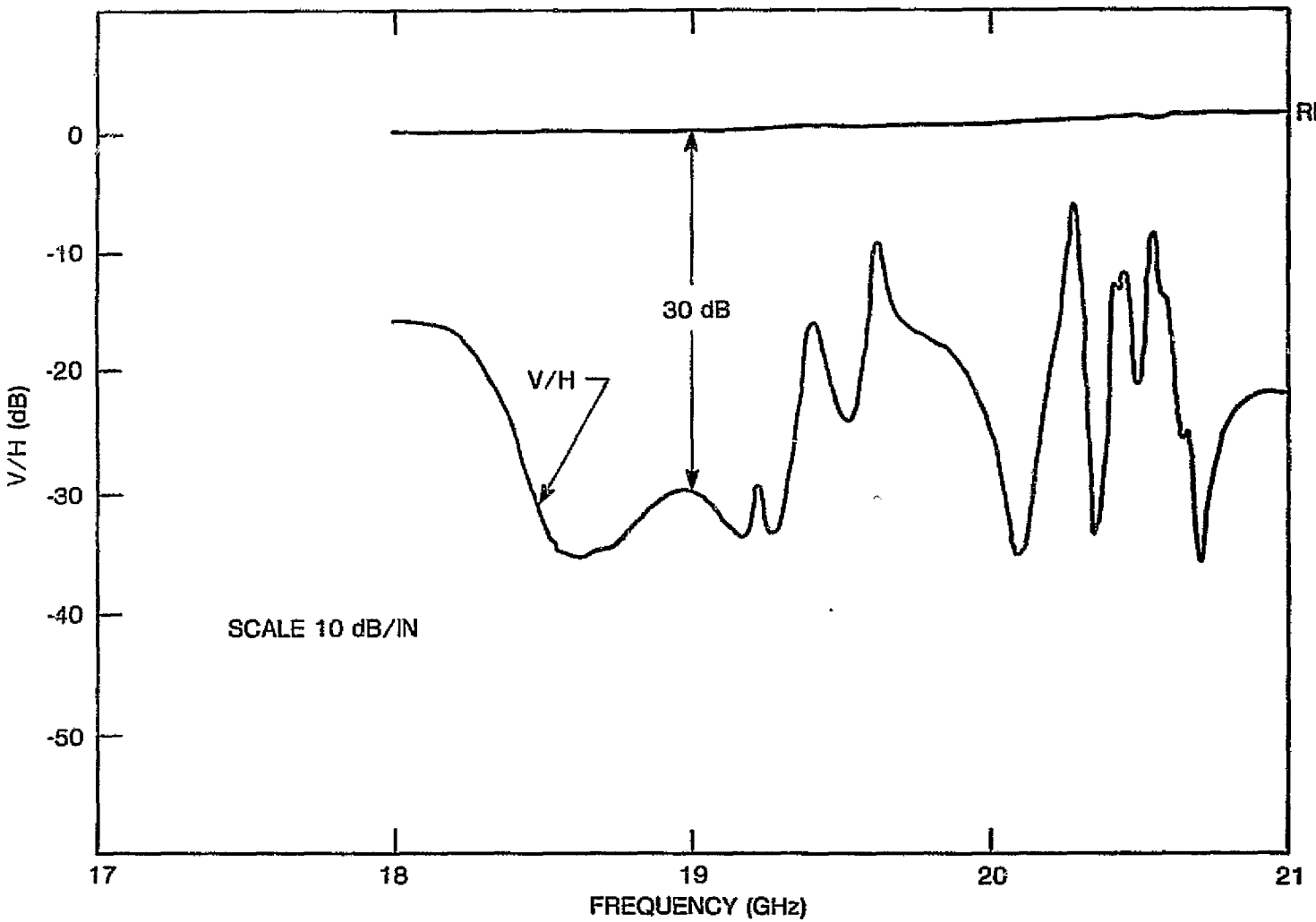

Figure 5-63. Vertical-to-Horizontal Cross-Polarization

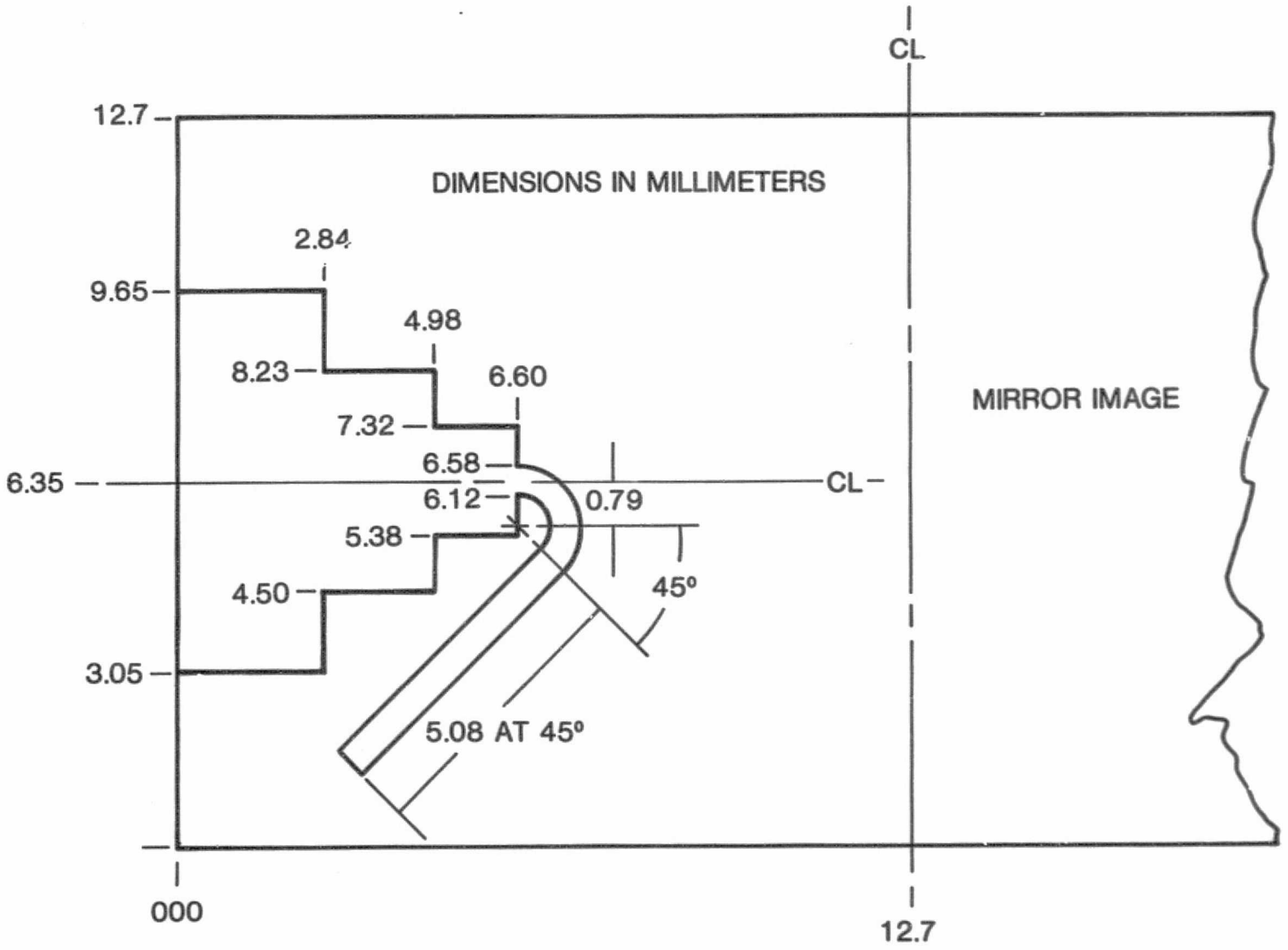

Figure 5-64. Drawing of Revised Square Waveguide Transition

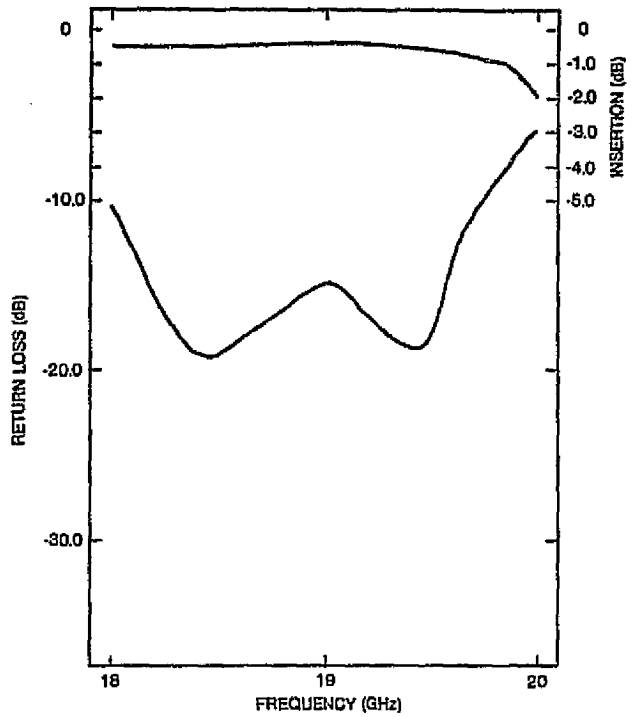

Figure 5-65. Measured Insertion Loss and Return Loss of Revised Square Waveguide Transitions

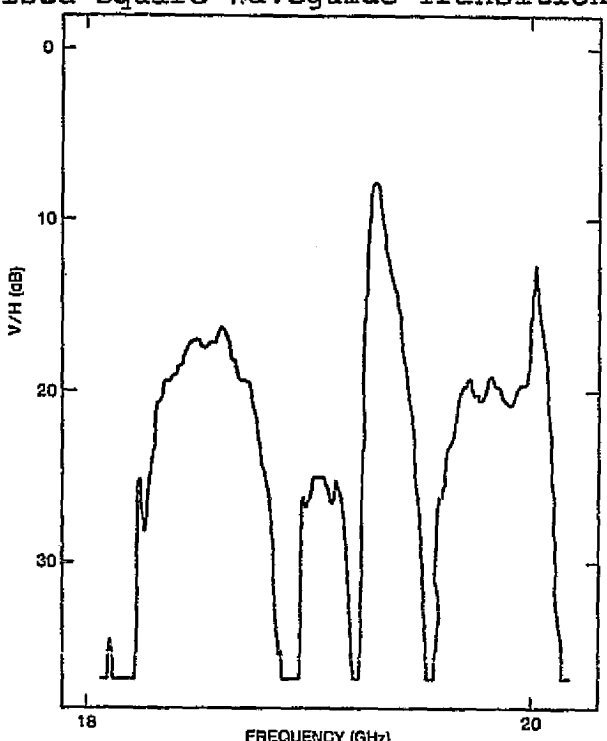

Figure 5-66. Cross-Polarization of Revised Square Waveguide Transition

Figure 5-67 is a drawing of the transition that was designed for the 9.65-mm (0.38-in.) housing. Table 5-5 gives the dimensions and electrical parameters of this transition, and Figures 5-68 and 5-69 are the calculated insertion loss and return loss for this structure. Tuning of this circuit proved to be difficult. Although good insertion loss and return loss were possible, the bandwidth under these conditions was only 1 to 2 percent; far below the expected value.

Table 5-5. Characteristics of 9.65-mm (0.38-in.) Transitions

Section	Z(P,I) (Ω)	W (mm)	ℓ (mm)
1	585	9.40	1.60
2	303	4.06	2.82
3	101	0.71	3.07
4	62.7	0.19	2.36

The primary difference between the 10.7-mm (0.42-in.) and the 9.65-mm (0.38-in.) transitions was the difference in characteristic impedances, especially at the large gap extreme. Under the assumption that the problem was caused by incorrect impedance levels, the 9.65-mm substrate was replaced with the 10.7-mm substrate (revised). Performance improved significantly. Figures 5-70 and 5-71 are plots of insertion loss and return loss for two different transitions that were assembled. Except for resonance at just above 19 GHz, which was traced to the two dual tapers used to transform to WR-42 waveguide, the insertion loss and return loss are quite good. The reason for the difference in the two transitions is that one was assembled with bondwires between the MMIC and the substrate and the other was assembled with ribbons, thus giving a lower inductance in series with the input.

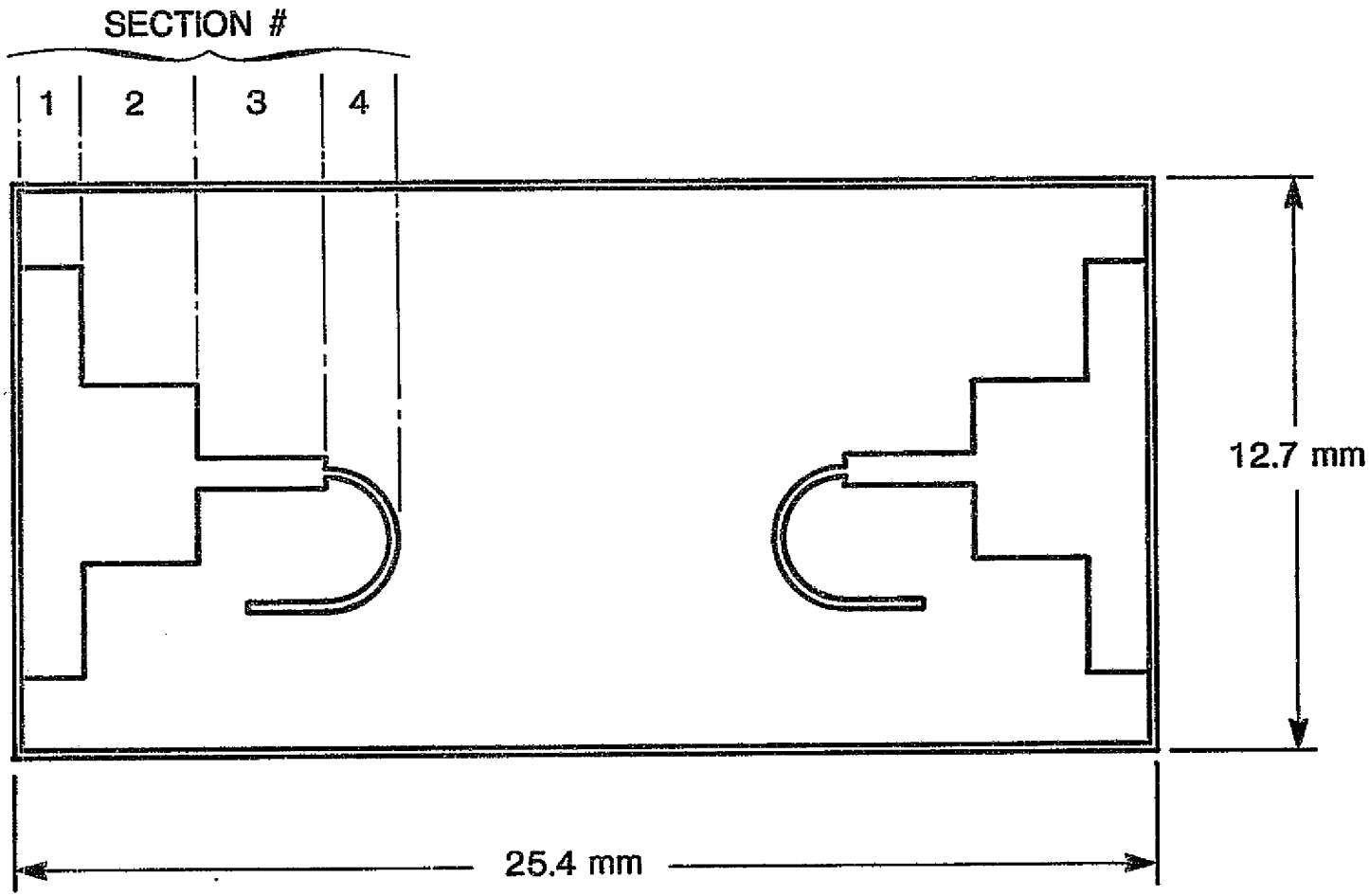

Figure 5-67. Drawing of 9.65-mm (0.38-in.) Square Waveguide Transition

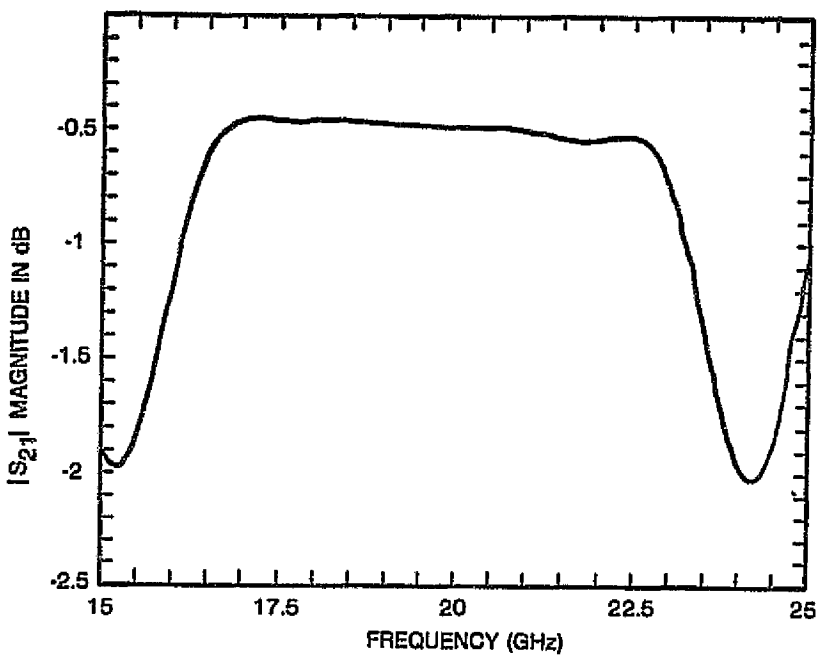

Figure 5-68. Calculated Insertion Loss of 9.65-mm (0.38-in.) Transition

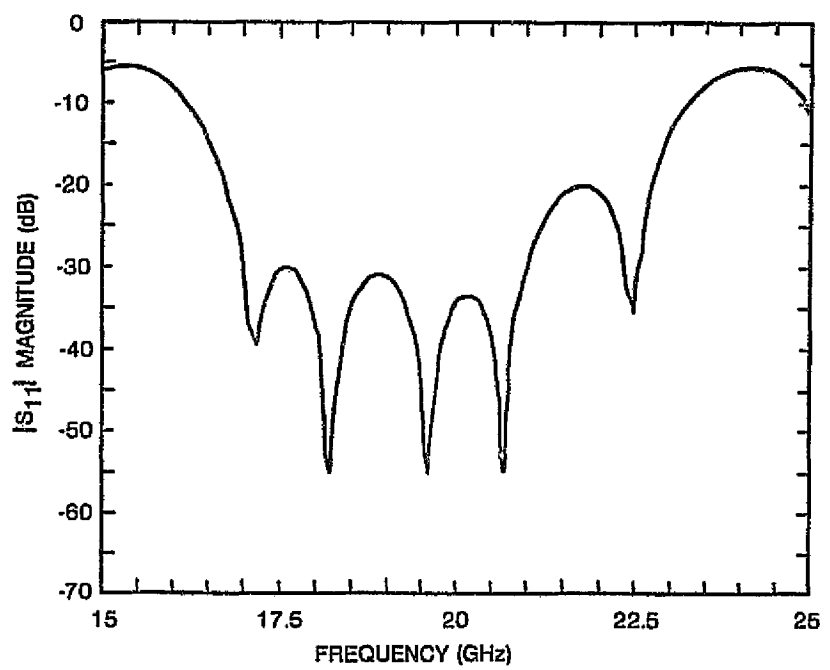

Figure 5-69. Calculated Return Loss of 9.65-mm (0.38-in.) Transition

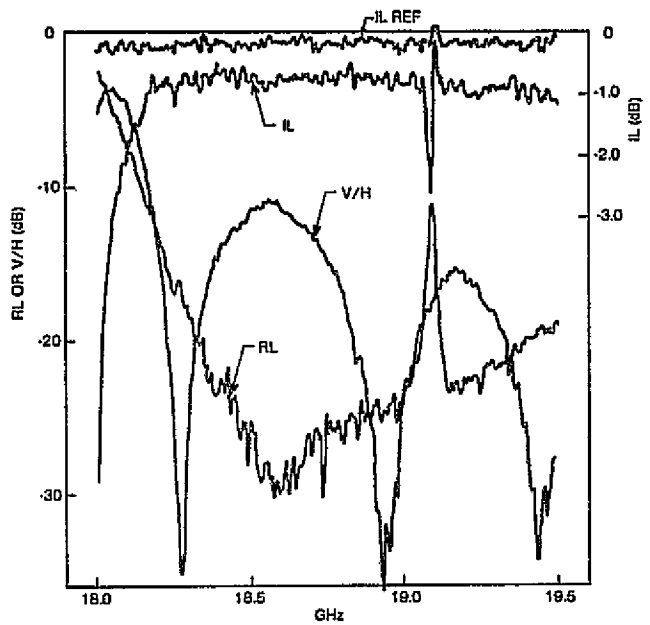

Figure 5-70. Performance of First 9.65-mm (0.38-in.) Transition With 10.7-mm (0.42-in.) (Revised) Substrate

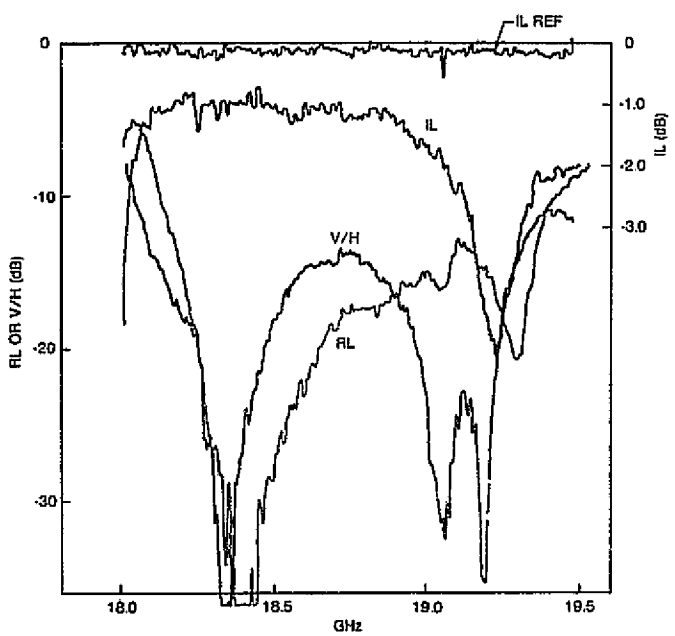

Figure 5-71. Performance of Second 9.65-mm (0.38-in.) Transition With 10.7-mm (0.42-in.) (Revised) Substrate

It is apparent that problems still exist in vertical-to-horizontal isolation and are probably caused by asymmetries and mechanical imperfections in the substrate assembly and housing.

5.7.4 3-WAY POWER COMBINER

As discussed in Subsection 5.6.1, Configuration C requires three independently scannable beams. This capability necessitates the use of a phase shifter for each beam, a 3-way power combiner, and a power amplifier. With the techniques developed under the present contract, it is possible to combine the five chips (the power amplifier, the 3-way combiner, and the three phase shifters) on a single motherboard coupled to rectangular waveguide. Figure 5-72 illustrates a possible configuration.

The circuit pictured in the figure differs from the MMIC/waveguide transition discussed earlier in several ways. A tapered rather than stepped finline transformer is shown, a broader bandwidth balun is used, and several functional modules are combined on one motherboard.

The specifications for the MMIC power amplifier and phase shifters are defined elsewhere on the basis of system operational requirements. The 3-to-1 combiner, however, should meet the requirements of low loss, small size, and good isolation. Several circuit configurations could be used [5-20], but the best candidate appears to be a single quarter-wavelength radial [5-21] or tapered [5-22] N-way combiner with resistive loading, as shown in Figure 5-72. The small size of this structure at 20 GHz makes it a good choice for a drop-in component on the motherboard. The substrate material for the combiner could be fused silica. The isolation between the three inputs should exceed 20 dB across the operating band.

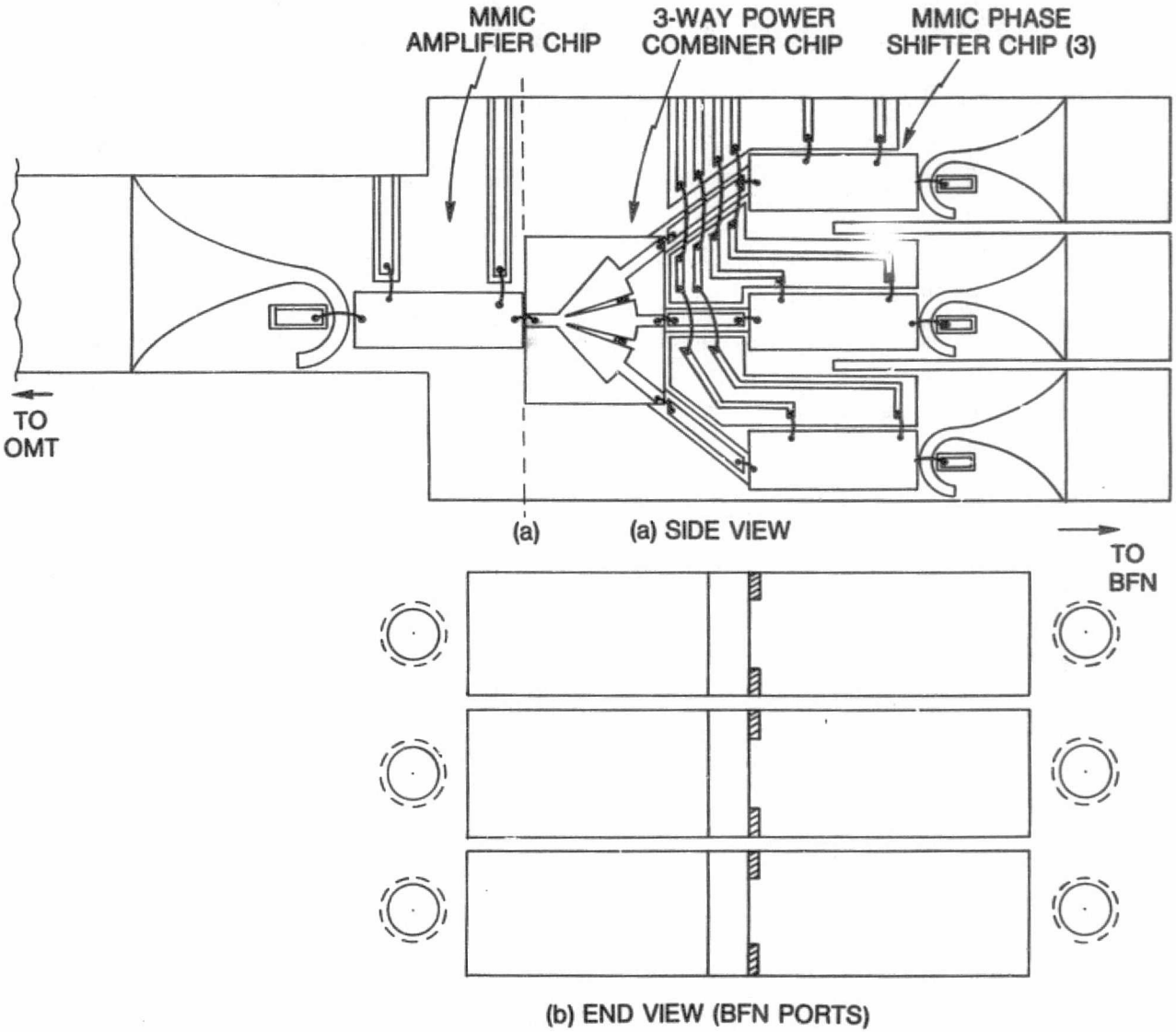

Figure 5-72. Three-Beam Integrated Element Configuration

5.7.5 CONCLUSIONS AND RECOMMENDATIONS

Several conclusions can be made at this point with regard to the planar finline transition, in both rectangular and square versions. First, the advantages of this type of MMIC mounting technique have been demonstrated. Electrically, the transition will couple energy with very low loss and over a broad bandwidth from waveguide into an MMIC or MIC circuit. Mechanically, it provides a single-piece, rugged, and easily reproduced module that can be produced inexpensively. And finally, the use of beryllia for the substrate material allows for a low thermal resistance structure.

Two areas need closer investigation: the characteristic impedance of finline and the step discontinuity effects. Without a firm understanding of these problem areas, the designer must use approximate or cut-and-try techniques, or rely on relatively long tapered sections which will increase the size of the transition.

Of the two forms, rectangular or square waveguide, it appears that the square structure will require considerably more development effort to become competitive with an OMT, at least in terms of cross-polarization performance. The use of a pair of rectangular (single polarization) transitions with a coaxial or microstrip RF power division or manifold structure coupled to an OMT appears to be the most promising approach at this time.

5.8 PHASED ARRAY THERMAL CONTROL

The thermal control effort of this study was concentrated on investigating techniques of extracting the heat generated in

the feed amplifiers and transporting it to a major spacecraft heat rejection surface. To accomplish this, the following assumptions were made regarding the spacecraft's heat rejection system:

a. The prime heat rejection surface (thermal radiator) is located remote from the feed array network.

b. The feed array's generated heat is transported to this radiator via a forced cooling loop whose design is not part of this study.

c. The amplifiers are designed to be mounted to a 0 to 70°C heat sink (reference the Statement of Work for 20-GHz transmit module and GaAs power amplifier). This means that the temperature gradient between the cooling loop and the amplifier must be minimized.

Initially, a passive technique of cooling the feed modules was examined. However, with the large power densities of the feed modules (0.775 to 1.55 W/cm^2), it became obvious that passive radiative cooling would be inadequate. Figure 5-73 shows the feed module temperature as a function of heat dissipation per unit area for an ideal radiator with no incident sun. As can be seen, to achieve a radiator temperature of 70°C, the power density cannot be greater than 0.078 W/cm^2 (which is far less than the expected range of feed module densities).

Several active feed array cooling techniques were investigated during this task. The one with the most potential at the present time is a heat pipe/fluid loop combination. This thermal control concept is illustrated in Figures 5-74 through 5-76. The heat generated in the amplifiers is transported to the fluid coolant loop via heat pipes attached to each waveguide section containing an amplifier chip assembly. The fluid loop then

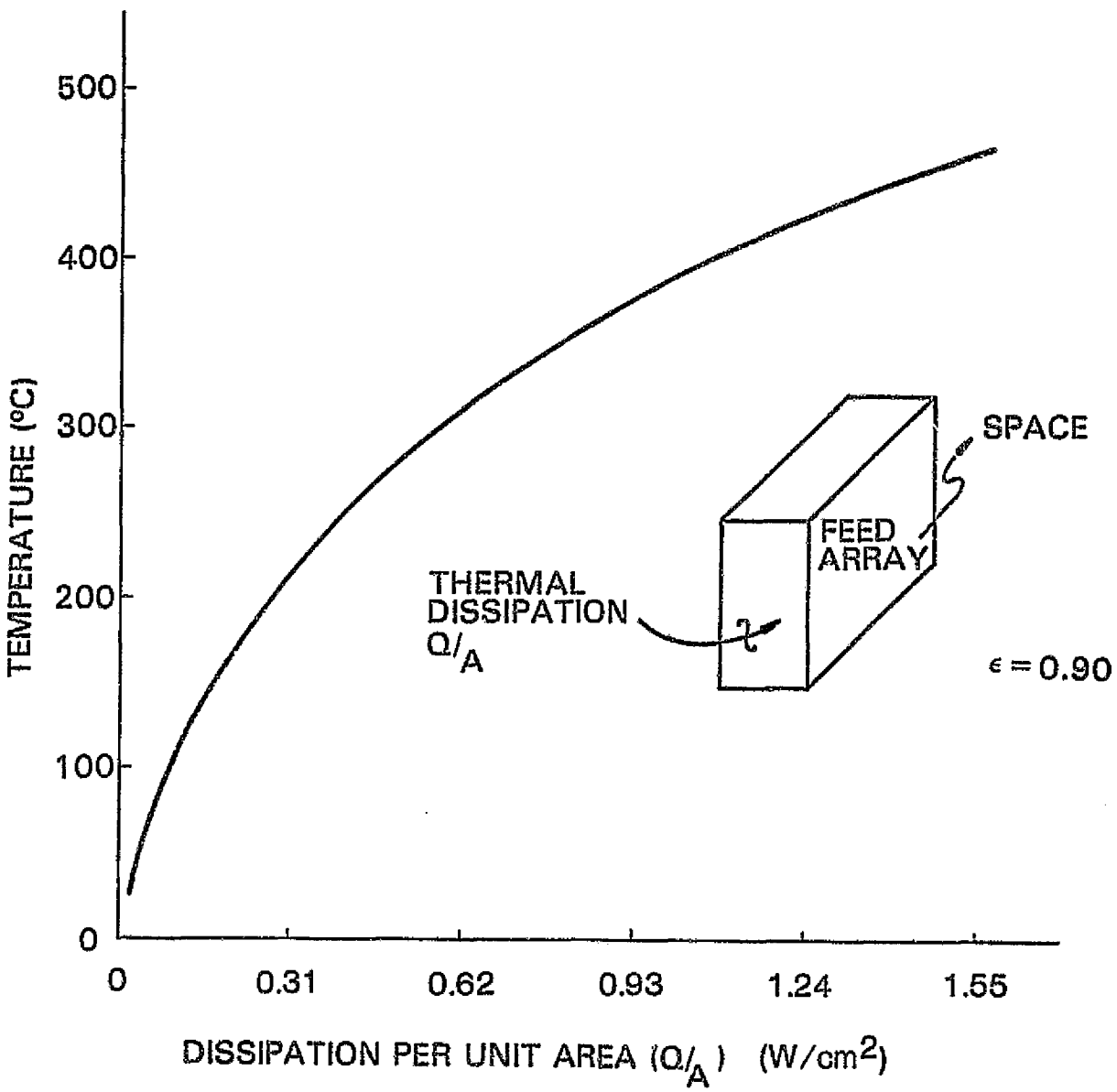

Figure 5-73. Passive Radiation Cooling of Feed Array

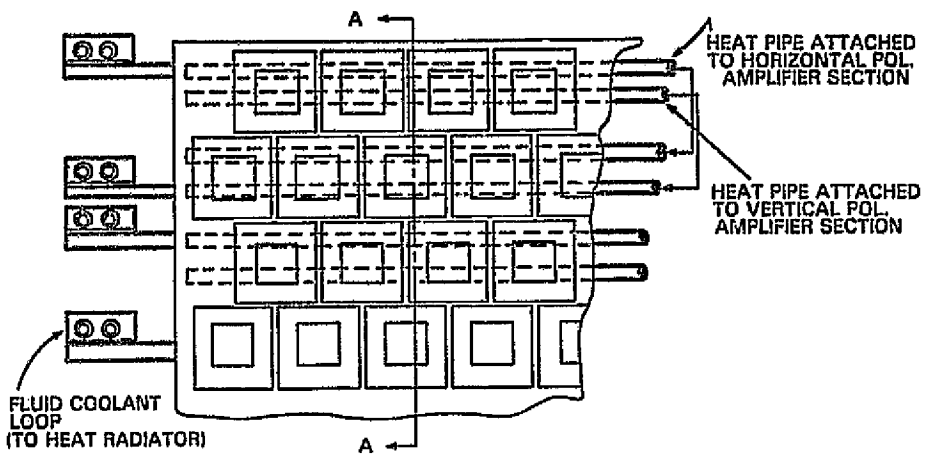

Figure 5-74. Phased Array Feed Thermal Control: Front View

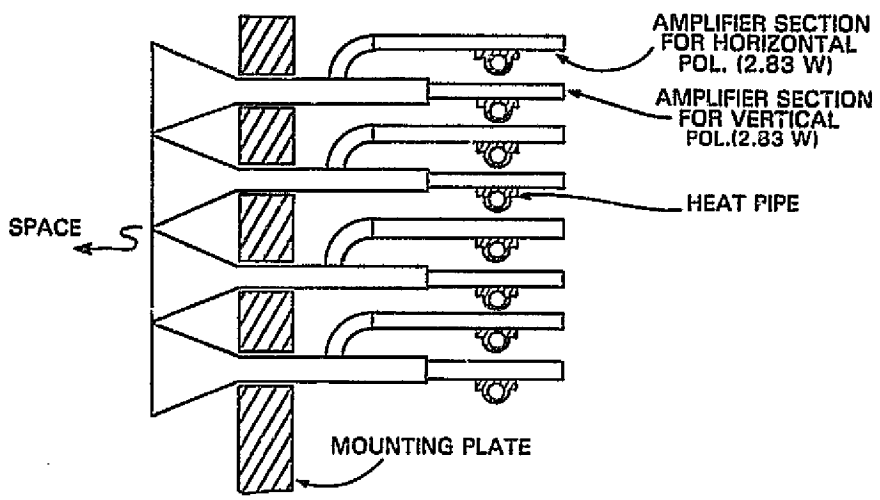

Figure 5-75. Phased Array Feed Thermal Control: Side View

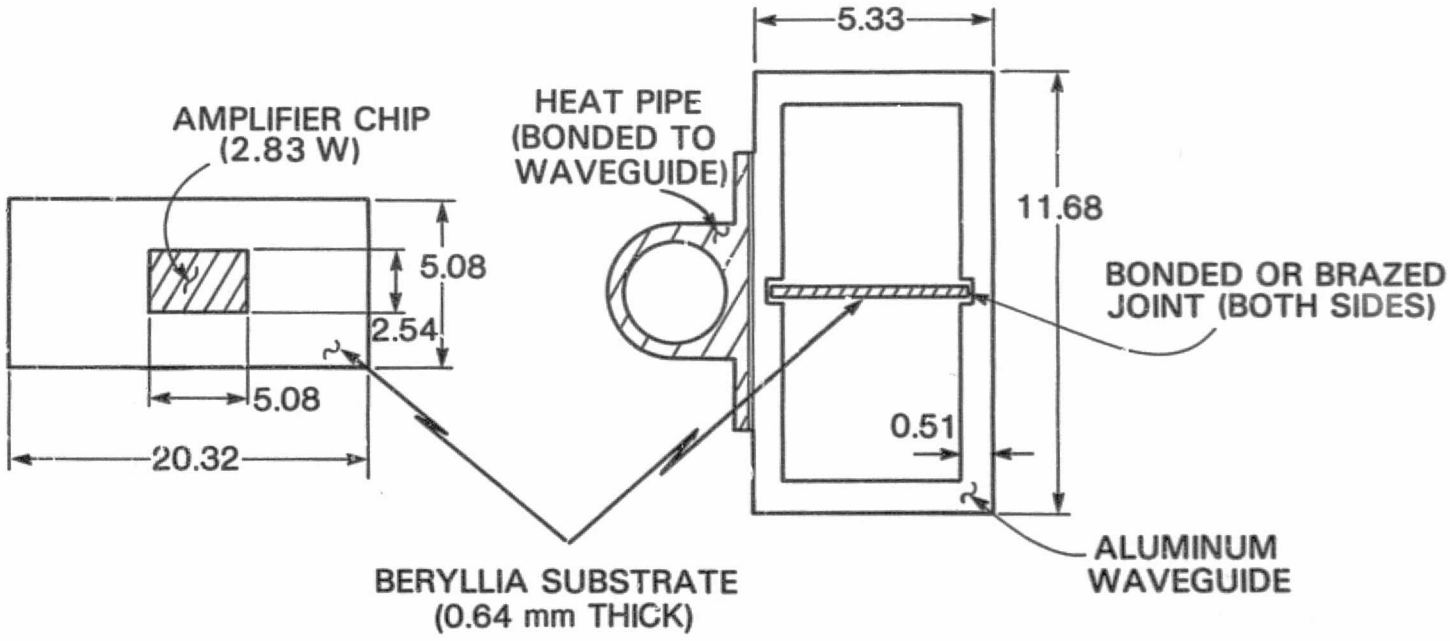

Figure 5-76. Amplifier Chip Thermal Design

carries the heat to the thermal radiator for rejection to space. With this concept, the heat pipes isothermalize the feed array and thus minimize the temperature gradient between the chip and the fluid loop.

The amplifier chip is mounted on a beryllia substrate to distribute its 2.83 W of generated heat. This chip is attached to the waveguide, as shown in Figure 5-76. An analytical thermal model of the substrate/waveguide assembly was developed assuming a bonded joint at the interface. It was found that the temperature gradient across this bonded joint was about 25°C, whereas the gradient in the substrate was only about 15°C. This interface between the substrate and waveguide can be improved by brazing, which would reduce the temperature gradient across the interface to about 9°C. The temperature gradient from the waveguide to the heat pipe vapor is 2.8°C. This means that, with a 70°C fluid loop temperature and utilizing a brazed joint, the amplifier chip will be about 97°C (70 + 2.8 + 9 + 15). This is well under the allowable chip temperature of 150°C.

The heat pipe transport capability limit will allow 48 amplifier sections (136 W) to be connected to any one heat pipe (this is a grooved aluminum heat pipe with ammonia as the working fluid). By coincidence, the physical layout of the feed array network has 24 elements in-line. This allows one heat pipe to be utilized in distributing the heat generated in two rows of amplifier elements to the forced cooling loop. In addition, reliability considerations will probably require a redundant heat pipe at each location (not shown in figures). The heat pipes considered for this application have an extensive flight history, having been developed by NASA-GSFC in 1970 and flown on ATS-6 and other spacecraft with no failures.

As presently conceived, all the heat pipes will be in a common plane. This will permit a valid ground thermal vacuum test

program to be performed on the feed array assembly. With the heat pipes in a horizontal position on earth, their heat transport performance is identical to the zero-gravity performance in space.

6. CONCLUSIONS

The results presented in this study substantiate, by analysis and hardware demonstration, the feasibility of phased-array-fed dual-reflector systems with distributed power and phase control. The conclusions drawn from this study are based on a detailed examination of two multiple scanning spot beam and two multiple fixed spot beam designs.

The two multiple scanning beam antenna designs that were developed utilized a 576-element phased array, but differed in their feeding systems: one was network-fed, incorporating both amplifier and phase shift modules, while the other was space-fed, using only the variable amplitude module. Both designs provide six simultaneous scanning beams and, with an appropriately sized main reflector, are capable of meeting all the isolation and e.i.r.p. requirements specified by NASA.

A comparison of the two approaches clearly showed that the space-fed array or lens offered a simpler beam-forming design; however, phase errors introduced across the radiating aperture contributed to both mispointing and gain loss. The network-fed phased array, which is more complex, has the advantage of producing precise amplitude and phase distributions to the radiating apertures and, hence, achieves lower scan losses and accurate pointing.

Both the bifocal and quadrufocal configurations were analyzed to select the best lens design. This analysis revealed that the bifocal lens has less scan loss over a half space than does the quadrufocal design. Expressions for the optimum feed locus for both designs were derived. Previously, the primary feed elements that illuminate the lens have been placed on a plane. This study showed that a feed placed on the optimum feed locus could achieve a higher gain for a fixed-scan direction.

For the multiple fixed spot beam configurations, both network-fed and space-fed 576-element phased array designs were considered, in addition to a more conventional focal-region-fed Cassegrain system which utilized 9-horn clusters to generate the fixed beams. All designs were capable, with an appropriately sized main reflector, of achieving the isolation and e.i.r.p. requirements desired by NASA. Of note was the Cassegrain design, which used an undersized 2.76-m (9-ft) reflector but was still able to achieve 30 dB of co-pol and cross-pol isolation between Boston and Washington by optimizing the feed element, feed locations, and excitations. This configuration also has a relatively simple beam-forming network when compared to the corporate-fed configuration, which becomes quite complex for 18 fixed beams.

Several key hardware elements were designed, built, and tested during this study. One of these was a waveguide-to-MMIC transition, which is a critical element in systems that use distributed power and phase control, since energy must be transitioned into and out of the MMIC circuit efficiently. The new design showed good performance over a 1-GHz bandwidth with a maximum insertion loss of 0.3 dB. The transition was designed in both rectangular and square waveguide. A wideband design that can operate over the full 2.5-GHz bandwidth was also considered.

A phased array element and a lens element, both incorporating the waveguide-to-MMIC transition, were also fabricated. The phased array element consisted of a square pyramidal horn, an OMT, and two rectangular waveguide-to-MMIC transitions. The lens element consisted of two square pyramidal horns and two square waveguide-to-MMIC transitions. For the dual-polarized element of the phased array, the rectangular waveguide transitions are connected to the two arms of an OMT that feeds the radiating horn. Cross-polarization isolation is also provided through the OMT. For the lens element, the square waveguide transition must offer

good isolation between the two orthogonal polarizations. An isolation of over 30 dB was measured across a 1-GHz bandwidth for the present design. Measurement of return loss, insertion loss, and isolation all showed good results for both elements.

The scanning performance and mutual coupling effects of the phased array were demonstrated through measurements. A 34-element array with eight excited central elements was assembled and tested for both polarizations. The measured scanned array pattern followed the embedded element pattern in both the E- and H-planes. Although element-to-element mutual coupling was small for the size of element fabricated, the cumulative effect on the radiation pattern was significant, especially for edge elements.

In conclusion, this configuration study demonstrated the performance achievable in an array-fed multibeam dual-reflector system. The information provided can serve as a data base for future work in this area. The results obtained demonstrate the advantages of using distributed power and phase control via MMIC modules, as compared to conventional systems, when high efficiency, high e.i.r.p., and rapidly scanned multiple beams are required.

7. REFERENCES

[2-1] "30/20 GHz Spacecraft Multiple Beam Antenna System," Ford Aerospace Report for NASA Contract NAS3-22498.

[2-2] "30/20 GHz Spacecraft Multiple Beam Antenna System," TRW Report for NASA Contract NAS3-22499.

[3-1] D. F. DiFonzo, "The Evolution of Communications Satellite Antennas," IEEE Antennas and Propagation Symposium, Albuquerque, New Mexico, May 1982, Digest, Vol. 1, pp. 358-361.

[3-2] A. Zaghloul and R. R. Persinger, "INTELSAT VI Antenna Subsystem Studies," COMSAT Laboratories Final Report, INTELSAT Task Order T4-81-100, August 1981.

[3-3] V. Krichevsky," Optimum Beam Scanning in Offset Single and Dual Reflector Antennas," COMSAT Laboratories Final Report for INTELSAT Contract INTEL-222, March 1982.

[4-1] W. D. Fitzgerald, "Limited Electronic Scanning with an Offset Feed Near-Field Gregorian System," MIT Lincoln Laboratory, Technical Report 486, DDC AD-736029, September 24, 1971.

[4-2] C. Dragone and M. J. Gans, "Imaging Reflector Arrangements to Form a Scanning Beam Using a Small Array," Bell System Technical Journal, Vol. 58, No. 2, February 1979, pp. 501-515.

[4-3] N. Amitay and M. J. Gans, "Design of Rectangular Horn Arrays With Oversized Aperture Elements," IEEE Transactions on Antennas and Propagation, Vol. AP-29, November 1981, pp. 871-884.

[4-4] W. Rotman and R. Turner, "Wide-Angle Microwave Lens for Line Source Applications," IEEE Transactions on Antennas and Propagation, Vol. AP-11, November 1963, pp. 623-632.

[4-5] J. B. L. Rao, "Multifocal Three-Dimensional Bootlace Lenses," IEEE Transactions on Antennas and Propagation, Vol. AP-30, November 1982, pp. 1050-1056.

[4-6] S. Silver, Microwave Antennas Theory and Design, MIT Radiation Laboratory Series, Vol. 12, New York: McGraw-Hill, 1949.

[5-1] A. I. Zaghloul and M. R. Chartoff, "Correlation Matrix Solution to Mutual Coupling Between Rectangular Apertures," IEEE International Symposium on Antennas and Propagation, Quebec, June 1980, Digest, pp. 170-173.

[5-2] J. B. Knorr, "Millimeter-Wave Fin-Line Characteristics," IEEE Transactions on Microwave Theory and Techniques, Vol. MTT-28, No. 7, July 1980, p. 737.

[5-3] P. J. Meier, "Integrated Fin-Line Millimeter Components," IEEE Transactions on Microwave Theory and Techniques, Vol. MTT-22, No. 12, December 1974, p. 1209.

[5-4] S. B. Cohn, "Slotline on a Dielectric Substrate," IEEE Transactions on Microwave Theory and Techniques, Vol. MTT-17, October 1969, p. 768-778.

[5-5] P. H. Vartanain et al., "Propagation in Dielectric Slab Loaded Rectangular Waveguide," IRE Transactions on Microwave Theory and Techniques, Vol. MTT-6, April 1958, pp. 215-222.

[5-6] E. J. Denlinger, "A Frequency Dependent Solution for Microstrip Transmission Lines," IEEE Transactions on Microwave Theory and Techniques, Vol. MTT-19, January 1971, pp. 30-39.

[5-7] T. Itoh and R. Mittra, "Spectral-Domain Approach for Calculating the Dispersion Characteristics of Microstrip Lines," IEEE Transactions on Microwave Theory and Techniques, Vol. MTT-21, July 1973, pp. 496-499.

[5-8] R. F. Harrington, Field Computation by Moment Methods, New York: Macmillan Company, 1968.

[5-9] J. B. Davies and D. Mirshekar-Syahkal, "Spectral Domain Solution of Arbitrary Coplanar Transmission Lines With Multilayer Substrate," IEEE Transactions on Microwave Theory and Techniques, Vol. MTT-25, February 1977, pp. 143-146.

[5-10] T. Itoh, "Spectral Domain Emittance Approach for Dispersion Characteristics of Shielded Microstrips with Tuning Septums," 9th European Microwave Conference, Brighton, England, 1979, Proceedings, pp. 435-439.

[5-11] R. H. Jansen, "High Speed Computation of Single and Coupled Microstrip Parameters Including Dispersion, High-Order Modes, Loss and Finite Strip Thickness," IEEE Transactions on Microwave Theory and Techniques, Vol. MTT-26, February 1978, pp. 75-82.

[5-12] T. G. Bryant and J. A. Weiss, "MSTRIP (Parameters of Microstrip)," IEEE Transactions on Microwave Theory and Techniques, Vol. MTT-19, April 1971, pp. 418-419.

[5-13] J. B. Knorr and P. M. Shayda, "Millimeter-Wave Fin-Line Characteristics," IEEE Transactions on Microwave Theory and Techniques, Vol. MTT-28, July 1980, pp. 737-743.

[5-14] R. H. Jansen, "Unified User-Oriented Computation of Shielded, Covered, and Open Planar Microwave and Millimeter-Wave Transmission-Line Characteristics," IEE Microwaves, Optics, and Acoustics, Vol. 3, January 1979, pp. 14-22.

[5-15] S. B. Cohn, "Slot Line on a Dielectric Substrate," IEEE Transactions on Microwave Theory and Techniques, Vol. MTT-17, October 1969, pp. 768-778.

[5-16] E. C. Jordan and K. G. Balmain, Electromagnetic Waves and Radiating Systems, Englewood Cliffs, NJ: Prentice-Hall, 1968.

[5-17] J. H. C. Van Heuven, "A New Integrated Waveguide-Microstrip Transition," IEEE Transactions on Microwave Theory and Techniques, Vol. MTT-24, No. 3, March 1976, pp. 144-146.

[5-18] W. J. Getsinger, Private communication.

[5-19] P. J. Meier, "Integrated Fin-Line Millimeter Components," IEEE Transactions on Microwave Theory and Techniques, Vol. MTT-22, No. 12, December 1974, pp. 1209-1216.

[5-20] N. Nagai, "New n-Way Hybrid Power Dividers," MTT Symposium Digest, 1977, pp. 503-505.

[5-21] M. Cohn, B. Geller, and J. Schellenberg, "A 10-Watt Broadband FET Combiner/Amplifier," MTT Symposium Digest, 1975, pp. 292-297.

[5-22] H. Yamaski, J. Schellenberg, and Z. Lemnios, "A Unique Approach to K_u-Band Power FETs," Electron Devices Meeting Digest, 1980, pp. 110-113.

APPENDIX A. MEASURED ELEMENT PATTERNS IN ARRAY ENVIRONMENT

This appendix contains plots of the radiation patterns measured for different elements in the 14-element array shown in Figure 5-17. The elements are horn 1, representing an edge element; horn 10, representing a central element; and a single horn representing an isolated element. Both vertical and horizontal polarizations were measured for horns 1 and 10; and E-plane patterns, H-plane patterns, and 45° cuts are included for all three elements. Co- and cross-polarized patterns are shown. The measurements were performed at 11.7, 11.95, and 12.2 GHz.

Figures A-1 through A-12 show the measured patterns for vertically polarized edge element 1, as follows:

- Figures A-1 to A-3 show the E-plane patterns at 11.7, 11.95, and 12.2 GHz, respectively.
- Figures A-4 to A-6 show the H-plane patterns at the same three frequencies.
- Figures A-7 to A-12 show the 45°-plane patterns at the three frequencies. For this plane, the co- and cross-pol patterns are shown on consecutive figures for each frequency.

Figures A-13 through A-24 show the measured pattern for horizontally polarized edge element 1, as follows:

- Figures A-13 to A-15 show the E-plane patterns at 11.7, 11.95, and 12.2 GHz, respectively.
- Figures A-16 to A-18 show the H-plane patterns at the same three frequencies.
- Figures A-19 to A-24 show the 45°-plane patterns at the three frequencies. The co- and cross-pol patterns are shown on consecutive figures for each frequency.

Figures A-25 through A-36 show the measured patterns for vertically polarized central element 10, as follows:

- Figures A-25 to A-27 show the E-plane patterns at 11.7, 11.95, and 12.2 GHz, respectively.
- Figures A-28 to A-30 show the H-plane patterns at the same three frequencies.
- Figures A-31 to A-36 show the 45°-plane patterns at the three frequencies. For this plane, the co- and cross-pol patterns are shown on consecutive figures for each frequency.

Figures A-37 through A-48 show the measured patterns for horizontally polarized central element 10, as follows:

- Figures A-37 to A-39 show the E-plane pattern at 11.7, 11.95, and 12.2 GHz, respectively.
- Figures A-40 to A-42 show the H-plane patterns at the same three frequencies.
- Figures A-43 to A-48 show the 45°-plane patterns at the three frequencies. For this plane, the co- and cross-pol patterns are shown on consecutive figures for each frequency.

Figures A-49 through A-60 show the measured patterns for the isolated element, as follows:

- Figures A-49 to A-51 show the E-plane patterns at 11.7, 11.95, and 12.2 GHz, respectively.
- Figures A-52 to A-54 show the H-plane patterns at the same three frequencies.
- Figures A-55 to A-60 show the 45°-plane patterns at the three frequencies. For this plane, the co- and cross-pol patterns are shown on consecutive figures for each frequency.

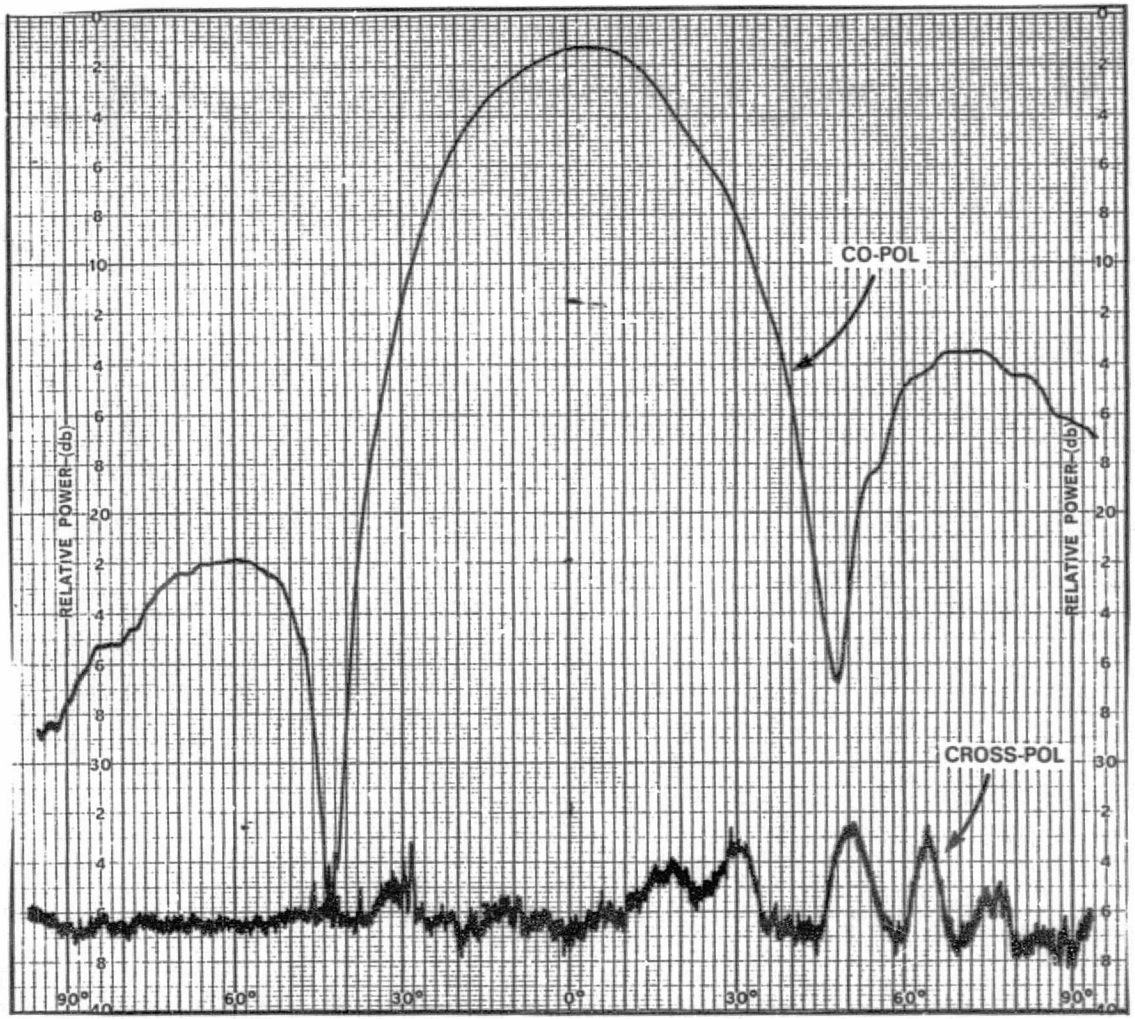

Figure A-1. E-Plane Pattern for Vertically Polarized Element 1 at 11.7 GHz

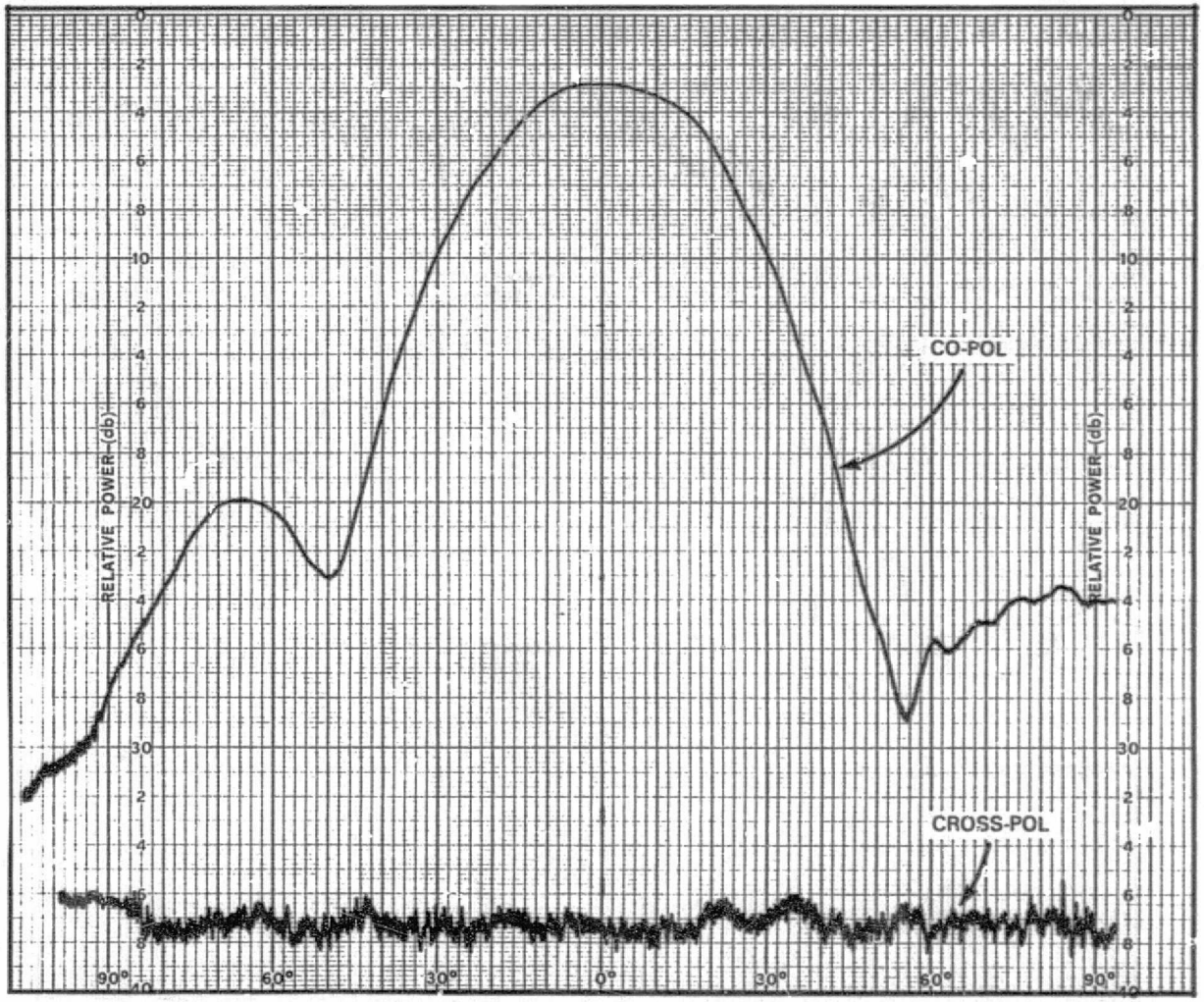

Figure A-2. E-Plane Pattern for Vertically Polarized Element 1 at 11.95 GHz

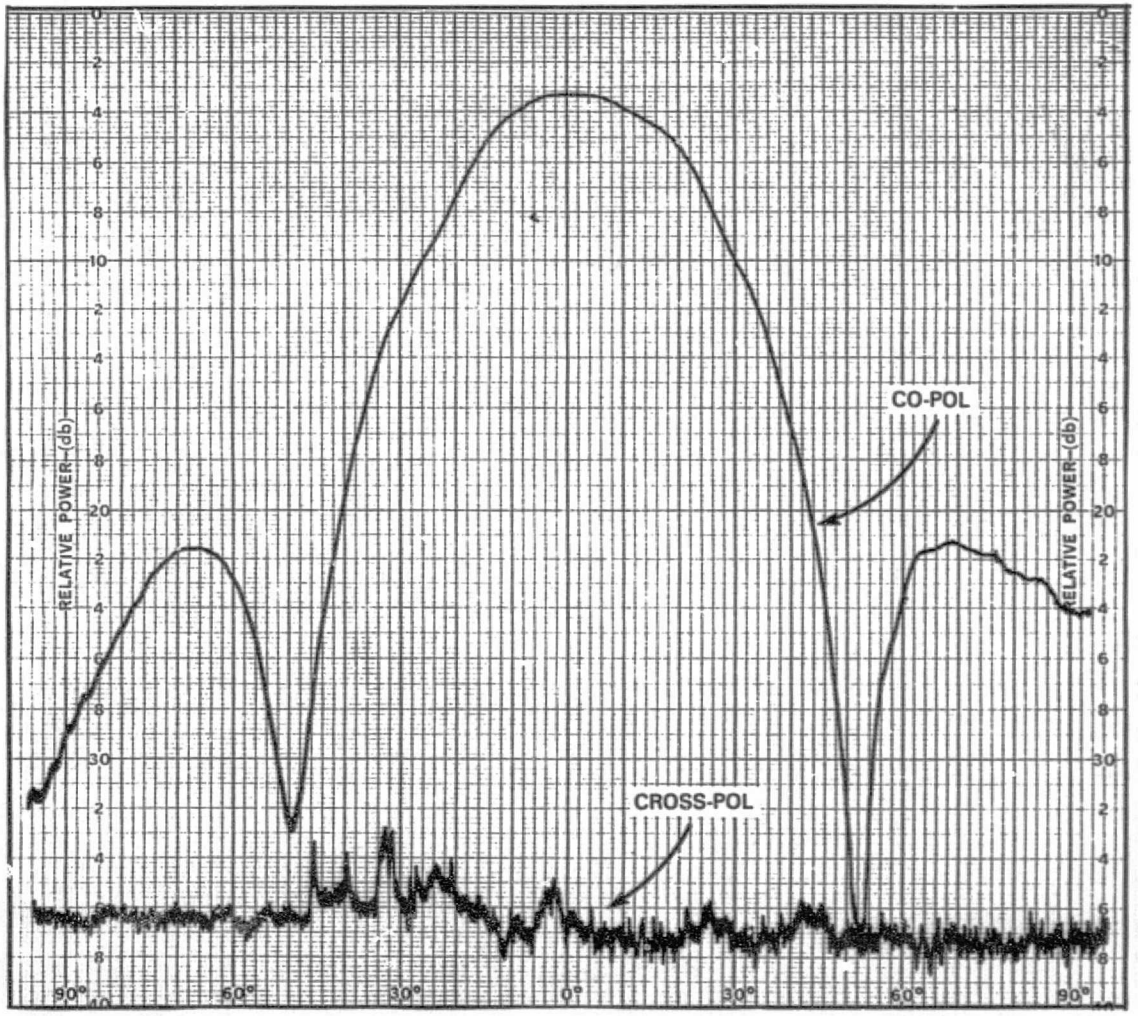

Figure A-3. E-Plane Pattern for Vertically Polarized Element 1 at 12.2 GHz

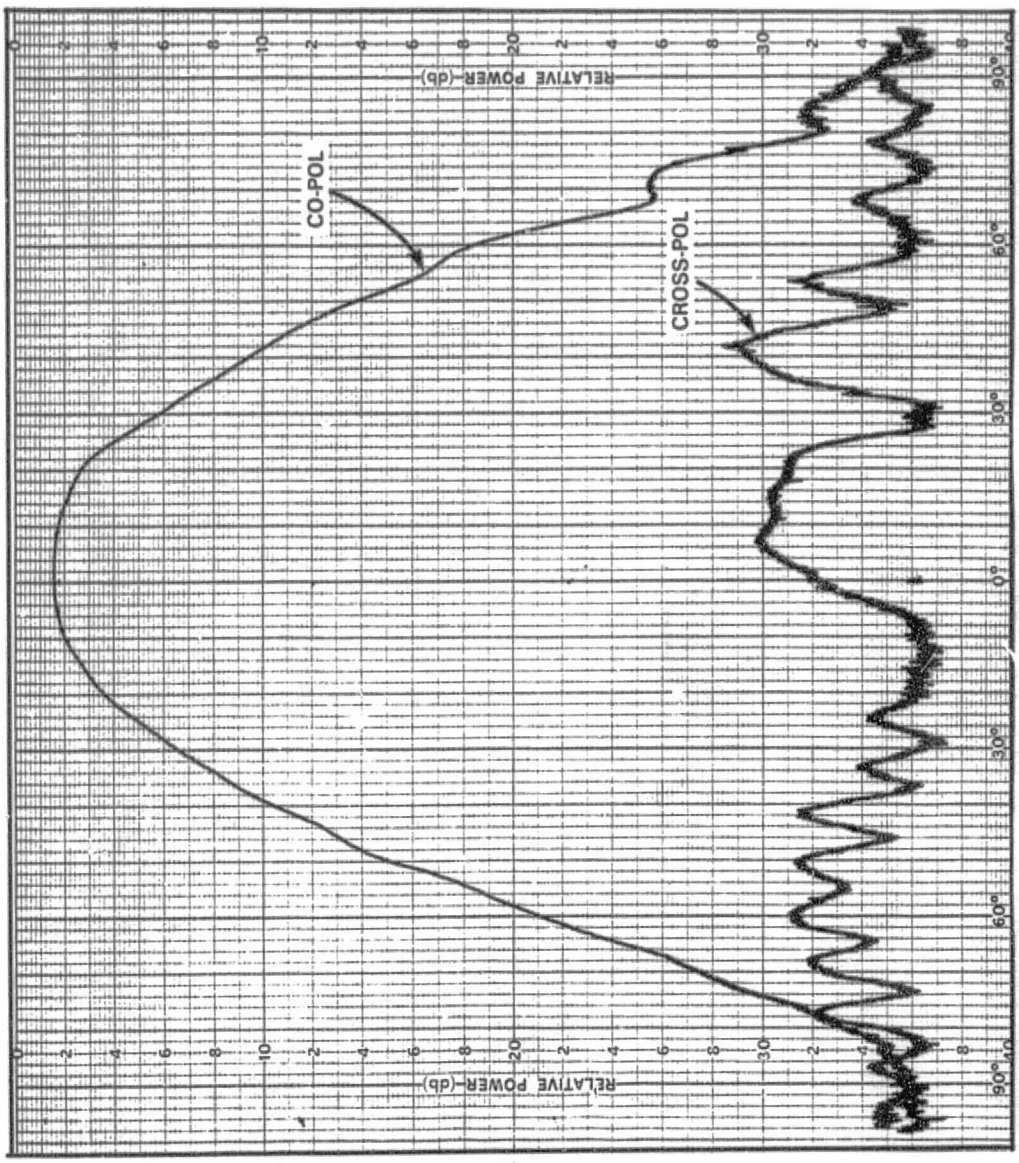

Figure A-4. H-Plane Pattern for Vertically Polarized Element 1 at 11.7 GHz

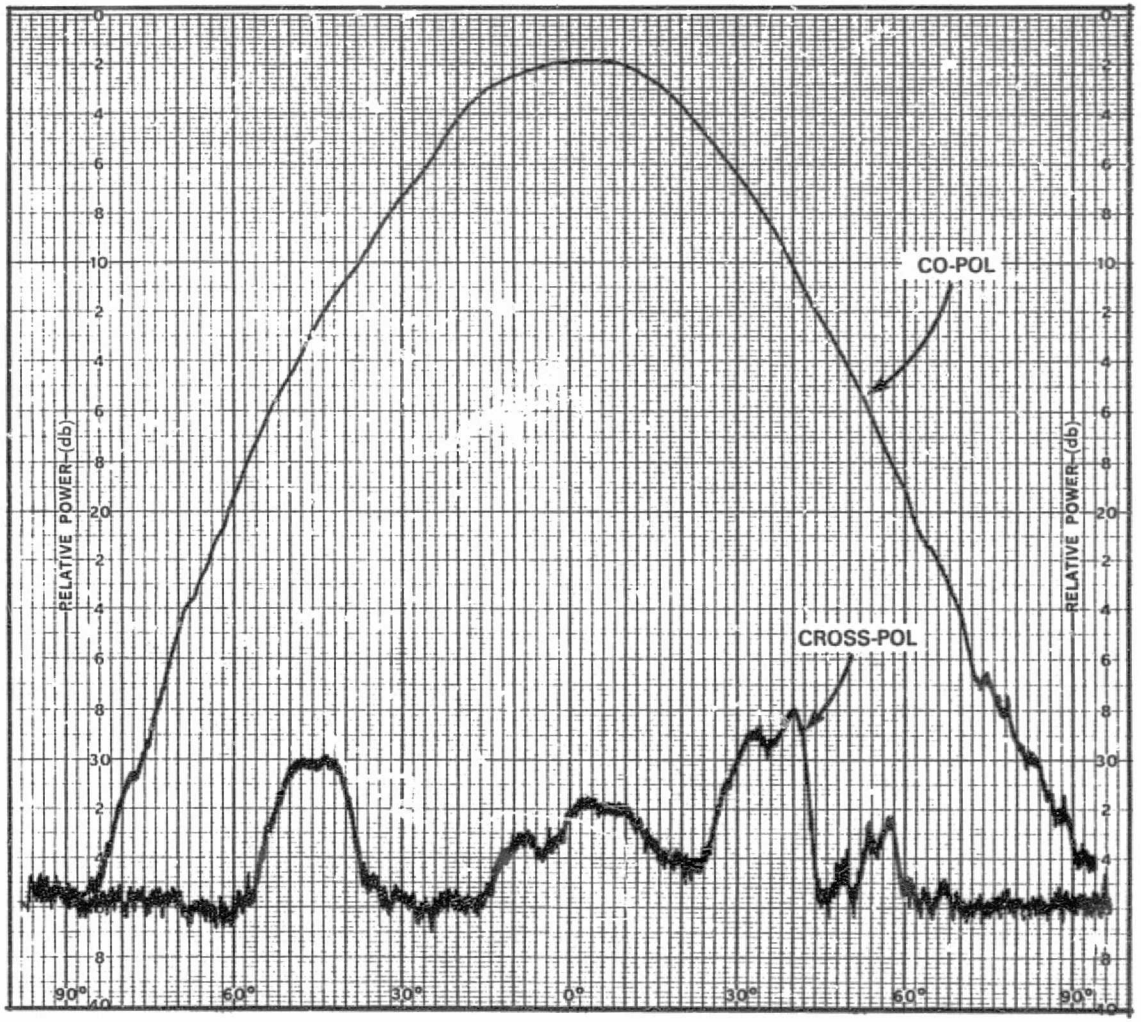

Figure A-5. H-Plane Pattern for Vertically Polarized Element 1 at 11.95 GHz

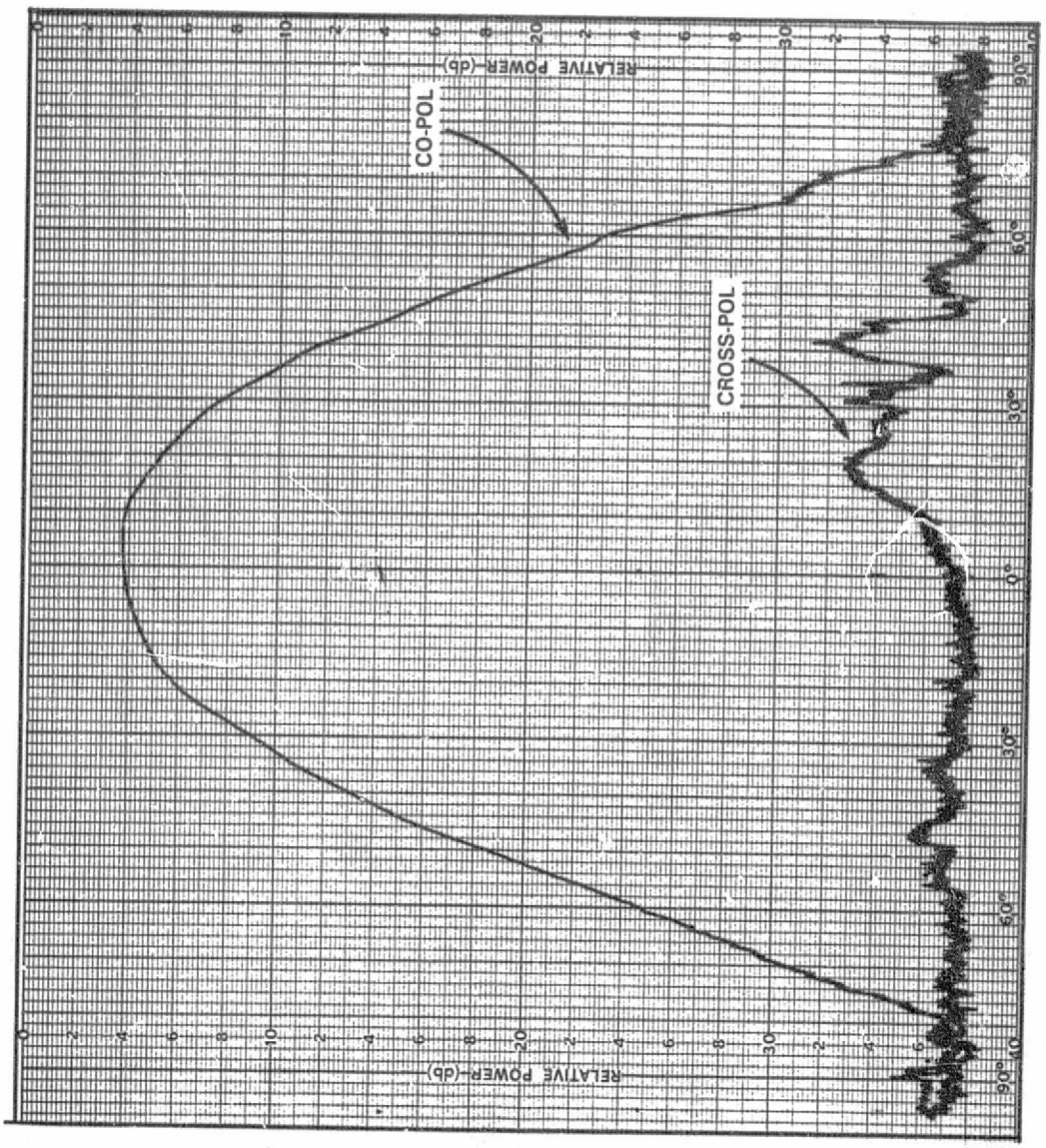

Figure A-6. H-Plane Pattern for Vertically Polarized Element 1 at 12.2 GHz

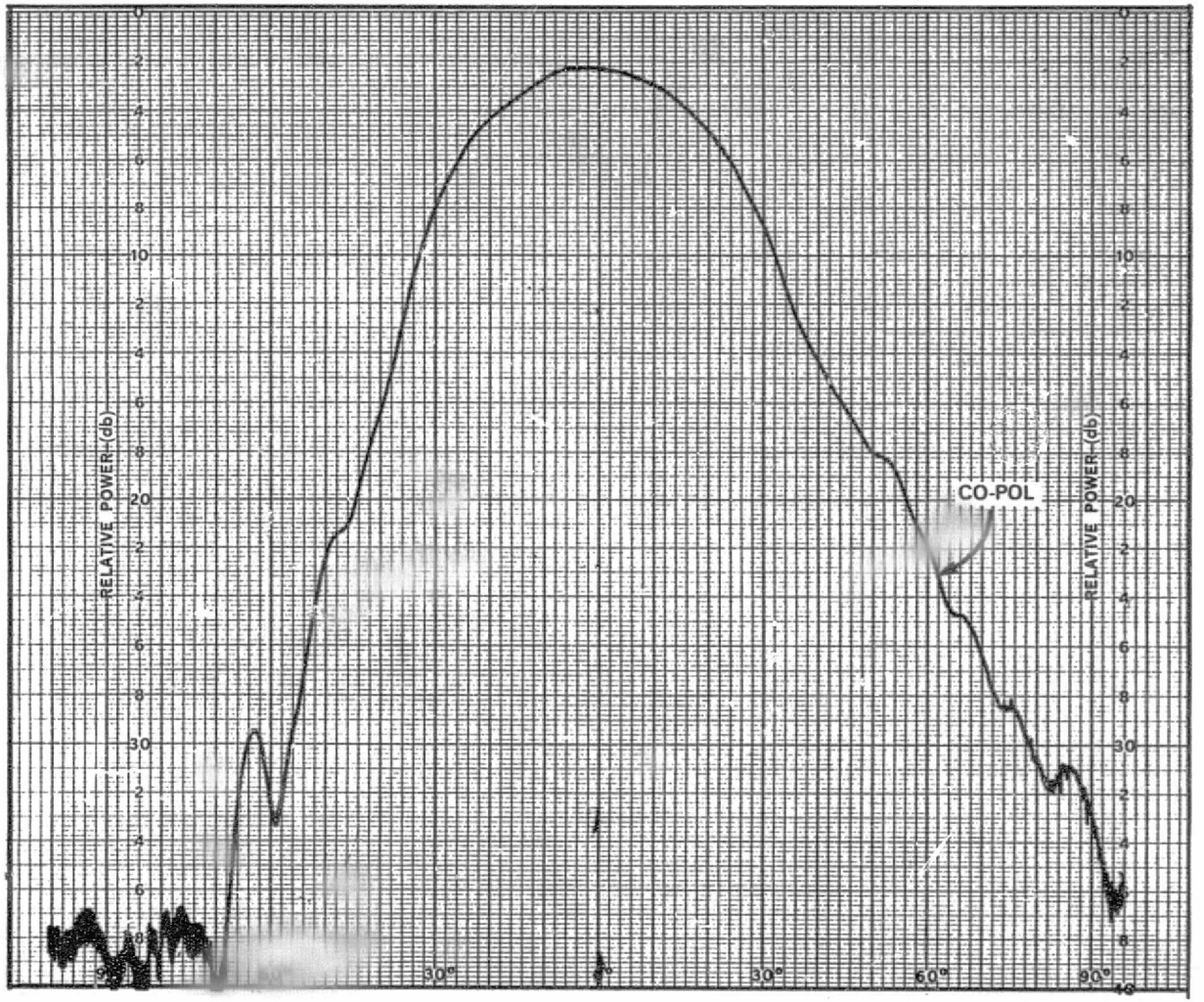

Figure A-7. Co-Pol 45°-Plane Pattern for Vertically Polarized Element 1 at 11.7 GHz

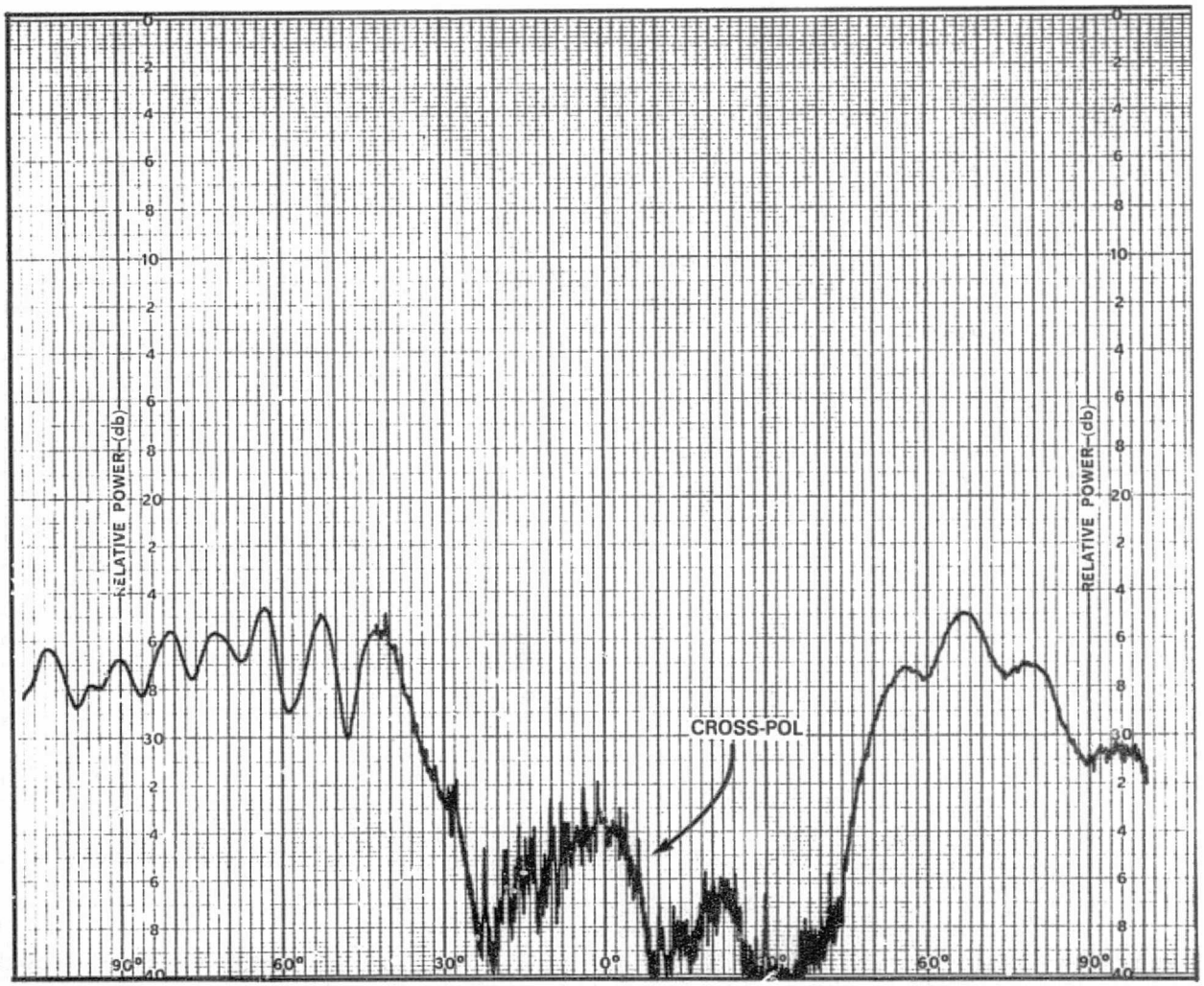

Figure A-8. Cross-Pol 45°-Plane Pattern for Vertically Polarized Element 1 at 11.7 GHz

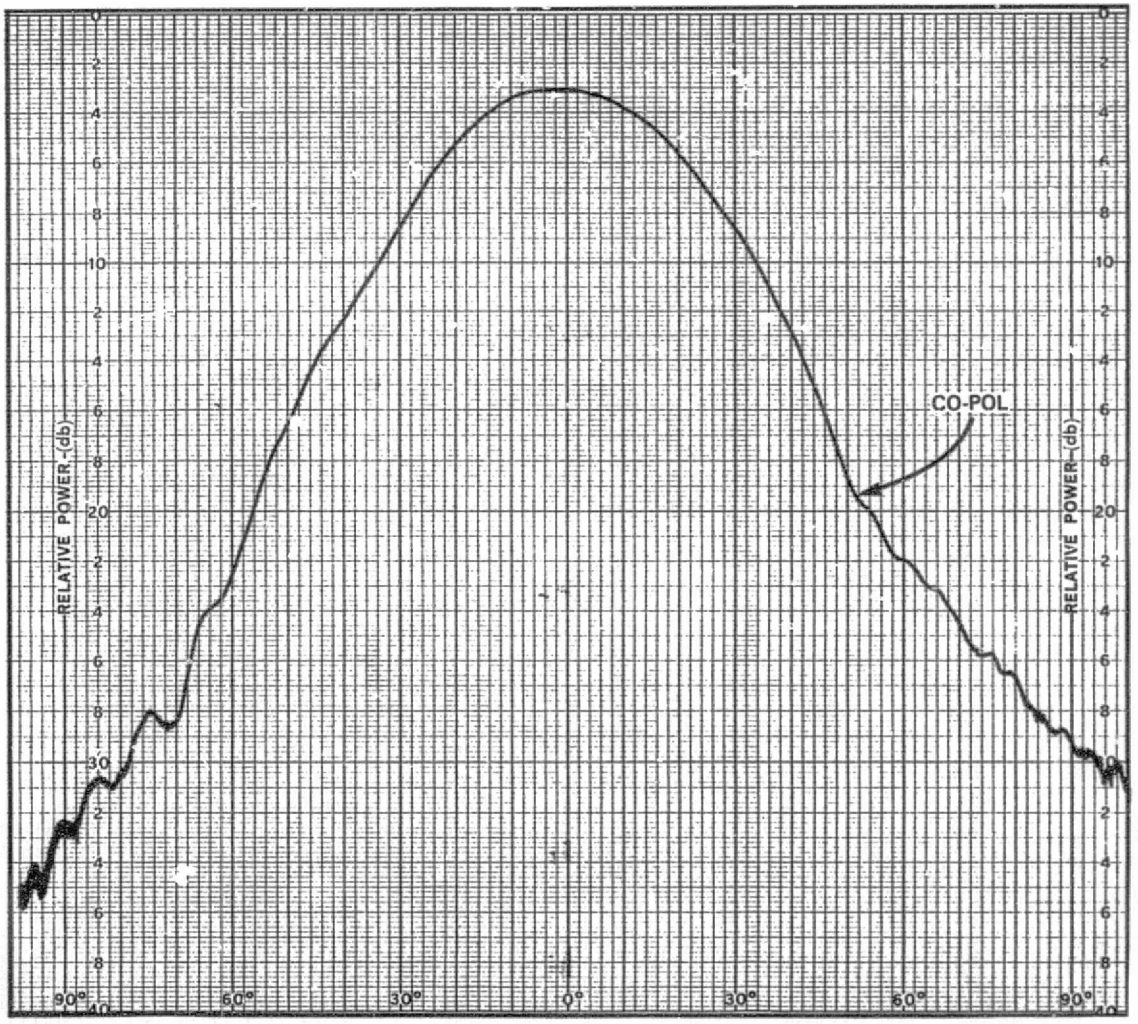

Figure A-9. Co-Pol 45°-Plane Pattern for Vertically Polarized Element 1 at 11.95 GHz

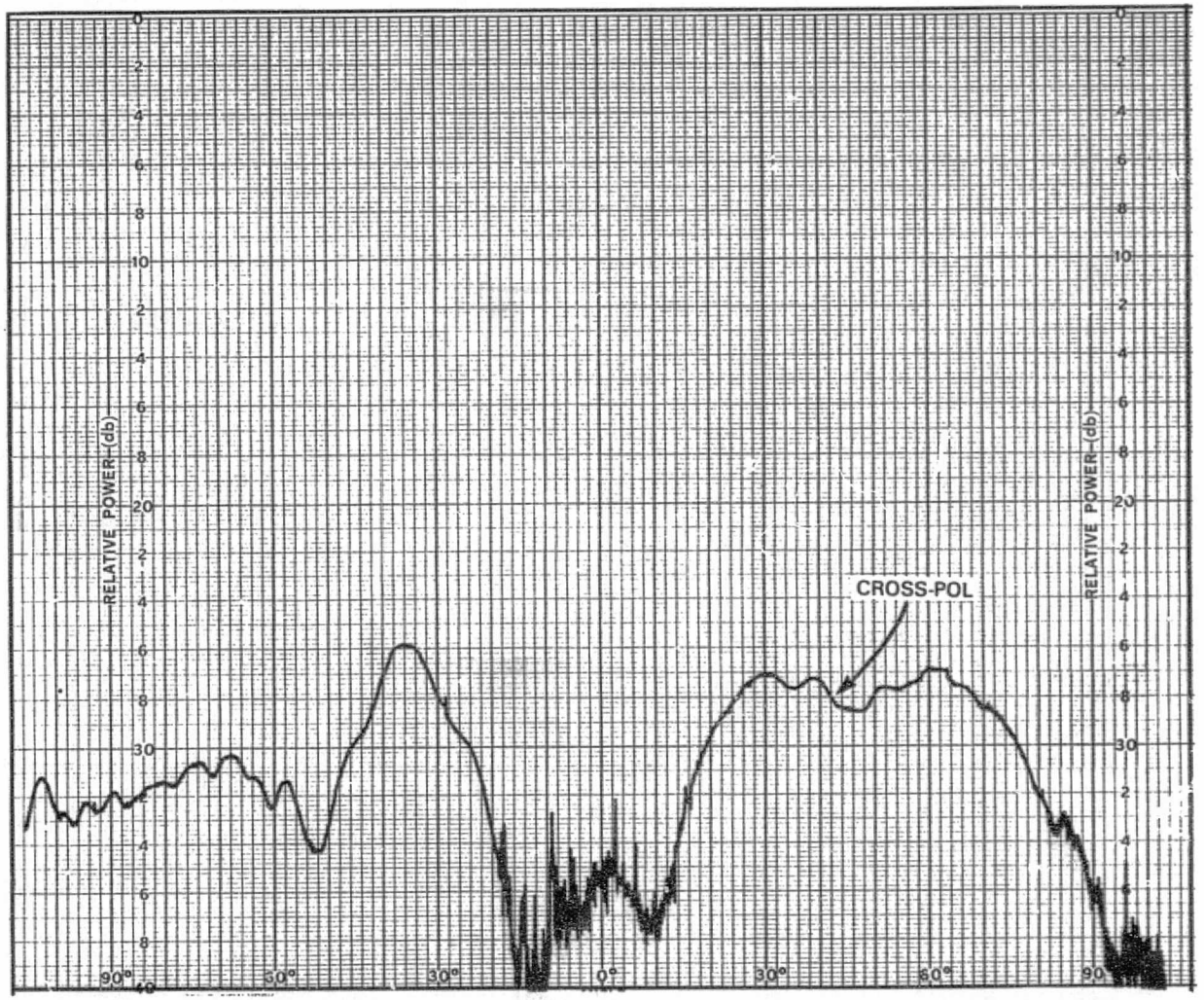

Figure A-10. Cross-Pol 45°-Plane Pattern for Vertically Polarized Element 1 at 11.95 GHz

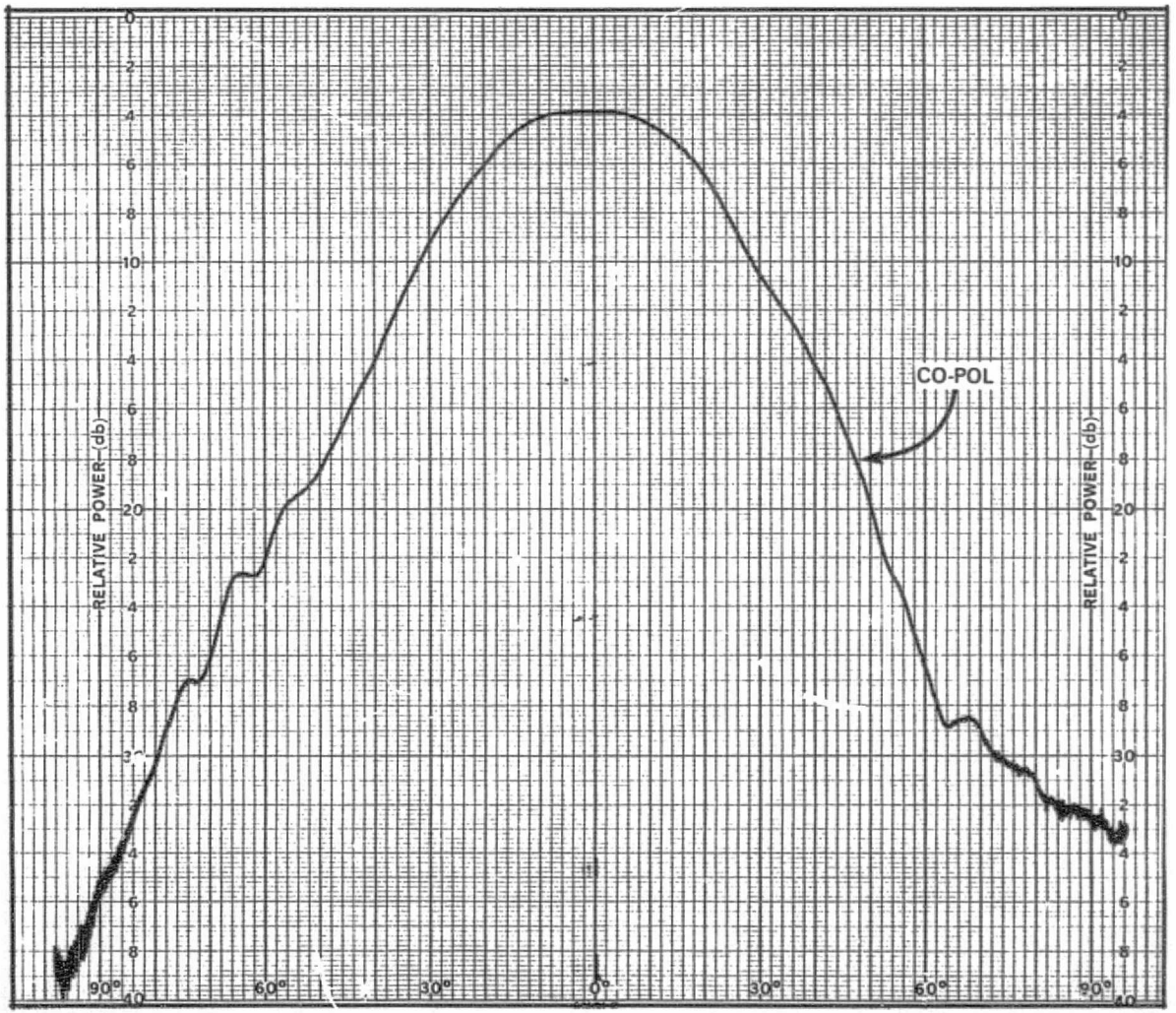

Figure A-11. Co-Pol 45°-Plane Pattern for Vertically Polarized Element 1 at 12.2 GHz

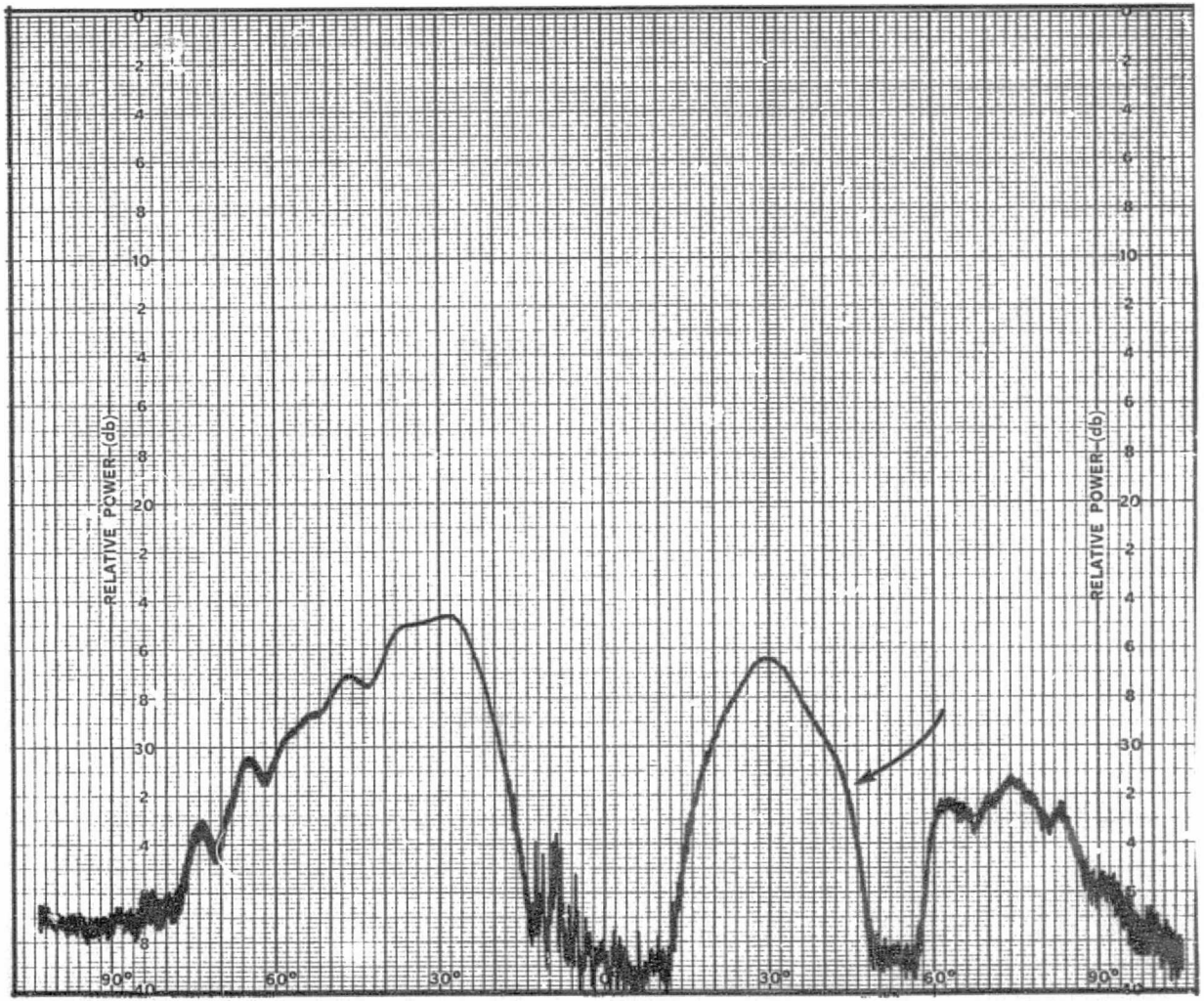

Figure A-12. Cross-Pol 45°-Plane Pattern for Vertically Polarized Element 1 at 12.2 GHz

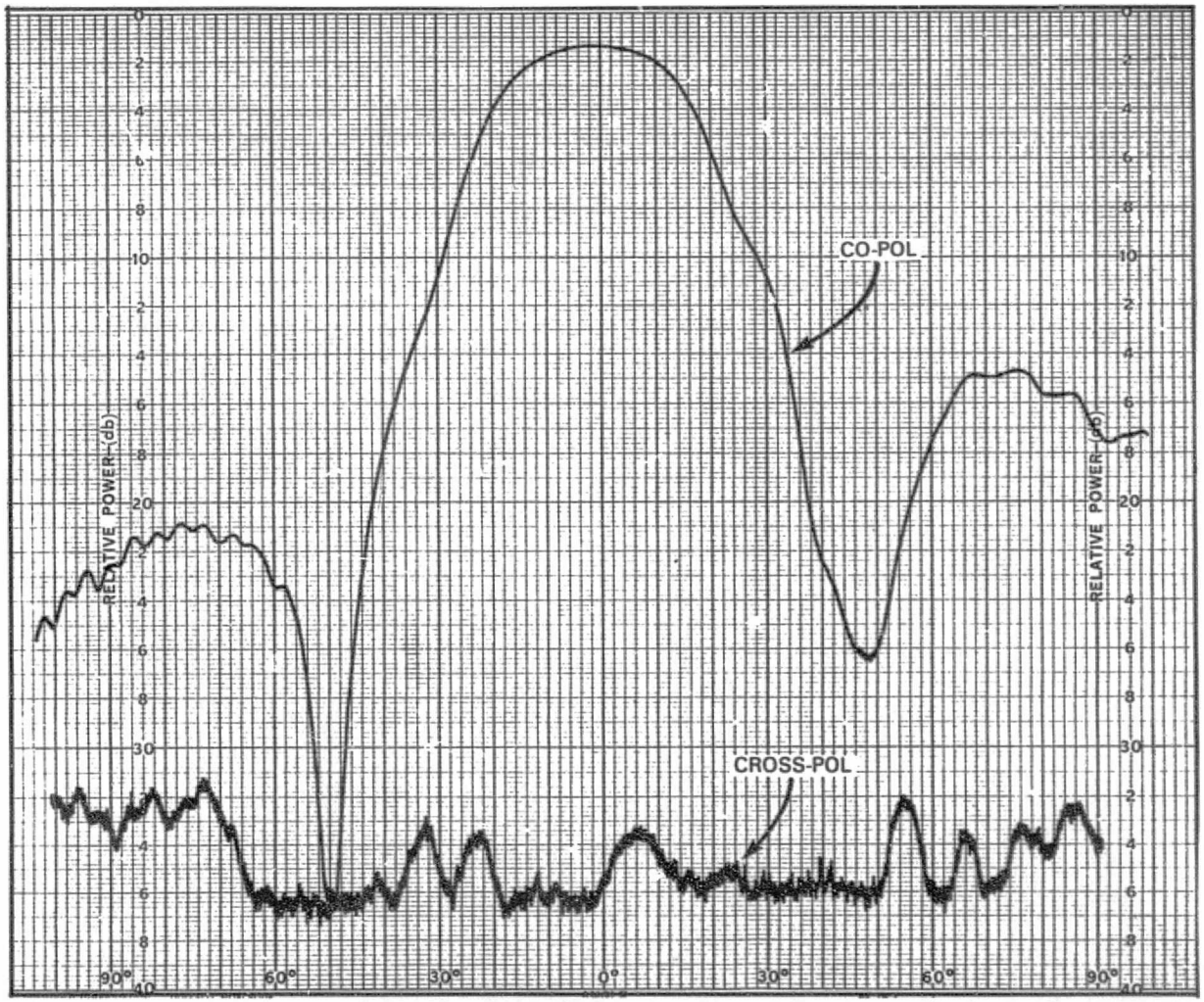

Figure A-13. E-Plane Pattern for Horizontally Polarized Element 1 at 11.7 GHz

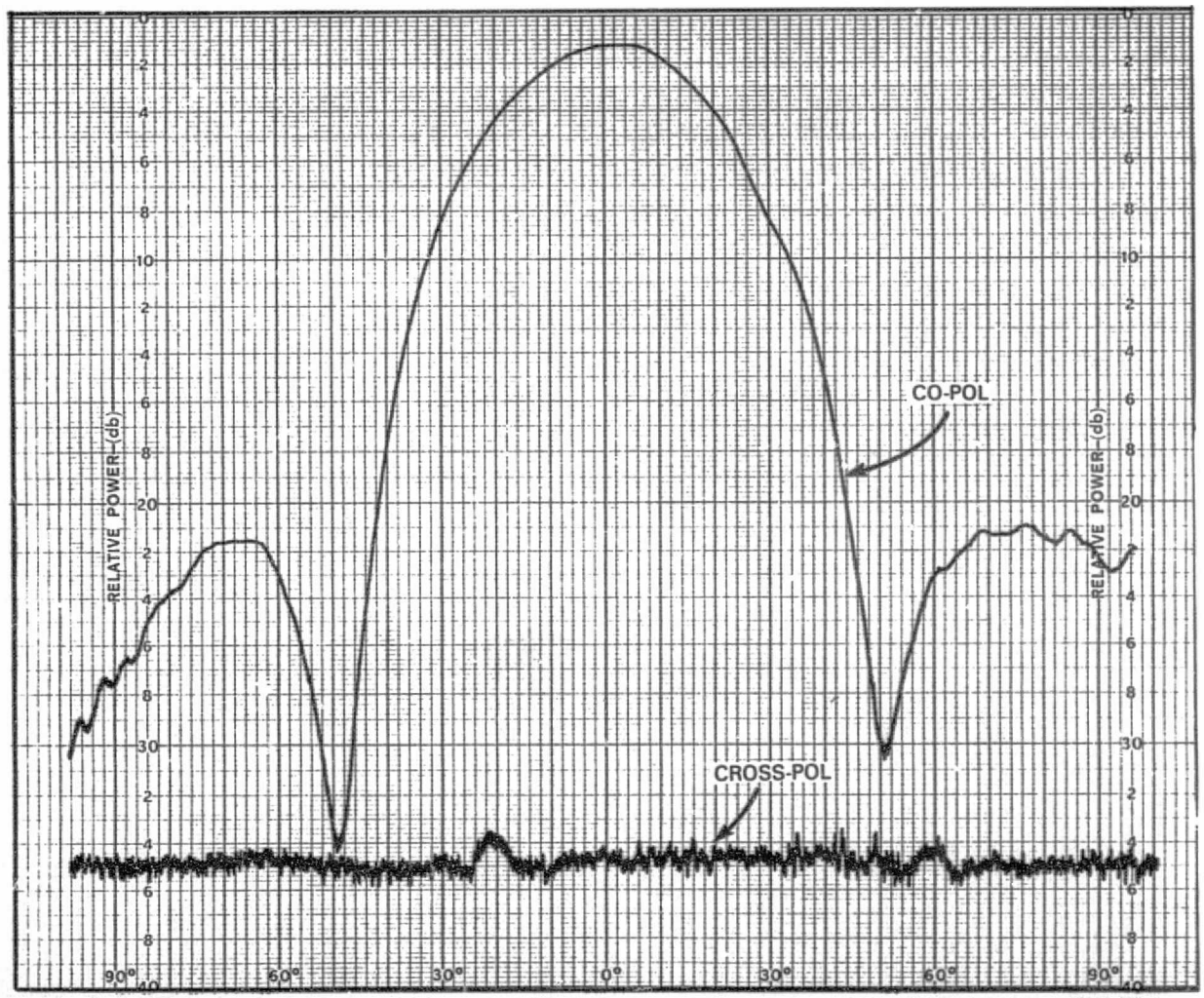

Figure A-14. E-Plane Pattern for Horizontally Polarized Element 1 at 11.95 GHz

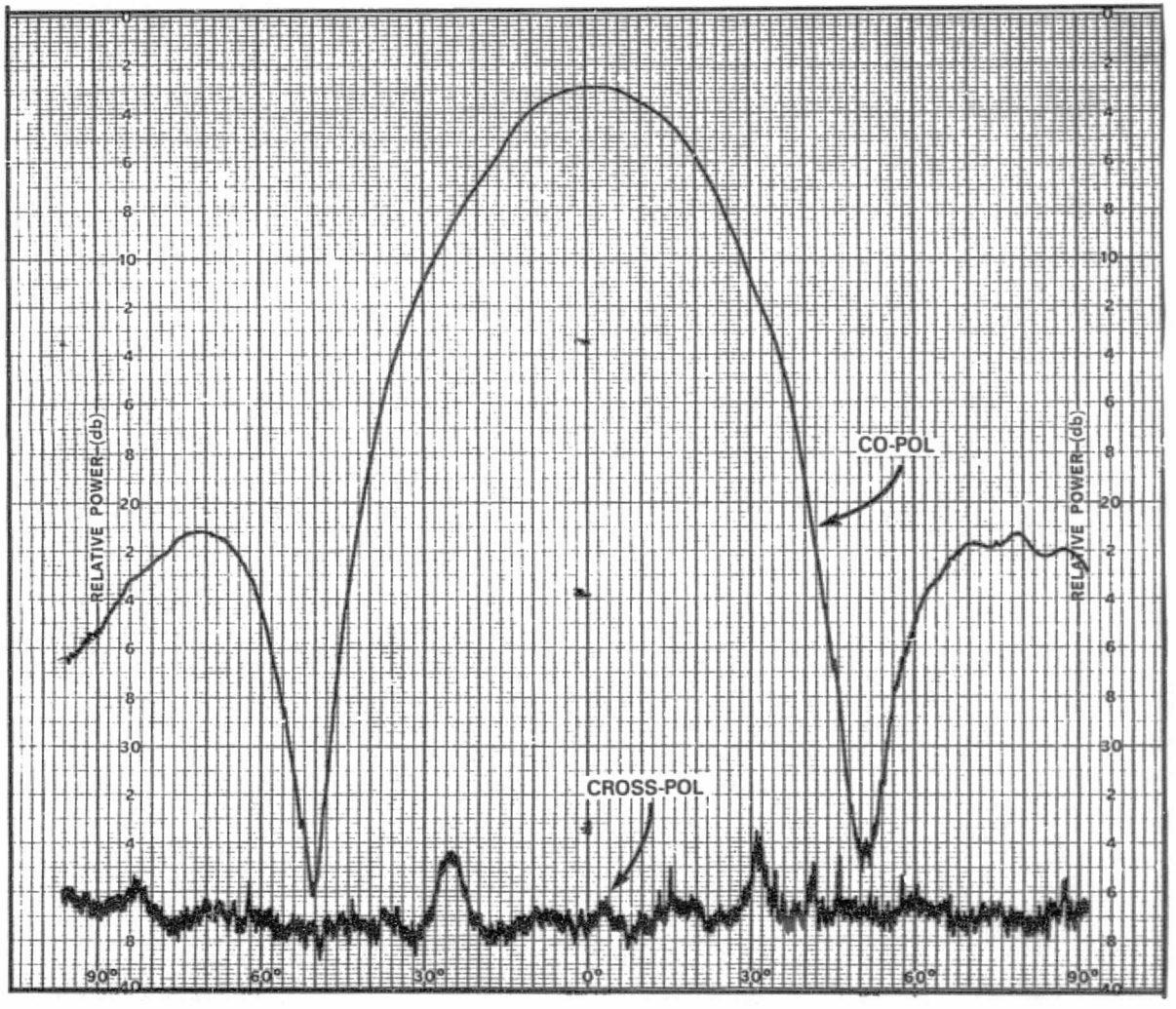

Figure A-15. E-Plane Pattern for Horizontally Polarized Element 1 at 12.2 GHz

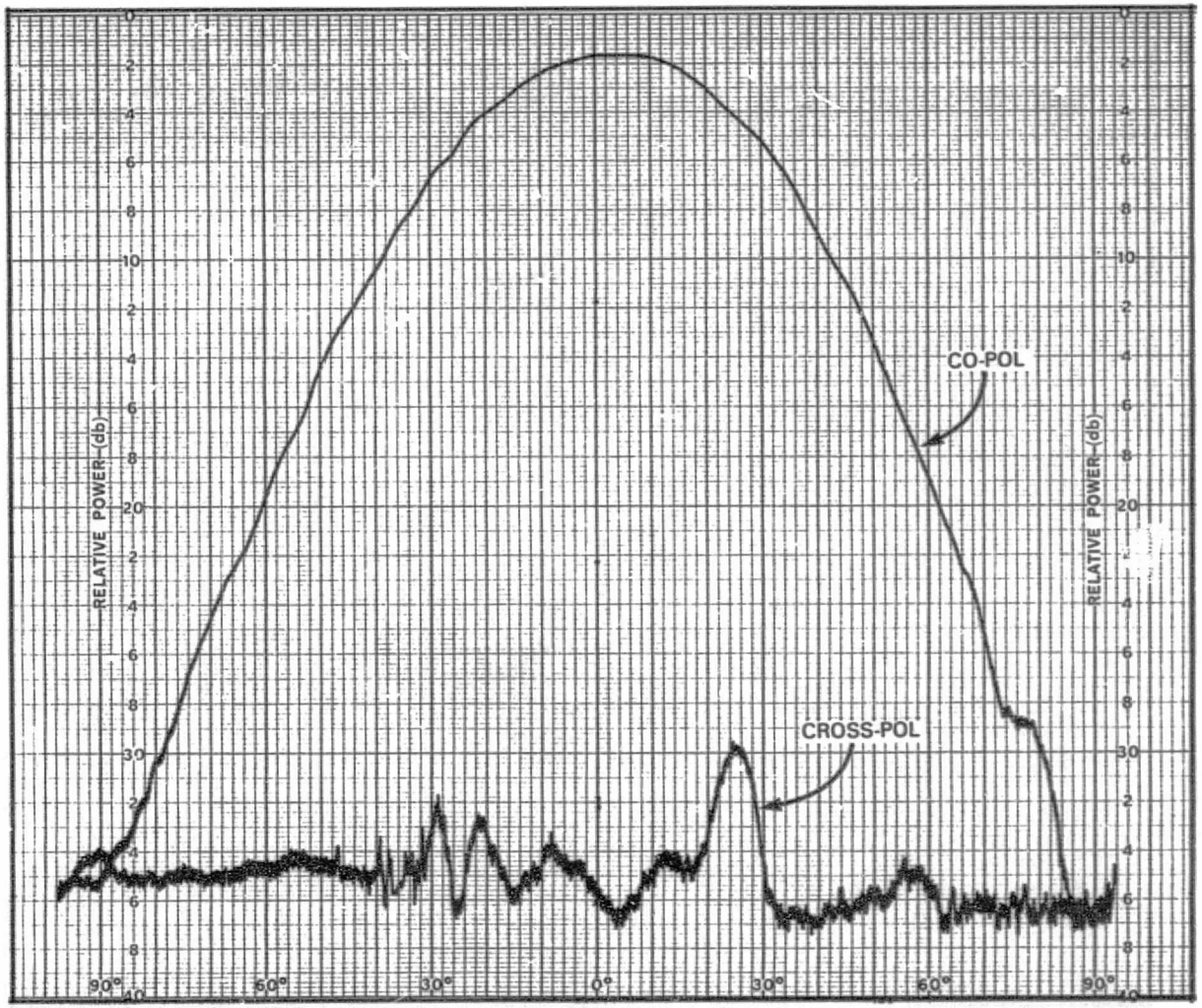

Figure A-16. H-Plane Pattern for Horizontally Polarized Element 1 at 11.7 GHz

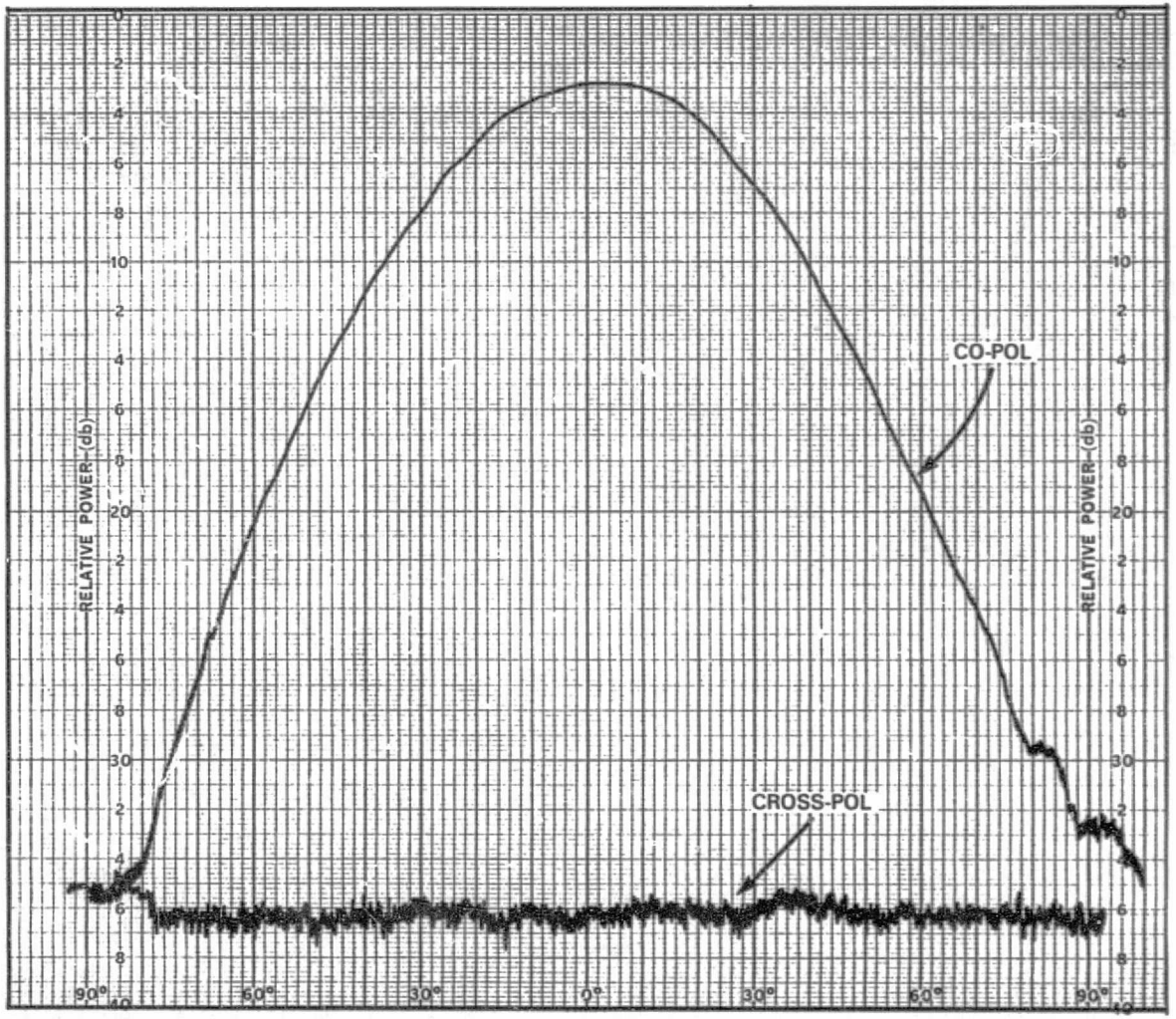

Figure A-17. H-Plane Pattern for Horizontally Polarized Element 1 at 11.95 GHz

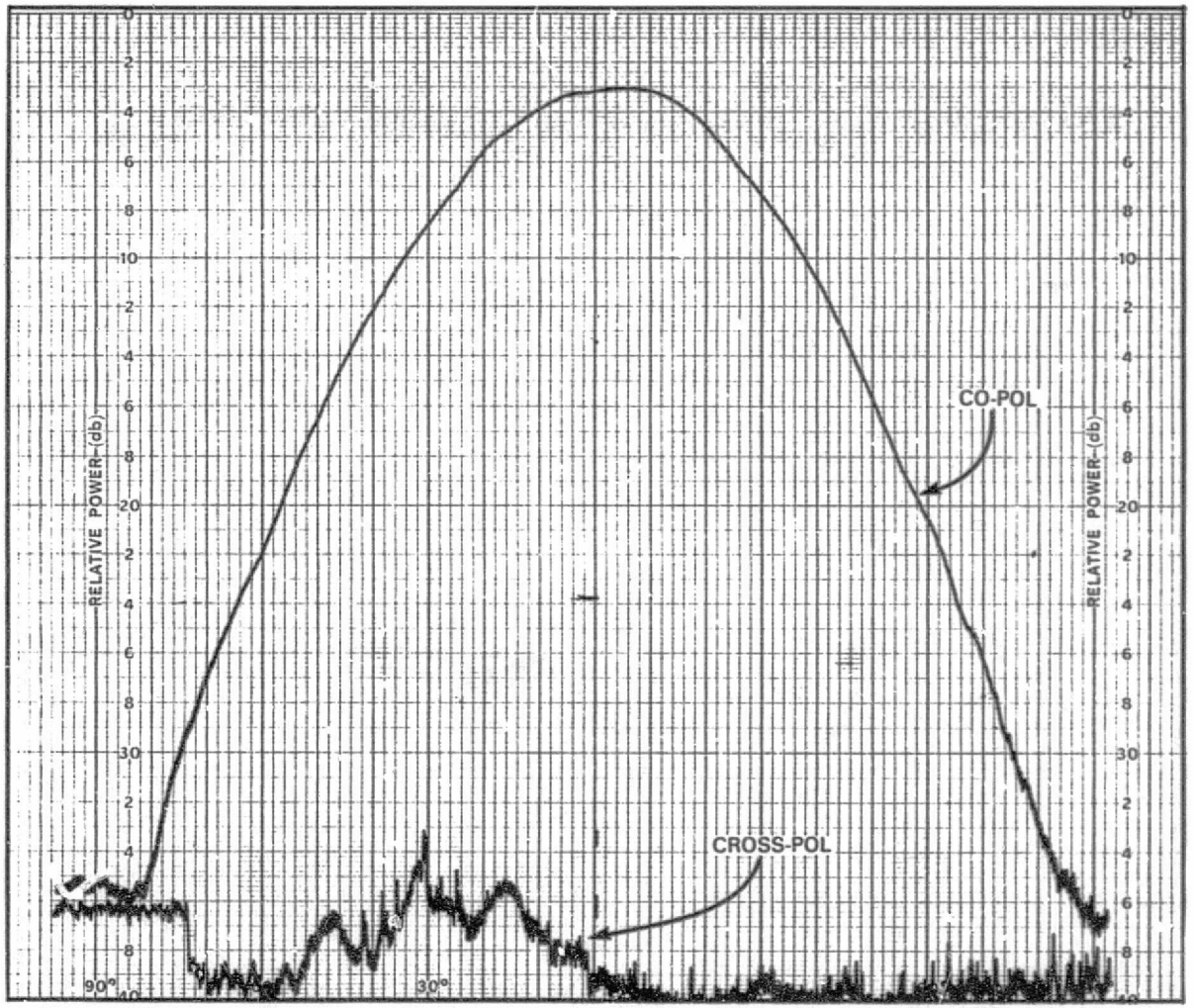

Figure A-18. H-Plane Pattern for Horizontally Polarized Element 1 at 12.2 GHz

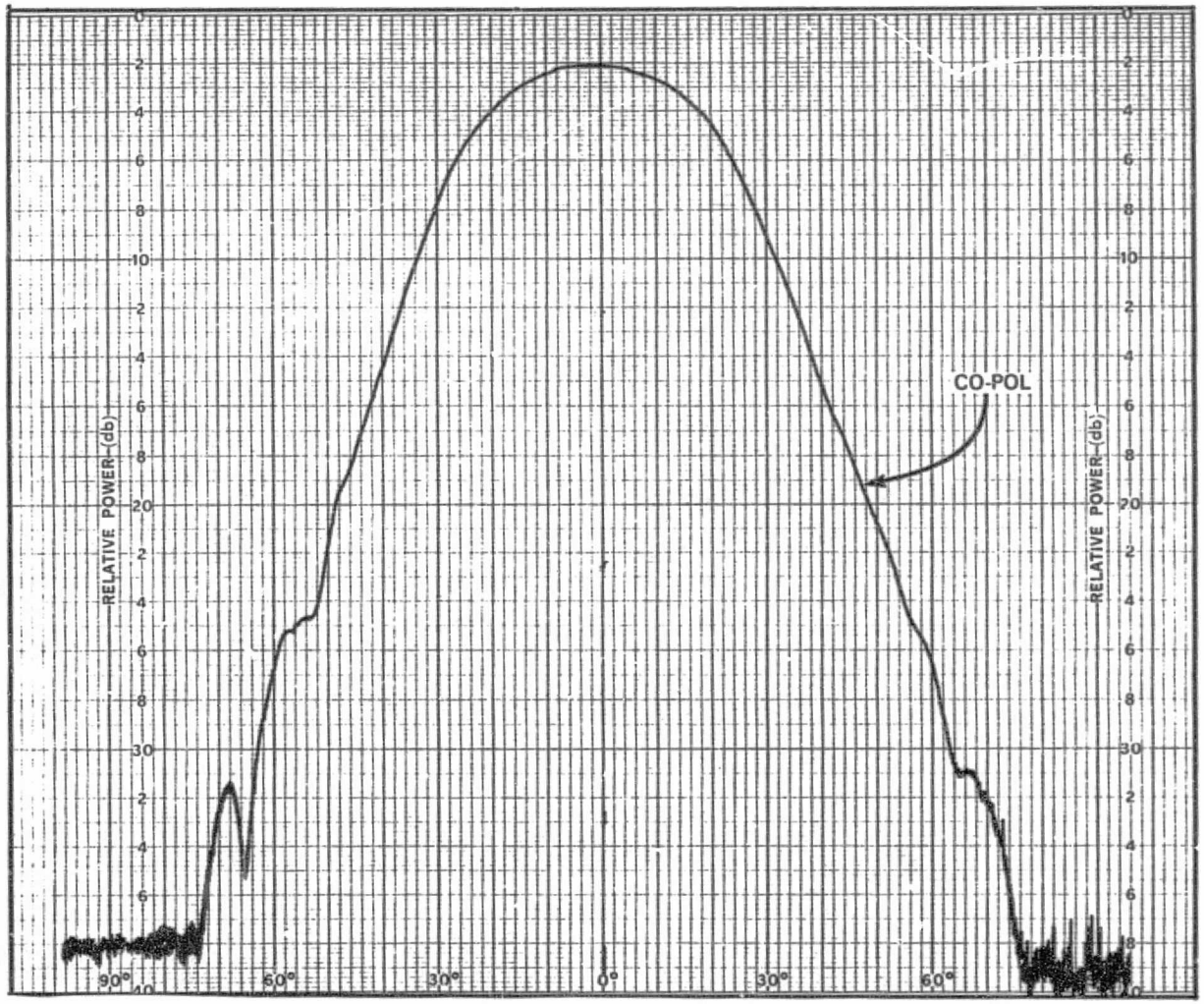

Figure A-19. Co-Pol 45°-Plane Pattern for Horizontally Polarized Element 1 at 11.7 GHz

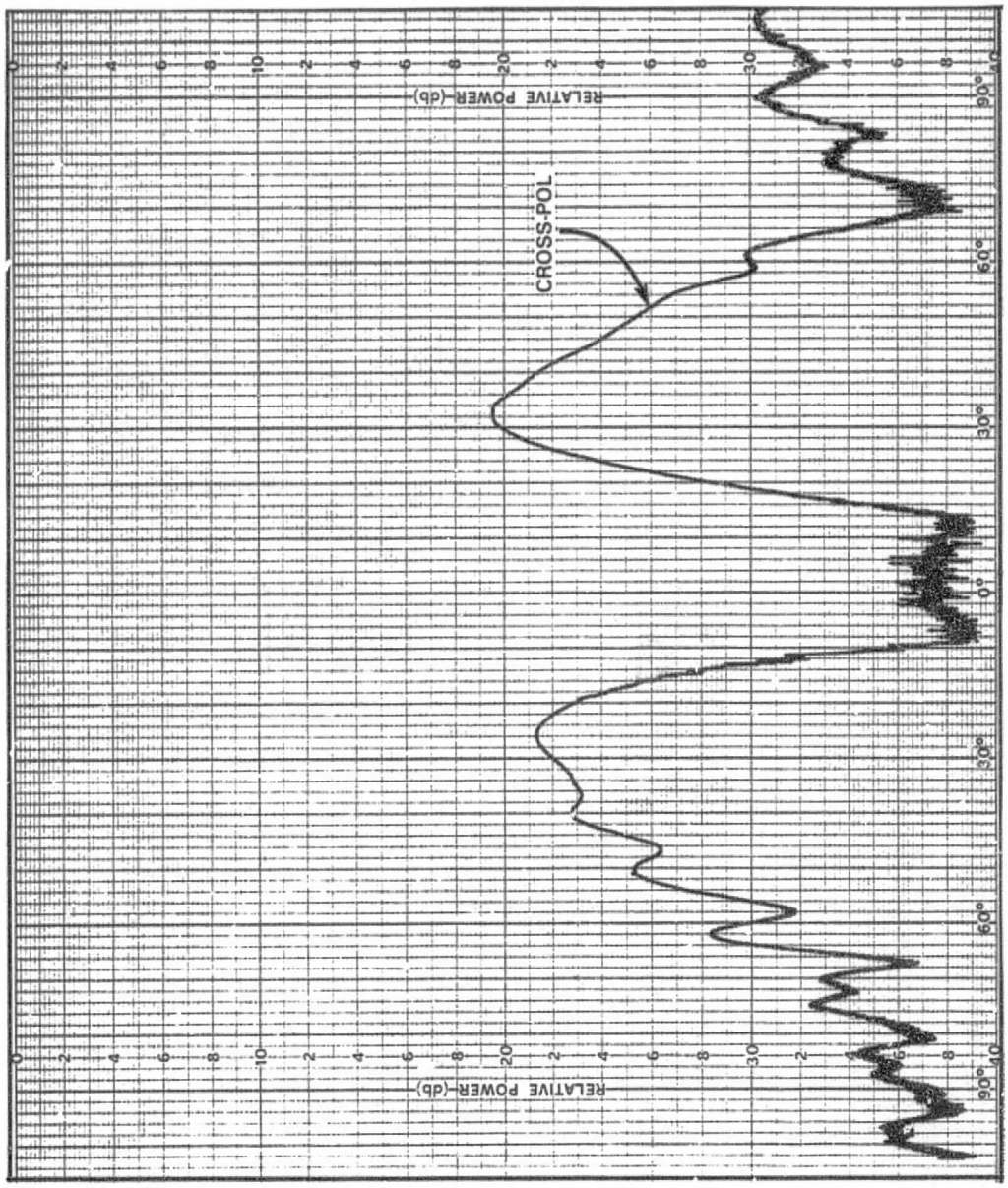

Figure A-20. Cross-Pol 45°-Plane Pattern for Horizontally Polarized Element 1 at 11.7 GHz

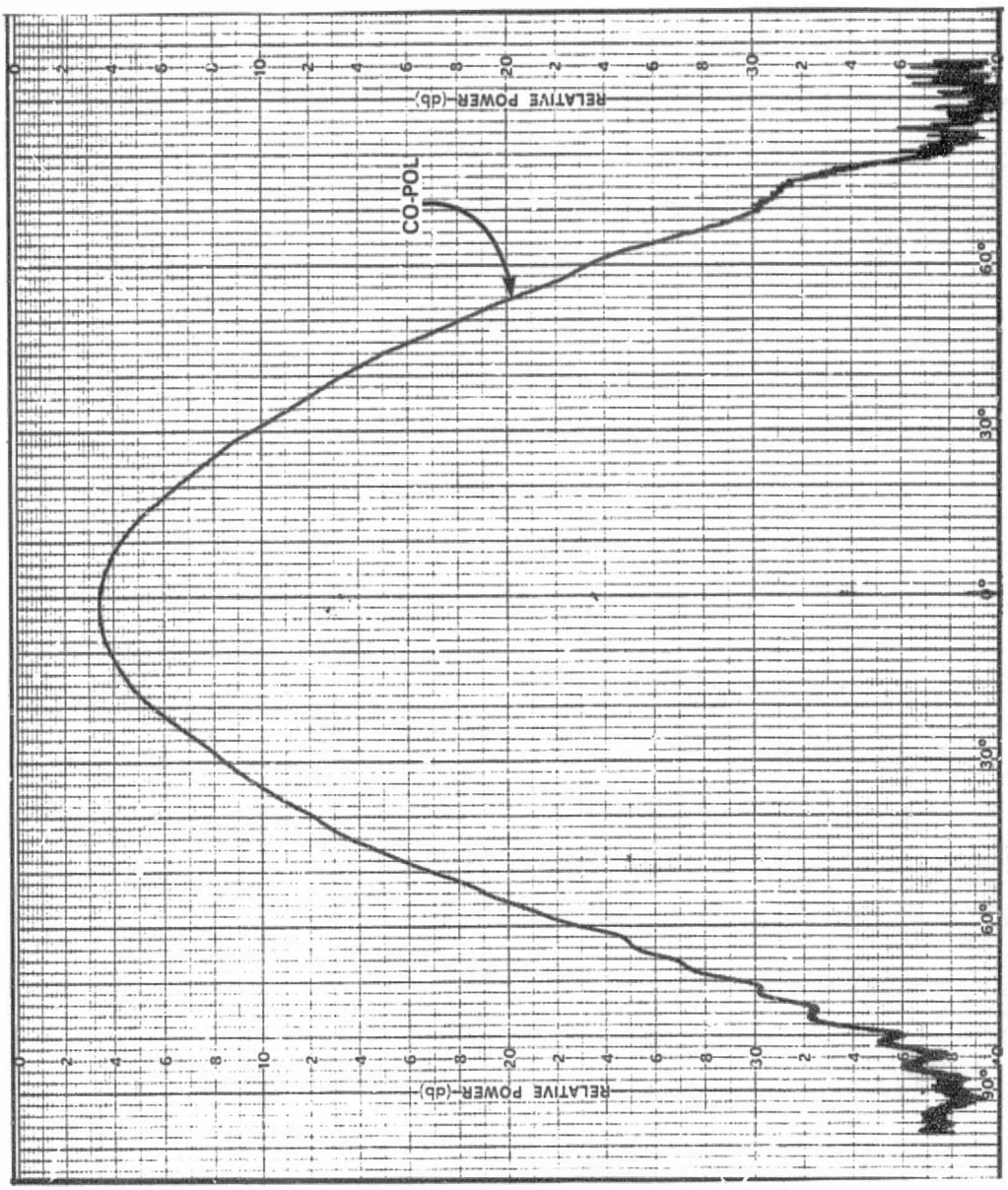

Figure A-21. Co-Pol 45°-Plane Pattern for Horizontally Polarized Element 1 at 11.95 GHz

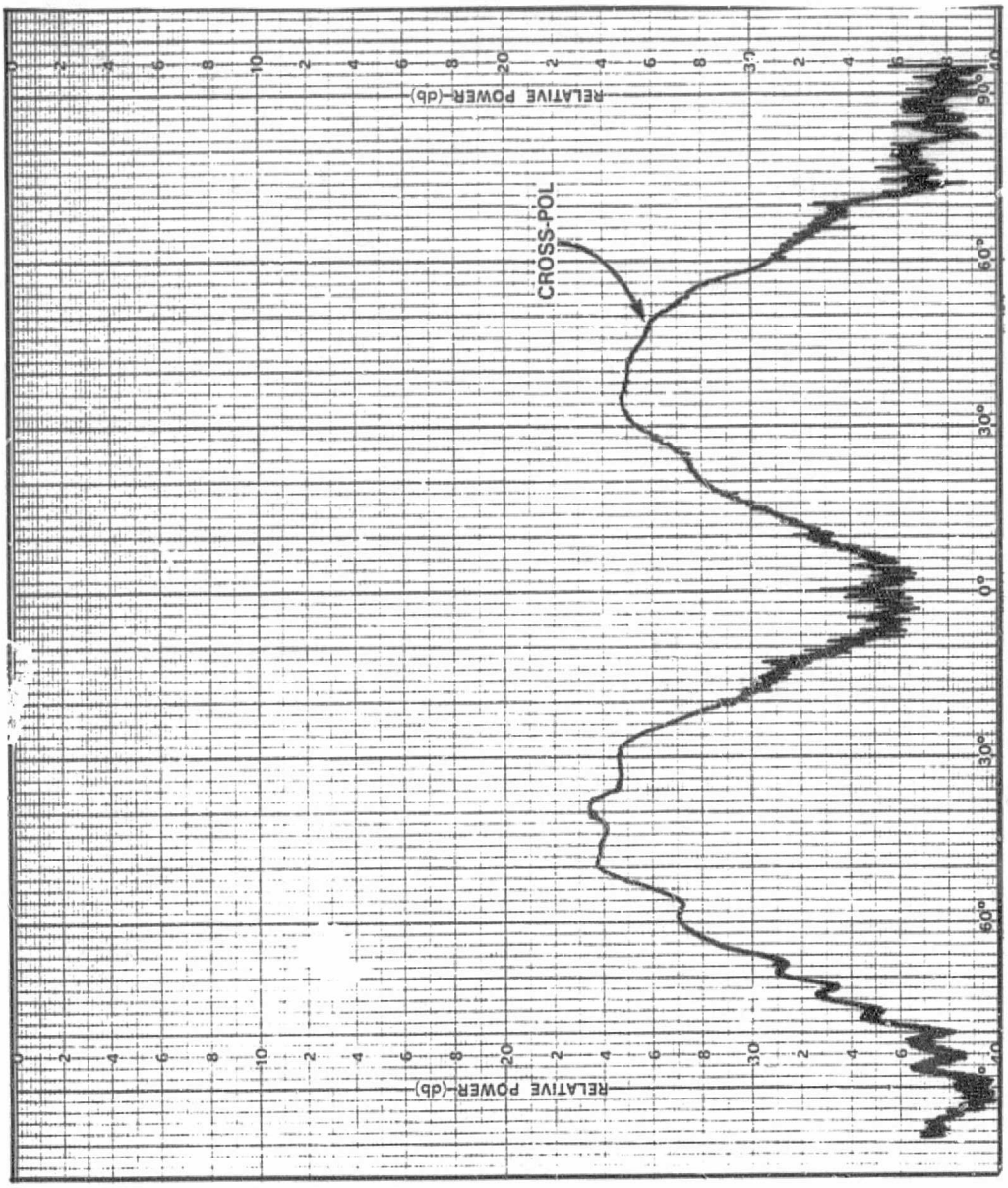

Figure A-22. Cross-Pol 45°-Plane Pattern for Horizontally Polarized Element 1 at 11.95 GHz

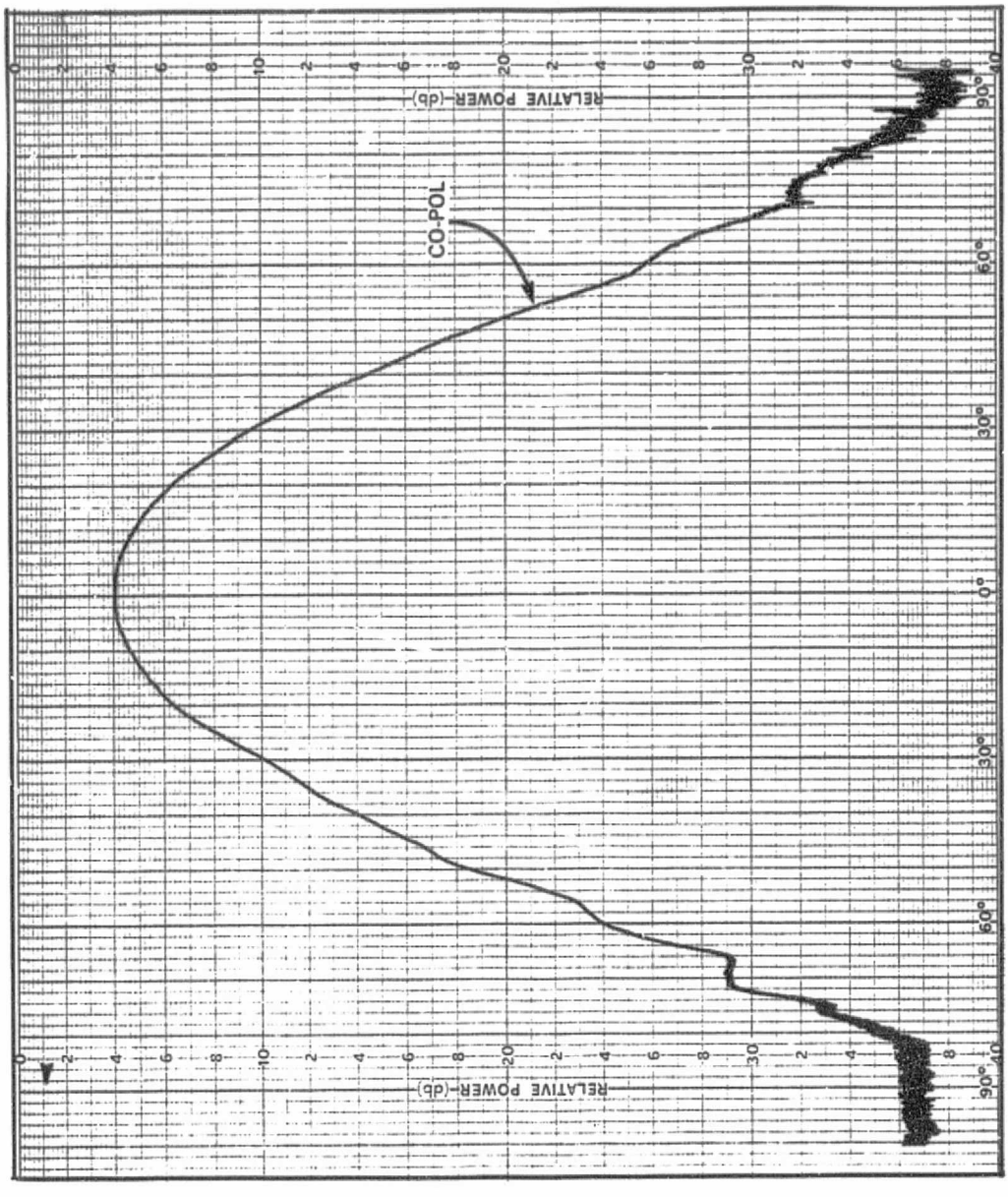

Figure A-23. Co-Pol 45°-Plane Pattern for Horizontally Polarized Element 1 at 12.2 GHz

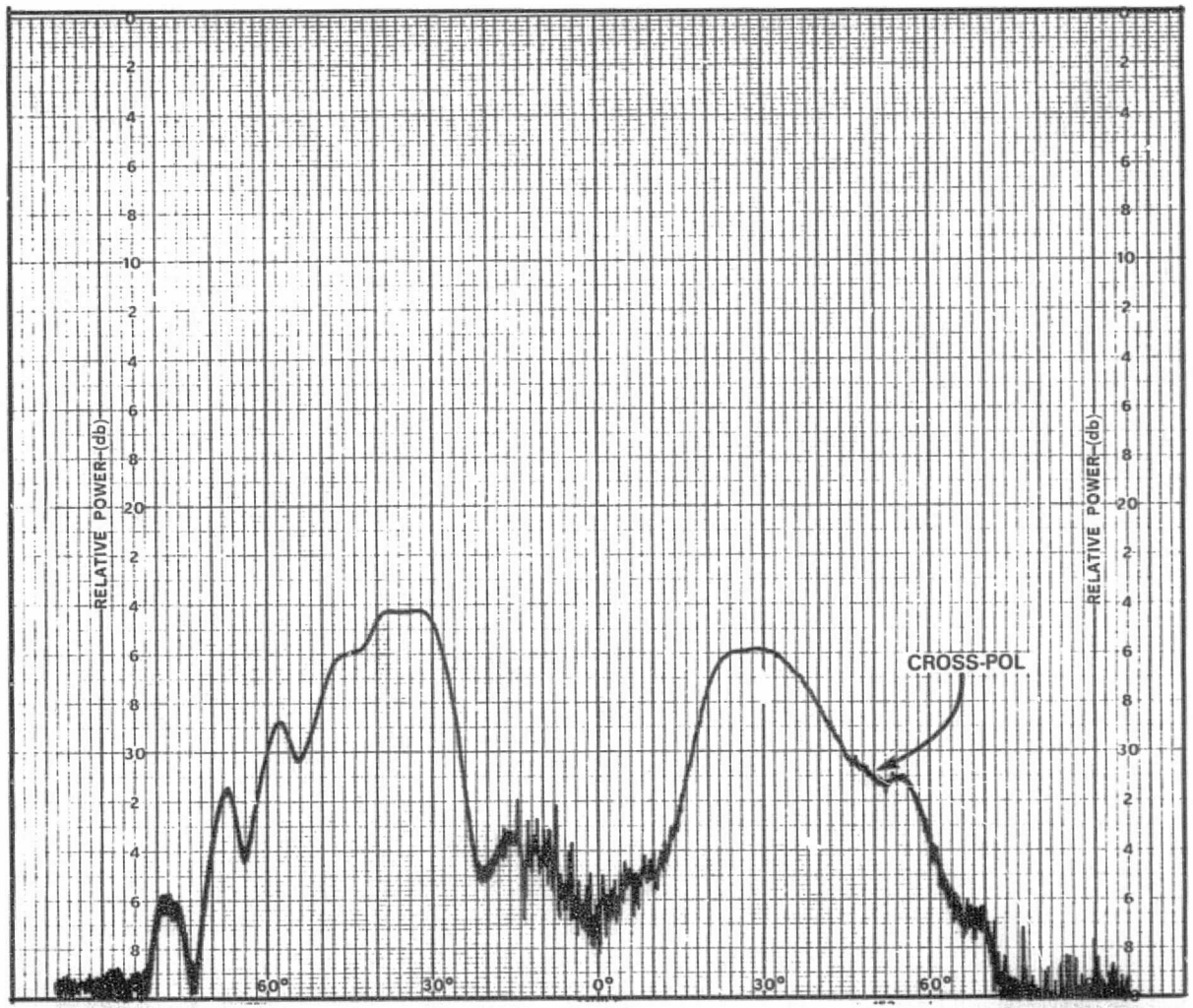

Figure A-24. Cross-Pol 45°-Plane Pattern for Horizontally Polarized Element 1 at 12.2 GHz

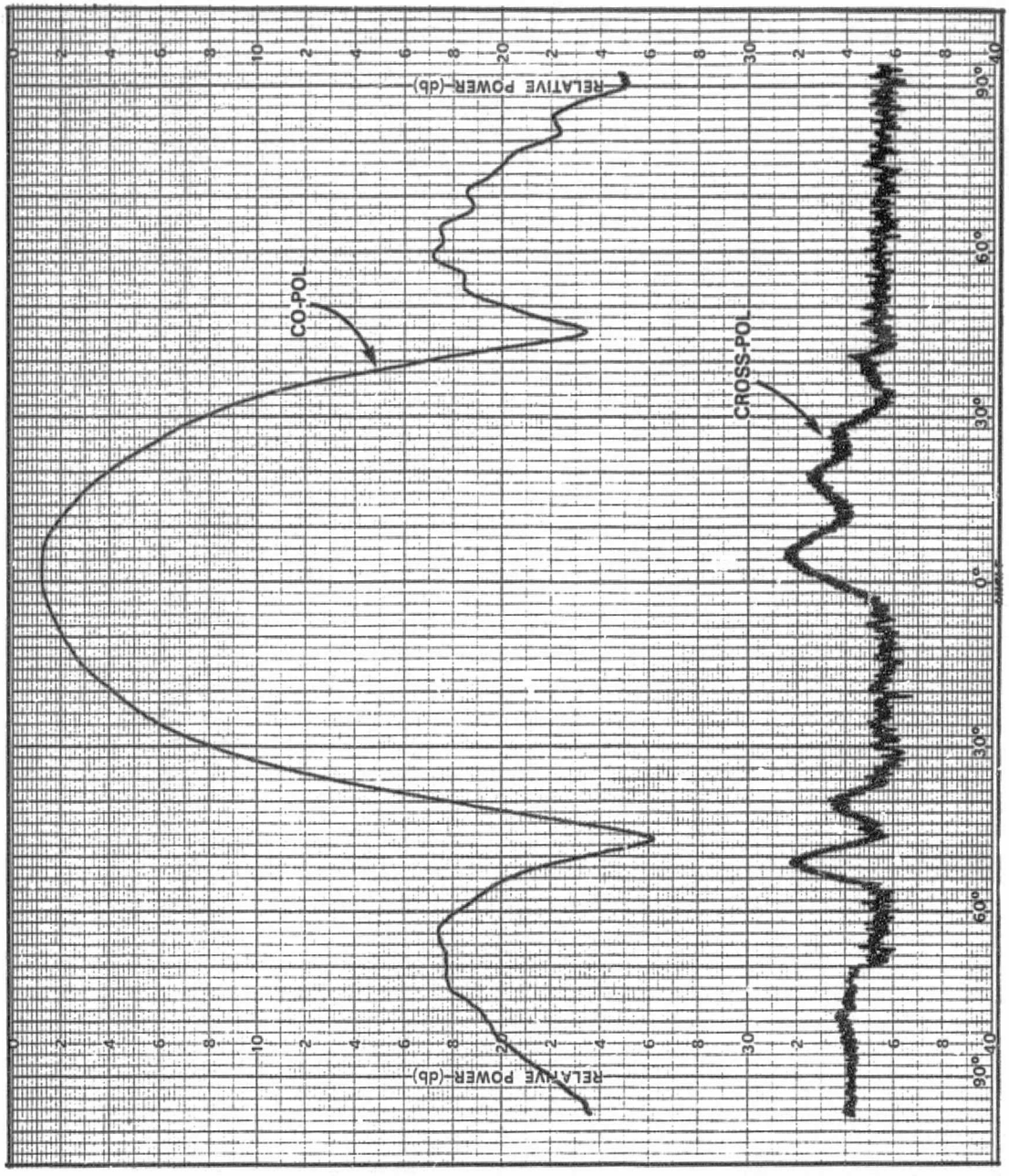

Figure A-25. E-Plane Pattern for Vertically Polarized Element 10 at 11.7 GHz

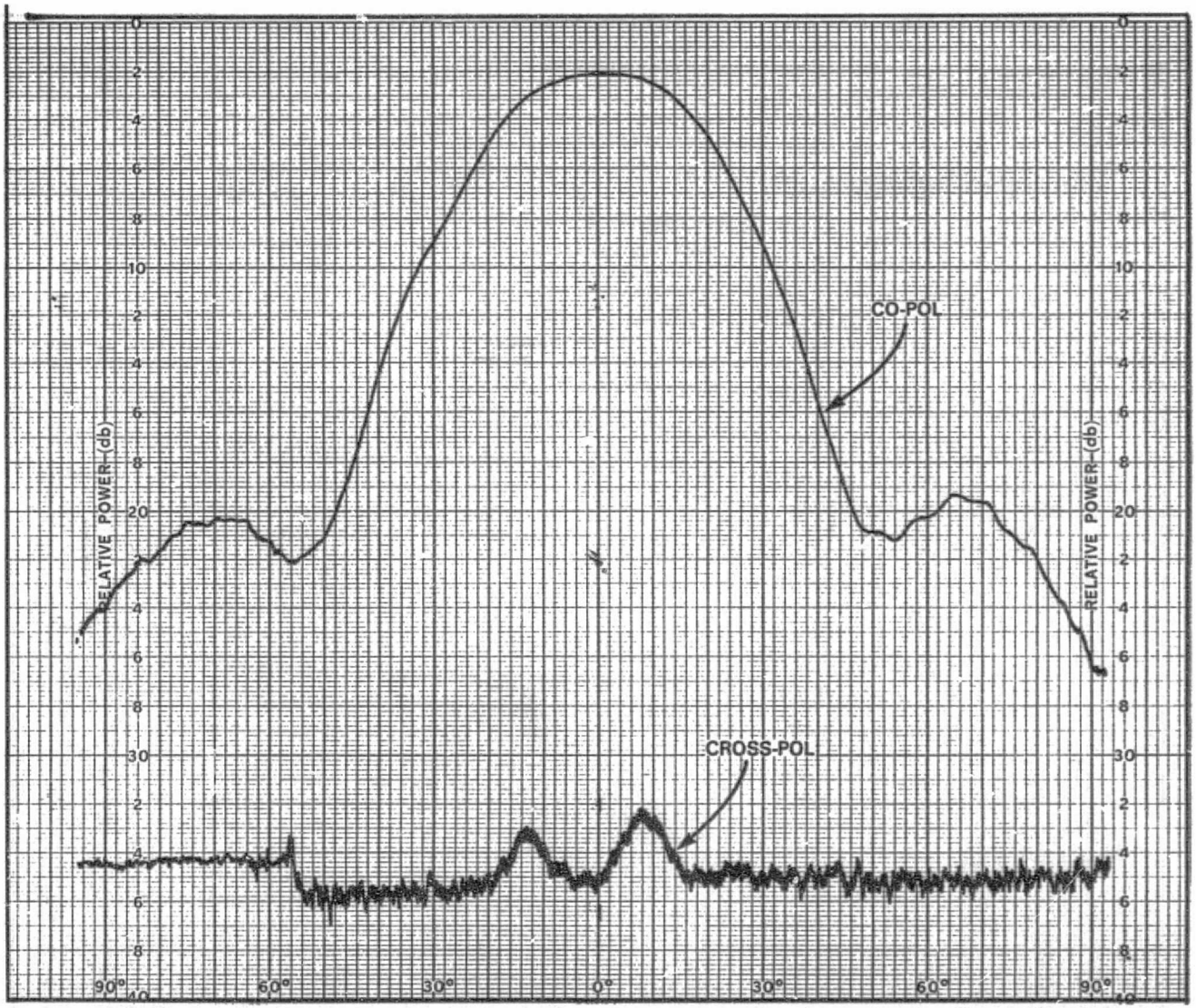

Figure A-26. E-Plane Pattern for Vertically Polarized Element 10 at 11.95 GHz

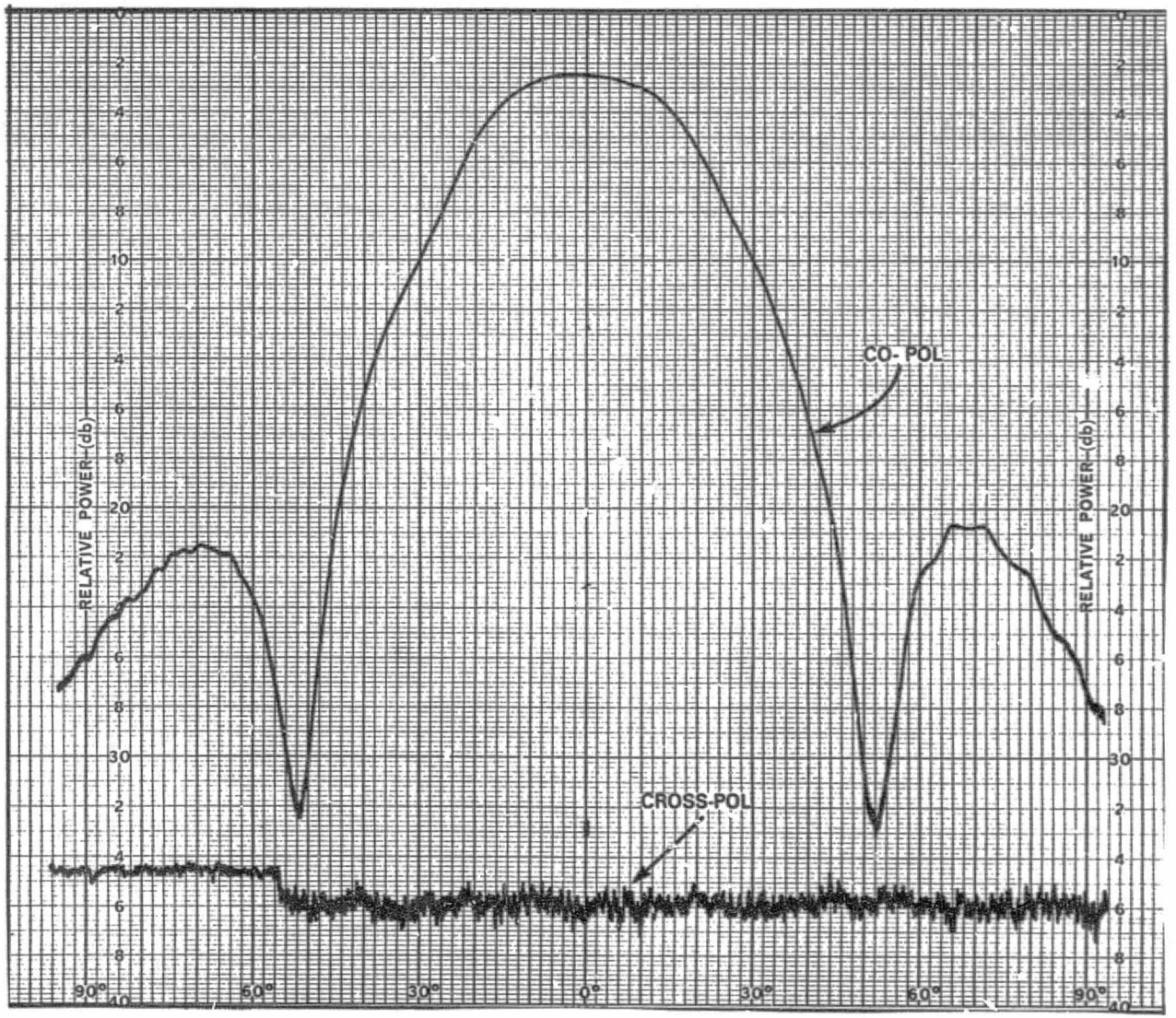

Figure A-27. E-Plane Pattern for Vertically Polarized Element 10 at 12.2 GHz

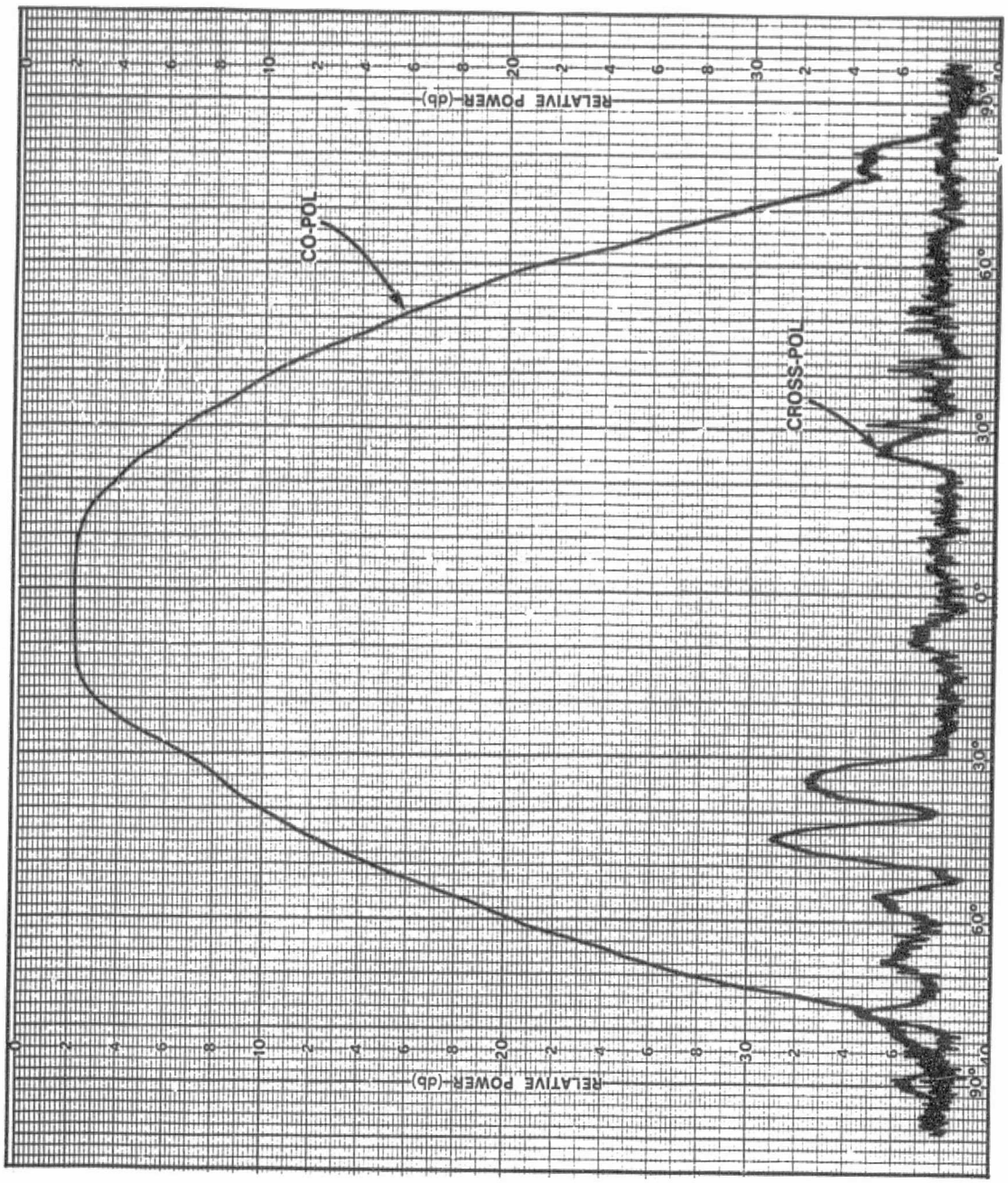

Figure A-28. H-Plane Pattern for Vertically Polarized Element 10 at 11.7 GHz

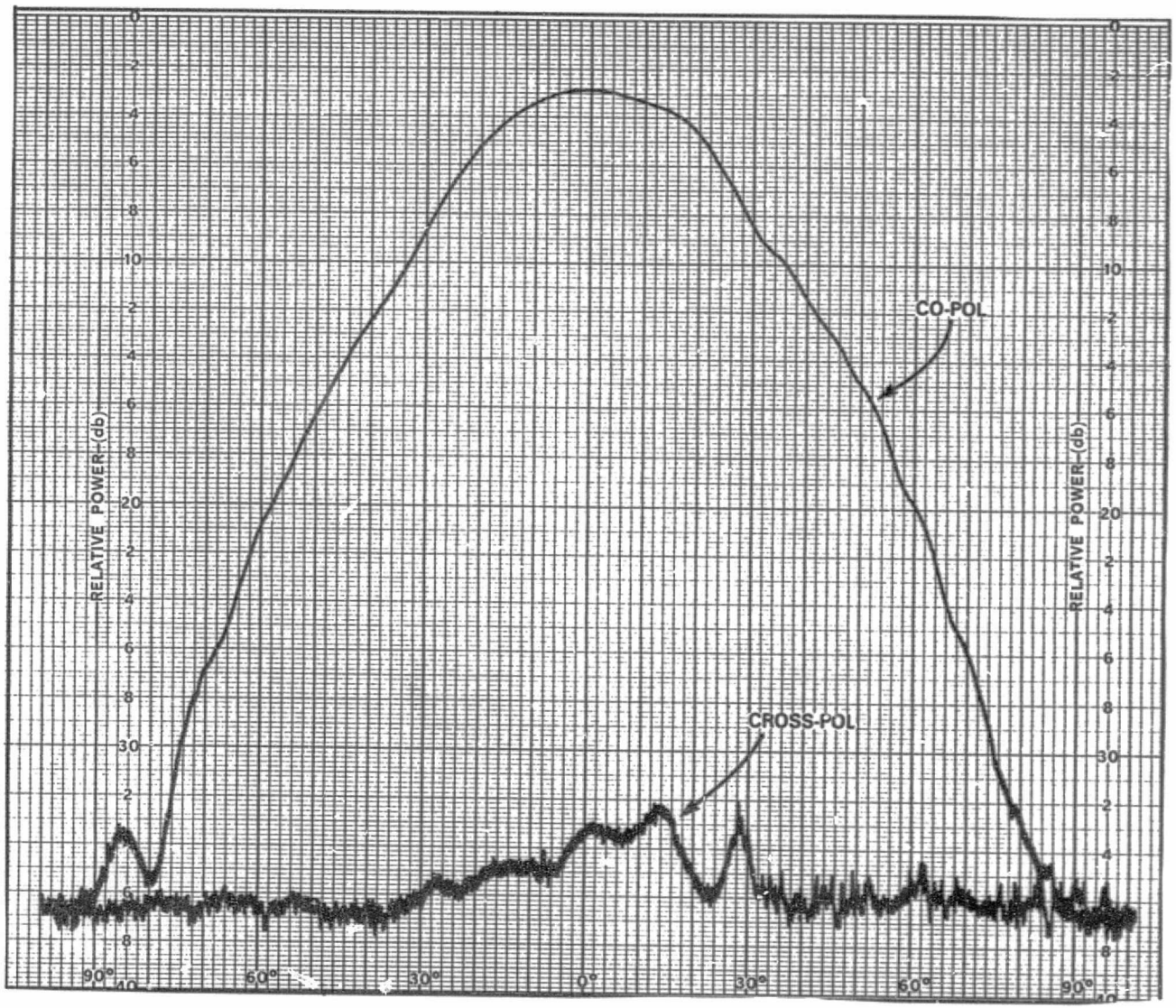

Figure A-29. H-Plane Pattern for Vertically Polarized Element 10 at 11.95 GHz

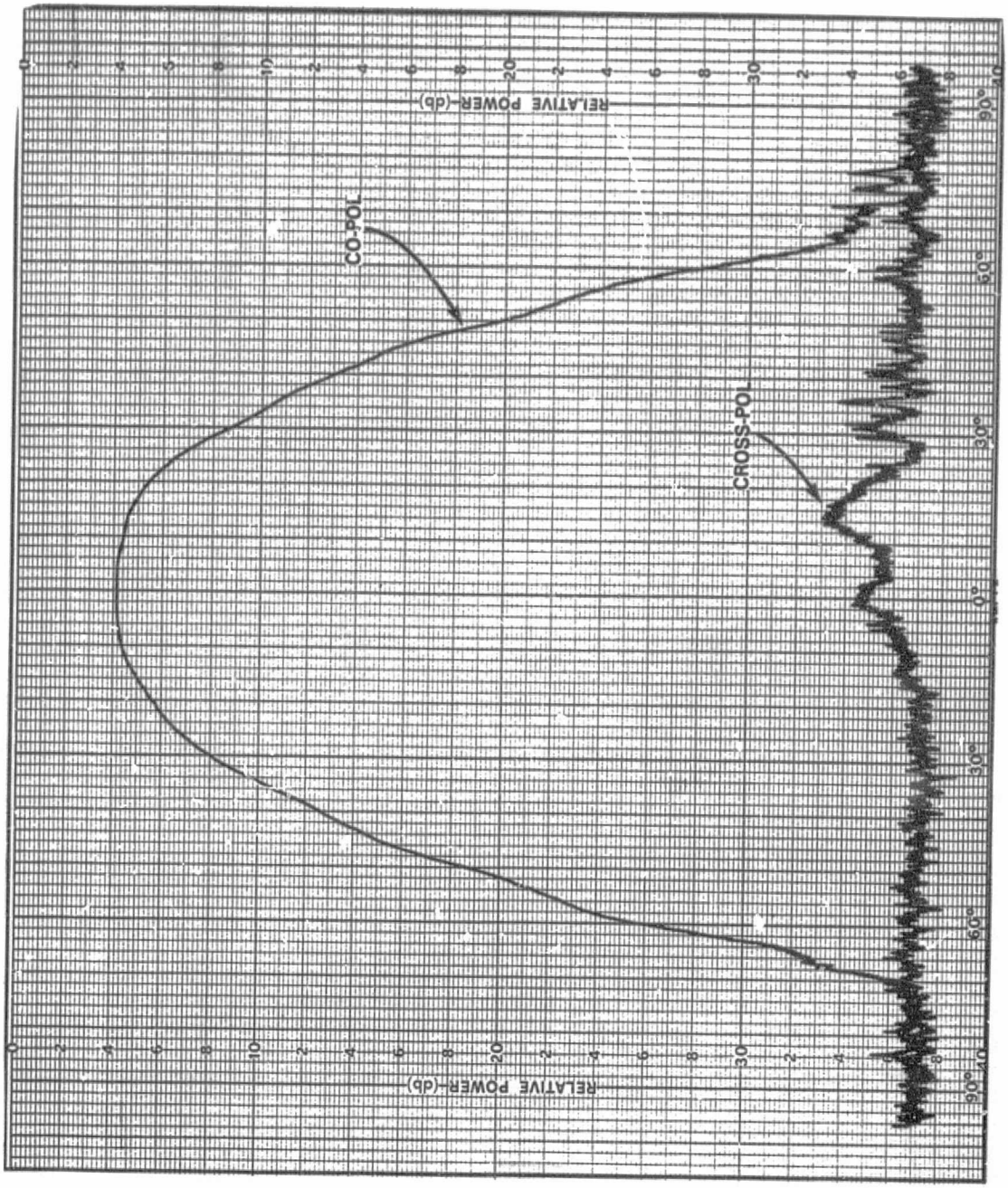

Figure A-30. H-Plane for Vertically Polarized Element 10 at 12.2 GHz

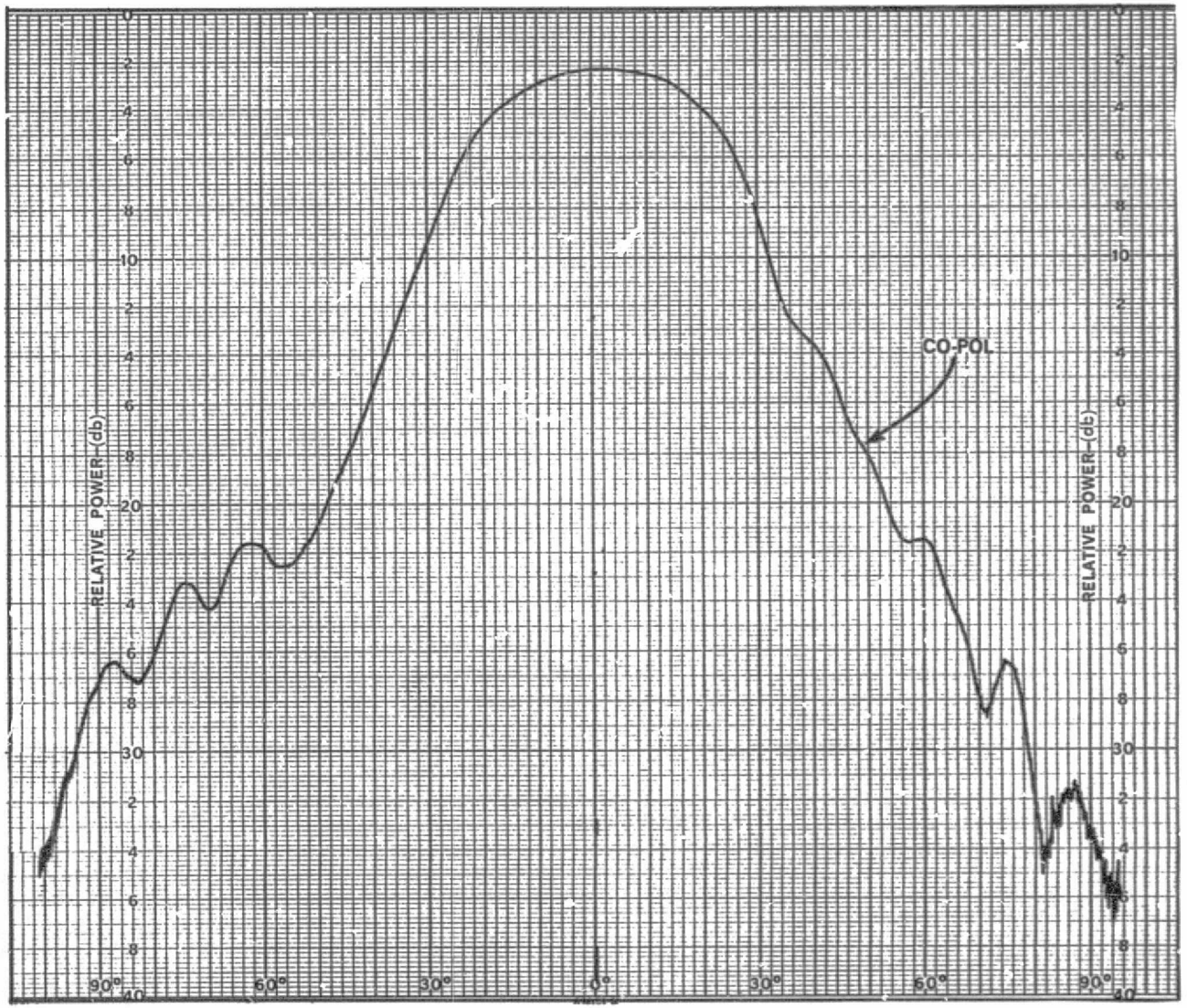

Figure A-31. Co-Pol 45°-Plane Pattern for Vertically Polarized Element 10 at 11.7 GHz

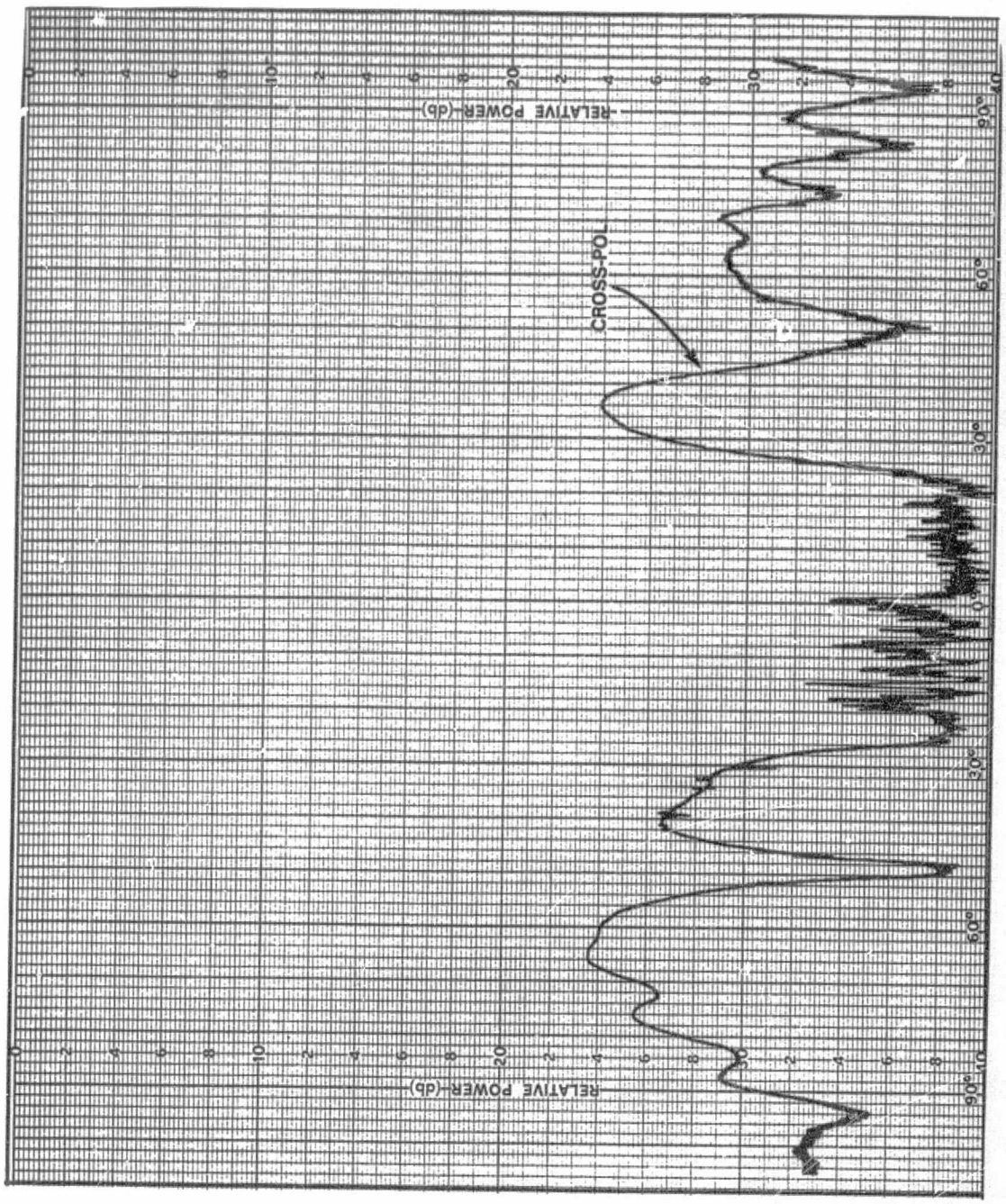

Figure A-32. Cross-Pol 45°-Plane Pattern for Vertically Polarized Element 10 at 11.7 GHz

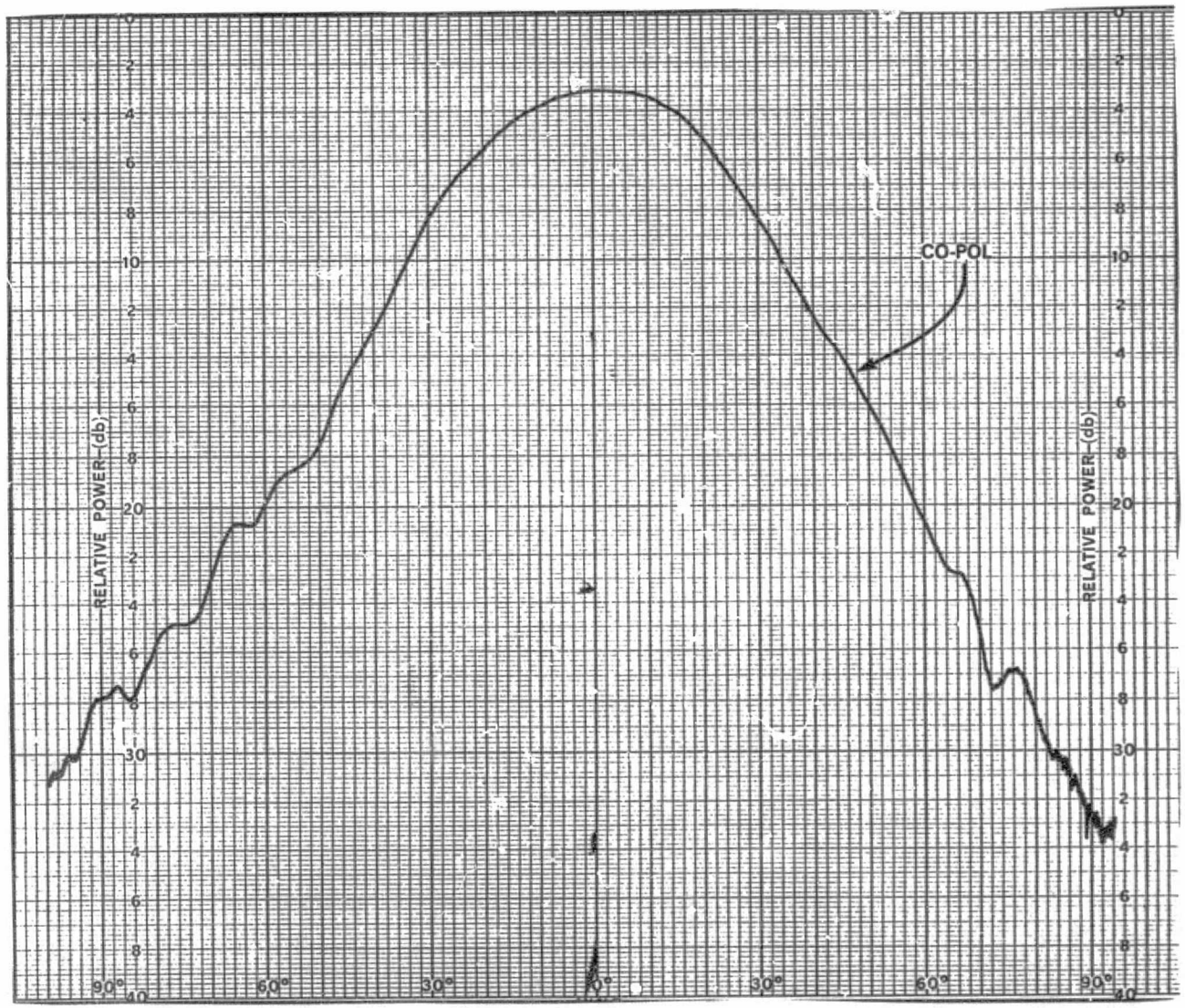

Figure A-33. Co-Pol 45°-Plane Pattern for Vertically Polarized Element 10 at 11.95 GHz

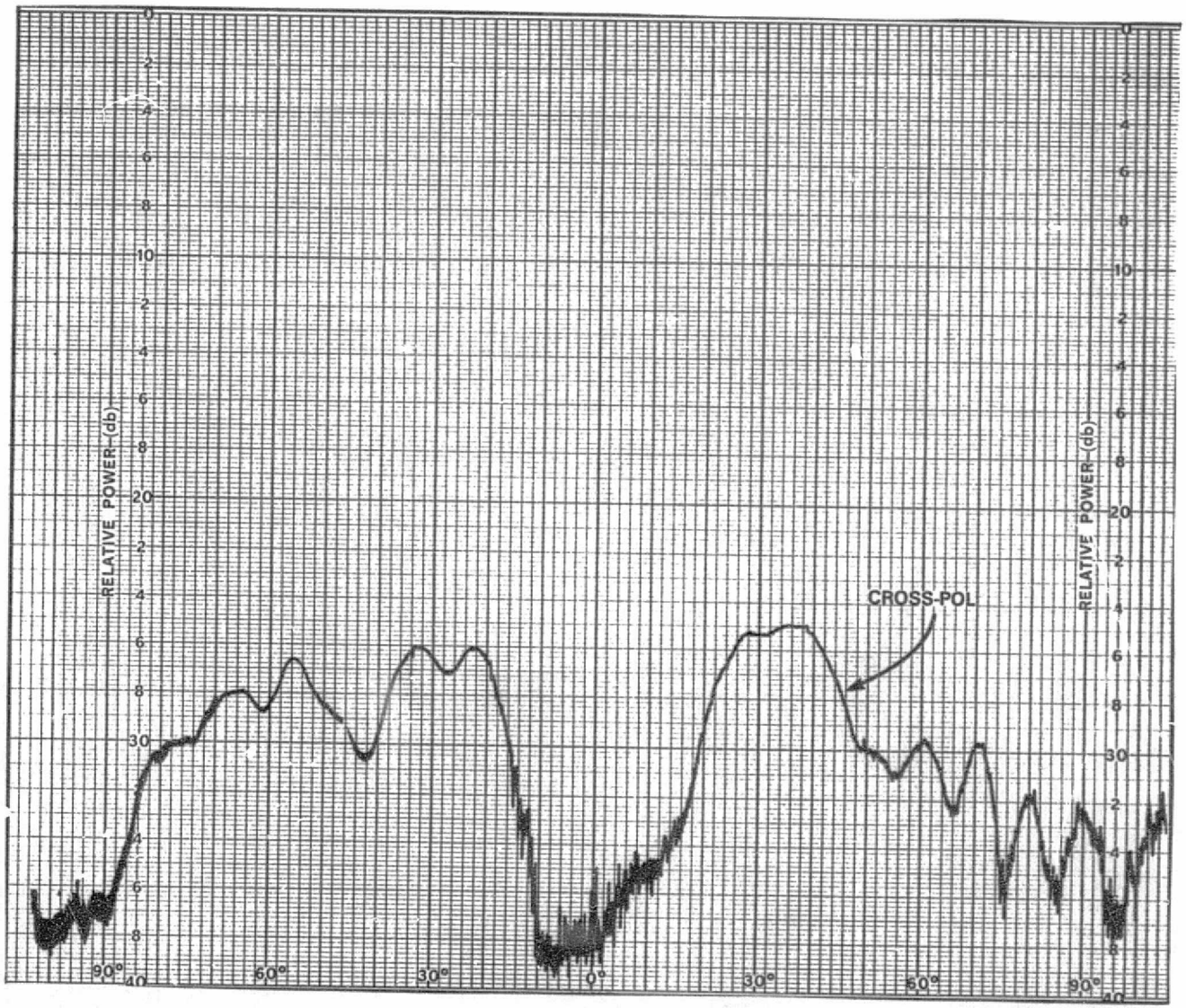

Figure A-34. Cross-Pol 45°-Plane Pattern for Vertically Polarized Element 10 at 11.95 GHz

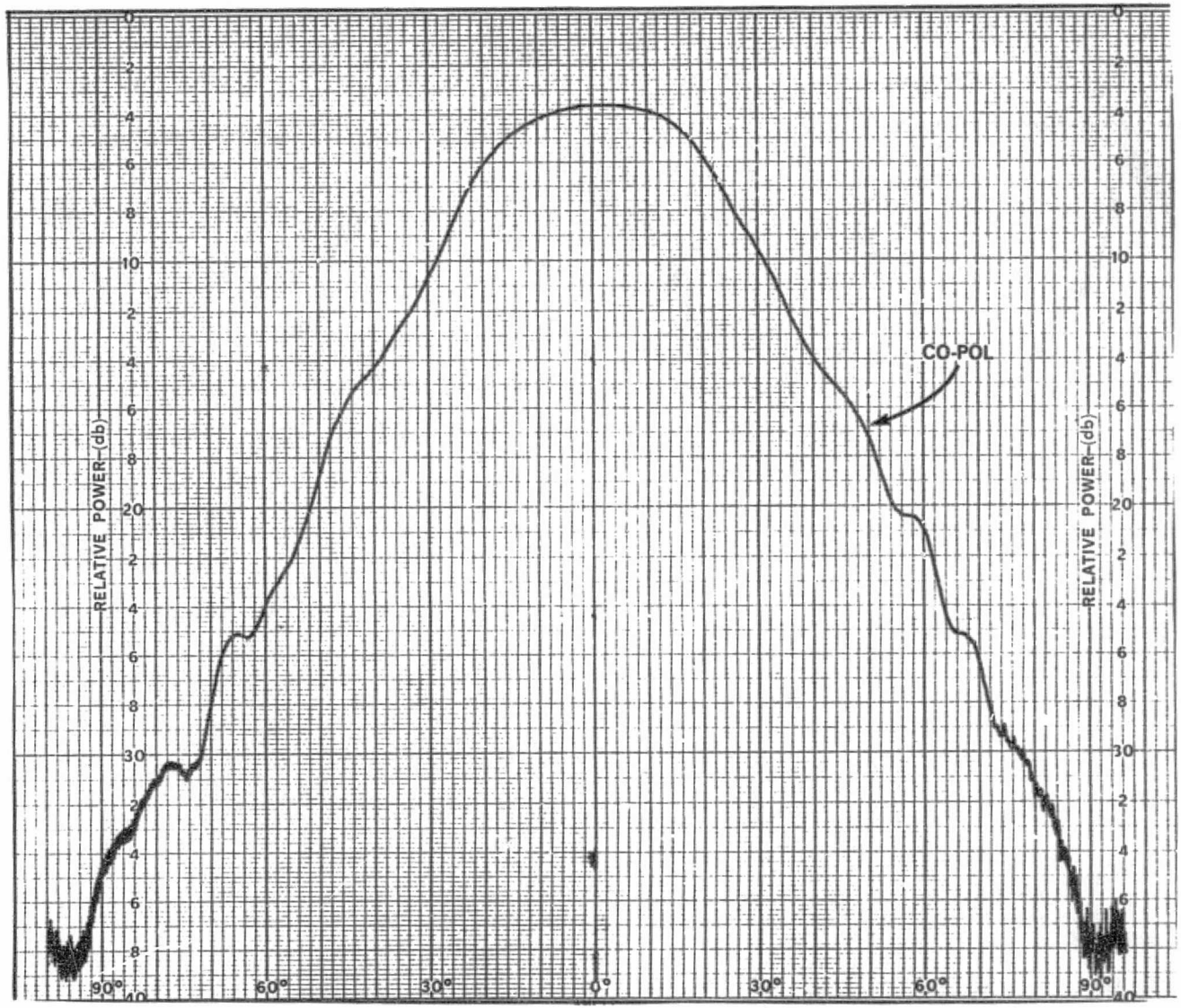

Figure A-35. Co-Pol 45°-Plane Pattern for Vertically Polarized Element 10 at 12.2 GHz

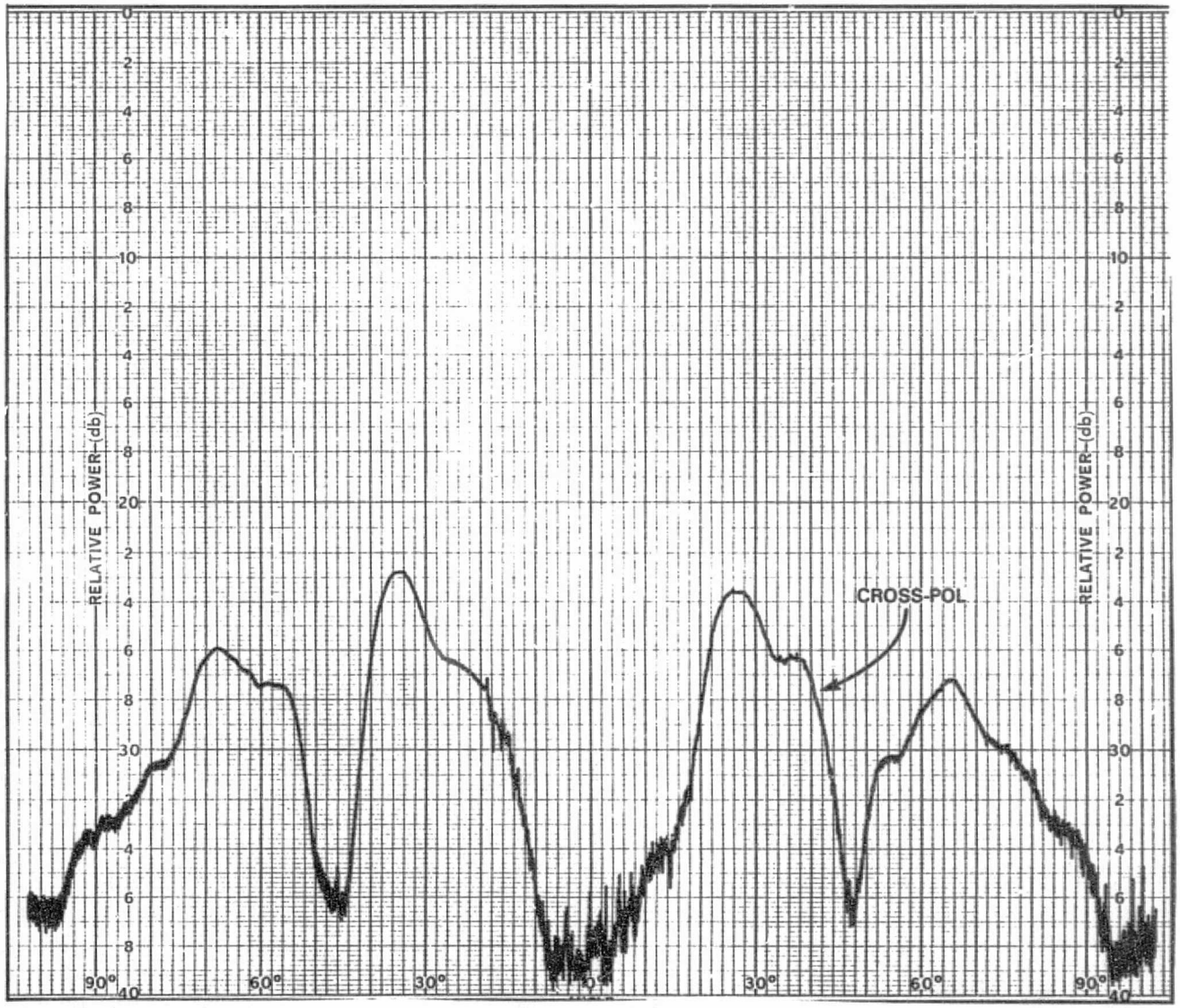

Figure A-36. Cross-Pol 45°-Plane Pattern for Vertically Polarized Element 10 at 12.2 GHz

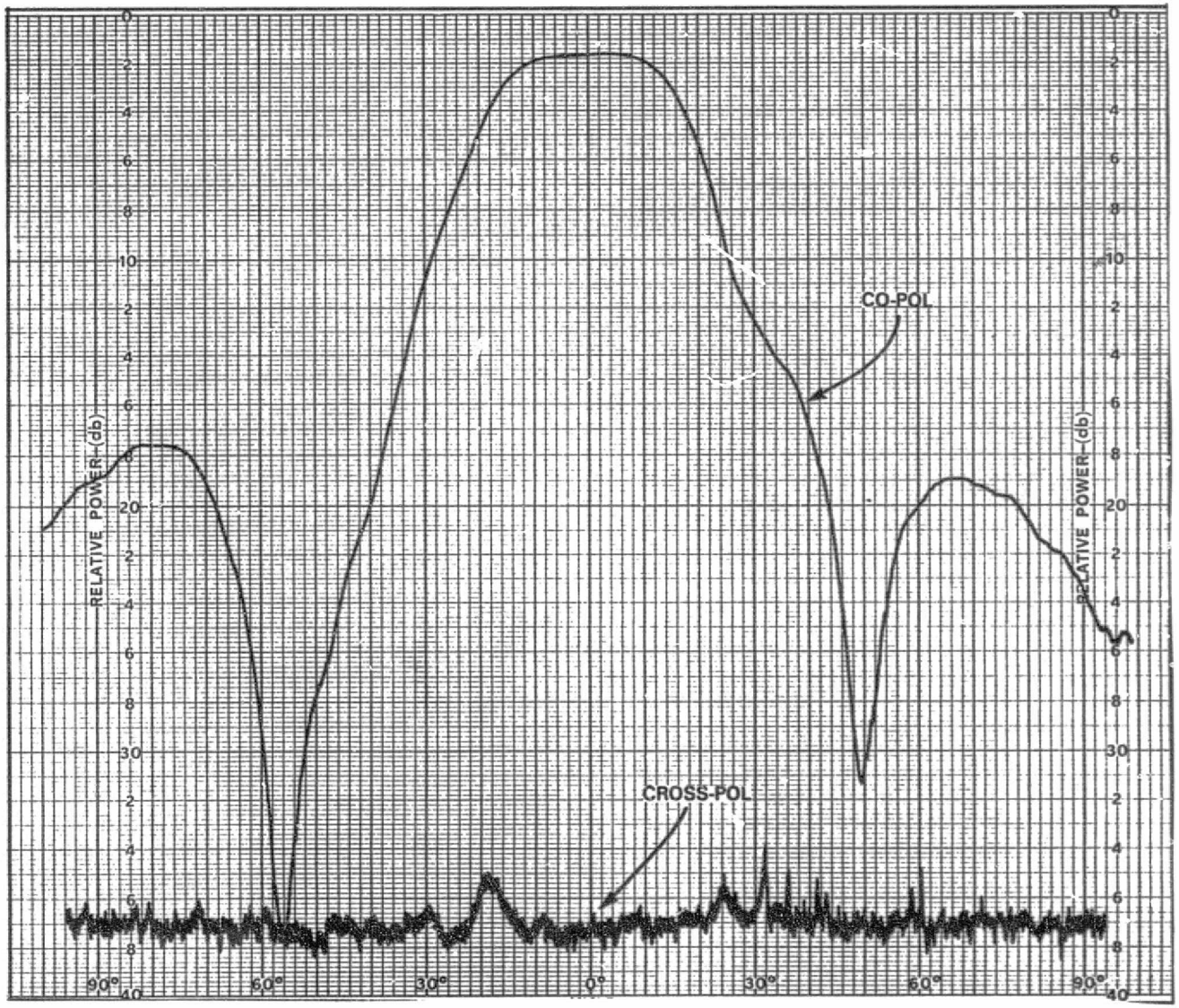

Figure A-37. E-Plane Pattern for Horizontally Polarized Element 10 at 11.7 GHz

Figure A-38. E-Plane Pattern for Horizontally Polarized Element 10 at 11.95 GHz

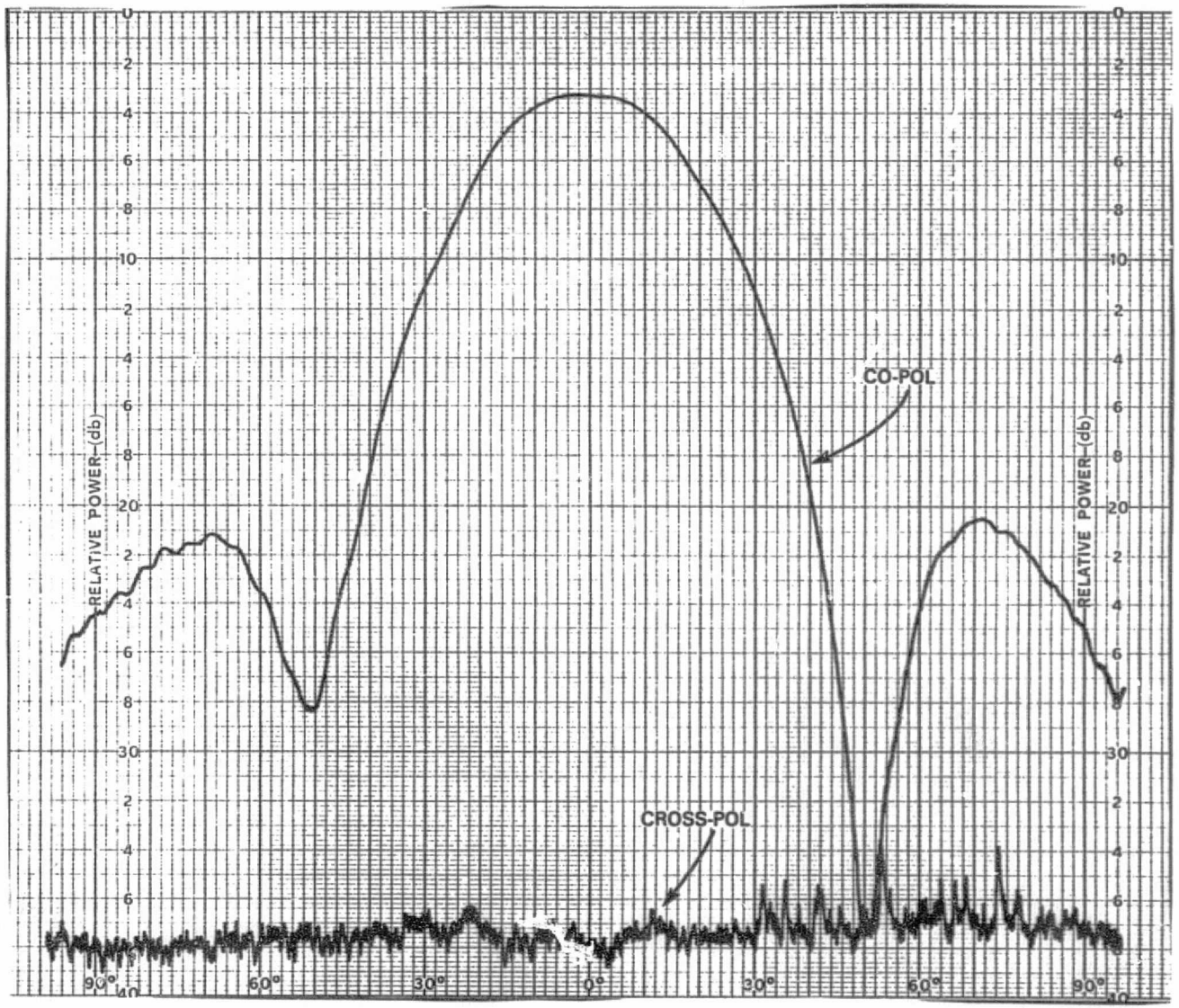

Figure A-39. E-Plane Pattern for Horizontally Polarized Element 10 at 12.2 GHz

Figure A-40. H-Plane Pattern for Horizontally Polarized Element 10 at 11.7 GHz

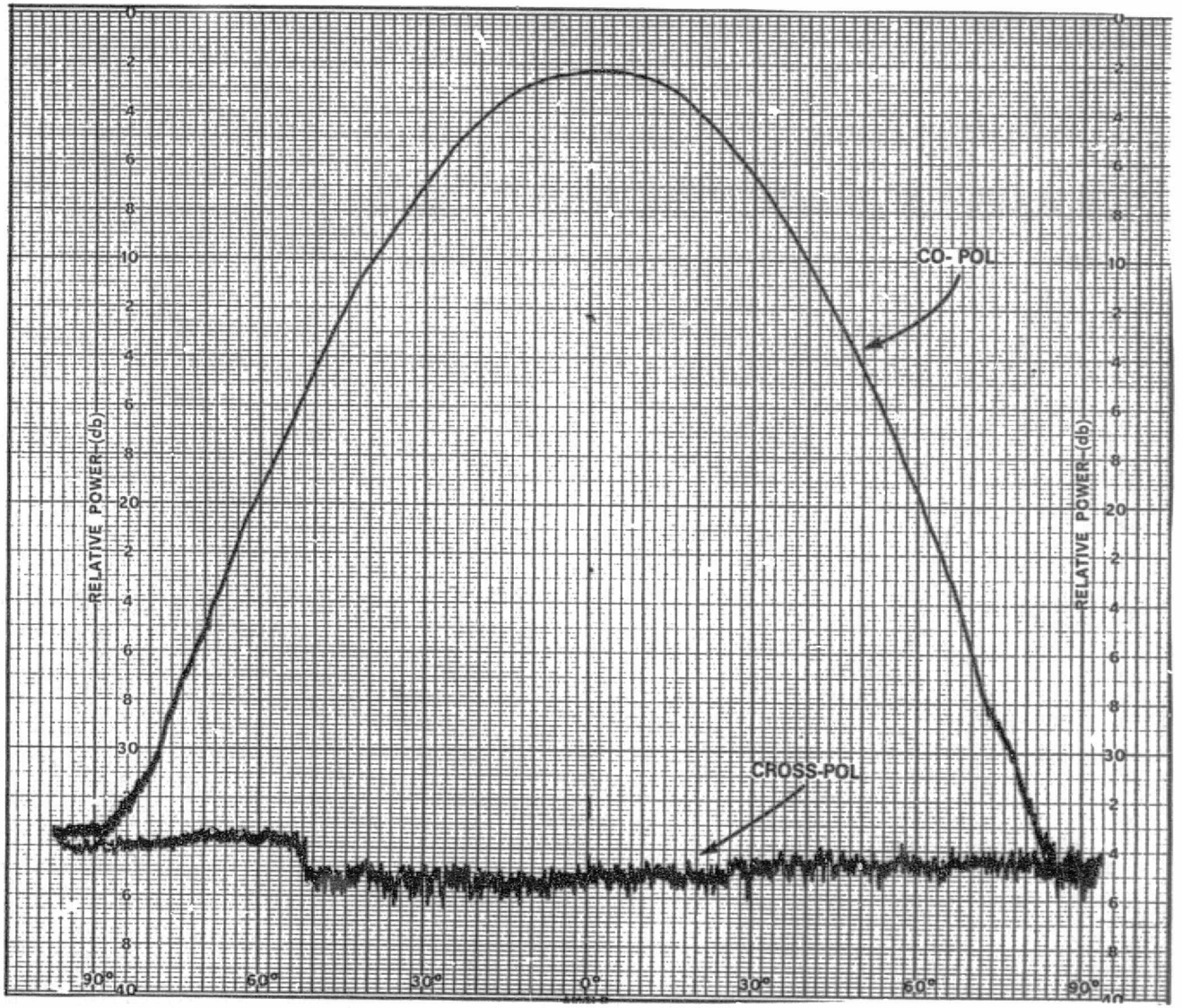

Figure A-41. H-Plane Pattern for Horizontally Polarized Element 10 at 11.95 GHz

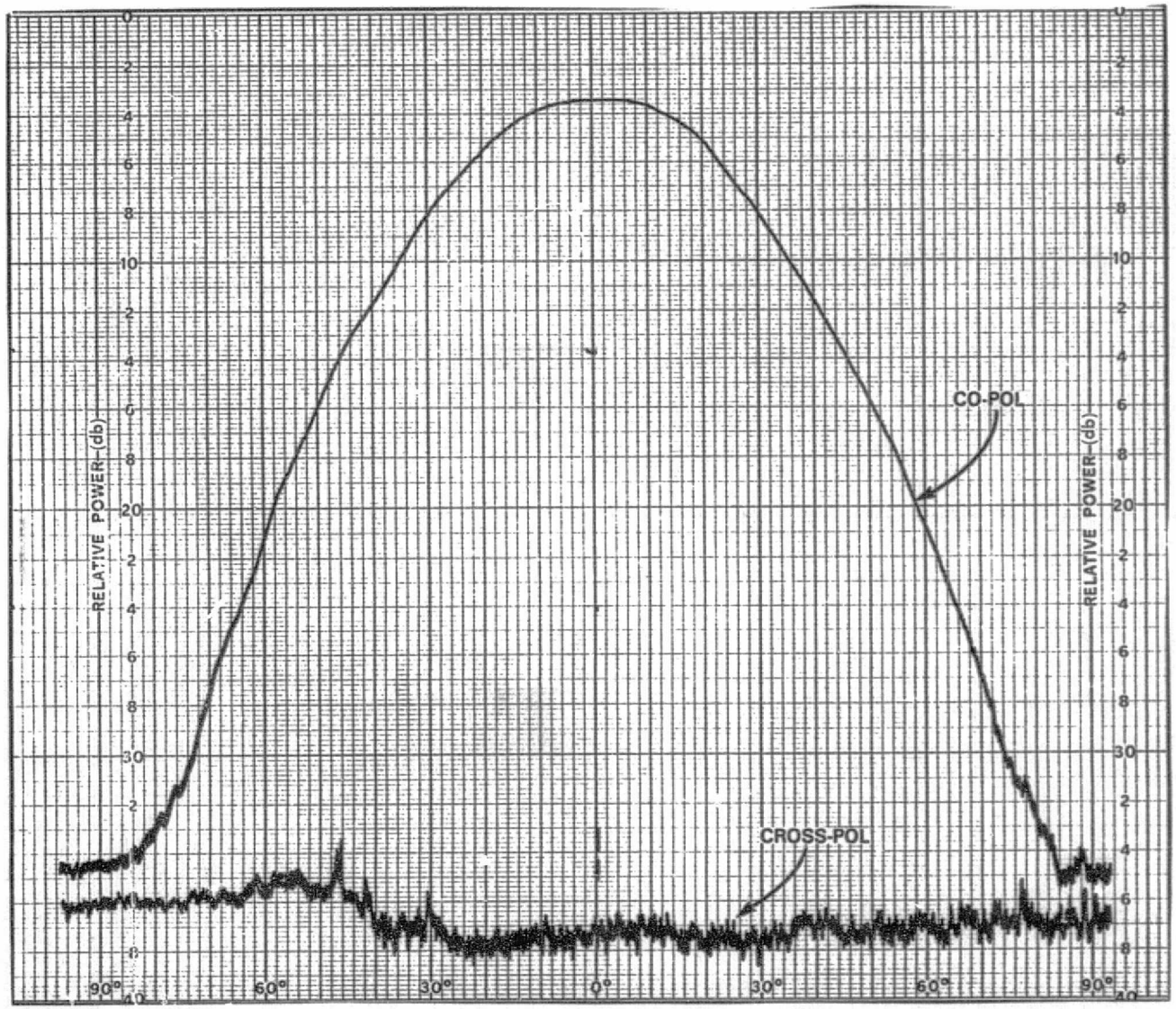

Figure A-42. H-Plane Pattern for Horizontally Polarized Element 10 at 12.2 GHz

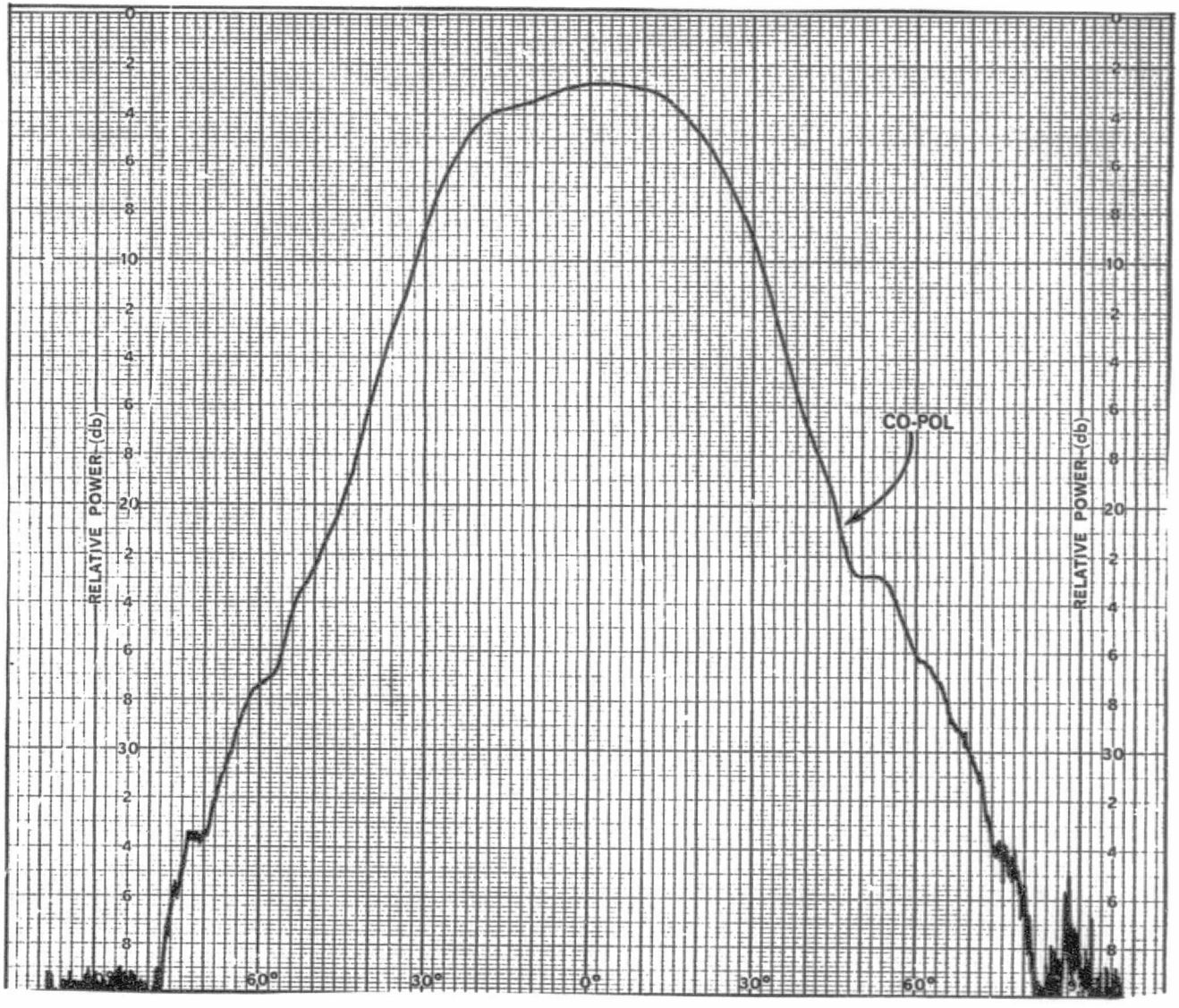

Figure A-43. Co-Pol 45°-Plane Pattern for Horizontally Polarized Element 10 at 11.7 GHz

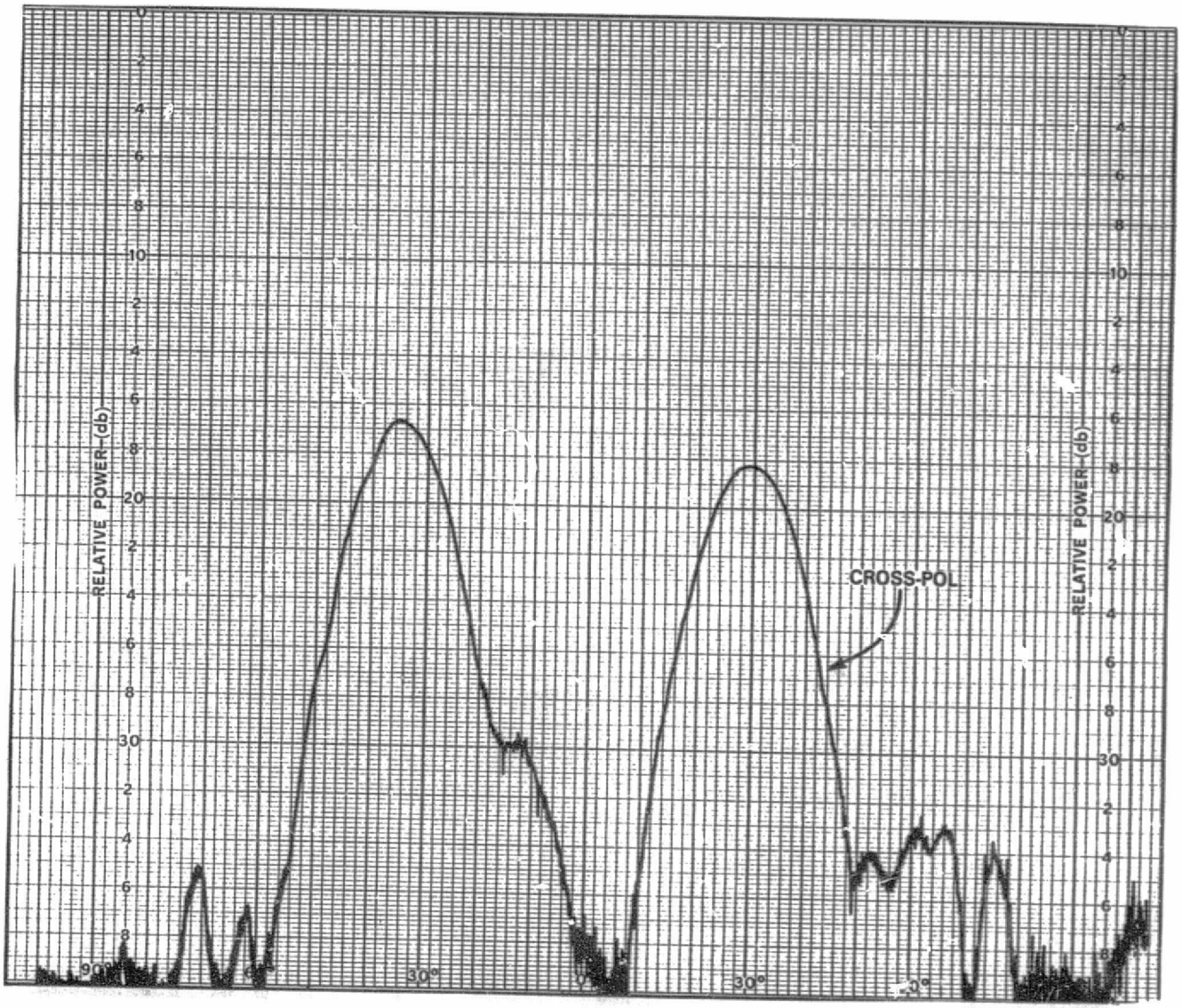

Figure A-44. Cross-Pol 45°-Plane Pattern for Horizontally Polarized Element 10 at 11.7 GHz

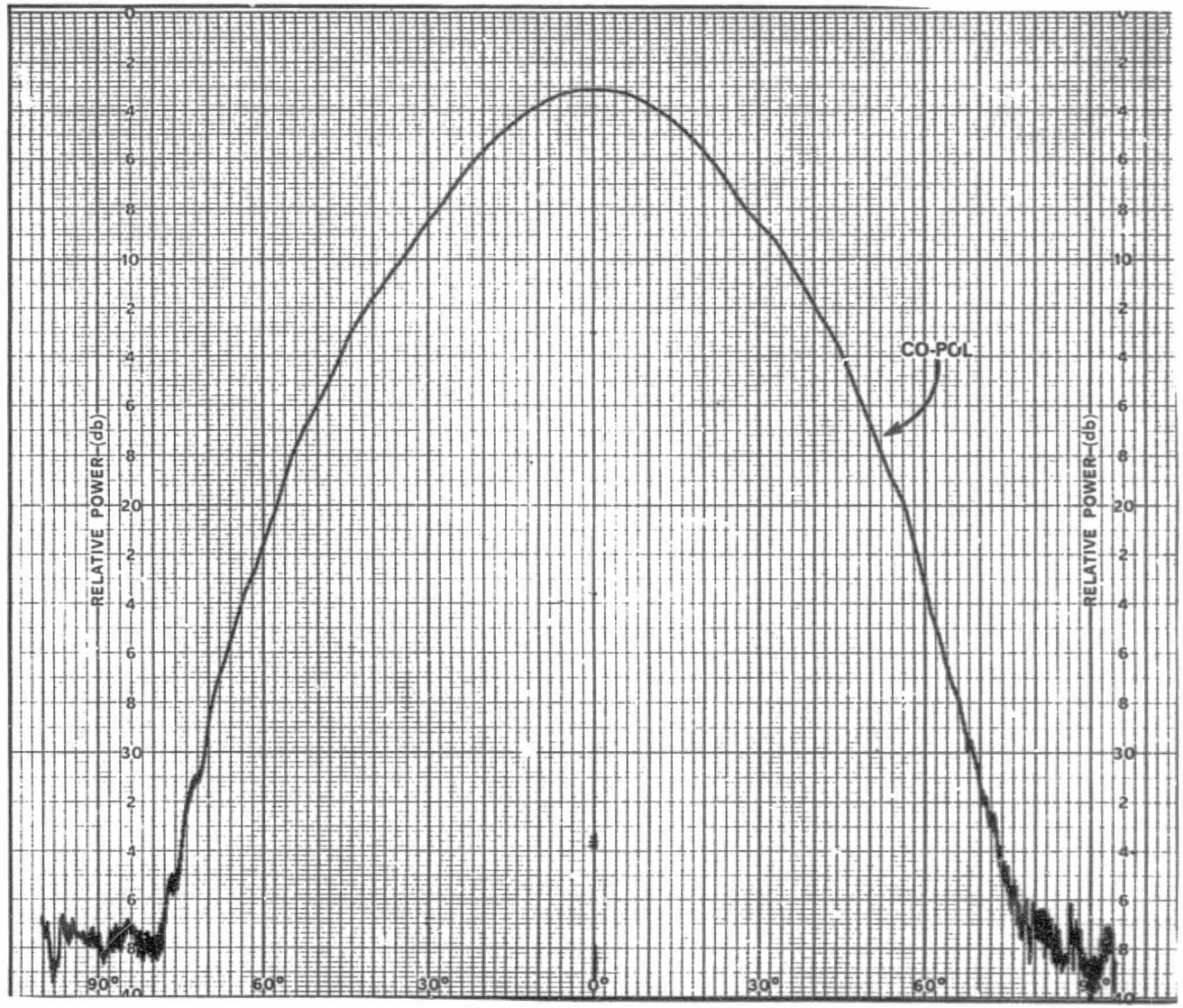

Figure A-45. Co-Pol 45°-Plane Pattern for Horizontally Polarized Element 10 at 11.95 GHz

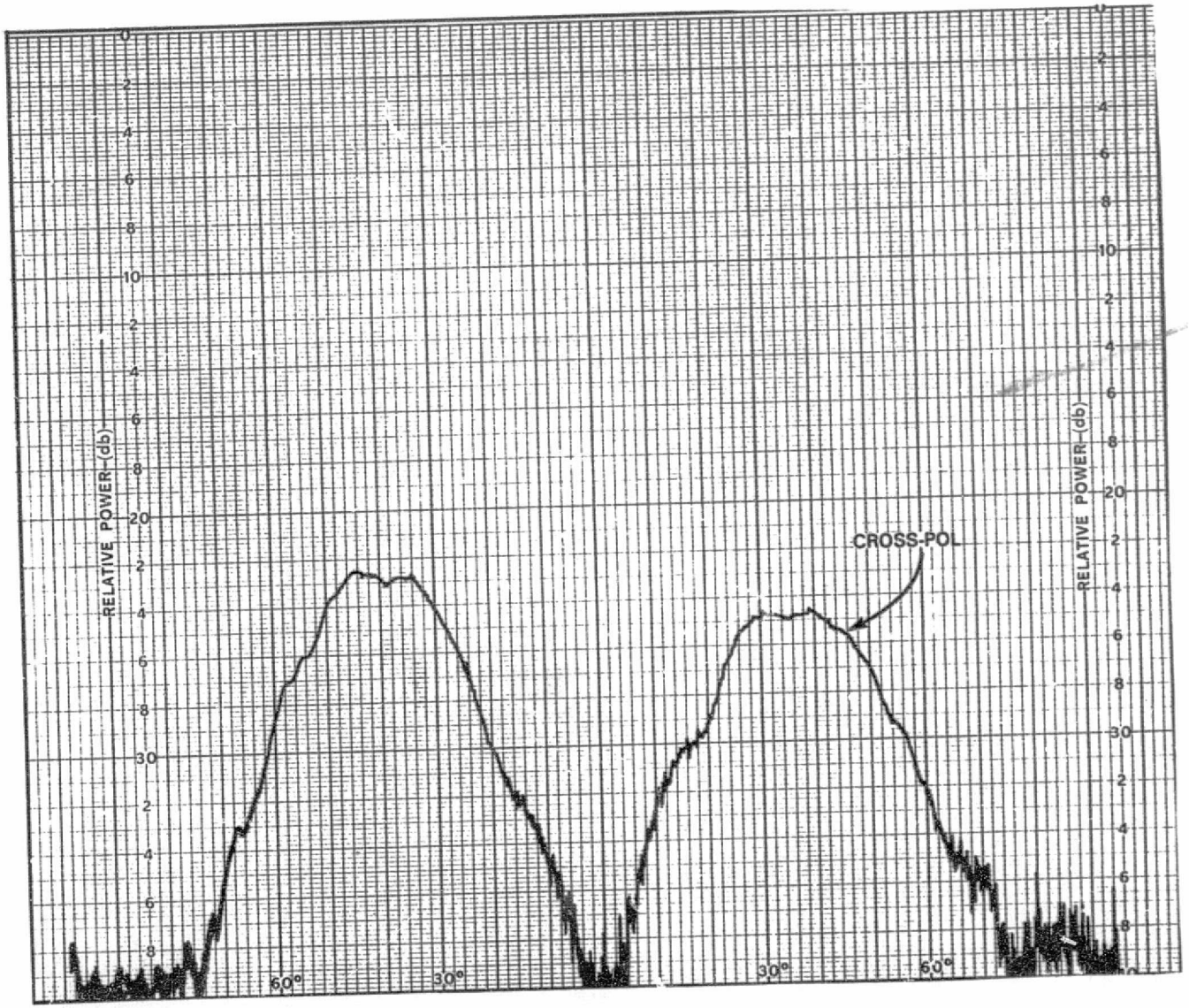

Figure A-46. Cross-Pol 45°-Plane Pattern for Horizontally Polarized Element 10 at 11.95 GHz

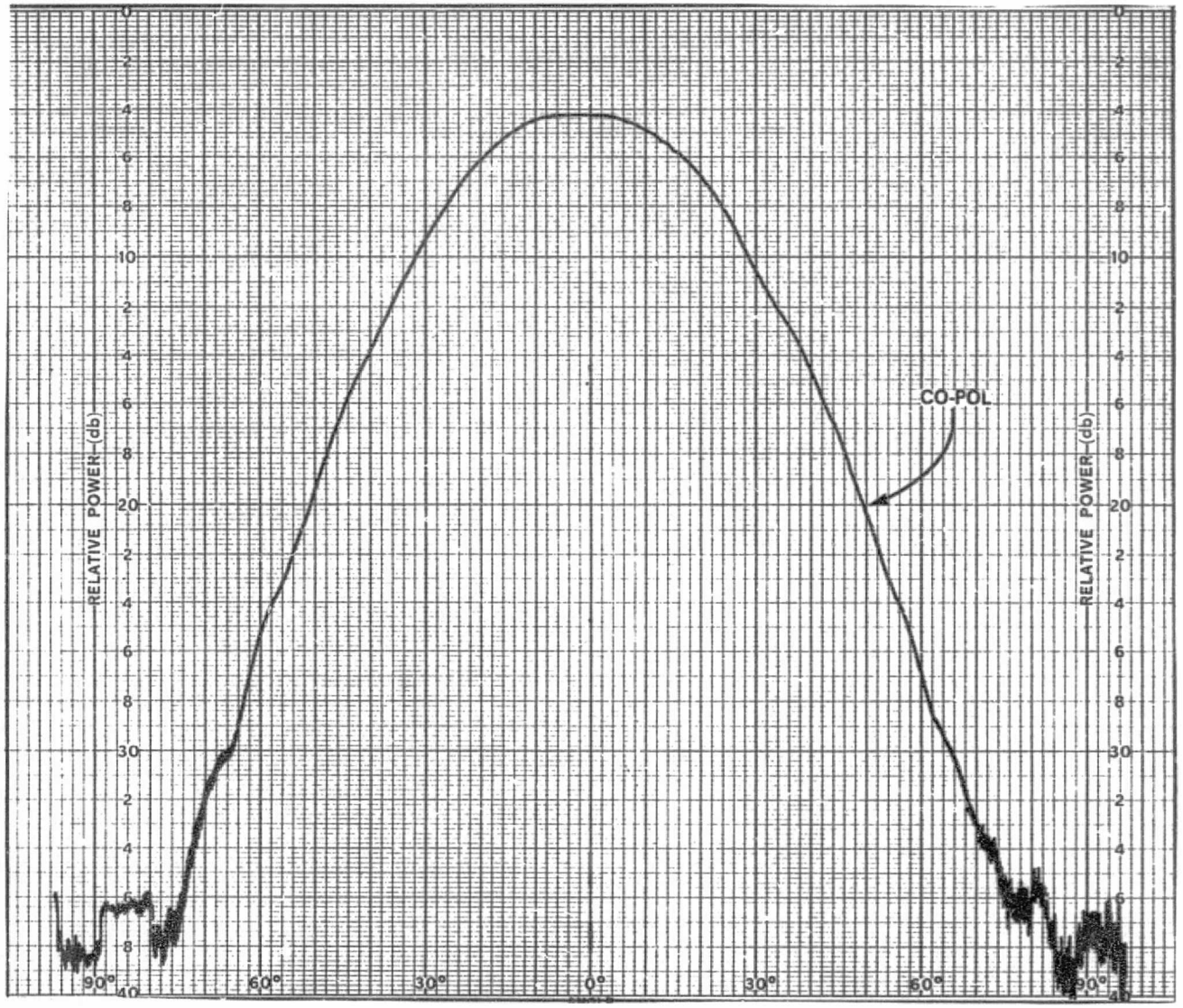

Figure A-47. Co-Pol 45°-Plane Pattern for Horizontally Polarized Element 10 at 12.2 GHz

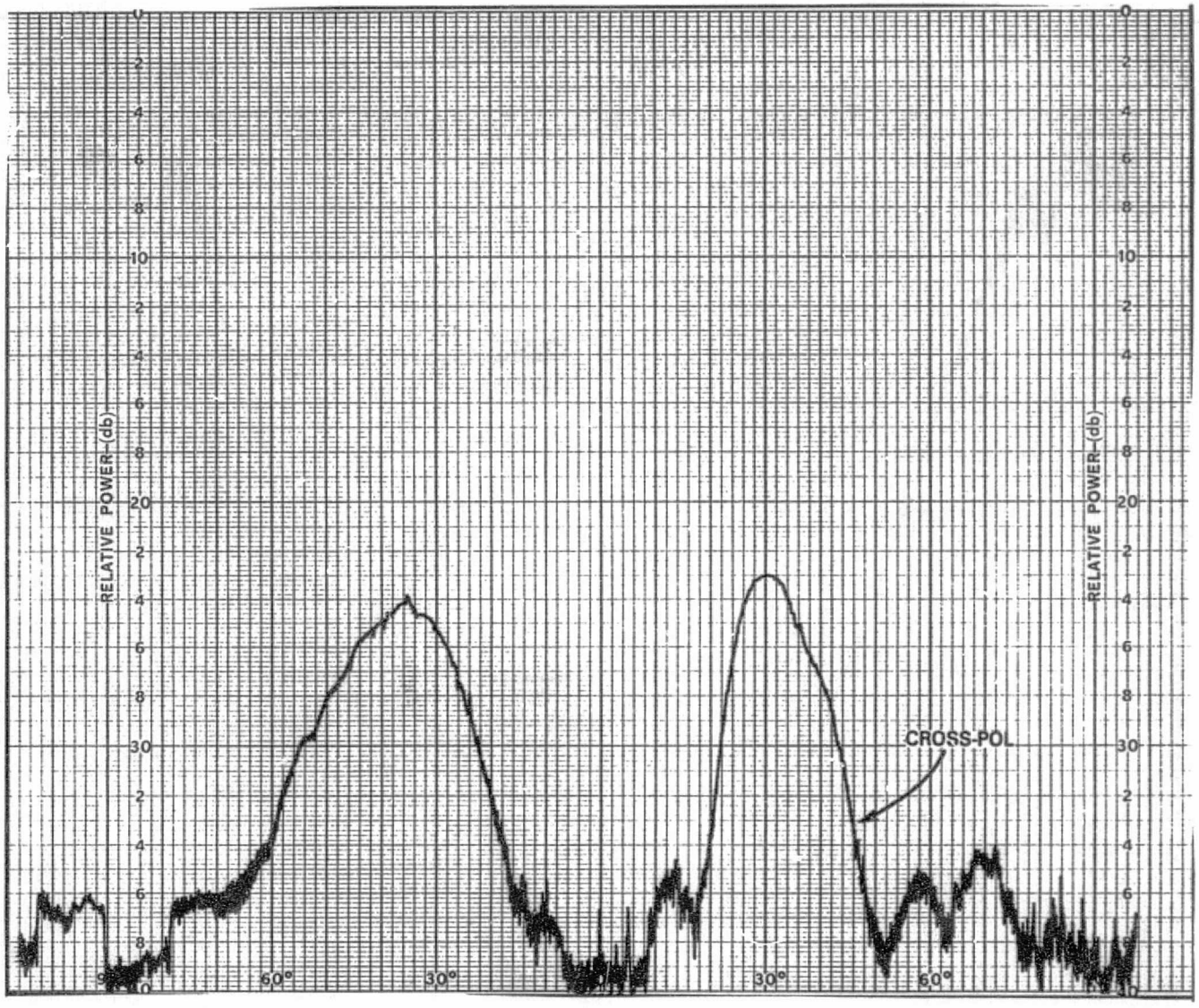

Figure A-48. Cross-Pol 45°-Plane Pattern for Horizontally Polarized Element 10 at 12.2 GHz

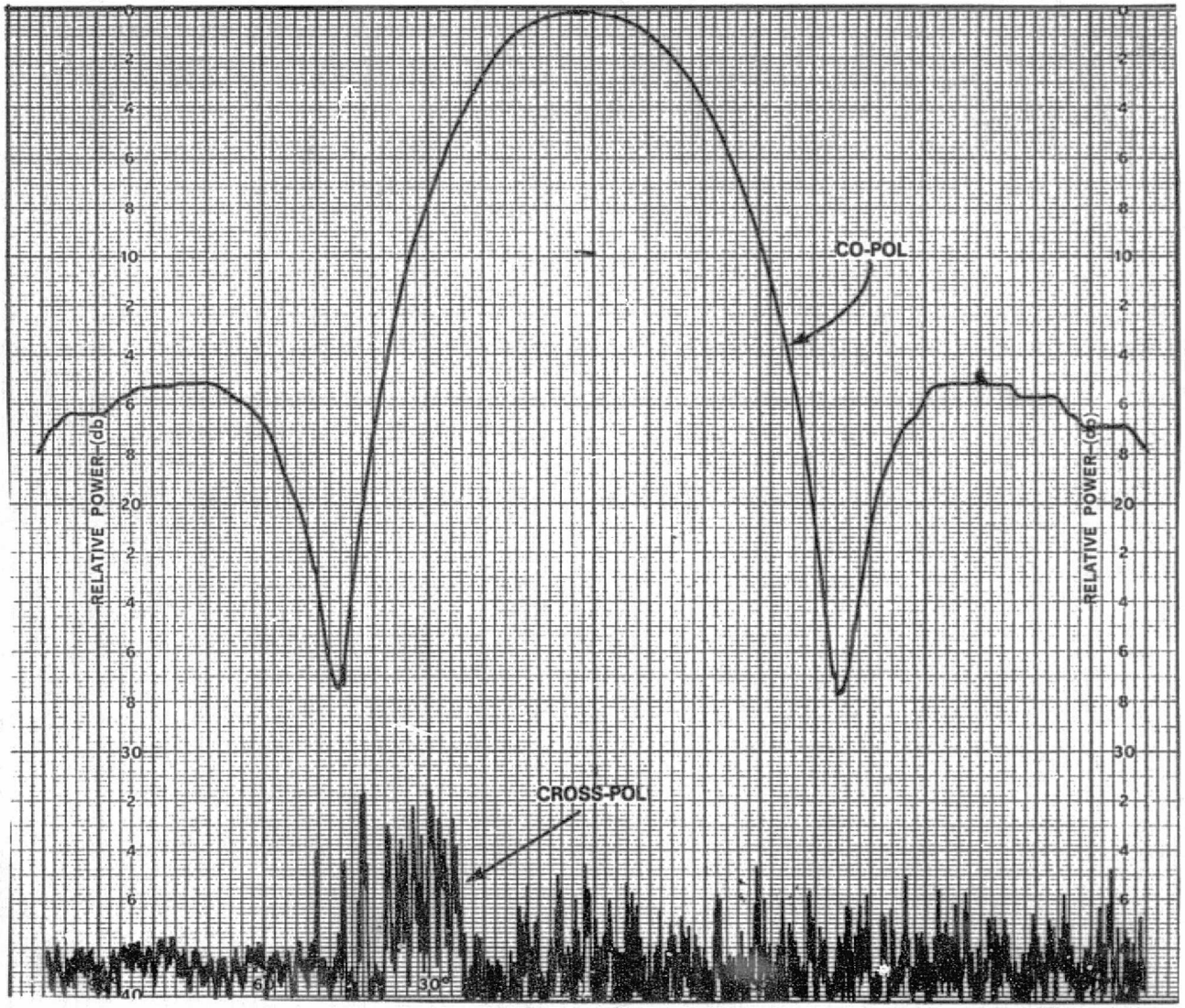

Figure A-49. E-Plane Pattern for Isolated Element at 11.7 GHz

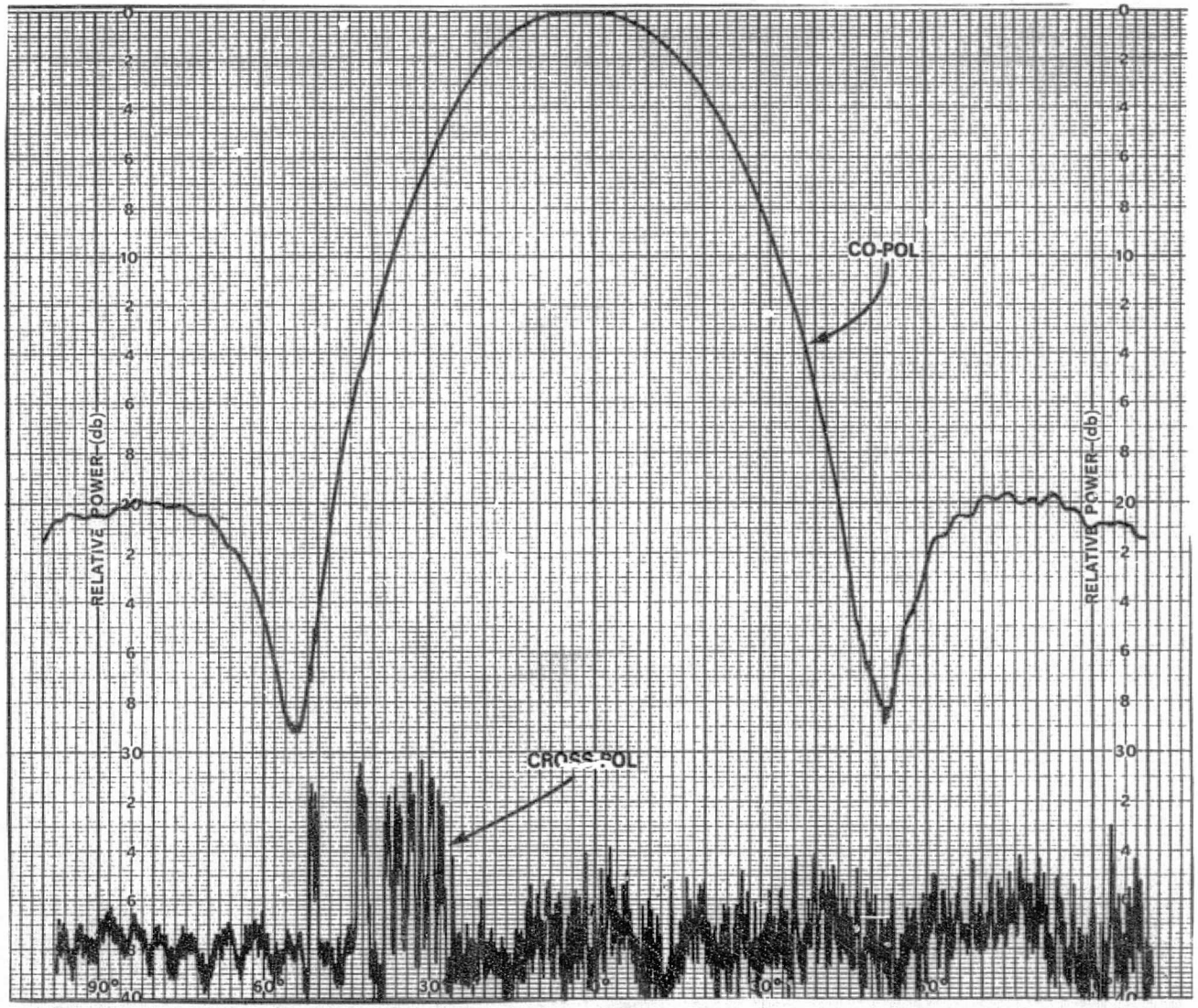

Figure A-50. E-Plane Pattern for Isolated Element at 11.95 GHz

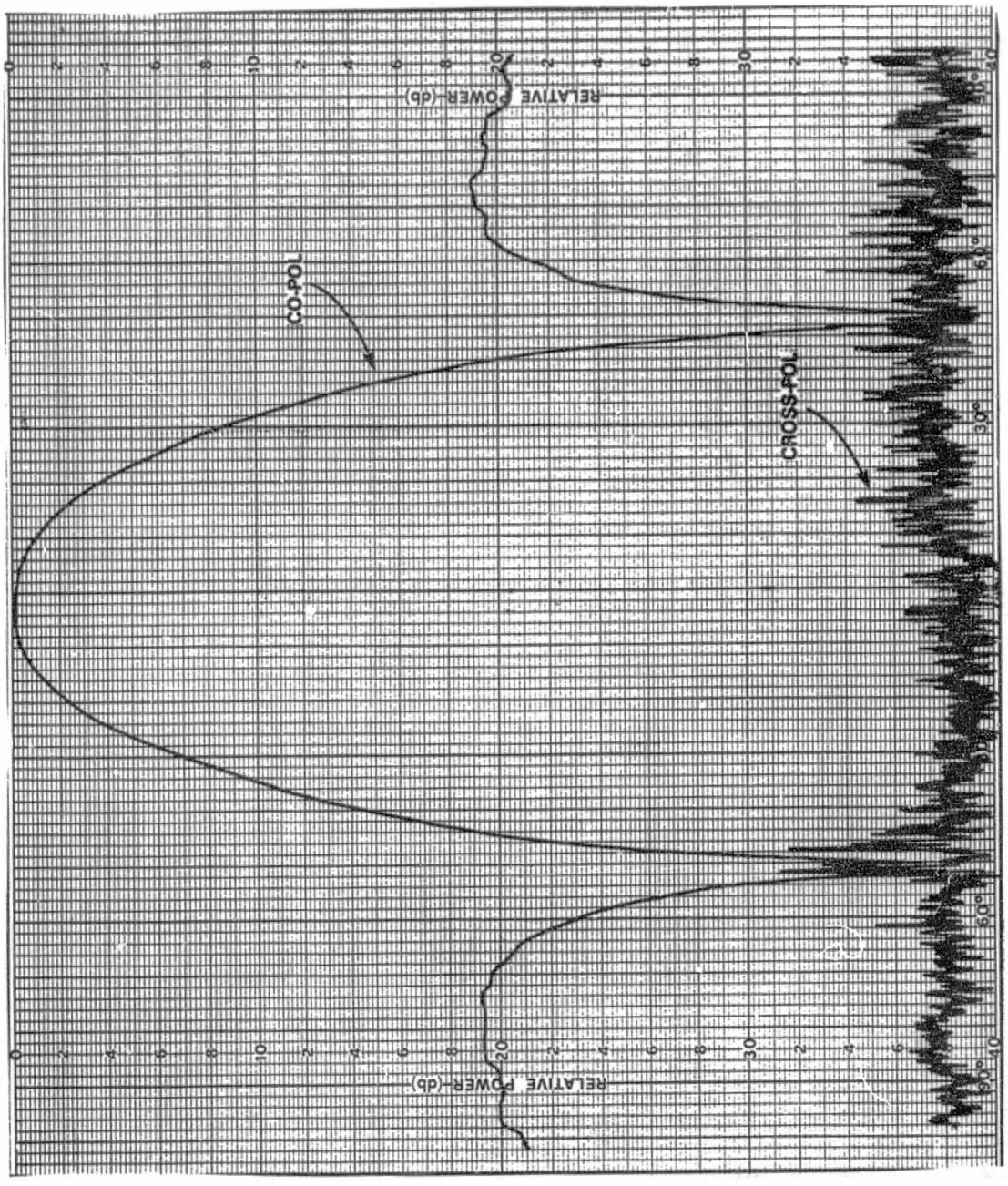

Figure A-51. E-Plane Pattern for Isolated Element at 12.2 GHz

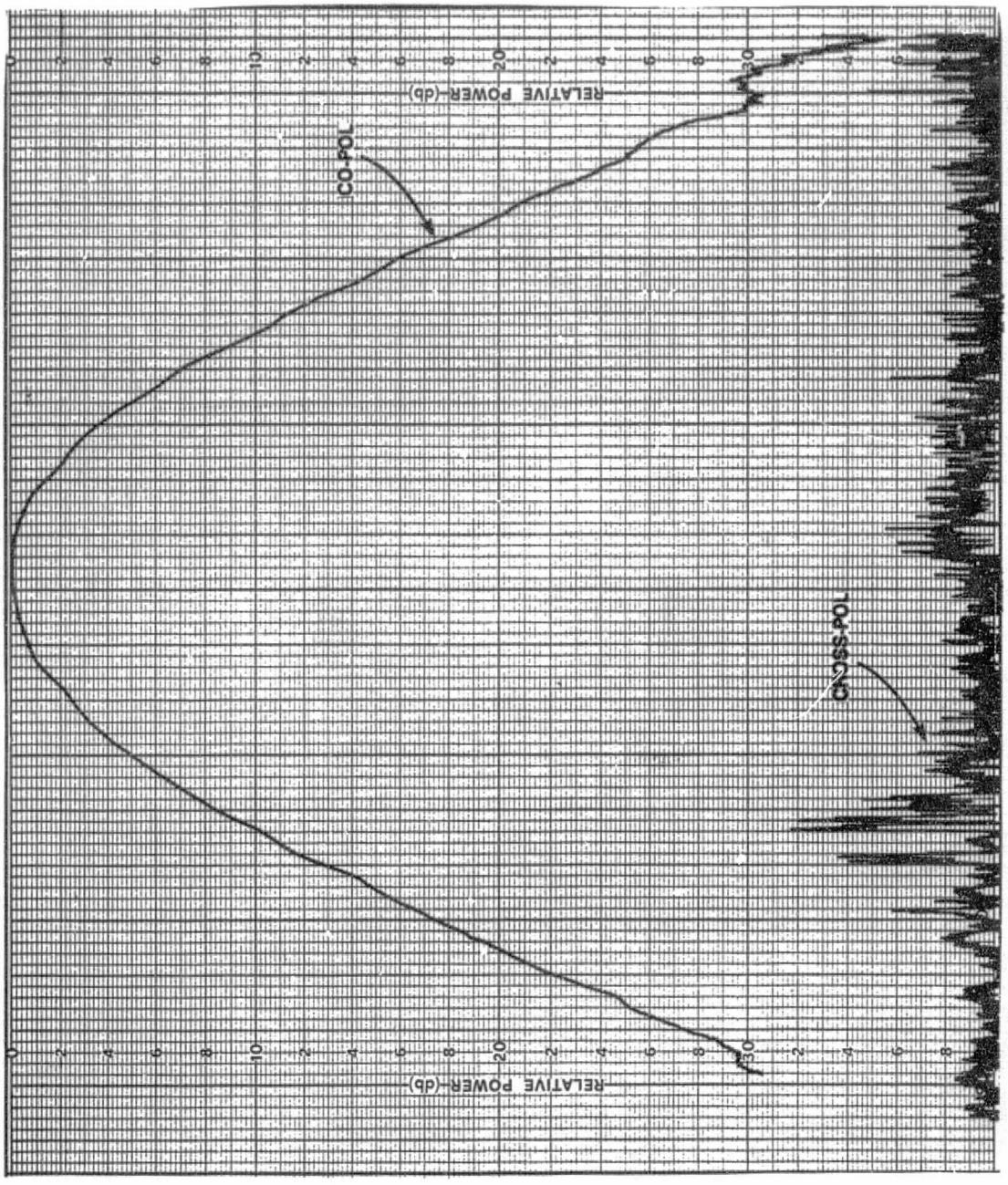

Figure A-52. H-Plane Pattern for Isolated Element at 11.7 GHz

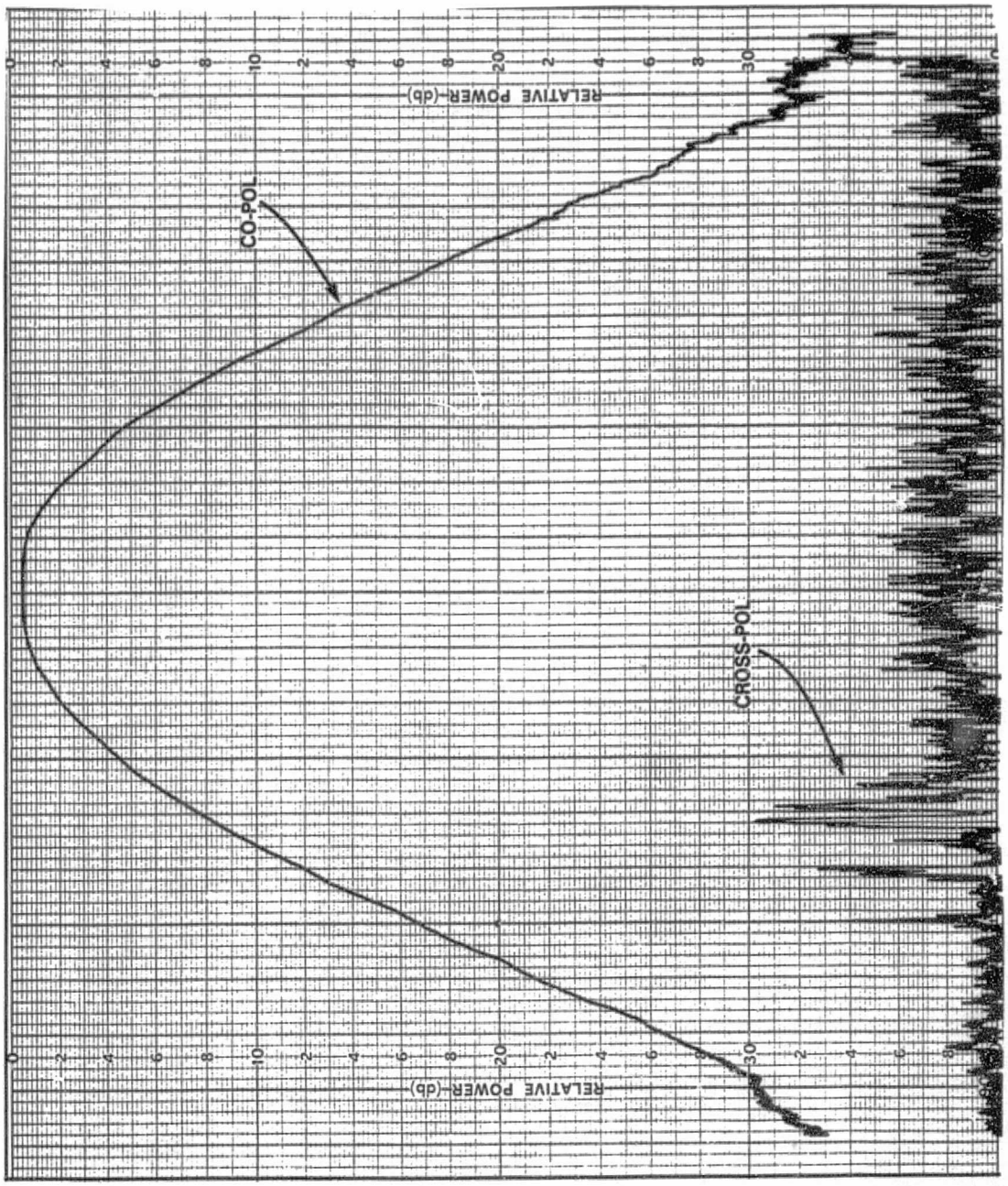

Figure A-53. H-Plane Pattern for Isolated Element at 11.95 GHz

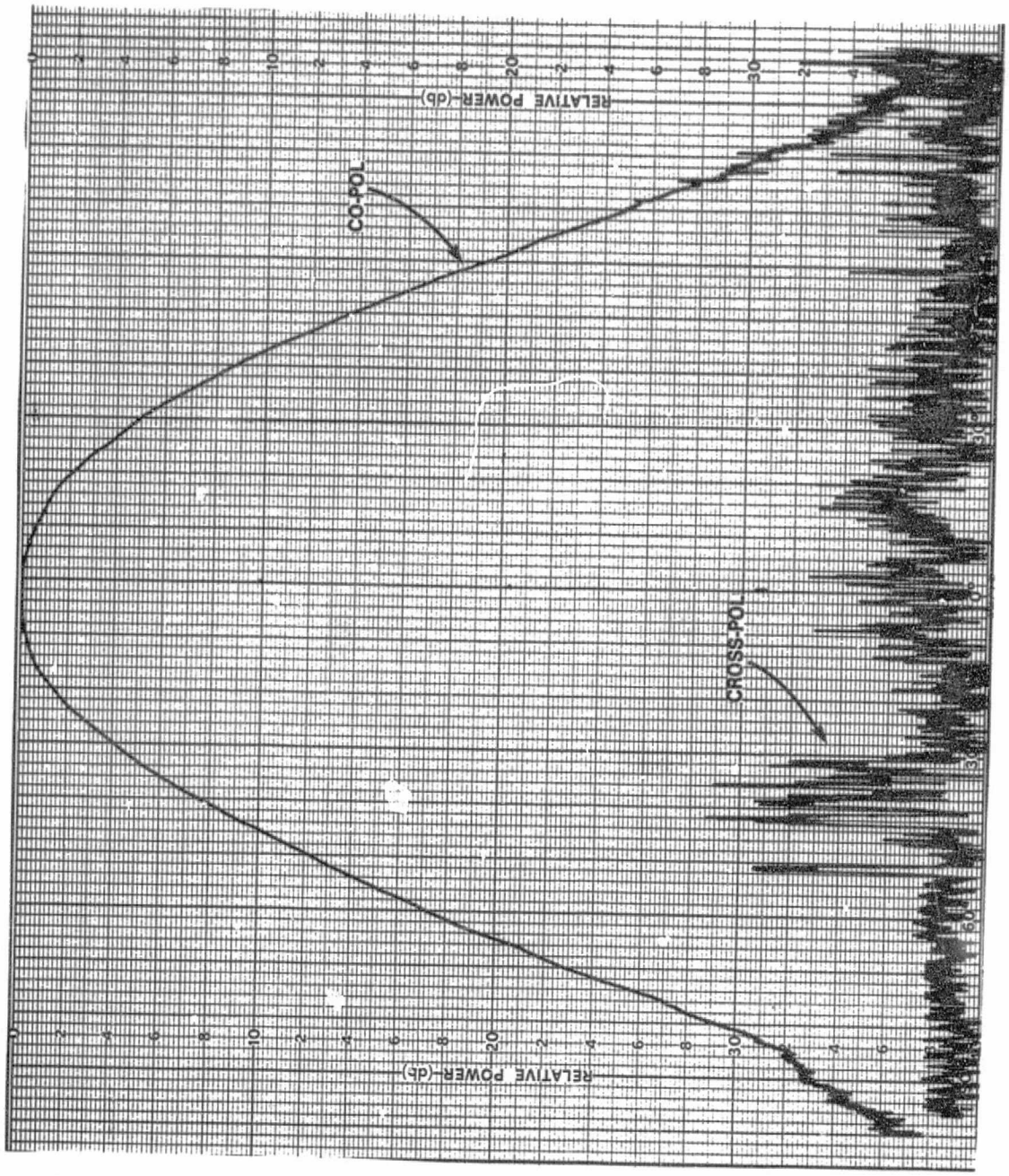

Figure A-54. H-Plane Pattern for Isolated Element at 12.2 GHz

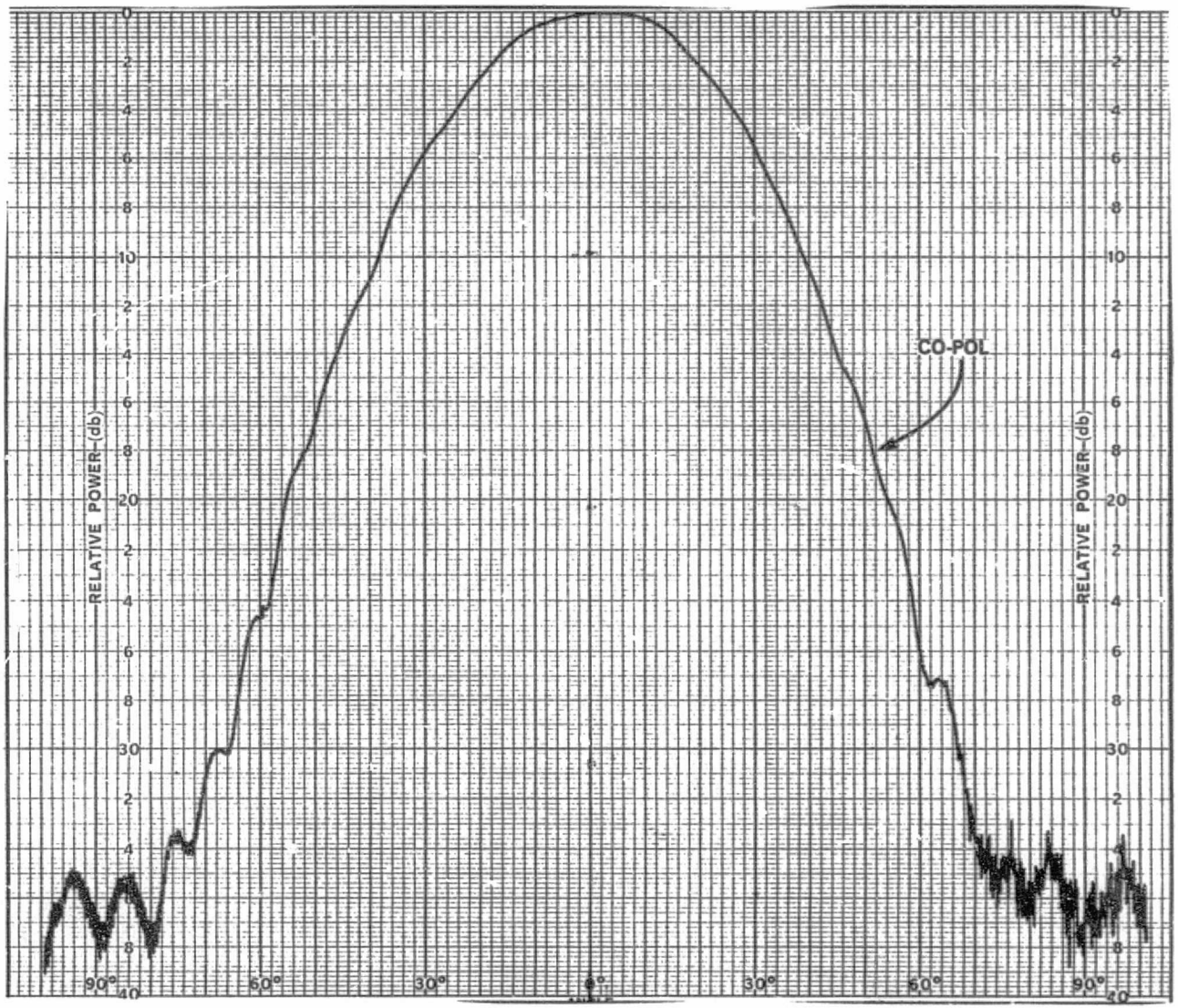

Figure A-55. Co-Pol 45°-Plane Pattern for Isolated Element at 11.7 GHz

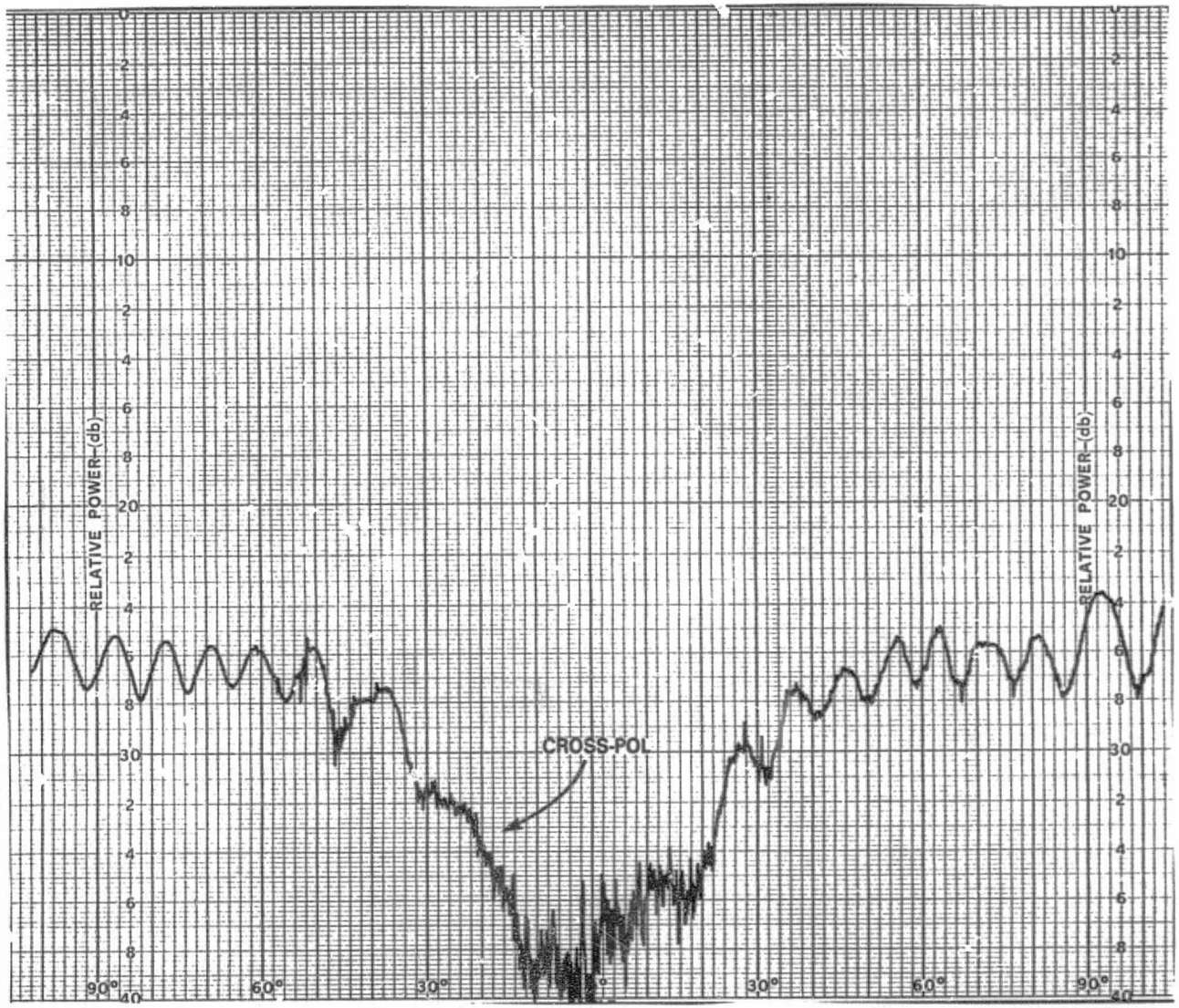

Figure A-56. Cross-Pol 45°-Plane Pattern for Isolated Element at 11.7 GHz

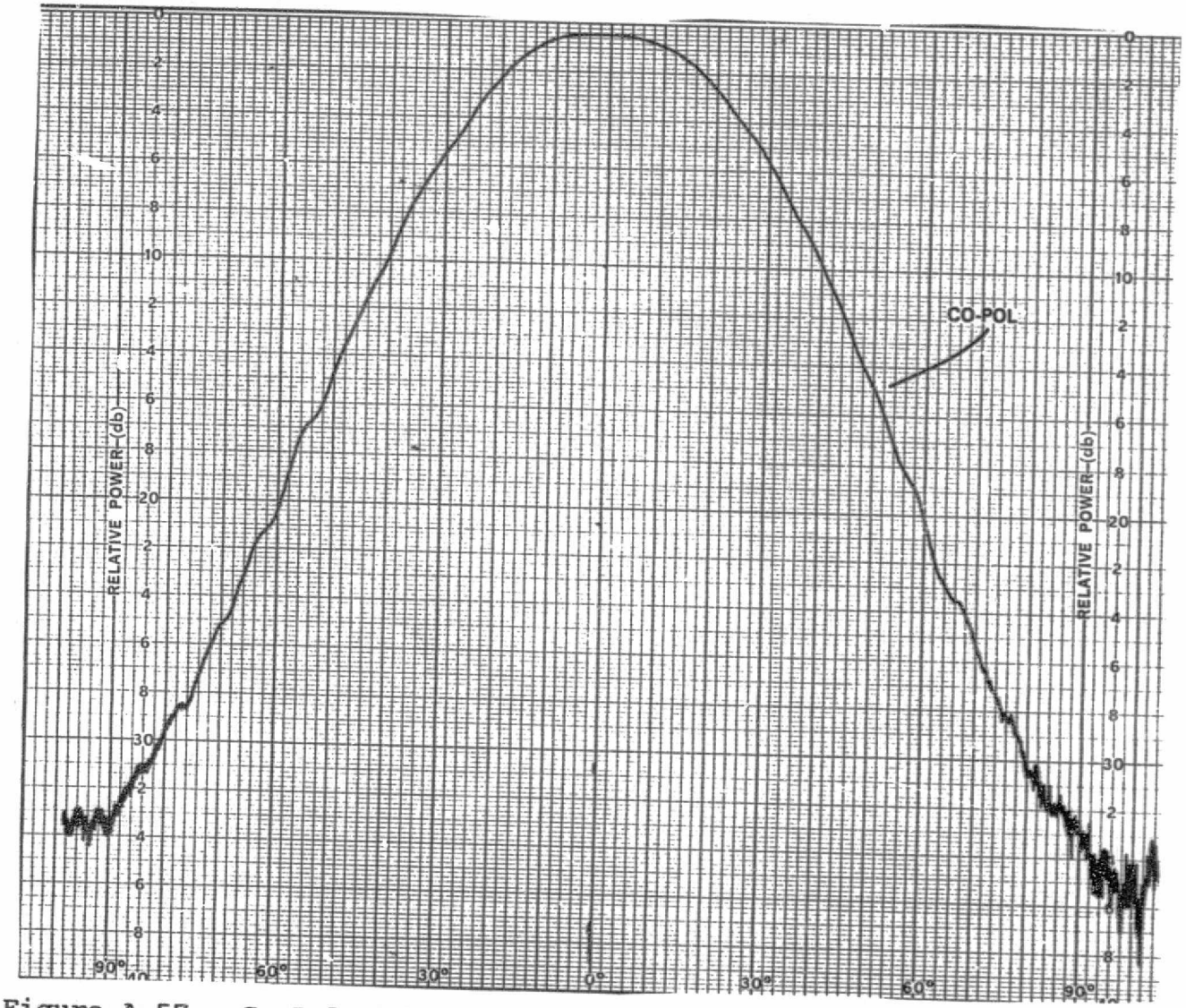

Figure A-57. Co-Pol 45°-Plane Pattern for Isolated Element at 11.95 GHz

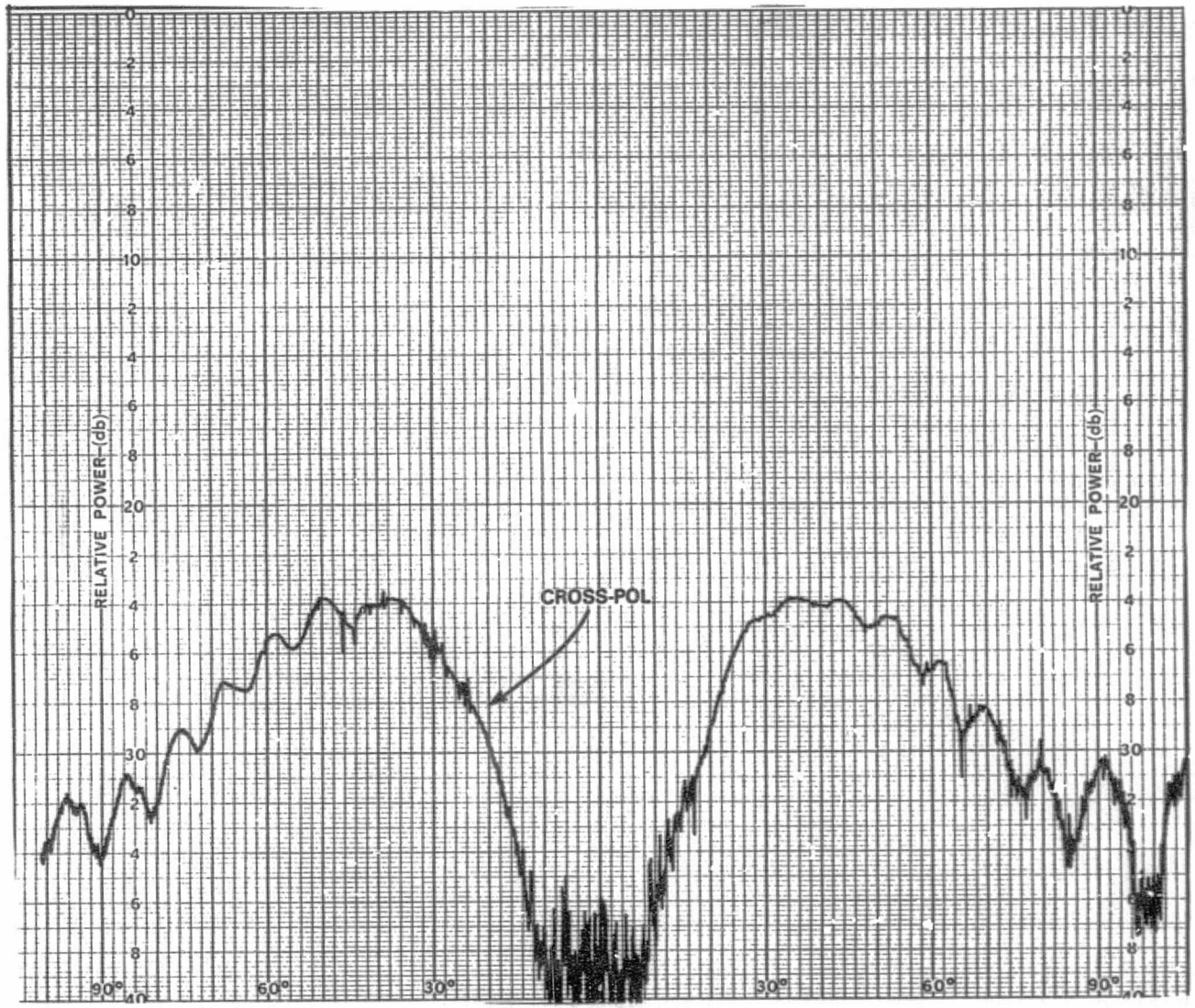

Figure A-58. Cross-Pol 45°-Plane Pattern for Isolated Element at 11.95 GHz

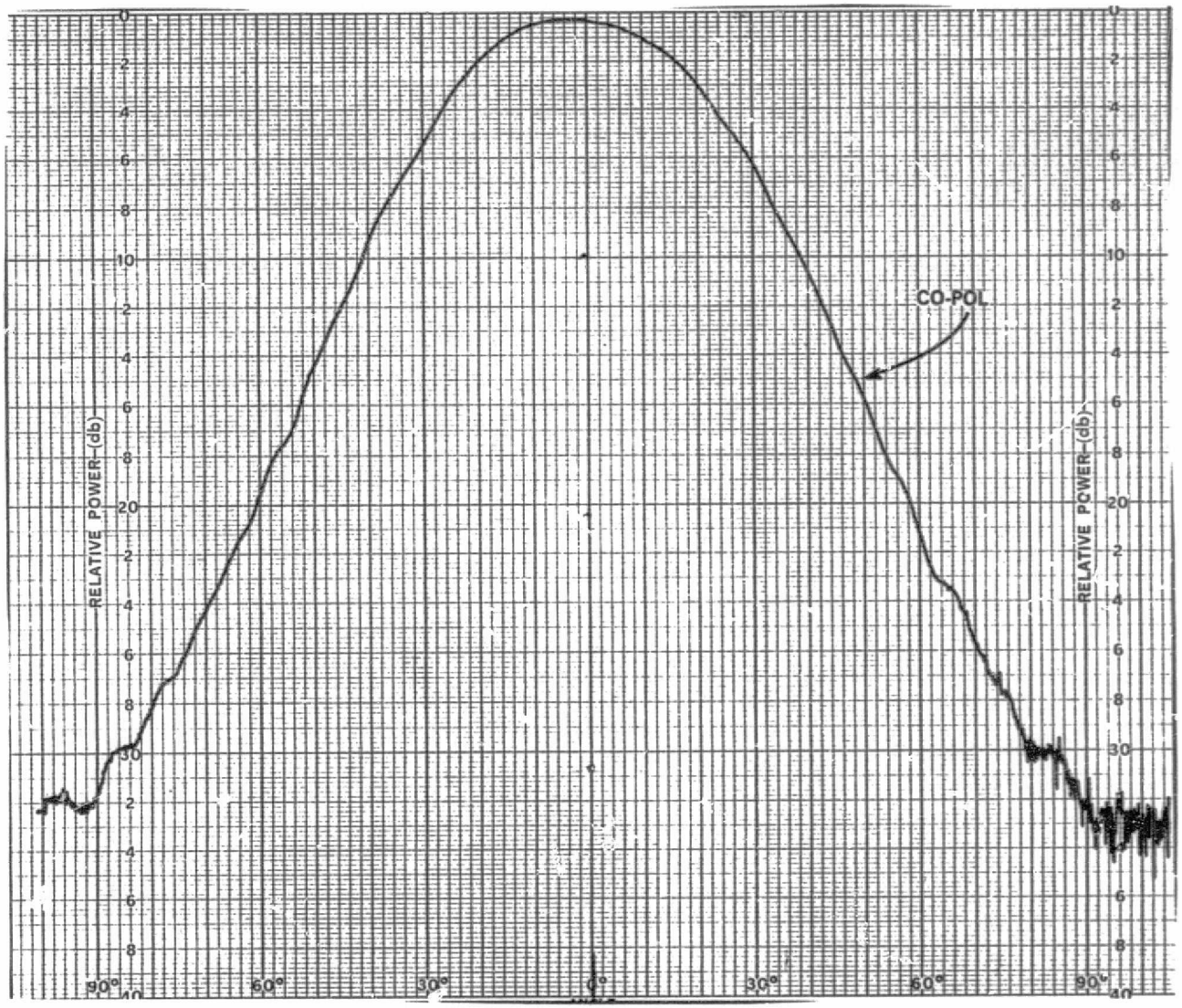

Figure A-59. Co-Pol ±45°-Plane Pattern for Isolated Element at 12.2 GHz

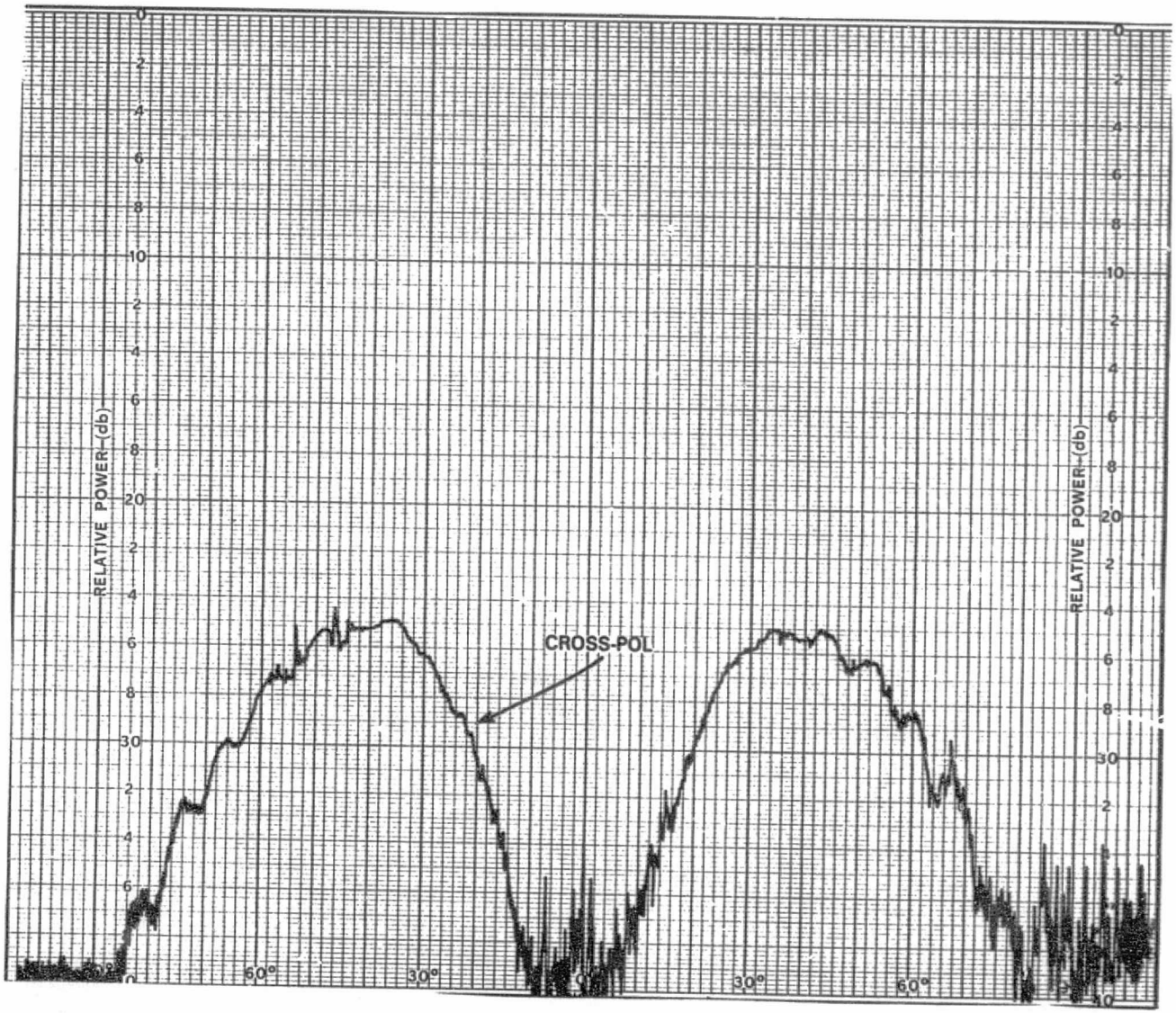

Figure A-60. Cross-Pol 45°-Plane Pattern for Isolated Element at 12.2 GHz

APPENDIX B. MEASURED SCANNING ARRAY PATTERNS

This appendix contains plots of the radiation patterns measured for the 8-element linear array embedded in the 34-element array shown in Figure 5-24. The array elements are fed to scan in five different directions from 0° to 20°. Three different amplitude distributions were used: uniform, 30-dB Taylor, and 30-dB quantized Taylor. The pattern cuts were taken in the plane of the linear array. When the elements are fed with vertical polarization, the cut represents an H-plane pattern. When the elements are fed with horizontal polarization, the cut represents an E-plane pattern. All the measurements were repeated at 11.7, 11.95, and 12.2 GHz.

Figures B-1 through B-30 show the measured patterns for the uniformly excited array, as follows:

- Figures B-1 to B-3 show the E-plane pattern when the elements are horizontally polarized and equally phased to radiate in the broadside direction. The figures show the measurements at 11.7, 11.95, and 12.2 GHz, respectively.
- Figures B-4 to B-6 show the H-plane pattern when the elements are vertically polarized for broadside radiation at the three frequencies.
- Figures B-7 to B-12 show the E-plane patterns at the three frequencies, followed by the H-plane patterns at the three frequencies, when the elements are excited with progressive phase differences of 45°.
- Figures B-13 to B-18 show the E-plane patterns at the three frequencies, followed by H-plane patterns at the three frequencies, when the elements are excited with progressive phase differences of 90°.

- Figures B-19 to B-24 show the E-plane patterns at the three frequencies, followed by H-plane patterns at the three frequencies, when the elements are excited with progressive phase differences of 135°.
- Figures B-25 to B-30 show the E-plane patterns at the three frequencies, followed by the H-plane patterns at the three frequencies, when the elements are excited with progressive phase differences of 180°.

Figures B-31 through B-42 show the measured patterns for the array when excited with 30-dB Taylor distribution, as follows:

- Figures B-31 to B-36 show the E-plane patterns at the three frequencies, followed by the H-plane patterns at the three frequencies, when the elements are equally phased for broadside radiation.
- Figures B-37 to B-42 show the E-plane patterns at the three frequencies, followed by the H-plane patterns at the three frequencies, when the elements are excited with progressive phase differences of 180°.

Figures B-43 through B-54 show the measured patterns for the array when excited with 30-dB Taylor distribution quantized to the relative amplitude levels of 0, -6, -10, and -16 dB, as follows:

- Figures B-43 to B-48 show the E-plane patterns at the three frequencies, followed by the H-plane patterns at the three frequencies, when the elements are equally phased for broadside radiation.

Figures B-49 to B-54 show the E-plane patterns at the three frequencies, followed by the H-plane patterns at the three frequencies, when the elements are excited with progressive phase differences of 180°.

To show the scanning performance of the array, the measured element patterns of a central element are given in Figures B-55 to B-60: first the E-plane patterns at the three frequencies, followed by the H-plane patterns at the three frequencies.

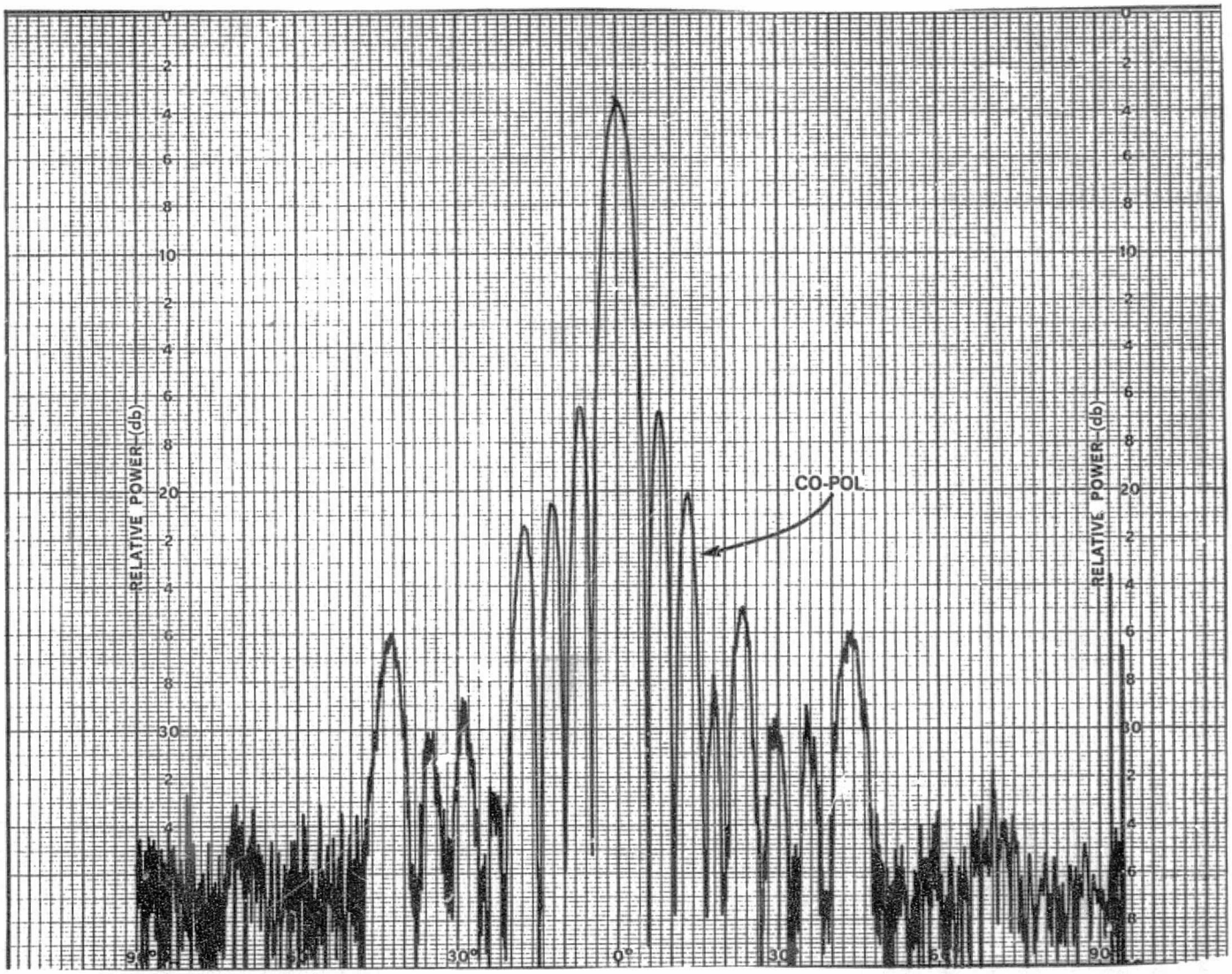

Figure B-1. E-Plane Pattern of Horizontally Polarized 8-Element Array, Uniform Amplitude, Equal Phase, 11.7 GHz

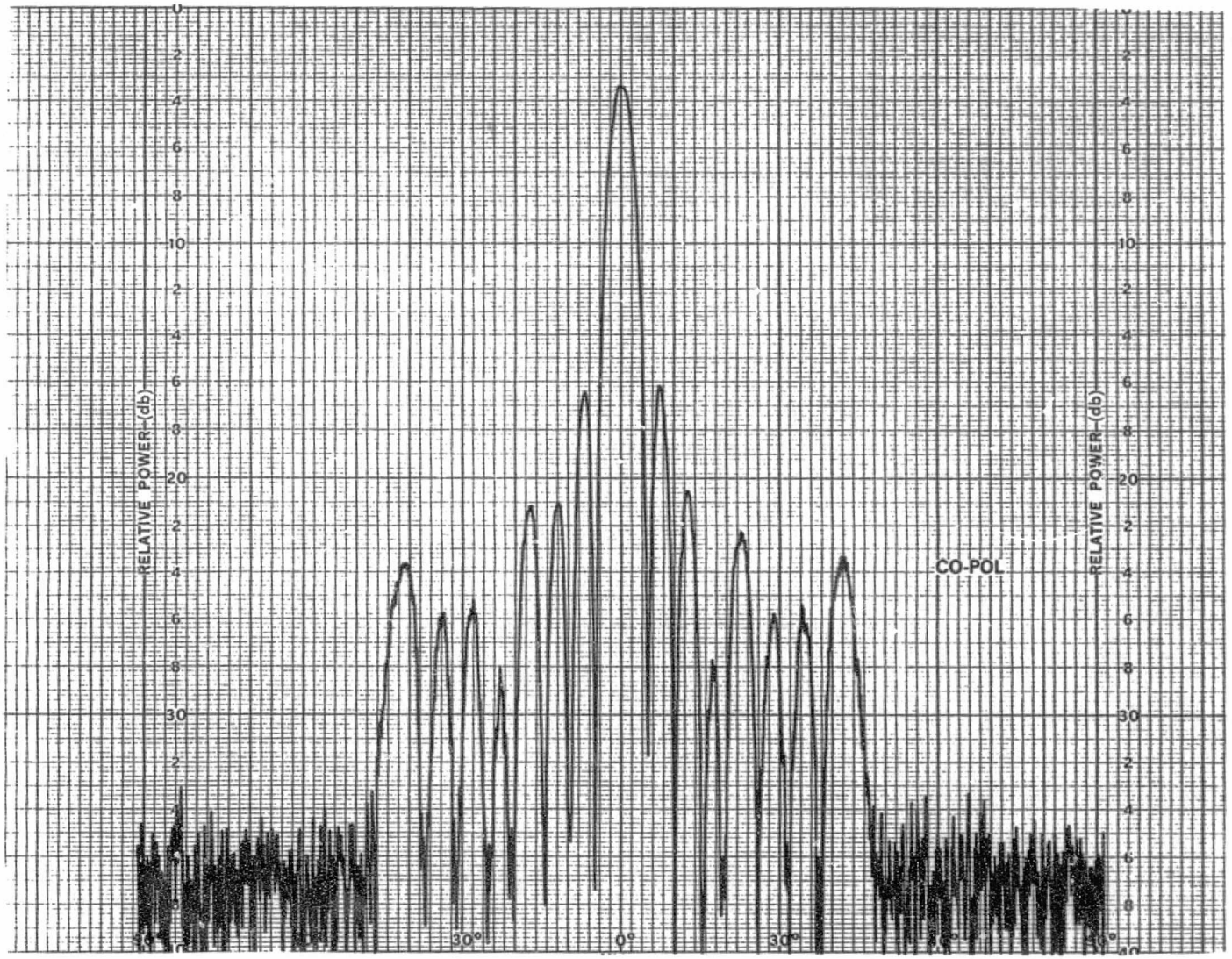

Figure B-2. E-Plane Pattern of Horizontally Polarized 8-Element Array, Uniform Amplitude, Equal Phase, 11.95 GHz

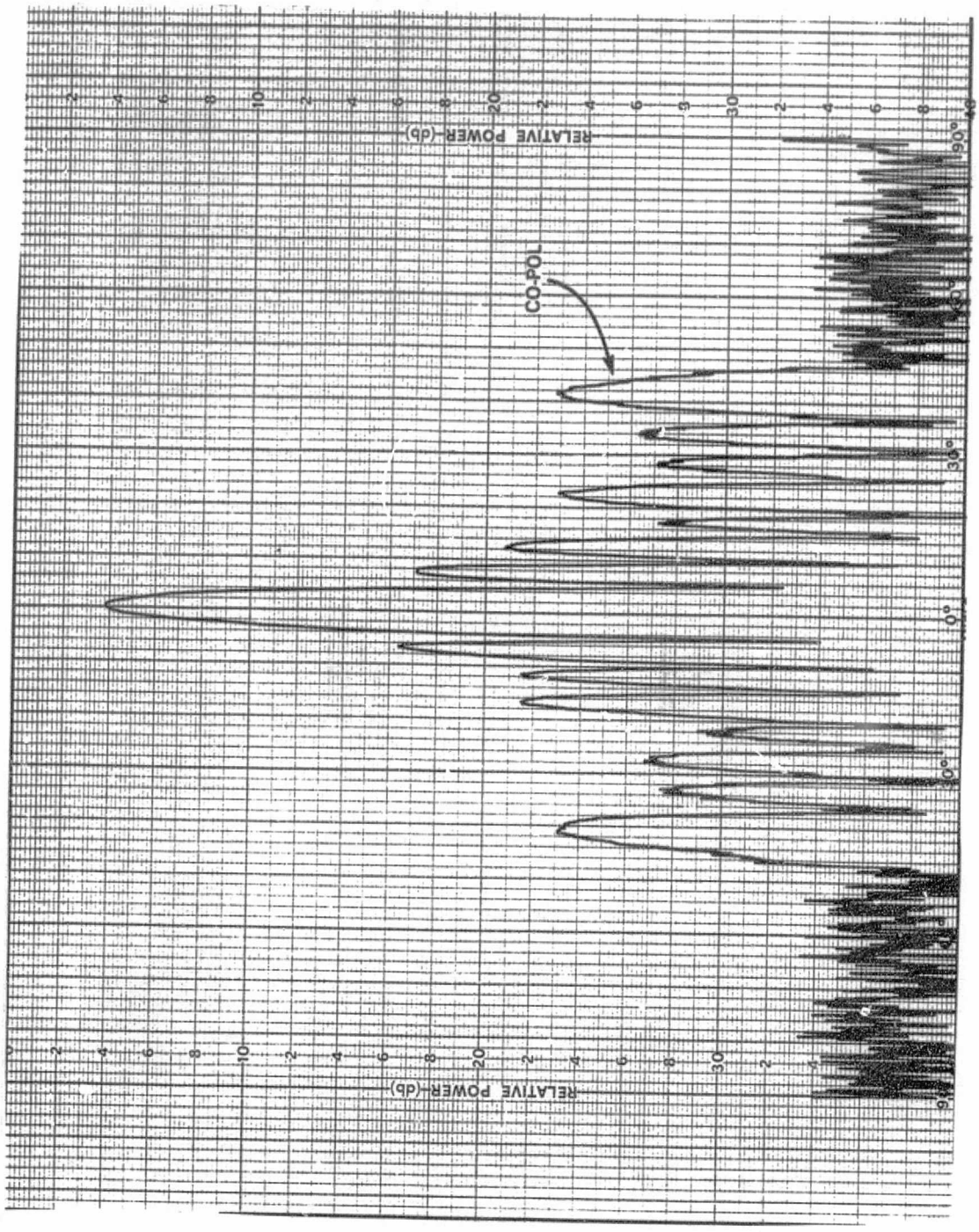

Figure B-3. E-Plane Pattern of Horizontally Polarized 8-Element Array, Uniform Amplitude, Equal Phase, 12.2 GHz

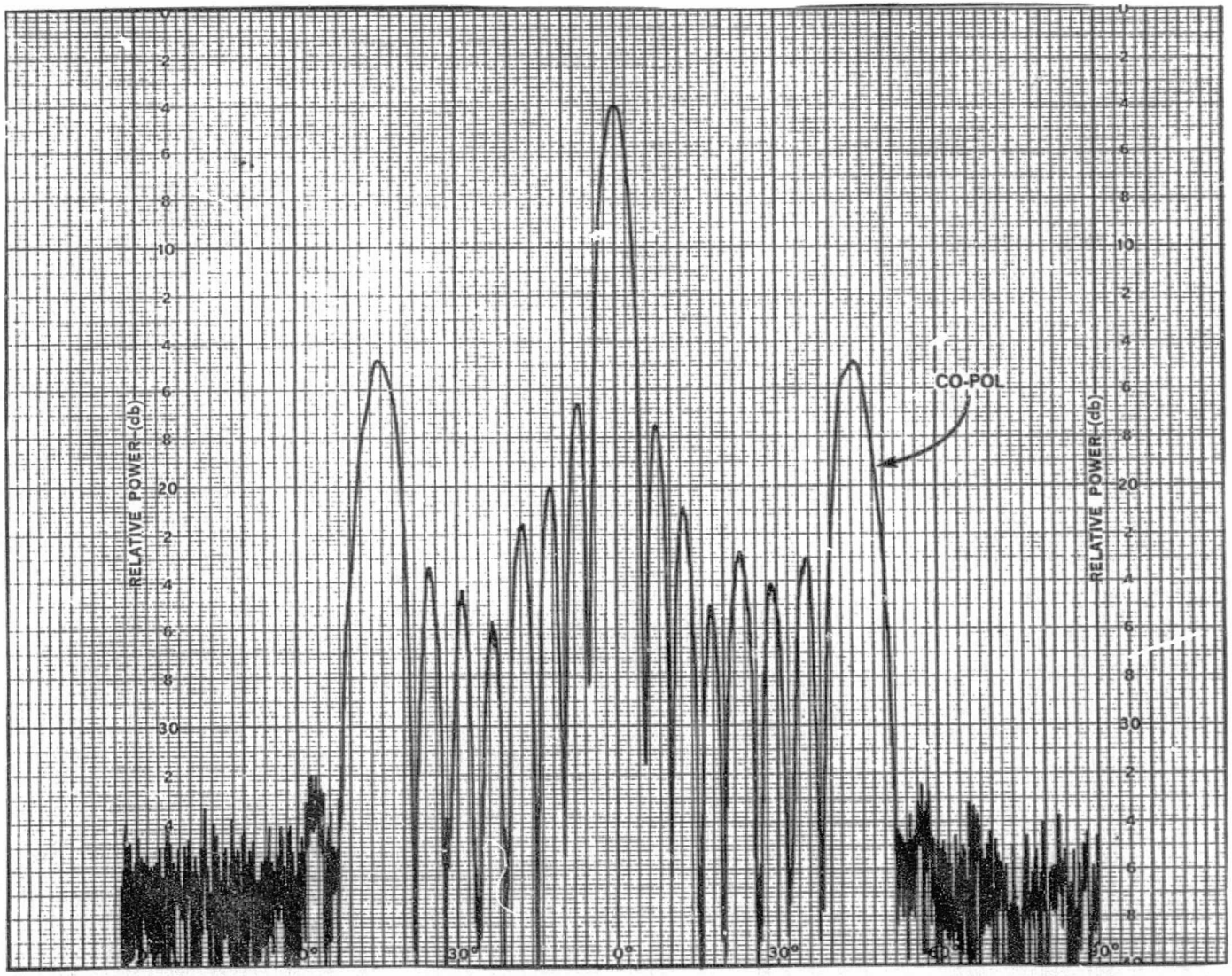

Figure B-4. H-Plane Pattern of Vertically Polarized 8-Element Array, Uniform Amplitude, Equal Phase, 11.7 GHz

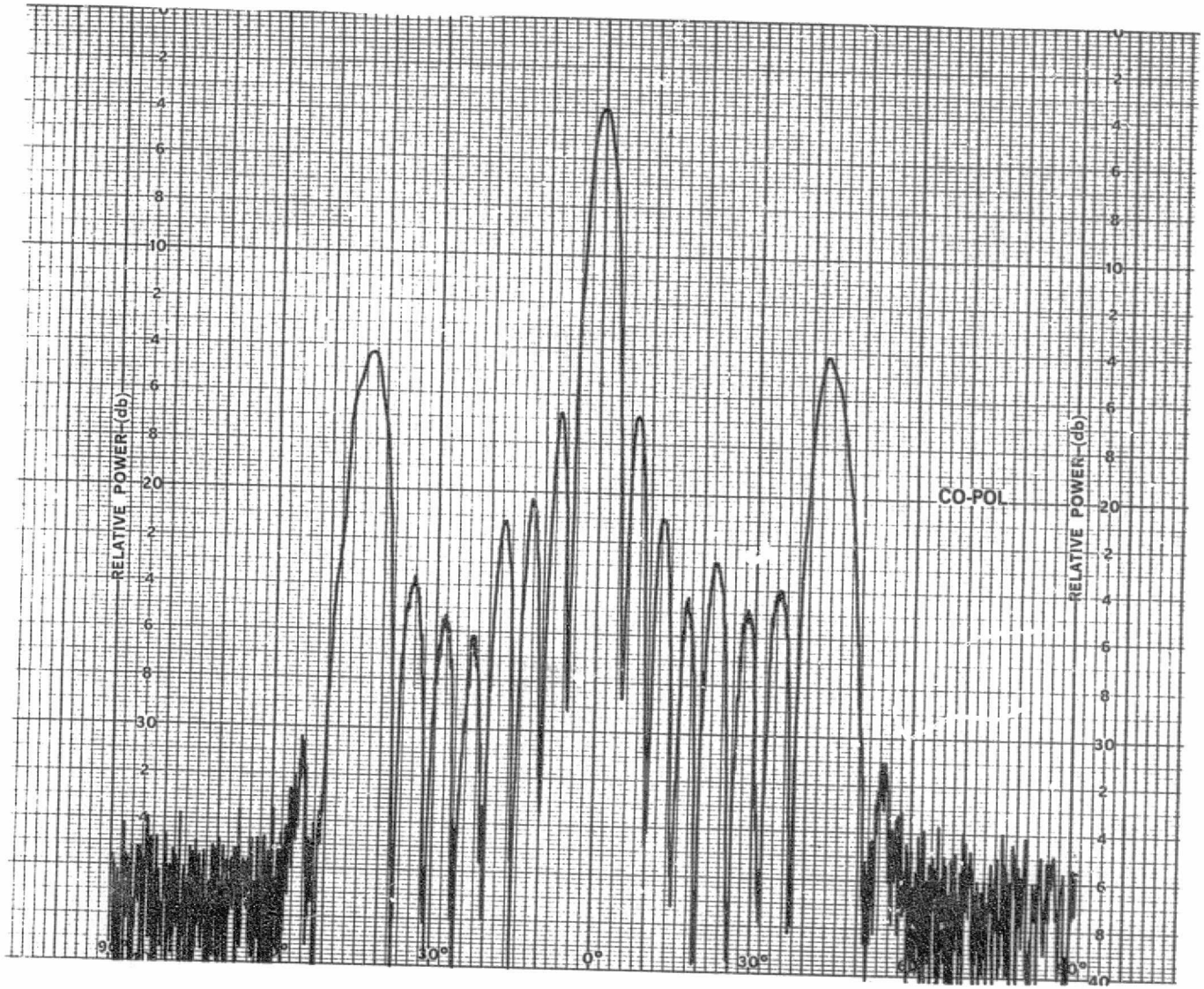

Figure B-5. H-Plane Pattern of Vertically Polarized 8-Element Array, Uniform Amplitude, Equal Phase, 11.95 GHz

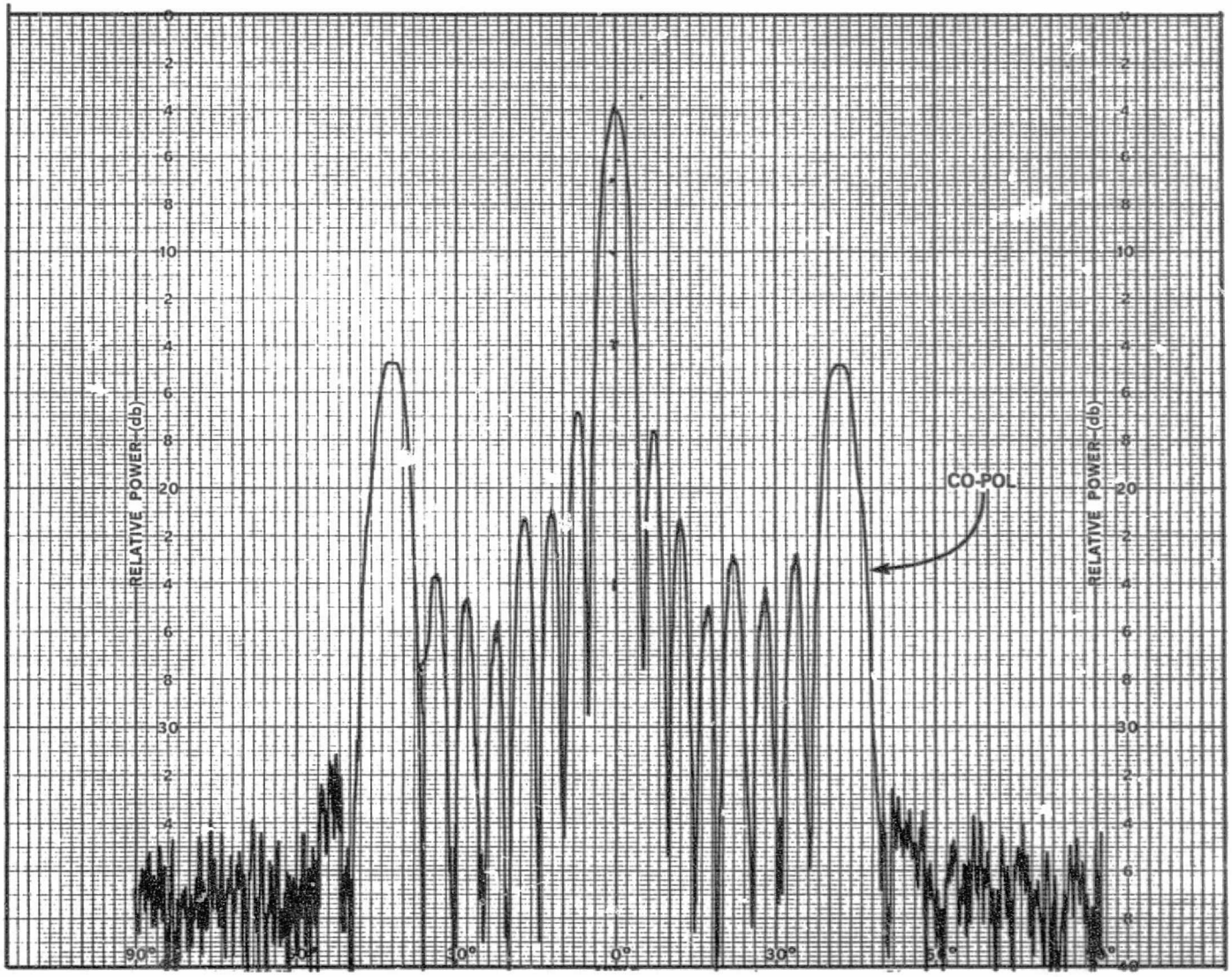

Figure B-6. H-Plane Pattern of Vertically Polarized 8-Element Array, Uniform Amplitude, Equal Phase, 12.2 GHz

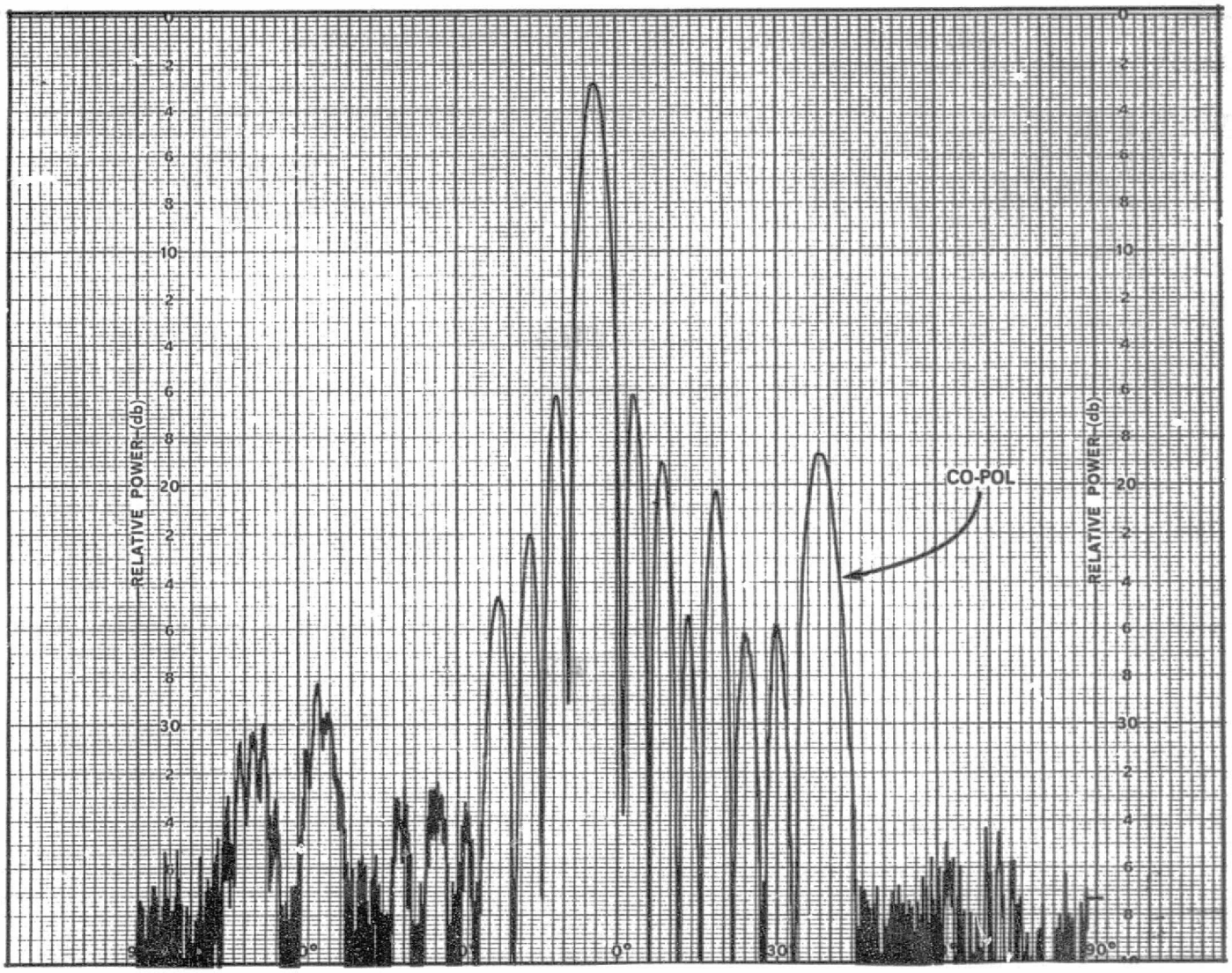

Figure B-7. E-Plane Pattern of Horizontally Polarized 8-Element Array, Uniform Amplitude, 45° Progressive Phase Difference, 11.7 GHz

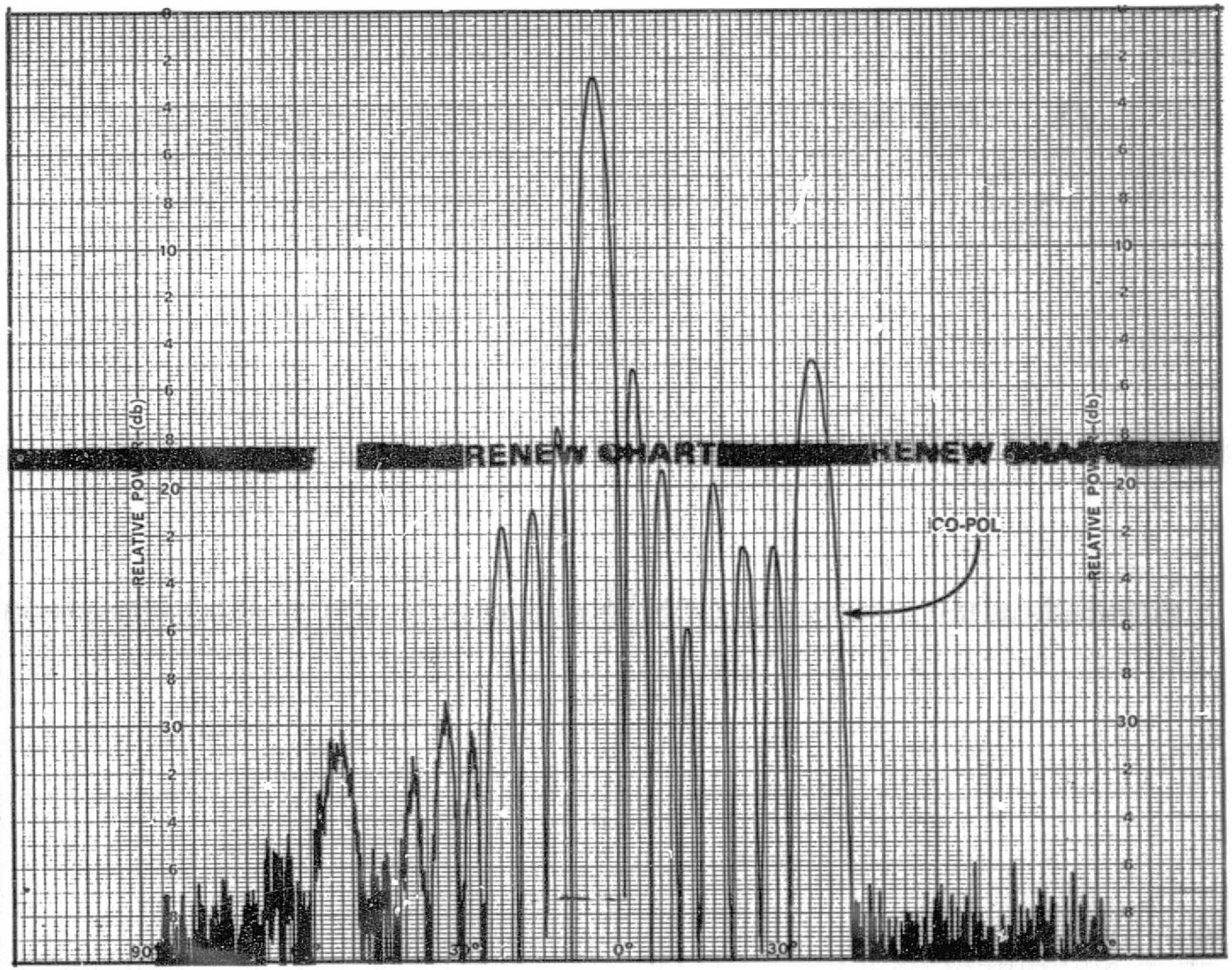

Figure B-8. E-Plane Pattern of Horizontally Polarized 8-Element Array, Uniform Amplitude, 45° Progressive Phase Difference, 11.95 GHz

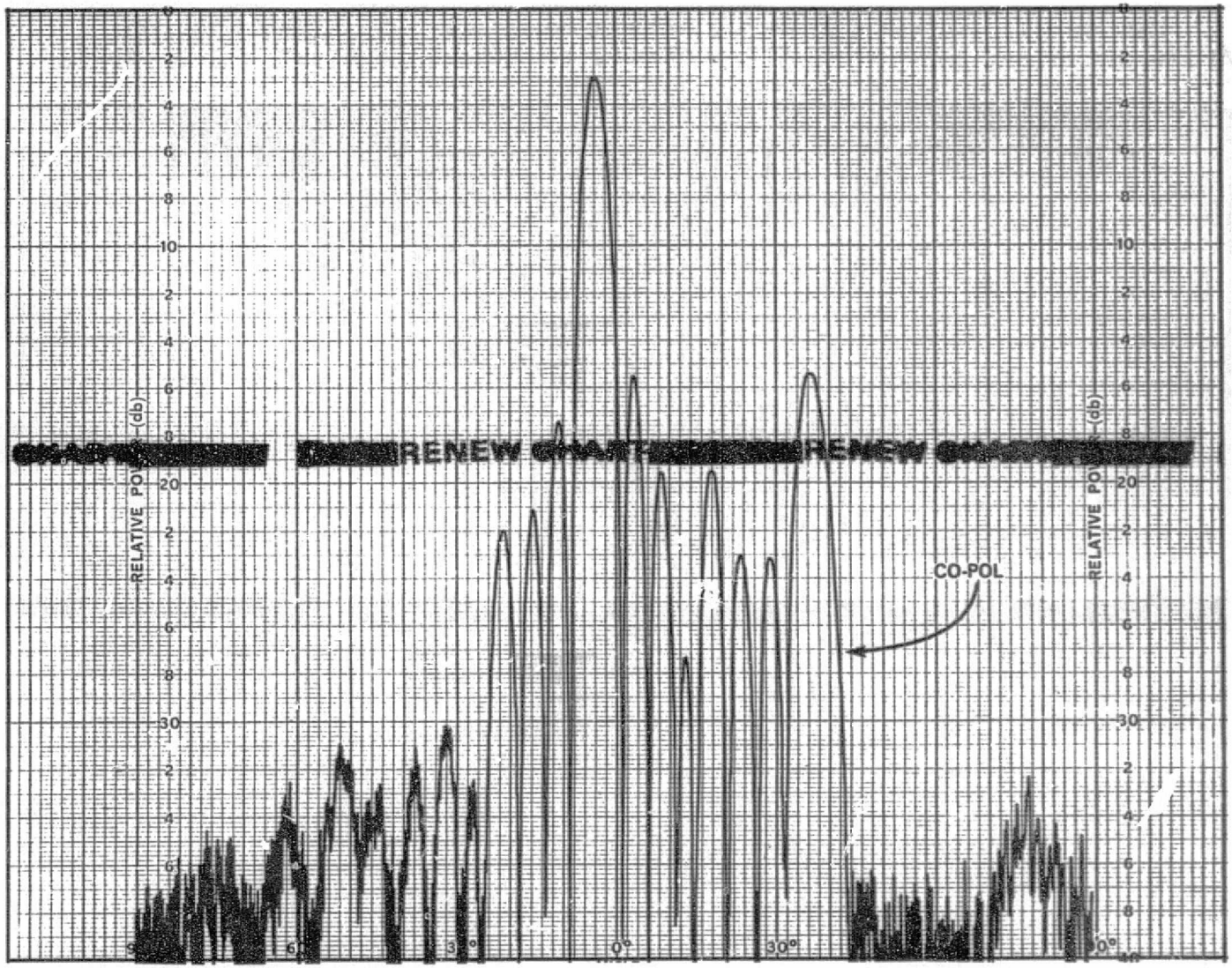

Figure B-9. E-Plane Pattern of Horizontally Polarized 8-Element Array, Uniform Amplitude, 45° Progressive Phase Difference, 12.2 GHz

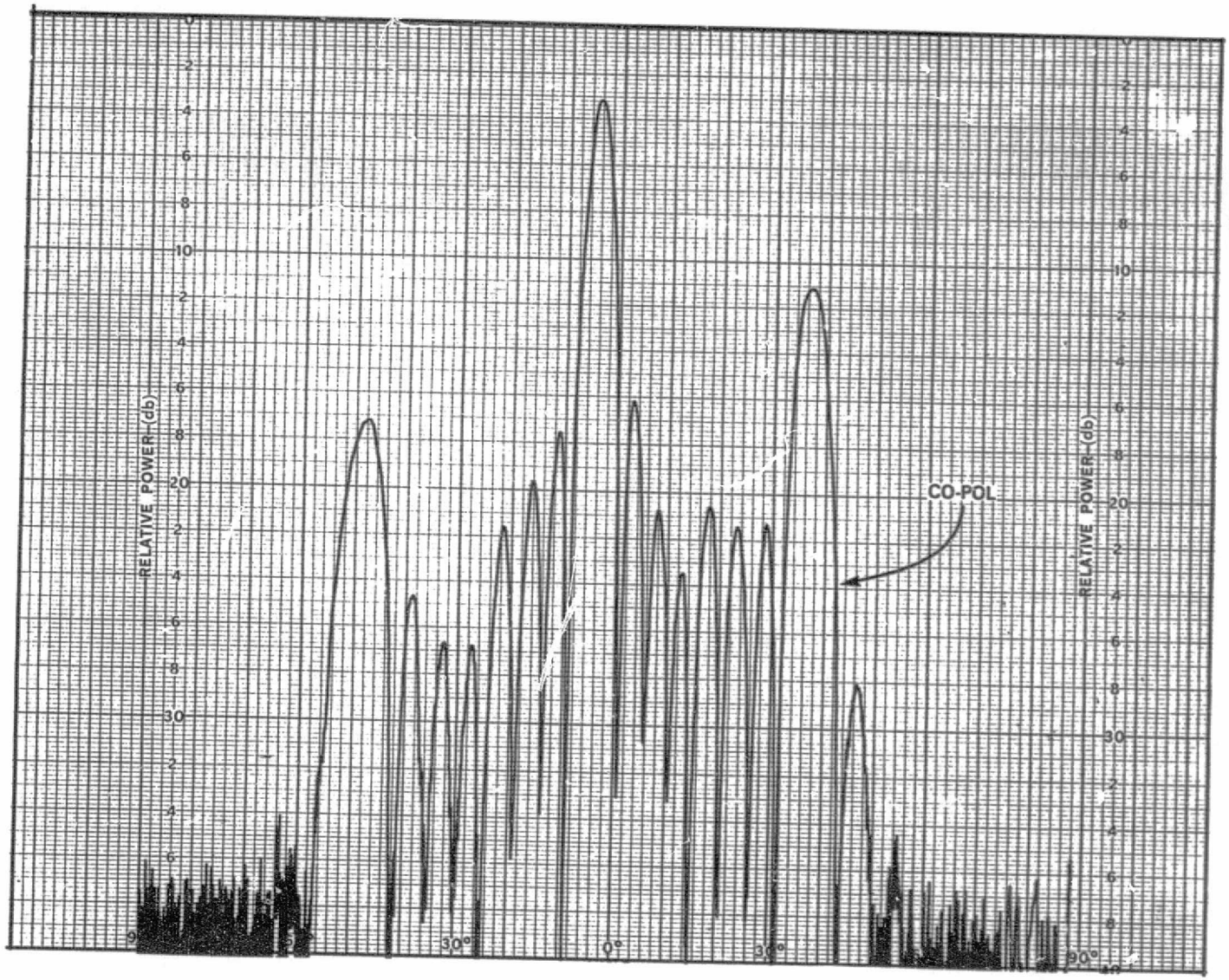

Figure B-10. H-Plane Pattern of Vertically Polarized 8-Element Array, Uniform Amplitude, 45° Progressive Phase Difference, 11.7 GHz

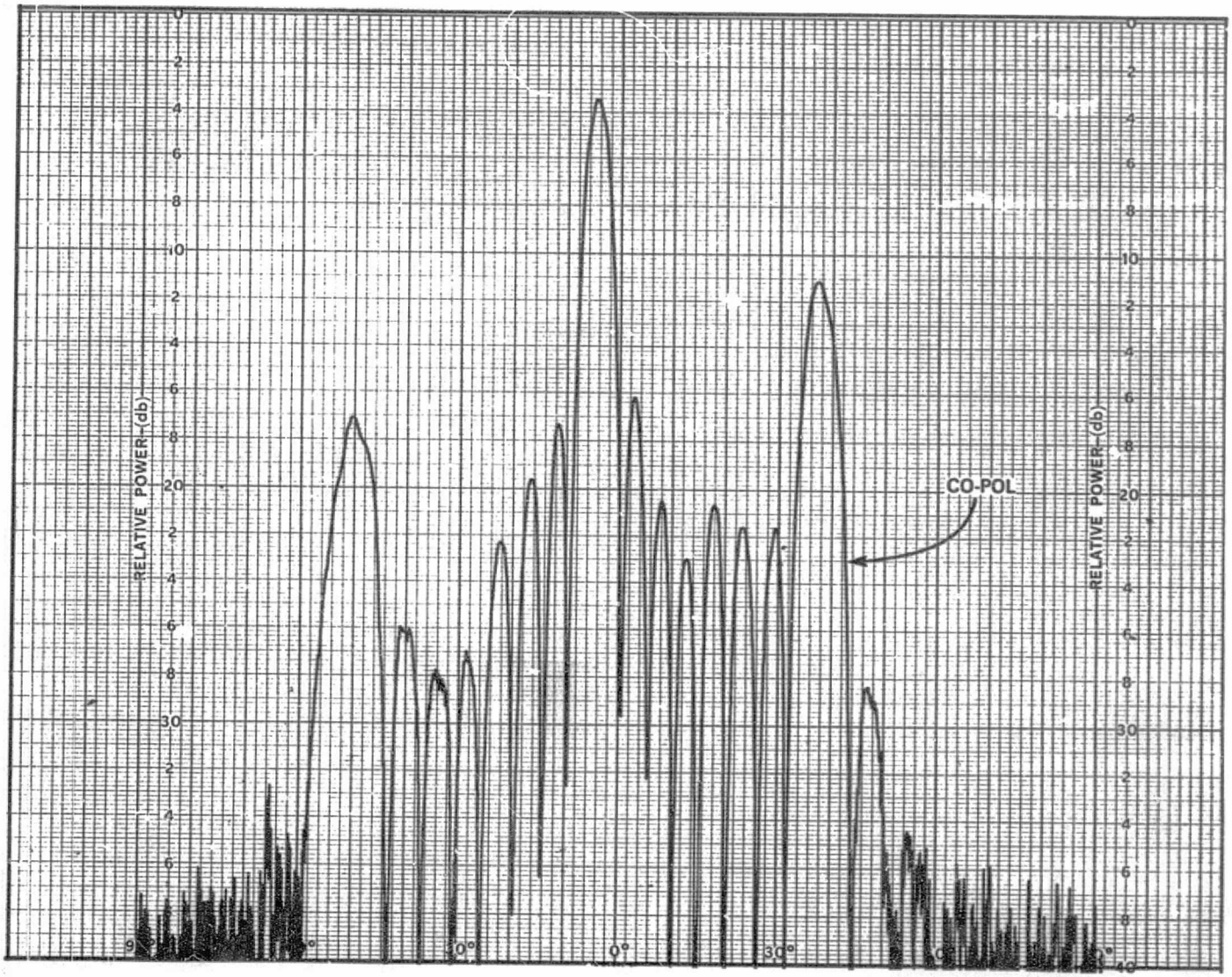

Figure B-11. H-Plane Pattern of Vertically Polarized 8-Element Array, Uniform Amplitude, 45° Progressive Phase Difference, 11.95 GHz

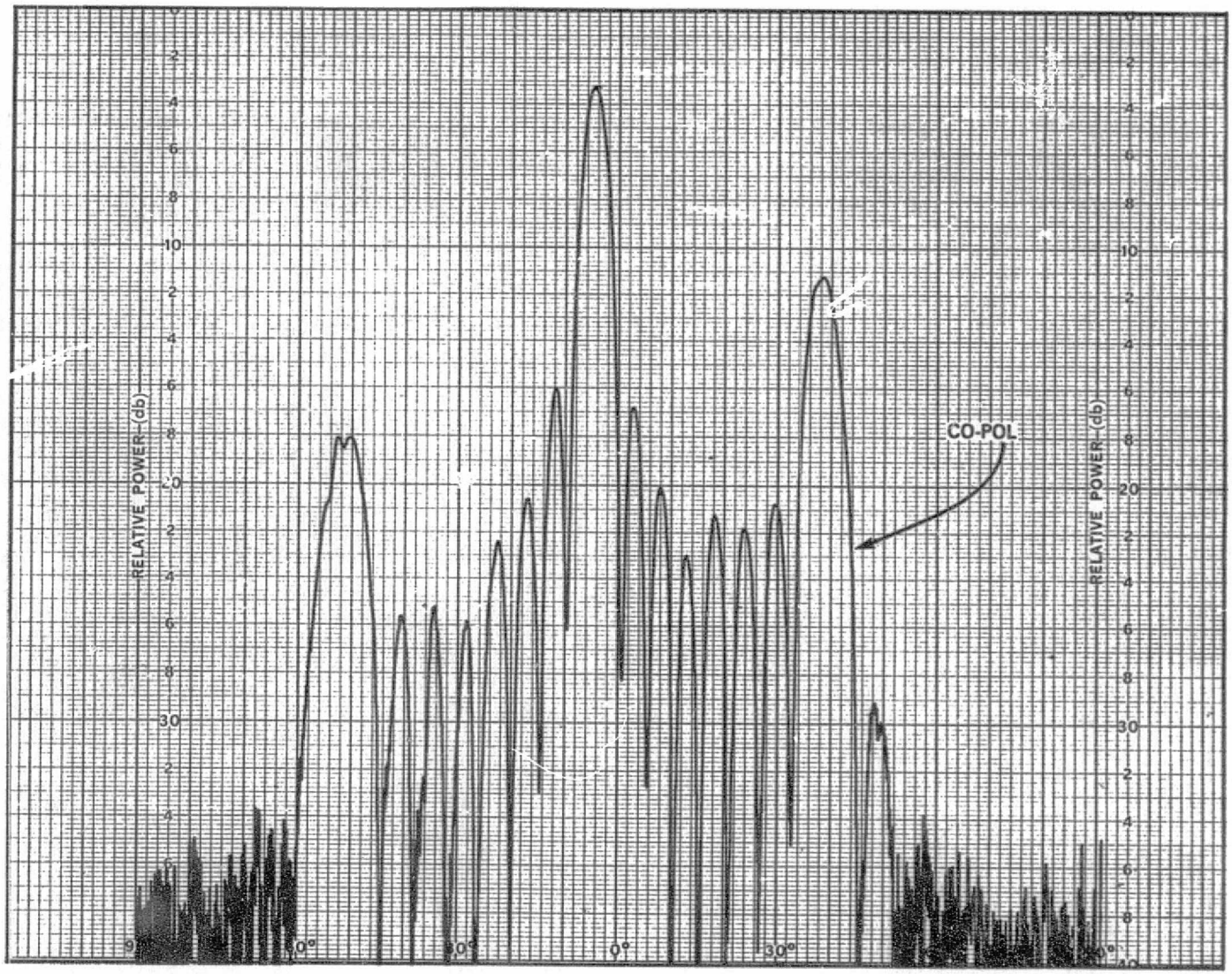

Figure B-12. H-Plane Pattern of Vertically Polarized 8-Element Array, Uniform Amplitude, 45° Progressive Phase Difference, 12.2 GHz

ORIGINAL PAGE IS
OF POOR QUALITY

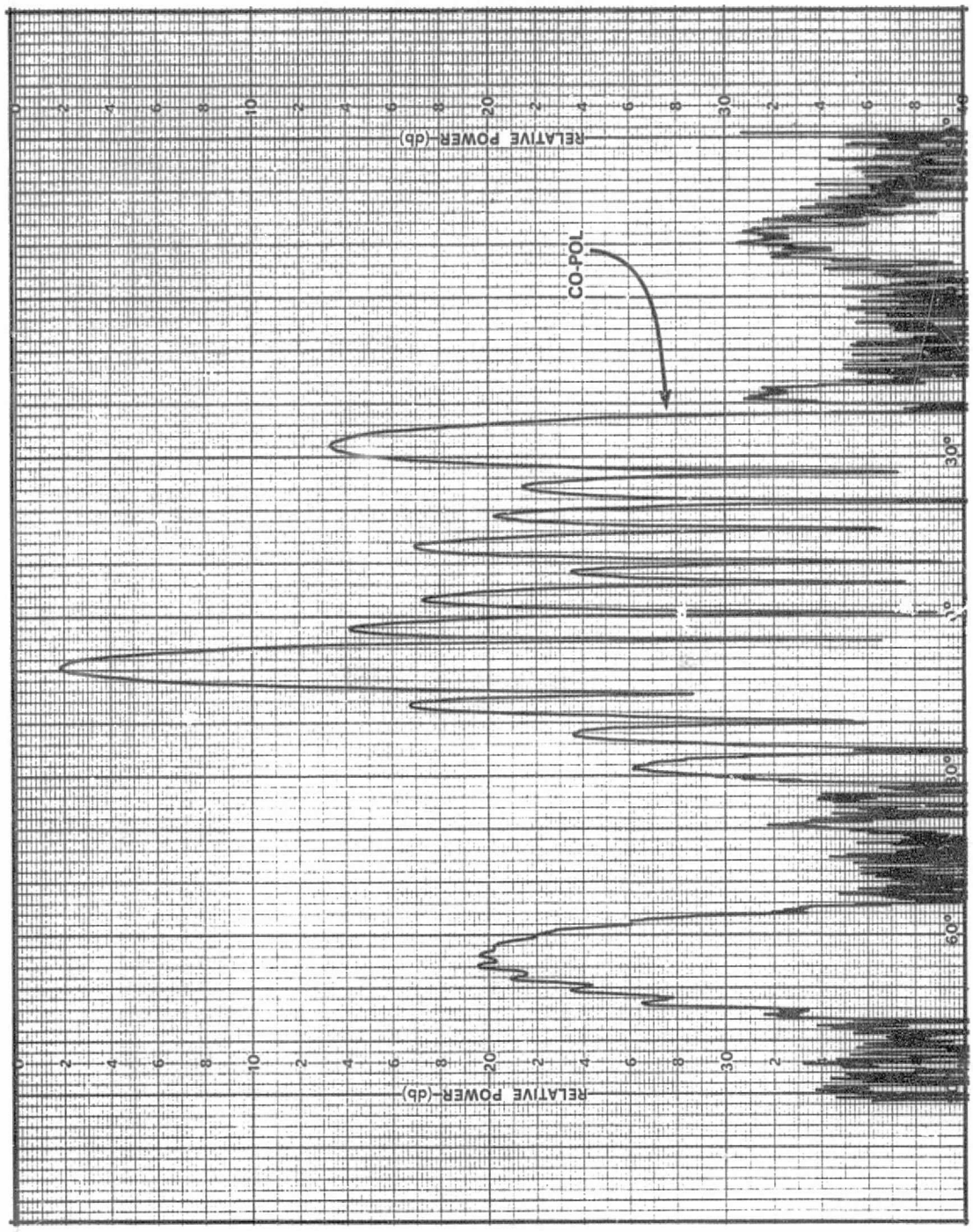

Figure B-13. E-Plane Pattern of Horizontally Polarized 8-Element Array, Uniform Amplitude, 90° Progressive Phase Difference, 11.7 GHz

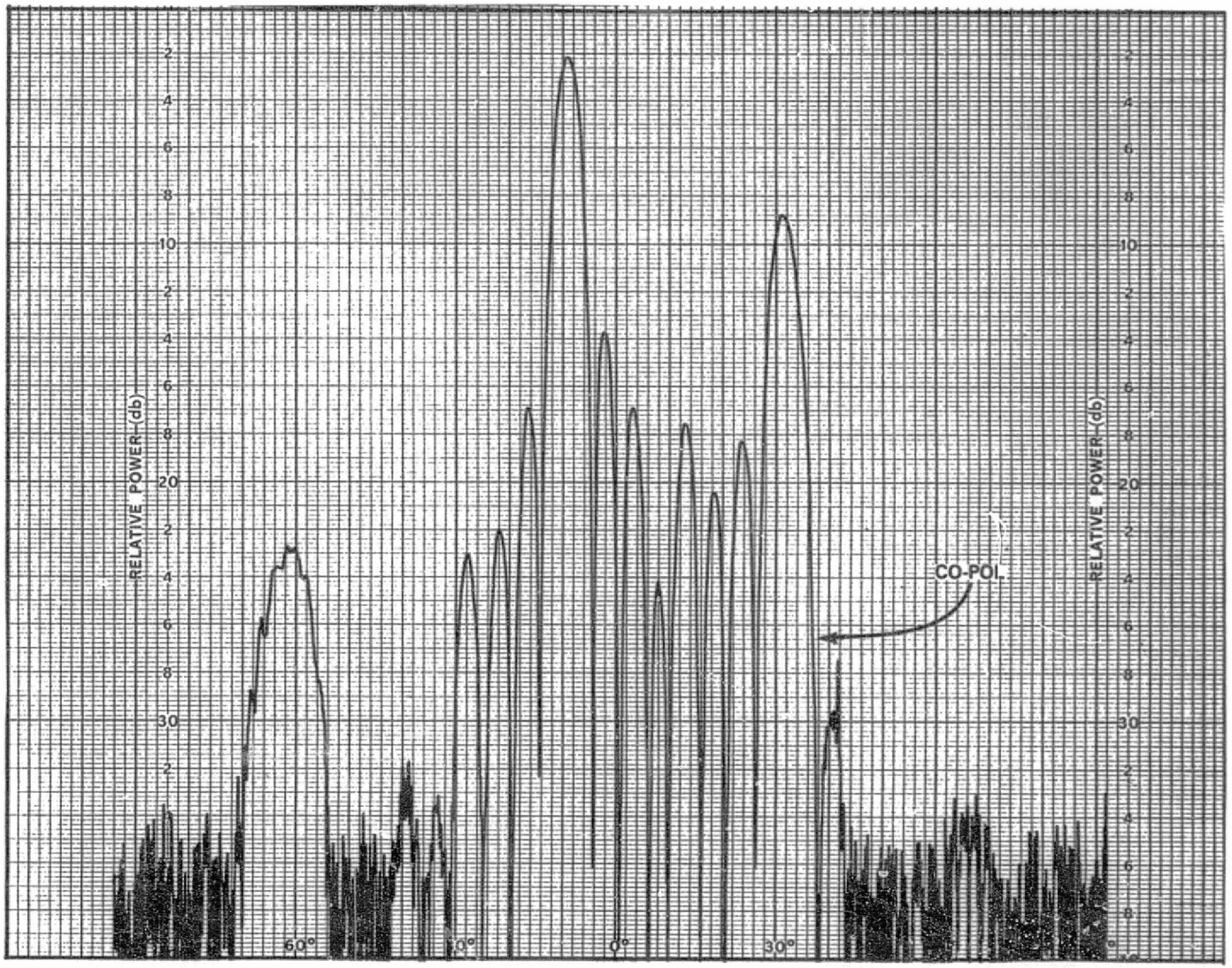

Figure B-14. E-Plane Pattern of Horizontally Polarized 8-Element Array, Uniform Amplitude, 90° Progressive Phase Difference, 11.95 GHz

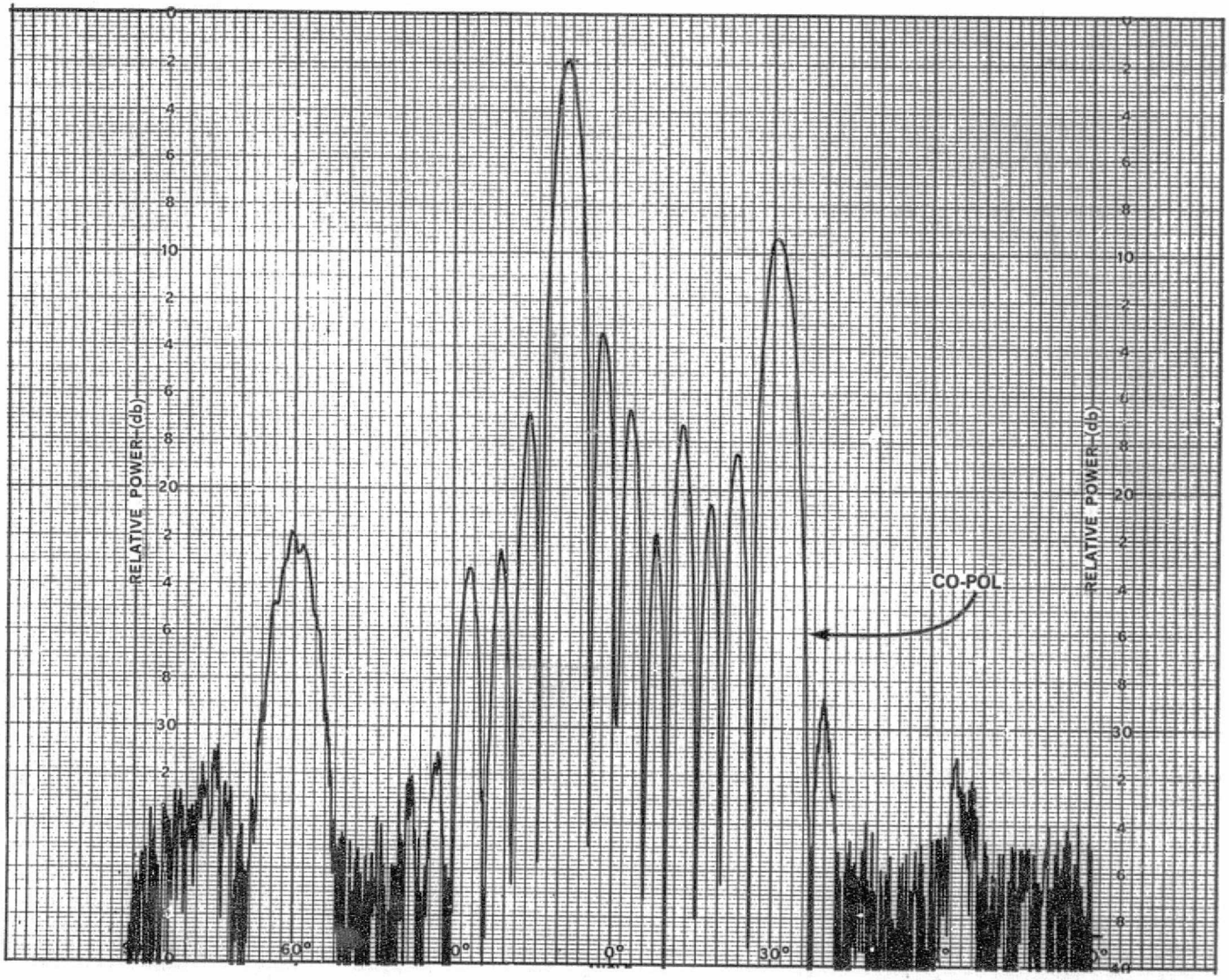

Figure B-15. E-Plane Pattern of Horizontally Polarized 8-Element Array, Uniform Amplitude, 90° Progressive Phase Difference, 12.2 GHz

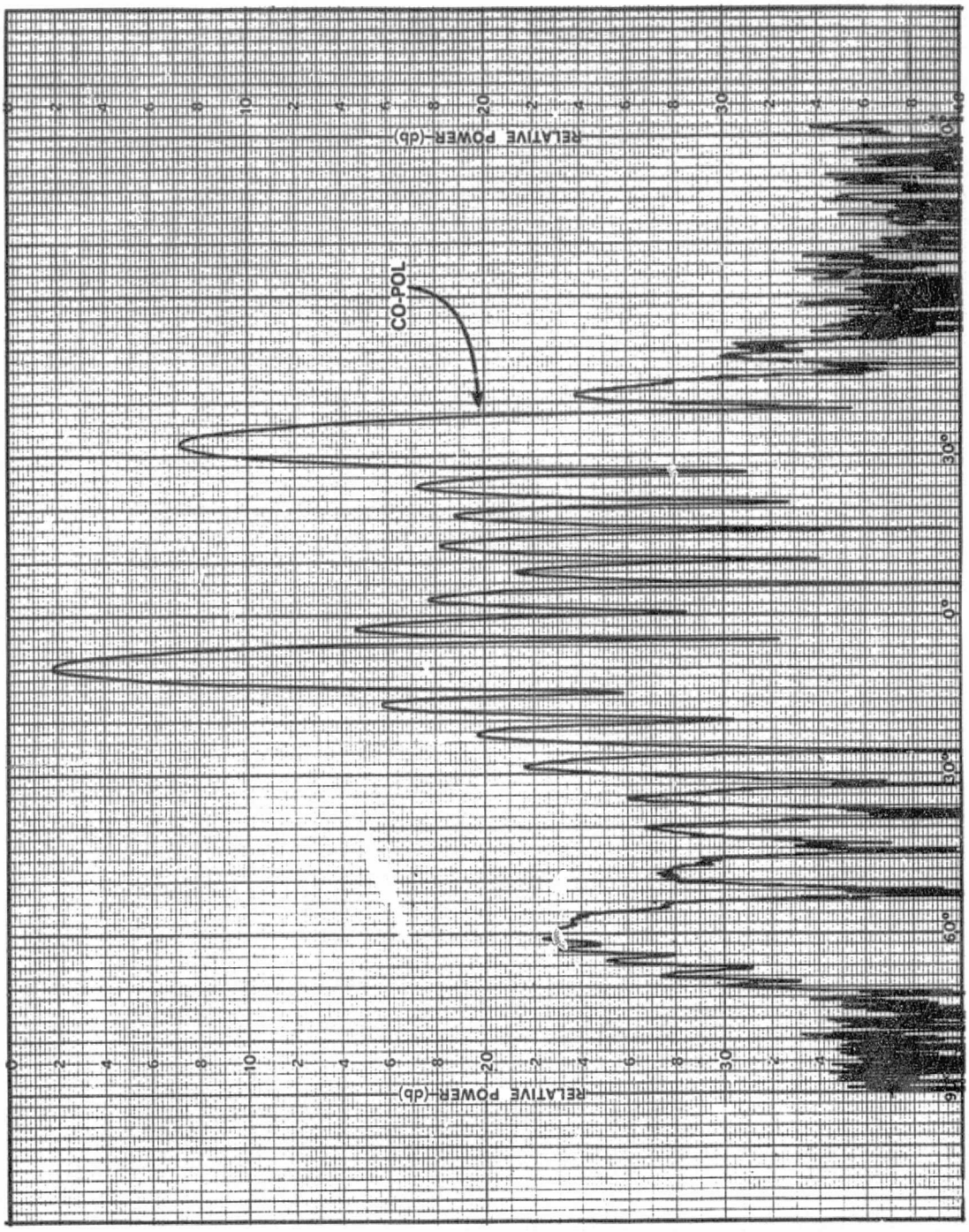

Figure B-16. H-Plane Pattern of Vertically Polarized 8-Element Array, Uniform Amplitude, 90° Progressive Phase Difference, 11.7 GHz

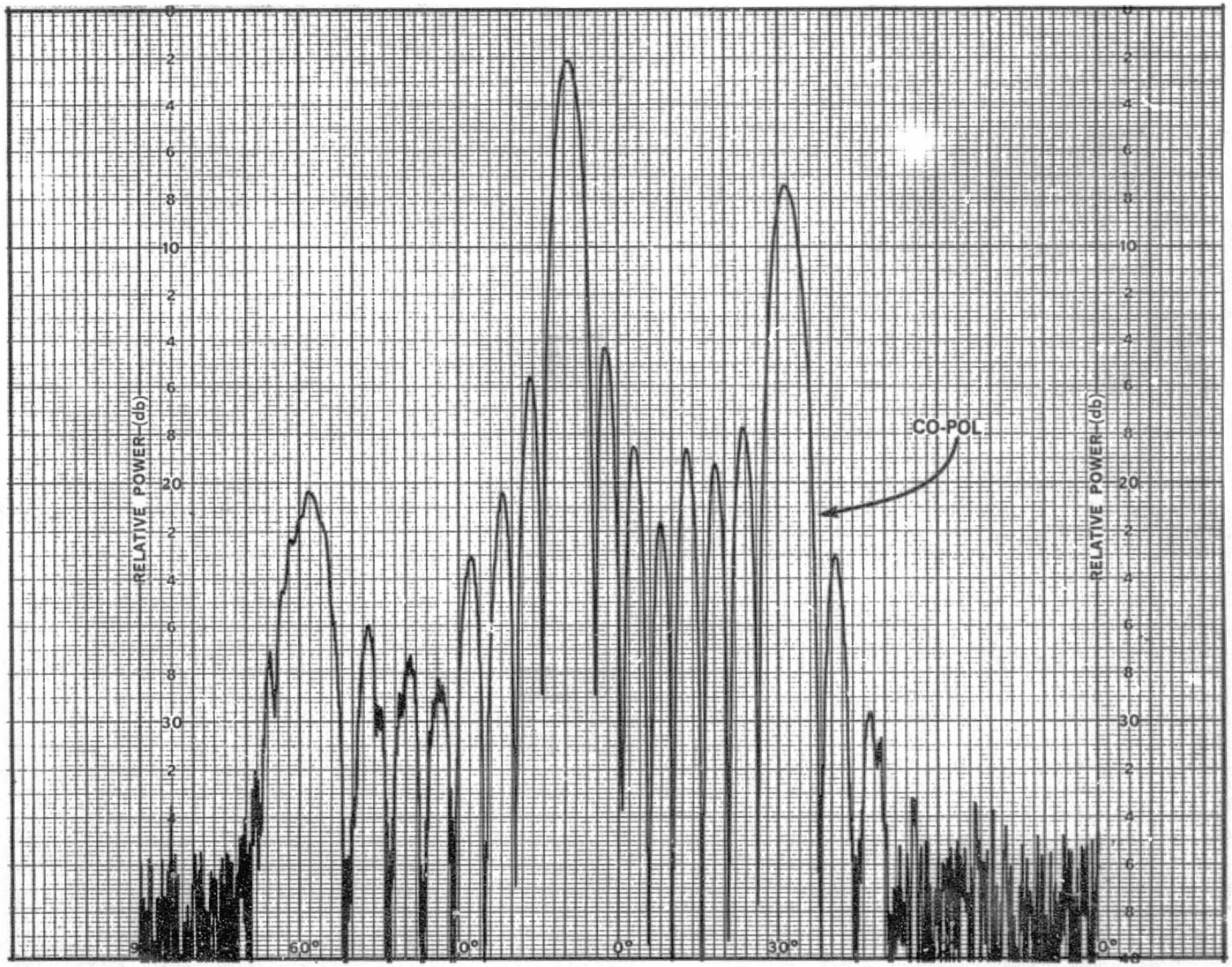

Figure B-17. H-Plane Pattern of Vertically Polarized 8-Element Array, Uniform Amplitude, 90° Progressive Phase Difference, 11.95 GHz

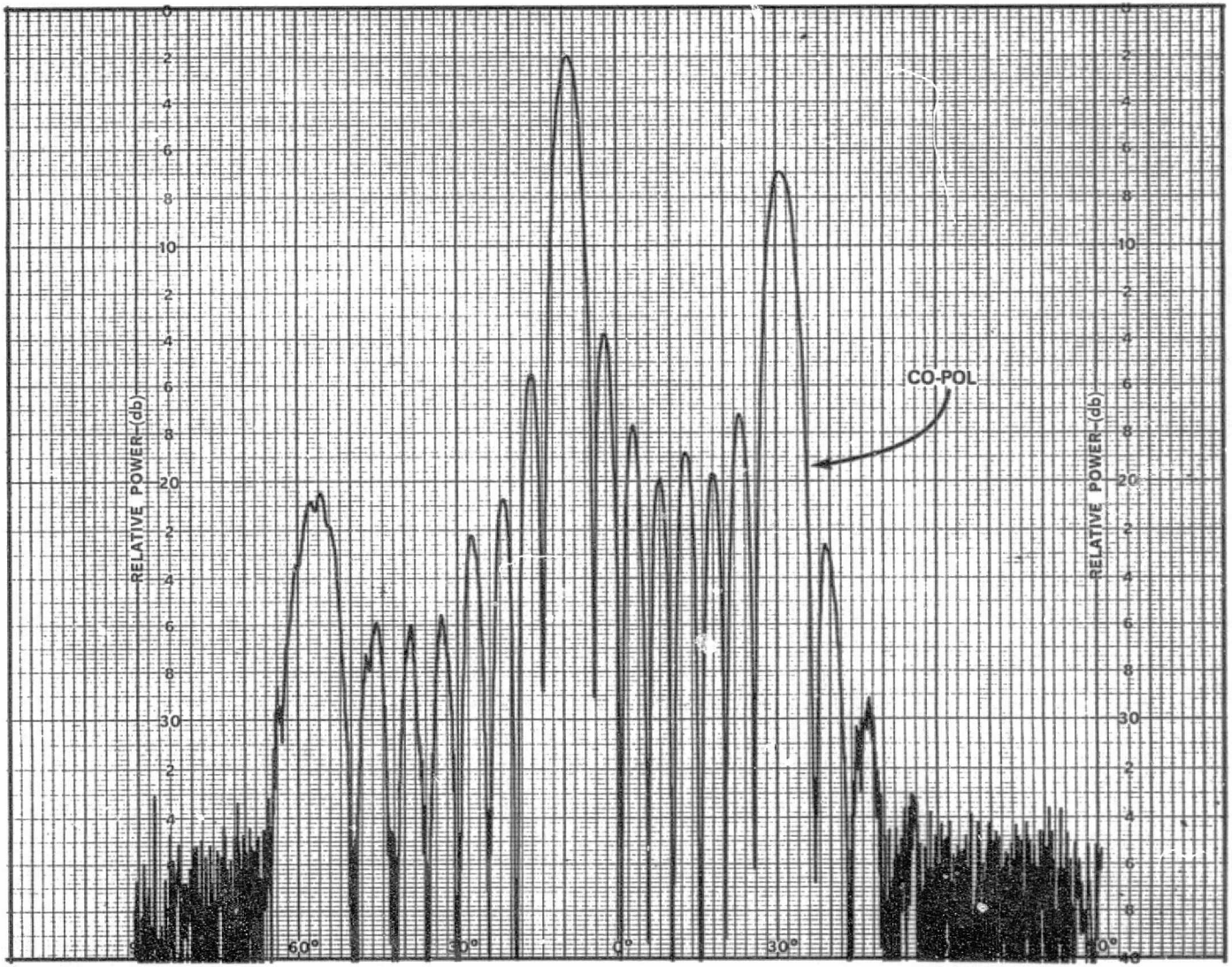

Figure B-18. H-Plane Pattern of Vertically Polarized 8-Element Array, Uniform Amplitude, 90° Progressive Phase Difference, 12.2 GHz

Figure B-19. E-Plane Pattern of Horizontally Polarized 8-Element Array, Uniform Amplitude, 135° Progressive Phase Difference, 11.7 GHz

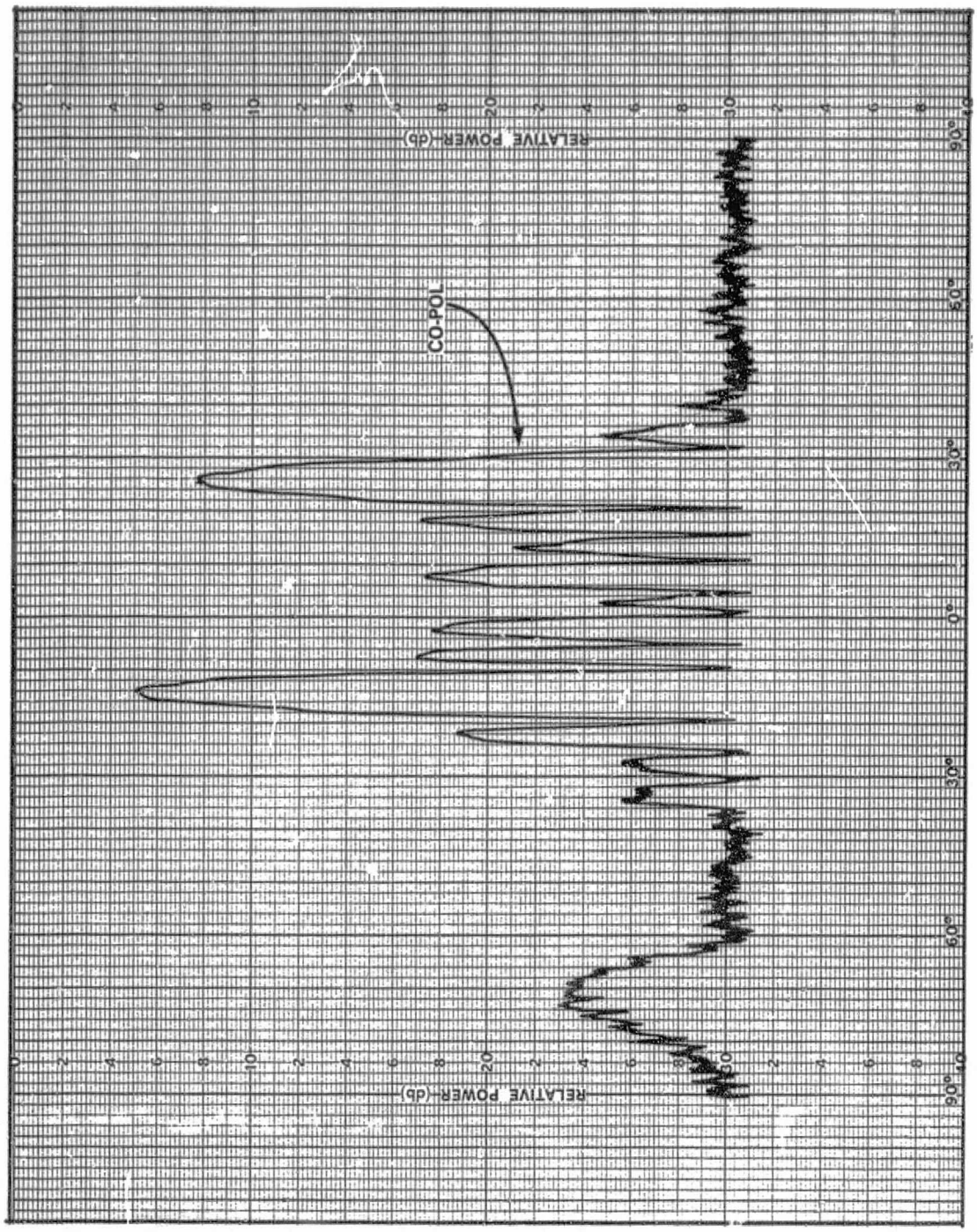

Figure B-20. E-Plane Pattern of Horizontally Polarized 8-Element Array, Uniform Amplitude, 135° Progressive Phase Difference, 11.95 GHz

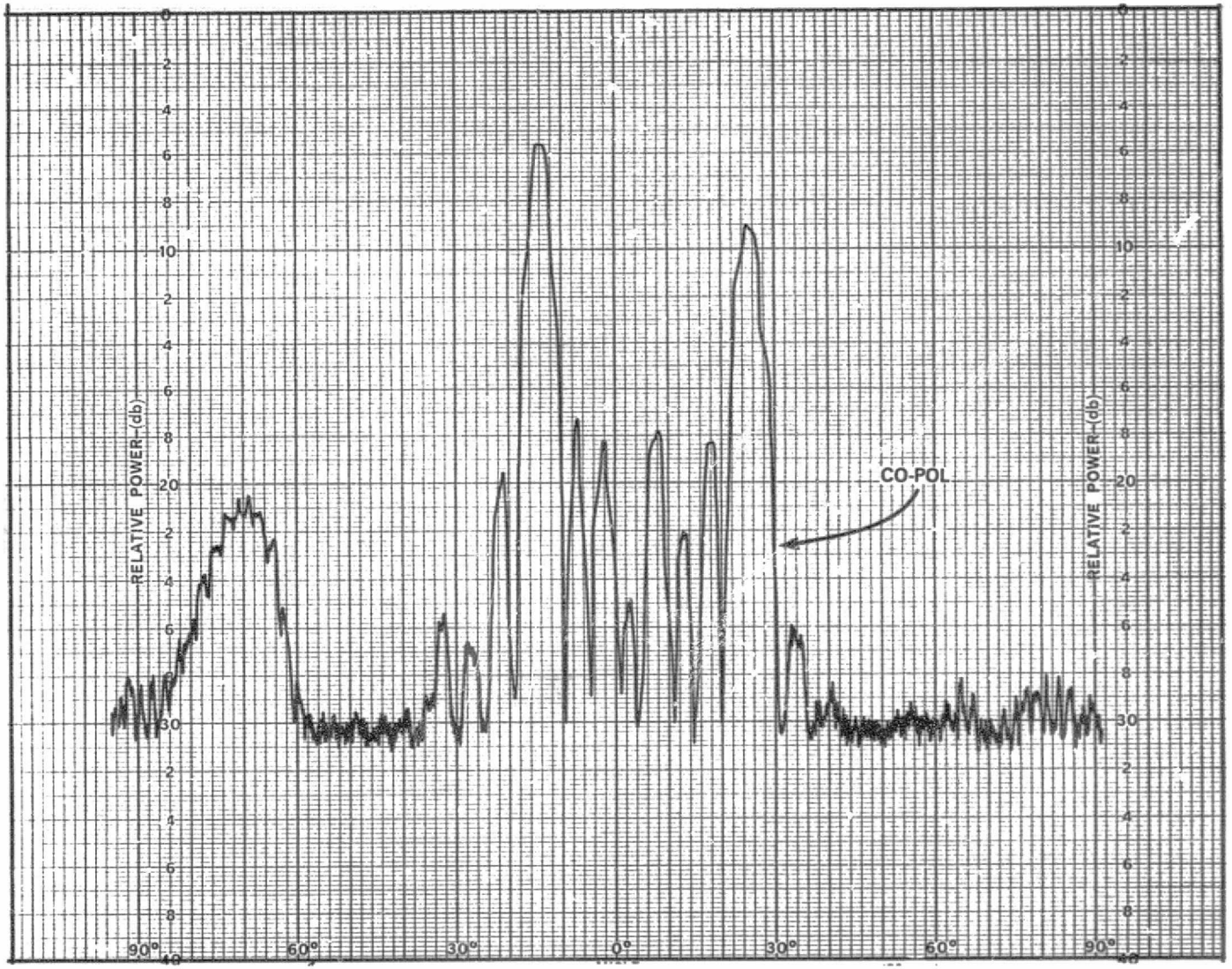

Figure B-21. E-Plane Pattern of Horizontally Polarized 8-Element Array, Uniform Amplitude, 135° Progressive Phase Difference, 12.2 GHz

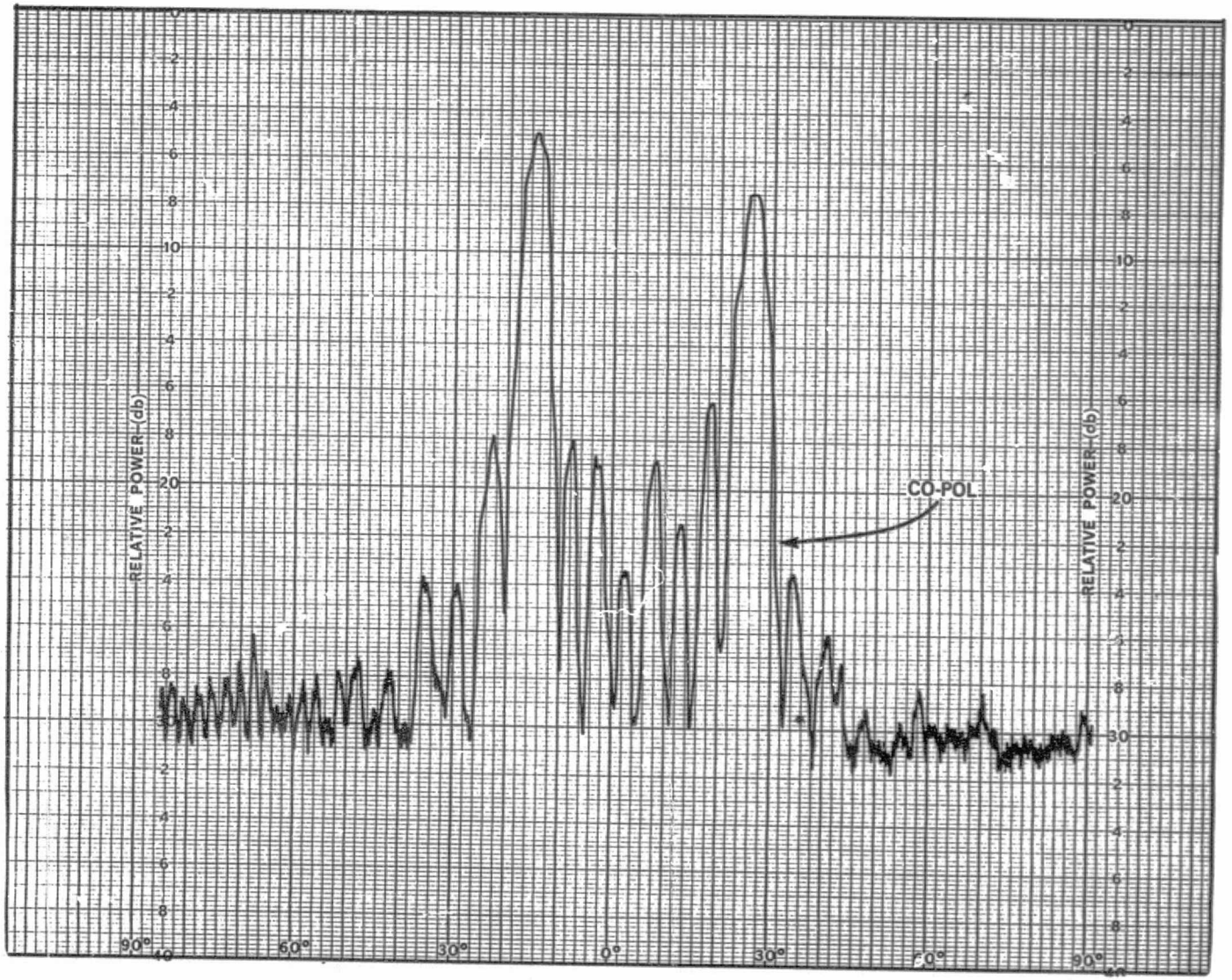

Figure B-22. H-Plane Pattern of Vertically Polarized 8-Element Array, Uniform Amplitude, 135° Progressive Phase Difference, 11.7 GHz

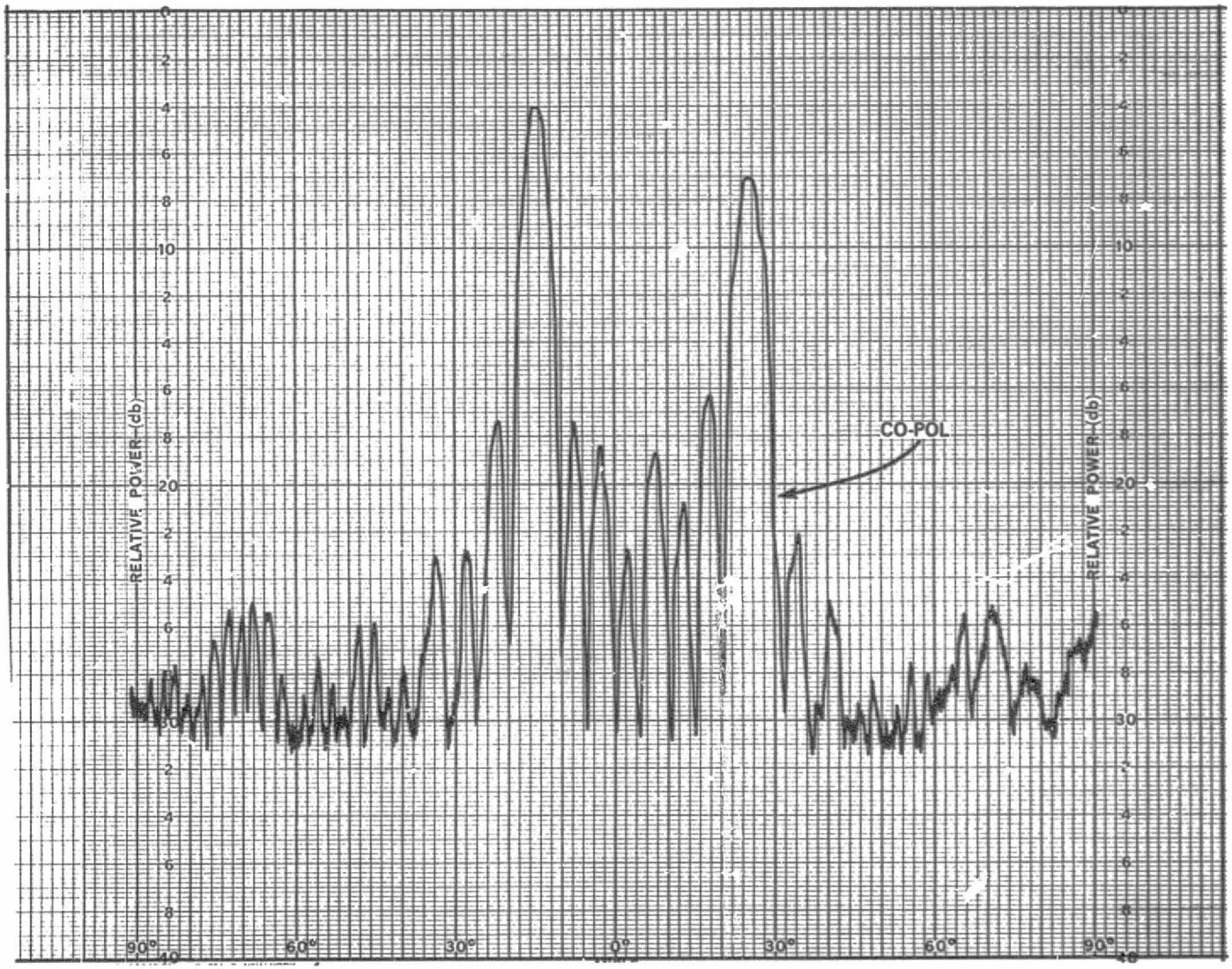

Figure B-23. H-Plane Pattern of Vertically Polarized 8-Element Array, Uniform Amplitude, 135° Progressive Phase Difference, 11.95 GHz

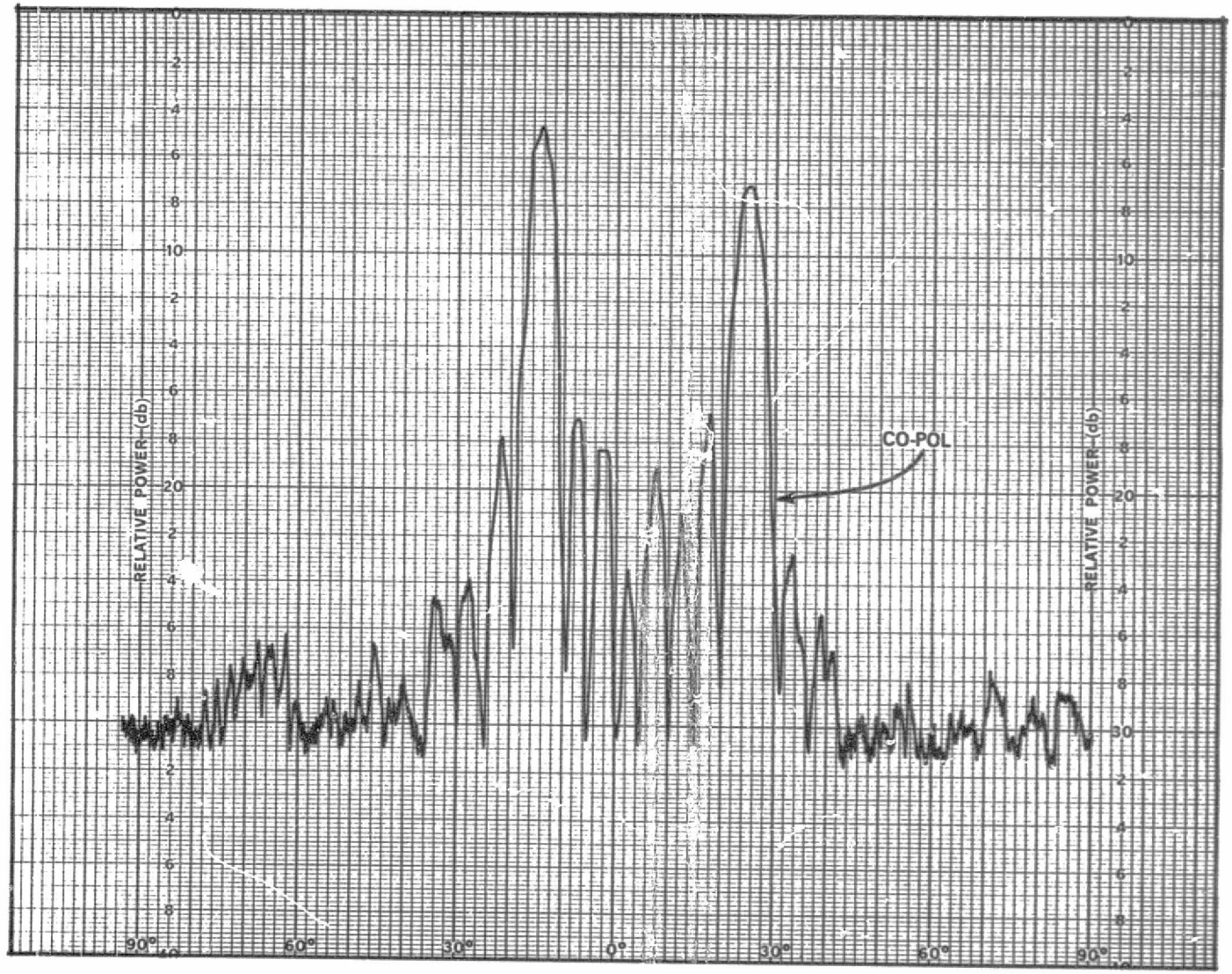

Figure B-24. H-Plane Pattern of Vertically Polarized 8-Element Array, Uniform Amplitude, 135° Progressive Phase Difference, 12.2 GHz

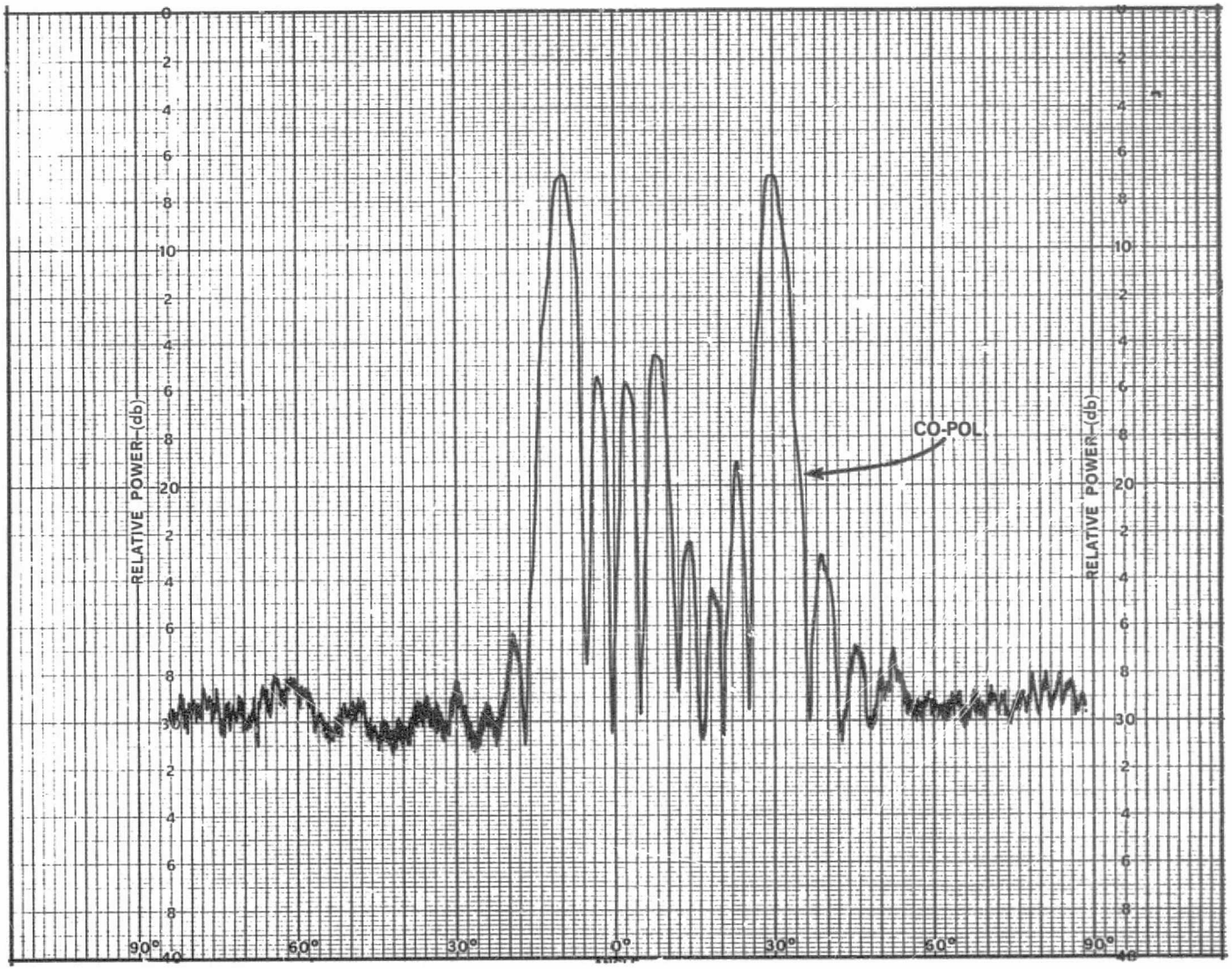

Figure B-25. E-Plane Pattern of Horizontally Polarized 8-Element Array, Uniform Amplitude, 180° Progressive Phase Difference, 11.7 GHz

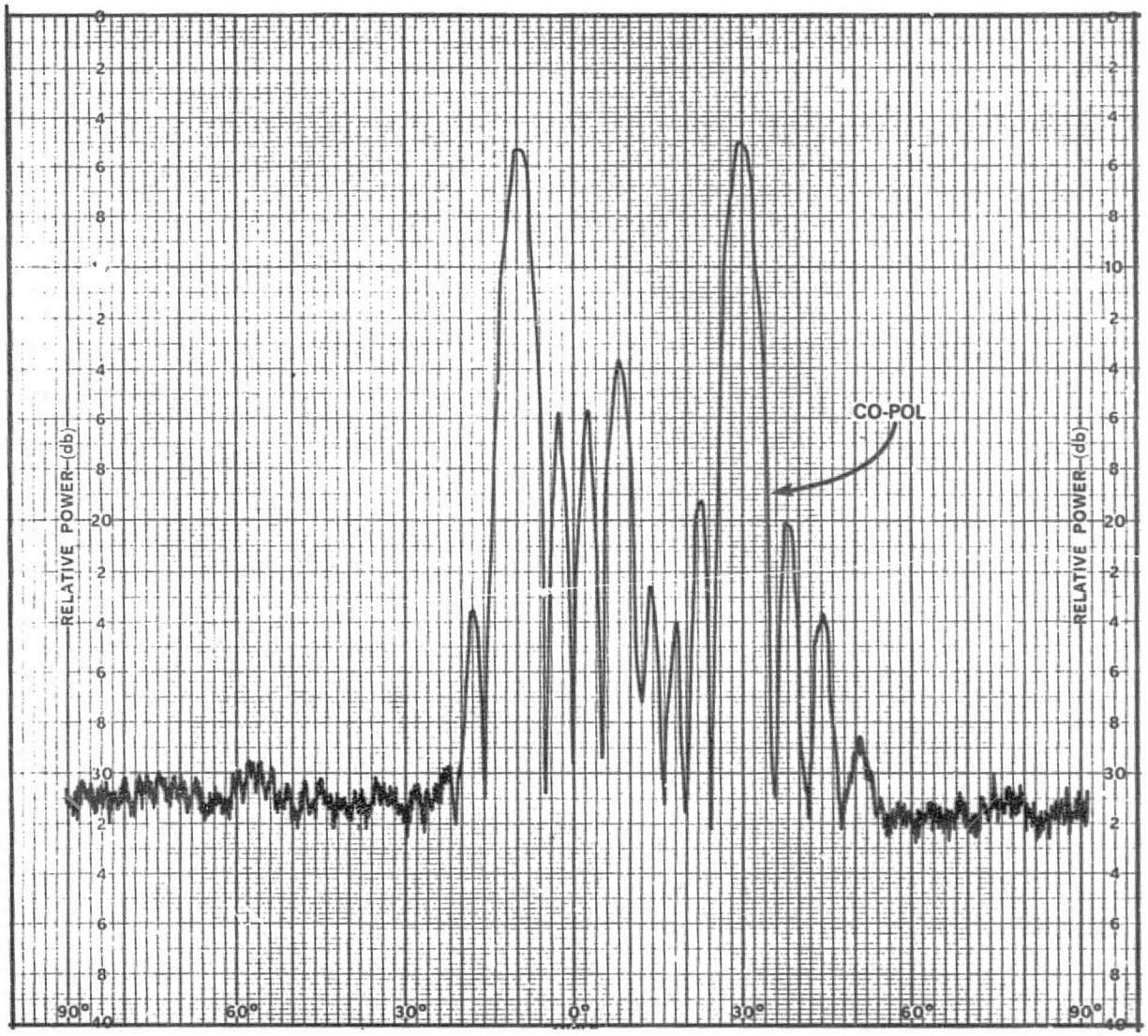

Figure B-26. E-Plane Pattern of Horizontally Polarized 8-Element Array, Uniform Amplitude, 180° Progressive Phase Difference, 11.95 GHz

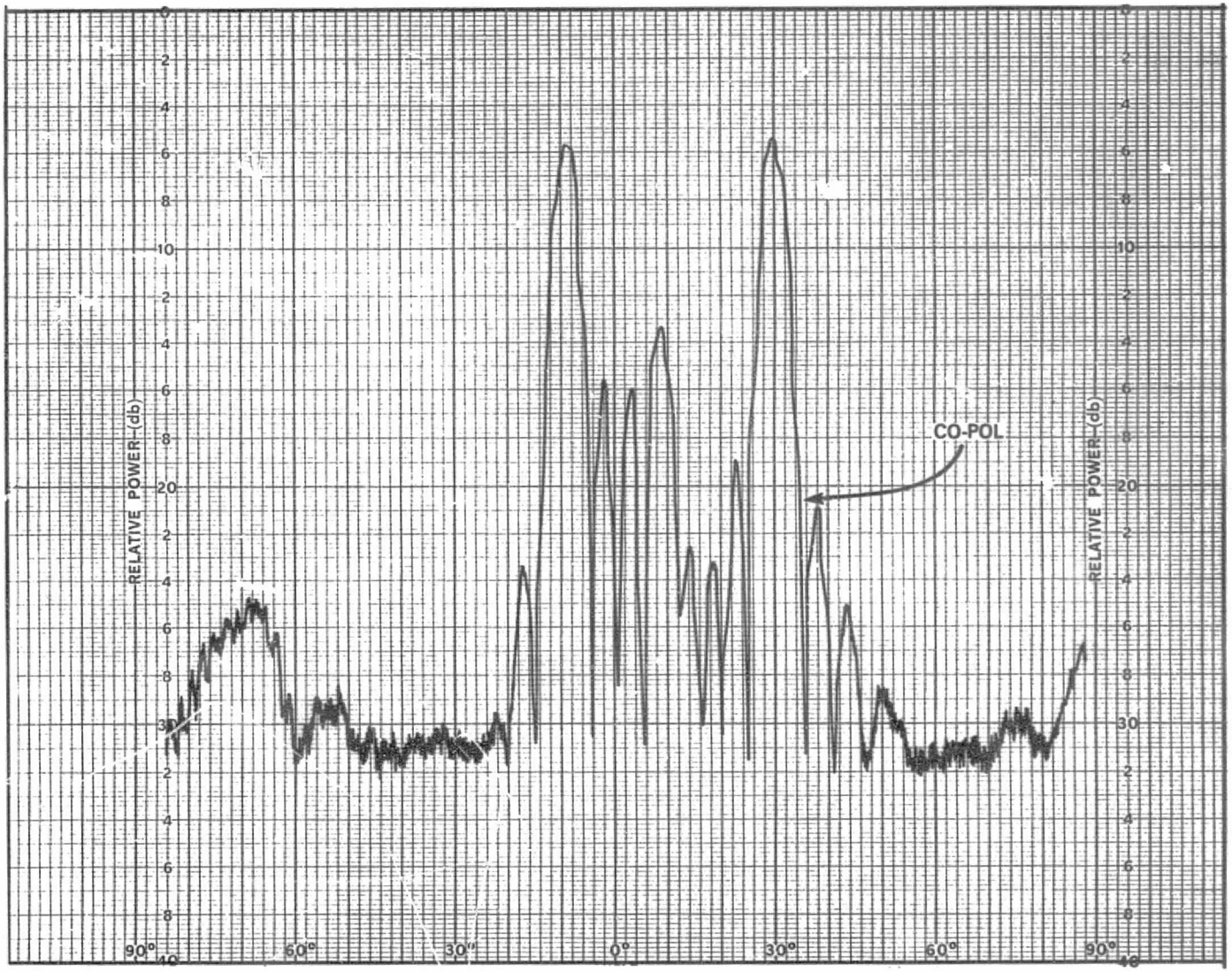

Figure B-27. E-Plane Pattern of Horizontally Polarized 8-Element Array, Uniform Amplitude, 180° Progressive Phase Difference, 12.2 GHz

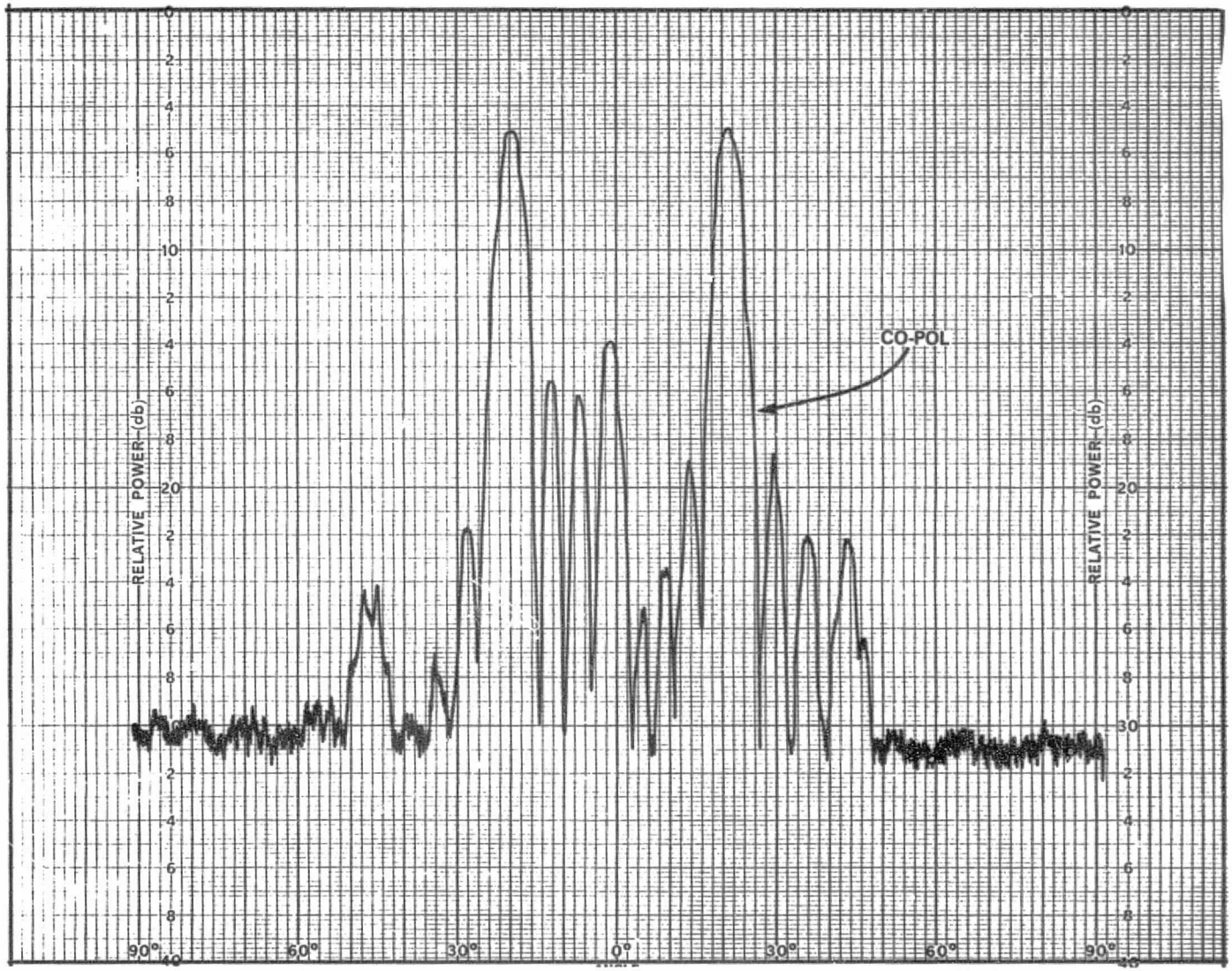

Figure B-28. H-Plane Pattern of Vertically Polarized 8-Element Array, Uniform Amplitude, 180° Progressive Phase Difference, 11.7 GHz

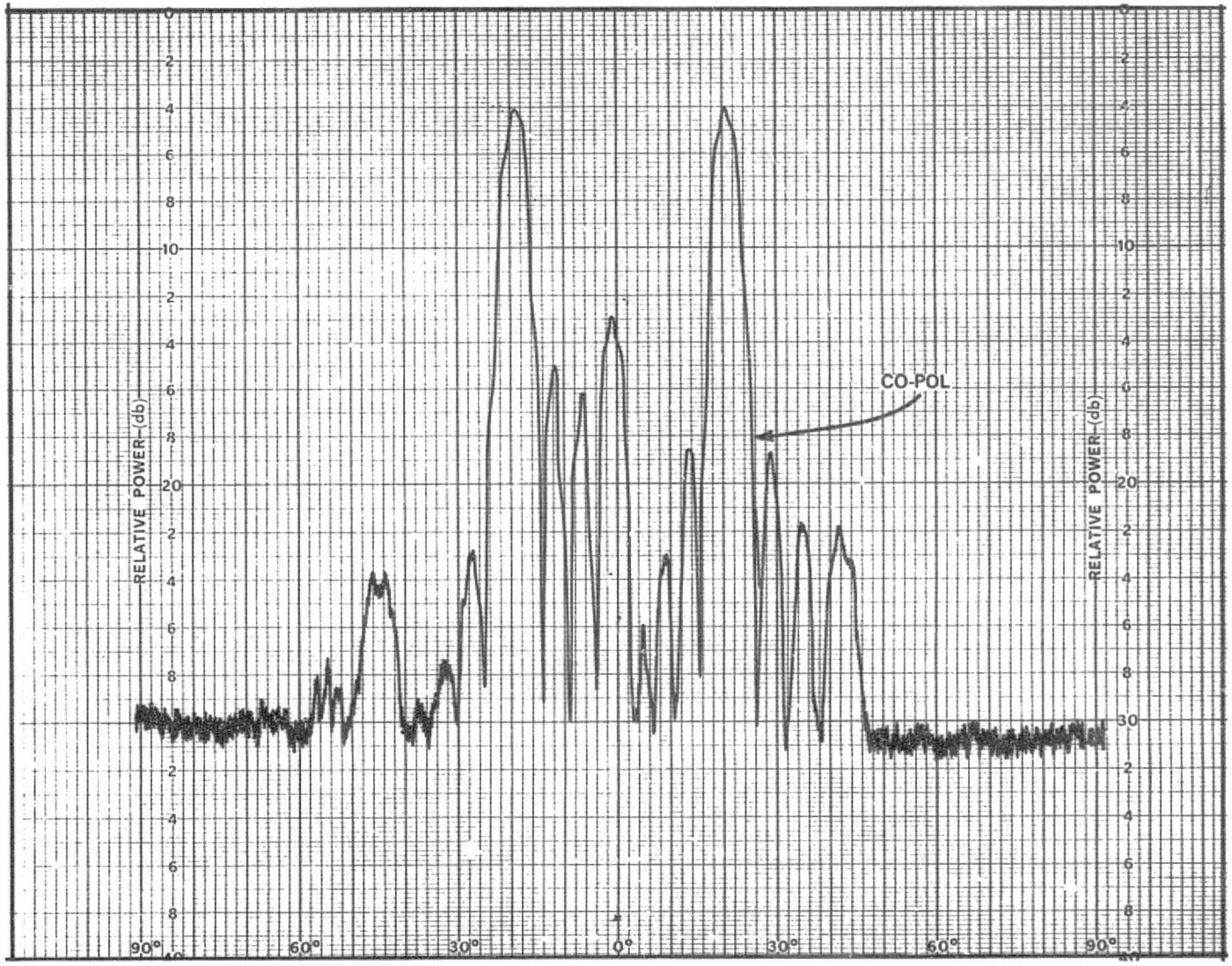

Figure B-29. H-Plane Pattern of Vertically Polarized 8-Element Array, Uniform Amplitude, 180° Progressive Phase Difference, 11.95 GHz

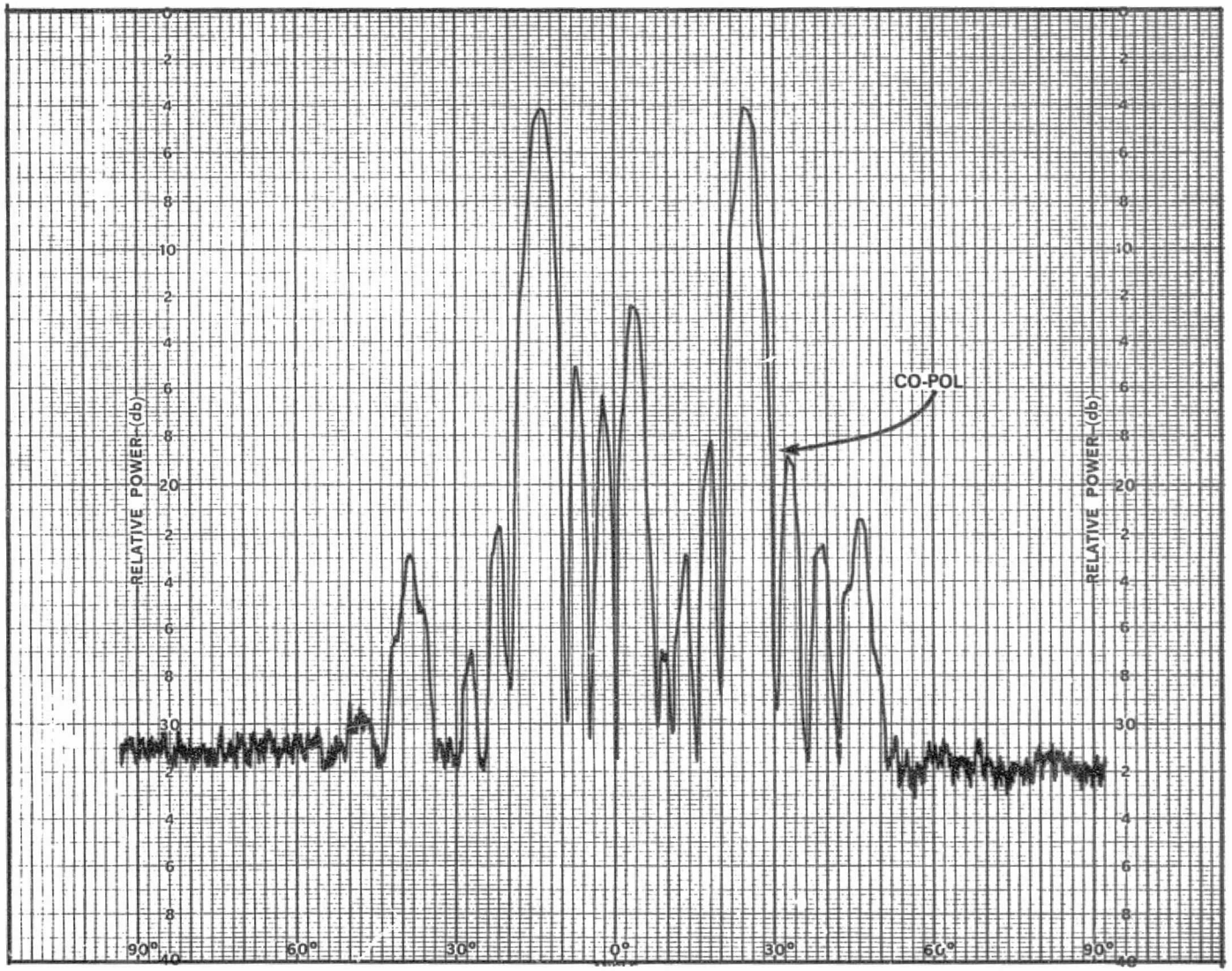

Figure B-30. H-Plane Pattern of Vertically Polarized 8-Element Array, Uniform Amplitude, 180° Progressive Phase Difference, 12.2 GHz

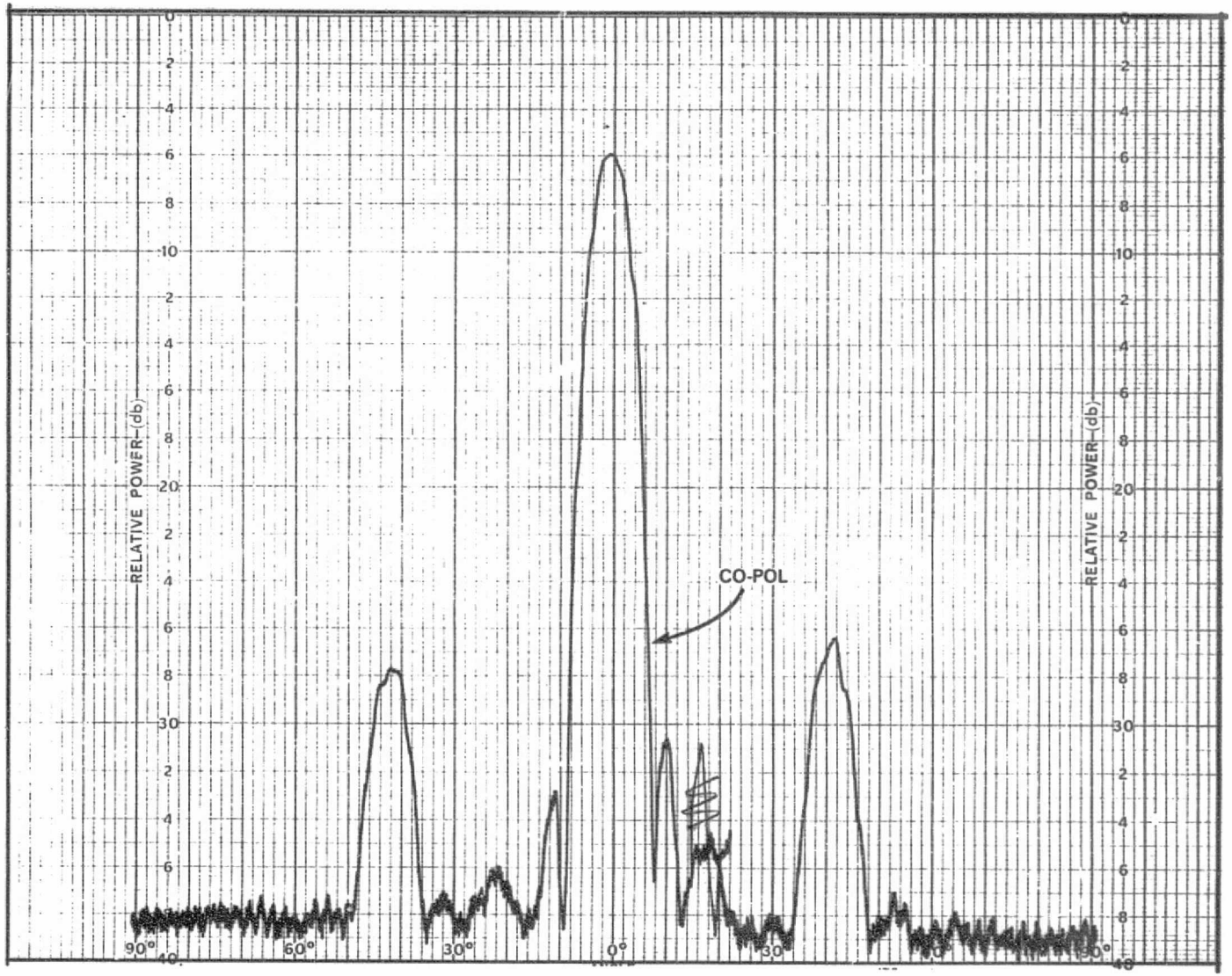

Figure B-31. E-Plane Pattern of Horizontally Polarized 8-Element Array, 30-dB Taylor Amplitude Distribution, Equal Phase, 11.7 GHz

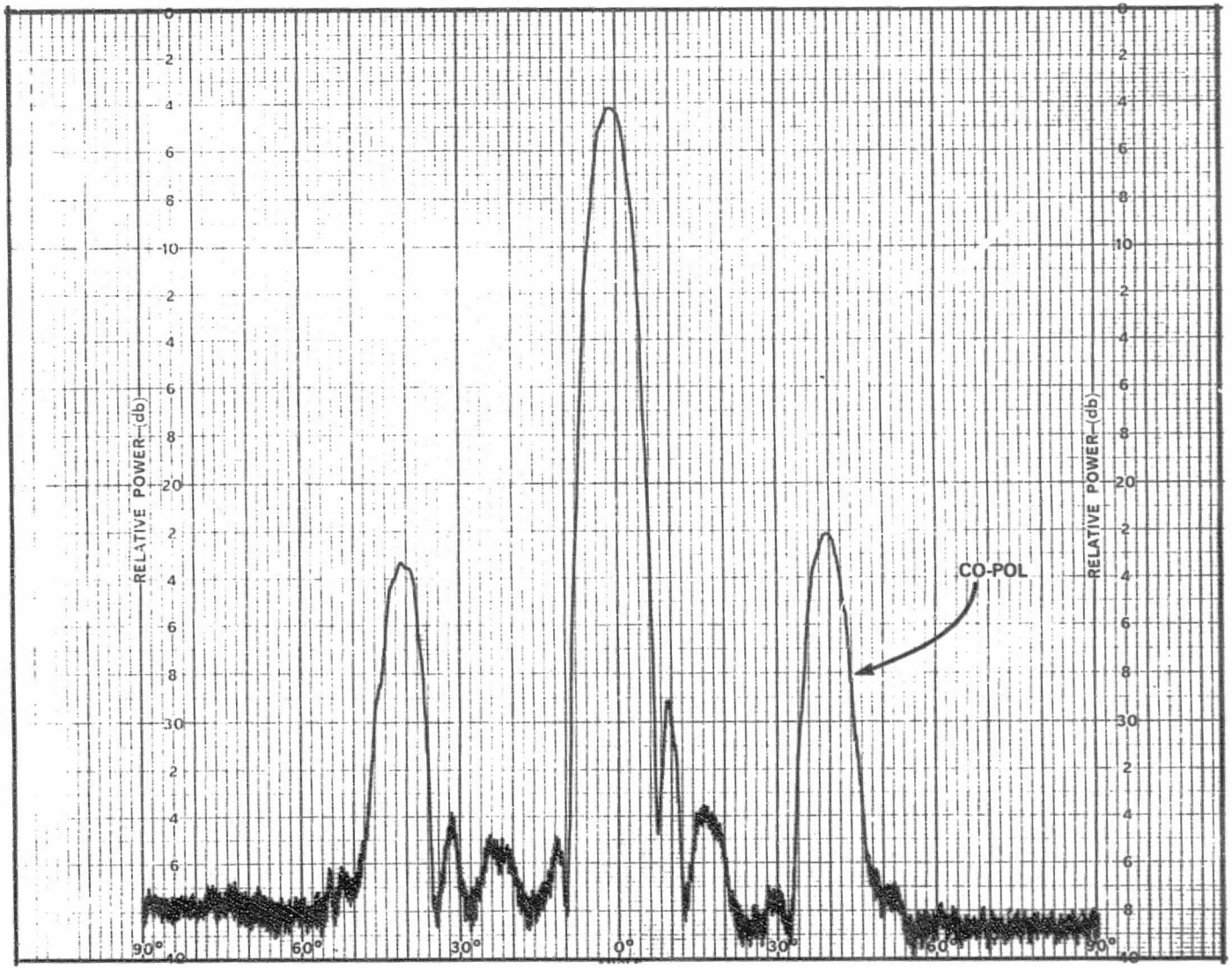

Figure B-32. E-Plane Pattern of Horizontally Polarized 8-Element Array, 30-dB Taylor Amplitude Distribution, Equal Phase, 11.95 GHz

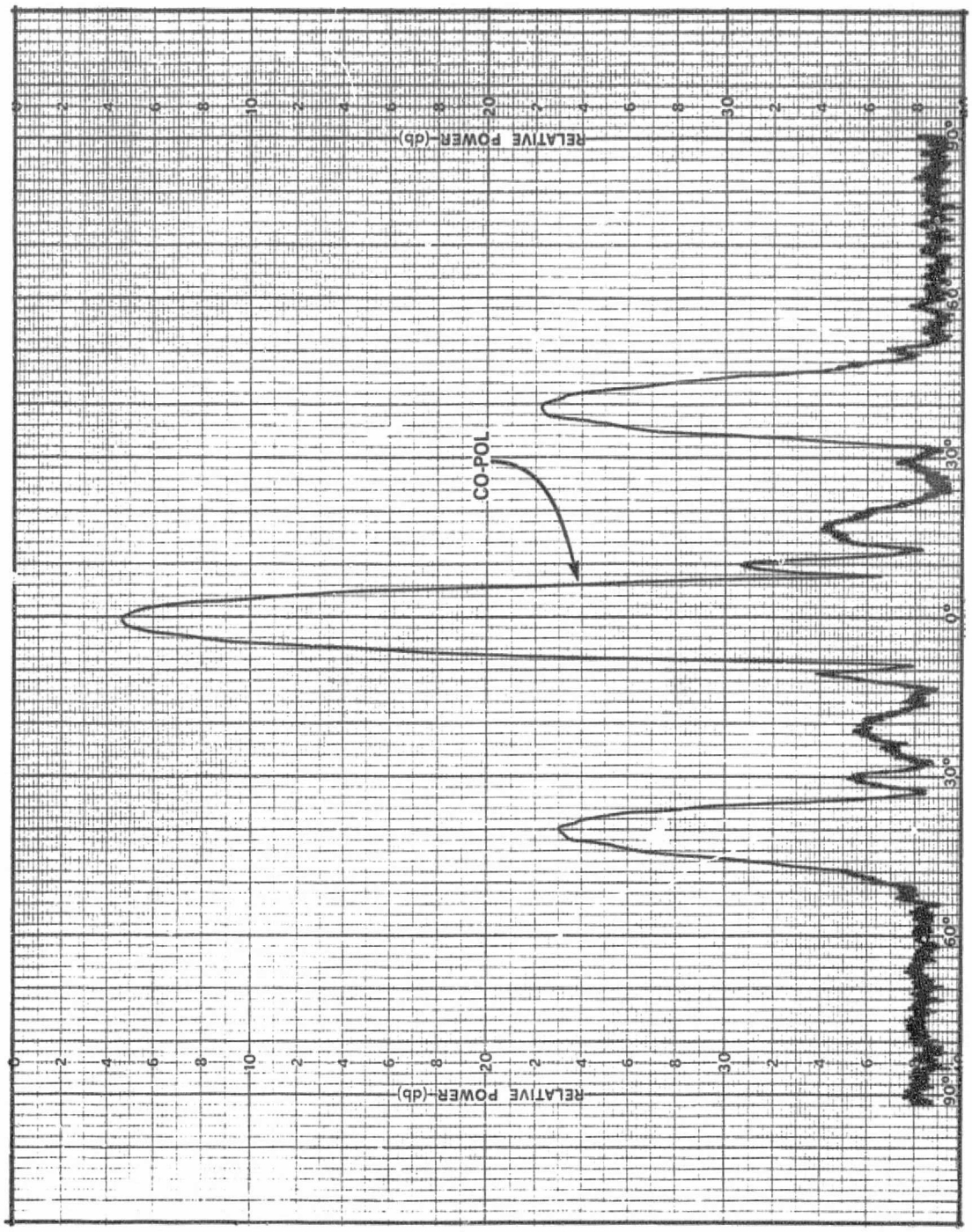

Figure B-33. E-Plane Pattern of Horizontally Polarized 8-Element Array, 30-dB Taylor Amplitude Distribution, Equal Phase, 12.2 GHz

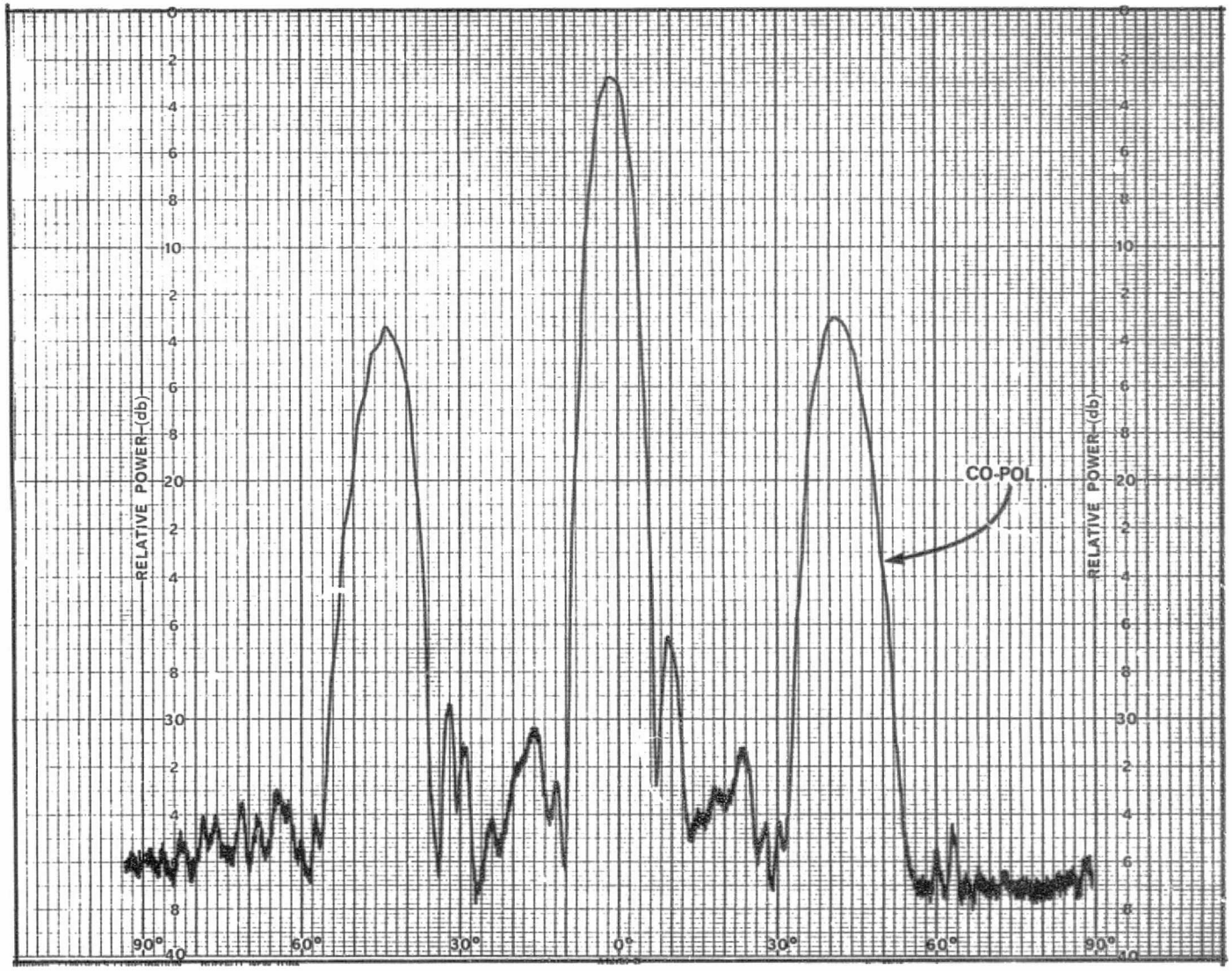

Figure B-34. H-Plane Pattern of Vertically Polarized 8-Element Array, 30-dB Taylor Amplitude Distribution, Equal Phase, 11.7 GHz

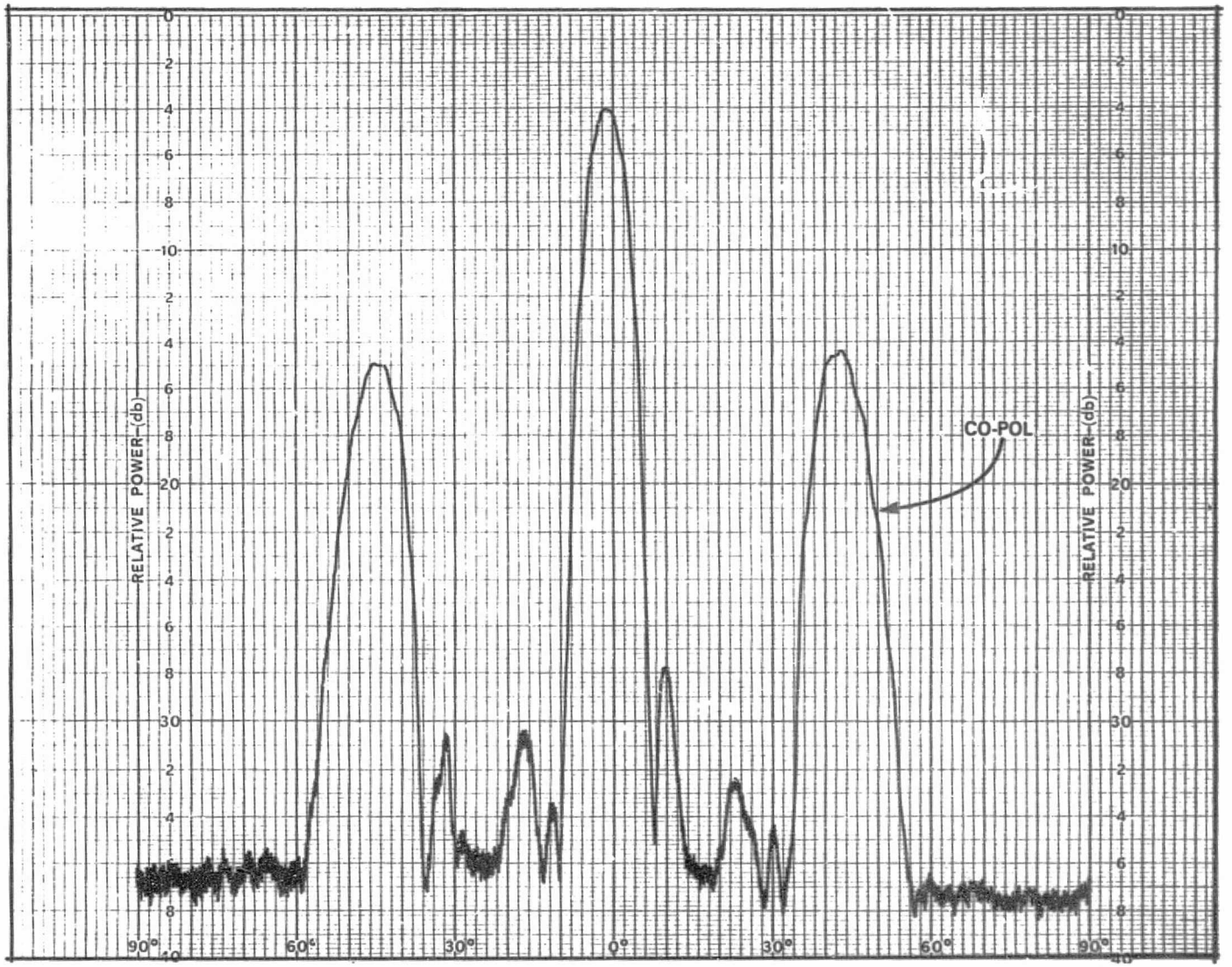

Figure B-35. H-Plane Pattern of Vertically Polarized 8-Element Array, 30-dB Taylor Amplitude Distribution, Equal Phase, 11.95 GHz

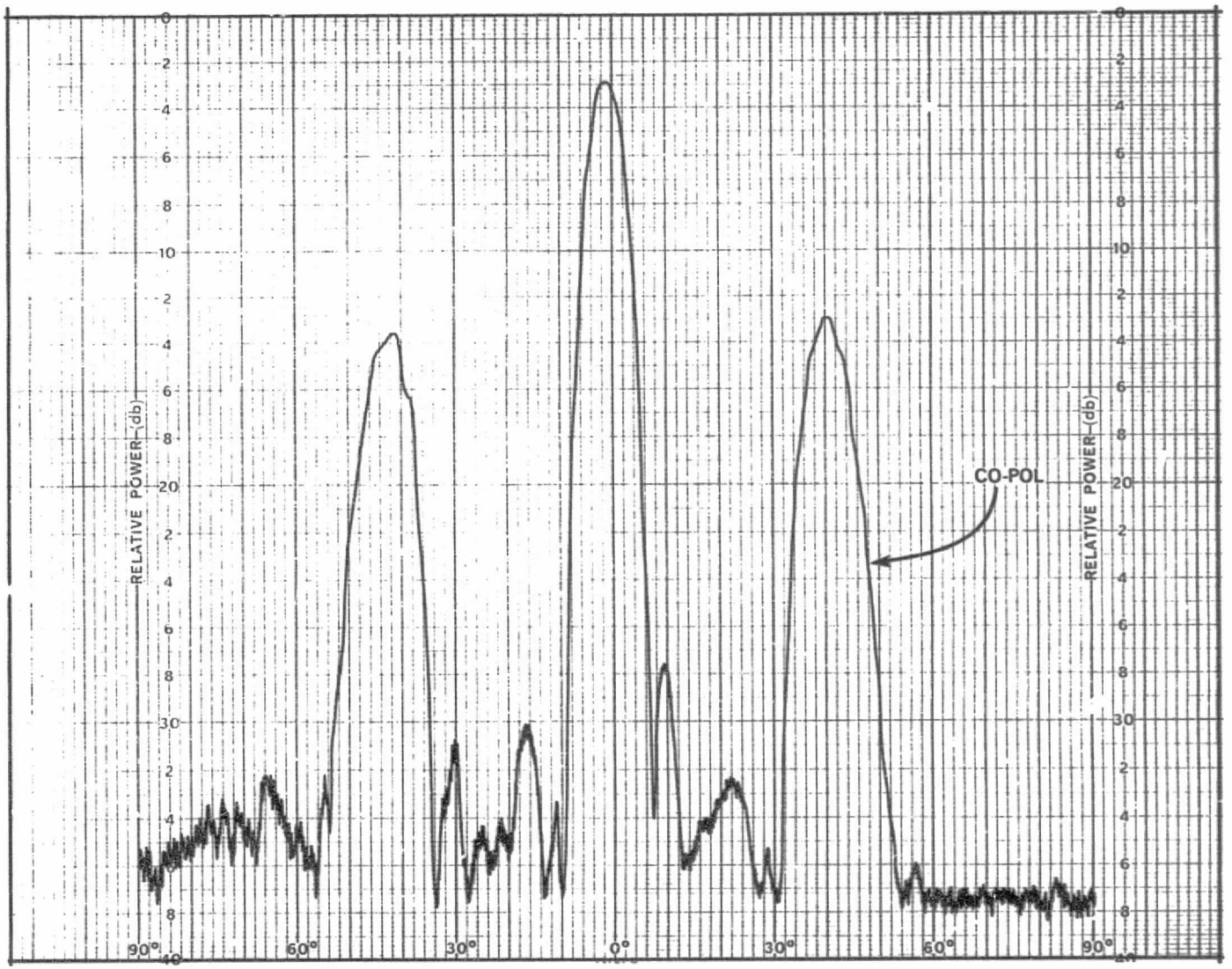

Figure B-36. H-Plane Pattern of Vertically Polarized 8-Element Array, 30-dB Taylor Amplitude Distribution, Equal Phase, 12.2 GHz

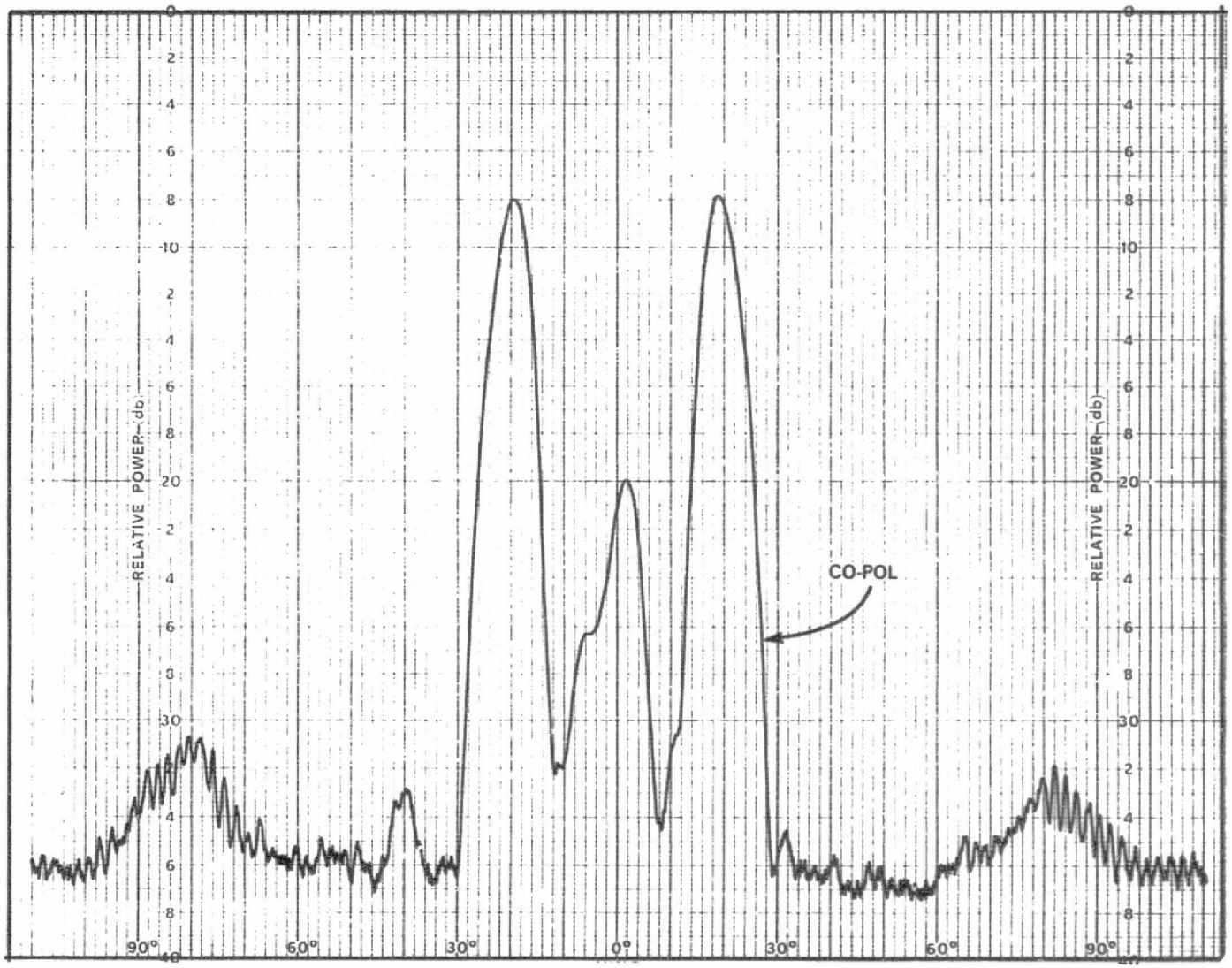

Figure B-37. E-Plane Pattern of Horizontally Polarized 8-Element Array, 30-dB Taylor Amplitude Distribution, 180° Progressive Phase Difference, 11.7 GHz

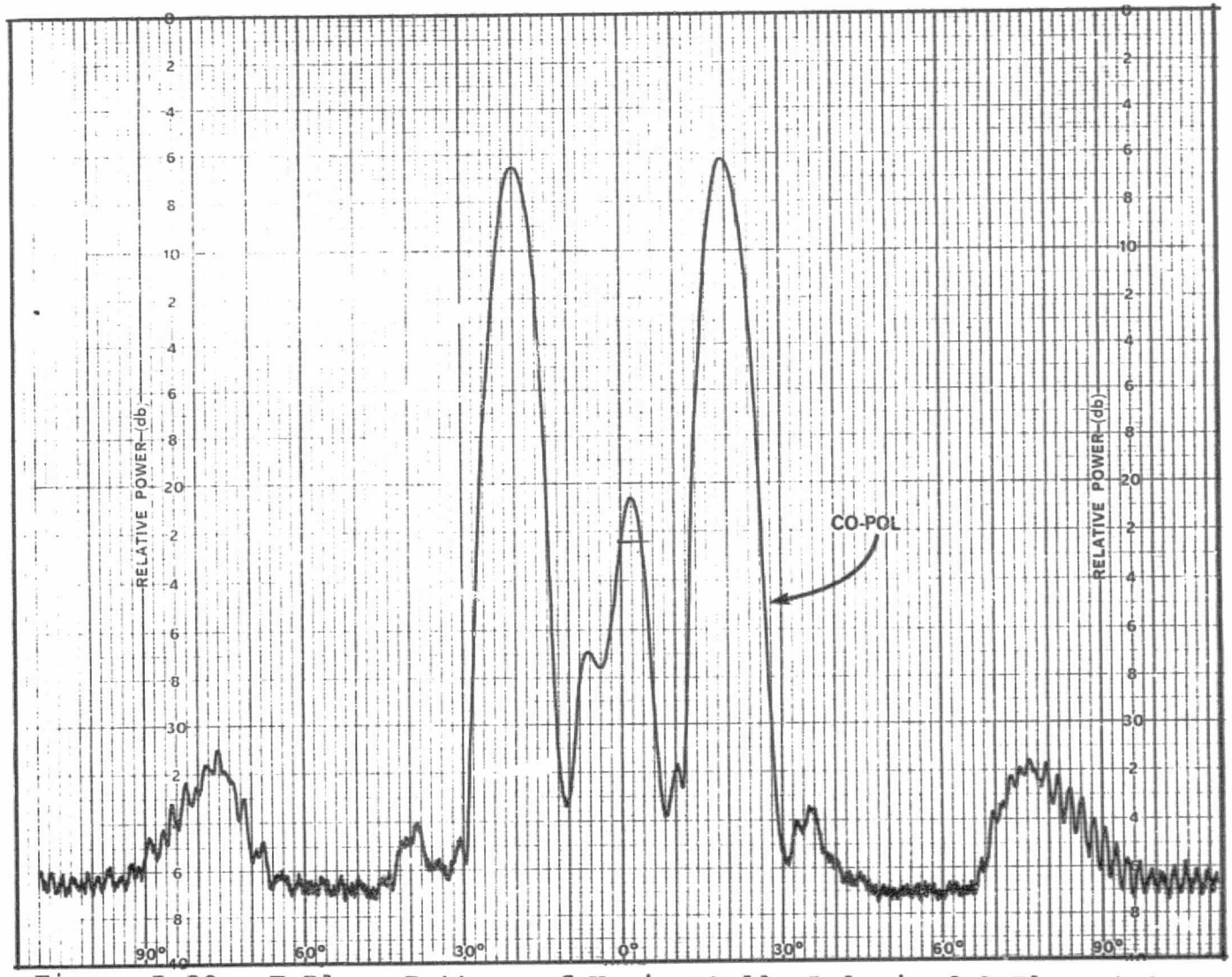

Figure B-38. E-Plane Pattern of Horizontally Polarized 8-Element Array, 30-dB Taylor Amplitude Distribution, 180° Progressive Phase Difference, 11.95 GHz

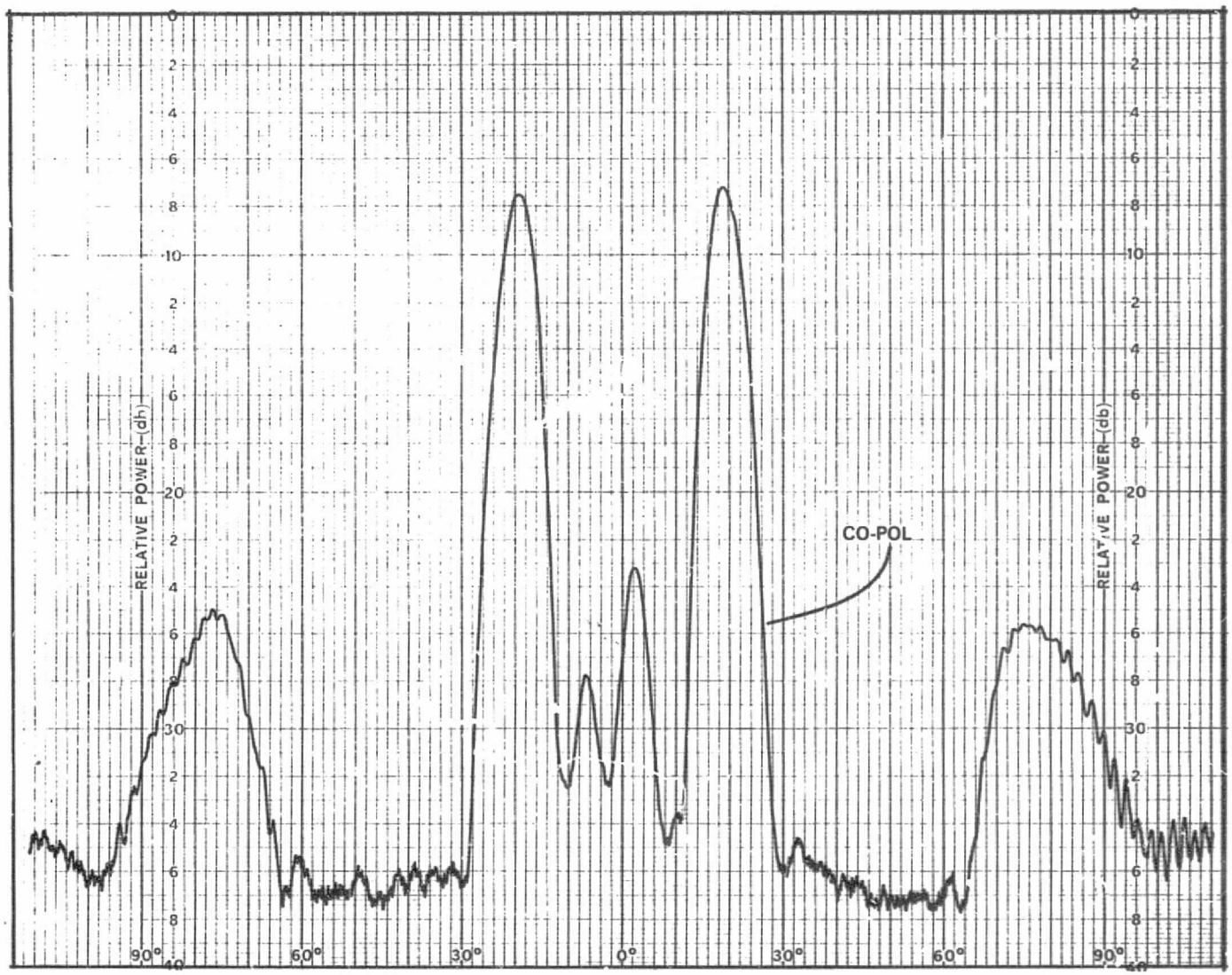

Figure B-39. E-Plane Pattern of Horizontally Polarized 8-Element Array, 30-dB Taylor Amplitude Distribution, 180° Progressive Phase Difference, 12.2 GHz

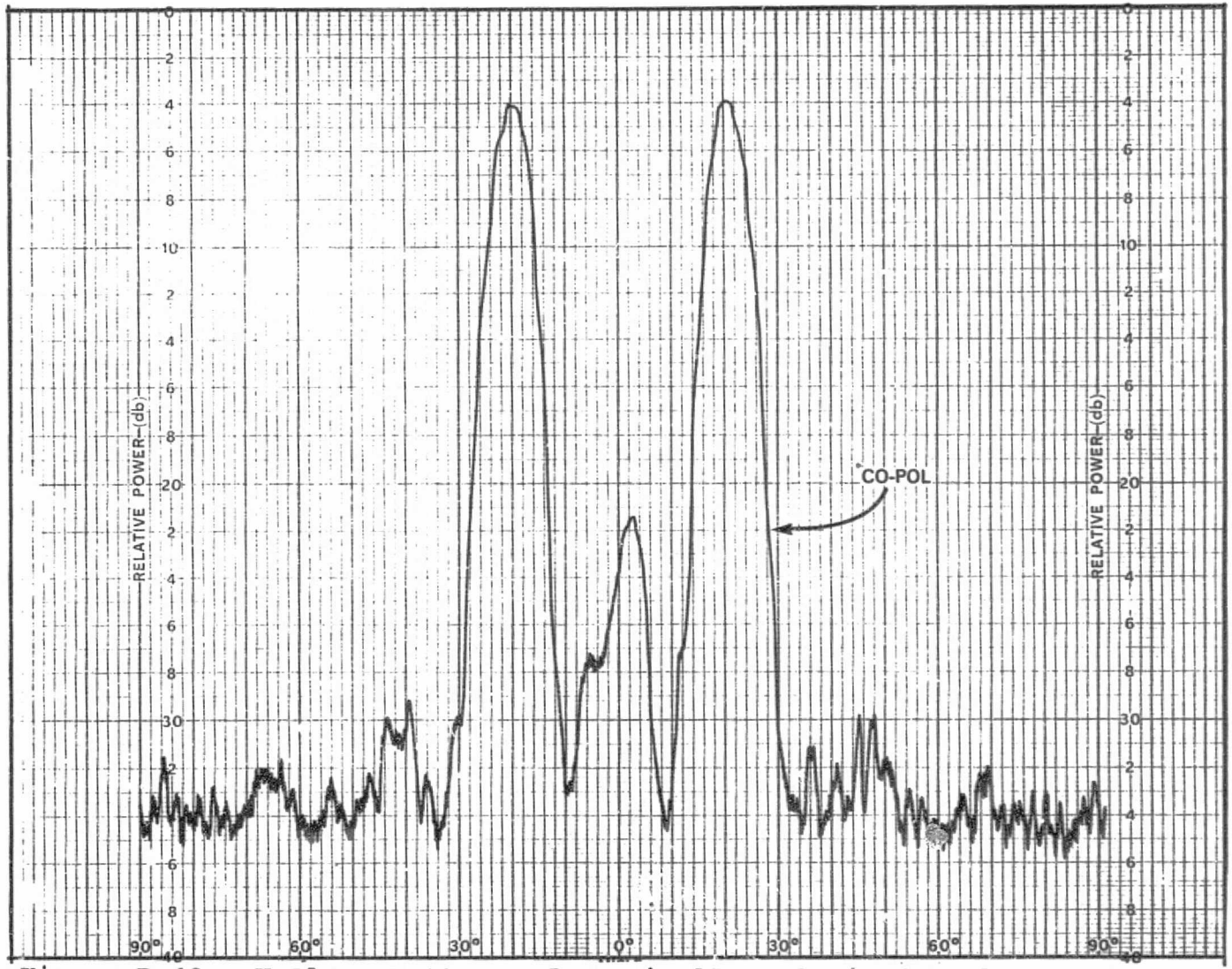

Figure B-40. H-Plane Pattern of Vertically Polarized 8-Element Array, 30-dB Taylor Amplitude Distribution, 180° Progressive Phase Difference, 11.7 GHz

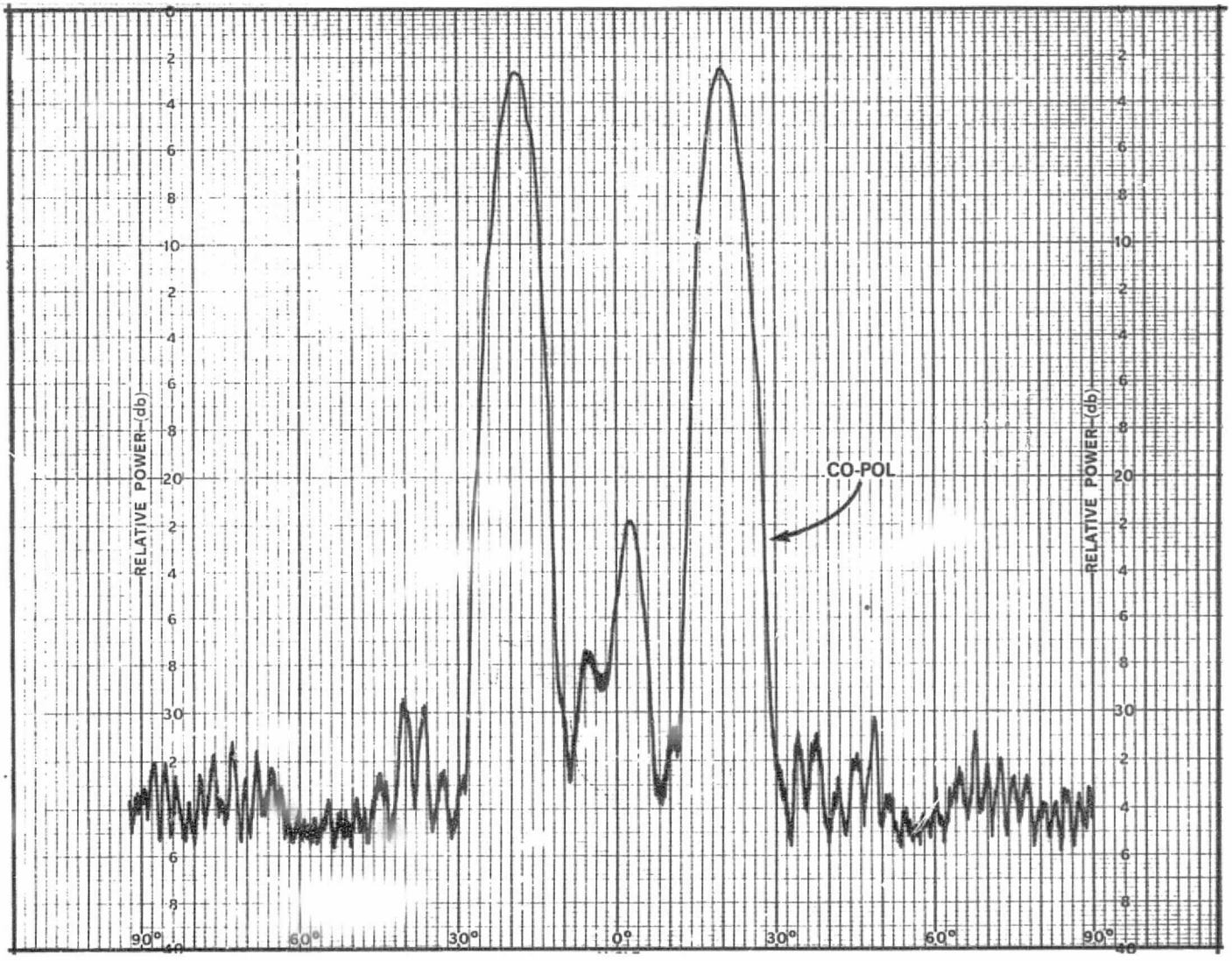

Figure B-41. H-Plane Pattern of Vertically Polarized 8-Element Array, 30-dB Taylor Amplitude Distribution, 180° Progressive Phase Difference, 11.95 GHz

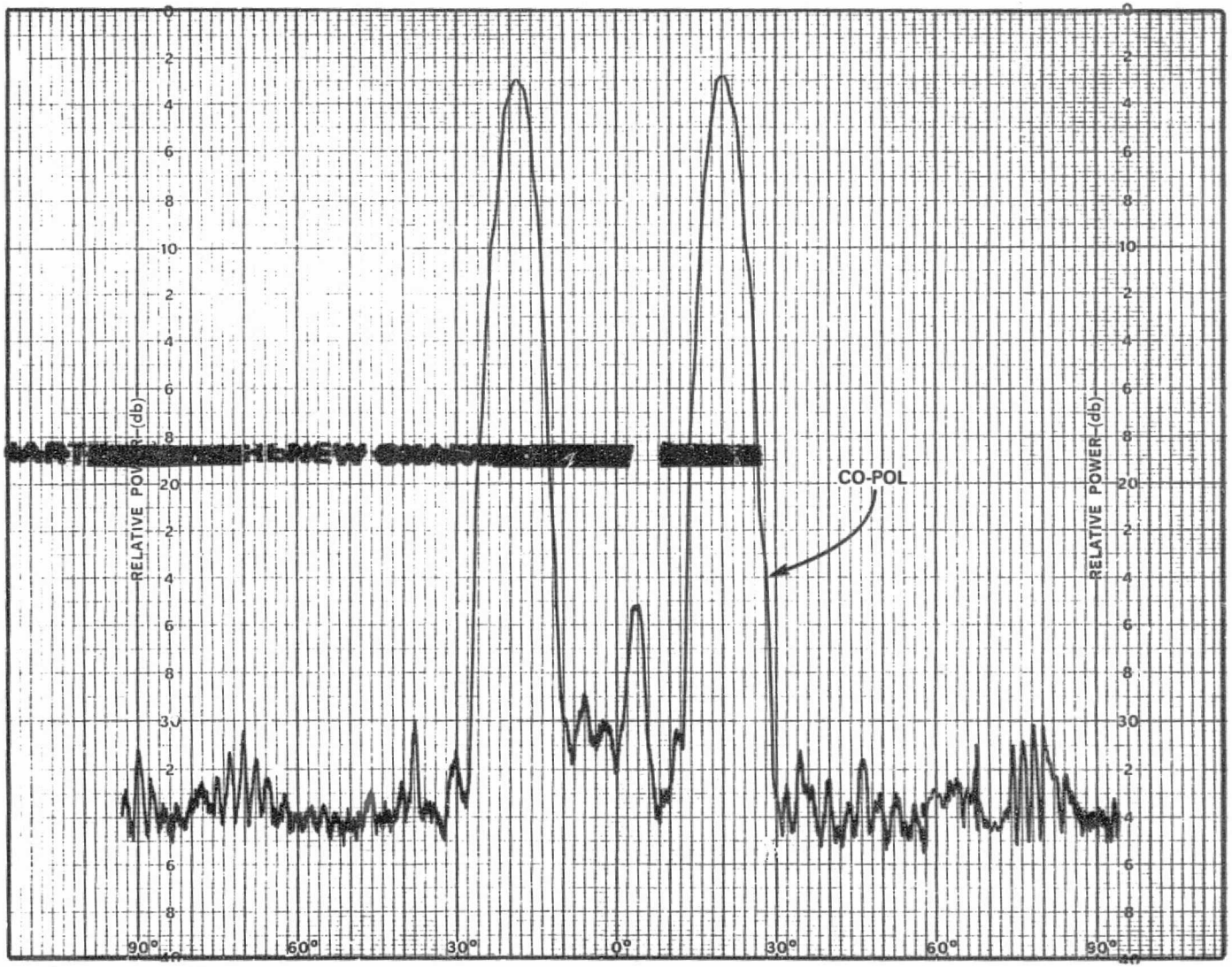

Figure B-42. H-Plane Pattern of Vertically Polarized 8-Element Array, 30-dB Taylor Amplitude Distribution, 180° Progressive Phase Difference, 12.2 GHz

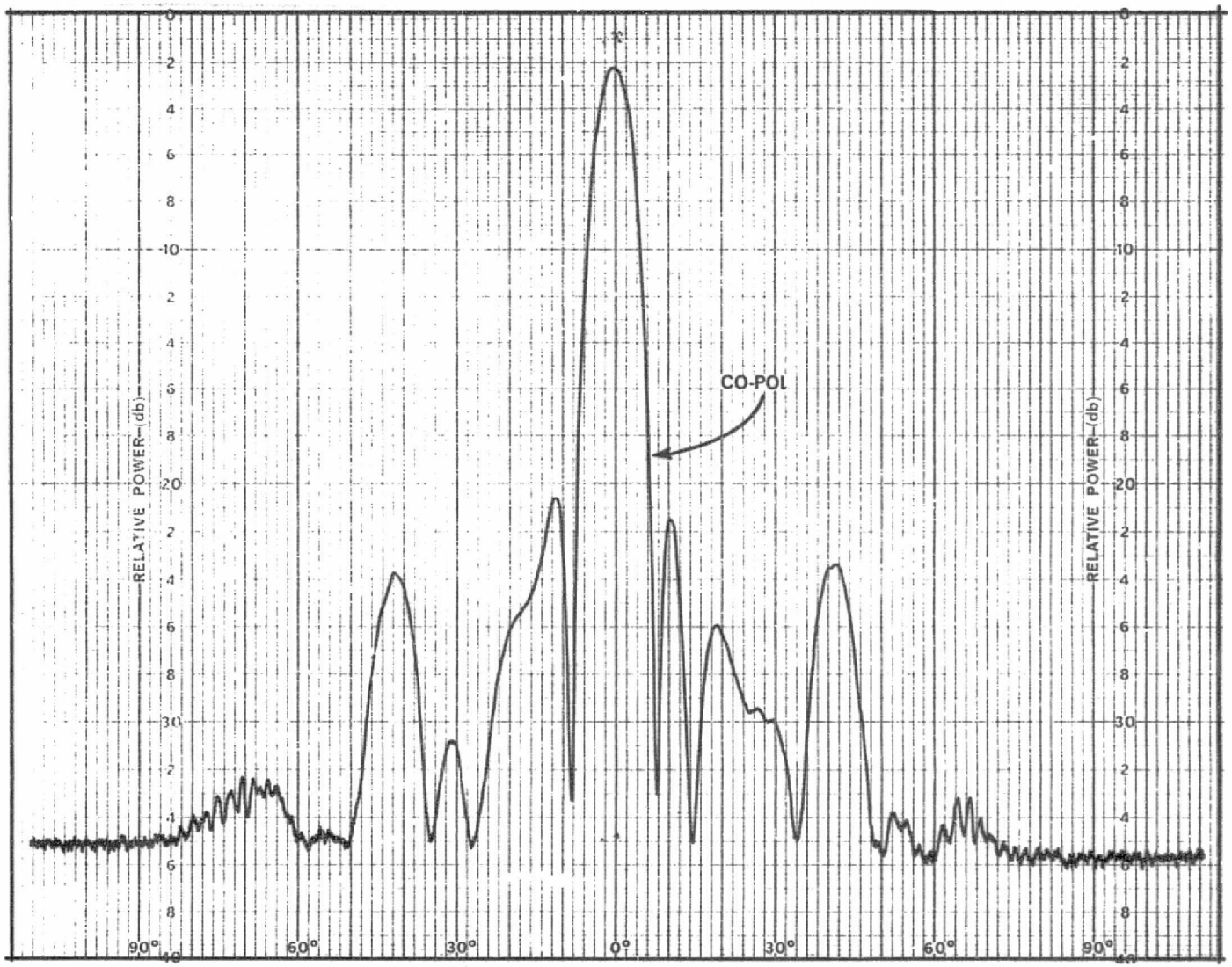

Figure B-43. E-Plane Pattern of Horizontally Polarized 8-Element Array, Quantized 30-dB Taylor Amplitude Distribution, Equal Phase, 11.7 GHz

Figure B-44. E-Plane Pattern of Horizontally Polarized 8-Element Array, Quantized 30-dB Taylor Amplitude Distribution, Equal Phase, 11.95 GHz

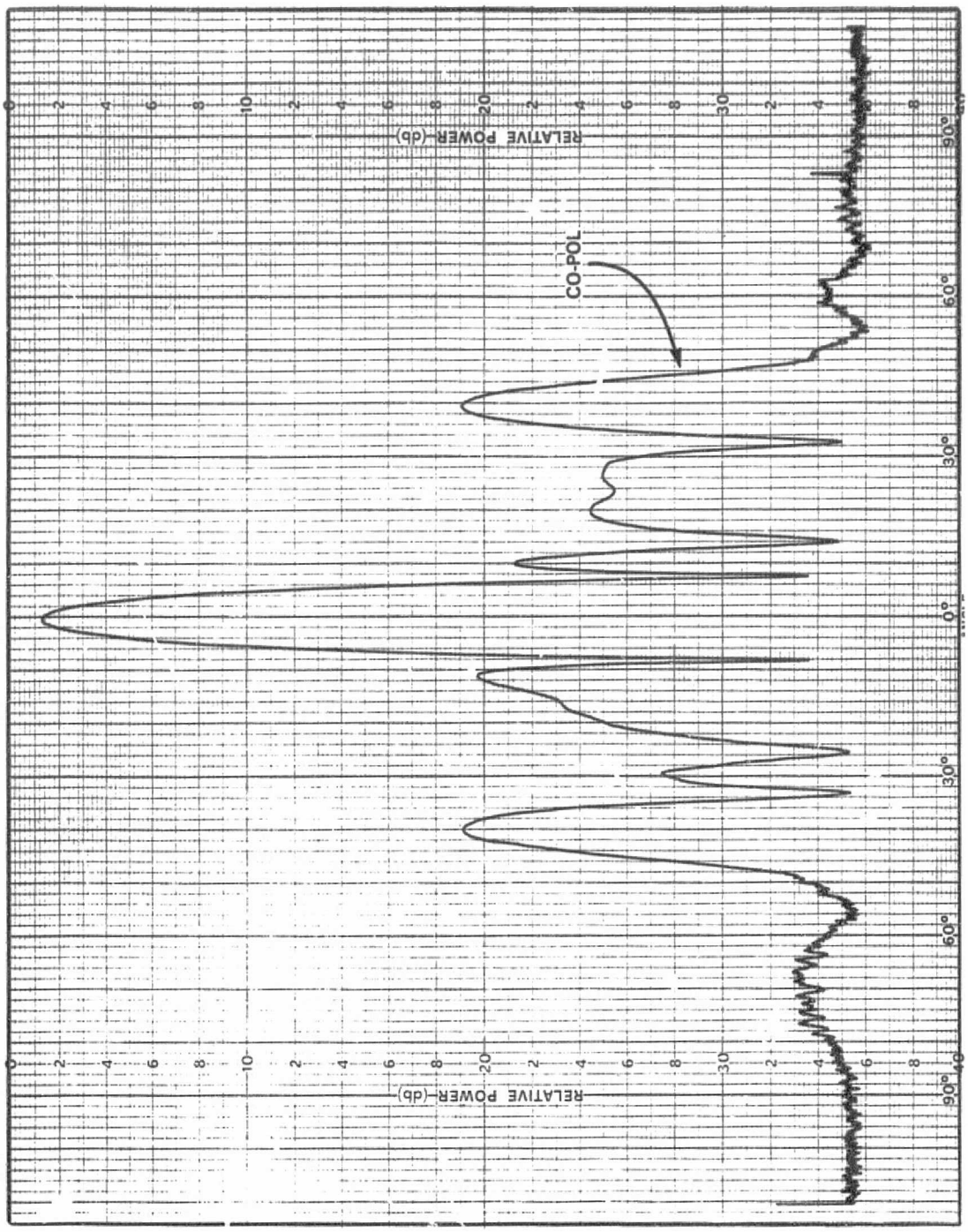

Figure B-45. E-Plane Pattern of Horizontally Polarized 8-Element Array, Quantized 30-dB Taylor Amplitude Distribution, Equal Phase, 12.2 GHz

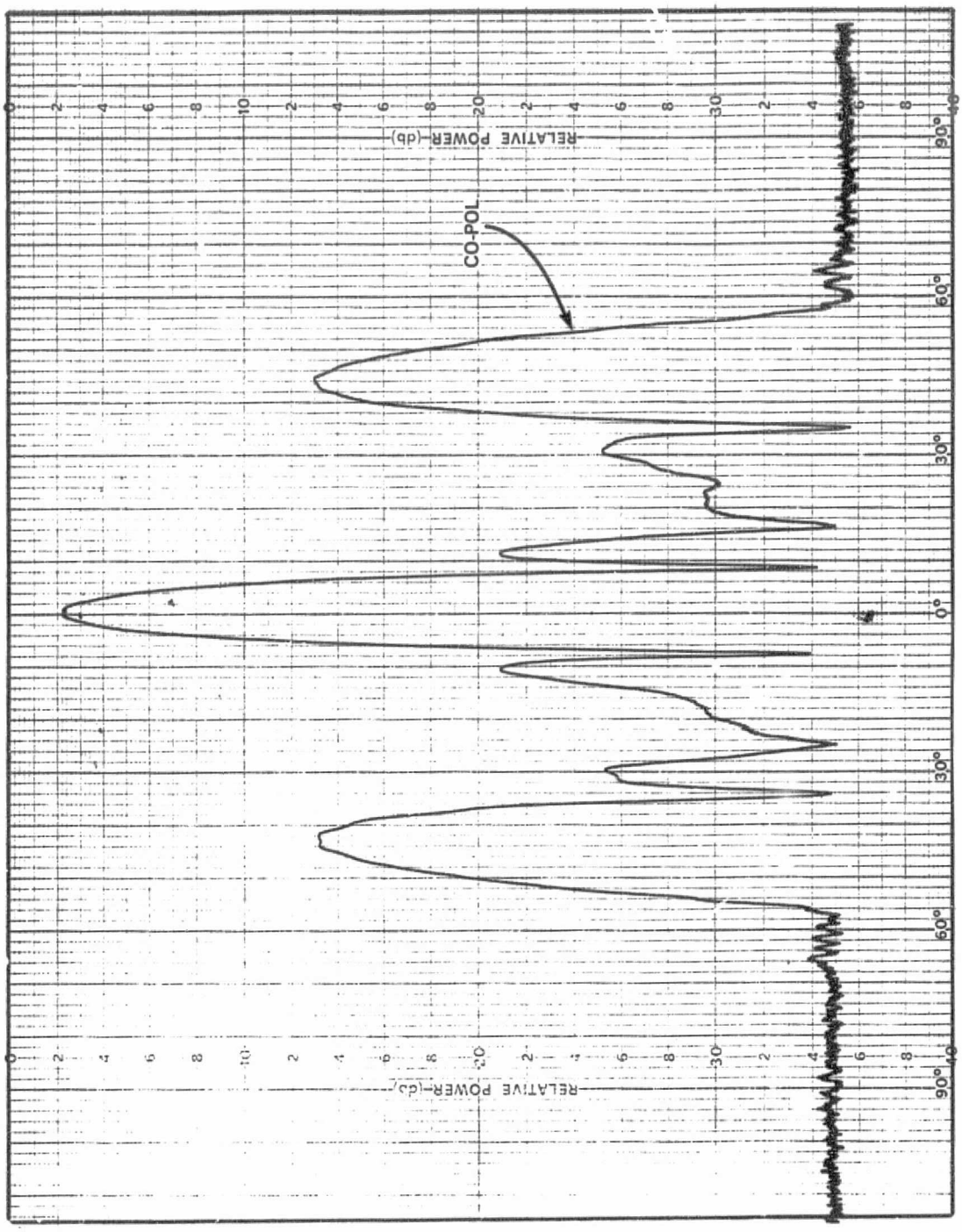

Figure B-46. H-Plane Pattern of Vertically Polarized 8-Element Array, Quantized 30-dB Taylor Amplitude Distribution, Equal Phase, 11.7 GHz

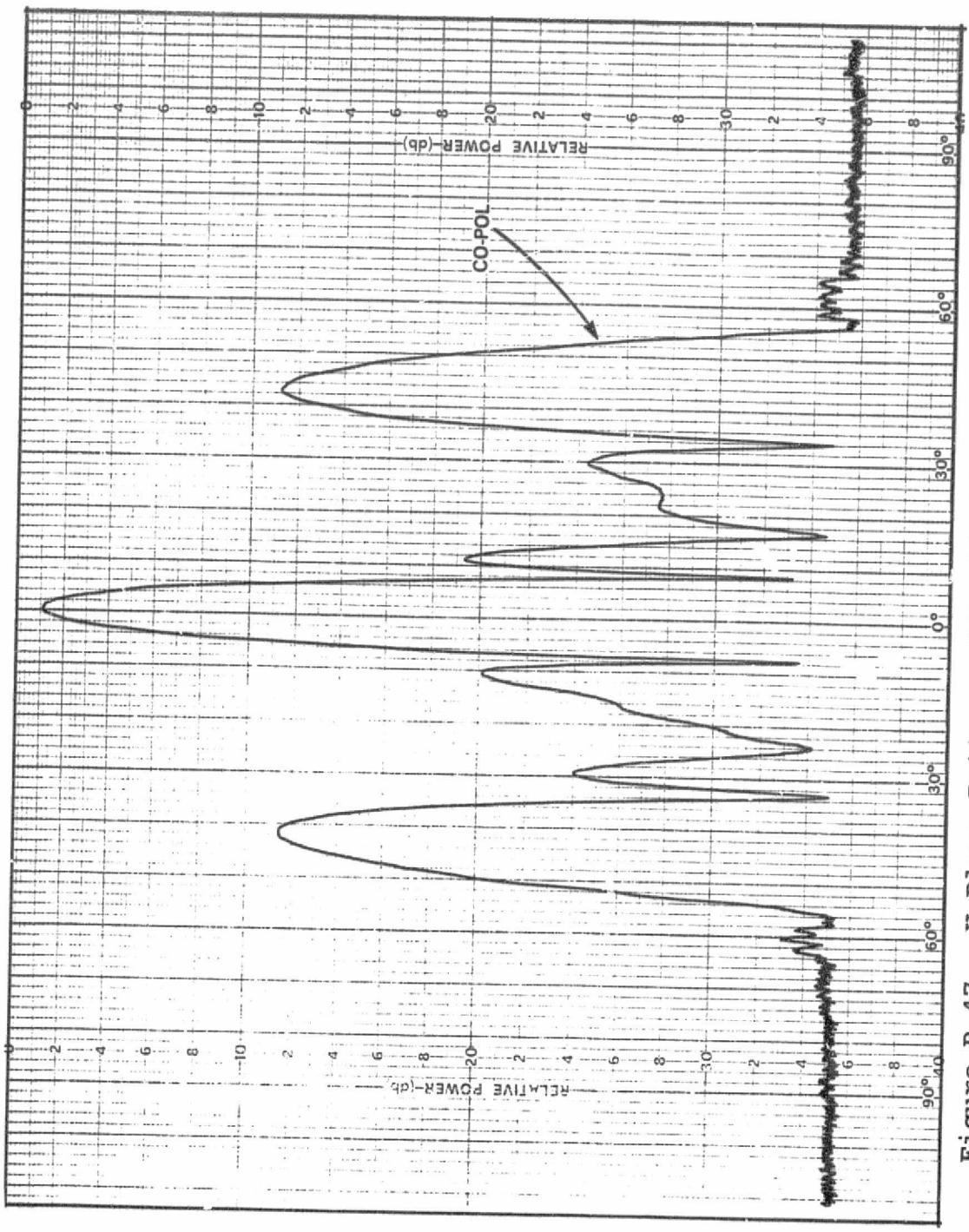

Figure B-47. H-Plane Pattern of Vertically Polarized 8-Element Array, Quantized 30-dB Taylor Amplitude Distribution, Equal Phase, 11.95 GHz

Figure B-48. H-Plane Pattern of Vertically Polarized 8-Element Array, Quantized 30-dB Taylor Amplitude Distribution, Equal Phase, 12.2 GHz

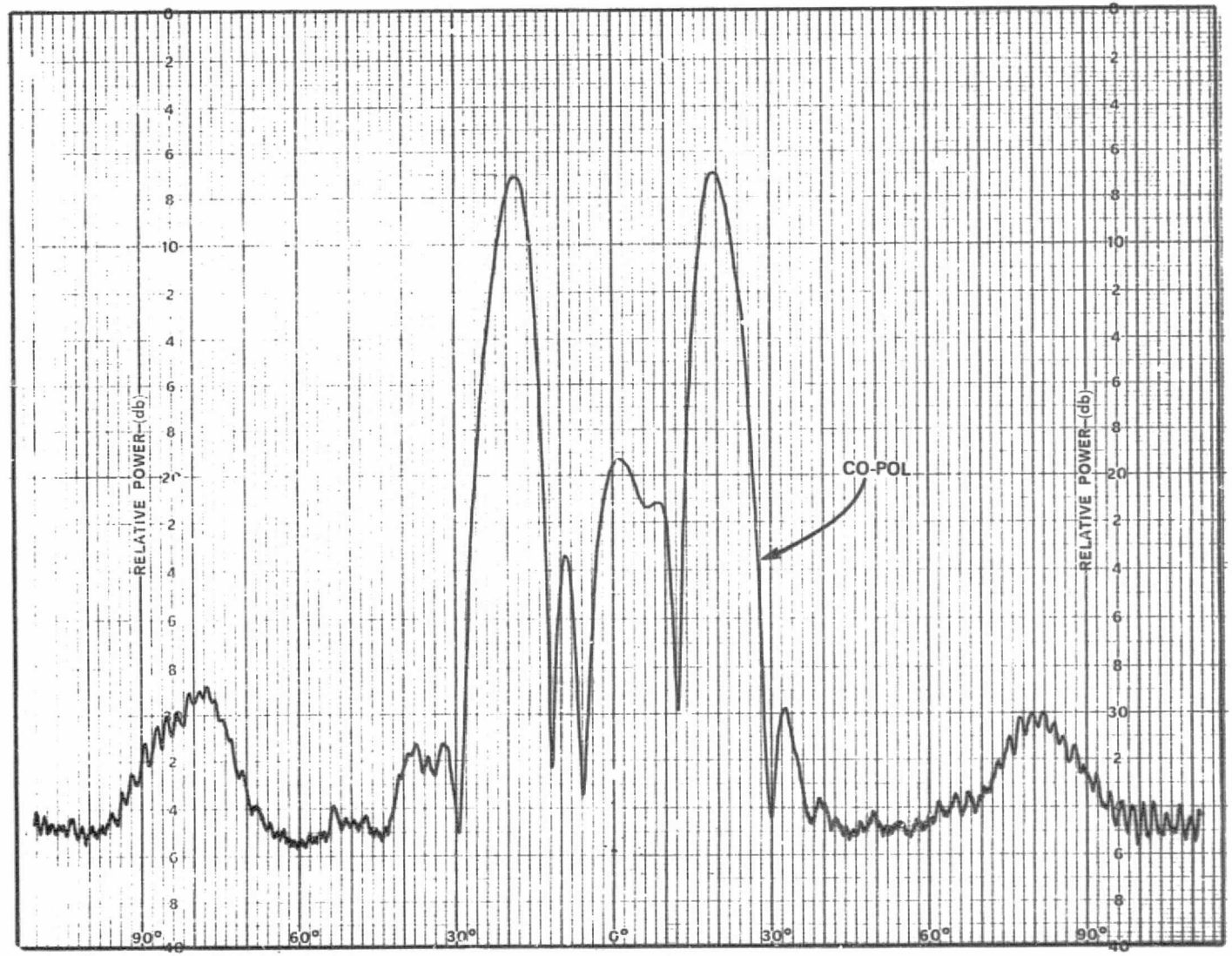

Figure B-49. E-Plane Pattern of Horizontally Polarized 8-Element Array, Quantized 30-dB Taylor Amplitude Distribution, 180° Progressive Phase Difference, 11.7 GHz

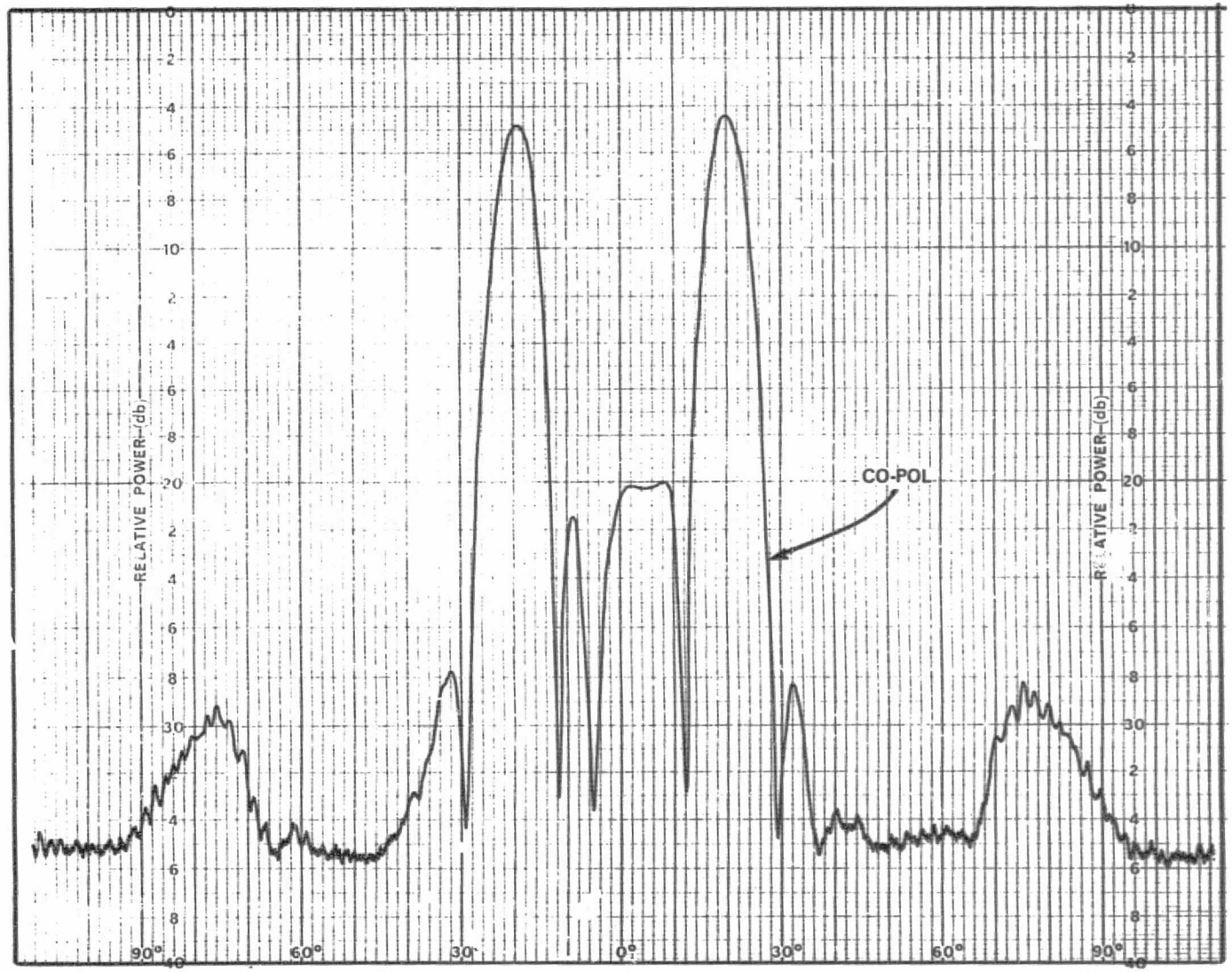

Figure B-50. E-Plane Pattern of Horizontally Polarized 8-Element Array, Quantized 30-dB Taylor Amplitude Distribution, 180° Progressive Phase Difference, 11.95 GHz

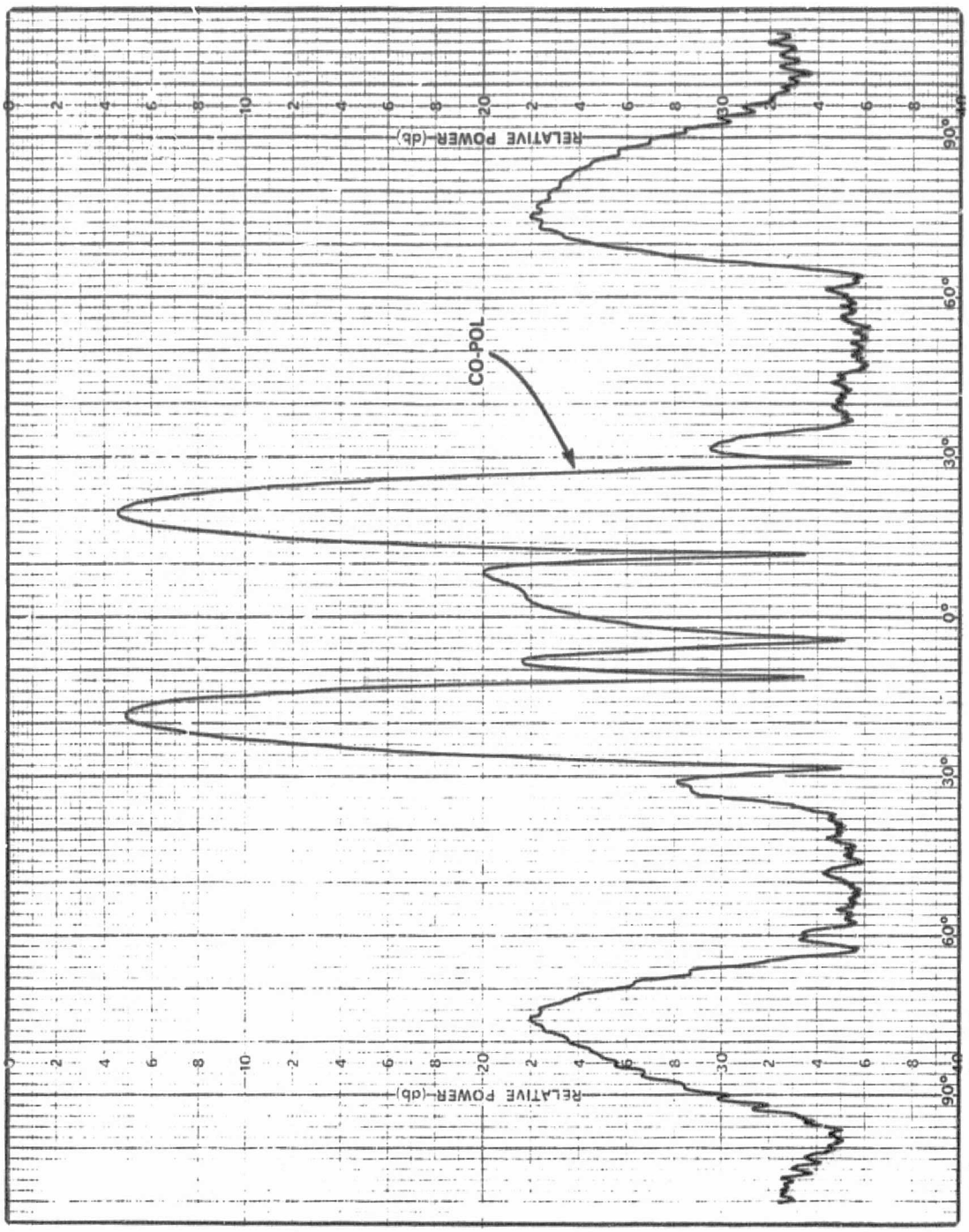

Figure B-51. E-Plane Pattern of Horizontally Polarized 8-Element Array, Quantized 30-dB Taylor Amplitude Distribution, 180° Progressive Phase Difference, 12.2 GHz

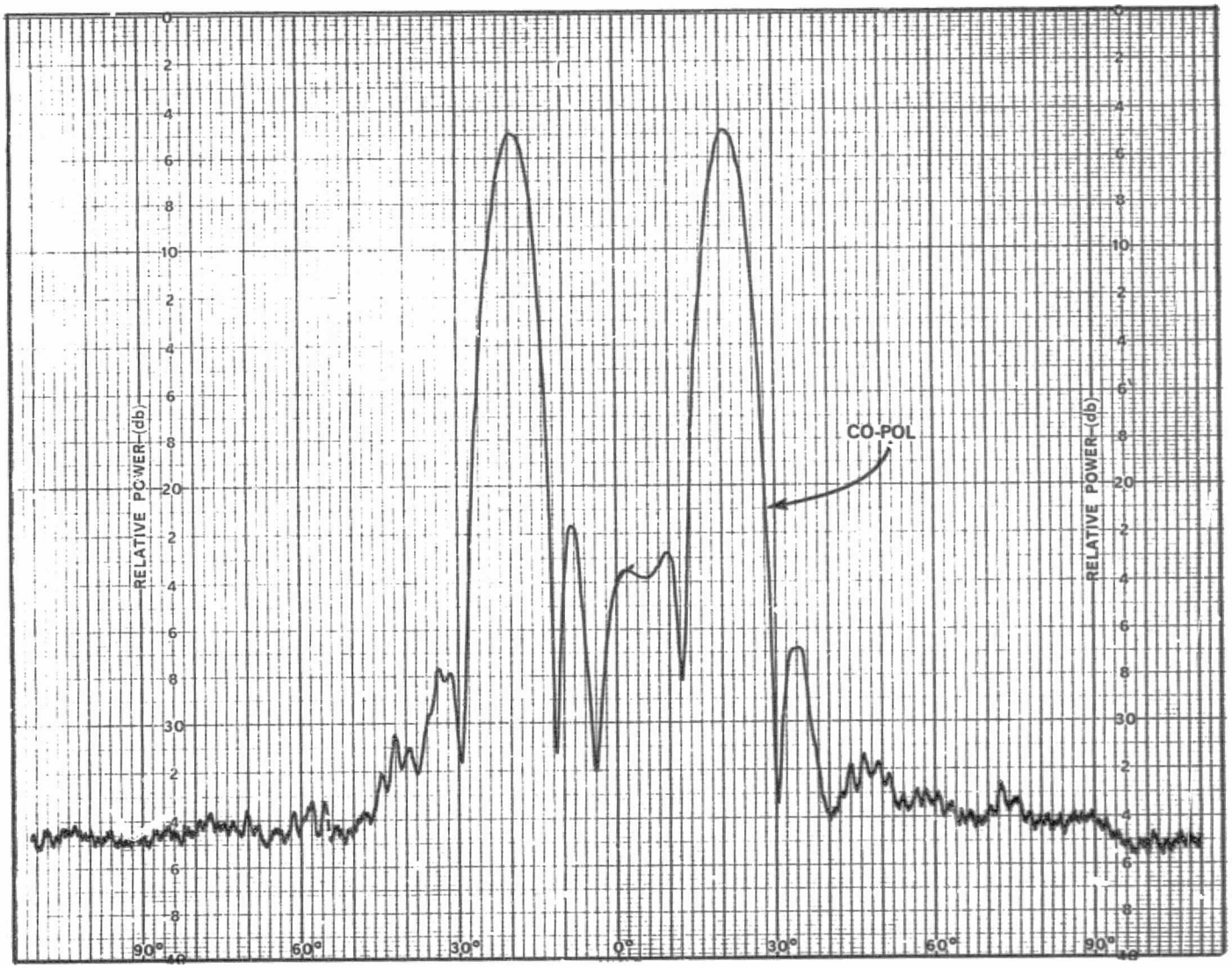

Figure B-52. H-Plane Pattern of Vertically Polarized 8-Element Array, Quantized 30-dB Taylor Amplitude Distribution, 180° Progressive Phase Difference, 11.7 GHz

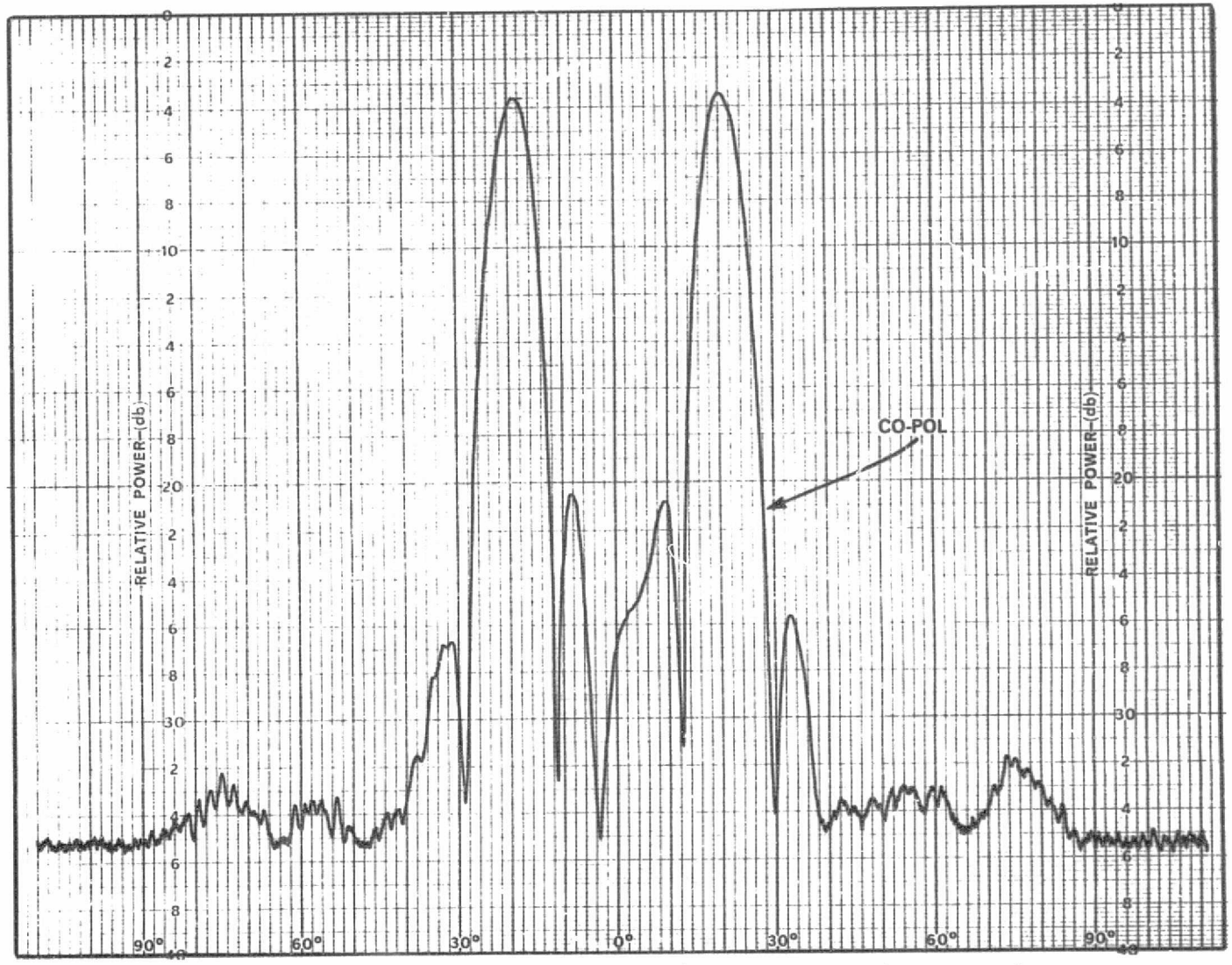

Figure B-53. H-Plane Pattern of Vertically Polarized 8-Element Array, Quantized 30-dB Taylor Amplitude Distribution, 180° Progressive Phase Difference, 11.95 GHz

C - 6

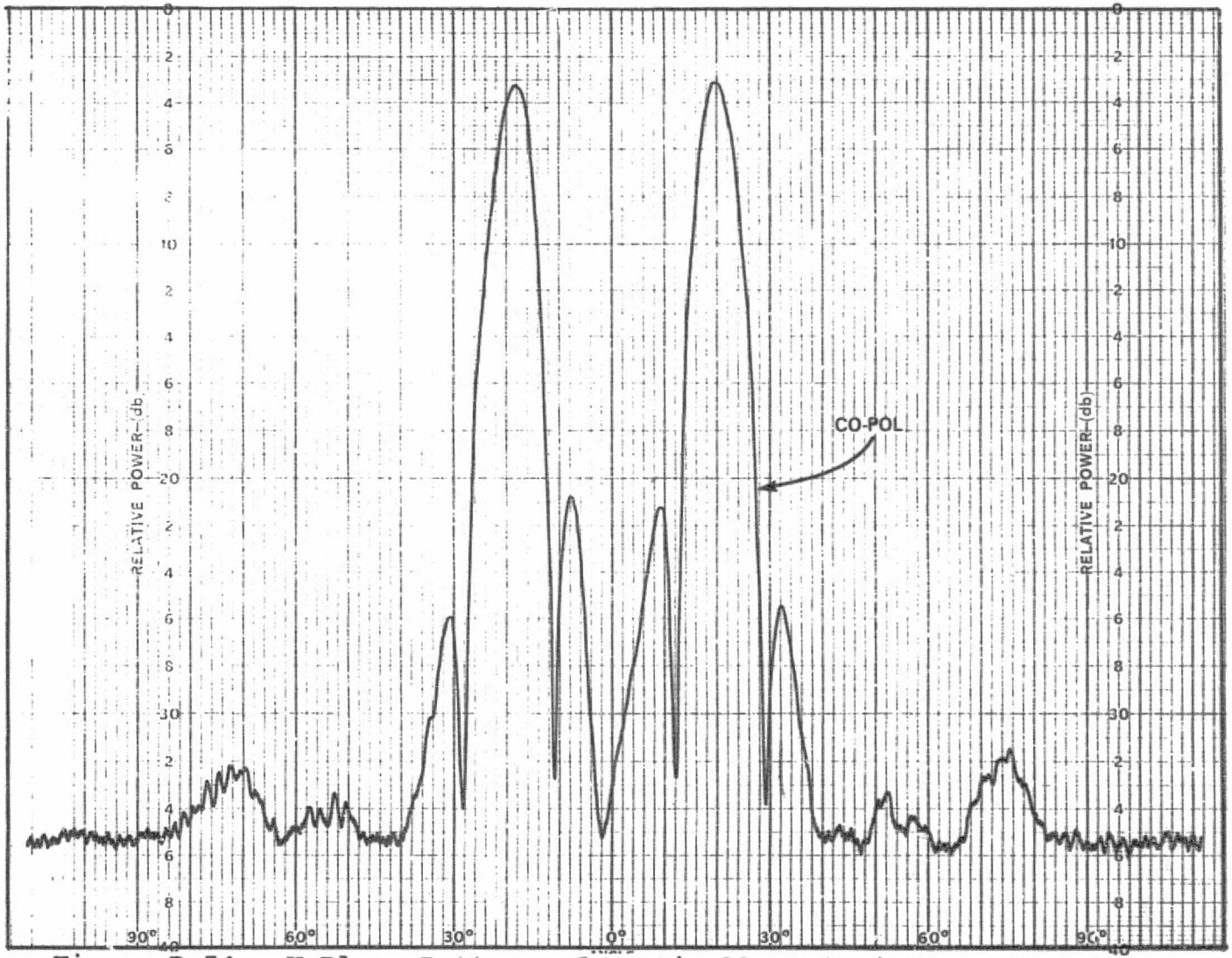

Figure B-54. H-Plane Pattern of Vertically Polarized 8-Element Array, Quantized 30-dB Taylor Amplitude Distribution, 180° Progressive Phase Difference, 12.2 GHz

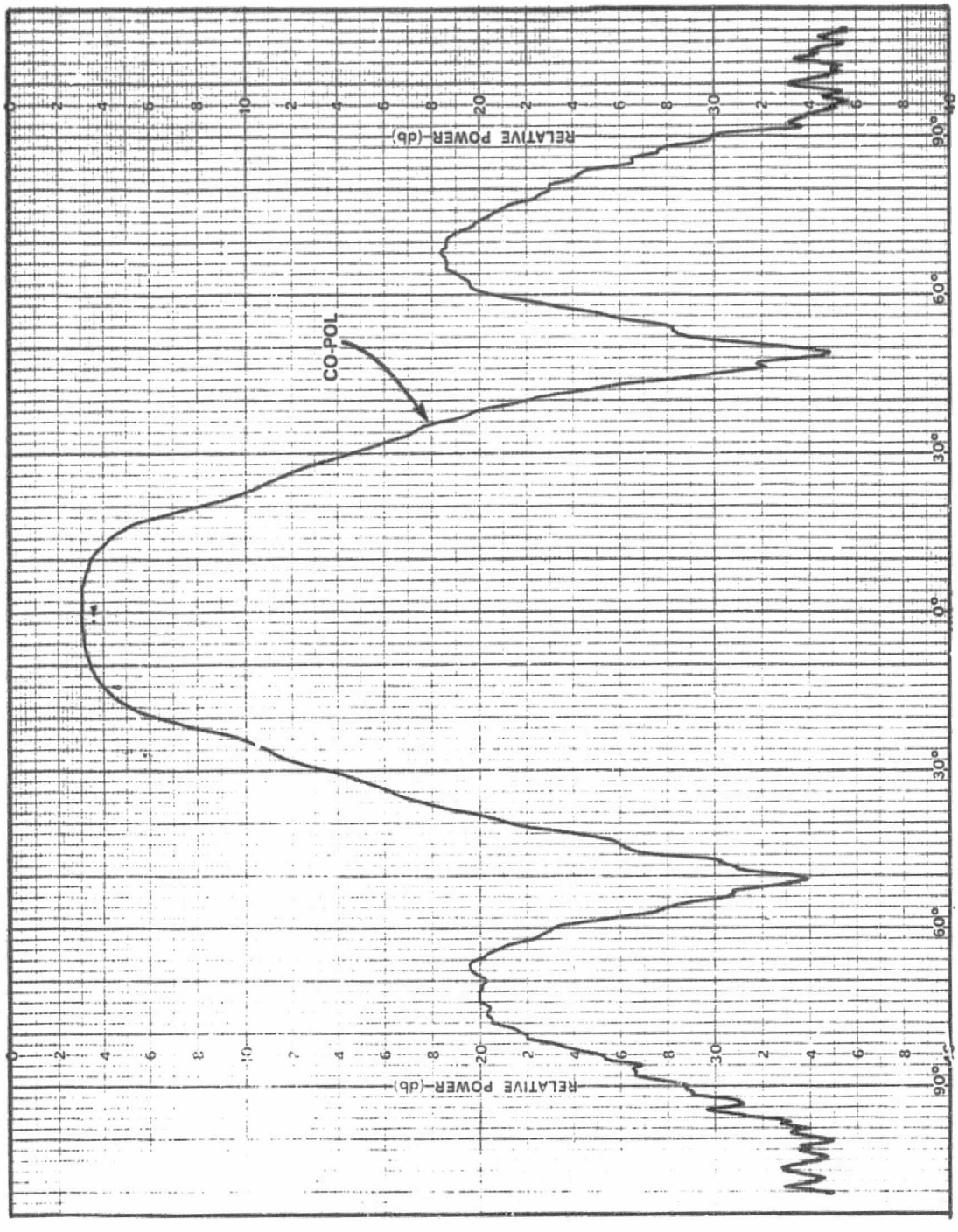

Figure B-55. E-Plane Pattern of Horizontally Polarized Central Element in the Array, 11.7 GHz

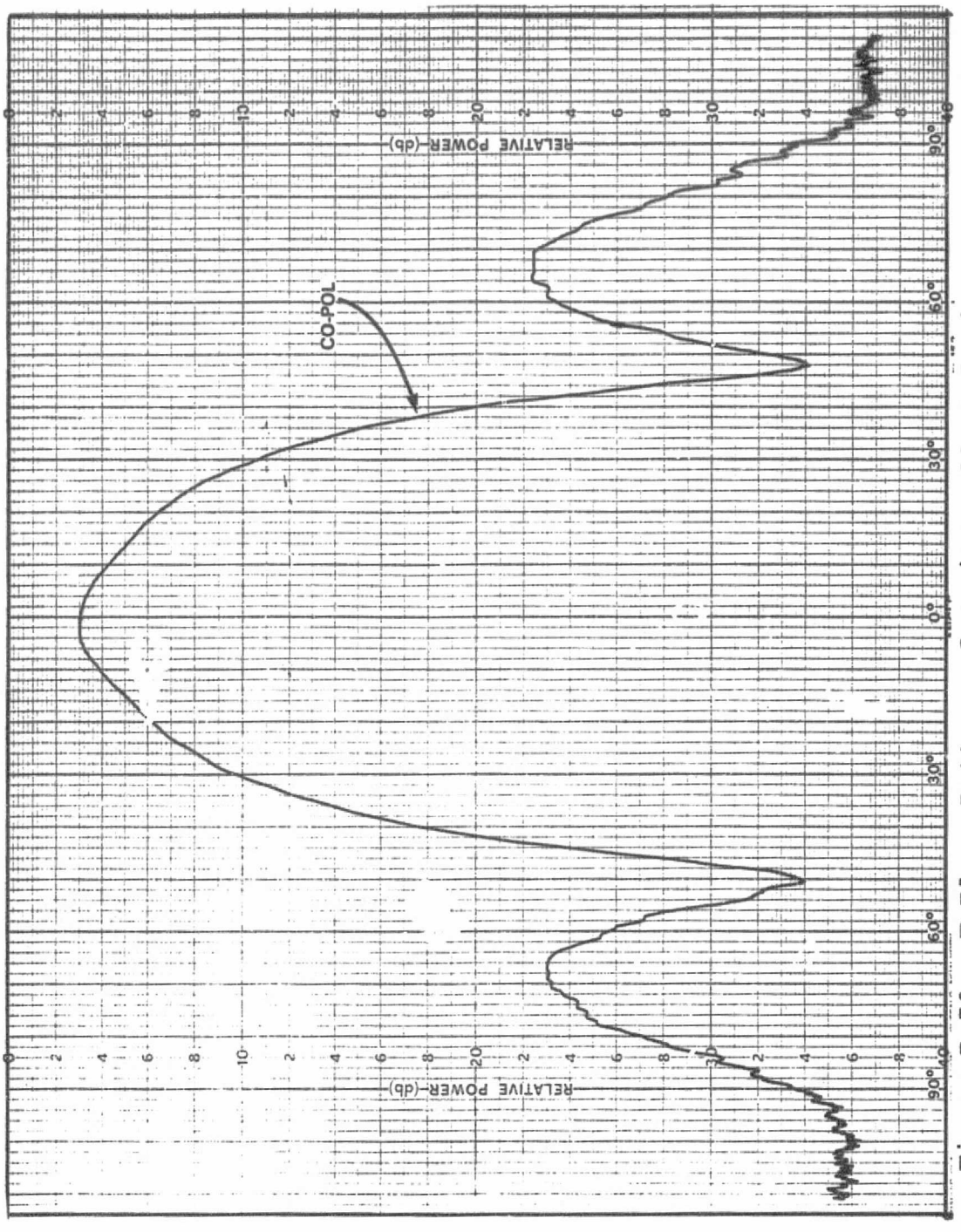

Figure B-56. E-Plane Pattern of Horizontally Polarized Central Element in the Array, 11.95 GHz

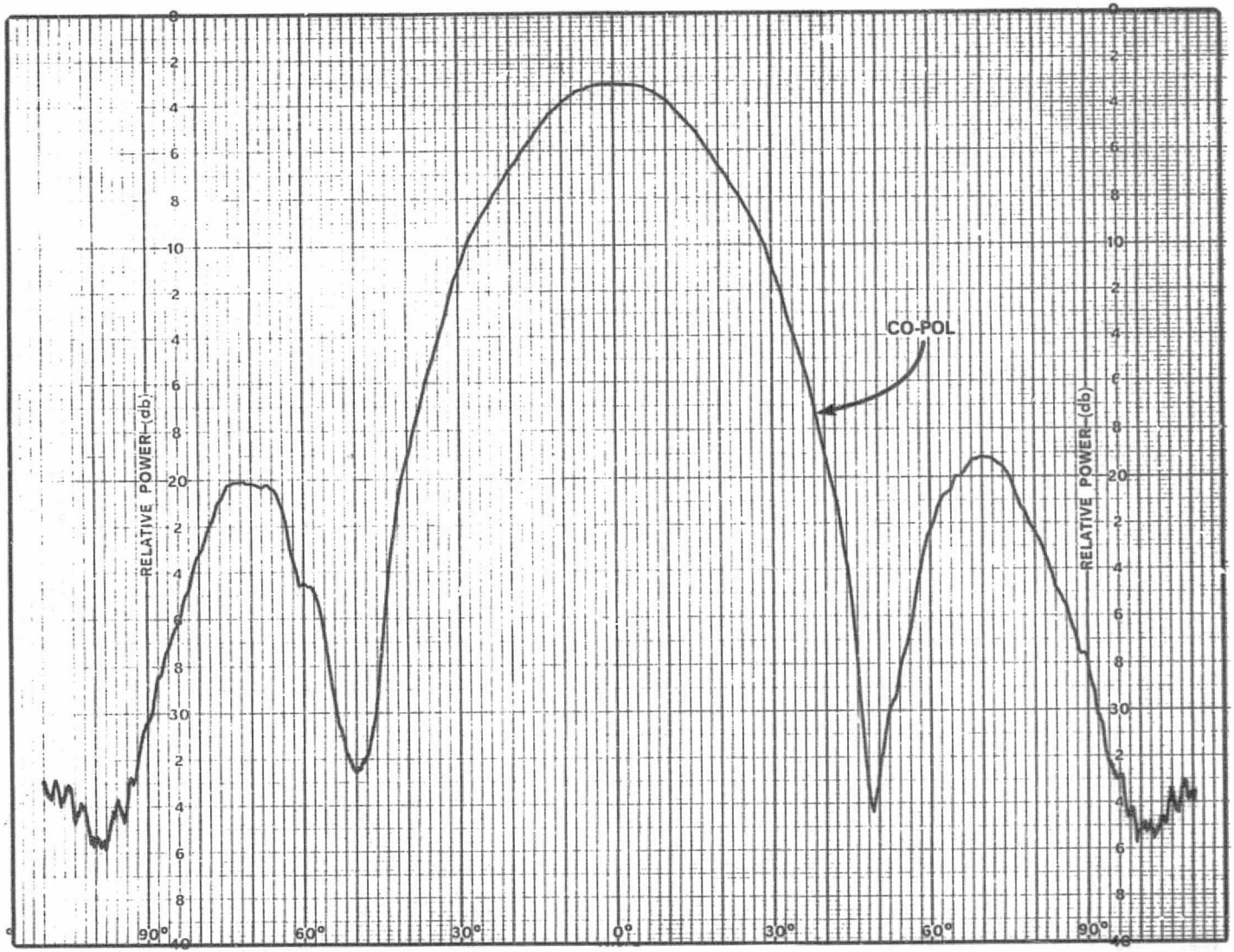

Figure B-57. E-Plane Pattern of Horizontally Polarized Central Element in the Array, 12.2 GHz

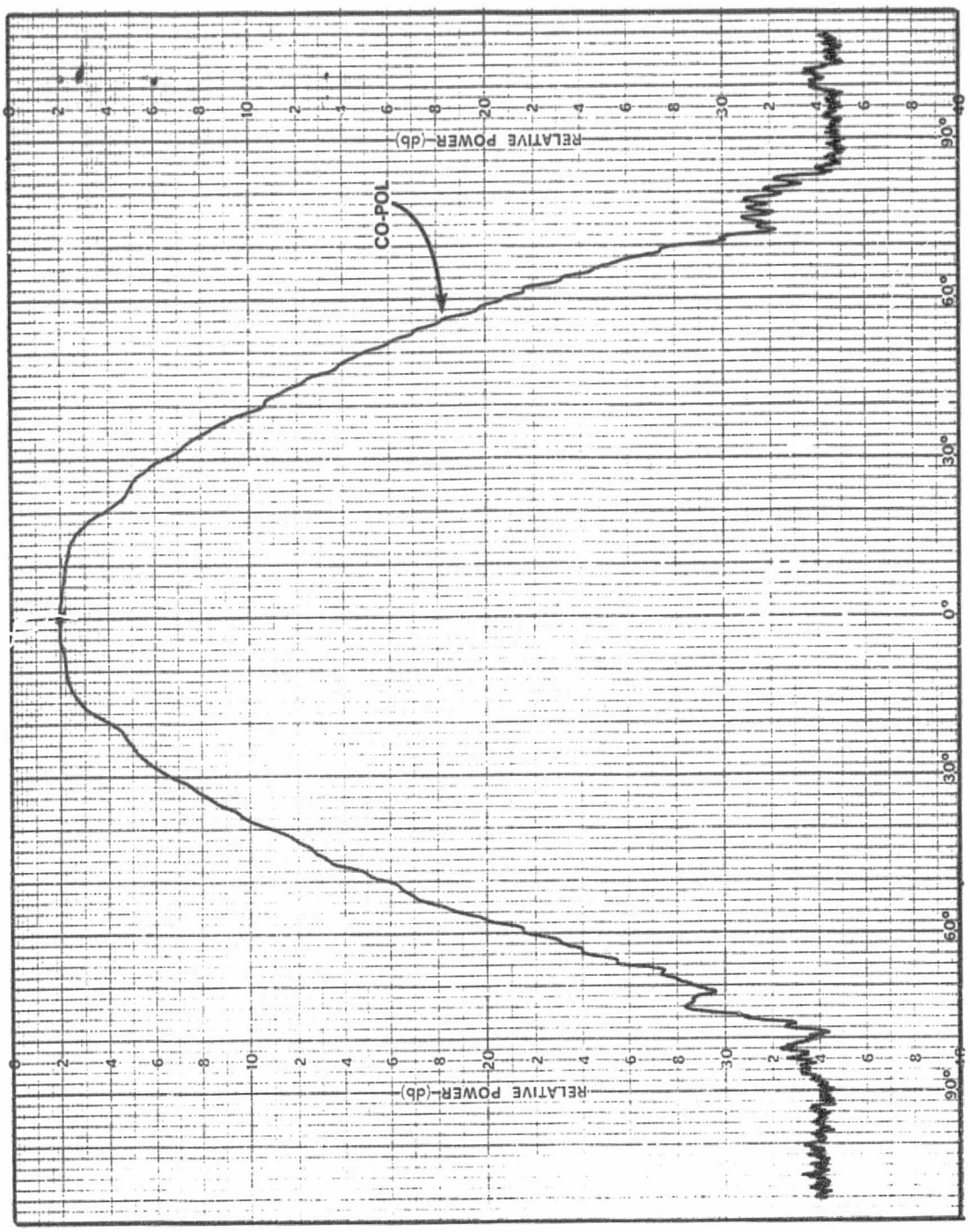

Figure B-58. H-Plane Pattern of Vertically Polarized Central Element in the Array, 11.7 GHz

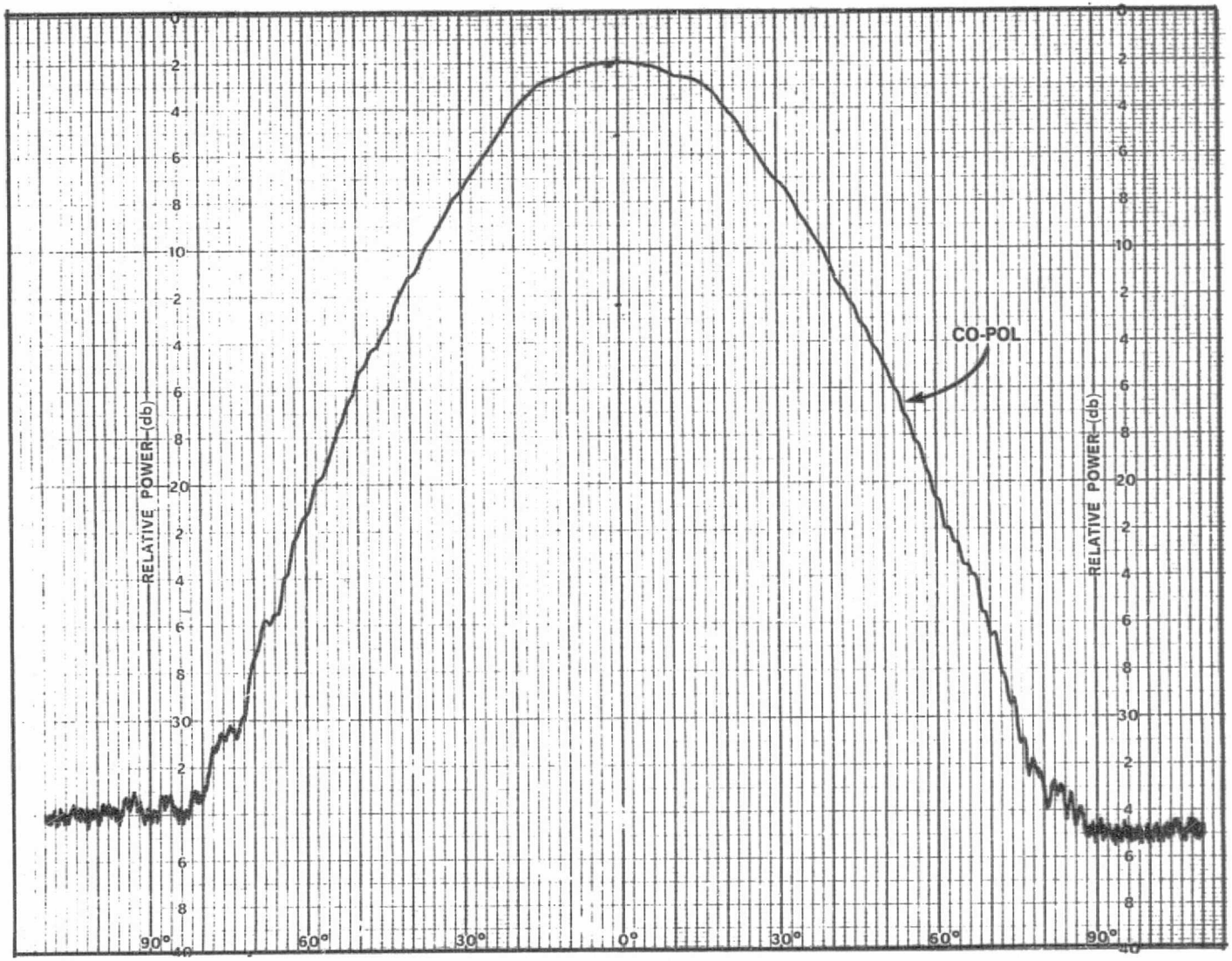

Figure B-59. H-Plane Pattern of Vertically Polarized Central Element in the Array, 11.95 GHz

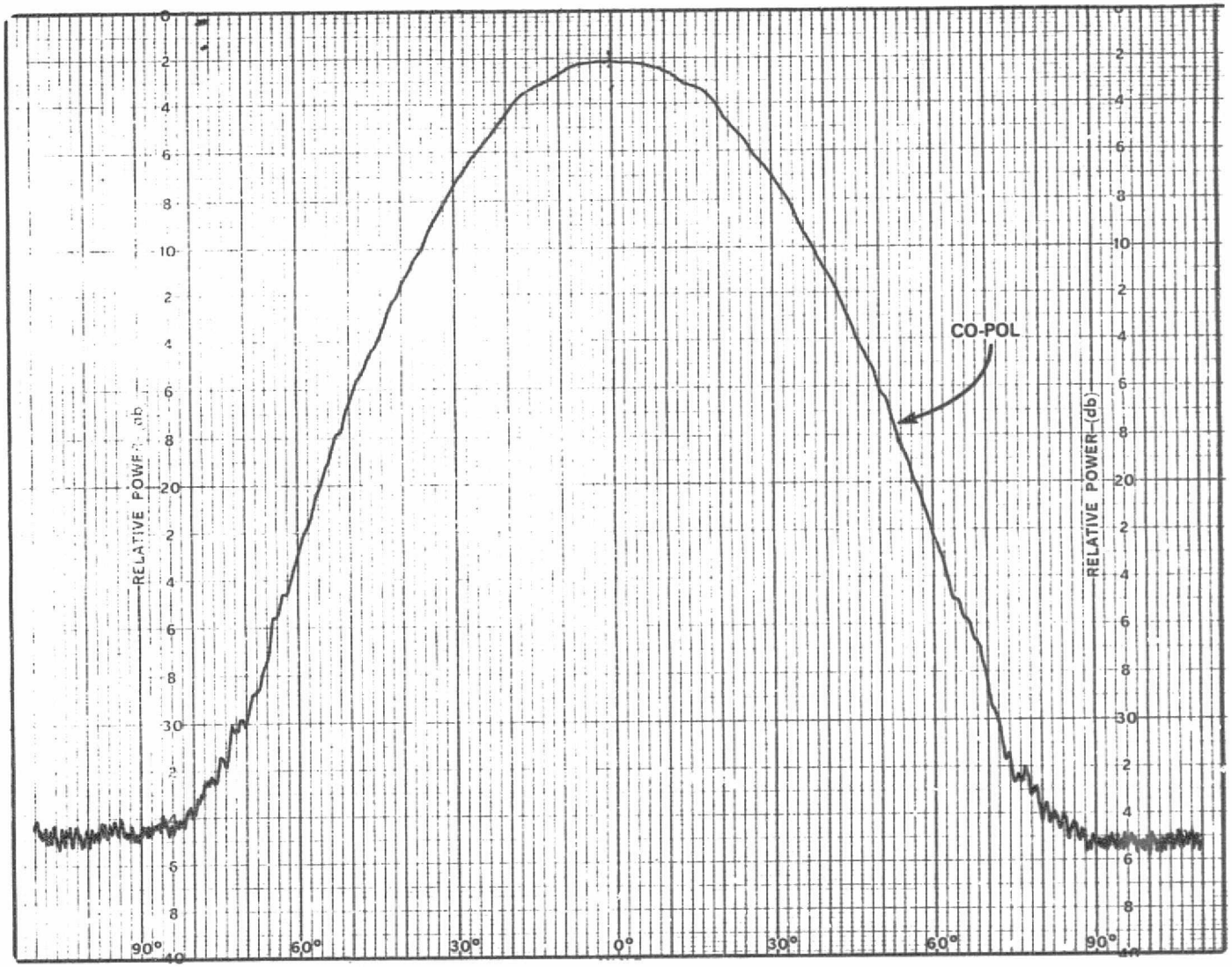

Figure B-60. H-Plane Pattern of Vertically Polarized Central Element in the Array, 12.2 GHz